Germanium and related elements in sulphide minerals: crystal chemistry, incorporation and isotope fractionation

Rémi Belissont

École doctorale RP2E — Ressources Procédés Produits Environnement
Université de Lorraine — LabEx Ressources21

Unités Mixtes de Recherche
GeoRessources
Centre de Recherches Pétrographiques et Géochimiques

Germanium and related elements in sulphide minerals: crystal chemistry, incorporation and isotope fractionation

Germanium et éléments associés dans les sulfures : cristallochimie, modes d'incorporation et fractionnement isotopique

par
Rémi Belissont

Thèse présentée pour l'obtention du titre de
Docteur de l'Université de Lorraine en Géosciences

Soutenance publique le 15 Mars 2016

Membres du Jury

Robert Moritz	Professeur, Université de Genève, Suisse	Rapporteur
Stefan Weyer	Professeur, Université Leibniz de Hanovre, Allemagne	Rapporteur
Nigel Cook	Professeur, Université d'Adélaïde, Australie	Examinateur
Etienne Deloule	Directeur de Recherche CNRS, CRPG, Nancy	Examinateur
Alain Manceau	Directeur de Recherche CNRS, ISTerre, Grenoble	Examinateur
Michel Cathelineau	Directeur de Recherche CNRS, GeoRessources, Nancy	Directeur de Thèse
Marie-Christine Boiron	Chargée de Recherche CNRS, GeoRessources, Nancy	Co-Directeur de Thèse
Béatrice Luais	Chargée de Recherche CNRS–HDR, CRPG, Nancy	Co-Directeur de Thèse

Abstract

Germanium and certain related elements (Ga, In) are critical in many high-tech industries (electronics, solar panels, fibre optics). Being distinctly siderophile, lithophile, chalcophile and organophile, Ge can be a useful geochemical tracer in a number of fields such as cosmochemistry, planetary differentiation, hydrothermal and tectonic activity. However, many studies witnessed the overall lack of data to clearly understand the Ge geochemistry and the factors controlling its concentration in Ge-bearing minerals and ore deposits. Germanium does not form specific deposits but rather occurs in trace to minor amounts in various types of ore deposits, and the most significant Ge enrichments occuring in low-T carbonate- or sediment-hosted Zn–Pb deposits (e.g., MVT, SedEx). Advances in LA-ICP-MS and MC-ICP-MS analytical developments now allow for acquiring large dataset of *in situ* minor/trace element contents and detecting small stable isotope variations, respectively.

Analyses of Ge by LA-ICP-MS has been refined in order to provide precise and reproducible data for Ge and related trace elements. Multivariate statistics, especially principal component analysis, was applied to the LA-ICP-MS dataset in order to gain statistical power in the identification of element correlations and their interpretation. These techniques were applied to the Saint-Salvy Zn vein-type, MVT-related deposit (French Massif Central), the Barrigão Cu vein-type, VMS-remobilsed deposit (Iberian pyrite belt, Portugal) and the Kipushi Zn–Cu carbonate-hosted deposit. Their most important Ge-bearing minerals are sphalerite (up to 2580 ppm Ge), chalcopyrite (up to 5750 ppm Ge), and renierite (5.0–9.1 wt.% Ge), respectively. Trace element signatures in sphalerite from various deposit types were compared in a common, statistically powerful perspective by principal component analysis, which clearly indicated a first order relation of Ge contents with temperature. Germanium, along with Ga and Sb, is associated with low-T, sediment- and carbonate-hosted deposits, while In is markedly incorporated in high-T, magmatic-related deposits.

Synchrotron-based XAFS spectroscopy was used to probe Ge crystal chemistry and Ge-doped sphalerites that were precipitated experimentally to study the temperature effect on Ge incorporation and to quantify the isotopic fractionation, $\Delta^{74}Ge_{ZnS-fluid}$. The results showed that Ge^{4+} occur in tetrahedral coordination in all investigated sulphides. Therefore, given the observed element correlations, Ge is chiefly incorporated through coupled substitutions like $3Zn^{2+} \leftrightarrow Ge^{4+} + 2(Cu,Ag)^{+}$ and $3Fe^{3+} \leftrightarrow 2Ge^{4+} + Cu^{+}$ in sphalerite and chalcopyrite, respectively. In particular, Ge^{4+} incorporation in sphalerite may be enhanced at high monovalent element activity (Cu or Ag) that are required for charge balancing. Nevertheless, significant Ge amounts were readily introduced into experimental sphalerite without the presence of monovalent elements, which indicate that Ge can be accommodated through the creation of vacancies like $2Zn^{2+} \leftrightarrow Ge^{4+} + \square$, especially at high S activity, when sphalerite is Zn deficient.

The positive $\delta^{74}Ge-Ge$ content correlation observed in sphalerite from Saint-Salvy could indicate that Ge partition coefficient, $K_d^{Ge} = [Ge]_{ZnS}/[Ge]_{sol}$, increases with temperature, implying an exothermic reaction. Ge isotopes in sulphides yield a large range of $\delta^{74}Ge$ values, spanning from –5.72‰ to +3.67‰. The light $\delta^{74}Ge$ compositions of Saint-Salvy and Barrigão ores appear to be related to variations in low to moderate fluid temperatures during Ge uptake in open system (e.g., fluid cooling), while the trend towards heavy $\delta^{74}Ge$ compositions observed at Kipushi likely translates a Rayleigh fractionation effect during ore formation in closed system, associated with significant fluid modification.

Résumé

Le germanium et certains éléments associés (Ga, In) sont considérés comme critiques dans nombre d'industries des hautes technologies (électronique, panneaux solaires, fibre optiques). Le Ge étant distinctement sidérophile, lithophile, chalcophile et organophile, il est par exemple un traceur géochimique important en cosmochimie et pour l'étude des systèmes hydrothermaux. Cependant, de nombreuses études relèvent un manque de données nécessaires à la compréhension de la géochimie du cycle du Ge et des facteurs qui contrôlent son incorporation dans les minéraux et les gisements métalliques. Il n'existe pas de gisement spécifique de Ge mais il est présent à l'état de traces dans de nombreux types de dépôts minéralisés, notamment les gisements à Pb–Zn de bassins (MVT, SedEx) associés à des fluides de basse température. Les développements analytiques en LA-ICP-MS et MC-ICP-MS permettent respectivement d'acquérir un grand nombre de données *in situ* de concentrations en éléments traces et de détecter de faibles variations isotopiques.

L'analyse du Ge par LA-ICP-MS a été affinée afin de pouvoir acquérir des mesures précises et reproductibles de la concentration en Ge et éléments associés dans les sulfures. L'utilisation de statistiques multivariées, notamment l'analyse en composantes principales (ACP), a été appliqué à ces données afin d'identifier les corrélations élémentaires et de préciser leur interprétation. Les cibles de cette étude concernent le gisement filonien à Zn de Saint-Salvy associé à des circulations de type MVT (Massif Central, France), le gisement filonien à Cu de Barrigão (Ceinture pyriteuse ibérique, Portugal) associé à une re-mobilisation de VMS, et le gisement à Zn–Cu de Kipushi (R.D. Congo). Dans ces gisements, les porteurs de Ge les plus importants sont respectivement la sphalérite (jusqu'à 2580 ppm), la chalcopyrite (jusqu'à 5750 ppm) et la réniérite (5,0–9,1 %). Une ACP appliquée aux signatures en éléments traces des sphalérites de nombreux gisements met en en évidence une relation de premier ordre entre la concentration en Ge et le type de gisement : Ge, Ga et Sb sont associés aux gisements de basse température (MVT, SedEx), alors que In est associé aux gisements de plus haute température lié à des processus magmatiques.

La spectroscopie d'absorption des rayons X par rayonnement synchrotron (XAFS) a permis d'étudier la cristallochimie du Ge. Des synthèses expérimentales de sphalérites dopées en Ge ont été conduites pour mesurer l'effet de la température sur le partage élémentaire et le fractionnement isotopique du Ge, $\Delta^{74}\mathrm{Ge}_{\mathrm{ZnS-sol}}$. Les résultats mettent en évidence la présence de Ge^{4+} en coordination tétraédrique dans tous les sulfures analysés. En tenant compte des corrélations élémentaires observées dans la sphalérite et la chalcopyrite, ceci suggère que le Ge est respectivement incorporé par substitutions couplées comme $3\mathrm{Zn}^{2+} \leftrightarrow \mathrm{Ge}^{4+} + 2(\mathrm{Cu,Ag})^{+}$ et $3\mathrm{Fe}^{3+} \leftrightarrow 2\mathrm{Ge}^{4+} + \mathrm{Cu}^{+}$. Une forte activité en éléments monovalents (Cu, Ag) pourrait alors favoriser l'enrichissement en Ge dans les sulfures. Les teneurs élevées en Ge des sphalérites expérimentales, sans l'intervention d'éléments monovalents, montrent que Ge peut être intégré grâce à la création de lacunes comme $2\mathrm{Zn}^{2+} \leftrightarrow \mathrm{Ge}^{4+} + \square$, spécialement à haute activité en S, lorsque la sphalérite est déficitaire en Zn.

La corrélation positive $\delta^{74}\mathrm{Ge} - [\mathrm{Ge}]_{\mathrm{ZnS}}$ des sphalérites de Saint-Salvy indiquerait alors que le coefficient de partage, $K_{\mathrm{d}}^{\mathrm{Ge}} = [\mathrm{Ge}]_{\mathrm{ZnS}}/[\mathrm{Ge}]_{\mathrm{sol}}$, augmenterait avec T, impliquant une réaction exothermique. Les compositions isotopiques en δ^{74}Ge des sulfures étudiés varient de –5,72‰ à +3,67‰. Les compositions légères mesurées dans les gisements de Saint-Salvy et Barrigão semblent liées à des variations de température des fluides (basse à moyennes T) lors de l'incorporation de Ge en système ouvert, alors que la tendance marquée vers les compositions isotopiques lourdes à Kipushi indiquerait un fractionnement de Rayleigh.

Avant-propos

Le présent manuscrit de thèse est intégralement rédigé en anglais pour plusieurs raisons. D'une part, les objets à l'étude sont en partie issus de collaborations internationales, notamment le 'Laboratório Nacional de Energia e Geologia' (LNEG, Alfragide, Portugal), par l'intermédiaire du Dr. Daniel D. Oliveira, et la 'Katholieke Universiteit Leuven' (K.U. Leuven, Belgium), par l'intermédiaire du Prof. Philippe Muchez. D'autre part, le jury est composé de membres internationaux, notamment les deux rapporteurs de la thèse, Prof. Robert Moritz (Université de Genève, Suisse) et Prof. Stefan Weyer (Université Leibniz de Hanovre, Allemagne), ainsi que l'examinateur, Prof. Nigel Cook (Université de Adelaide). Un résumé étendu en français est inclus au manuscrit.

Remerciements

Ce travail a été co-financé par le laboratoire d'excellence LabEx Ressources 21 et la Région Lorraine. Le programme Observatoire Terre Environnement Lorraine (OTELo), et le projet INSU–CESSUR (CNRS) ont également participé au financement de ce travail. Les recherches ont été menées au sein des laboratoires GeoRessources et du Centre de Recherches Pétrographiques et Géochimiques (CRPG). Je remercie mes deux laboratoires d'accueil pour avoir mis à disposition les moyens analytiques et humains pour mener à bien ce travail.

Pour commencer, je tiens bien sûr à remercier Marie-Christine Boiron et Béatrice Luais, mes co-directrices de thèse, pour leur confiance, leur disponibilité et la bienveillance dont elle ont fait preuve pendant ces années de thèse. Je les remercie également pour toute la science qu'elles ont chercher à me transmettre. Merci à Michel Cathelineau, mon directeur de thèse, pour les discussions en métallogénie. Je suis reconnaissant envers les membres du jury qui ont accepté d'examiner ce travail : Robert Moritz, pour son expertise en métallogénie, Stefan Weyer, pour son expérience en géochimie isotopique, Nigel J Cook, un acteur incontournable dans le domaine des éléments stratégiques en métallogénie, Alain Manceau, pour sa grande expertise en cristallochimie et spectroscopie d'absorption des rayons X, et enfin, Etienne Deloule, pour sa grande connaissance en géochimie isotopique appliquée à la métallogénie.

Je remercie chaleureusement toutes les personnes nous ayant fourni les échantillons indispensables pour mener ma mission à terme, ou celles avec qui j'ai pu collaborer ; Catherine Lerouge et Daniel Cassard du BRGM, pour les échantillons de la mine de Saint-Salvy ; Philippe Muchez (K.U. Leuven, Belgium), pour nous avoir permis d'accéder à l'ensemble des collections d'échantillons de la mine de Kipushi ; et enfin Daniel PS de Oliveira (LNEG, Portugal), pour les échantillons de la mine de Barrigão. Merci également à Philippe Marion (ENSG, Nancy) et Christian Marignac (Mines Nancy) pour la transmission de plusieurs échantillons de leur collection.

Merci à l'ESRF (Grenoble) pour les facilités lors des deux sessions d'analyses par rayonnement synchrotron (Octobre 2013 et Septembre 2015). Un très grand merci à Manuel Muñoz (ISTerre, Grenoble) et Olivier Mathon (ESRF, Grenoble) pour leur investissement considérable dans nos deux sessions au synchrotron, pour leur savoir-faire, et pour tout ce qu'ils m'ont appris. Encore merci à Manuel pour m'avoir accueilli à l'ISTerre pendant une semaine et pour m'avoir enseigné quelques uns des rouages d'Athena et des calculs FEFF. Merci à Laurent Truche (GeoRessources, Nancy) pour son aide inestimable pour les expérimentations en autoclave.

Merci également à ceux par qui toute analyse minéralogique débute, les litholamelleurs de GeoRessource, Cédric Demeurie et Alexandre Flammand, pour leur écoute et l'intérêt constant qu'ils portent à nos besoins. Je tiens à remercier Chantal Peiffert et Philippe Lach pour les nombreuses discussions que nous avons pu avoir et leur aide précieuse dans le développement de l'analyse des sulfures en LA-ICP-MS. Je remercie l'équipe du SCMEM de GeoRessources, Sandrine Mathieu, pour son aide et sa patience lors des séances de MEB et les nombreuses discussions sur les techniques d'analyses par rayons X, ainsi qu'Olivier Rouer pour les analyses en microsonde électronique. Merci à Isabelle Bihannic et Renaud Gley (LIEC, Nancy) pour les analyses des poudres par diffraction X. Merci également à Delphine Yeghicheyan au SARM pour les analyses des éléments en traces en solutions. Je remercie

aussi toutes les personnes de l'équipe Sondes ioniques du CRPG pour leur aide de l'analyse isotopique du soufre, Claire Rollion-Bard, Andrey Gurenko et Emilie Thomassot, Nordine Bouden, sans oublier Étienne Deloule. Pareillement, je remercie Christian France-Lanord et Thomas Rigaudier pour m'avoir aider à réaliser des analyses isotopiques globales du soufre par EA-IRMS.

Enfin, j'aimerais ici te rendre l'hommage que je n'ai jamais pu te témoigner, Pete. Je n'oublierai jamais ton humanité débordante et ton extrême sympathie. Ta voix fera écho encore très longtemps dans les murs de ce laboratoire pour tous ceux qui t'ont côtoyé, tu nous manques beaucoup ici.

J'aimerais exprimer ma profonde gratitude envers Damien Cividini, pour son amitié, son aide et son implication dans les analyses isotopiques sur le Neptune. Merci pour toutes ces discussions scientifiques stimulantes concernant l'analyse isotopique, mais aussi pour m'avoir un peu transmis de ta passion du cinéma et de la musique (surtout Pink Floyd). Un grand merci également à Aimeryc Schumacher, qui, avec Damien, forment un tandem incontournable. Merci pour ton aide précieuse en salle blanche et sur le Neptune, ainsi que pour ta grande gentillesse. Je n'oublie pas de remercier mes amis et collègues de bureau au CRPG qui m'ont accueilli pour la deuxième partie de ces années de thèse, Léo, mon camarade depuis plus de huit ans déjà, Guillaume et Romain. Merci à vous pour tous ces moments partagés à travailler, à s'entraider, et fort heureusement, à blaguer, à parler films, jeux-vidéos, ou à écouter de la musique. Je n'oublie pas Yves, un visiteur régulier de notre bureau, pour avoir partagé avec nous sa bonne humeur comme ses légendaires coups de gueule.

Bien entendu, merci à mes premiers compagnons à GeoRessources, Wilfried et Philippe, puis à Jérémy qui leur succéda. Merci à tous mes compagnons doctorants du CRPG et de GeoRessources — Martin, Jesse, Maïa, Julien, Matthieu, Roland, Maxime, Guillaume, Christophe, et bien sûr, Guimou et Quentin — toujours disponibles pour bavarder, boire un café, jouer à la pétanque ou toute autre activité hautement scientifique. Je n'oublie pas de remercier tous mes amis lorrains — Jérémy & Élodie, Maxime & Camille, Virginie & Marc, Julien & Cindy, Nadège, Josselin, Mélanie et Aurélie, et mes amis de toujours, Sandro, Rémi, Amar, et Fred & Julie — pour m'avoir toujours épaulé.

Je suis extrêmement reconnaissant envers mes parents, pour leur soutien indéfectible, leur confiance et la liberté qu'ils m'ont offert pour me hisser jusqu'à l'âge d'homme. Merci également à mon grand frère, Julien, qui a toujours veillé sur moi et a largement contribué, surement sans le savoir, à mon développement en étant pour moi un modèle. Merci à toi Julie, pour ton soutien, ta patience, et surtout, pour ton amour. Il faut reconnaitre que la vie s'est bien jouée de nous, toi qui détestais tant la géologie à l'école, et moi, le ton autoritaire des institutrices qui sait si bien me remettre d'aplomb aujourd'hui. Aussi, j'aimerais remercier la famille de Julie, ses parents, Annick et Jean-Michel, et ses soeurs, Alex et Margaux, qui m'ont respectivement accueilli comme un fils et un frère ; sans oublier Roger et ses bonnes bouteilles de vin. Enfin, merci à mes grands-parents qui ont grandement contribué à façonner mon esprit ; à Mamie Denise, pour le goût de la Musique et des « bonnes choses » ; merci à Papy Maurice, pour m'avoir transmis un peu de son ingéniosité et de sa curiosité ; à Papy Jeannot, pour sa passion du football, sans quoi je ne saurais comment décompresser. Enfin, je souhaite dédier cette thèse à ma Mamie Jeanette ; ton immense tendresse a été pour moi un havre de réconfort, et ce sentiment restera toujours profondément ancré en moi.

Résumé des travaux

Introduction

Les métaux tels que le germanium, l'indium, le gallium, le scandium et les terres rares sont de plus en plus utilisés dans les industries de haute technologie (énergies renouvelables, fibres optiques, smartphones). La situation à risque en ces métaux, dits stratégiques ou critiques, ainsi créée (European Commission, 2010, 2014) encourage une exploration accrue et nécessairement des recherches comprenant le cycle géologique de ces métaux et les facteurs contrôlant leur concentration, le mode d'incorporation à l'état de trace dans certains minéraux majeurs (par exemple, Ge dans la sphalérite), la distribution à l'échelle de gisements ou de provinces est en grande partie inconnue. La communauté internationale, s'est en partie emparée de ces nouveaux enjeux, et travailler à l'échelle de provinces métallogéniques est primordial. Les métaux stratégiques sont rarement des produits primaires de minéralisations mais sont le plus souvent des sous-produits de l'exploitation de minéraux majeurs, et sont ainsi extraits en quantités faibles. Le germanium, qui est l'objet de cette étude, n'est pas extrait de gisements spécifiques mais on le retrouve à l'état de traces dans les minéraux majeurs de nombreux types de gisements comme le montrent les compilations récentes de Höll et al. (2007) et Melcher and Buchholz (2013). Par son comportement chalcophile, le Ge est souvent enrichi dans certains sulfures (jusqu'à plus de 3000 ppm) par le biais de processus de mobilisation par des fluides minéralisateurs associés à des conditions de température et de redox variées, et ce, en fonction des types de gisements.

Les minéraux porteurs de Ge et autres éléments stratégiques associés, leurs conditions d'incorporation en solution solide et/ou en micro-inclusions (selon les éléments) sont mal connus. Actuellement, la sphalérite (ZnS) est considérée comme le minéral porteur de Ge le plus significatif, ce qui en fait une des principales sources de Ge dans le monde. Des études récentes par microscopie optique et LA-ICP-MS sur des sphalérites provenant de différents gisements de classe mondiaux de type Pb–Zn–F–Ba montrent que ces sulfures sont parfois fortement zonés, leurs teneurs en métaux stratégiques sont très variables, et ce jusqu'à plusieurs ordres de grandeur. Ainsi, les teneurs peuvent atteindre 5000 ppm Ge, 10% In, et 1000 ppm Ga (Cook et al., 2009; Ye et al., 2011). Ces travaux montrent également une tendance à l'incorporation préférentielle de cortèges élémentaires spécifiques selon le type de gisement. Les gisements basses températures non liés à une source magmatique sont plutôt enrichis en Ge, Ga, Cd, Tl et As, notamment ceux du type Mississipi-Valley (MVT). Parmi les gisements liés à une source magmatique, les gisements du volcanisme sous-marin, les amas sulfurés volcanogéniques (VMS) ou les gisements types stratiformes (SedEx), sont généralement plus riches en In, Sn et Ga, alors que les gisements du métamorphisme de contact (skarns) ou du volcanisme aérien (épithermaux) sont enrichis en In, Sn, Co et Mn.

L'objectif majeur de cette thèse est focalisé sur le traçage élémentaire et isotopique du germanium (Ge) dans les différents types de gisements à différentes époques métallogéniques où le Ge est un sous-produit significatif, qu'il soit à l'état de traces dans certains minéraux

majeurs (e.g. sphalérite, chalcopyrite) ou soit présent sous forme de minéraux du Ge à fortes teneurs mais en plus faible volume (e.g. renierite, germanite). Le but est de comprendre les mécanismes et les conditions physico-chimiques liées à la formation des minéralisations enrichies en Ge et métaux stratégiques associés. L'originalité de cette approche est de coupler des traceurs géochimiques élémentaires (Ge et cortège multi-élémentaire Cu, Ga, In, Ag, Cd, Fe, etc.) et isotopiques (isotopes de Ge, S, Fe) à différentes échelles pour tenir compte de l'hétérogénéité des minéraux (e.g. sphalérites zonées) : analyses élémentaires et isotopiques ponctuelles et globales, ainsi que l'étude de la cristallochimie par spectroscopie d'absorption des rayons X par rayonnement synchrotron (XAFS). Trois principaux types de gisements encaissés dans des roches sédimentaires, carbonatées ou métamorphiques sont étudiés : le gisement filonien à Zn de Saint-Salvy (Sud-ouest massif central, France), le gisement filonien à Cu de Barrigão (Ceinture pyriteuse ibérique, Portugal), et le gisement Zn–Cu de Kipushi (R.D. Congo). Une approche expérimentale, visant à simuler la précipitation de sphalérites dopées en Ge en conditions hydrothermales, a été associée dans cette étude pour quantifier les mécanismes d'incorporation du Ge et déterminer son fractionnement isotopique.

Les travaux de recherche ont tenté d'établir le lien entre les concentrations en Ge d'un gisement et le contexte géologique de sa mise en place. Ceci implique de comprendre dans quelles phases et à quelles teneurs sont distribués le Ge et les métaux stratégiques associés, et quels sont les mécanismes et conditions de leur incorporation. Les problématiques des études métallogéniques sont les suivantes : traçage de la source des métaux, de l'origine des fluides, des mécanismes pré-concentrations, de l'évolution de la composition et des paramètres physico-chimiques des fluides hydrothermaux, ainsi que les moteurs des circulations hydrothermales.

Techniques analytiques et méthodes

L'approche analytique de ces travaux, présentée dans la Figure 1, comprend dans un

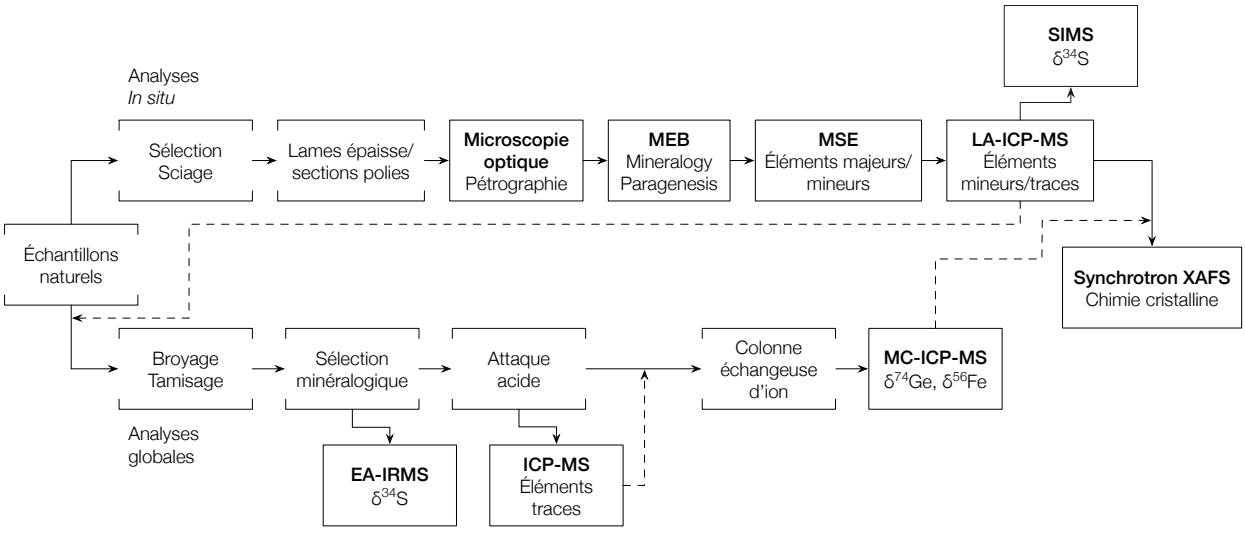

Fig. 1 – Approche analytique développée dans ces travaux. Les lignes en traits pleins indiquent le cheminement des échantillons, les lignes en pointés représentent une prise de décision postérieur à une analyse.

premier temps une caractérisation pétrographique et minéralogique classique afin de sélectionner les échantillons qui seront montés en lames épaisses polies ou sections polies. L'étude minéralogique approfondie se poursuit sur sections/lames polies par microscopie optique, puis par microscopie électronique à balayage (MEB) afin d'affiner l'identification des minéraux et leur relation génétique. L'analyse de la composition chimique des minéraux en éléments majeurs et mineurs est réalisée par microsonde électronique (MSE). Les éléments mineurs et traces sont alors analysés *in situ* par ablation laser couplée à un spectromètre de masse à source plasma induit (LA-ICP-MS). Des analyses globales des minéraux en éléments traces et isotopiques (Ge, Fe, S) vont compléter la caractérisation de ces échantillons. Les échantillons macroscopiques sélectionnés sont ensuite broyés et tamisés et les minéraux sont triés par séparation magnétique et/ou par sélection sous stéréo-microscope. Les échantillons sont dissout par attaque acide en salle blanche de chimie sous atmosphère contrôlée, les éléments traces sont analysés par ICP-MS. Les analyses isotopiques du Ge impliquent un processus séparation et de purification du Ge sur colonnes de résine échangeuses d'ions, puis les mesures isotopiques du Ge sont réalisées par spectrométrie de masse à multi-collection (MC-ICP-MS).

Éléments traces et isotopes du Ge dans la sphalérite de Saint-Salvy

Une première étude minéralogique et géochimique intégrée a été conduite sur les sphalérites (ZnS) du principal gisement de Ge d'Europe occidentale : le filon à Zn–Ge–Ag–(Pb–Cd) de Noailhac – Saint-Salvy (Tarn, France) où la concentration en Ge peut dépasser 2500 ppm dans certaines zonations très caractéristiques. Ces résultats font l'objet de la publication suivante : Belissont R., Boiron M.-C., Luais B. and Cathelineau M. (2014) LA-ICP-MS analyses of minor and trace elements and bulk Ge isotopes in zoned Ge-rich sphalerites from the Noailhac – Saint-Salvy deposit (France): Insights into incorporation mechanisms and ore deposition processes. *Geochimica et Cosmochimica Acta* **126**, 518–540.

L'analyse du Ge par LA-ICP-MS a été développée afin d'obtenir des mesures précises et reproductibles de la concentration du Ge et des traces associées dans les sulfures à étudiés. À la différence des protocoles d'analyse présentés dans la littérature récente, nous démontrons l'importance de l'utilisation de l'isotope ^{74}Ge et d'un standard de sulfures approprié, le polysulfure synthétique MASS-1 (Wilson et al., 2002), pour l'analyse de la sphalérite. Par ailleurs, une place importante a été consacrée à l'utilisation de statistiques descriptives multivariées afin d'améliorer la compréhension et l'interprétation des données ponctuelles en élément trace jusqu'alors peu usité dans ce domaine. L'analyse statistique en composantes principales (ACP) des données élémentaires LA-ICP-MS met en évidence un enrichissement préférentiel des éléments traces dans certaines faces cristallines – ou contrôle cristallographique – lors la croissance de la sphalérite, entraînant la formation de plusieurs types de zonations (Fig. 2). Les zonations sectorielles – plans (111) – sont enrichies en Ge, Cu, Ga et Sb, alors que les bandes rythmiques – plans (110) – sont enrichies en Fe, Cd, In et Sn. Les éléments divalents intègrent le réseau de la sphalérite par substitution directe, $Zn^{2+} \leftrightarrow (Fe,Cd)^{2+}$, alors que les éléments tri- et tétravalents l'intègrent par substitutions couplées avec des élément monovalents (essentiellement le cuivre), par exemple, selon la relation $3Zn^{2+} \leftrightarrow Ge^{4+} + 2Cu^{+}$ dans le cas du germanium. À ce stade cependant, nombre d'éléments hétérovalents ont plusieurs états d'oxydation possible et leur état dans la sphalérite est encore mal contraint. Dans le cas du Ge, l'état Ge^{4+} est dominant par rapport à Ge^{2+}, cependant, son état d'oxydation n'a pas été, pour le moment, formellement identifié.

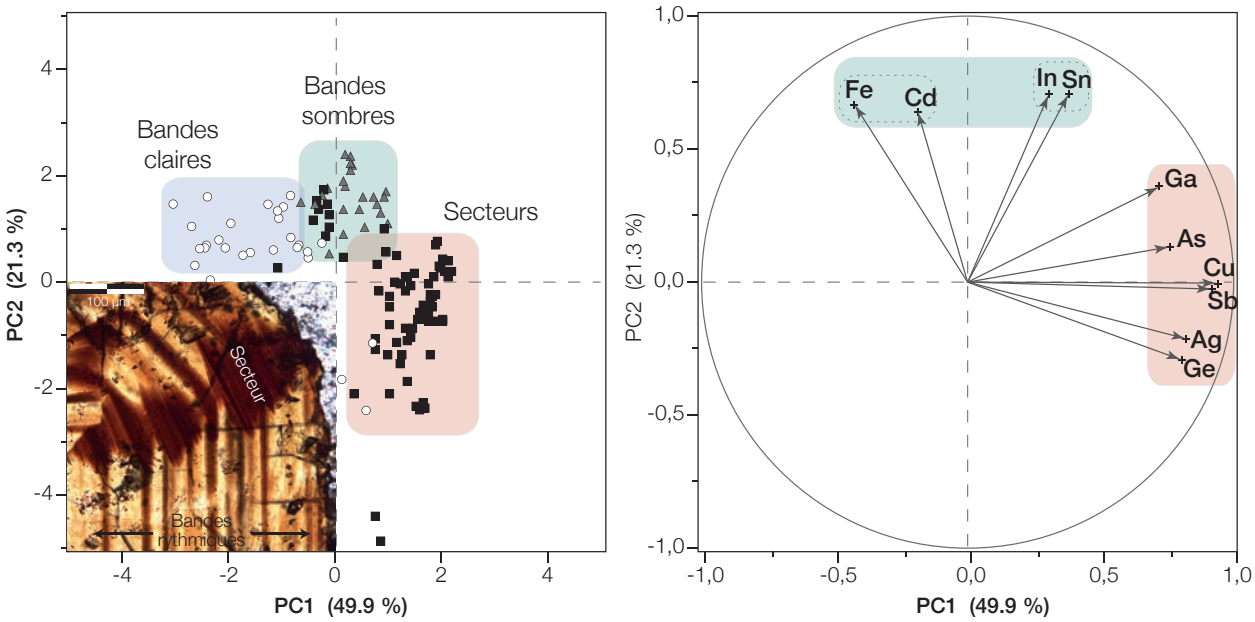

Fig. 2 – Analyse en composante principale (ACP) des données en éléments traces par LA-ICP-MS sur les sphalérites de Saint-Salvy. L'encart en bas à gauche est une microphotographie optique d'une sphalérite de Saint-Salvy où figurent les deux types de zonations caractéristiques.

Les analyses du rapport isotopique $^{74}Ge/^{70}Ge$, dont les variations — en notation $\delta^{74}Ge$ — sont exprimées en ‰ par rapport à un standard international de Ge (NIST 3120a), mettent en évidence une large gamme de compositions isotopiques comparée aux autres réservoirs terrestres (croûte/manteau supérieur), variant de –2,07‰ à +0,91‰ (±0,25‰ à 2σ SD en moyenne, Fig. 3). Ce fractionnement isotopique important est caractéristique de la précipitation de sphalérite à basse température (80–140°C). Une corrélation positive entre la concentration en Ge et son rapport isotopique $\delta^{74}Ge$ suggère un dépôt de sphalérite en milieu ouvert avec des apports réguliers de fluides hydrothermaux.

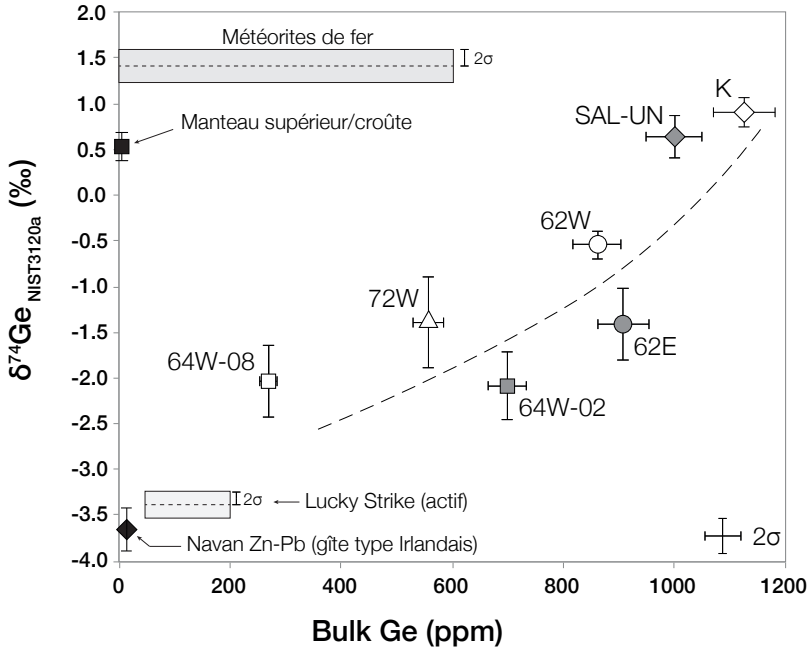

Fig. 3 – Composition isotopique ($\delta^{74}Ge$) *vs* concentration en Ge pour les sphalérites de Saint-Salvy, du gisement à Zn–Pb de Navan (Irlande) et des sulfures hydrothermaux de Lucky Strike (ride médio-atlantique; Escoube et al., 2012), comparée à la composition de réservoirs terrestres et météoritiques.

Enfin, une ACP intégrant les concentrations en éléments traces des sphalérite de Saint-Salvy et celles provenant d'autres types de gisements mondiaux (données de la littérature) ont permis de confirmer que la signature en éléments traces des sphalérites est fortement dépendante de leurs conditions de dépôt. Par exemple, les fortes teneurs en germanium sont associées aux gisements de basses températures (Type MVT, par exemple), alors que celles en indium sont associées aux gisements de plus hautes températures, liés aux processus magmatiques.

Cristallochimie et mécanismes d'incorporation de Ge dans les sulfures

Les mécanismes d'incorporation des éléments et le fractionnement isotopique associé dépendent de leur état d'oxidation. Les états d'oxydation de Ge, Cu et Fe ont été déterminés dans les sphalérites de Saint-Salvy par rayonnement synchrotron en spectrométrie d'absorption des rayons X par micro-faisceaux (μ-XANES) couplée à la cartographie en fluorescence X (μ-XANES). Ces travaux font également l'objet d'une publication : Belissont R., Muñoz M, Boiron M.-C., Luais B. and Mathon O. (2016) Distribution and oxidation state of Ge, Cu and Fe in sphalerite by μ-XRF and K-edge μ-XANES: insights into Ge incorporation, partitioning and isotopic fractionation. *Geochimica et Cosmochimica Acta* (**en ligne**).

Cette étude vise à améliorer notre compréhension des mécanismes de substitution et de l'incorporation en éléments traces et la quantification du fractionnement isotopique du Ge dans la sphalérite. Des spectres XANES au seuil K de nombreux minéraux porteurs de Ge, Cu et Fe sont intégré à l'étude et comparés à ceux des sphalérites. De plus, des spectres théoriques au seuil K du Ge ont l'objet de calculs *ab initio* pour compléter l'étude.

Les résultats montrent parfaite similarité entre les spectres au seuil K du Ge de la sphalérite en comparaison avec les sulfures de Ge que sont la reniérite, la germanite et la briartite, mettant en évidence Ge^{4+} en géométrie tétraédrique (Table 1). Par ailleurs, les spectres aux seuils K de Cu et Fe suggèrent la présence respective de Cu^{+} et de Fe^{2+} en site tétraédrique. Aucune différence d'état d'oxydation de ces métaux n'est mise en évidence au sein et entre les différents types de zonations de la sphalérite, ainsi qu'entre les différents échantillons.

En accord avec l'étude minéralogique et géochimique et des éléments traces, l'incorportation de Ge^{4+} dans la sphalérite a donc bien lieu dans le site tétraédrique de Zn^{2+} par une substitution couplée pour atteindre l'électroneutralité, qui peut s'écrire sous la forme $(2x{+}3y)Zn^{2+} \leftrightarrow (x+2y)(Cu,Ag)^{+} + x(Ga,In,Sb)^{3+} + y(Ge,Sn)^{4+}$. Par rapport à ce qui est suggéré dans la précédente étude de Johan (1988), les éléments divalents ont été retirés de cette équation : ils sont trop peu corrélés aux éléments hétérovalents d'une manière générale, car ils intègrent simplement le réseau de la sphalérite par substitution directe du Zn. Plus spécifiquement, à Saint-Salvy, la forte corrélation élémentaire Ge *vs* Cu+Ag penche en faveur d'un mécanisme du type $3Zn^{2+} \leftrightarrow Ge^{4+} + 2(Cu,Ag)^{+}$ (Table 1). Par ailleurs, il est possible que le Ge intègre la sphalérite à travers la formation de lacunes cristallographiques du type $2Zn^{2+} \leftrightarrow Ge^{4+} + \square$ (lacune).

L'état tétravalent du Ge est compatible avec un fractionnement isotopique lié à la température et permet d'expliquer simplement la large gamme de δ^{74}Ge mesurée dans la sphalérite

de Saint-Salvy. Finalement, l'enrichissement exceptionnel de ces sphalérites en Ge ainsi que sa grande variabilité en teneurs globales ne semblent pas liés à un effect de redox mais plutôt à l'effet d'un fractionnement élémentaire lié à la température. La corrélation positive δ^{74}Ge–contenu en Ge suggère que le coefficient de partage $D_{\mathrm{Ge}} = [\mathrm{Ge}]_{\mathrm{ZnS}}/[\mathrm{Ge}]_{\mathrm{sol}}$ augmenterait avec la température, auquel cas la réaction d'incorporation du Ge serait exothermique ($\Delta \mathrm{G} < 0$) et spontanée d'un point de vue purement thermodynamique.

Une étude similaire a été conduite sur des sulfures de Cu, notamment la chalcopyrite, qui, comme nous le verrons dans la partie suivante, peut contenir des concentrations exceptionnelles en Ge. Comme pour la sphalérite, Ge^{4+} en coordination tétraédrique est formellement identifiée dans tous les sulfures de Cu porteurs de Ge (Table 1). Ainsi, à l'instar des sulfures dans lesquels Ge est un composant essentiel, comme la reniérite, la germanite ou la briartite, les sulfures de Cu dans lequel il se trouve à l'état de trace, comme la chalcopyrite ou la covellite, et également dans certaines micro/nano-inclusions de sulfures de Ge présents dans une sphalérite de Kipushi, ont tous Ge^{4+} en coordination tétraédrique.

Table 1 – Caractéristiques principales du germanium dans les trois plus importants sulfures porteurs de Ge de cette étude.S: Saint Salvy, B: Barrigao, K: Kipushi.

	Sphalerite **ZnS**	**Chalcopyrite** **$CuFeS_2$**	**Renierite** **$Cu_{10}ZnGe_2Fe_4S_{16}$**
Gisement	Saint-Salvy Kipushi	Barrigão Kipushi	Kipushi
Texture du minerai	*Saint-Salvy*: Brèche en cocarde, croissance lente de en milieu ouvert *Kipushi*: Localement massif ou en équilibre dans les minerais mixtes Pb–Zn et Zn–Cu. Chalcopyrite 'disease' par endroit	*Barrigão*: Grains subautomorphes interloqués avec le cuivre gris, textures de remplacement par endroit. *Kipushi*: Principalement en équilibre dans les minéralisations à Zn–Cu ou localement massive	Principalement en équilibre dans les minéralisations à Zn–Cu ou localement massive
Chimie cristalline de Ge	Tétraédrique Ge^{4+}	Tétraédrique Ge^{4+}	Tétraédrique Ge^{4+}
Concentrations en Ge	jusqu'à 2576 ppm (S) jusqu'à 5930 ppm (K)	2 – 5750 ppm (B) 13 – 686 ppm (K)	5.03 – 16.63 wt.%
Mécanismes de substitution	$3Zn^{2+} \leftrightarrow Ge^{4+} + (Ag,Cu)^{+}$ $2Zn^{2+} \leftrightarrow Ge^{4+} + \square$	$3Fe^{3+} \leftrightarrow 2(Ge,Sn)^{4+} + Cu^{+}$ $2Fe^{3+} \leftrightarrow Ge^{4+} + (Pb,Zn)^{+}$	–
Distribution à l'échelle du grain	*Saint-Salvy*: zonations sectorielles dans des grains subautomorphes à croissance lente par contrôles cristallographiques. *Kipushi*: Homogène ou rarement sous forme de micro/nano-inclusions de sulfures de Ge.	*Barrigão*: Halos riche en Ge–Sn bordant les reliques de chalcopyrites antérieure, à la périphérie des grains dans les réseaux de micro-fractures, ou sous forme de veinules. *Kipushi*: Homogène	Homogène
Timing de l'incorporation du Ge	*Saint-Salvy*: Synchrone, contrôles cristallographiques (zonations sectorielles) et variations de compositions de fluides à l'interface cristal–fluide (bandes de croissance). *Kipushi*: Probablement lié à un événement ponctuel minéralisateur rich en Ge (Ge peak), contemporain ou temporellement proche de la précipitation des sulfures de Ge.	*Barrigão*: Surimpression hydrothermale tardive *Kipushi*: Probablement lié à un événement ponctuel minéralisateur rich en Ge (Ge peak), contemporain ou temporellement proche de la précipitation des sulfures de Ge.	Charactéristique d'un événement riche en Zn–Cu–Ge, probablement sous haute activitée en soufre comme l'atteste la présence de sulfosels (tennantite).

Éléments traces dans les minerais de Barrigão et de Kipushi.

La chalcopyrite de Barrigão contient environ 2 à 5750 ppm de Ge avec une moyenne de 1080 ppm sur l'ensemble des analyses (Table 1). À l'échelle du grain, la distribution du Ge est hétérogène : des zones enrichies en Ge–Sn apparaissent sous forme de halo autour de reliques de chalcopyrite, sur la bordure des grains dans certains réseaux de micro-fractures, ainsi que sous forme de veinules dans certains grains de plus grande taille. L'analyse en composantes principales met en évidence un groupe de corrélation (Ge, Ga, Sn, As, Ag, Sb) nettement anti-corrélé à Fe, qui suggère notamment le mécanisme $3Fe^{3+} \leftrightarrow 2(Sn,Ge)^{4+}+Cu^{+}$ pour les éléments hétérovalents par rapport au Fe, et une substitution direct Fe $Fe^{3+} \leftrightarrow M^{3+}$ pour les éléments isovalents, par exemple, Ga, As, In et Sb.

La solution solide tennantite–tétraédrite (cuivre gris) à Barrigão, en équilibre textural avec la chalcopyrite, contient environ 1 à 90 ppm. L'analyse en composante principale des teneurs élémentaires met en évidence une corrélation (Ge, Ga, In) avec As, qui représente le pôle de la tennantite, alors que Ag est correlé avec Sb, représentant le pôle tétraédrite. Les éléments divalents Zn, Mn, Pb et Cd sont par contre anticorrélés au Fe. L'enrichissement en Ge vers le pôle de la tennantite peut s'expliquer par la proximité des rayons atomiques de Ge et As qui sont respectivement 1,20 Å et 1.19 Å en liaison covalente d'une part, et par la précipitation de tennantite durant l'épisode hydrothermal tardif riche en Ge–Sn d'autre part, qui est responsable de la formation de zonations enrichies en Ge dans les chalcopyrites. En faveur de cette hypothèse, on note notamment une forte corrélation de As avec Ge dans ces zones d'enrichissement.

Dans les sulfures de Kipushi, à l'inverse, la distribution du Ge est relativement homogène. Le principal sulfure de Ge, la reniérite, contient de 5,0 à 9,1% Ge. Les sulfures de Ge accessoires, la germanite et la briartite, titrent respectivement 4,9–9,2% et 16,6% Ge (Table 1). Au sein des minéraux portant le Ge à l'état de trace, la concentration moyenne en Ge décroit dans l'ordre suivant : chalcopyrite (13–686 ppm, ∼218 ppm), sphalerite (max. 5930 ppm, ∼128 ppm), tennantite (1–182, ∼32 ppm), pyrite (max. 148 ppm, ∼8 ppm) et bornite (2–14 ppm, ∼6 ppm). Les concentrations en traces, plus particulièrement dans la sphalérite et la chalcopyrite, sont homogènes par échantillon. Ainsi, les sphalérite et de chalcopyrite les plus riches en Ge pourraient être des indicateurs minéralogiques de l'arrivée progressive de Ge dans le fluide qui, de manière synchrone, est responsable de la précipitation de sulfures de Ge, notamment, les sphalérites et chalcopyrites qui, en équilibre textural avec la reniérite, sont les plus riches en Ge.

Implications des isotopes du Ge sur les processus de dépôt

La composition isotopique du Ge présent dans les sulfures étudiés varient, en δ^{74}Ge, de –5,72‰ à +3,67‰ (Table 2). Un fractionnement isotopique d'une amplitude de 5,97‰ est mesuré dans la sphalérite de Saint-Salvy, de 1,52‰ et 2,50‰ respectivement dans la chalcopyrite et le cuivre gris de Barrigão, et de 3,41‰ dans la paragenèse sulfurée Kipushi. Les compositions isotopiquement légères mesurées dans les gisements filoniens de Saint-Salvy et Barrigão semblent liés à des variations dans les basses à moyennes températures des fluides. Les fluides associés à la précipitation de sphalérite à Saint-Salvy ainsi que ceux de l'événement

tardif riche en Ge à Barrigão semblent avoir peu varié au cours d'une précipitation en système hydrothermal ouvert. Par contre, compte tenu des températures plus élevées (290–300°C), de l'absence de différences systématiques entre les valeurs de δ^{74}Ge des minéraux de Kipushi, et de la tendance marquée vers les compositions isotopiques lourdes, la température ne serait pas le facteur principal de fractionnement isotopique à Kipushi. Ce dernier serait plutôt lié fractionnement de type Rayleigh. Si tel est le cas, la composition des fluides minéralisateurs à Kipushi aurait donc pu évoluer significativement par précipitation de sulfures en système clos.

Table 2 – Comparaison des caractéristiques principales des gisements de Saint-Salvy (France), Barrigão (Portugal) et Kipushi (R.D. Congo).

	Saint-Salvy French Massif Central	**Barrigão** Iberian pyrite belt	**Kipushi** Central-african copperbelt
Typologie	Filonien à Zn encaissé dans les métasédiments Caractéristiques de fluides type MVT	Filonien à Cu encaissé dans les métasédiments Re-mobilisation de VMS	Gîte Cu–Zn de type Kipushi encaissé dans des carbonates
Âge	Trias sup. – Jurassique inf. (~180 Ma) Tardi varisque, régime extensif	Tardi varisque, Surimpression précoce de la phase alpine possible	Ordovicien sup. (~451 Ma) Post Lufilien (pic de déformation à 530 Ma)
Type de minerai	Brèche type cocarde	Brèche	Sulfures massifs
Paragenèse	Sp	Cp, Tn–Tht et Py mineure	Sp, Cp, Bn, Cc, Py, Apy, Tn, Gn et Rn, Shg accessoirs
Éléments	Zn ± Ge, Ag, Cd, Pb	Cu ± Ge, Sn	Zn, Cu ± Pb, Ge, Ga, Mo, W, V
Nature des fluides	H_2O–NaCl–$CaCl_2$	Non estimé *	NaCl–KCl–$CaCl_2$
Salinité	23–25 wt.% NaCl eq.	2–25 wt.% NaCl eq.*	~30–43 eq.wt.% NaCl eq.
Température	80–140°C	260–300°C * probablement plus bas pendant la surimpression de fluides riches en Ge	~290–380°C
Source des métaux	Schistes noirs cambriens ± granite du Sidobre ?	re-mobilisation de VMS et/ou métasédiments	Lessivage du socle felsique
δ^{74}Ge (‰)	–5.06‰ à +0.91‰ (5.97‰ au total)	–3.50‰ à –1.44‰ dans Cp (1.52‰ au total) –5.72‰ à –3.22‰ dans Tn–Tht (2.50‰ au total)	–0.36‰ to 3,67‰ (3.41‰ au tot.)
Processus proposé	Effet de température, refroidissement ?	Effet de température	Processus de fractionnement de Rayleigh

* Considérations théoriques de Mateus et al. (2003)
Abréviations: Sp, sphalérite; Cp, chalcopyrite: Tn, tennantite; Tht, tétraédrite; Bn, bornite; Cc, chalcocite; Py, pyrite; Gn, galena; Rn, reniérite, Shg, shungite

Contents

List of Figures

List of Tables

Chapter 1

Introduction

1.1 Definition of critical metals

Raw materials are fundamental to the economy and growth of countries. Recent years have seen a growth in the demand for materials used across a wide range of products. Securing reliable, sustainable and undistorted access of the necessary raw materials is of growing concern within the E.U. and across the globe. In consequence, the 'Raw Materials Initiative' was instigated to manage responses to raw materials issues at the level of the European Union. The purpose of this work was defining the critical raw materials for the EU's economy. These critical raw materials combine both high economic importance and high supply risk (Fig. 1.1). The first criticality analysis for raw materials was published in 2010 by the European Commission (2010). Fourteen critical raw materials were identified from a list of 41 materials of economic importance. According to a recent update of this analysis, 20 compounds are now seen as critical, from a list of 54 candidate raw materials. This list includes the metals and metalloids, antimony, gallium, germanium, indium, tungsten, platinum group metals (PGM), light and heavy Rare Earth elements (REE), beryllium, magnesium, cobalt, chromium, silicon, and raw materials such as phosphates, borates, magnesite, coking coal, natural graphite.

Economically, minor metals such as Ge, In, Ga, Sc and REE are increasingly used for high-tech applications (e.g., electronic/solar applications, infra-red optics, fibre optics). The demand has overpassed their worldwide production in recent years. The deficit in these critical metals is driving renewed explorations and researches on the geological cycles of these metals and the factors controlling their incorporation, concentration, and distribution from the scale of host minerals to ore deposits, up to an entire metallogenic province. No ore deposits are mined solely for its critical metal contents, which are rather recovered as by-products from base metal mining operations and extracted in low quantities. For instance, primary germanium is recovered from zinc concentrates or fly ash from coal.

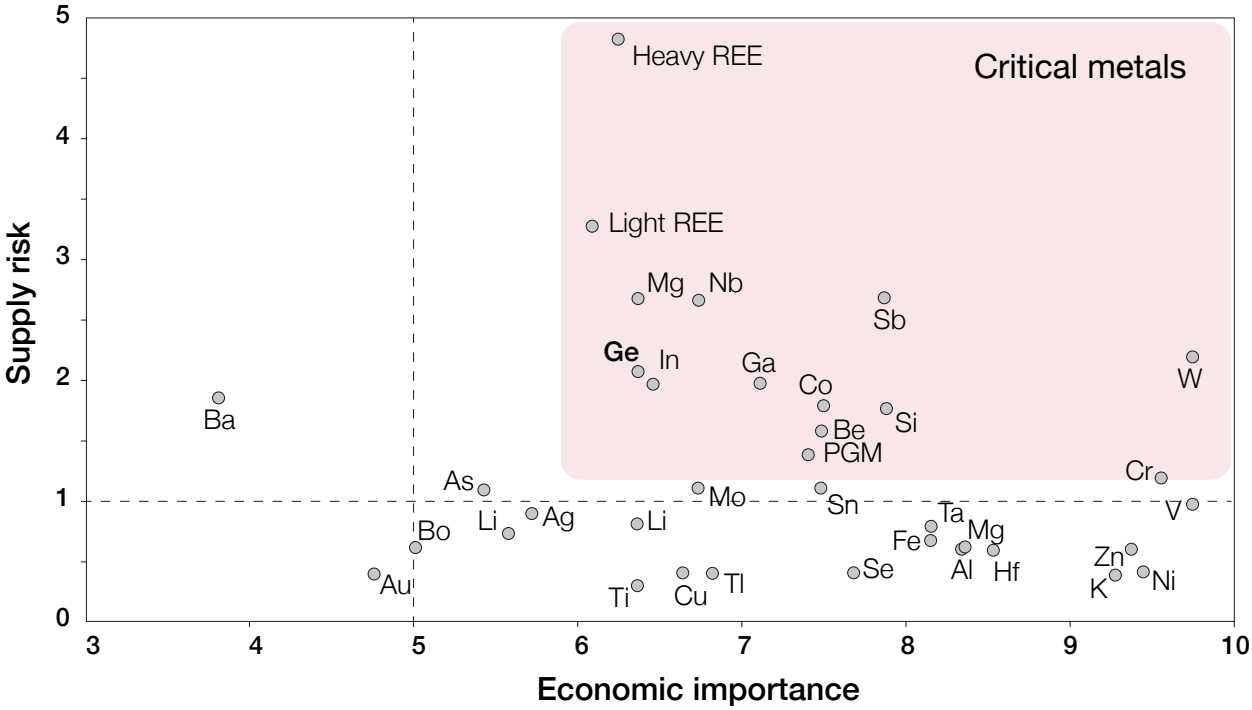

Fig. 1.1 – Criticality diagram of metals and metalloids according to the European Commission (2014).

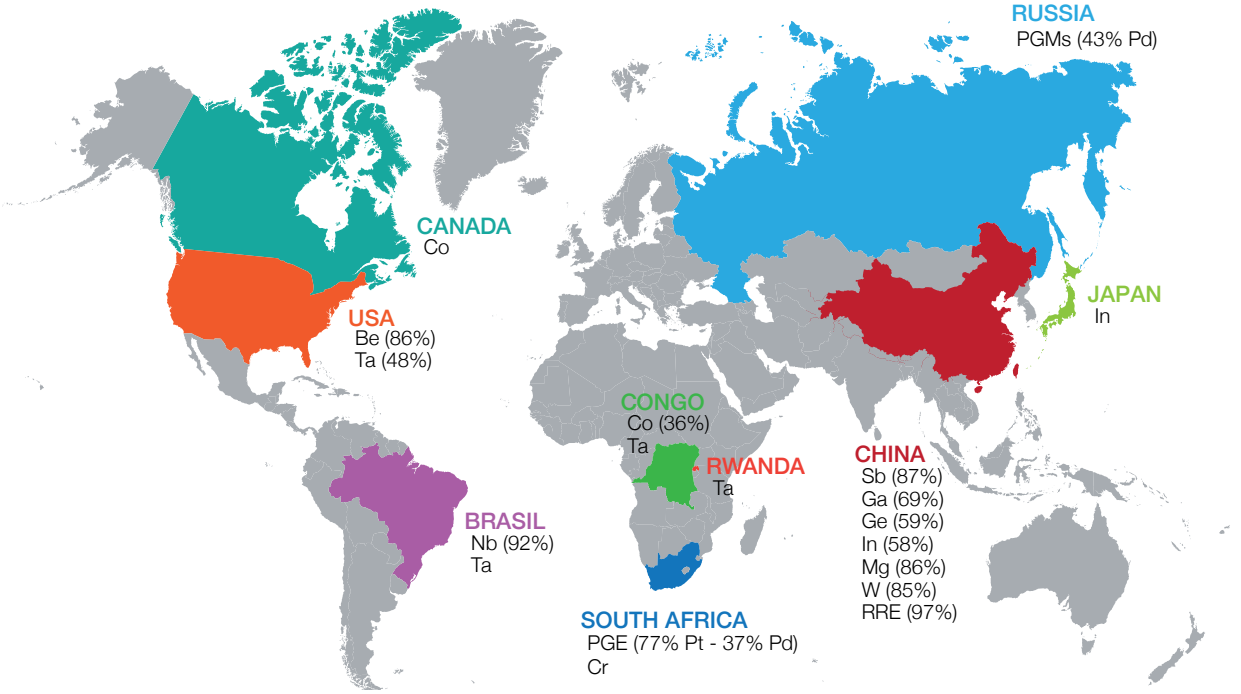

Fig. 1.2 – Map of critical metals global production (European Commission, 2014).

1.2 General aims

The rapid increase in the economic importance of Ge due to some of its major applications being modern high-tech economies, especially developing fields of sustainable energy and communication, which caused a significant demand increase in recent year, combined with a production now largely dominated by China, encourage for enhanced exploration as well as intense research for better understanding the geological cycle of Ge and the factors controlling Ge occurrences and concentrations.

Germanium, as with critical metals in general, does not form specific deposits but rather occurs in trace to minor amounts in various types of ore deposit and minerals, as shown by the recent reviews of Höll et al. (2007), Melcher and Buchholz (2013) and Frenzel et al. (2014). It is widely recognised that Ge displays chalcophile and organophile behaviours, and that most significant Ge enrichments occur through low-T ore-forming processes in carbonate- or sediment-hosted Zn deposits (e.g., MVT, SHMS), and that there is a consistent association of Ge with coal and lignite reservoirs.

In ore deposits, there is substantial lack of data regarding the way Ge distributes from the scale of district or within a given deposit. Even at the scale of Ge-bearing minerals, the incorporation mechanism of Ge and its association with other critical metals is still unclear. The recent development and maturation of new analytical techniques, especially laser ablation and multi-collector inductively coupled plasma mass spectrometers, found many applications to gain insights on this matter, yet, the Ge uptake in ore-forming systems and minerals remain mostly unclear.

In this context, this thesis is an attempt to provide answers regarding Ge distribution and associated enrichment processes in distinct geological frameworks with the help of recent techniques. In a first part, this thesis manuscript presents a review of the current background knowledge about Ge geochemistry and details most specifically the goals and strategy of this study, while the second part describes the analytical techniques and methods. Results and discussions are presented by topic, which are (1) minor and trace elements in Ge-bearing sulphides, (2) Ge crystal chemistry in sulphide minerals, (3) its isotopic fractionation in selected ore deposits and finally, (5) an experimental study of Ge partitioning and isotope fractionation in sphalerite. The last part summarises the main features of this work and assesses some research perspectives arising from it.

Chapter 2

State of the art

2.1 Germanium properties, uses and stakes

2.1.1 The element germanium

Germanium (Ge) is a grayish-white, hard, brittle metalloid, that was first isolated and described by Clemens Winkler in 1886 in the silver sulphide argyrodite (Ag_8GeS_6) from Freiberg, Saxony, Germany. Its existence was predicted earlier in 1864 by John Newlands, who postulated the existence of an element intermediate between silicon and tin in his scheme of elemental octaves. This idea was put forward in 1871 by Dmitri Mendeleïev in the periodic table of elements and was then named eka-silicon (beyond silicon, Haller, 2006).

Germanium has the atomic number 32, atomic weight 72.59 g.mol^{-1}, electron configuration [Ar] $3d^{10}4s^24p^2$, and is located in period 4, group 14 in the periodic table of the elements. Ge is nominally tetravalent but possesses two main oxidation states, +2 and +4, the latter forming the most common and stable compounds. Divalent Ge species (e.g., GeO and GeS) are usually not stable under atmospheric conditions (Bernstein, 1985). Natural germanium occur as a mixture of five stable isotopes – by weight, ^{74}Ge (35.94 %), ^{72}Ge (27.66 %), ^{70}Ge (21.23 %), ^{73}Ge (7.73 %), and ^{76}Ge (7.44 %). In addition, at least 27 synthetic radioisotopes have been artificially produced from ^{58}Ge to ^{89}Ge with half-lives ranging from 110 ηs to 270.95 d (Audi et al., 2003).

2.1.2 Properties and uses

Ge first came into use in the second half of the 20$^{\text{th}}$ century in radar units and as the material from which the first transistor was made (Bell laboratories, 1947) and quickly became essential in many new solid-state electronic and optical devices. Germanium owes its usefulness to three kind of salient properties (Thomas et al., 2000):

Electrical – Germanium is an intrinsic n-type semiconductor, which in the pure state and in the absence of any impurities, conduct electricity but poorly due to a strong resistivity of 53 Ω·cm at 25°C, compared with $1.7{\cdot}10^{-6}$ Ω·cm for copper. It is particularly effective

at high frequencies and low operating voltages.

Optical – Germanium and its oxide, whether in the crystalline or glassy states, are both transparent to part of the infrared spectrum (1800-23000 nm), have exceptionally high refractive index for the IR spectrum (4.0026 at 11000 nm), and exhibit low chromatic dispersion (the variation of refractive index with wavelength).

Chemical – Germanium is a glass-former, in analogy to Si, Ge is able to form extended three-dimensional networks of more or less randomly ordered Ge-O tetrahedra. Ge dioxide is a catalyst in some chemical reactions, among which the polymerization of polyethylene terephthalate (PET).

Today, Ge compounds are used primarily as a semiconductor and substrate in electronic circuitry (transistors, diodes) and solar cells, in infrared optic industry for night vision devices, in fibre optics for telecommunication networks, as polymerization catalyst for polyethylene terephthalate (PET) plastics (Butterman and Jorgenson, 2005).

Electronics and optoelectronics

Electronics was the main use of germanium from the 1950s to most of the 1970s, and drastically diminished afterwards, as silicon-based transistors and diodes were preferred to germanium due to a more easily manufacture and operating conditions. In the late 1990s, since manufacturers faced problems with the continued shrinking of silicon semiconductors, germanium is experiencing a revival. Successful advancements in the techniques for growing exceedingly thin epitaxial layers of germanium on silicon (SiGe) with atomic layer accuracy lead to the manufacture of microscopic heterojunction bipolar transistors now equipping cell phones, computers, and lasers (Haller, 2006). Single-crystal Ge is used as a substrate in the production of LEDs, laser diodes, and high-efficiency multijunction photovoltaic solar cells used in solar panels of terrestrial and space applications.

Infrared optical systems

The optical behaviour of germanium metal and oxide glasses to transmit IR radiations found many application in military forward looking infrared (FLIR) systems such as night vision goggles, binoculars, gunsights, surveillance cameras, and IR-seeking missiles. Civilian uses include detecting overheating bearings, fire fighting in dense smoke, locating lost hikers in wilderness areas, monitoring of rock surface temperatures in mines, satellite mapping, medical diagnosing, and detecting faults in structural materials (Hilton, 1993). The high refractive index and low chromatic dispersion allow the use of germanium windows and lenses for industrial IR lasers. Germanium photoconductors have been used in a range of infrared astronomical experiments, both airborne and space-based (Young et al., 2003).

Fibre optics

The most important commercial fibres are essentially composed of silica glass doped with up to 4 wt.% GeO_2, designed for the transmission of analogue or digital data in the near-IR spectrum, owing to its transparency for this part of the spectrum, high refractive index, and its low chromatic dispersion. Two kinds of optical fibres incorporate GeO_2, thin single-mode fibres for long-distance land and submarine cables (7–10 μm), and multi-mode fibres (50–300 μm) used for transmission over much shorter distances such as between office buildings or local-area computer networks (Lecoy, 2013).

Catalysts

Germanium dioxide (GeO_2) is used as a polycondensation catalyst in the late-stage polymerization of PET that benefits of better transparency and whiteness than with other catalysts. PET is a commodity plastic largely employed in bottles, but also in food packaging, films, and many other products. GeO_2 catalyst was mainly used during the early years in film applications. Today, most of germanium catalyst is consumed by Japanese polyester producers for bottle applications (Thiele, 2001). Germanium fluoride (GeF_4) is a highly selective catalyst for the fluorination of hydrocarbons at room temperature and pressure, leading to a more efficient production of environmental-friendly hydrofluorocarbons (HFCs) refrigerants (e.g., Omotowa, 2010).

Other uses

Germanium is mixed in various amounts with gold, silver, copper, and palladium in dental alloys, and with silicon in thermoelectric devices. Mixed in very small amounts, it acts as a hardener of metals, such as aluminum, magnesium, and tin. Owing to its high refractive index and low chromatic dispersion, GeO_2 has long been a component of the glass used in wide-angle camera lens. Single-crystal germanium are used in detectors for γ-rays in spectral analysis and in X-ray monochromators for high-energy physics (e.g., synchrotron beamlines).

The worldwide germanium end-use pattern for 2015 (Fig. 2.1), estimated by Guberman (2016), was – by importance, 30% in fibre optics, 20% for catalysts, 20% in IR optics, 15% in electronics/solar applications, and 15% for other purposes (e.g., phosphors, metallurgy, and chemotherapy). In 2014, China remained the leading global consumer and producer of Ge, ensuring more than 70% of Ge world production, which is estimated at 165 t. Stockpiling activities in China have triggered global price increases since 2010 by limiting the amount of germanium available for consumers. The Chinese trade policies have been modified in recent years, such as a 5% export tax placed on GeO_2, in order to reduce the exports of minor metals and favour the export of downstream products (Guberman, 2013).

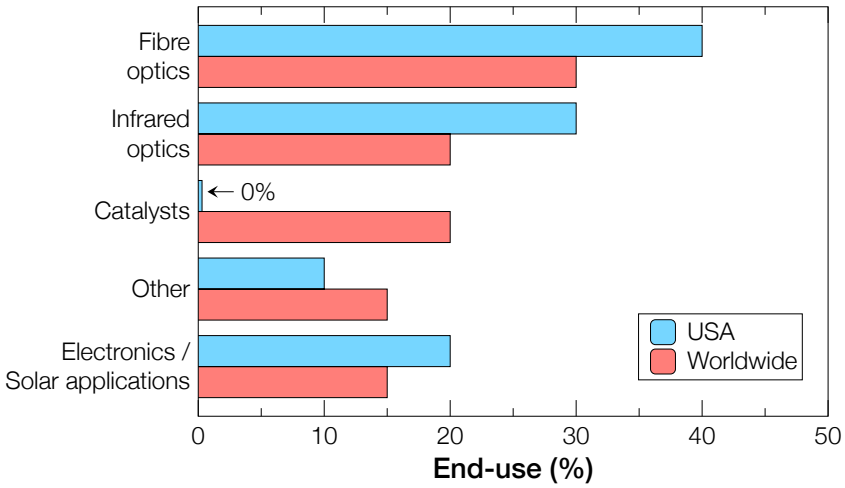

Fig. 2.1 – End-use patterns of Ge worldwide and in the USA in 2015 (data from Guberman, 2016).

2.1.3 Production

Data for global Ge reserves, resources and refinery production are not readily available or are of poor quality (Höll et al., 2007; Melcher and Buchholz, 2013). Primary Ge is chiefly recovered as a by-product from many ore deposit types in hydrometallurgical processes, especially sediment-hosted Pb–Zn and/or Cu ore deposits, generally containing Ge-bearing sphalerite and/or wurtzite (ZnS polymorphs), as shown by the compilations of Bernstein (1985), Höll et al. (2007), and Frenzel et al. (2014). Remarkably, the Apex Mine (Utah, USA) is so far the only mine that has been operated primarily for germanium and gallium production, where Ge was concentrated mainly in gœthite, hematite and limonite (Bernstein, 1986a). Important amounts of primary Ge are extracted from coal ashes, making China one of the major Ge producer since it entered the market around 1985.

Secondary Ge can be produced by recycling. Due to the small quantities in which germanium is used in most manufactured products, little (if any) germanium is recovered from old post-consumer scrap. Recycling from new manufacturing scrap, however, is more widespread in the production of Ge-bearing electronics, fibre optics and optical devices. Worldwide, about 25–35% of the total Ge used is derived from recycled scrap, while in the US economy, more than 50% of the Ge used originates from recycled scrap (Butterman and Jorgenson, 2005; Melcher and Buchholz, 2013).

Before 1978, D.R. Congo, Namibia, Japan and USA dominated global Ge refinery by producing 60–80 t/yr (Fig. 2.2). Afterwards, followed a period of over-production at more than 100 t/yr, led by USA and other western producers, including France (with the Saint-Salvy Zn–(Ge) deposit; Foglierini et al., 1980). Since 2001, China has taken the lead in global Ge refinery production. In 2012, world refinery production is estimated at about 128 t Ge, produced in China (70%), USA (~2%), Russia (~4%), and other countries including Canada, Spain, India, Finland and Australia (Guberman, 2013; Melcher and Buchholz, 2013). In 2014, China produced about 60% of total Ge according to the European Commission (2014).

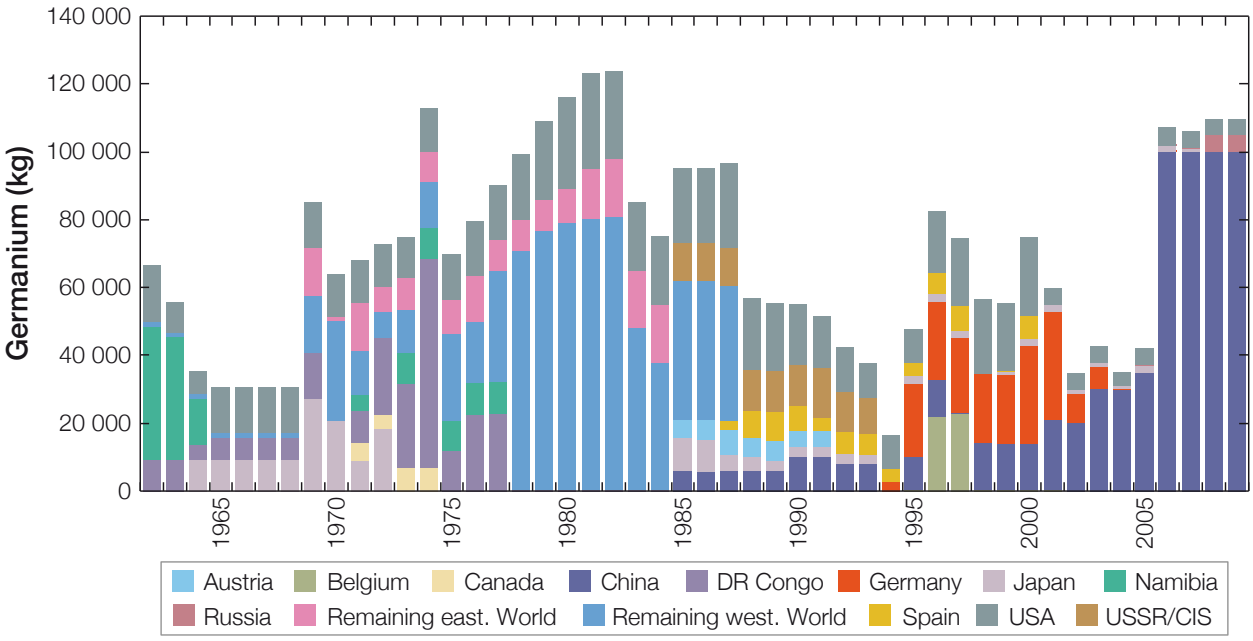

Fig. 2.2 – World germanium production, by country, from 1962 to 2009 (from Melcher and Buchholz, 2013, BGR database).

2.2 Germanium geochemistry

2.2.1 Distribution and geochemical behavior

Germanium concentrations are commonly low in most rocks, and given the analytical difficulties for measuring it, Ge is a widely unreported trace element in most geochemical studies. A most interesting feature about Ge is that it exhibits siderophile, lithophile, chalcophile as well as organophile behaviours and occurs in a wide variety of geologic environments (Bernstein, 1985; Höll et al., 2007).

The *siderophile* behaviour of Ge is mostly expressed through important concentrations (up to 600 ppm) occurring in the iron phase of meteorites and telluric iron. For instance, in composite stony-iron meteorites, Ge is usually found to be enriched in the metal fraction by a 10 to 70 fold relative to the silicate-oxide fraction (Bernstein, 1985). Carbonaceous chondrites (17.0–34.4 ppm Ge) display the highest Ge contents. Ordinary chondrites have lower Ge contents (9–13 ppm Ge), while enstatite chondrites are strongly depleted in Ge (30–50 ppb; Luais, 2015, and references therein; Fig. 2.3). Most remarkably, Ge is enriched in iron meteorites, though its content is highly variable, generally ranging from less than 0.1 ppm up to several hundred ppm, and sometimes up to several thousand ppm, e.g., the exceptional content of 2000 ppm Ge was measured in the Butler meteorite (Wasson, 1966). Ge is therefore a useful trace element for classifying iron meteorites (Bernstein, 1985; Luais, 2015, and references therein). On Earth, Ge is hence thought to be enriched in the core, for which the estimations give 18.7 ppm (McDonough, 2003) and 31–58 ppm (Righter et al., 2011), compared to 7 and 11–21 ppm for the bulk Earth, respectively.

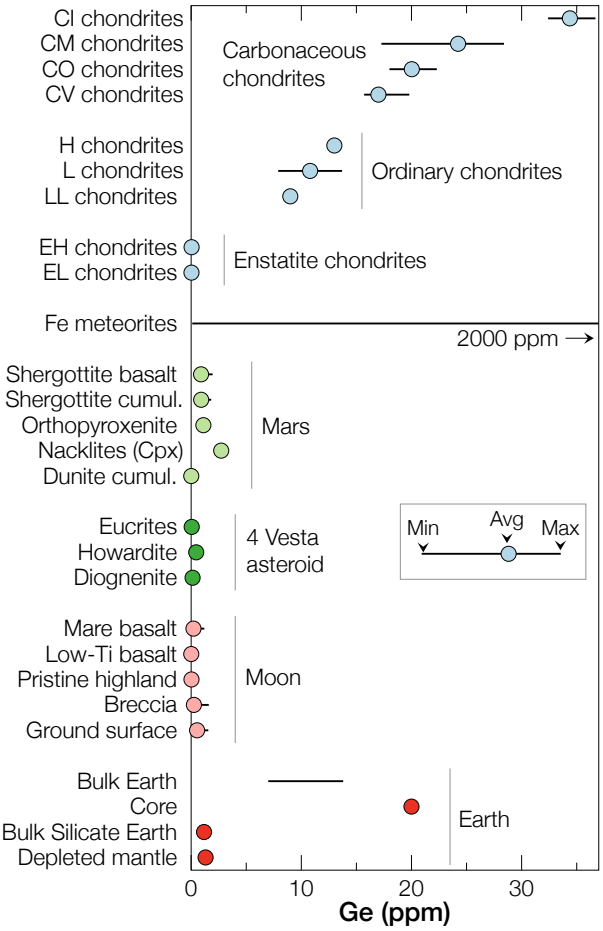

Fig. 2.3 – Ge concentrations in Chondrites and Fe meteorites, Mars, Vesta and Moon rocks Luais (data compiled by 2015), and Earth reservoirs (data compiled by El Korh et al., in rev.). Number of analyses: carbonaceous chondrites, n=28; ordinary chondrites, n=48; enstatite chondrites, n=14; Mars, n=39, Vesta, n=25; Moon, n=206, Earth, n=654.

The *lithophile* behaviour of germanium is indicated by slight enrichments of the bulk Earth crust (about 1.3 ppm) relatively to the primitive mantle (1.1 ppm; Dasch, 1996). Most Ge is largely incorporated in low concentrations in silicate minerals, because of the isovalent substitution by Ge^{4+} of the chemically similar Si^{4+}. Igneous rocks generally host

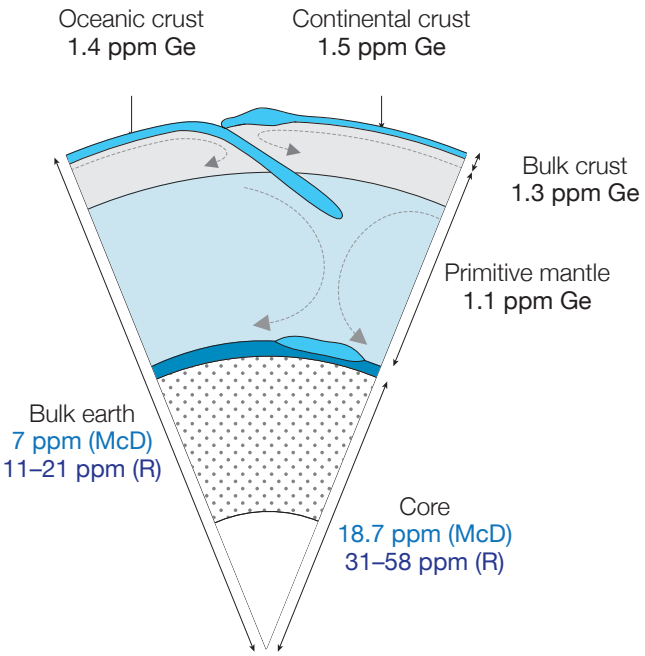

Fig. 2.4 – Ge concentrations in the Earth's reservoirs; oceanic and continental crust (Taylor and McLennan, 1995), bulk crust (updated in Hu and Gao, 2008), primitive mantle (Dasch, 1996), core (McDonough, 2003; Righter et al., 2011) and bulk Earth estimates (McDonough and Sun, 1995; Righter et al., 2011).

0.5 to 6 ppm Ge, with little variations in the Ge content of mafic to felsic rocks, and plutonic to volcanic rock types. However, Ge is found to be slightly enriched in late magmatic differentiates (e.g., muscovite granites) and in other rocks that crystallize in the presence of a high volatile concentration (e.g., pegmatites, greisens and skarns). The alteration of such rocks and the breakdown of their Ge-bearing minerals, mostly micas (especially muscovite) and and other species, including topaz and garnet, may release a significant amount of Ge (Höll et al., 2007). Germanium concentrations in rocks from the Moon, the 4 Vesta asteroid and Mars are generally below the ppm level, except orthopyroxene and clinopyroxene cumulates from Mars, grading 1.1 and 2.7 ppm Ge, respectively (Fig. 2.3).

The *chalcophile* behaviour of Ge, unlike Si, is shown by the systematic occurence of Ge in a variety of sulphide ore deposits, which sometimes, even conduct to the formation of Ge-sulphides. A high sulphidation environments (high fS_2), allowing the formation the thiocomplex $[GeS_4]^{4-}$, is thought to trigger the formation of thiogermanates. Alternatively, in Zn–Pb deposits of low to moderate sulphidation, and often low temperatures, Ge is preferentially incorporated into Zn sulphides (sphalerite and wurtzite). In addition, regardless of the sulphidation state, Ge is often related to Cu- and/or Ag-rich parageneses (Bernstein, 1985). The reader can refer to Section 2.3 for further details on Ge-bearing sulphide deposits.

The *organophile* behaviour of Ge is suggested by its overall enrichment in organic matter-rich environments. Ge is reported to have one of the highest affinities for organic matter of all the elements commonly associated with carbonaceous sediments (Bernstein, 1985), and based on statistical analyses, Ge is the only element for which a consistent organic association can be demonstrated (Höll et al., 2007). Enrichments in organic matter is operated through chemisorptive processes, forming simple and relatively stable organo-complexes (e.g., with lignin and humic acids), which gain progressive stabilisation during lignification/coalification with the formation of chelates or highly condensed aromatic organo-germanium species (Höll et al., 2007; Rosenberg, 2008).

Due to these distinct geochemical behaviors, according to Bernstein (1985), Ge is found to be enriched (1) in Fe–Ni phases (meterorites and Earth core), (2) in Zn-Pb(–Ag)-rich and Cu-rich sulphide ores (sphalerite, Cu-sulphides, sulfosalts, Ge-sulphides), (3) in Iron-oxide deposits (hematite, magnetite, goethite), (5) in oxidized zone of Ge-bearing sulfide deposits (hydroxides, oxides, hydroxy-sulfates, and arsenates), (6) in pegmatites, greisens, and skarns (topaz, garnets, micas), and (7) in coal and lignite (bound to organic matter). A better understanding of this pattern of distbution would require the knowledge of thermodynamic data regarding the stability fields of Ge-bearing minerals, and their solubility with respect to fluids of different nature and temperature–pressure conditions. Thermodynamic data for Ge-compounds are relatively scarce. The stability fields of Ge, GeS_2 and GeO_2 as related to the activities of S_2 and O_2 for different temperatures are presented in Fig. 2.5a–c.

2.2.2 Mineralogy and crystal chemistry

Coordination and bonding properties

Germanium has the electronic configuration $[Ar]3d^{10}4s^24p^2$ and generally occur in the stable form of Ge^{4+} in the environment and natural compounds, whereas Ge^{2+} only exists in synthetic compounds that are usually unstable in atmospheric conditions (Bernstein, 1985; Rosenberg, 2008). The relatively high electronegativity of Ge (2.01 according to Pauling) favours the formations of predominantly covalent bonds with O and even more with S (Bernstein, 1985).

Ge has a strong affinity for the tetrahedral coordination. For instance, in the Earth's crust, most Ge is present in small amounts (up to a few ppm) in silicate minerals due to the isomorphous substitution of Ge^{4+} (39 ρm ionic, 121 ρm covalent) for the chemically similar Si^{4+} (26 ρm ionic, 116 ρm covalent). Notably, germanates and silicates form isostructural compounds. Ge also occur in tetrahedral coordination in Ge sulphides, in which Ge^{4+} forms highly covalent tetrahedral sp^3 hybrid bonds to S (Bernstein et al., 1989; Tettenhorst and Corbato, 1984; Bernstein, 1985), all of which having pseudoisometric derivative of the sphalerite structure. Hence, it is not surprising to commonly find Ge in minor/trace amounts in sphalerite, and other sulphides having sphalerite-like structures, e.g., chalcopyrite, enargite, bornite. In constrast, Ge show a greater tendency for the octahedral coordination than Si. For instance, GeO_2 (argutite) crystallises in the rutile–like structure (r-GeO_2), not in the quartz–like structure (q-GeO_2). Ge is also found octahedral coordination in oxide minerals, e.g., in hematite and goethite (Bernstein and Waychunas, 1987).

Mineralogy

In contrast to Si, the number of Ge minerals is very limited, the most common are the sulphides, such as argyrodite (7% Ge), briartite (14–18% Ge), germanite (6–10% Ge), renierite (4–8% Ge), and the hydroxide, stottite (32% Ge). Other Ge minerals are extremely rare or even unique to one locality. The most significant amounts of Ge therefore occur in non-silicate crustal reservoirs (see Sec.2.3). The minerals encountered in this study are renierite and briartite (with minor respects) from the Kipushi deposit (D.R. Congo), and german-

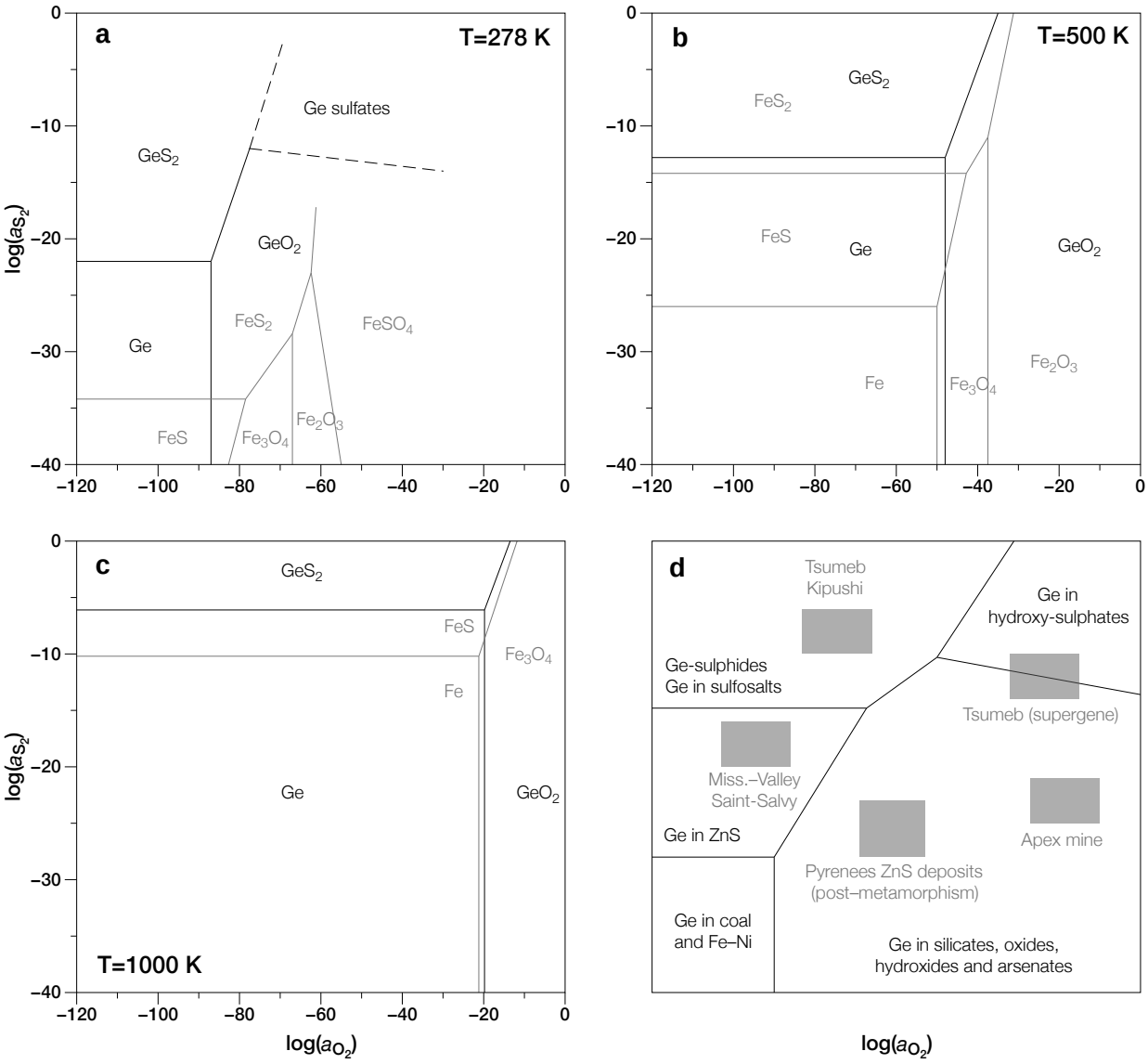

Fig. 2.5 – The known stability fields of Ge, GeS_2 and GeO_2 as related to the activities of S_2 and O_2 at 278 K (**a**), 500 K (**b**) and 1000 K (**c**) at 1 atm. Stability fields of some Fe compounds are shown for comparison. **d**. Schematic diagram proposed for the geochemical behavior of Ge in various geologic environments according to the known stability fields of Ge compounds and natural observations (at ∼300–600 K, 1 atm). Grey boxes corresponds to characteristic Ge-bearing ore deposits, for which further details can be found in Sec. 2.3. Modified from (Bernstein, 1985, and references therein).

ite from the Tsumeb deposit (Namibia). Renierite forms a continuous solid-solution series, $Cu_{10}(Zn_{1-x},Cu_x)(Ge_{2-x},As_x)Fe_4S_{16}$ where $(0 \leqslant x \leqslant 1)$, and passing from the Zn and the As end-member occur through the coupled substitution $Zn^{2+}+Ge^{(4+)} \leftrightarrow Cu^{+}+As^{5+}$ (Bernstein, 1986b; Bernstein et al., 1989). Renierite is tetragonal and has a pseudoisometric derivative of the sphalerite structure type. Briarite, $Cu_2(Fe,Zn)GeS_4$, and germanite, $Cu_{13}Fe_2Ge_2S_{16}$, also have sphalerite-like structures (Imbert et al., 1973; Tettenhorst and Corbato, 1984, , respectively). However, such Ge minerals only form under specific conditions, associated to a restricted number of deposits. Economically, sphalerite, because mined in large amounts, and with concentrations of up to 3000 ppm Ge, associated to a wide bunch of minor/trace elements, is the most important of all Ge-bearing minerals.

Sphalerite

The geochemical features of sphalerite have been investigated for many decades, e.g., the pioneer works of Stoiber (1940) questionned the link between trace element content in sphalerite and its genetic type. Notably, several studies showed a temperature control on Ge and Ga contents in sphalerite (Möller and Dulski, 1993, 1996). A wide range of minor/trace elements can easily substitute for Zn within its tetrahedral sites in sphalerite (Fig. 2.6a), offering valuable by-products in sphalerite processing (e.g. Ge, In, Ga; (Höll et al., 2007)). The presence of some elements (e.g. Ag, Cu) is thought to enhance minor/trace element incorporation. Several studies have pointed out that direct substitution of Zn^{2+} by bivalent cations accounts for the presence of common minor elements in sphalerite, i.e., Fe^{2+}, Mn^{2+}, Cd^{2+}, Co^{2+} or Ni^{2+} (Cook et al., 2009). Johan (1988) proposed a theoretical general coupled substitution mechanism, extended to tri- and tetravalent elements. This mechanism implies that incorporation of these cations in sphalerite is related to the formation of donor–acceptor pairs with monovalent ions.

Copper-sulphides

Germanium is a trace to major component in many Cu-sulphides with sphalerite-type structures (e.g., Fig. 2.6b), in which it is thought to occur as tetrahedral Ge^{4+} (Bernstein, 1985). Strikingly, in deposits containing Cu-sulphides (e.g., bornite, chalcopyrite) or even Ge-sulphides (e.g., renierite, germanite), sphalerite is usually not the major Ge carrier (Höll et al., 2007). Cook et al. (2011) observed that Ge concentrations are typically below the ppm level in bornite, chalcocite and digenite from various deposits, with the exception of bornite from Sasca Montană (Cu–Au skarn, Romania), Radka and Chelopech (high to intermediate sulphidation, epithermal Cu–Au deposits, Bulgaria), which shows is enriched in Ge (means 31, 20 and 6 ppm, respectively). Reiser et al. (2011), however, reported an average Ge concentration of 0.19 wt.% in chalcopyrite from Barrigão (Cu vein-type deposit, Portugal).

The mechanisms by which Ge enters the lattice of chalcopyrite ($CuFeS_2$) is not well understood, it is thought to be incorporated via coupled substitutions in the Fe tetrahedral site towards a stannite group phase such as briartite ($Cu_2(Zn,Fe)GeS_4$). In enargite (Cu_3AsS_4), a coupled substitution $As^{5+}+Cu^{+} \leftrightarrow Ge^{4+}+Zn^{2+}$ towards the renierite join $Cu_4(Zn_{1-x}Cu_x)(Ge_{2-x}As_x)Fe_4S_{16}$ is suggested (Bernstein, 1985). Germanium crystal chemistry in Cu-sulphides remain largely undocumented and needs to be addressed using highly sensitive techniques.

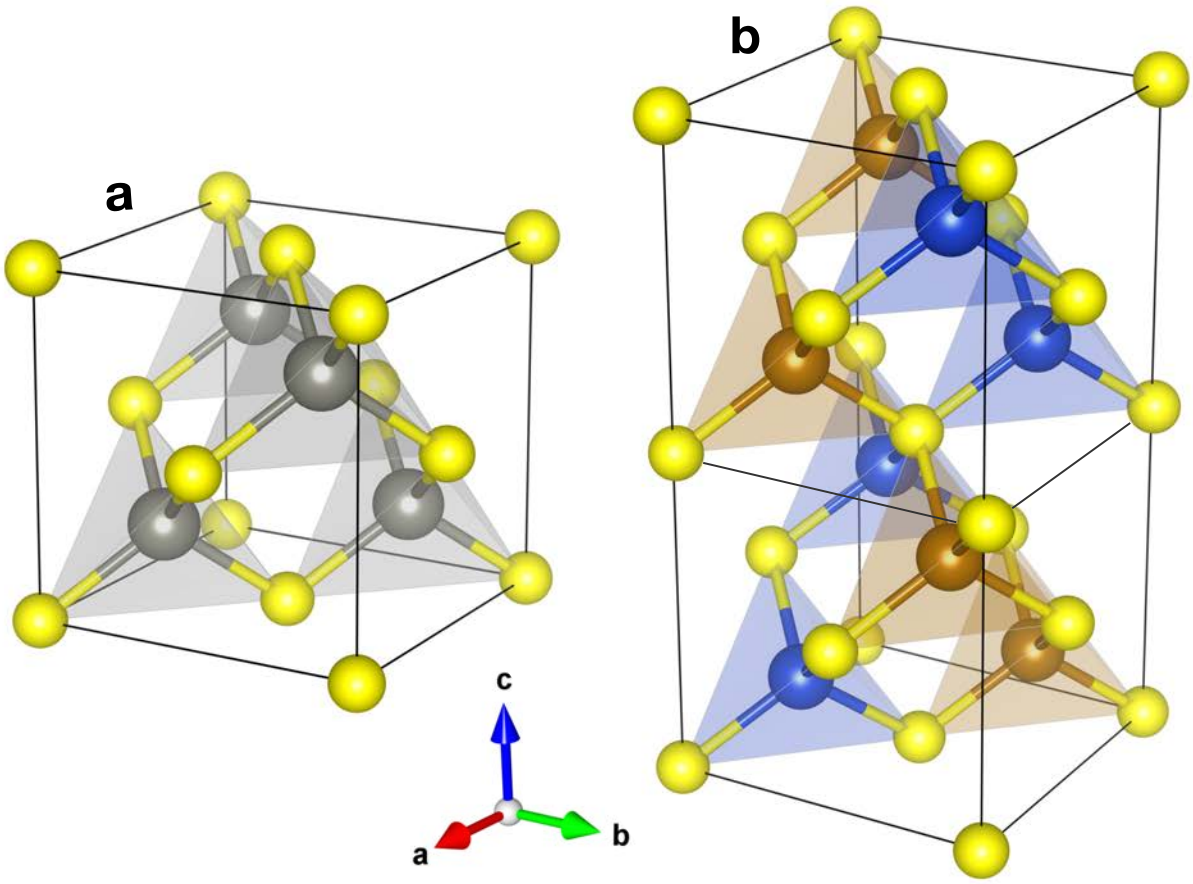

Fig. 2.6 – Crystal structure of sphalerite (a) and chalcopyrite (b). Colors: S, yellow; Zn, grey; Cu, blue; Fe, brown.

2.2.3 Germanium hydrogeochemistry

The chemical behaviour of Ge with respect to aqueous fluids of various natures plays a key role in the solvation, transport and deposition of Ge between different crustal reservoirs, which eventually conduct to the formation of economically-interesting, finite Ge-bearing reservoirs (e.g., in sulphide or carbonaceous deposits). Ge concentrations in river water and seawater is of 0.05 to 0.1 ppb (e.g., Froelich et al., 1985; Murnane and Stallard, 1990). More locally, Ge concentrations of up to 48 ppb have been reported in groundwater of ore deposits, and up to 293 ppb in highly alkaline, high-Na, low-Ca, thermal waters. The partition coefficient of Ge between granitic melts and coexisting aqueous fluids, $D_{\mathrm{Ge}} = [\mathrm{Ge}]_{\mathrm{fluid}}/[\mathrm{Ge}]_{\mathrm{melt}}$, increases with pressure, and preferably in a CO_2-rich fluid than in a (Na,K)Cl-rich fluid (Höll et al., 2007, and references therein).

Aqueous complexes

Similarly to Si, the most important forms of Ge in aqueous solution are germanic acid $Ge(OH)_4^0$ and its dissociation products, $GeO(OH)_3^-$ and $GeO_2(OH)_2^{2-}$. Pokrovski and Schott (1998b) showed that $Ge(OH)_4^0$ is the dominant Ge-bearing species at concentrations up to at least 0.05 m over a wide range of pH (0–8) and temperatures (20–350°C), while $GeO(OH)_3^-$ only forms in alkaline solutions (pH>8–9; Fig. 2.7). The dominant aqueous Ge complex, $Ge(OH)_4^0$, show very little changes in a wide temperature–density (pressure) range (20–500°C, 1.1–0.2 g.cm^{-3}; Pokrovski et al., 2005).

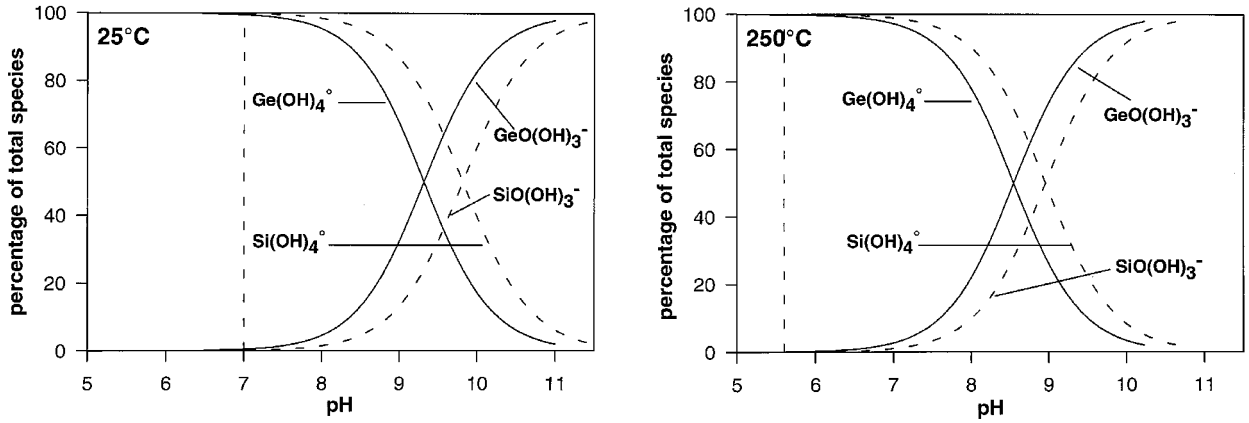

Fig. 2.7 – Distribution of Ge and Si hydroxide species as a function of pH at 25 and 250°C, and P_{sat}. The vertical dashed lines stand for the pH of the neutrality point of water at a given temperature. From Pokrovski and Schott (1998b).

The enrichment of Ge in topaz, and to a lesser extent in fluorite and muscovite, and in F-bearing hot springs, suggest that aqueous Ge fluoride and hydroxy-fluoride species may form, e.g., $[GeFe_6]^{2-}$. Such species have been identified in a number of experimental studies, and they could potentially play a role in Ge mass transfer in fluoride-rich environments, such as those in which greisenization occurs (Wood and Samson, 2006). There is, however, an overall lack of agreement regarding the stoichiometries and stability constants for these species. Chloride complexes do not become important until Cl as high as 4 M (at 25°C). The enrichment of Ge in hydrothermal sulphide deposits, and the formation of Ge-sulphides

minerals at high S activities, suggest the formation of thiogermanate complexes, e.g., $[GeS_4]^{4-}$ (Höll et al., 2007). Such complexes may only occur as reaction intermediates in the Ge-sulphide deposition process in high sulphur activity environments. Ge–chloride and Ge-sulphide complexes are therefore unlikely to play any significant role in the aqueous transport of Ge.

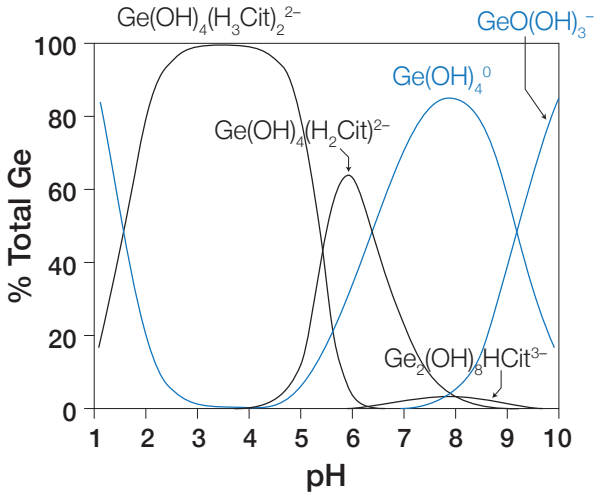

Fig. 2.8 – Distribution of Ge aqueous species at 25°C in the H^+–$Ge(OH)_4$–citric acid system (0.005 M $Ge(OH)_4$ + 0.02 M citric acid + 0.1 M NaCl). It can be seen that Ge-citrate complexes dominate Ge speciation in the pH range of 2–7. From (Pokrovski and Schott, 1998a).

In organic-rich waters, the formation of Ge can form complexes with aqueous organic species, such as methylated Ge species, CH_3–Ge^{3+} or $(CH_3)_2$–Ge^{2+}. In contrast to inorganic Ge species, the methylated complexes are though not to be involved in the biogeochemical cycling of germanium, and that concentrations of these species vary linearly with the salinity of the estuary or ocean (Rosenberg, 2008). In addition, (Pokrovski and Schott, 1998a) showed that in organic-rich surficial waters, Ge may also form complexes of chelate type with a variety of functional groups, e.g., the presence of humic acids can considerably affect Ge speciation in aqueous solution. For example, Fig. 2.8 shows the distribution of Ge aqueous species in the presence of citric acid as a function of pH.

Solubility

In order to fully constrain genetic models of supergene and hydrothermal deposits of Ge, the challenge is to calculate the solubilities of Ge-bearing mineral species. In addition to the knowledge of stability constants of the pertinent aqueous complexes, the solubility products of the Ge-bearing solid phases must be known, as a function of temperature and pressure. However, solubility products are unavailable for most of the rare minerals in which Ge is an essential component, but a substantial amount of data exists for more common minerals in which Ge is incorporated as a minor/trace element (e.g., sphalerite). To calculate the solubility of Ge in solid solution, the solubility products for the pure, end-member phase (commonly hypothetical) containing Ge is required, and a mixing model with which to calculate the activity of this end-member in the solid solution (Wood and Samson, 2006).

Nevertheless, the pure end-member might not be stable. For instance, for Ge in sphalerite (ZnS), the Ge end-member would be a hypothetical Ge-sulphide (i.e., GeS), with the sphalerite structure. The actual GeS is orthorhombic and composed of a double layer structure in which Ge^{2+} occurs in a (3+2)-fold coordination with ionic and covalent bonds (Wiedemeier

and Schnering, 1978), which is far from the cubic, diamond-like structure of sphalerite. In such a case, direct experimental measurements of the solubility product of the end-member phase is irrelevant.

Remarkably, this calculation is possible for Ge-bearing silicates (where Si is partially substituted by Ge) or oxides (using the data of Pokrovski and Schott, 1998b) which include the solubilities of the tetragonal and hexagonal polymorphs of $GeO_{2\,(s)}$. The solubility of the hexagonal polymorph is much higher than that of the tetragonal polymorph (by more that 4 orders of magnitude at 25°C; Fig.2.9a). The tetragonal polymorph would be the stable pure $GeO_{2\,(s)}$ phase in nature and its solubility is independent of pH in most geologic environments (i.e., pH<8; Fig.2.9b). However, if we consider Ge occuring in solid solution in quartz, the thermodynamics of the hexagonal phase are most relevant to solubility calculations. For instance, Pokrovski and Schott (1998b) were able to calculate, as a function of temperature, the $Ge(OH)_{4\,(aq)}/Si(OH)_{4\,(aq)}$ molal ratio in an aqueous solution in equilibrium with a Ge-bearing wollastonite $Ca(Si_{1-x}Ge_x)O_3$ (Fig. 2.10).

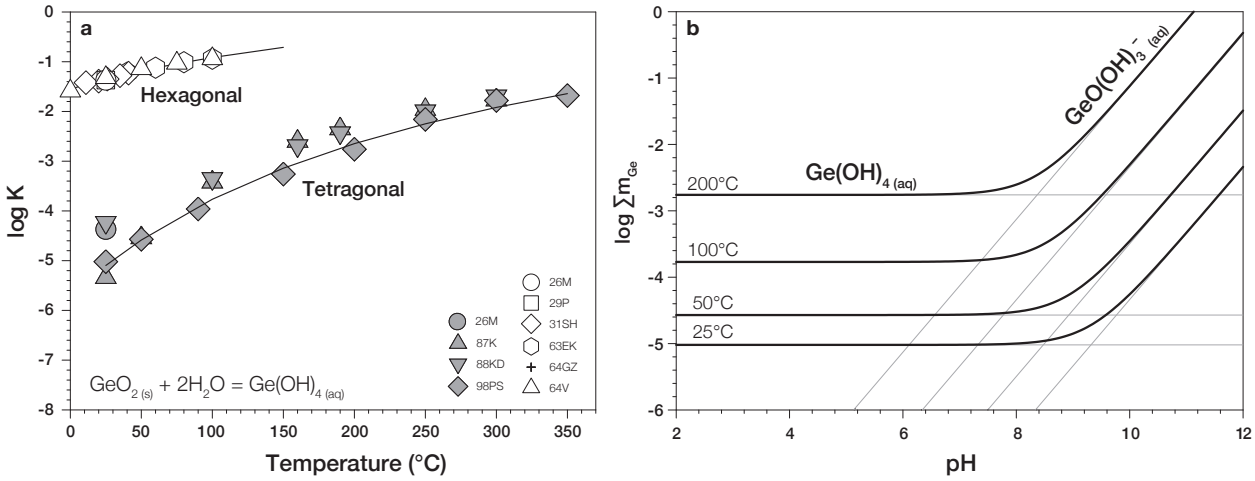

Fig. 2.9 – a. Literature values for the equilibrium constants for the dissolution reactions of hexagonal and tetragonal GeO2 as a function of temperature at SWVP (modified from Wood and Samson, 2006, see references therein). **b**. The solubility of tetragonal GeO_2 as a function of pH and temperature at SWVP. The dotted lines show the concentrations of $Ge(OH)_4^0$ and $GeO(OH)_3^-$ in equilibrium with tetragonal GeO_2 at each temperature. The heavy curves represent the total solubility. Modified from Wood and Samson (2006) after the data of Pokrovski and Schott (1998b).

2.3 Germanium-bearing deposits

Germanium does not form specific ore deposits but instead occurs in a variety of ore deposits of different ages (Fig. 2.11). Reliable Ge data are often lacking in the literature (even for large ore deposits), however, some of the conditions influencing the concentration processes of Ge during the Earth's crust evolution have been inferred (Bernstein, 1985; Höll et al., 2007). The metallogenesis of Ge greatly coincides with the geologic evolution of hydrothermal base-metal deposits (Zn, Pb, and Cu) in which it is largely associated (Table 2.1). The evolution of the atmosphere following the appearance of the photoautotrophic, oxygen-producing

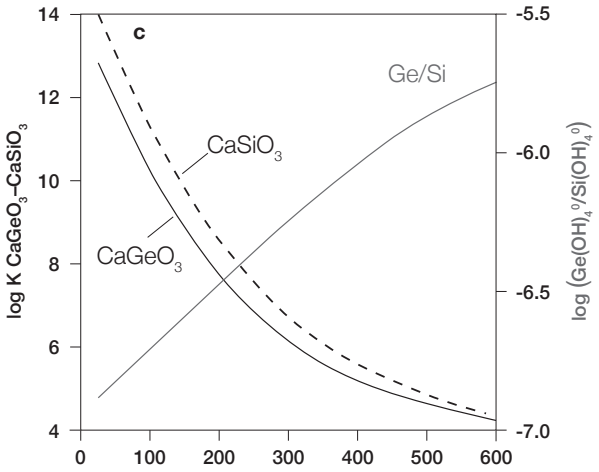

Fig. 2.10 – Log K of $CaSiO_3$ (wollastonite) and $CaGeO_3$, the pure end-member, with the $Ge(OH)^0_{4\,(aq)}/Si(OH)^0_{4\,(aq)}$ ratio in a solution in equilibrium with a Ge-bearing wollastonite containing 1.4 ppm Ge, as a function of temperature at 1 kbar. From Pokrovski and Schott (1998b).

cyanobacteria triggered the oxidation of Fe^{2+} to Fe^{3+} in the oceans around 2.3–2.4 Ga. The formation of Fe^{3+}-hydroxides have facilitated the chemisorptive concentration of Ge and its integration in large amounts of banded iron formations (BIF). The appearance of cellulose-producing eucariotes in Proterozoic time and the transformation of cellulose into lignin and humic acid permitted an enhanced adsorptive mechanism for concentrating Ge in carbonaceous rocks such as lignite, coal and coaly black shales. During the Phanerozoic time, the Ge geochemistry were influenced by the evolution of the biosphere and Ge-bearing organic matter as well as the change from prevailing dolostones to limestones. The requirements for sulfate-reducing bacteria and organic matter to form sulphide species and release Ge, respectively, favoured the slight Ge enrichments occurring in Phanerozoic low-temperature sulphide deposits hosted in organic-rich sedimentary rocks (e.g., shales).

2.3.1 Volcanic-hosted massive sulphide deposits

Volcanic-hosted massive sulphide (VHMS) deposits, including those of the volcanogenic type (VMS), occur in submarine volcanic rocks of various ages and tectonic settings, from Archean volcanic strata to currently active seafloor hydrothermal systems. Such deposits are of syngenetic or early diagenetic origin, and related to the interaction of hydrothermal fluids with volcanic rocks and overlying sediment rocks in submarine settings. They are generally characterised by massive or banded stratiform to lens-like sulphide orebodies lying above strongly altered pyrite-dominated feeder-zones (Large et al., 2001). Briefly, their classification is based on ore composition (Zn, Cu, Pb, Ba), host lithology, and tectonic setting, which encompass (i) the Cyprus-type (Cu–Zn), hosted in ophiolites, (ii) the Abitibi-type, hosted in mafic–felsic volcanic sequences, (iii) the Kuroko-type (Cu–Zn–Pb(–Ba)), occurring in bimodal volcanic suites in island arc or back-arc setting, and other hybrids or sub-types (Franklin et al., 1981).

The few data reporting Ge concentrations in Archean Abitibi-type ore deposits does not indicate the presence of significant amount of Ge. In the giant VHMS of Kidd Creek (Ontario, Canada), traces of Ge are reported in low-temperature Zn-rich ores whereas the high-temperature Cu-rich ore is devoid of Ge (Hannington et al., 1999). In the Bousquet 2 Mine (SE Greenstone Belt, Quebec, Canada), up to 85 ppm Ge are reported in Cu–Zn ores samples, expressed in renierite and mawsonite (Tourigny et al., 1993).

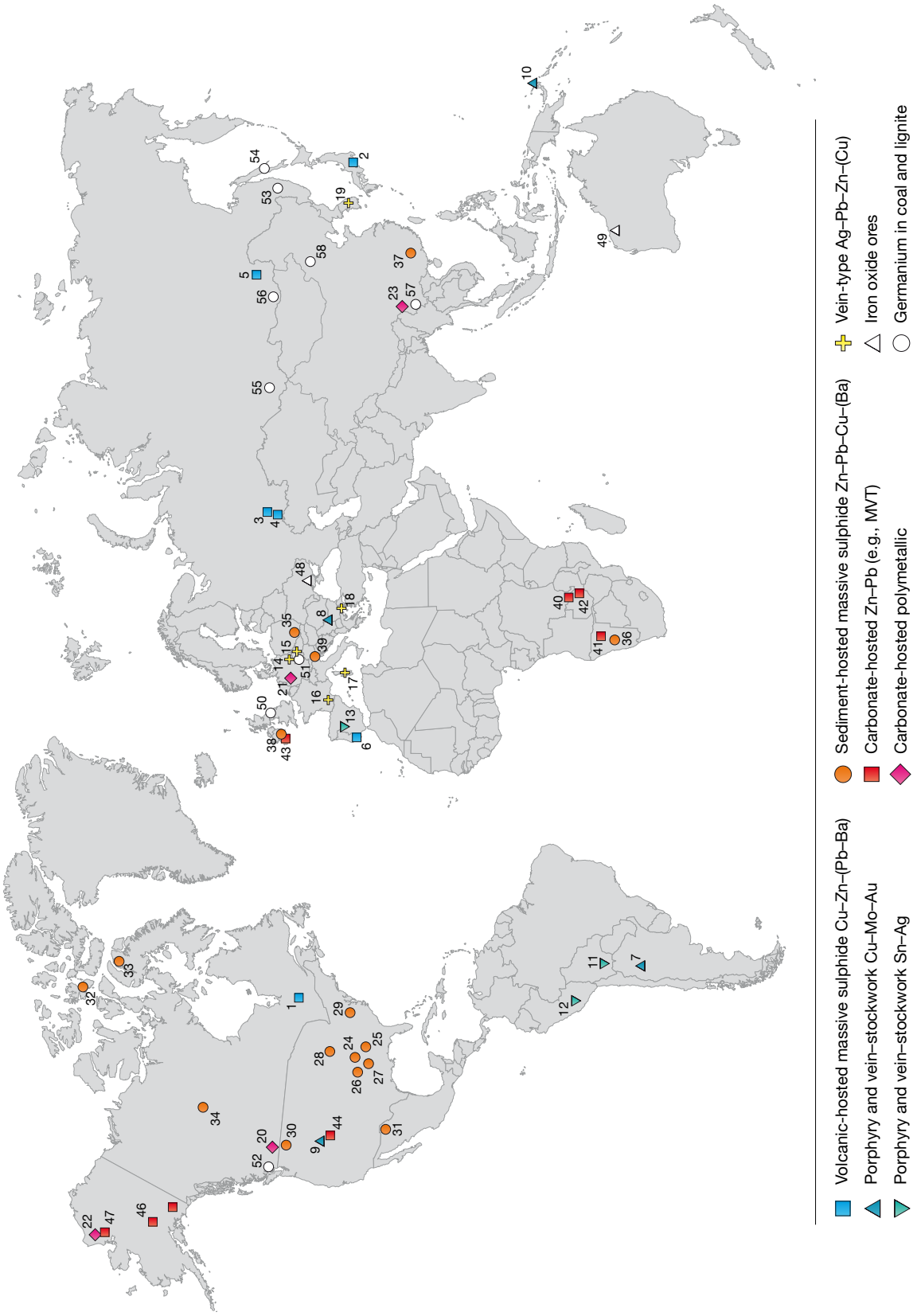

Fig. 2.11 – Germanium-bearing ore deposits (*continued on the next page*)

Fig. 2.11 – Volcanic-hosted massive sulphide (VHMS) Cu–Zn(–Pb)(–Ba) deposits: 1 Abitibi–Belt: Kidd Creek, Noranda, Bousquet 2 Mine, Canada; 2 Kuroko-type (and Besshi-type) deposits, Japan; 3 Gaiskoje, Russia; 4 Bakr Tau, Russia; 5 Gorevskoe and Ozernoe, Russia; 6 Iberian Pyrite Belt: Neves Corvo, Portugal. **Porphyry and vein–stockwork Cu–Mo–Au deposits**: 7 Capillitas, Argentina; 8 Bor, Serbia, and Chelopech, Bulgaria; 9 Bingham, USA; 10 Lihir Island, Papua-New Guinea. **Porphyry and vein–stockwork Sn–Ag deposits**: 11 Potosi, Colquechaca, and Porco, Bolivia; 12 Sayapullo, Peru; 13 Barquilla, Spain. **Vein-type Ag–Pb–Zn(–Cu) deposits**: 14 Freiberg, Germany; 15 Kutna Hora and Pribram, Czech Republic; 16 Noailhac – Saint-Salvy, France; 17 Sardinia, Italy; 18 Kirki, Greece; 19 Wolyu, Korea; **Sediment-hosted massive sulphide (SHMS) Zn–Pb–Cu(–Ba) deposits**: 20 Sullivan, Canada; 21 Meggen, Germany; 22 Red Dog Mine, Alaska, USA; 23 Jinding, China. **Carbonate-hosted base metal (Zn–Pb) deposits** (Mississippi Valley-type, MVT; Irish-type, IRT; and Alpine-type, APT): 24 Central Missouri, USA; 25 Southeast Missouri (Old Lead Belt, Viburnum Trend, Indian Creek), USA; 26 Tristate District, USA; 27 Northern Arkansas, USA; 28 Upper Mississippi Valley (Illinois–Wisconsin), USA; 29 Elmwood–Gordonsville, USA; 30 Pend Oreille, USA; 31 Tres Marias Mine, Mexico; 32 Polaris Mine, Canada; 33 Nanisivik, Canada; 34 Pine Point, Canada; 35 Upper Silesia, Poland; 36 Mount Aukas, Namibia; 37 Fankou, China; 38 Irish-type: Navan, Lisheen, Silvermines, Galmoy and Tynagh, Ireland; 39 Alpine-type: Bleiberg, Austria; Cave de Predil, Italy; Mezica and Topla, Slovenia. **Carbonate-hosted polymetallic Cu–Pb–Zn–Ge deposits of the Kipushi-type**: 40 Kipushi, Democratic Republic of Congo; 41 Tsumeb, Tsumeb West, Kombat and Tschudi, Namibia; 42 Kabwe, Zambia; 43 Gortdrum, Ireland; 44 Apex Mine, USA; 45 Kennecott Mine, Alaska, USA; 46 Ruby Creek, Alaska, USA; 47 Omar, Alaska, USA. **Iron oxide ores**: 48 Kremenchuk–Krivoi Rog, Ukraine; 49 Hamersley Range, Australia. **Germanium in coal and lignite**: 50 Durham Coalfield, England; 51 Plzeň, Czech Republic; 52 Lang Bay, Canada; 53 Shkotovskoye and Spetsugli, Russia; 54 Sakhalin Island, Russia; 55 Kuzbas Basin, Russia; 56 Chitinskaya Basin, Russia; 57 Lincang, China; 58 Xilinhaote, China. Modified from Höll et al. (2007).

In the Cu–Zn–Pb–Ba ores from Kuroko-type deposits in Japan, up to 370 ppm Ge are reported in sphalerite and the presence of renierite and Ge-bearing bornite (e.g., Shakanai deposit) and colusite (e.g., Ezuri Kuroko deposit) have been described (Shikazono, 2003). Among the Kuroko-type VMS deposits of the Iberian Pyrite Belt (IPB, Spain and Portugal), 10 to 60 ppm Ge have been measured in the giant Neves-Corvo polymetallic deposit (Portugal, Oliveira et al., 1997). The few Ge data available for VHMS deposits in the Ural Mountain Range (Russia) report 25 ppm Ge in sphalerite (Gaiskoye and Bakr Tau Cu–Zn deposits) and in bornite-rich ore. Ge occur among the by-products of Zn concentrates from the Gorevskoe Pb–Zn deposit and appear in the mining project of the giant Ozernoe Zn–Pb deposit (Avdonin and Sergeeva, 1999).

Huge reserves/resources are predicted for VMS/VHMS deposits, providing major sources of the world's Zn, Cu, Pb, Ag and Au, but they contain only low to moderate amounts of Ge (average content far below 100 ppm), from which Ge is a by-product, along with Cd, In, Ga, Sn, Sb, Bi, and many other elements (Höll et al., 2007).

2.3.2 Porphyry and vein–stockwork deposits

In porphyry and vein–stockwork Cu–Mo–Au deposits, the by-products generally include Rh, Se, Te, and In. Germanium is associated with ores hosted in the peripheral zones of porphyry systems, including late-stage epithermal veins, stockworks and breccias, in which it occurs in Cu, Sn and Zn sulphides. Ge is commonly enriched in bornite (up to 1000 ppm Ge), enargite, tennantite, luzonite, stannite, and covellite (e.g., at Bor, Serbia, at Chelopech, Bulgaria, at Bingham, Utah, USA, and at Chuquicamata, Chile; Höll et al., 2007).

In the Bor deposit (Banatitic Magmatic and Metallogenetic Belt, Serbia), Ge was reported in microphases such as germanocolusite, germanite, and Ge-bearing arsenosulvanite (Ciobanu et al., 2002; Cook et al., 2002). In the Chelopech high-sulphidation epithermal Cu–Au deposit (Panagyurishte district, Bulgaria), germanite, renierite, germanocolusite, and Ge-bearing arsenosulvanite have been described (Bonev et al., 2002). In the Landolam deposit (Lihir Island, Papua New Guinea), 550 ppm Ge has been reported in chalcopyrite from a hydrothermal breccia, and 120 ppm Ge in tennantite of a late-stage silicate–pyrite vein (Müller et al., 2002).

The Capillitas diatreme (Catamarca Province, Argentina) host large porphyry Cu–Au deposits and related epithermal vein-type deposits. The epithermal veins are hosted in rhyolite, ignimbrite and granite. Several stages of mineralization were identified, which show a complex polymetallic paragenesis with a number of valuable trace metals, including Ge. Low- and high- sulphidation environments have been identified but Ge occurs mainly in the former. The low-sulphidation paragenesis occurs in remote veins and consists of galena, sphalerite, chalcopyrite, pyrite, Ag-bearing minerals, rhodochrosite, barite and quartz. Ge occurs in argyrodite and is along with native silver, acanthite, proustite and pearceite (Paar et al., 2004; Paar and Putz, 2005).

Another type of porphyry and vein–stockwork includes Sn–Ag deposits. They mainly consist of stockworks and a set of ore veins in subvolcanic felsic intrusions (chiefly dacite to rhyodacite of A-type to S-type). Ge is an accessory component of ore deposits in the Bolivian Ag–Sn belt (Höll et al., 2007). Argyrodite, associated with Ag-sulphides and Ag-sulphosalts has been reported in Colquechaca. Argyrodite and Ge-bearing Sn minerals have been described at Potosi, Chocoya-Animas, Tatatsi-Portugalete and other Ag–Zn–Pb–Sn deposit of this region (Moh, 1976; Bernstein, 1985). In the Sn-bearing polymetallic Sayapullo ore deposit (Cordillera Occidental, Peru), concentrations of up to 310 ppm Ge and 855 ppm Ga have been reported (Soler, 1987). Of interest, Pascua et al. (1997) discovered the unique occurence of barquillite $Cu_2(Cd,Fe)GeS_4$ in Sn–Ge–Cd–Cu–Fe-bearing sulphides and sulfosalts from the vein-type deposit of Barquilla (Salamanca, Spain). In addition, the Ag–Zn–Pb–Sn Porco deposit (Bolivia) host vein-like mineralisations in which a high-grade Ge ore occur. Ge is related to argyrodite, the latter being associated with a high-grade Ag mineralisation and galena which yielded bulk contents of up to 2000 ppm Ge (Paar and Putz, 2005).

2.3.3 Sediment-hosted massive sulphide deposits

Sedimentary-hosted massive sulphide (SHMS) deposits, including sedimentary-exhalative (SedEx) deposits, are mostly stratiform deposits of syngenetic or early diagenetic origin, and related to the interaction of hydrothermal fluids with clastic sediments. Such deposits are hosted in basinal sedimentary rocks (marine and clastic, including black shales) along continental margins or in intracratonic rift settings. They form massive to semi-massive accumulations of sulphide and sulphate (e.g., barite) minerals as stacked, lens-like, tabular bodies, on or below the seafloor. The mineralisation is concordant and continues laterally into distal sedimentary facies, where it expresses as minor sulphides, barite, iron oxide, chert and carbonates. The lack of clear magmatic affiliation is one of the distinguishing features between the SHMS-type deposits and the, otherwise often similar, VHMS-type deposits (Sangster, 1990; Goodfellow et al., 1993; Sangster, 2001).

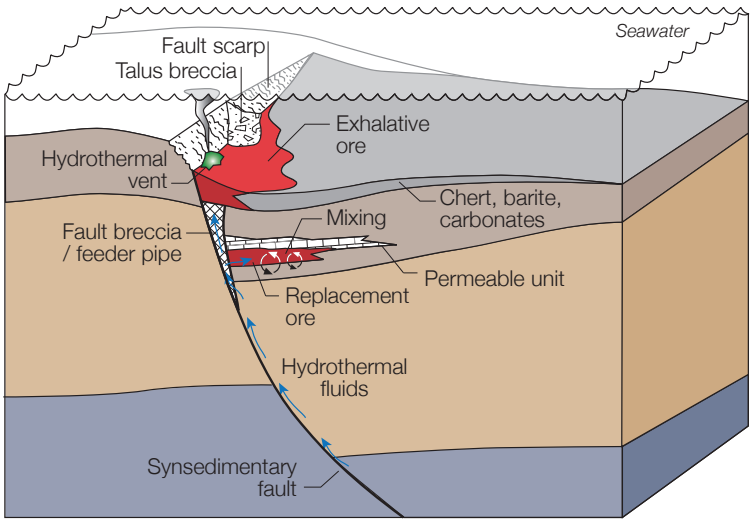

Fig. 2.12 – Typical geological setting and features of a SedEx deposit. Modified from Wilkinson (2014).

SHMS deposits are among the largest Pb–Zn deposits worldwide, and examples from the Proterozoic to the recent seafloor are known. Most of these deposits contain only low to moderate Ge concentrations, usually below 50 ppm, in Zn sulphides from Proterozoic SHMS (e.g., Broken Hill, Australia; Sullivan, Canada), and Phanerozoic deposits (e.g., Meggen and Rammelsberg, Germany; Graz, Austria; Höll et al., 2007, and references therein). Sandstone-hosted Zn–Pb(–Ba)(–F) deposits, usually Pb-dominated, are relatively poor in Ge, with the exception of the giant Zn–Pb Jinding deposit (Yunnan, China). Sphalerite, galena and pyrite form the main paragenesis, along with a significant amount of celestine and barite. Ge concentrations of up to 75 ppm have been reported in sphalerite, though they are usually of few tens of ppm (Ye et al., 2011; Meng et al., 2015).

The Red Dog Zn–Pb–Ag district (Brooks Range, Alaska) is an exceptional Ge-rich SHMS deposit. It is the most productive Zn mine district in the world as well as the largest source of Ge in the U.S.A. Strata-bound massive sulphide ore-bodies are hosted in the Carboniferous Kuna Formation which consists of finely laminated, black, siliceous and carbonaceous shale and mudstone with locally abundant carbonate turbidites. Sulphide deposition took place in a passive continental margin under extensional tectonic setting, in anoxic bottom waters with evidences of high organic matter production. The reserves are estimated to a total of 140.6 Mt grading 16.6% Zn and 4.6% Pb. The massive sulphide paragenesis consists

primarily of sphalerite and galena, with accessory iron sulphides, in a quartz- or barite-rich gangue. The deposition comprise several stages, including early precipitations, hydrothermal recrystallization, replacements, and late-stage remobilisations along with thrusting processes during the Brookian orogeny (Leach et al., 2004; Kelley et al., 2004). Sphalerite is the main Ge carrier. Of the four sphalerite deposition stages, Ge concentrations range 1.5–426 ppm, with an median around 145 ppm. Late stage sphalerite is reported to host higher Ge concentrations than early sphalerite. An average grade of 60 ppm Ge has been reported in zinc concentrate from the 29 Mt of mined ore (Kelley et al., 2004). Whole-rock geochemical analyses of unaltered and unmineralised Paleozoic host lithologies (e.g., shales, black shales, cherts) report Ge concentrations of up to 3.2 ppm. Altered wall rocks with Ge averaging up to 6.5 ppm, with a series of anomalies in Zn, Pb, Tl, As, Sb, and Eu, recommended for mineral exploration (Slack et al., 2004). Stable isotope data (Zn, S) and their interpretations are reported in Sec. 2.4.3.

2.3.4 Carbonate-hosted deposits

Carbonate-hosted deposits are low-temperature (commonly T<250°C) Zn–Pb deposits, characterised by epigenetic, stratiform to lens-shaped, massive, stockwork-like or disseminated deposits, often irregular in shape. The ore is hosted in stable carbonate platforms (chiefly dolostones, or limestones, with possible shales), without any obvious relationship to contemporary magmatic activity. The ore mineralogy is relatively simple, as characterised by sphalerite, galena, fluorite, barite, with dolomite, calcite, and quartz. The ore-forming hydrothermal fluids are usually characterized by temperatures below 250°C (mostly 100–150°C) and salinities in the range of 10 to 30 wt.% NaCl eq. (i.e., brines from evaporated seawater or evaporite-derived fluids), associated to large-scale migrations in deep sedimentary basins with basement/cover interactions. Mixing with other fluids, e.g., seawater or meteoric water, may play an important role in the precipitation mechanisms. Favourable conditions for MVT mineralization are generally met in orogenic forelands and adjacent thrust belts, or possibly in extensional settings. Carbonate-hosted Zn–Pb deposits occur worldwide, from the early Proterozoic to Cenozoic (Höll et al., 2007).

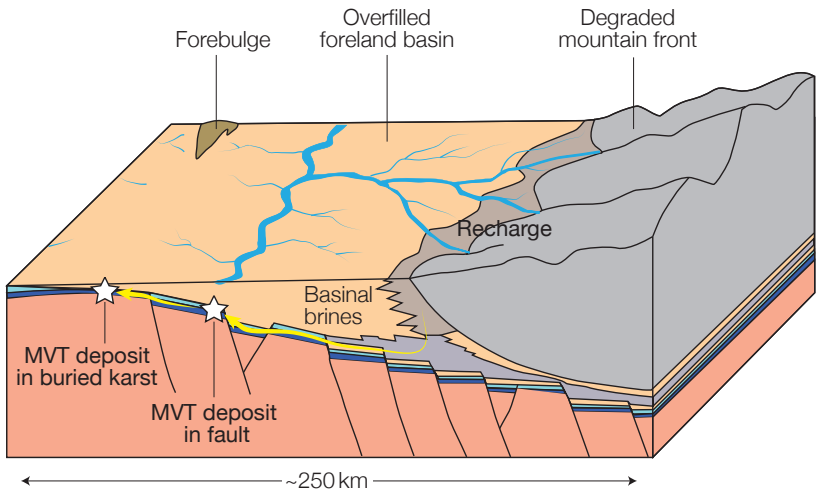

Fig. 2.13 – Tectonic setting for MVT ore genesis at the post-collisional orogenic stage when the foreland basin has filled, which creates a topographic slope toward the previously exposed forebulge region. Permeable carbonates are ideal host rocks for mineralisation that is precipitated from connate brines migrating away from the eroding mountain belt. Redrawn from Bradley and Leach (2003).

Mississippi Valley-type deposits (MVT) occur in platform carbonate sequences at flanks of basins or in foreland thrust belts (Fig. 2.13). They have been forming since the Proterozoic and one of their characteristic feature is sulphur originating from thermochemical sulfate reduction (TSR, $\delta^{34}S > 0\,‰$) (Sangster, 1990; Leach et al., 2001). Most of them are generally poor in Ge, however, those with large Zn tonnages and enhanced Ge contents may provide a significant Ge production. Ge occurs in sphalerite and wurtzite, with notable correlation with other trace to minor elements such as Ga, Cu or Ag. The classic major MVT districts in the U.S.A. contains moderate Ge concentrations(Höll et al., 2007). Viets et al. (1992) showed a correlated enrichment of Ge (up to a few hundreds of ppm), Ga, and Cu in the sequences of light-colored sphalerite (Northern Arkansas, Tristate and Central Missouri). The Elmwood-Gordonsville Zn–Pb district (Tennessee, U.S.A.) contained an average grade of about 400 ppm Ge in Zn concentrates (Misra et al., 1996). The Pend Oreille deposit (Washington State, U.S.A.) is predicted to become the second major source of Ge in the U.S.A. after the Red Dog district, due to a large amount of Ge-rich Zn concentrate. Data for Ge concentrations remain lacking or undisclosed (Höll et al., 2007). The deposits of Polaris, Pine Point and Nanisivik (Arctic Canada) show commonly moderate Ge contents, although up to 400 ppm Ge has been reported in the latter, and being correlated to Ag (Leach et al., 2001). The MVT deposits from the Upper Silesian district (Poland) have Ge grades below 100 ppm in Zn concentrates, primarily in sphalerite, in which it shows correlation with Pb, Tl, and As. Of note, ore mineralization involve coal field water and the formation of Ge-humate is thought to be responsible for the low Ge grades (Höll et al., 2007).

Irish-type deposits (IRT), which are mostly characterised by a sulphur source dominantly bacteriogenic (BSR, $\delta^{34}S = -15 \pm 10\,‰$), host from a few tens ppm Ge in sphalerite (Navan group), to above 100 ppm Ge (Silvermines–Lisheen group, southern Ireland; Wilkinson et al., 2005a). In the Lisheen deposit, Wilkinson et al. (2005b) reported 400–900 ppm Ge in sphalerite, 200–1300 ppm in galena, and 200–1000 in tennantite, high Ge content being associated to enhanced Ag and Cu. The deposition model involve rapid supersaturation, caused by fluid mixing, at relatively high temperature (about 240°C). Metal-bearing solutions leached the basement (Zn, Pb, Fe, Cd) was therefore mixed with shallow, saline (about 25 wt.% NaCl eq.) and H_2S-rich (bacteriogenic) formation waters. Minor metals (Cu, As, Ni, Co, and perhaps Ge) are thought to have been acquired from the hydrothermal alteration of the footwall Old Red Sandstone.

Alpine-type deposits (APT) are mostly consituted by the four large carbonate-hosted Zn–Pb of the Alps, namely, Bleiberg (Austria), Mežica (Slovenia), Cave de Predil and Salafossa (Italy). All of them show characteristics relatively similar to the Irish-type deposits, mostly due to the bacteriogenic sulphate origin ($\delta^{34}S < 0\,‰$). The mineralisation, mainly consisting of sphalerite and galena, were affected by burial and locally by metamorphism during the Alpine orogeny (Schroll, 2005). Of note, Möller and Dulski (1993) constructed their Ga/Ge sphalerite geothermometer in samples from Bleiberg, suggesting that metals were leached at low temperatures (about 100°C). The latter has never been successfully used elsewhere. At Bleiberg, Ge concentrations of 160–550 ppm have been reported, with significant enrichments in late-stage botryoidal sphalerite (up to 1500 ppm), which contrasts with Ge-depleted recrystallised sphalerite. About 200 ppm Ge are reported in the sphalerite concentrate (Schroll, 2005). At Mežica, higher Ge contents are described in fine-grained sphalerites from the first and last mineralising stages (about 200 ppm in Zn concentrate), and at Cave di Predil, the highest Ge concentrations occur in the last-stage

mineralisation in botryoidal sphalerite (500 ppm Ge in the Zn concentrate). A Ge–Tl–As correlation group was observed in these Alpine deposits, negatively correlated with a Cd–Sb–Ga group. Moreover, an upper crustal origin of Ge, As and Tl was inferred from Pb isotope data (Kuhlemann et al., 2001).

Kipushi-type deposits (KPT) consist of epigenetic, massive, pipe-like to tabular orebodies, hosted in dolomite, limestone and metamorphic equivalents. The main, usually Cu–Pb–Zn, mineralisation is often associated with rare elements such as Ge, Ga, Ag, In, As, Cd, Sn, Co, Ni, Sb, Mo, Re, V, W and Au. Common characteristics of KPT deposits involve a high sulphidisation mineral assemblage, e.g., marked by the presence of enargite, tennantite–tetrahedrite, colusite, and thiogermanates; an irregular shape – they are often discordant and elongated; the proximity to a redox boundary, e.g., between reduced carbonates and oxidised clastic sediments; and the presence of evaporites levels, which enhanced brine salinity and provided sulphur. Host rocks are inherited from intracratonic platform and rifted continental margin sedimentary sequences. KPT deposits are associated to basinal and orogenic fluid circulations at relatively high-temperature (250 to 450°C). They generally occur in the vicinity of MVT Zn–Pb and stratiform Cu deposits, with which they share a number of common features. The main ore minerals are sphalerite, chalcopyrite, galena, bornite, chalcocite, tennantite–tetrahedrite and enargite. In particular, Ge concentrations in sphalerite are usually moderate (mostly below 100 ppm Ge), and therefore, sphalerite is typically not the major Ge host. The most significant Ge carriers are the thiogermanates, renierite, germanite, briartite, argyrodite and germanosulvanite. High concentrations of Ge are also reported in stannoidite, enargite and tennantite–tetrahedrite (Melcher, 2003; Kampunzu et al., 2009).

Kipushi-type deposits include the polymetallic sulphide deposits of the African copper-belt, among which the major deposits of Tsumeb (Namibia), Kipushi (D.R.Congo) and Kabwe (Zambia). Fluid transport and ore deposition within host carbonates resulted from fluid expulsion during (∼530–680 Ma, e.g., Tsumeb, Kabwe) of after (∼455 Ma; e.g., Kipushi) tectonic movements associated with the Pan-African orogenesis (Schneider et al., 2007; Heijlen et al., 2008; Van Wilderode et al., 2013). Germanite and renierite-rich ores, locally abundant at Tsumeb and Kipushi, respectively, are thought to have formed in early stages of Cu sulphide precipitation (De Vos et al., 1974; Dimanche, 1974; Intiomale and Oosterbosch, 1974; Melcher, 2003; Heijlen et al., 2008). Remarkably, the formation of KPT deposits in the African copper-belt are related to an extreme climatic signature (Snow ball Earth), associated with enhanced production of organic matter in Neoproterozoic time (Melcher, 2003). For the Kipushi deposit, further details are given in Sec. 4.3 and the trace element features of sphalerite and Cu-sulphides are presented in Sec. 5.3.2.

Other examples of Ge-bearing KPT deposits can be found outside Africa. The deposits of Apex (Utah, U.S.A.) is somewhat unique but displays the features of KPT deposits. Though the ore consist of a supergene, oxidised mineral assemblage of iron oxides/hydroxides, the primary ore was composed of pyrite, galena, sphalerite and chalcopyrite, preserved as relics. The significant abundance of in Cu, Ge, Ga and As suggests the former presence of germanite, renierite and gallite in the primary ore (Bernstein, 1986a). Other KPT deposits includes these of Kennecott, Ruby Creek and Omar (Alaska, USA) and Gortdrum (Ireland). Further details are available in the review of Höll et al. (2007).

Finally, high Ge concentrations are reported in supergene, oxidation zones, of KPT deposits, most particularly, at Tsumeb and at the Apex Mine. The oxidation, caused by

meteoric water infiltrations, altered the thiogermanates (mostly germanite and renierite) into secondary Ge-bearing species such as Ge oxides (brunogeierite – that was previously thought to host Ge^{2+}, otjisumeite, bartelkeite), Ge hydroxides (stottite, manganostottite) and Ge hydroxy-sulphates (itoite, fleischerite, schaurteite), and a variety of other Ge-bearing secondary minerals (Intiomale and Oosterbosch, 1974; Melcher, 2003). For instance, goethite was the most important ore mineral for Ge at the Apex mine, with Ge concentrations of up to 5310 ppm, along with hematite, containing up to 7000 ppm Ge (Bernstein, 1986a).

2.3.5 Vein-type deposits

Very typical occurences of Ge-bearing deposits are of the vein type Ag–Pb–Zn. Vein-type deposits are of clearly epigenetic origin. Somewhat heterogeneous, they are hosted in sedimentary or magmatic rocks, as well as their metamorphic equivalent, and they are found in different tectonic settings. They are commonly structurally controlled and result from space-filling deposition processes rather than replacement processes. The filling occurs within steeply dipping faults and fractures. Some are related to igneous intrusions or metamorphic processes, while others lack such clear indications of their origin (Frenzel et al., 2014).

The polymetallic Freiberg ore deposit (Saxony, Germany), from which Ge was first isolated, host Ag–Pb–Zn(–Cu) mineralization with a substantial Ge enrichment. In almost the entire mined Zn ore, Ge was estimated at only 1 to 3 ppm, but a notable amount of Ge, estimated at about 100 ppm, was in a few part of the Zn ore that was interpreted as a late-stage, low-temperature, Ag-rich mineralisation. Here, Ge was concentrated mainly in argyrodite and botryoidal Zn sulphide. Similarly, at Wolyu (South Korea), the mineralisation occurs in polymetallic ore veins in Cretaceous sedimentary and volcanic rocks, and contains galena, sphalerite, chalcopyrite and electrum. A late, low-temperature mineralising stage is associated to the deposition of argyrodite. Sphalerite is the Ge carrier, though in variable concentrations, in the deposits of the Harz Mountains (Germany) and the Pribram ore district (Czech Republic).

The Noailhac – Saint Salvy Zn–Ge–Ag–Pb–Cd deposit (Tarn, France), was one of the major Ge source in western Europe (20% of the world's Ge before 1980), with a production of about 500 t Ge for a total of 547 300 t of Zn concentrate grading 750 ppm Ge (Cassard et al., 1994). The deposit is hosted within the Cambrian black schists of the pre-Variscan basement. The vein-system develops against a late-Variscan granite batholith in which the mineralised, subvertical vein structure is about 10 km long, for an average thickness of 25 m. Several mineralising stages are described, from skarn to low-temperature hydrothermal ore mineralisation. The deposit probably formed in at the late Triassic–early Jurassic transition (about 180 Ma) (Munoz et al., 1994; Marignac and Cuney, 1999). The sphalerite of the economically important mineralising stage, and shows exceptional Ge concentrations, reaching up to 2500 ppm (Barbanson and Geldron, 1983), and strong compositional zonings (Johan, 1988). Further details are presented in Sec. 4.1. Trace elements and Ge isotopes are presented in 5.2.

Other vein-type deposits generally host moderate Ge concentrations. This comment is valid for the Pb–Zn–Ba ore deposits in Sardinia (Italy). They are hosted in Cambrian (meta)sediments and form late- to post-Variscan Zn–Pb–Ba–Ag–Cu skarn, vein and pale-

okarst deposits (Boni et al., 1996). The Kirki (St. Phillippi) Ag–Pb–Zn ore deposit (Thrace, Greece) may represents an upper volcanic, base metal-bearing portion of a porphyry system, where sphalerite and wurtzite ores contain up to 70 ppm Ge and enhanced Ga concentrations (Tsirambides and Filippidis, 2012; Skarpelis, 1995).

2.3.6 Iron-oxide ores

The presence of Ge in iron oxide ores has often been reported. No significant amounts of Ge are reported in Fe-oxide minerals either in high-temperature hydrothermal replacement (HTHR) ores, including Skarn deposits, (Frenzel et al., 2014), nor in oolitic Fe-ores (e.g., Lorraine basin, France), all of which containing less than 10 ppm Ge. Of greater interest, Ge has been reported to occur in the Archean–Paleoproterozoic Algoma-type banded iron formations (BIF) and the predominantly Paleoproterozoic Superior-type BIF. The highest Ge concentrations occur in the oxide facies; up to 38 ppm Ge is reported in the ore from the Hamersley Range (Australia); average grades of 27 and 43 ppm Ge are reported in hematite and magnetite from Kremenchuk-Krivoi Rog (Ukraine), respectively; while average grades of 8 (up to 20) and 40 (up to 100) ppm Ge are reported in hematite and magnetite from the small Lahn–Dill-type BIF (Germany), respectively (Höll et al., 2007).

2.3.7 Coal and lignite deposits

Coal and lignite deposits contain Ge, with grades that vary over several orders of magnitude (Bernstein, 1985). In general, coal often contains low Ge contents (about 1 ppm), but after coal combustion, its content in ashes can see an tenfold increase. However, some coal deposits show significant Ge enrichment, for instance, average grades of 276 ppm and 348 ppm Ge are reported in coal and coal argillites from Novikovskoye (Russia), respectively, and some 1043 ppm Ge are described in coal ash from Shkotovskoye (Russia). In particular, China is the world's major Ge producer thanks to coal and lignite resources. The Ge resources of Yunnan Province (e.g., Lincang lignite deposits) are estimated at 1112 t Ge, and up to 1600 t of Ge is estimated in the coal deposit of Xilinhaote (Höll et al., 2007; Qi et al., 2011, eastern Inner Mongolia;).

Table 2.1 – Key features of the main Ge-bearing deposit types, with Ge concentrations, past and the estimated future potential (though data of Ge grade in concentrates are often lacking). Modified after Melcher and Buchholz (2013) and Höll et al. (2007).

Deposit type	Brief description	Features	Examples	Ge-bearing species	Past production	Future potential	Typical ore grade (ppm Ge)
Volcanic-hosted massive sulphides Cu-Zn(-Pb)(-Ba)	Lenticular seafloor massive sulphides orebodies, often with footwall stringer zones	In extensional oceanic settings; associated with volcanic (mafic to felsic) rocks. Ge concentrations up to 100 ppm in recent ores, up to 370 ppm in Kuroko-type deposits	Kuroko-type ores (Japan); Neves Corvo Cu-Sn-Zn (Ag-Se-In-Ge) (Portugal); Gorevskoe Pb-Zn (Russia); Ozernoe Zn-Pb (Russia)	Sphalerite (bornite, Ge-sulphides)	low	medium	<<100 (–300)
Porphyry and vein-stockwork Cu-Mo-Au	Medium to large, low-grade stockwork of quartz veinlets and disseminations in felsic intrusive rocks	In compressional tectonic settings; Ge-bearing sulphides occur in peripheral zones of porphyry systems, including late-stage epithermal veins	Capillitas (Argentina); Bor (Serbia); Chelopech (Bulgaria); Ladolam (Papua New Guinea)	Cu-As sulphides, bornite, sphalerite	low	low	10–100
Porphyry and vein-stockwork Sn-Ag	Stockworks and arrays of ore veins in subvolcanic, felsic intrusions	Mineralization includes argyrodite and Ge-bearing Sn minerals	Potosi/Bolivian Ag-Sn belt; Barquilla (Spain)	Argyrodite, sphalerite	low	medium	10–100
Vein-type Ag-Pb-Zn(-Cu)	Ore veins hosted by sedimentary and magmatic rocks	Heterogeneous group of vein deposits found in different tectonic settings	Freiberg (Germany); Saint Salvy (France); Kirki (Greece)	Argyrodite, sphalerite	high until 1993	low	100–1000
Sediment-hosted massive sulphides Zn-Pb-Cu(-Ba)	Concordant lenses of stratiform massive to semi-massive sulphides and sulfates (baryte), often with footwall stringer zones and stockworks	Hosted by clastic marine sediments, including black shales, along continental margins or in intracratonic rift settings	Red Dog (Alaska, U.S.A.); Jinding/Lanping (China)	Sphalerite, wurtzite	high	high	10–100

Table 2.1 – *Continued*

Deposit type	Brief description	Features	Examples	Ge-bearing species	Past production	Future potential	Typical ore grade (ppm Ge)
Mississippi Valley-type (MVT) Zn-Pb-Fe(-Cu)(-Ba)(-F)	Hosted in carbonate successions since the Paleoproterozoic; very common type	Signifcant age difference between host rock and mineralization;sulphur derived from TSR	Elmwood-Gordonsville district (Tennessee, U.S.A.); Pend Oreille (Washington, U.S.A.); Très Marias (Mexico); Fankou, Huize (China)	Sphalerite, wurtzite	high	high	100–1000
Irish-type (IRT) Zn-Pb(–Ag)(–Ba)	Hosted in Lower Carboniferous carbonate rocks	Bacteriogenic sulphur source (BSR)	Navan, Tynagh, Lisheen (all Ireland)				
Alpine-type (APT) Zn-Pb	Hosted in Triassic limestones	Bacteriogenic and non-bacteriogenic sulphur sources	Bleiberg (Austria); Mezica (Slovenia); Cave de Predil (Italy)				
Kipushi-type (KPT) polymetallic Cu-Zn-Pb-Ag-As	Hosted in Neoproterozoic limestones (central and SW Africa)	High-temperature fluids (250-450°C); sulphur derived from TSR Highest Ge grades known	Tsumeb (Namibia); Kipushi (DR Congo); Kabwe (Zambia); Ruby Creek (Alaska, U.S.A.)	Ge-sulphides, Cu-sulphides (sphalerite)	high until 2000	medium	10–1000
Oxidation zones of KPT deposits	Extensive oxidation of primary sulphide ores	Ge in Fe-hydroxides, and forming secondary Ge minerals	Tsumeb (Namibia); Apex (Utah, U.S.A.)				
Iron oxide ores	Precambrian banded iron formations; Phanerozoic volcanogenic-sedimentary deposits	Ge in iron oxides from sedimentary deposits; low Ge in Fe skarn deposits	Hamersley Range (Australia), Krivoi Rog (Ukraine), Atasu type (Kazakhstan)	Hematite, magnetite, goethite	none	low	10–50
Coal and lignite	Extensive beds of coal and lignite close to bedrock contacts	Up to 3000 ppm Ge in fly ash from coal combustion	Lincang, Wulantuga (China); Tarbagataisk, Shotovsk (Russia); Lugansk (Ukraine); Angrensk (Uzbekistan)	Organic matter – coal/lignite – ashes	 medium high	 high high	 100–1000 10–1000

2.4 Stable isotope geochemistry

Stable isotope analysis of light elements (H, Li, B, C, N, O, and S), referred to as *traditional* isotopes, has been successfully applied for many decades to study their geochemical and biogeochemical cycling in many different settings and played a major role in advancing the understanding of mineralising systems. The isotopes of metals (e.g., Cr, Fe, Cu, Zn, Mo, Cd, W, Hg) and metalloids (Ge, Sb), referred to as *non-traditional* isotopes, received less attention because (i) they were thought to be too heavy to fractionate, and (ii) due to the lack of suitable techniques to resolve natural variations in the stable isotope ratios of these elements (Wiederhold, 2015; Johnson et al., 2004b). Non-traditional stable isotope systems have added powerful new tools for assessing the source of elements, their fractionation in many geochemical and biogeochemical processes, which is particularly useful for the study of mineral deposits.

2.4.1 Basic principles and equations

Isotopes of the same element share nearly identical chemical and physical properties, but small mass differences may result in fractionation of isotopes during chemical reactions or physical processes. Isotopic fractionations between species or phases depend on a number factors, most of which involving the relative mass difference, the nature of the bonding environment, and redox state. The range in only mass-dependent isotopic variations is expected to decrease with increasing atomic number (Z) because the relative mass difference ($\Delta m/\bar{m}$) decreases (Fig. 2.14a–b).

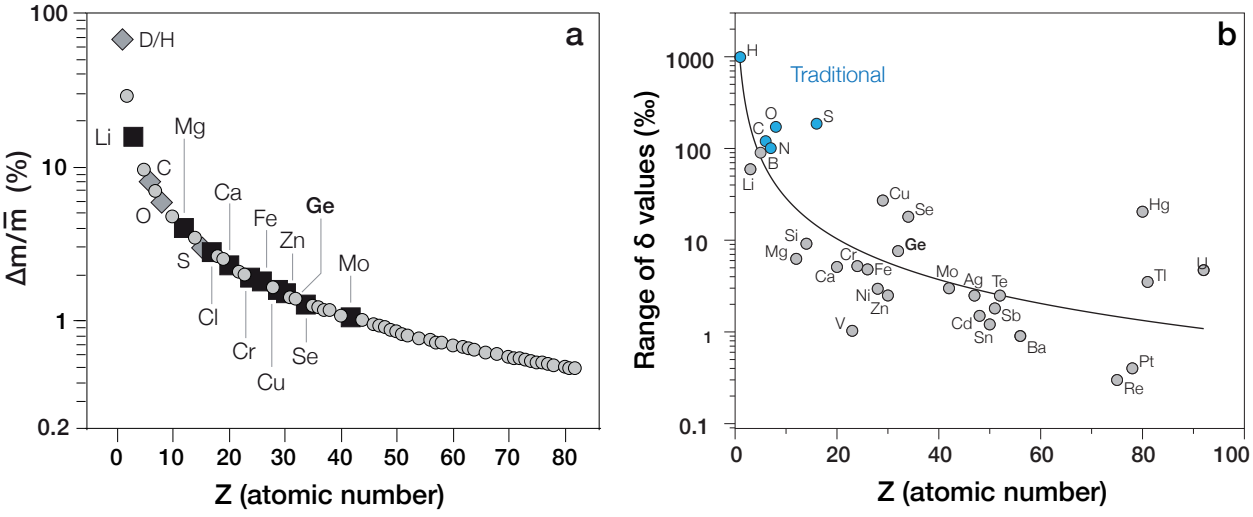

Fig. 2.14 – a. Relative mass differences for elements that have two or more isotopes, shown as $\Delta m/\bar{m}$, where Δm is the unit mass difference ($\Delta m = 1$), and $\bar{m}$ is the average mass of the isotopes of that element, as a function of atomic number (Z). Grey diamonds are *traditional* stable isotopes, large black squares and grey circles are *non-traditional* stable isotopes. Modified from Johnson et al. (2004b). **b**. Range of delta values observed so far in natural samples on a logarithmic scale with the inferred (mass-dependent) fractionation trend. Modified after Wiederhold (2015).

Ratios of isotopes of a given element are usually chosen with the heavier isotope of major abundance in the denominator, and one of the lighter, less abundant isotope in the numerator. The delta (δ) scale has been defined to express the ratios as small numbers with one or two decimals. For germanium isotope studies, the $^{74}Ge/^{70}Ge$ ratio (35.94 and 21.23% in abundance, respectively) is most commonly used, and expressed in δ^{74}Ge as

$$\delta^{74}\mathrm{Ge}_{\mathrm{std}}(\mathrm{sam}) = \left(\frac{(^{74}\mathrm{Ge}/^{70}\mathrm{Ge})_{\mathrm{sam}}}{(^{74}\mathrm{Ge}/^{70}\mathrm{Ge})_{\mathrm{ref}}} - 1 \right) \times 1000$$

The delta scale converts very small variations in isotope ratios to delta values in per mill (‰), which represent deviation from a reference (e.g., the NIST 3120a Ge standard). If $\delta^{74}\mathrm{Ge} > 0$, the sample is isotopically heavier (higher heavy/light ratio) than the standard, and inversely, if $\delta^{74}\mathrm{Ge} < 0$ the sample is isotopically lighter than the standard.

When two substances are in isotopic equilibrium, the distribution of isotopes between substances is controlled by energy considerations (i.e., bond strength). Equilibrium isotopic partitioning can be described using the fractionation factor, α, which by definition is

$$\alpha_{\mathrm{A-B}} = \frac{R_{\mathrm{A}}}{R_{\mathrm{B}}}$$

where R is the isotope ratio of interest in substance A or B. In practice, α can be related to δ values using the approximation

$$\Delta_{\mathrm{A-B}} = \delta_{\mathrm{A}} - \delta_{\mathrm{B}} \simeq 1000 \ln \alpha_{\mathrm{A-B}}$$

Experimental studies of stable isotopic fractionation between coexisting phases generally show linear or smooth curves correlating $1000 \ln \alpha$ with inverse temperature (T), and generally modelled using two parameters (A, B) as:

$$1000 \ln \alpha_{\mathrm{A-B}} = \frac{A}{T^2} + B$$

This relation leads to geothermometry, which utilises measured isotope values and fractionation data between coexisting phases (in isotopic equilibrium) to calculate temperatures of equilibration. Geothermometry is a very important tool in understanding the conditions of mineralising systems.

Naturally occurring variations in stable isotope ratios are can be related to a range of fractionation processes. *Mass-dependent fractionation* is strictly governed by relative mass differences among different isotopes of an element and include equilibrium and kinetic fractionations. In thermodynamic equilibrium, it is common that species having stronger bonds preferentially concentrate the heavier isotope. Kinetic effects are caused by different reaction rates affecting light and heavy isotopes, associated with incomplete and unidirectional processes. The corresponding measurements always show a preferential enrichment of the lighter isotope in the reaction products, e.g., during biological reactions such as photosynthesis or bacterial processes.

Reservoir effects occur when substances may leave the system and, therefore, not respond to later changes in the system. Such process occur in the precipitation of a mineral, which behaves 'inertly' after precipitation and does not continue to re-equilibrate if the system

evolves or conditions change. One typical reservoir effect is the Rayleigh distillation, when a precipitated mineral is isolated from isotopic exchange in a non-renewed but evolving fluid system, which is expressed as

$$R = R_0 \, f^{\alpha-1}$$

where R is the isotopic ratio of interest, R_0 is the initial isotopic ratio of the compound, f is the fraction of that substance remaining as the Rayleigh distillation proceeds, and α is the equilibrium or kinetic fractionation factor between the two coexisting phases. An example of the Rayleigh fractionation that could occur during the Ge incorporation in sphalerite and quartz is presented in Fig. 2.15, using the δ-scale equivalent of the equation above:

$$\delta^{74}\mathrm{Ge} = (\delta^{74}\mathrm{Ge}_0 + 1000)\, f^{\alpha-1} - 1000$$

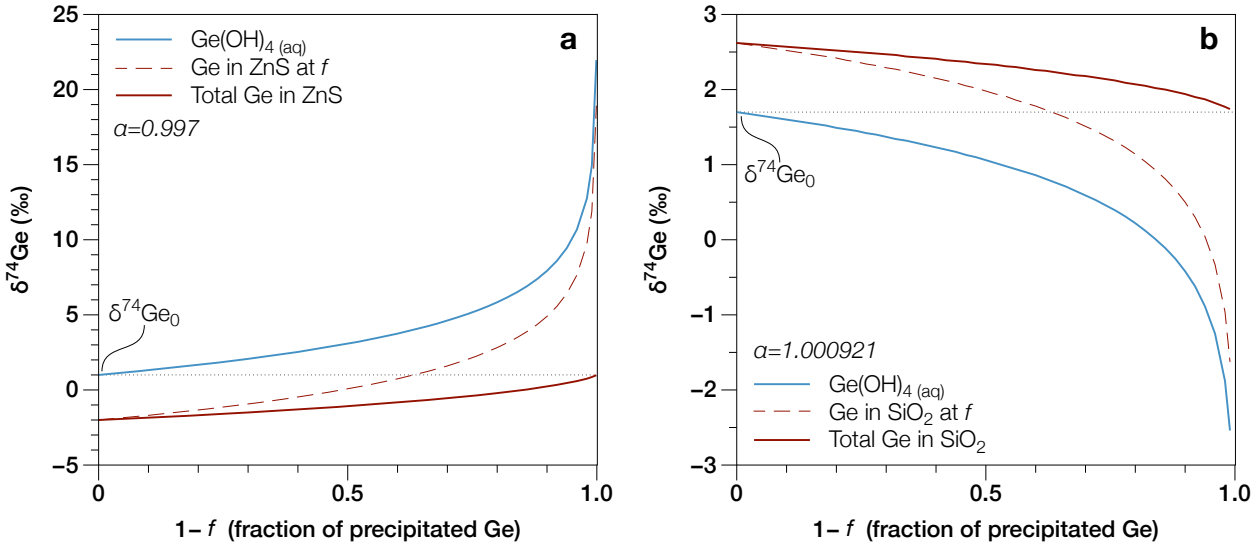

Fig. 2.15 – Rayleigh plot for Ge isotopic fractionations during the incorporation in sphalerite (**a**) and quartz (**b**). For sphalerite, the isotopic fractionation factor, α, is assumed to be 0.997, and the starting isotopic composition, $\delta^{74}\mathrm{Ge}_0$, is 1.00‰. For quartz, $\alpha = 1.000921$ and $\delta^{74}\mathrm{Ge}_0 = 1.7$. α values were inferred from the *ab initio* predictions of Li et al. (2009).

Mass balance effects affect the measured isotopic fractionation because modal proportions of substances can change during a chemical reaction. They are especially important for elements in situations where these coexist in molecules of reduced and oxidized compounds. The mixing of reservoirs with different isotope signatures, which is commonly used for source tracing, require mass balance considerations. If the isotopic compositions of the involved end-members are known and sufficiently distinct, contributions of different source materials in a sample can be quantified by mixing calculations. Conservation of mass in an n component system can be described by

$$\delta_{\mathrm{mix}} = \sum_i x_i \, \delta_i$$

where x_i is the mole fraction of the element in question for each of n phases within the system. Isotopic fractionation depends on a number of other factors and processes briefly described below.

Chemical composition – The nature of the chemical bonds within a mineral plays to a high degree on its isotopic composition. For instance, sphalerite preferentially concentrates ^{34}S relative to coexisting galena. Covalent bonding mostly occurs in sulphide minerals, while ionic bonding occurs in silicate and oxides minerals.

Crystal structure – Secondary in importance after the effect of chemical composition. Heavy isotopes favour the more closely packed or well-ordered structure, which depends on coordination symmetry and bond length. For instance, a relatively large isotopic fractionation is observed in the transition between graphite and diamond (Hoefs, 2009).

Oxidation state – The oxidation state, together with ligands and coordination numbers, is one of the key parameters involved in inducing large isotopic equilibrium fractionation at low temperatures (e.g., Schauble, 2004). Heavy isotopic compositions typically correlate with high oxidation states, e.g., $^{56}Fe/^{54}Fe$ ratios are usually higher in Fe^{3+}-bearing compounds than in Fe^{2+}-bearing compounds (e.g., Polyakov and Mineev, 2000).

Diffusion – Ordinary diffusion is more or less limited to ideal gases, for which light isotopes are more mobile than heavy isotopes, leading to significant isotope fractionations. Diffusion also includes the process of thermal diffusion under a temperature gradient, which results in a mass transport. The greater the mass difference, the greater is the tendency of the two species to separate by thermal diffusion (e.g., Richter et al., 1999, 2003).

Mass-independent fractionation – Also referred to as MIF. Such a process generate an isotopic fractionation that is not strictly governed by relative mass differences among the isotopes of an element, and therefore, violates the mass-dependent rules. MIFs were first observed in meteorites and in ozone (Hoefs, 2009). Significant mass-independent S isotope fractionation have been reported in sulphides older than 2.4 Ga (i.e., the great oxidation event; Farquhar et al., 2000).

For instance, the combined effects of chemical composition, crystal structure and oxidation state on the Ge isotopic fractionation has been studied in Li et al. (2009) for oxide, silicate minerals, and sphalerite, with respect to the aqueous Ge complex, $Ge(OH)_4$ (Fig. 2.16). The results predict that Ge in sulphides could be extremely light relative to Ge-bearing oxides or silicates.

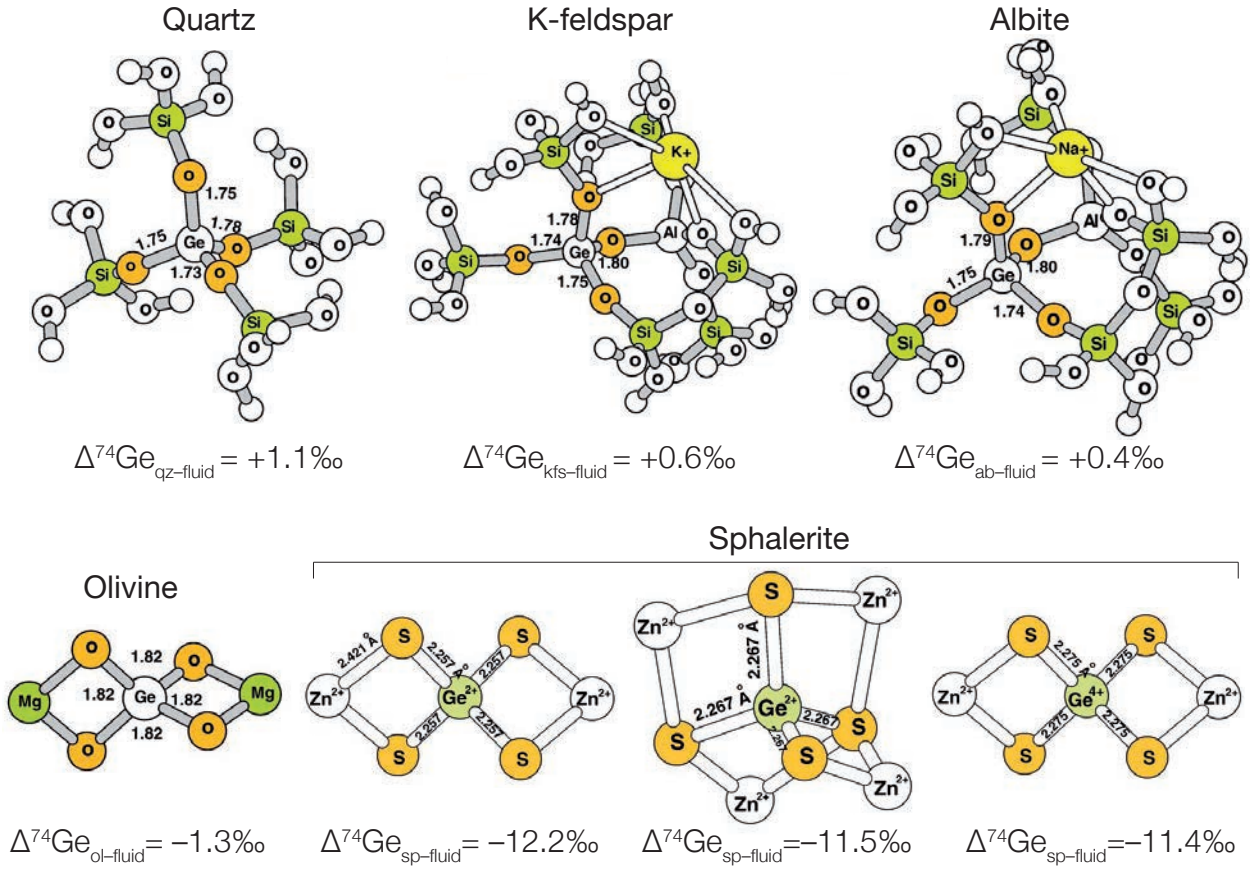

Fig. 2.16 – Cluster models for the structures of quartz, olivine, albite, K-feldspar, and sphalerite, with predicted Ge isotope fractionation between $Ge(OH)_4$ in fluid and mineral species at 25°C. For sphalerite, three tetrahedral clusters are simulated, $[Ge^{2+}S_4Zn_2]^{2-}$, $[Ge^{2+}S_4Zn_4]^{2+}$ and $[Ge^{4+}S_4Zn_2]^0$, yielding distinct $\Delta^{74}Ge$ due to variations in Ge–S bond lengths and Ge oxidation state. Cluster sketches and data from the study of Li et al. (2009).

2.4.2 Germanium isotopes

Being distinctly siderophile, lithophile, chalcophile and organophile (Sec. 2.2.1), Ge is found in a variety of geological environments, making it a useful geochemical tracer in the fields of cosmochemistry (Dickinson et al., 1989), planetary differentiation (Luais, 2007, 2012), hydrothermal (Arnórsson, 1984) and tectonic activity during metamorphism in specific geodynamic settings (El Korh et al., in rev.), the study of oceanic systems (Rouxel et al., 2006), as well as continental weathering (e.g., Murnane and Stallard, 1990; Kurtz et al., 2002). The Ge isotope system (see Sec. 2.1.1) can provide useful information regarding processes triggering variable Ge contents in terrestrial reservoirs, but to date, relatively few Ge isotope data are available for meteorites (Hirata, 1997; Xue et al., 1997; Luais, 2003, 2007), terrestrial rocks (Rouxel et al., 2006; Luais, 2012; Escoube et al., 2012; Meng et al., 2015; Qi et al., 2011) and fluids (Siebert et al., 2006; Escoube et al., 2015). Recent advances in the development of multi-collector inductively coupled mass spectrometry (MC-ICP-MS) has improved the precision and reproducibility of heavy stable isotope measurements, reducing uncertainties to about 0.05‰ (depending on the element), allowing small isotopic anomalies to be detected (Luais, 2012).

Germanium isotope compositions of the various rocks and minerals studied in the literature are compiled in Fig. 2.17 with respect to the SRM NIST 3120a Ge standard. Germanium isotope compositions in sulphide ore minerals were first reported in Luais (2007) and Luais (2012) for two sphalerite samples from the Saint-Salvy Zn(–Ge) vein-type deposit (France), having negative δ^{74}Ge values of -1.05 ± 0.15‰ and -2.06 ± 0.15‰. In comparison, Escoube et al. (2012) reported average δ^{74}Ge values as low as -3.65 ± 0.57‰ in sphalerite from the Navan Pb–Zn MVT deposit, and -3.37 ± 0.44‰ in sphalerite from the Lucky Strike active hydrothermal system (Azores). In addition, Meng et al. (2015) analysed Ge isotopes in sulphides from the Jinding, Shanshulin, and Tianqiao Zn–Pb SHMS deposits in China (see Sec. 2.3). Sphalerite, pyrite and galena show δ^{74}Ge values from –4.94‰ to +2.07‰. In the Shanshulin and Tianqiao deposits, they found the paragenetic sequence – in chronological order, pyrite, sphalerite, and galena, to be related with increasing δ^{74}Ge such as $\delta^{74}Ge_{pyrite} < \delta^{74}Ge_{sphalerite} < \delta^{74}Ge_{galena}$. They attributed this trend towards heavier compositions to kinetic or Rayleigh fractionation (see Fig. 2.15 in the previous section).

In contrast, Ge isotopic composition of the bulk crust/upper mantle, also referred to as Bulk Silicate Earth (BSE), has been estimated to $+0.56 \pm 0.18$‰ (Rouxel et al., 2006; Luais, 2012; Escoube et al., 2012), including the analysis of a number igneous rock references such as continental basalts and oceanic basalts (MORB and OIB), dolerite, granites, anorthosite and ultra-mafic rocks. Deep sea clays have δ^{74}Ge values similar to this average, whilst modern deep sea sponges, glauconite in marine sediments (GL-O, $+2.44 \pm 0.14$‰), and iron formation (IF-G, $+1.03 \pm 0.10$‰) have δ^{74}Ge values heavier than the upper mantle/crust rocks (Escoube et al., 2012, and references therein). The commonly negative δ^{74}Ge values (i.e., depletion in heavy isotopes) in sulphide minerals from ore deposits and modern seafloor hydrothermal systems therefore contrast with the generally positive Ge isotope values found in many silicates and oxide/hydroxide minerals from igneous and sedimentary rocks.

Moreover, Escoube et al. (2015) studied the behaviours of Ge and Si in seafloor hydrothermal fluids relative to seawater, using Ge isotope and Ge/Si ratio systematics. Their study compared the low-temperature hydrothermal vents from Loihi Seamount (Pacific Ocean,

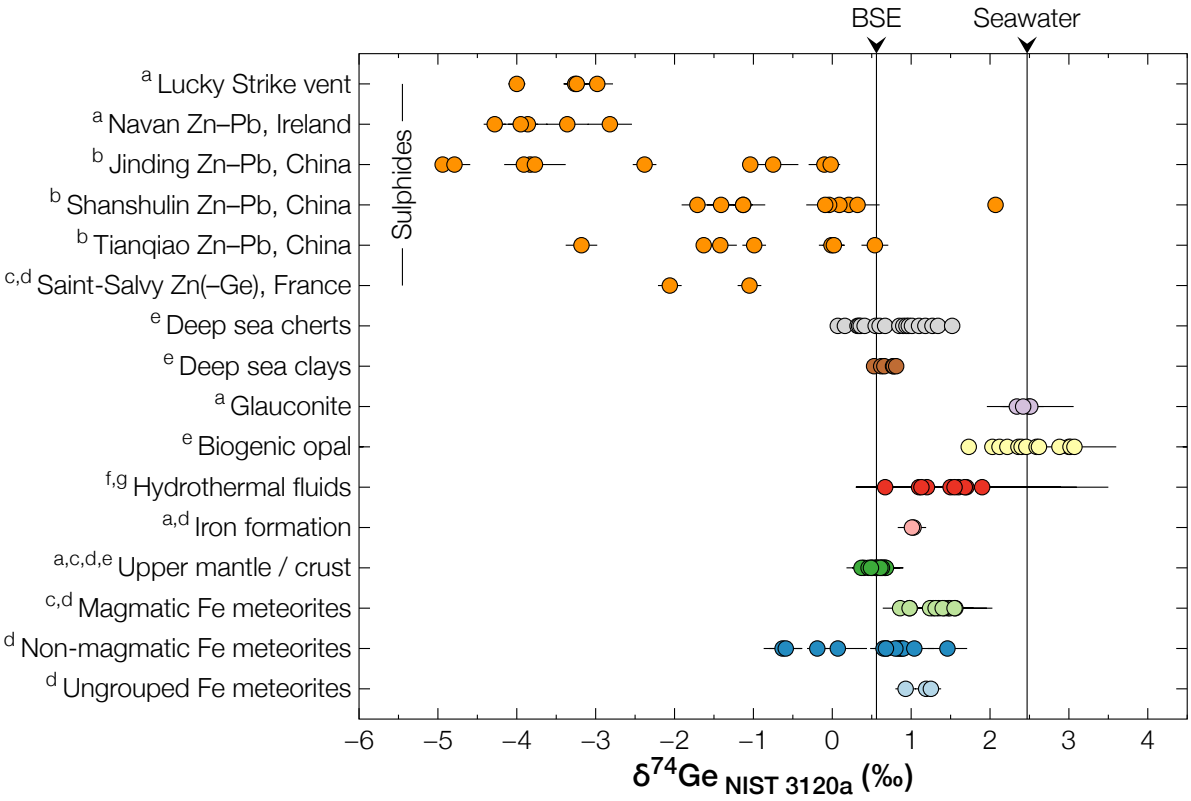

Fig. 2.17 – Compilation of Ge isotope compositions of various rocks and minerals from (a) [a]Escoube et al. (2012), [b]Meng et al. (2015), [c]Luais (2007), [d]Luais (2012), [e]Rouxel et al. (2006), [f]Siebert et al. (2006, 2011) and [g]Escoube et al. (2015). Errors in 2σ SD. Bulk Silicate Earth (BSE) and seawater δ^{74}Ge were estimated from averages compositions of upper crust/mantle-derived rocks and biogenic opal, respectively.

$T \simeq 20$–50°C) to high-temperature vents from the East Pacific Rise (EPR, $T \simeq 330$–380°C). They observed that both Ge/Si and δ^{74}Ge in hydrothermal fluids are fractionated relative to the basaltic host rocks, with $\Delta^{74}\text{Ge}_{\text{fluid}-\beta}$ up to +1.15‰ at EPR and +1.64‰ at Loihi, which are explained by the precipitation of Ge-bearing minerals (e.g., quartz, Fe-oxyhydroxides, sulphides) during higher temperature, seawater–rock reactions in the subsurface. Such a heavy isotopic composition was also reported for the Cascades high-T terrestrial hydrothermal fluids, with an average of $+1.20 \pm 0.30$‰ (Siebert et al., 2006, 2011). Moreover, Escoube et al. (2015) calculated the following average Ge isotope fractionation factors, $\alpha_{\text{ferrihydrite}-\text{fluid}} = -2.0 \pm 0.6$‰ and $\alpha_{\text{sulphide}-\text{fluid}} = -5.6 \pm 0.6$‰ ($2\sigma$ SD) at $T < 250$°C. They suggested that the 'missing Ge sink' may correspond to Ge sequestration into authigenic Fe-oxyhydroxides in marine sediments.

Finally, theoretical *ab initio* prediction of Ge isotope fractionation by Li et al. (2009), who estimated equilibrium fractionation factors between the dominant aqueous species in seawater, $Ge(OH)_4$ and $GeO(OH)_3^-$ as well as Ge-bearing organic complexes, and Ge in crystal structure of quartz/opal, albite, K-feldspar, olivine and sphalerite (see Fig. 2.16 in Sec. 2.4.1). These predictions are in good agreement with Ge isotopes in natural samples, i.e., the heavier isotope should be sequestered in silicates, whereas the lighter isotope should be incorporated in sphalerite (and possibly other sulphide phase with sphalerite-like structure). Given the isotopically light composition of most hydrothermal fluids, while both quartz and

sulphides may be incorporating Ge, sulphide precipitation may be the dominant factor for Ge isotope fractionation in hydrothermal fluids, triggering that they become progressively enriched in the heavy isotope as they cool.

2.4.3 Stable isotopes in metallogeny

Stable isotope studies provided diverse and powerful tools to address the typical problems in metallogenic studies dealing with source rocks, ore-forming fluids, rock alterations, and the deposition of ore (and gangue) minerals. Stable isotope variations are best interpreted in combination with other tools, such as fluid inclusion studies and elemental geochemistry. This section presents few applications of metal stable isotope that were found to be useful for the study of ore-forming systems, especially those concerning sediment- and carbonate-hosted deposits, which represent significant sources of economically recoverable Ge.

The sulphur isotope systematics has been extensively applied for more than seven decades to the study of sulphide-bearing mineral deposits. A considerable body of knowledge exists on the S isotopic fractionation in sulphide minerals (Fig. 2.18; Seal, 2006, and references therein). The sulphur isotope system is commonly used to study S sources and rock contaminations in high-temperature settings (e.g., mafic igneous rocks commonly record the fingerprint of contamination by crustal sedimentary sulphur), the sulphate reduction process in hydrothermal systems at lower temperatures (bacteriogenic if $\delta^{34}S \ll 0$ for $T < 100°C$, thermochemical if $\delta^{34}S \geqslant 0$), and if at least two sulphide minerals formed in equilibrium, it can be utilised to determine their deposition temperatures (e.g., the sphalerite–galena geothermometer, Ohmoto and Rye, 1979)

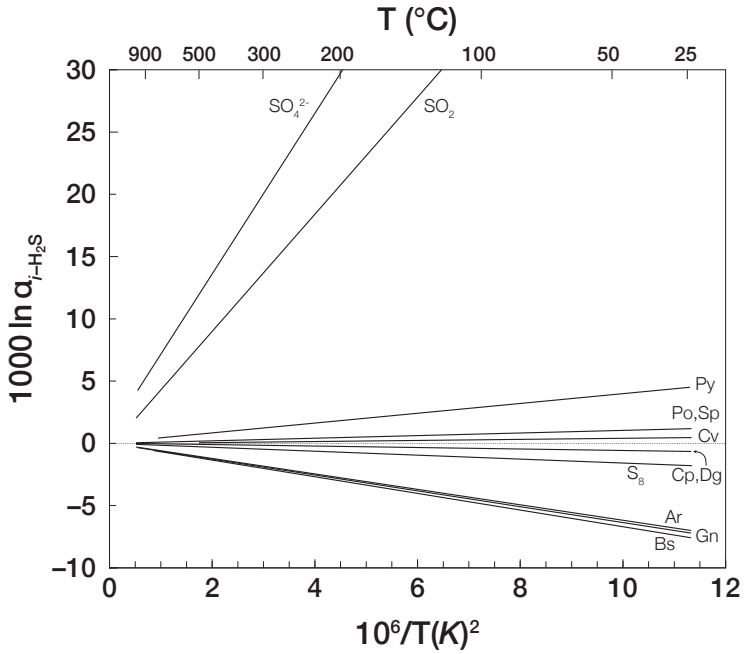

Fig. 2.18 – Temperature dependence of experimentally determined equilibrium S isotope fractionation factors relative to H_2S for a variety of sulphur species and sulphide minerals. The dashed line indicates a nil $1000 \ln \alpha$ value. Abbreviations: Ar argentite, Bs bismuthinite, Cp chalcopyrite, Cv covellite, Dg digenite, Gn galena, Po pyrrhotite, Py pyrite, Sp sphalerite. Modified after Seal (2006, and references therein).

As mentioned in Sec.2.3, the Red Dog SedEx Zn–Pb–Ag deposits (Brooks Range, Alaska) is a beautiful example for which Zn and S isotopes were combined to gain further insights into ore-deposition processes. Kelley et al. (2004) and Johnson et al. (2004a) report the variations in $\delta^{34}S$. They inferred a paragenetic sequence that involves early, low-temperature barite with

δ^{34}S values close to that of ambient seawater sulphate, and related sphalerite and pyrite with negative δ^{34}S ranging from –45 to –5‰, suggesting that S is derived from BSR of early barite or ambient seawater. Later mineralisation occurred at 100–200°C (Leach et al., 2004) accompanied by fracturing and deposition of sphalerite, galena, pyrite and/or marcassite, in veins with banded and crustiform habits suggesting open-space filling. Sulphides of that paragenetic stage show positive δ^{34}S values in the range of about 5 to 12.3‰ (mean of 3‰), suggesting that S was derived from TSR during barite dissolution, which, given the temperatures, is associated to a fractionation of about 15‰.

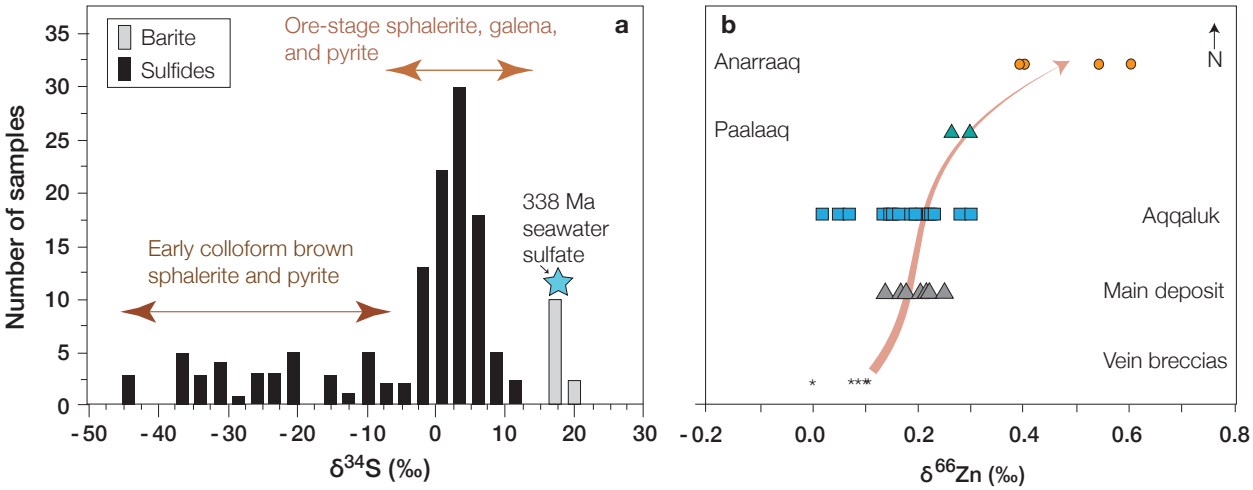

Fig. 2.19 – a. Frequency distribution of δ^{34}S with respect to the VCDT standard, for sulphides and ore-related barite. Data were obtained by *in situ* analysis using ion microprobe techniques. Barite data were obtained by conventional bulk analysis. **b**. Comparison of vein–breccia occurrences with the individual shale-hosted massive sulphide deposits in the Red Dog district. Modified from Shanks (2014), after data from Johnson et al. (2004a) and Kelley et al. (2009) for S and Zn isotopes, respectively.

Kelley et al. (2009) measured Zn isotopes in the Red Dog deposits. Zn isotope values (δ^{66}Zn) range from 0 to 0.6‰ and lack significant variation with paragenetic stages in any of the deposits. However, they observed a marked trend across the deposits, from low δ^{66}Zn values in the vein breccias, which are interpreted to be feeder zones for the ascending hydrothermal fluids, to higher δ^{66}Zn values in the overlying massive sulphides. They suggested that δ^{66}Zn values increase due to a kinetic isotope effect during precipitation and Rayleigh fractionation as the fluids migrated to upper or more distal ore zones. Wilkinson et al. (2005b) and Wilkinson et al. (2005a) report similar patterns in δ^{66}Zn variations in the Irish Midlands Zn–Pb MVT deposits. Kelley et al. (2009) showed that δ^{66}Zn does not correlate with δ^{34}S, and suggested that Zn is provided by the hydrothermal fluid, whereas H_2S is formed through by TSR at the site of ore deposition. All of these studies emphasise that further understanding of δ^{66}Zn systematics requires enhanced experimental and theoretical studies of the Zn, fluid–sulphide, isotopic fractionation.

Gagnevin et al. (2012) investigated the extent, causes and consequences of Zn and Fe isotope fractionation in a large hydrothermal system by studying the world-class Navan Zn–Pb deposit, Ireland. Large variations in Zn, Fe and S isotope compositions have been measured in growth banded, colloform sphalerite. Sphalerite bands were microdrilled with a spatial resolution of 100–300 μm. *In-situ* S isotopic analyses of sphalerite display a sub-

stantial δ^{34}S range, from –13.2‰ to +14.6‰ (total of 28‰). The chiefly light δ^{34}S indicate abundant bacteriogenic H_2S, while the few heavy δ^{34}S data may result from fractionation of the hydrothermal source. A total isotopic range of 0.55‰ and 2‰ has been measured for δ^{66}Zn and δ^{56}Fe, respectively, in sphalerite microsamples. δ^{66}Zn and δ^{56}Fe display a well-defined positive correlation (Fig. 2.20a) and both δ^{66}Zn and δ^{56}Fe evolve from lighter to heavier isotopic values with sphalerite growth and correlate with δ^{34}S (Fig. 2.20b). Light Fe and Zn isotopes are associated with early precipitation of sphalerite from the hydrothermal system, and the correlations observed are interpreted as the results of the combined effects of kinetic Zn and Fe isotope fractionation during sphalerite precipitation, and S isotope variation through mixing of hot, metal-rich hydrothermal fluids and cool, bacteriogenic sulphide-bearing brines. Gagnevin et al. (2012) suggested that incoming pulses of metal-rich hydrothermal fluid triggered sulphide mineralisation, and that rapid precipitation of sphalerite from hydrothermal fluids lead to strong kinetic fractionation of Zn and Fe isotopes at very short time and length scales. The authors emphasised the limited use of Fe and Zn isotopes as exploration tools within deposits, but suggested the possibility of detecting new deposits from isotopically heavy Zn–Fe geochemical halos.

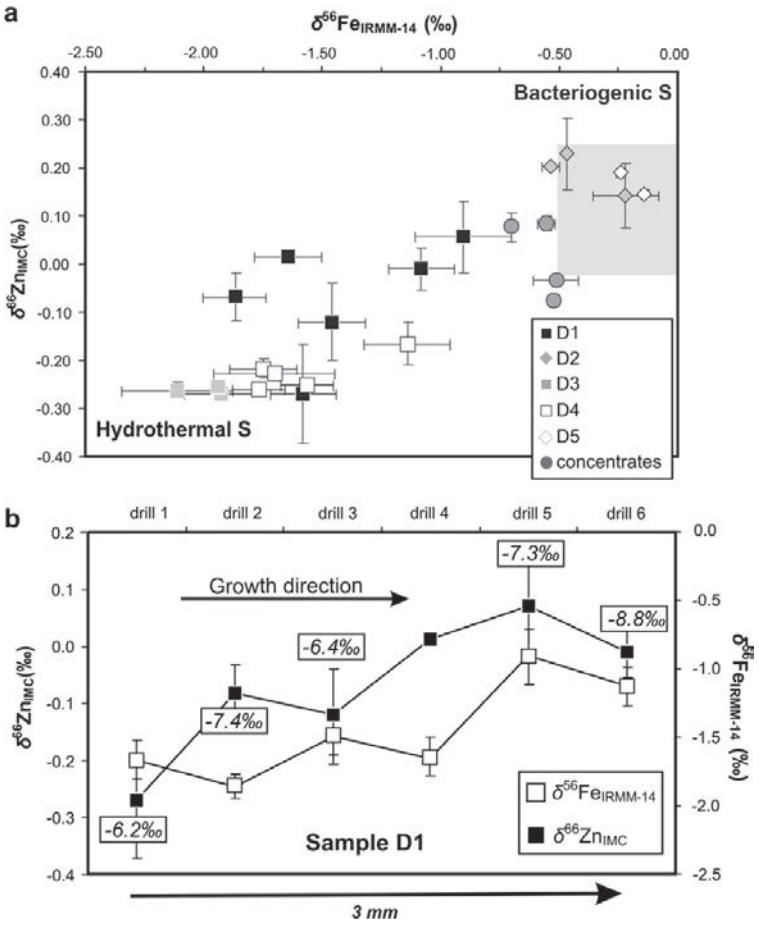

Fig. 2.20 – a. Correlation between $\delta^{56}Fe_{IRMM-14}$ and $\delta^{66}Zn_{IMC}$ for the five sphalerite samples and mine concentrates studied in Gagnevin et al. (2012). The sphalerite Zn and Fe isotope data exhibit a well-defined correlation (R^2=0.79). These δ^{66}Zn data (from –0.32‰ to +0.23‰) overlaps with that reported in Wilkinson et al. (2005b) for the Irish midlands orefield (–0.17‰ to 0.34‰, omitting two heavy δ^{66}Zn values of 0.64‰ and 1.33‰). The grey box represents the isotopic range of the basement samples. **b**. Small scale Fe and Zn isotopic variations between successive layers in sphalerite (sample D1). δ^{34}S data are also presented in boxes above or below each δ^{66}Zn data point.

Stable isotopes such as Zn, Cu, Fe, Mo, and Tl have already provided striking new insights into mineralisation processes and metal sources (Shanks, 2014; Albarède, 2004). Given the broad variability of metal and metalloid *non-traditional* isotopic compositions in the mineral and biological worlds, they hold a tremendous potential for better understanding ore-forming systems, although enhanced theoretical and experimental isotope-exchange studies are required to constrain the interpretations.

2.5 Goals and strategy

The studies presented above outlined the main features of the Ge metallogenesis as illustrated in Fig. 2.21. Germanium does not form specific ore deposits and rather occurs in trace to minor amounts in various ore deposit types, but most significant Ge enrichments occur in low-T sediment-hosted Zn–Pb and/or Cu deposits (e.g., MVT, SedEx) and carbonaceous deposits (coal and lignite). Germanium contents can vary over several orders of magnitude in sulphide minerals, but concentrations of up to thousand ppm are reported, especially in sphalerite and Cu-sulphides. Potential pre-enriched sources of Ge can be late differentiates such as muscovite granites and volatile-rich rocks, and organic-rich sedimentary rocks such as black shales. However, given the analytical difficulties for determining Ge concentrations, a broad lack of reliable data has been largely recognised across the literature, even for large ore deposits.

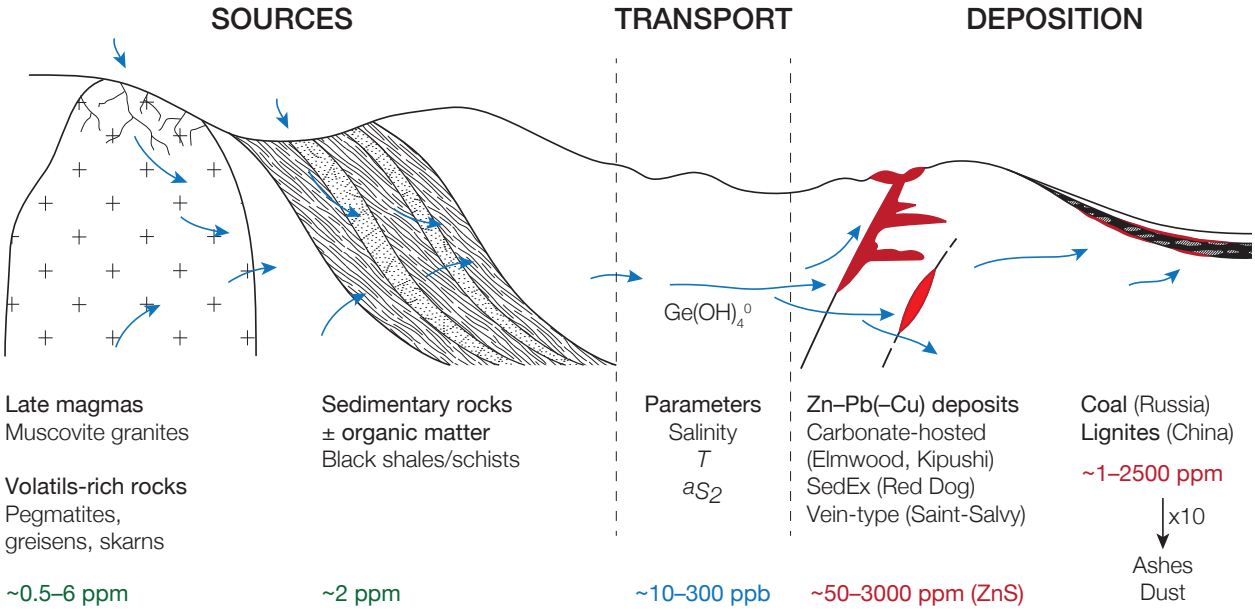

Fig. 2.21 – Conceptual frame of the Ge metallogeny considering potential pre-enriched sources of Ge (igneous and organic-rich sedimentary rocks), Ge transport (mainly as $Ge(OH)_4^0$) and deposition in the two main type of Ge-bearing deposits, Zn–Pb(–Cu) deposits (chiefly in sphalerite, ZnS) and carbonaceous rocks (coal and lignite).

The advent of accurate, high-resolution trace element analysis by laser ablation inductively coupled plasma mass spectrometers has enabled addressing the lack of data regarding Ge and related trace elements in Ge-bearing sulphide ore deposits. However, resolving issues isobaric interferences and external standard calibration are required to guarantee high precision analyses of low Ge concentrations. In addition, the overall lack of statistical power in data interpretation is a problematic addressed in this thesis.

The development and improvements of multi-collector inductively coupled plasma mass spectrometers provide new opportunities to identify small variations in stable isotope ratios, which are useful for tracing deposition temperatures, origin, nature, and evolution of ore-forming fluids, as well as the sources of the ore components and depositional mechanisms. Despite the recent growing interests in the study *non-traditional* stable isotope in ore-forming

systems, the mechanisms and thermal-chemical conditions involved in the incorporation, partitioning, isotope fractionation of Ge, remain incompletely understood and requires to be refined. The novelty of this thesis lies in the integration of mineralogical and geochemical studies, achieved in combining trace element analyses with stable isotope systematics on contrasted Ge-bearing deposit types.

For each case study, the approach is built around four central points: (1) at the scale of the deposit, the first step consist in identifying Ge-bearing sulphide phases, whether Ge occurs in the form of Ge-sulphides (rare) or as minor/trace amounts in major ore components (e.g., sphalerite), their distribution and the relations with the paragenetic sequence. (2) At the scale of the mineral, when Ge occurs in trace to minor amounts, it is essential to determine whether Ge is homogeneously distributed or in zoning patterns, and whether it occurs in nano/micro-inclusions or in solid solutions, in which case, the nature of substitution mechanisms (direct or coupled) should be understood, which require the knowledge of the substituted site, element correlations and crystal chemical constraints. (3) Isotope signatures are measured, especially Ge isotopes, that are possibly combined with other isotopic systems (e.g., Fe, S), and finally, (4) these observations are combined to decipher the effect of distinct ore-forming conditions and processes into the enrichment of Ge in sulphide minerals and deposits.

Finally, as most of the existing work on Ge geochemistry is limited to studies based on natural objects, which, in some way, exceed the experimental and theoretical basis required for fully interpret the results. Little is known about elemental partitioning and isotopic fractionation of Ge between coexisting phases in controlled environments, especially for the most common Ge-bearing sulphide, sphalerite. This study therefore includes the first experimental attempt to decipher the fluid–sphalerite, Ge partitioning and isotopic fractionation.

Chapter 3

Analytical techniques and Methods

3.1 Overview

The analytical approach of this study is presented in Fig. 3.1. Hand sample specimens were visually characterised and mounted into polished thick plates or sections for traditional optical petrographical characterisations. Further mineralogical and textural characterisations of the samples (or experimental products) were achieved by secondary electron microscopy (SEM). Further analyses of selected samples were performed with both *in situ* and bulk techniques. *In situ* analysis of major/minor elements were performed by electron-probe micro-analysis (EPMA), then minor/trace elements were analysed by laser ablation inductively coupled plasma mass spectrometry (LA-ICP-MS). For bulk analyses, minerals of interest in selected samples were separated by crushing–sieving operations, then purified by magnetic separation and/or hand-picking under stereo-microscope. Trace element analyses of digested minerals were performed using ICP-MS, Ge isotopes were analysed using multi-collector ICP-MS after a process of column purification. Finally, few samples were selected for in situ synchrotron experiments.

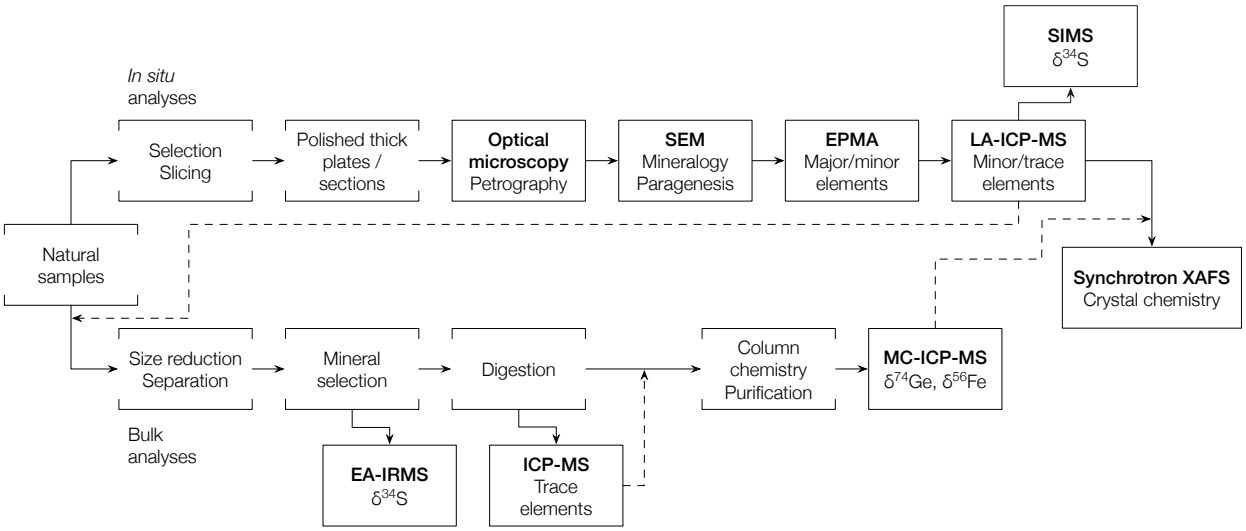

Fig. 3.1 – Typical analytical flowchart utilised in this study. Solid lines indicate the path of samples, dashed lines a decision in the sample selection.

3.2 SEM and EMPA analyses

Non-destructive analyses are carried out using a scanning electron microscope (SEM) and an electron microprobe analyser (EMPA) at the GeoRessources laboratory, Vandoeuvre-lès-Nancy, France, in order to study major/minor element distribution within the studied minerals. Back-scattered electron images and X-ray maps were recorded using a Jeol J7600F with both an energy dispersive spectrometer (EDS, SSD type) for major elements and a wavelength dispersive spectrometer (WDS, Oxford Wave) suitable for the mapping of minor/trace elements. For sulphide minerals, the beam current is usually set to 100 ηA, with an accelerating voltage of 25 kV in order to enhance chemical contrasts.

Major and minor element analyses were performed using a Cameca SX100 electron microprobe analyser (EMPA) with five wavelength dispersive spectrometers. Peak calibration on each element was carried out using reference materials. For example, in order to analyse sphalerite, pure sphalerite and metal Ge were used to calibrate Zn and Ge, respectively, and to optimize the measurements. The beam current was of 100 ηA with an accelerating voltage of 25 kV. The following 13 elements (with respective standards, analytical lines, and monochromators) were used for measurements: S (ZnS, Kα, PET), Fe (FeS_2), Kα, LIF), Zn (ZnS, Kα, LIF), Mn (Mn, Kα, LIF), Co (Co, Kα, LIF), Cu (Cu, Kα, LIF), Ga (AsGa, Lα, LIF/TAP), Ge (Ge, Lα, LIF/TAP), Ag (Ag, Lα, LPET), Cd (Cd, Lα, PET), In (InP, Lα, LPET), Sn (Sn/SnO_2, Kα, PET) and Pb (PbS, Mα, LPET). Peak counting times were scaled from 10 to 60 s, which were reduced by a half for background counting, depending on the element. Internal Cameca procedures were used for data reduction (i.e., quantification of element contents, uncertainties and limits of detection).

Using this setup, the calculated Ge detection limit was of 470 ppm, even though it was measured only in spots richer than 1000 ppm (on 32 analyses in sphalerite from Saint-Salvy, see section 5.2). Reducing this limit of detection to about 170 ppm is possible by counting 60 s on the Kα with a LLIF monochromator (Olivier Rouer, personal communication). However, this procedure enhances the overall counting time and reduces the number of measurable elements.

3.3 *In situ* trace elements analysis by LA-ICP-MS

Laser ablation inductively coupled plasma mass spectrometry (LA-ICP-MS) is used to circumvent the EMPA limitations in order to analyse a wide range of trace elements (especially, Ge, Ga, In and Sn for our study). Trace element analyses are carried out using LA-ICP-MS at the GeoRessources laboratory (Vandoeuvre-lès-Nancy, France), which is composed of a 193 ηm MicroLas Pro ArF Excimer coupled with the Agilent 7500c quadrupole ICP-MS. Analytical settings for laser ablation are detailed in Leisen et al. (2012) and Lach et al. (2013). Laser ablations are generally performed with a constant 5 Hz pulse rate at 90 mJ laser energy. The number of pulses depended on the section thickness, in the case of thin plates, 100 to 200 pulses are allowed, which is sufficient to form a sufficiently long and stable signal for integration. The ablated material is transported using a constant He flow and mixed with Ar in a cyclone coaxial mixer prior to entering the ICP torch and being ionized. The ions are then sampled, accelerated and focussed before being separated and analysed in

the quadrupole mass spectrometer. Data were collected during a 30 ms dwell time per channel to enhance the number of counts for trace elements. Specific areas of the sample plates were ablated with 32, 44 or 60 μm spot diameters. The following isotopes were monitored: ^{57}Fe, ^{64}Cu, ^{66}Zn, ^{71}Ga, ^{74}Ge, ^{75}As, ^{107}Ag, ^{111}Cd, ^{115}In, ^{118}Sn, and ^{121}Sb. The choice of ^{74}Ge over ^{72}Ge, which is commonly used in the literature (e.g., Cook et al., 2009; Danyushevsky et al., 2011; Ye et al., 2011) is discussed in the next paragraph. The total acquisition time was limited to 170 s, allowing a maximum of 2–3 spots per acquisition, generally in the same crystal.

Data reduction are carried our using in-house software LASP (Leisen, 2011) or the Iolite software (Paton et al., 2011), both following the standard methods of Longerich et al. (1996) and using the internal standard method (e.g., in sphalerite the Zn content is used and known from prior EPMA analyses), which is expressed as:

$$w^i_{\text{sam}} = w^i_{\text{std}} \frac{I^i_{\text{sam}}}{I^i_{\text{std}}} \left(\frac{I^{is}_{\text{std}}}{I^{is}_{\text{sam}}} \frac{w^{is}_{\text{sam}}}{w^{is}_{\text{std}}} \right)$$

where w is the concentration of an element i, is is the internal standard and I is the intensity on the LA-ICP-MS transient signal.

No correction factors are introduced in the calculation. For sphalerite and Cu-sulphides, the external standard calibration was performed with the synthetic polymetallic sulphide material MASS-1 (Wilson et al., 2002) using the certified Ge concentration of 57.8±2.6 ppm (Dr. Stephen Wilson, personal communication). Limit of detection (LOD) and uncertainty generally depends on the ablation spot diameter and the analysed element. For each analysis, LOD was calculated using the 3σ criterion (Longerich et al., 1996) as:

$$LOD = \frac{3\sigma_{\text{bg}}}{S} \qquad \text{where} \qquad S = \frac{I^{is}_{\text{sam}}}{w^{is}_{\text{sam}}} \left(\frac{I^i_{\text{std}}}{w^i_{\text{std}}} \frac{I^{is}_{\text{std}}}{w^{is}_{\text{std}}} \right)$$

where S is the analysis sensitivity. Uncertainty was calculated as in Lach et al. (2013) when using LASP, including the uncertainties on the net transient signal (σ) and the internal standard concentration. It is calculated as an error ($\sigma/\sqrt{n}$) in the net transient signals when using Iolite, as described in Longerich et al. (1996). Minimum LOD are usually lower than 1 ppm for the trace elements analysed at ablation spot diameters from 32 to 60 μm.

Cook et al. (2009) and Danyushevsky et al. (2011) emphasised analytical issues in the quantification of low Ge contents using LA-ICP-MS related to external standard calibration and to isobaric interferences. In this study, these issues have been overcome by testing isobaric interferences on Ge isotopes in well-characterised matrix-matched materials, and using proper external standards to better limit any matrix effects during laser ablation. The main interferences on Ge isotopes are the following: ^{70}Ge with ^{70}Zn and ^{36}Ar^{34}S; ^{72}Ge with ^{40}Ar^{32}S and ^{56}Fe^{16}O; ^{73}Ge with ^{40}Ar^{33}S, ^{57}Fe^{16}O, and ^{56}Fe^{16}O^{1}H; and ^{74}Ge with ^{40}Ar^{34}S and ^{58}Ni^{16}O. We used two homogeneous sphalerites whose bulk elemental concentrations have previously been analysed by the Service d'Analyses des Roches et des Minéraux (SARM) in the Centre de Recherches Pétrographiques et Géochimiques (CRPG-Nancy, France) by routine procedure of liquid chromatography ICP-MS (Table 3.1). The two samples consist of a Ge-poor sphalerite (S1) from the epithermal ore deposit of Cavnic, Romanian Carpathians Mountains, and a Ge-rich sphalerite (S2) from the Zn-F vein-type deposit of Peyrebrune, S.W. Massif Central, France. Bulk Ge contents of these sphalerites are 0.4±0.1 and 1363±97

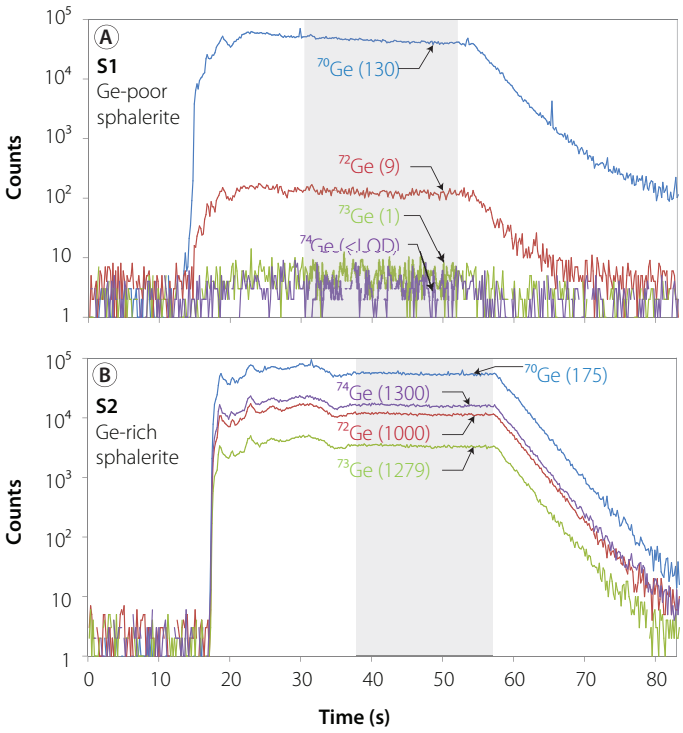

Fig. 3.2 – Determination of the most effective isotope for accurate Ge analysis in sphalerite using LA-ICP-MS. Signals of ^{70}Ge, ^{72}Ge, ^{73}Ge and ^{74}Ge intensity in (A) Ge-poor sphalerite (S1, 0.4 ppm Ge) in order to quantify isobaric interferences, and (B) in Ge-rich sphalerite (S2, 1360 ppm Ge) to verify the precision of the measurement. Calculated contents are indicated for each signal (in ppm). In Ge-poor sphalerite, interferences on ^{70}Ge, ^{72}Ge, ^{73}Ge have been detected. No detectable interferences on ^{74}Ge make it the most relevant mass for accurate Ge content measurement using LA-ICP-MS (see text for details).

ppm Ge, respectively. LA-ICP-MS analyses were performed using the experimental setup detailed above except that the masses monitored were limited to ^{66}Zn, ^{70}Ge, ^{72}Ge, ^{73}Ge, and ^{74}Ge. The Ge-poor sphalerite S1 was used to test which Ge isotope is least affected by interferences in a sphalerite matrix. The Ge-rich sphalerite S2 was used to test the precision of the calculations using the different Ge isotopes, and so to track interferences in the external standard.

Table 3.1 – Elemental compositions (in ppm) of S1 and S2 sphalerites analysed at the SARM (Nancy, France) using quadrupole ICP-MS.

		Mn	Fe	Co	Cu	Zn	Ga	As	Ge	Cd	In	Sb	Sn	Pb
S1	Content (ppm)	3330	117294	4.8	52	547400	4.3	<LOD	0.4	2030	0.3	46	17.6	11212
	Error (1σ SE, ppm)	238	5972	0.8	6	27870	0.4	–	0.1	103	0.1	2	2.0	571
S2	Content (ppm)	<LOD	26228	17.4	2296	661200	129	9.5	1363	1704	19.5	413	53.2	310
	Error (1σ SE, ppm)	–	1435	2.0	164	33664	9	1.1	97	87	1.4	21	3.8	16

LOD: limit of detection.
*Dissolution according to Luais (2007, 2012), trace element measurements at the SARM.

The resulting LA-ICP-MS ablation signal in S1 (Fig. 3.2a) shows major interferences on ^{70}Ge and ^{72}Ge leading to biased concentrations of 130 and 9 ppm respectively (true value of ~0.4 ppm). However, very limited interferences are seen on ^{73}Ge and ^{74}Ge, leading to concentrations of 1.1 and 0.1 ppm, respectively, which falls, within error, fairly close to the bulk ICP-MS value. Calculations on S2 (Fig. 3.2b) showed that the best accuracy was obtained for ^{74}Ge and ^{73}Ge with concentrations of 1300 and 1280 ppm, respectively (true value of ~1360 ppm). However, Ge content using ^{70}Ge is only of 175 ppm. This large underestimation is due to significant interference by ^{70}Zn that is a major component in sphalerite. Ge content using ^{72}Ge is of 1000 ppm. Remarkably, this underestimation is due to the presence of oxygen in the MASS-1 external standard (~12.9 wt.%), allowing the formation of ^{56}Fe^{16}O

that interferes on ^{72}Ge and introduces a bias in the calculation. Therefore, the isotopes least affected by isobaric interferences are ^{73}Ge and ^{73}Ge, and, considering their relative isotopic abundances (7.73% and 36.28%, respectively; Audi et al., 2003), ^{74}Ge appears to be most suitable for LA-ICP-MS analysis in sphalerite (relative to the MASS-1 external standard). Interferences on this isotope being negligible, there is no need for further corrections.

3.4 Multivariate statistics by PCA

Multivariate statistical analyses provide unique tools to bring out concise description of multi-dimensional data and highlight relationships among variables. Principal component analysis, one type of such multivariate statistical analysis, is a powerful variable-reduction technique designed to project data in two-dimensions with minimal data loss. Principal components are defined as orthogonal linear combinations of the initial variables, producing maximum variance and minimising data loss. They are directly computed as the eigenvectors of the covariance matrix, $S = (s_{ij})$, for which each term is expressed as:

$$s_{ij} = cov(X_i, X_j) = \frac{1}{n}\sum_{k=1}^{n}(x_{ik} - \bar{x_i})(x_{jk} - \bar{x_j})$$

Eigenvectors are ordered by decreasing eigenvalues, hence, the two first principal components carry the highest attributed variance and correspond to the most significant relationships between the variables.

Principal component analysis is widely used in the field of geochemical exploration on large-scale datasets (e.g., Samama et al., 1989) as it helps to better understand underlying ore mineralization and its organisation. Consequently, PCA is implemented in many geo-modelling softwares (e.g., Lafferière et al., 2000). PCA has also found applications in isotope geochemistry (e.g. Cadoux et al., 2007; Iwamori et al., 2010) and sulphide geochemistry (e.g. Winderbaum et al., 2012) though it is still rarely used to treat large LA-ICP-MS datasets. In addition, we use multivariate statistics to better interpret in situ minor/trace element data in mineral geochemistry, and understand their relationship.

3.5 Element-specific crystal chemistry by synchrotron-based XAFS

Synchrotron K-edge X-ray absorption fine structure (XAFS) spectroscopy is a powerful element-specific technique that details how an atom in a given material absorbs X-rays at energies near and above its core-level binding energies. Specifically, for a given atom, a XAFS spectrum records the modulation of the X-ray absorption probability due to its chemical and physical state, and is therefore sensitive to the formal oxidation state, bond nature and lengths, as well as coordination symmetry, nature and number of atoms surrounding the probed element. The XAFS spectrum is typically divided into two regions (Fig. 3.3): X-ray absorption near-edge structure (XANES) and extended X-ray absorption fine-structure (EXAFS). This distinction is particularly convenient for the interpretation.

XANES is strongly sensitive to the formal oxidation state and coordination symmetry (e.g., octahedral *vs* tetrahedral) of the absorbing atom, while the EXAFS part of the spectrum is used to determine bond lengths, coordination number, and nature ligands surrounding the absorbing atom (Newville, 2014; Brugger et al., 2010, e.g.,).

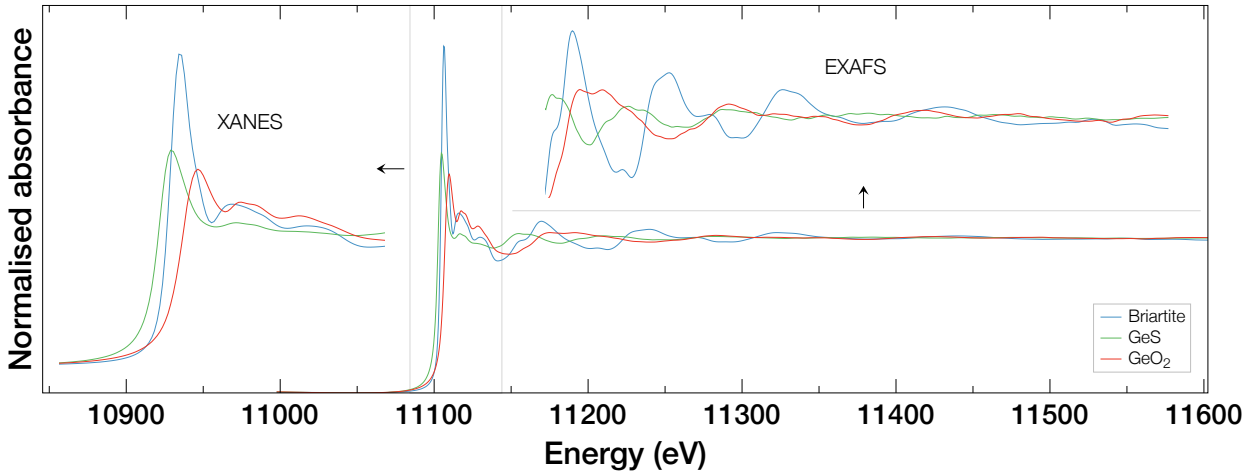

Fig. 3.3 – XAFS spectra at the Ge *K*-edge for GeS (Ge^{2+}), GeO_2 (Ge^{4+}), and briartite (natural Ge^{4+} sulphide), highlighting the XANES and EXAFS regions.

XAFS measurements were performed at the BM23 beamline of the European Synchrotron Radiation Facility (ESRF, Grenoble, France). The storage ring was operated at in multi-bunch mode, X-rays were generated using a bending magnet (BM), and monochromatised with a fixed-exit double-crystal Si(111) monochromator. Micro-focusing of X-rays into an incident beam of $\sim$5×5 μm^2 to $\sim$3×3 μm^2 was achieved using two mirrors in the Kirkpatrick-Baez (KB) geometry. μ-XRF maps were collected in order to choose the XAFS spots that followed. XAFS spectra were collected in fluorescence mode using a Vortex silicon-drift energy-dispersive detector located at 90° from the incident beam. The results presented in this thesis were obtained during experimental sessions on BM23, the first, performed in October 2013, focused on the oxidation of Ge, Fe and Cu in sphalerite; the second, performed in September 2015, focused on the oxidation state of Ge in chalcopyrite.

Complementary XANES spectra were collected at the ID26 beamline (ESRF, Grenoble, France) during the experimental session of October 2013. X-rays were generated using an insertion device (ID), monochromatised using a cryogenically-cooled fixed-exit double-crystal Si(111) monochromator, and focused into an incident beam of $\sim$1×2 mm^2 with high X-ray photon flux. Five analyser crystals were used to resolve the interferences on Ge-Kα, allowing for absorption studies on very dilute samples. More details on the XAFS phenomenon and experimental set-up can be found in the 'Ge crystal chemistry in sulphide minerals' chapter (6).

3.6 Germanium isotopes by MC-ICP-MS (bulk)

Stable isotope variations of metals are new tracers of sources and fate of metals as well as characterising ore-forming fluids and their evolution (Asael et al., 2012; Gagnevin et al., 2012). The advent of high-precision and reproducible analyse (i.e., < 0.05 ‰ per amu) using Multi-collector inductively Coupled Plasma Mass Spectrometry (MC-ICP-MS) for measuring heavy stable isotopes (e.g., Zn, Cu, Fe; Wilkinson et al., 2005b; Gagnevin et al., 2012), provides opportunities to measure and detect small variations of Ge isotopes in meteorites and terrestrial rocks (Hirata, 1997; Xue et al., 1997; Luais et al., 2000; Luais, 2003, 2007, 2012; Rouxel et al., 2006; Siebert et al., 2006, 2011; Escoube et al., 2012). Bulk Ge isotopic measurements were carried out using a GV Instruments MC-ICP-MS Isoprobe and ThermoScienfic Neptune *Plus* at the CRPG–Nancy (France). The chemical procedures used to isolate Ge from the samples follow the analytical methods for iron meteorites and Ge-bearing ores (sphalerite ores included) developed by Luais (2007). Full descriptions of chemical procedures and Ge isotopic measurements have been detailed in Luais (2007, 2012).

3.6.1 Chemistry procedure

Hand-sized ore samples were ground using both jaw and roll crushers, and sieved into three size-fractions of $<$150 μm, 150–300 μm and $>$300 μm, from which only the 150–300 μm fraction is used for further purification. The removal of gangue minerals and the sorting of sulphide minerals was performed using a laboratory Frantz magnetic separtor, operated in different conditions for discriminating minerals relatively to their Fe content and its magnetic state. Further purification was performed by handpicking under a stereomicroscope, avoiding mixed grains or grains with visible inclusions (i.e., sphalerite, which is transparent). About 10–30 mg were picked for each sample, depending on the known Ge average concentration. Note that about 1 μg Ge is sufficient for several replicates using the MC-ICP-MS.

The sulphide samples were cleaned from any surface impurities by a weak acid leaching in 0.2M HNO_3 during 5 min in ultrasonic bath, then rinsed in ultra-pure water (18.2 MΩ.cm), dried, weighed, ground in agate mortar, and finally digested using HNO_3 in screw-top Teflon vials at 60–80°C. The digestion started in HNO_3 4N in order to avoid the possible formation of a less-soluble sulphate coating around the grains, with progressive additions of concentrated HNO_3 (15N) until complete digestion. The sample was then dried at 60°C (hot plate under laminar flow hood) and dissolved into HNO_3 0.5N. This solution (0.5 ml) is loaded onto 2 ml AG50W–X8 cation-exchange resin (hydrogen form, 200–400 mesh) and Ge is eluted with 2 ml of HNO_3 0.5N, whereas other elements remain absorbed on the resin (Fig. 3.4a). The resin was formerly cleaned by alternate loadings of HCl 6N and H_2O, and conditioned with HNO_3 0.5N prior to sample introduction. The recovered Ge is dried and dissolved into HNO_3 0.01N for the analysis. In parallel, a total chemistry blank, and the JMC and Aldrich Ge standards were submitted to the same procedure for control samples. Total procedural blanks were better than 30 ρg Ge and 4ηg Zn.

Experimental solutions, that contained high concentrations of Na (see section **??**), were purified using the two-step column process detailed in Luais (2012) for silicate minerals. About 280 mL of solutions were evaporated in 60 mL Teflon vials at 60°C. The dry residue,

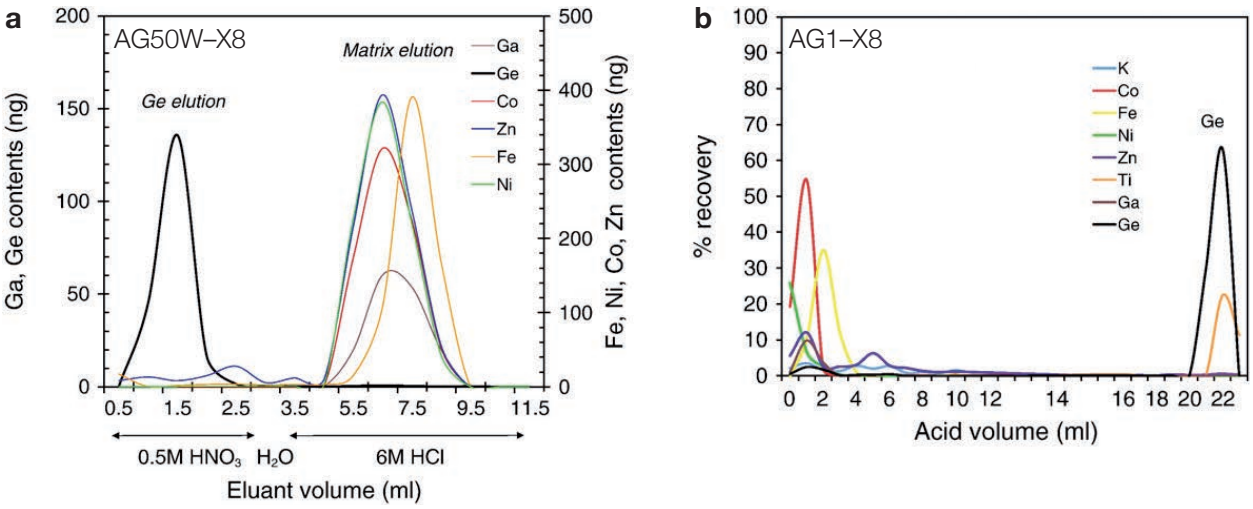

Fig. 3.4 – a. AG50W–X8 elution curves for Ge and other elements from a synthetic Fe–Ni metallic solution of Fe-meteorites (1 ppm Fe, Ni, Co, Zn, and 0.2 ppm Ge and Ga). The 2.5 ml HNO_3 for totally eluting Ge includes 0.5 ml of sample introduction. **b**. AG1-X8 elution curves for Ge and matrix elements in the ultramafic reference material PCC-1. After Luais (2012).

a Na-rich salt, was dissolved in 1 ml HF 1M, centrifuged in tubes equipped with 0.2 μm filter, then loaded onto 2 ml AG1-X8 anionic-exchange resin (1st step). For this process, the resin is previously cleaned with successive elution of HCl 0.2N, H_2O, HNO_3 0.5N, and H_2O, then conditioned with HF 1N. The addition of 13 ml HF 1N allows the elution of alkalis (e.g., Na) and metals (Mn, Zn, Ga, Ni, Co and Cu, plus most Al and Fe), while Ge and Ti are retained. The resin is then rinsed with 2 ml H_2O and 4 ml HNO_3 0.2N, and Ge ($\pm$ Al and Fe, and traces of Ti) is recovered with 3 ml HNO_3 0.2N (Fig. 3.4b). This fraction is dried at 60°C, dissolved in 0.5 ml HNO_3 0.5N and loaded onto 2 ml AG50W–X8 cation-exchange resin (2nd step) similarly to sulphide samples (see above). Again, Ge is eluted with 2 ml of HNO_3 0.5N, dried, and dissolved into HNO_3 0.01N for the analysis.

3.6.2 Analytical process

Analytical settings for measuring Ge isotopes have been described by Luais et al. (2000) and Luais (2007, 2012). The multi-collection system simultaneously measures ^{70}Ge, ^{72}Ge, ^{73}Ge and ^{74}Ge for isotopic ratio calculations, ^{68}Zn for interference corrections on ^{70}Ge (particularly important for analysing sphalerite), and ^{69}Ga and ^{71}Ga for external mass bias corrections or monitoring (Table 3.2).

The external mass fractionation of Ge isotopic ratios is calculated relatively to the international Ga isotopic standard SRM 994 (^{69}Ga/^{71}Ga=1.50676; Machlan et al., 1986), with which Ge from the standard or sample is doped in a 10:1 ratio. Luais et al. (1997) showed that mass fractionation, which results from variable focusing parameters between sessions (e.g., torch position, gas flows, extraction modes) can be parametrised using exponential laws as:

$$\left(^{74}\mathrm{Ge}/^{70}\mathrm{Ge}\right)_{\mathrm{true}} = \left(^{74}\mathrm{Ge}/^{70}\mathrm{Ge}\right)_{\mathrm{meas}} \times \left(\mathrm{m}_{74}/\mathrm{m}_{70}\right)^{f_{\mathrm{Ge}}}$$

$$\left(^{71}\mathrm{Ga}/^{69}\mathrm{Ga}\right)_{\mathrm{true}} = \left(^{71}\mathrm{Ga}/^{69}\mathrm{Ga}\right)_{\mathrm{meas}} \times \left(\mathrm{m}_{71}/\mathrm{m}_{69}\right)^{f_{\mathrm{Ga}}}$$

Table 3.2 – Isotope abundances, cup configuration and isobaric/polyatomic interferences according to May and Wiedmeyer (1998) and Luais (2012).

Isotope	Abundance	Cup	Interference
^{68}Zn	18.75 %	L3	$^{40}Ar^{14}N_2$
^{69}Ga	60.11 %	L2	–
^{70}Ge	20.84 %	L1	$^{40}Ar^{14}N^{16}O$, $^{35}Cl^{17}O^{18}O$, $^{37}Cl^{16}O^{17}O$, $^{34}S^{18}O_2$, $^{36}S^{16}O^{18}O$, $^{36}S^{17}O_2$, $^{34}S^{36}S$, $^{36}Ar^{34}S$, $^{38}Ar^{32}S$, $^{35}Cl_2$, $^{54}Fe^{16}O$
^{71}Ga	39.89 %	Center	–
^{72}Ge	27.54 %	H1	$^{36}Ar_2$, $^{37}Cl^{17}O^{18}O$, $^{35}Cl^{37}Cl$, $^{36}S^{18}O_2$, $^{36}S_2$, $^{36}Ar^{36}S$, $^{40}Ar^{32}S$, $^{56}Fe^{16}O$, $^{40}Ar^{16}O_2$, $^{40}Ca^{16}O_2$
^{73}Ge	7.73 %	H2	$^{36}Ar_2H$, $^{37}Cl^{18}O_2$, $^{36}Ar^{37}Cl$, $^{38}Ar^{35}Cl$, $^{40}Ar^{33}S$
^{74}Ge	36.28 %	H3	$^{40}Ar^{34}S$, $^{36}Ar^{38}Ar$, $^{37}Cl^{37}Cl$, $^{38}Ar^{36}S$

where m_x are the isotope atomic masses, f_{Ge} and f_{Ga} the mass bias parameters for Ge and Ga, respectively. Three methods of mass bias corrections are discussed in Luais (2012), namely, the sample–standard bracketing method (SSB), f_{Ga} correction method (assuming $f_{Ge} = f_{Ga}$), and the regression method (with $f_{Ge} \neq f_{Ga}$ and $f_{Ge}/f_{Ga} = cte$), which give a strong quantification of mass bias correction. Here, we used the two first correction methods, hence, measuring f_{Ga} allows the $^{74}Ge/^{70}Ge$ ratio to be corrected.

Samples were analysed at Ge concentrations of 50 to 500 ppb. Each analytical session begins with the optimisation of gas flow rates, torch and ion lenses parameters using a solution of the NIST SRM 3120a Ge standard. Gain calibration is performed to calibrate the Faraday cups, followed by peak centering and optimisation of the peak shapes. Samples are analysed by sample-standard bracketing, which consist of alternating measurements of standard (NIST SRM 3120a Ge) and samples. Each measurement starts with a washout time of 200 s in HNO_3 0.6 N, then 2×30 integration cycles of 8 s in HNO_3 0.1 N, and finally, 60 cycles in the sample. Ge isotope ratios are measured using the sample-standard bracketing method and expressed the δ unit (‰) with respect to the NIST 3120a Ge standard as (x = 72 to 74):

$$\delta^x Ge_{std}(sam) = \left(\frac{(^xGe/^{70}Ge)_{sam}}{(^xGe/^{70}Ge)_{std}} - 1 \right) \times 1000$$

Part of the germanium isotopes data were measured using a GV Instrument *Isoprobe* MC-ICP-MS (i.e., sphalerite from Saint-Salvy, see section 5.2). The analytical settings have been described in Luais et al. (2000). Argide interferences are resolved using an hexapole-collision cell with an hydrogen flow (Fig. 3.5a). At Ge concentration of 200 ppb, measurements of external JMC and Aldrich Ge standards give long-term reproducibility better than 0.15, 0.20 and 0.25‰ for δ^{72}Ge, δ^{73}Ge and δ^{74}Ge, respectively. Chemistry-processed and unprocessed JMC and Aldrich Ge standards are both measured to ensure that no analytical isotopic fractionation occured during chemistry processing. The data were initially measured by sample-standard bracketing relative to the JMC Ge standard and re-normalised relative to the NIST SRM 3120a Ge standard as in (Escoube et al., 2012):

$$\delta^x Ge_{NIST}(sam) = \left(\frac{\delta^x Ge_{JMC}(sam) + 1000}{\delta^x Ge_{JMC}(NIST) + 1000} - 1 \right) \times 1000$$

using the measured δ^{72}Ge, δ^{73}Ge and δ^{74}Ge$_{JMC}$ of the NIST SRM 3120a standard of +0.197±0.051, +0.261±0.109 and +0.366±0.131‰ (2σ SD external reproducibility), respectively (Luais, 2012).

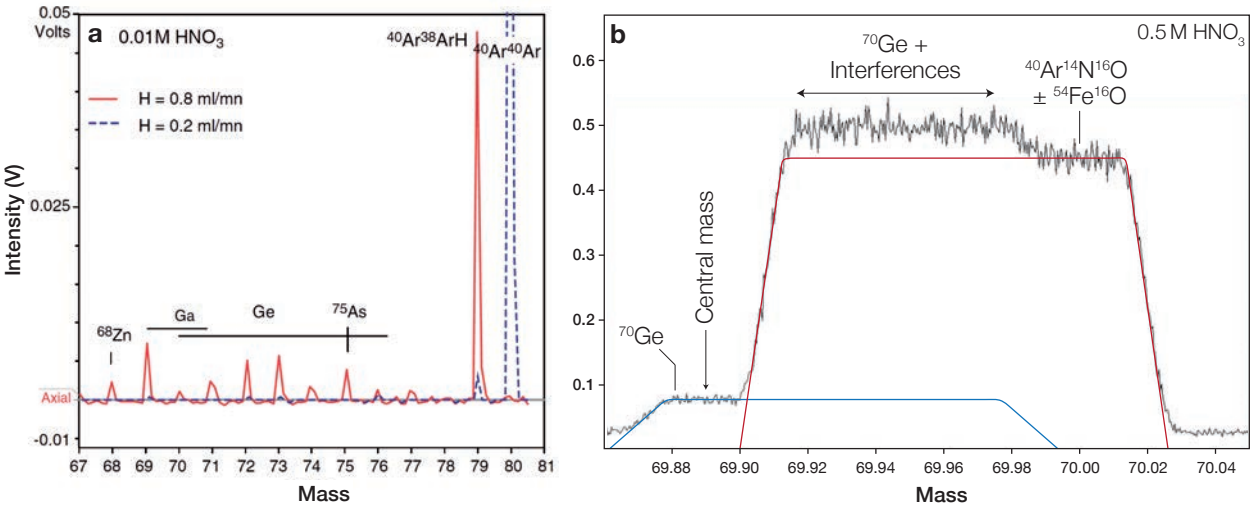

Fig. 3.5 – a. Isoprobe MC-ICP-MS – Effect of hydrogen addition in the hexapole collision cell on the removal of Ar dimers. Mass scan performed on the axial collector on blank solution. A high Ar dimer signal on mass 80 (^{40}Ar^{40}Ar) is seen with low hydrogen addition of 0.2 ml/mn, whereas complete removal of ^{40}Ar^{40}Ar can be obtained with a hydrogen flux of 0.8 ml/mn (after Luais, 2012). **b**. Neptune *Plus* MC-ICP-MS – Mass spectrum of ^{70}Ge peak and overlapping interferences measured at medium resolution (M/ΔM=6000) in blank solution (< 0.5 ppb Ge) using electron multiplier (SEM) counting mode. The central mass is set to 69.89 to avoid Ar interferences.

The most recent Ge isotopes data were measured on the ThermoFisher Scientific Neptune *Plus* MC-ICP-MS. Samples with confortable Ge amounts were introduced into the torch using a cyclonic spray chamber, whereas those with low Ge contents were introduced using an Apex HF desolvation nebulizer. In general, compared to the spray chamber, the Apex HF increase sensitivity by a factor of 4, but have less forgiving handling and overall stability. The instrument was operated in static mode at medium resolution (M/ΔM = 6000) in order to avoid counting Ar interferences (Fig. 3.5b). Cup configuration and analytical procedure, i.e., sample-standard bracketing, isobaric interference correction (^{68}Zn) and external mass bias monitoring (^{69}Ga/^{71}Ga), are similar to those used on the Isoprobe MC-ICP-MS in preceding paragraph. Similarly, JMC and Aldrich Ge standards were used to estimate accuracy and precision of the isotopic measurements. The Aldrich Ge standard have δ^{72}Ge, δ^{73}Ge, δ^{74}Ge reference values of -1.03 ± 0.12‰, -1.54 ± 0.17‰, and -2.01 ± 0.23‰, respectively; and the JMC Ge standard have δ^{72}Ge, δ^{73}Ge, δ^{74}Ge reference values of -0.16 ± 0.07‰, -0.23 ± 0.12‰, and -0.29 ± 0.10‰, respectively (Luais, 2012).

3.7 Sulphur isotopes by SIMS (*in situ*) and EA-IRMS (bulk)

Sulphur isotopes can provide information on S sources and S reduction pathways from sulphate in hydrothermal systems (e.g., thermochemical or bacteriogenic, Pfaff et al., 2011, and references therein), and related conditions. *In situ* sulphur isotope analyses were performed using the Cameca IMS 1270 secondary ion mass spectrometer at the CRPG–Nancy (France). Analytical settings are detailed in Rollion-Bard et al. (2007) and Thomassot et al. (2009). Samples were sputtered with a primary mass-filtered Cs^+ beam with an impact energy of 10 kV and an intensity of ∼7 ηA. The aperture-delimited primary ion beam resulted in flat-bottomed 15 × 25 μm ellipsoid spots. Sulphur isotopes were counted simultaneously in multi-collection mode by two off-axis Faraday cups (L'2 and H1) to yield ($^{34}S/^{32}S$) ratios. A pre-sputtering of 5 min was necessary before the analyses. The typical acquisition time was of 90 s, comprising 30 cycles of 3 s analysis per cycle. Both Faraday cups were inter-calibrated at the beginning of each analytical session. Before each analysis, an automated procedure of peak centering was performed. Values are reported in δ notation (in ‰) relative to the Vienna–Cañon Diablo troilite (VCDT, Ding et al., 2001) as:

$$\delta^{34}S_{VCDT}(sam) = \left(\frac{(^{34}S/^{32}S)_{sam}}{(^{34}S/^{32}S)_{VCDT}} - 1 \right) \times 1000$$

The instrumental mass fractionation (IMF) due to the analytical setting and matrix effect (e.g., Rollion-Bard and Marin-Carbonne, 2011) were corrected using the NBS-123 sphalerite standard of homogeneous isotopic composition (+17.44‰ VCDT, Zhang and Ding, 1989). This instrumental fractionation, defined as the difference between the measured and the true isotopic values of the standard (‰ $\Delta_{inst} = \delta^{34}S_{meas} - \delta^{34}S_{true}$), was measured at the beginning of each daily session and applied to correct each sample measurement (‰ $\delta^{34}S_{corr} = \delta^{34}S_{meas} - \Delta_{inst}$). On the overall data acquisition, the IMF averaged ∼2.5‰. The precision, including errors from counting statistics and reproducibility based on repeated measurements of the standard, were of ±0.13‰ to ±0.29‰ (1σ SD) depending on the analytical session. The average overall precision was of ±0.25‰ (1σ SD).

Sulphur isotope in bulk sphalerite samples were analysed using elemental analyzer-isotopic ratio mass spectrometer (EA-IRMS) at the CRPG-Nancy (France). Compared to SIMS, EA-IRMS show better accuracy and precision (±0.1‰ 1σ SD) of $\delta^{34}S$ values determined for bulk S-bearing geological materials. The general analytical technique has been described by various authors (e.g., Grassineau, 2006, and references therein). Precise masses of finely ground samples are loaded with careful attention into Sn capsules that are then tightly crimped. For S extraction, each capsule is dropped individually into a catalytic combustion furnace at a temperature around 1040°C. O_2 injection triggers the Sn oxidation, which creates an exothermic 'flash combustion' at about 1800°C responsible for the complete combustion and oxidation of the sample, producing SO_2. Reduced Cu absorbs the excess O_2 and SO_2 is carried by a He gas flow via a water trap for subsequent phase separation on a gas chromatographic column (tungstic oxide on alumina) before entering the mass spectrometer source. $^{34}S/^{32}S$ ratios for samples and standards are obtained by measuring the integrated peak areas corresponding to $^{34}S^{16}O_2$ (mass 66) divided by those of $^{32}S^{16}O_2$ (mass 64). S

isotopic values, δ^{34}S (‰), are reported relative to the Vienna–Cañon Diablo troilite using the equation above. The S-isotopic slope calibration is derived from a set of standards with δ^{34}S values ranging from –46.7‰ (CJP pyrite) to +20.3‰ (NBS 127 barite).

Chapter 4

Material

In the first comprehensive review of Ge geochemistry by Bernstein (1985), based on natural observations, experimental and thermochemical data, the latter outlines that Ge occurrences and forms appear to be chiefly related to sulphur and oxygen activities, and temperature (Fig. 4.1). Since then, the new Ge geochemical data that were issued in several compilations that followed are still consistent with these observations (e.g., Höll et al., 2007; Melcher and Buchholz, 2013; Frenzel and Woodcock, 2014). According to this conceptual diagram, we chose to study three distinct types of Ge occurrences and associated ore-formation conditions: Ge-bearing sphalerite from the vein-type Zn–Ge–Ag deposit of Saint-Salvy (French Massif Central), Ge-bearing chalcopyrite in the VMS-remobilised Cu deposit of Barrigão (Iberian pyrite belt, Portugal) and Ge-sulphides in the carbonate-hosted polymetallic deposit of Kipushi (Central-African copper belt, D.R. Congo).

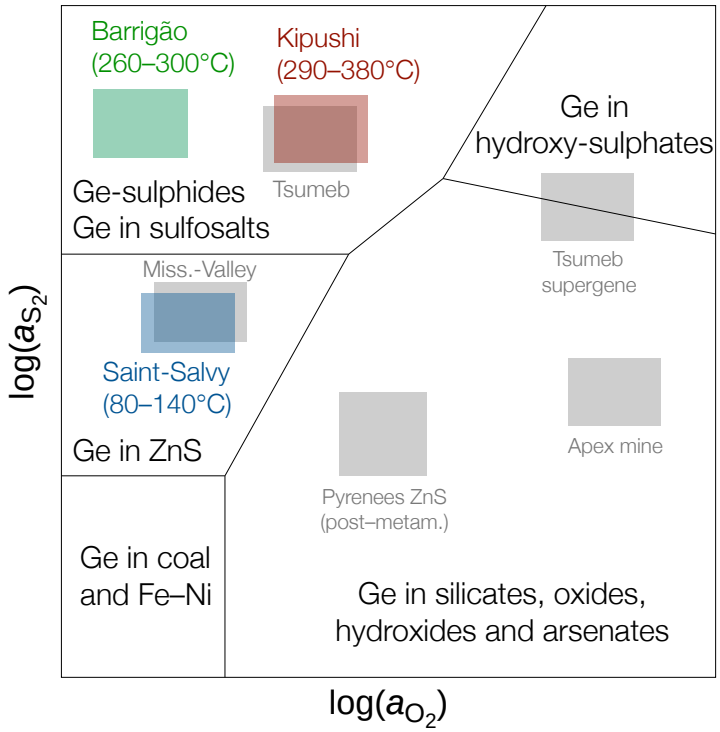

Fig. 4.1 – Schematic diagram of Ge behavior in different geologic environments as related to oxygen and sulphur activities (modified from Bernstein, 1985) and the three Ge-bearing deposits studied in this thesis.

4.1 The Saint-Salvy Zn deposit (France)

4.1.1 Geological setting

The Saint-Salvy Zn–Ge–Ag vein-type deposit is located on the S border of the Sidobre granite massif, SW edge of the French Massif Central (Fig. 4.2). The vein system is hosted by the western part of the Cambrian–Silurian schist unit. The ore body is 3 km long and lies along a sub-vertical ENE–WSW strike slip fault (Cassard et al., 1994). The mineralisation occurs as decametric veins of massive sphalerite and metric lenses of implosion-collapse breccias filled with siderite, quartz, and sphalerite. Ore deposition occurred during the Lias-Dogger transition under an extensional strike-slip regime, from high-salinity (H_2O–NaCl–$CaCl_2$, 23–25 wt.% NaCl eq.) and low-T (80–140°C) fluids (Munoz et al., 1994). Similar surface-derived brines have been described for most of the Pb–Zn–(F–Ba) deposits of the southern Massif Central margins, for example Peyrebrune (Munoz et al., 1997), Les Malines (Charef and Sheppard, 1988) and Trèves (Leach et al., 2006), which belong to a widespread early Jurassic hydrothermal event in western Europe that formed a number of large F-Ba-Pb-Zn mineralisations (e.g., Bruce et al., 1998; Muchez et al., 2005; Boiron et al., 2010; Cathelineau et al., 2012; Munoz et al., 2015). Further details are presented in section 5.2.

4.1.2 Ore paragenesis

Seven ore samples were collected from deep mine faces of the main mine, which is about 600 m deep and 1450 m long: 62E, 62W, 64W (64W-02 and 64W-08) and the deepest one, 74W (the first number indicates the mine level (depth) whereas the second indicates longitudes, see Cassard et al., 1994). Two additional samples representative of the mined ore were added to our study, K and SAL-UN. The samples were taken from economic veins so that only sphalerite from the economic mineralization stage was investigated. These samples consist of implosion-collapse breccias containing angular to rounded schist clasts coated with – in chronological order – palissadic layers of siderite and/or quartz, and Ge-bearing sphalerite, and terminal quartz filling. This paragenesis forms the typical 'cockade' breccia texture (e.g., Cassard et al., 1994; Frenzel and Woodcock, 2014). Accessory sulphides such as pyrite, pyrrhotite or galena (Cassard et al., 1994), have not been observed in our samples. Detailed descriptions of the Saint-Salvy ore paragenesis can be found in Halfon and Rosique (1973), Barbanson and Geldron (1983), Moisy (1993), Cassard et al. (1994) and Munoz et al. (1994). The latter is more geochemistry-oriented, featuring fluid inclusion and stable isotopes studies ($\delta^{18}O$, δD, $\delta^{34}S$). Fig.4.3 suggest a main mineralising event during the Late Triassic – Early Jurassic transition (∼180 Ma).

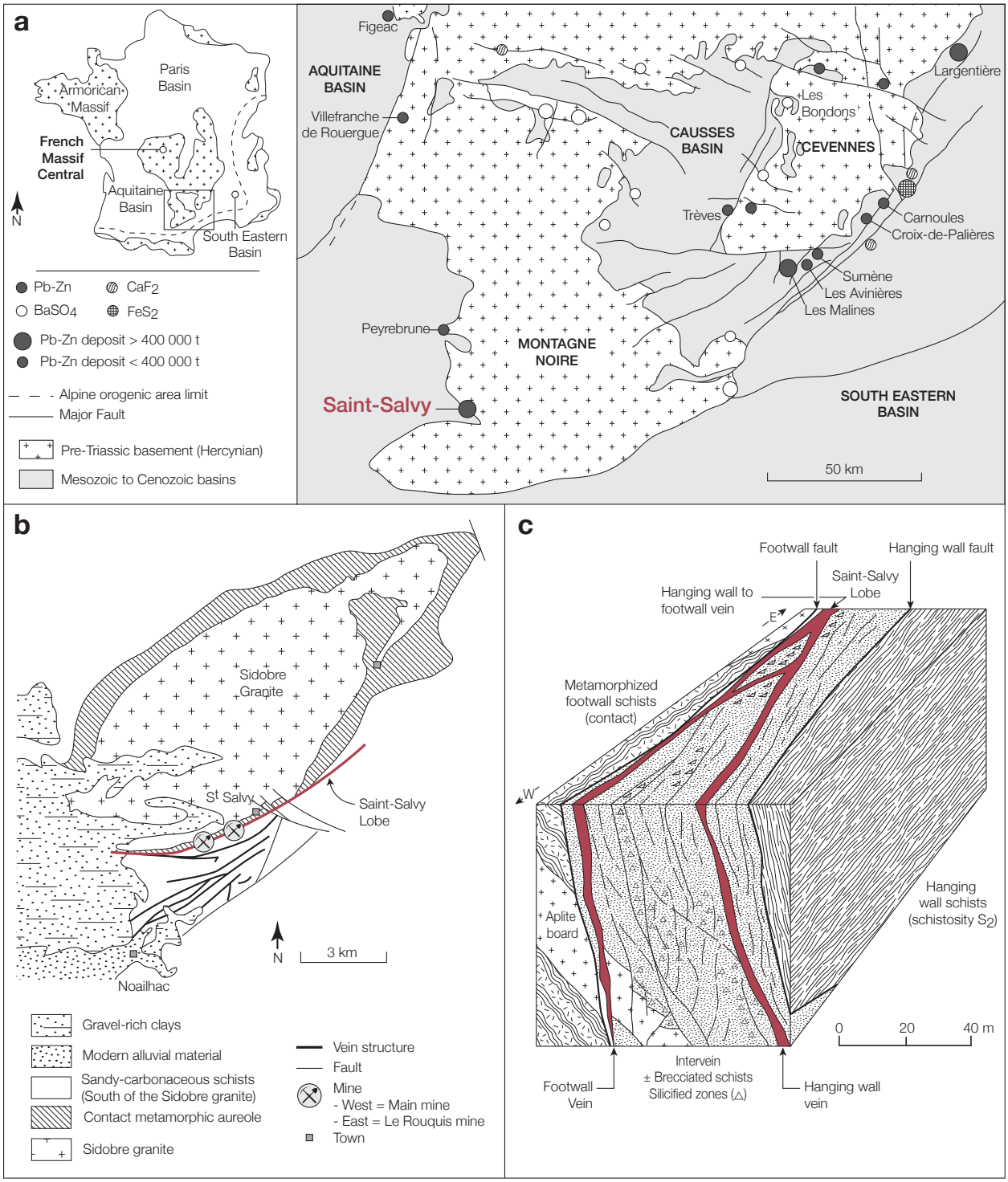

Fig. 4.2 – **a**. Location of the Saint-Salvy deposit in the French Massif Central and other major deposits (modified from Leach et al., 2006). **b**. Location of the Saint-Salvy lobe south of the Sidobre granite, including the contact-metamorphism aureole. **c**. Main features of the East–West block diagram of the Saint-Salvy vein structure (b/c modified from Cassard et al., 1994).

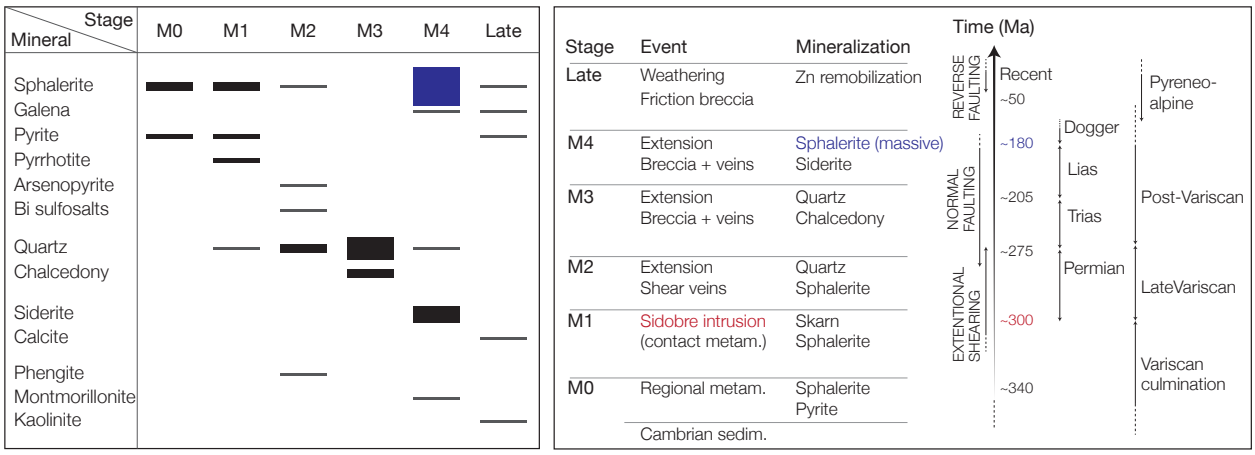

Fig. 4.3 – Mineral paragenesis and deposition timing at Saint-Salvy (modified after Munoz et al., 1994).

Optical microscope observations of the Ge-bearing sphalerite on 150 μm-thick polished sections reveal well-developed supra-millimetric crystals heterogeneously coloured from light brown to dark reddish-brown without any micro-inclusions of other sulphide species (e.g., chalcopyrite). Two main typical optical compositional zoning patterns can be identified within sphalerite crystals, (i) *rhythmic bandings*, (110) faces, occurring as alternating parallel dark brown and light brown growth bands, from the core to the rim (Fig. 4.4a-b). They frequently associated with adjacent (ii) *sector zonings*, (111) faces, occurring as crosscutting-like dark brown zones consisting of a series of small and parallel truncation planes highly variable in size, and accounts for their highly indented boundaries (Fig. 4.4a-b). Face indexation for this sphalerite is presented in Johan (1988). This sphalerite also shows dark brown geometric patterns such as triangles or multiple quadrangles highlighting complex twinning (e.g., polysynthetic twins). These patterns can form complex areas over several dozens of μm^2 in some crystals.

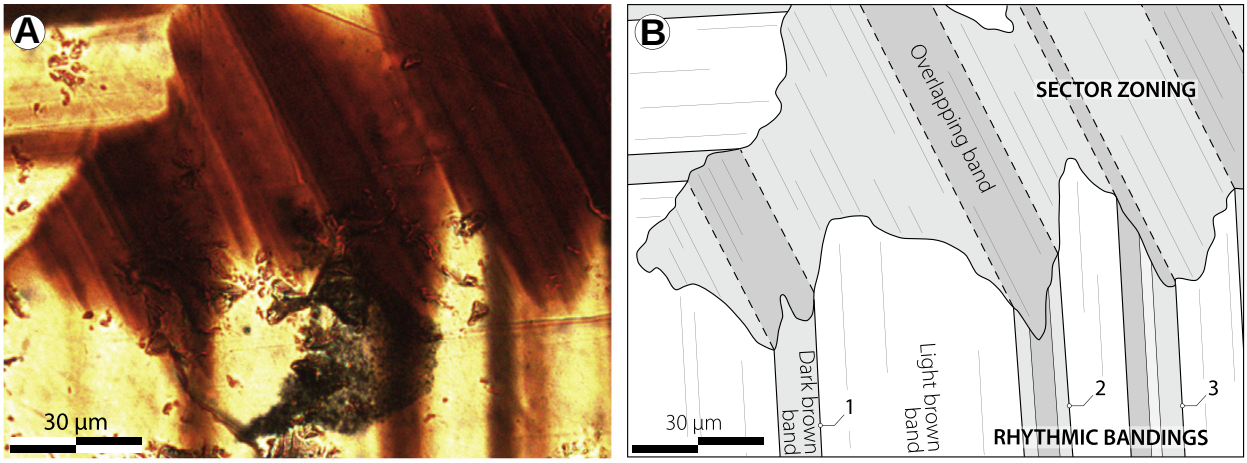

Fig. 4.4 – Zoning patterns in sphalerite from Saint-Salvy. (A) Colour zoning patterns under transmitted light microscopy, i.e. rhythmic banding and sector zoning. (B) Interpretative scheme.

4.2 The Barrigão Cu deposit (Portugal)

4.2.1 Geological setting

The Barrigão Cu-rich deposit is located within the SE part of the Iberian Pyrite Belt (Portuguese side), which is one of the greatest mining district in the world, famous for its largest concentrations of massive sulphide deposits, including several world-class volcanic-hosted massive sulphide deposits (VHMS, e.g., Neves Corvo; Fig. 4.5). Strata-bound massive sulphide deposits are intercalated within volcano–sedimentary successions of Late Devonian to Early Carboniferous age. The latter underwent post-depositional low-grade regional metamorphism associated with thrusting and folding during the Variscan orogeny, which resulted in the tectonic dismembering of the volcano–sedimentary successions and ore deposits, as well as in the development of late fault-related veins, distributed throughout the South Portuguese and Ossa Morena zones, often hosting copper deposits (Reiser et al., 2011).

Barrigão is one of these late vein-type deposits and consists of two converging metric-thick vein structures of ∼1800 m long. The mineralisation is hosted within Visean shales and greywackes of the Mértola Formation, a subunit of the Baixo Alentejo Flysch Group (Reiser et al., 2011). Because of the impossibility to safely gather samples in the underground mine, ore samples were collected from the mine dumps located in the northern sector of the Barrigão mine by the team of Daniel P.S. de Oliveira, Laboratório Nacional de Energia e Geologia (LNEG), Lisbon, Portugal. The sample collection is composed of duplicates from the study

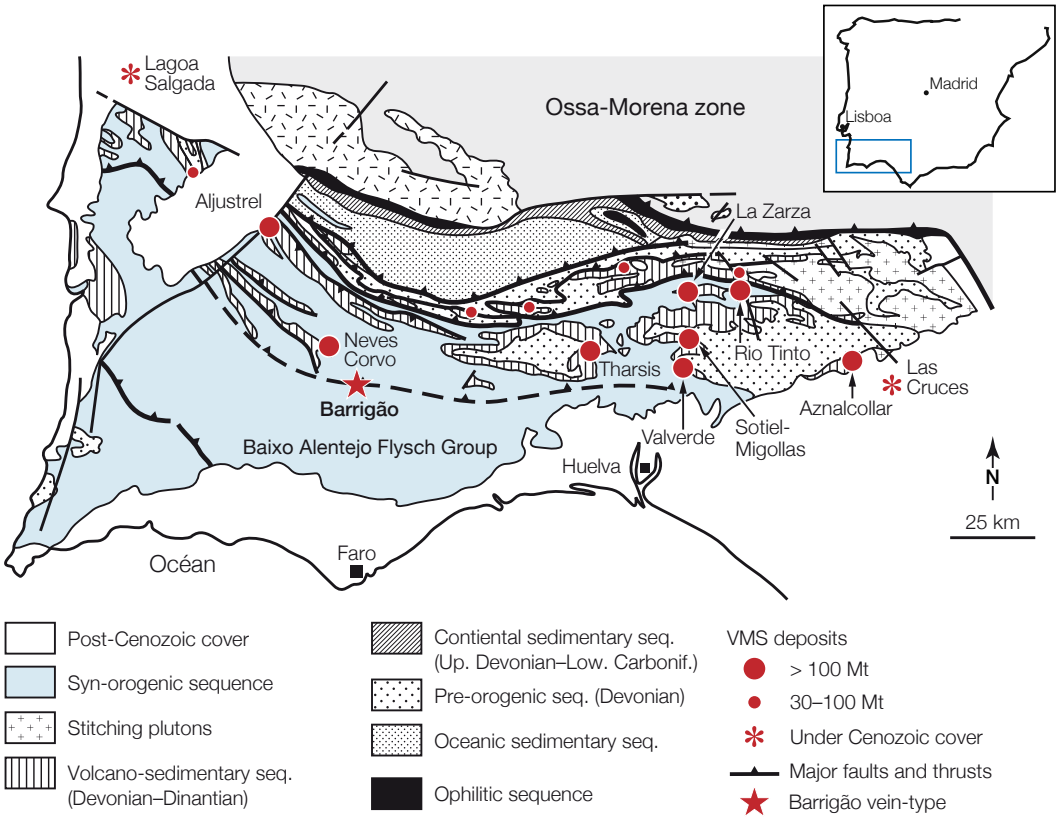

Fig. 4.5 – Location of the Barrigão deposit in the Iberian Pyrite Belt, Portugal.

of Reiser et al. (2011), for a total number of 21 samples. Samples were mounted into polished 150–200 μm thick plates at the GeoRessources laboratory, Université de Lorraine, France.

4.2.2 Ore paragenesis

The Barrigão copper ore occurs in fault breccias chiefly composed of chalcopyrite and tennantite–tetrahedrite (fahlore), pyrite, and minor/rare arsenopyrite, löllingite, sphalerite in a matrix of quartz, angular fragments of black shale, and carbonates. Reiser et al. (2011) described the presence of native bismuth (reported in tennantite) and an undetermined Cu–Sn–Ge-sulphide. The host rocks are siliceous greywackes and shales, consisting of quartz, feldspars, phyllosilicates, rutile, apatite, and locally abundant graphite. The host rocks schistosity is preserved in the foliation of mica and, if present, graphite. Four texture types have been recognised and suggest four mineralising stages; three successive hydrothermal stages ending with a supergene-driven mineralising event. The paragenetic sequence is shown in Fig. 4.6.

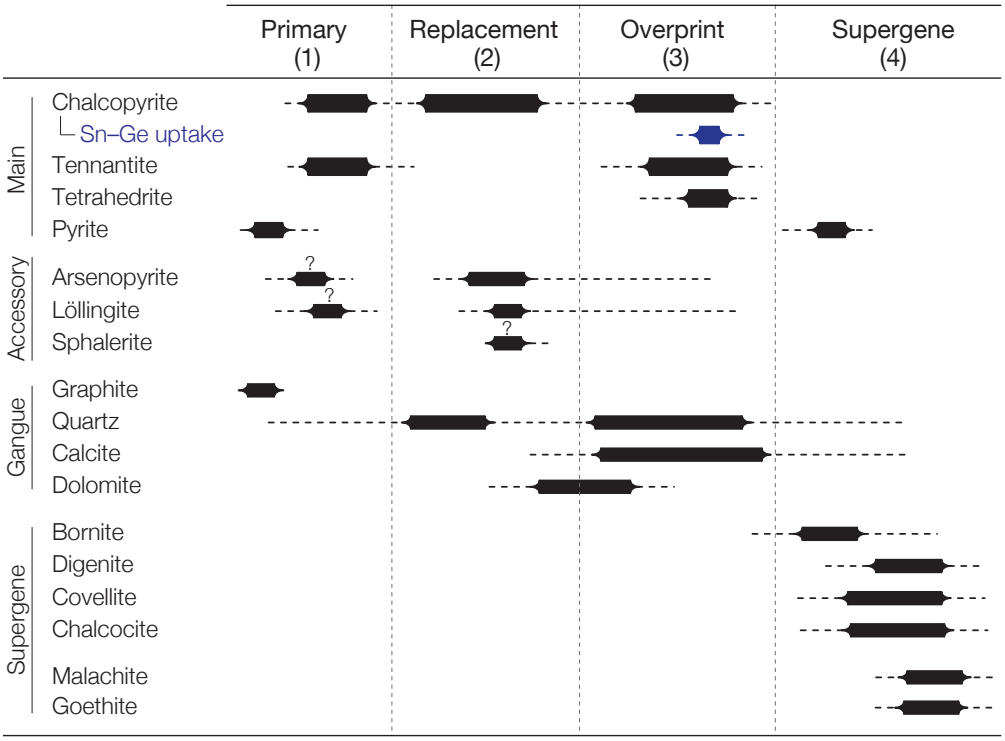

Fig. 4.6 – Paragenetic sequence of mineralisation at Barrigão (modified from Reiser et al., 2011)

Most of the sulphide mineralisation are expressed trough medium to coarse grained layers or aggregates of coeval chalcopyrite and fahlore. They both show smooth interlocking boundaries and in places subhedral to euhedral textures (Fig. 4.7b,c). Small pyrite relics (below 200 μm) are commonly observed in chalcopyrite (Fig. 4.7a), themselves containing marcassite relics and/or euhedral löllingite (Reiser et al., 2011). Subhedral to anhedral tennantite relics, often fractured or porous, are hosted in nearly fracture-free chalcopyrite, associated with replacement textures or atoll-like morphologies, evoke a second mineralising stage. A hydrothermal overprint is marked by the development of quartz-carbonate veins

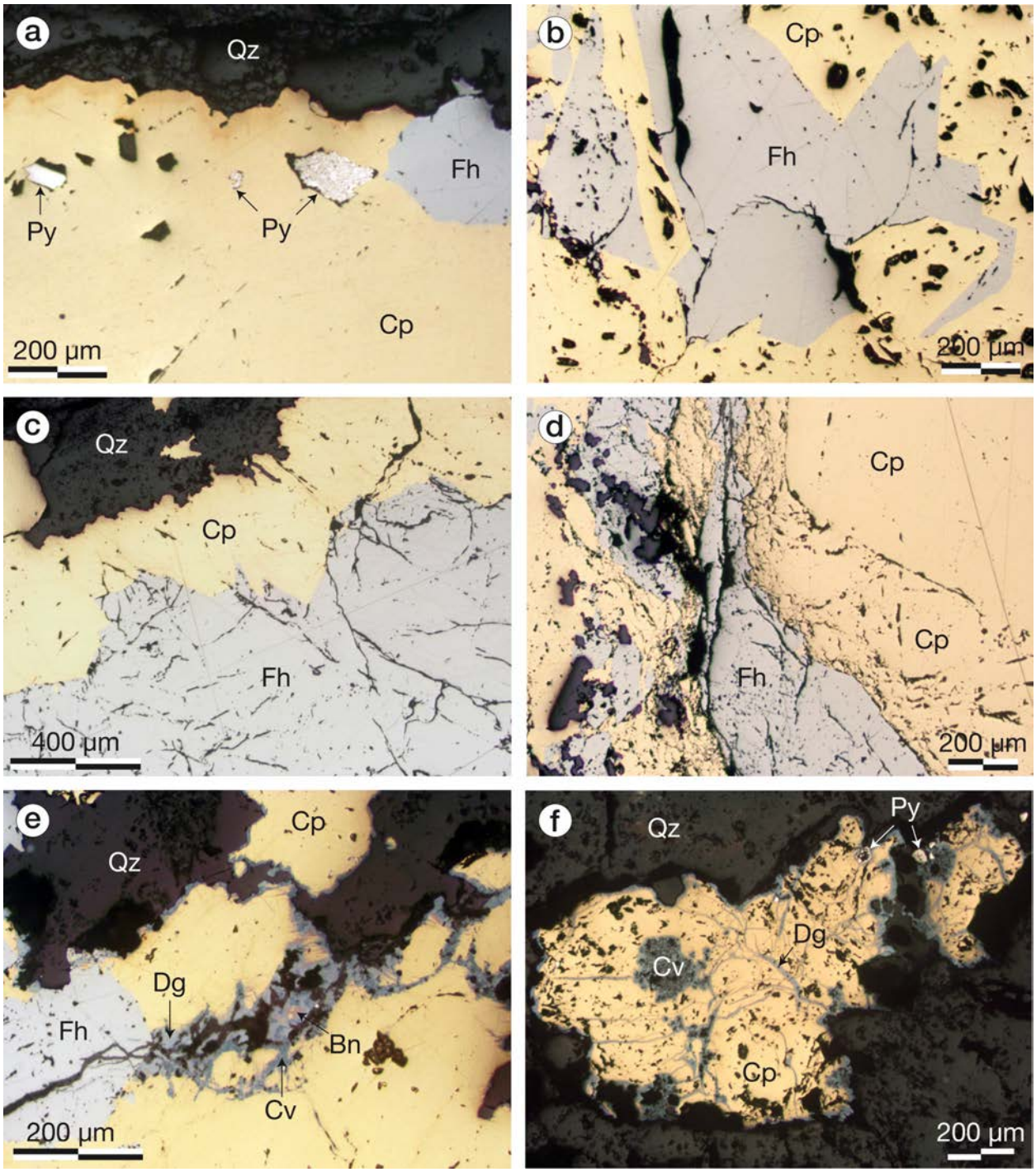

Fig. 4.7 – Microphotographs of typical Barrigão ore assemblages and textures. **a** – Pyrite (Py, euhedral and aggregate) replacement by chalcopyrite (Cp) and tennantite–tetrahedrite (fahlore, Fh). Late grain corrosion noted by a highly indented grain boundary against quartz (Qz) cement (sample 2Barr5). **b**–**c** – Chalcopyrite and fahlore in equilibrium (samples Barr8 and Barr3, respectively). **d** – Hydrothermal overprint marked by a fractured/porous chalcopyrite–fahlore texture (left-hand side) around an unaltered chalcopyrite grain (right-hand side; sample Barr1). **e**–**f** – Late hydrothermal shown as a reworking of the former chalcopyrite–fahlore assemblage (corroded irregular quartz-cemented grain boudaries) and supergene modifications marked by the development of a bornite–digenite–covellite succession (Bn–Dg–Cv) in vein margins and grain boundaries, as well as pyrite in vugs (samples 2Barr8 and 2Barr17, respectively).

showing fragment transport and marginal corrosion of the chalcopyrite–fahlore assemblage, as well a dynamic re-crystallisation in veins and highly fractured zones (Fig. 4.7d–f). This overprint is also marked by the presence of patchy and vein-like zoning patterns in chalcopyrite (Fig. 4.8a–c) as well as veins of tetrahedrite in tennanite (Fig. 4.8f), indicating an hydrothermal reworking of former ore minerals. A late supergene destabilisation of chalcopyrite appears in the development of tens of micrometers wide layers of bornite, digenite and covellite in fractures and corroded margins, generally related to quartz–carbonate-cemented veins, and pyrite deposition in vugs (Fig. 4.7e–f) as well as copper hydroxysulphate, brochantite $Cu_4SO_4(OH)_6$ (Fig. 4.8d,e).

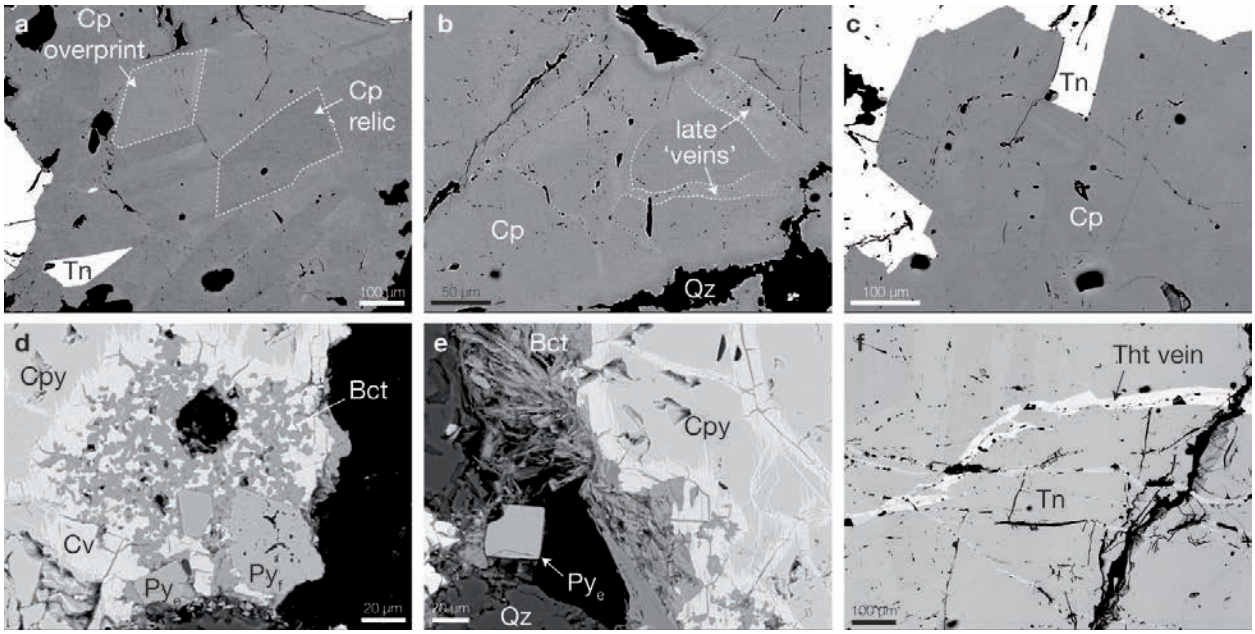

Fig. 4.8 – Secondary electron microscope observations of typical textures in samples from Barrigão. **a**. Patchy zonation in chalcopyrite showing relics of chalcopyrite (Cp) surrounded by heavier in Z halos. **b**. Late vein-like zoning in chalcopyrite. **c**. Equilibrium texture between chalcopyrite and tennantite (Tn) and zoning patterns in chalcopyrite. **d**. Supergene alteration textures in chalcopyrite, late As-rich, framboidal pyrite (Py_f) and euhedral pyrite (Py_e). **e**. Supergene alteration textures with the Cu hydroxysulphate, brochantite (Bct). **f**. Late veins of tetrahedrite (Tht) in tennantite (Tn).

4.3 The Kipushi Zn–Cu deposit (D.R. Congo)

4.3.1 Geological setting

The Kipushi carbonate-hosted Zn–Cu deposit is located in the southeastern part of the Central African Copperbelt (Fig. 4.5), an exceptionally rich metallogenic province, which extends along the Lufilian orogenic belt, itself running along the borders of the Angola to the northwest, Democratic Republic of Congo, and Zambia to the southeast. The ore lenses are situated on the northern flank of an anticline dipping 75–85°NE. The brechified axis, known as the Axial Breccia, is crosscut by the subvertical NE-directed Kipushi fault along which the mineralisation forms a pipe-like orebody, irregular to elliptical in cross-section, trending 28°NE, 20–60 m thick on its 200–600 m length, and dipping ~70°NW (Kampunzu et al., 2009).

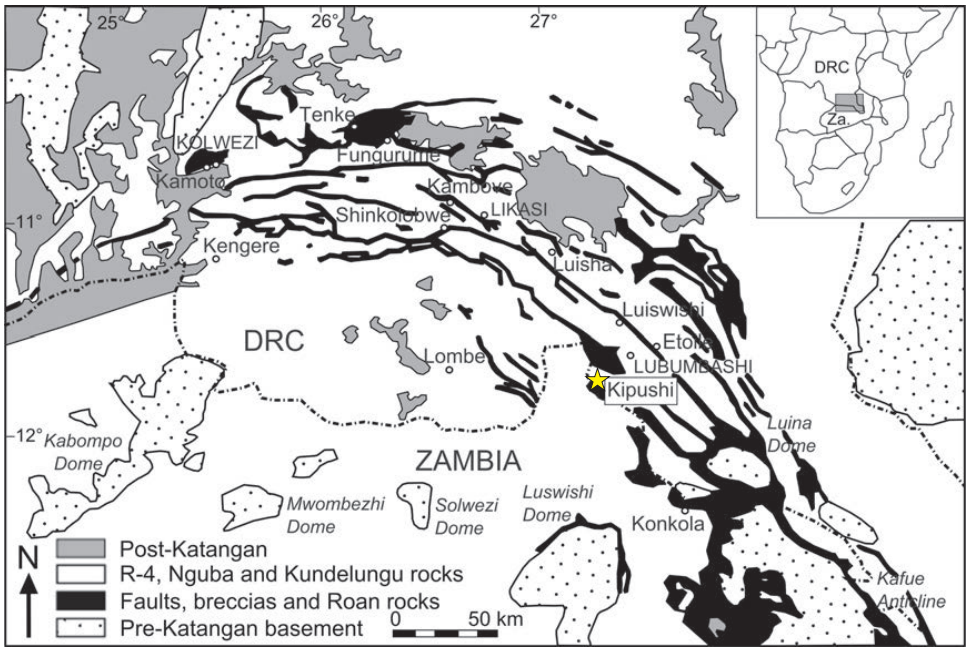

Fig. 4.9 – The Central African Copperbelt and the Kipushi deposit (from Van Wilderode et al., 2013).

The complex Zn–Cu sulphide mineralisation (described below, section 4.3.2) is hosted in dolomitic shales and dolomites filling cavities and collapse breccias along fractures and bedding planes. Distinct ores types are organised in a coherent zonal distribution with respect to host lithologies (Intiomale, 1982). From the surface down to the 1500 m level, progressing northward along the Kipushi fault, the main part of the mineralisation evolves as: (1) Zn–Pb-rich ores at the top of the Kakontwe Formation and Zn-rich ores at the base of the Kipushi Formation; (2) Zn–Cu-rich ores in carbonates of the Kipushi Formation, (3) Cu-rich ores in shales and carbonates of the Katete Formation in the northern part of the deposit (Fig. 4.10, level 600). Moreover, in the southern part of the orebody, lenticular Zn–Cu and Cu ores parallel to the Kipushi Fault in the central to lower carbonates of the Kakontwe Formation, become more significant with increasing depth (Fig. 4.10, level 1300). Below the 1350 m level, the concentration of Zn in the Zn–Cu ores decreases while the amount of Fe progressively increases (Intiomale, 1982; Intiomale and Oosterbosch, 1974).

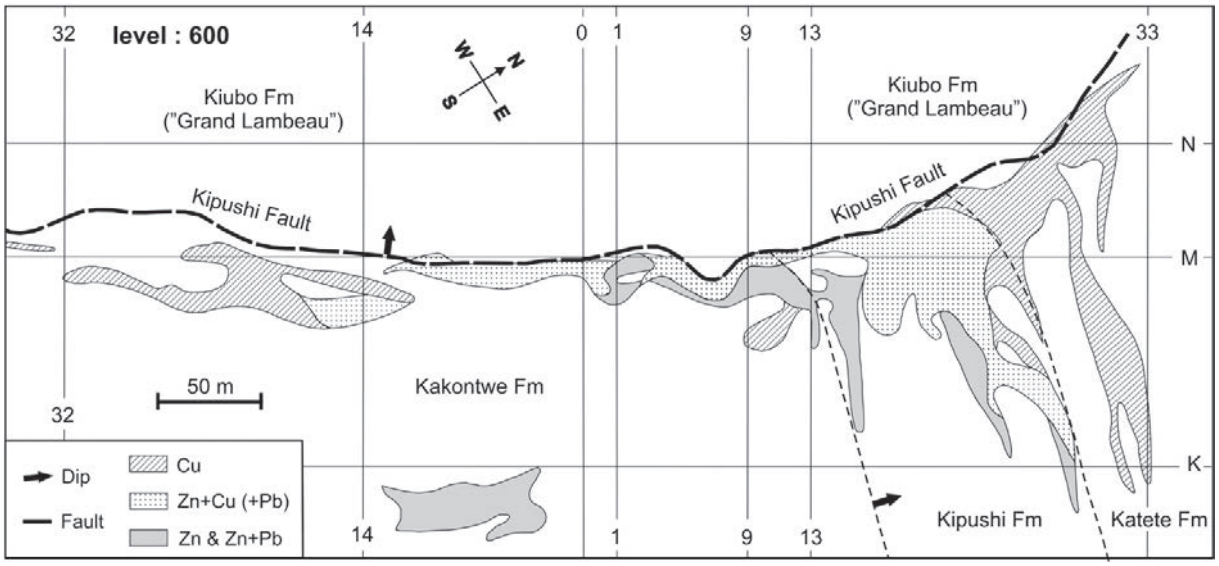

Fig. 4.10 – Structural organisation of the Kipushi ore types at level (Z) 600. From Kampunzu et al. (2009) and references therein.

Ore formation is though to result from ascending metal-bearing brines channelled in Kipushi fault. The Grand Lambeau slab at the hangingwall provided an impermeable lithologic boundary against which the mineralisation could develop (Magnée and Francois, 1988). The main orebody could have formed by hot ascending fluids through karstic cavities, whereas the ore offshoots have formed laterally by descending cooling fluids penetrating through the host dolomites, implying a convective system (Intiomale and Oosterbosch, 1974). The strong salinity of the NaCl–KCl–$CaCl_2$ fluids (30–43 wt.% eq. NaCl) suggests the dissolution of halite and the relatively high metal content (Ba, Zn, Fe, Pb) indicates that the source rocks may have included felsic basement (Heijlen et al., 2008).

The textural relationships between Zn- and Cu-dominated ores suggest different mineralising events, but the uniform Pb isotope signature suggests that both type of ores formed from the same fluid system (Schneider et al., 2007; Van Wilderode et al., 2013). Schneider et al. (2007) determined concordant Rb–Sr and Re–Os ages on sphalerite–bornite and bornite–renierite of 451 Ma, which suggest that the Kipushi orebody is not related to metamorphogenic fluids mobilised syntectonically during the Pan-African-Lufilian orogeny. Finally, according to Heijlen et al. (2008), the best estimate of the ore formation temperature is given by sphalerite and chlorite geothermometry, yielding relatively hot temperatures ranging between ∼290°C and 380°C.

The ore samples originate from different locations all along the Kipushi mine galleries, at levels from 290 to 850 m below the surface (Table 4.1, Fig. 4.11). The samples are fairly aligned on a plane along the Kipushi fault, therefore, in order to deal with the position information in a more comprehensive manner, principal component analysis was performed on the (X,Y,Z) coordinates in order to reduce the number of variables to two within the orebody, an upward coordinate ('Up') and a longitudinal, North-eastward coordinate ('NE'). These component are shown in Fig. 4.11. Most of them originate from the collection of Dr. P. Antun, available at the Department of Earth and Environmental Sciences, KU Leuven (Leuven, Belgium). A total number of 40 samples were mounted into either polished sections

Table 4.1 – Mineralogy and position of the selected samples from Kipushi. Coordinates 'Up' and 'NE' were calculated by PCA applied on (X,Y,Z) coordinates.

		Preparation		Coordinates in mine (m)			Coordinates in orebody	
Samples	Mineralogy	Plate	Section	X	Y	Z	Up	NE
P712	Rn, Cp, Sp, Tn	✓	✓	-217.5	125	-290	2.091	-1.761
P715	Sp (brown-orange), Cp, Py ± Cv	✓	✓	-140	7	-360	1.712	-0.373
P717	Sp (massive), Py ± Cp, Cv, Tn, Bn	✓		-238.3	189	-384	1.865	-2.365
P722	Py (massive), Cp ± Sp, Tn		✓	-156	65.7	-417	1.636	-0.920
P724	Bn (massive) ± Tn, Sp, Shg		✓	-27	-50	-417	1.792	0.697
P725	Bn (massive) ± Cp, Tn, Cv, Gn (rare)		✓	-228.5	-73	-434	0.682	-0.159
P726	Bn (massive) ± Tn, Cv, Cp, Dg, Cc		✓	-93	-73	-434	1.321	0.547
P735	Sp (massive) ± Py		✓	-86.5	-30	-450	1.456	0.234
P743	Sp, Cp, Gn ± Tn, Py	✓		-87.5	-70	-467	1.226	0.560
P749	Sp (massive, yellow-green) ± Cp, Tn, Py	✓		-120	-92	-500	0.853	0.580
U4	Rn, Sp, Cp, Gn, Tn		✓	–	–	–	–	–
U5	Rn		✓	–	–	–	–	–
U15	Cp, Sp, Rn, Gn ± Tn		✓	-246	100	-500	1.011	-1.644
U17	Py, Sp ± Gn, Cp, Rn, Shg	✓		-123	-43	-500	1.031	0.164
U22	Sp, Cp, Bn ± Cv, Tn, Rn	✓		-135	-102	-500	0.743	0.584
U25	Sp ± Cp (DIS)	✓		-50	-75.5	-500	1.248	0.810
U29	Bn, Cp, Dg		✓	-24.5	-75.5	-500	1.368	0.943
U31	Py, Sp (yellow-green), Cp, Gn, Tn	✓		-153	-137	-700	-0.287	0.834
U37	Py, Sp ± Gn, Cp, Apy, Tn	✓		-181	-131	-700	-0.395	0.639
U42	Cp, Sp, Tn , Apy ± Gn		✓	-73	-136	-600	0.499	1.213
U48	Sp (grey), Gn, Bn, Tn, Cp, Cv, Rn, Gm	✓		-162	-82	-600	0.290	0.309
U51	Sp (red), Py, Apy	✓		-198	-37	-600	0.297	-0.246
K1703	Rn, Sp		✓	–	–	-290	–	–
K2221	Rn, Sp, Cp		✓	–	–	–	–	–
K2208	Rn		✓	–	–	–	–	–
A38	Dolomite w/ Sp (yellow-brown) ± Apy, Shg	✓		-226	-132	-850	-1.217	0.456
A45	Sp	✓		-315	-130	-850	-1.630	-0.024
A50	Sp (massive)	✓		-347	-94	-850	-1.639	-0.484
A51	Sp (massive, red) ± Cp, Py, Cv	✓		-350	-89	-850	-1.634	-0.541
A78	Schist w/ Py ± Cp, Tn	✓		-457	79	-850	-1.480	-2.470
A87	Py ± Sp, Cp		✓	-492	135	-850	-1.426	-3.110
A100	Sp (massive, yellow) ± Cp, Py, Shg, Cv, Tn	✓		-249	-156	-850	-1.420	0.533
A104	Cp (massive) ± Tn, Cv, Sp, Py		✓	-252	-180	-850	-1.528	0.713
A106	Sp (massive, yellow), Cp, Tn, Apy	✓		-252	-186	-850	-1.552	0.762
A108	Bn, Sp (orange-yellow) ± Cv, Cp	✓		-251	-197	-850	-1.590	0.857
A109	Sp, Cv ± Bn, Sp	✓		-251	-200	-850	-1.602	0.882
A114	Bn (massive), Sp, Tn		✓	-252	-220	-850	-1.685	1.040
A118	Sp, Gn	✓		-78	-72	-850	-0.283	0.737
B40	Breccia w/ Cp, Py ± Sp	✓	✓	–	–	-800	–	–
D32	Sp (vein), Cp, Py		✓	-94	143	-700	1.090	-1.146

Abbreviations: Sp, sphalerite; Cp, chalcopyrite; Tn, tennantite; Bn, bornite; Cc, chalcocite; Dg, digenite; Py, pyrite; Apy, arsenopyrite; Gn, galena; Rn, renierite, Gm, germanite; Shg, shungite

for opaque-rich samples or polished 150–200 μm thick plate for sphalerite-dominated samples (Table 4.1). Care was taken to ensure a representative sampling of the orebody in both space and mineral assemblage. Host rocks are also available in this collection, they are studied in Van Wilderode et al. (2013).

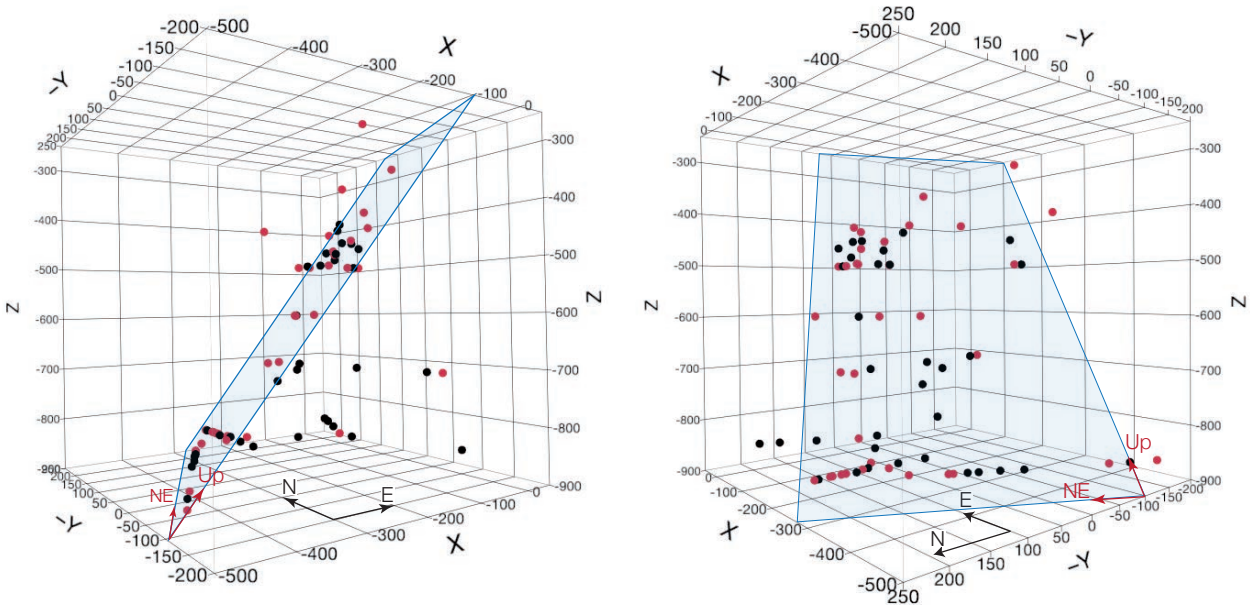

Fig. 4.11 – Kipushi sample positions in a 3D plot. Samples in red were selected for analysis, those in black where not studied. The samples are fairly aligned on a plane along the Kipushi fault. Coordinates 'Up' and 'NE' were calculated by PCA applied on (X,Y,Z) coordinates.

4.3.2 Ore paragenesis

The primary ore sulphide minerals that massively replaced of the dolomite host rocks and cements include – with decreasing abundance – sphalerite, chalcopyrite, bornite, chalcocite, pyrite, arsenopyrite, tennantite, and galena. Accessory minerals include thiogermanates with locally abundant renierite $(Cu,Zn)_{11}(Ge,As)_2Fe_4S_{16}$, minor briartite $Cu_2(Zn,Fe)GeS_4$ and rare germanite $Cu_{26}Fe_4Ge_4S_{32}$, Cu-rich species such as covellite, digenite, tetrahedrite, and rare sulphides such as gallite $CuGaS_2$, carrollite $Cu(Co,Ni)_2S_4$, ovamboite $Cu_{20}(Fe,Cu,Zn)_6W_2Ge_6S_{32}$, betekhtinite $Cu_{10}(Fe,Pb)S_6$, cobaltite CoAsS, linnaeite Co_3S_4, molybdenite MoS_2, cosalite $Pb_2Bi_2S_5$, bismuthinite Bi_2S_3, tungstenite WS_2, and stromeyerite AgCuS. Secondary supergene minerals occuring in the superficial oxidized include cerussite, malachite, smithsonite, calamine, cuprite, chalcocite, and a variety of rare Cu–Zn minerals (Intiomale and Oosterbosch, 1974).

As shown above, two main paragenesis overlap along the deposit and form a zonal distribution with respect to host lithologies – progressing northward: a Zn-dominated mineralisation (Fig. 4.13), consisting of sphalerite, galena, pyrite, and arsenopyrite, with locally abundant renierite; and a Cu-dominated mineralisation chiefly represented by chalcopyrite and bornite (e.g., Intiomale and Oosterbosch, 1974). The paragenetic sequence is shown in Fig. 4.12 implies several mineralising stages described in many studies (Intiomale and Oosterbosch, 1974; De Vos et al., 1974; Heijlen et al., 2008; Van Wilderode et al., 2013). The first stage includes the deposition of pyrite and arsenopyrite, present as corroded relics or agglomerates in a massive groundmass of later sphalerite and chalcopyrite. The second mineralising stage includes cogenetic sphalerite and chalcopyrite (possibly slightly latter), sharing sv, with accessory tennantite, briartite and germanite, primarily occurring as inclusions, and late galena, showing replacement textures in sphalerite (Fig. 4.13a,b,d). The third stage implies the replacement of chalcopyrite by bornite, chalcocite (Fig. 4.13e), and renierite. A late stage corresponds to the replacement of chalcocite by pyrite, and chalcopyrite, bornite and digenite in thin veins.

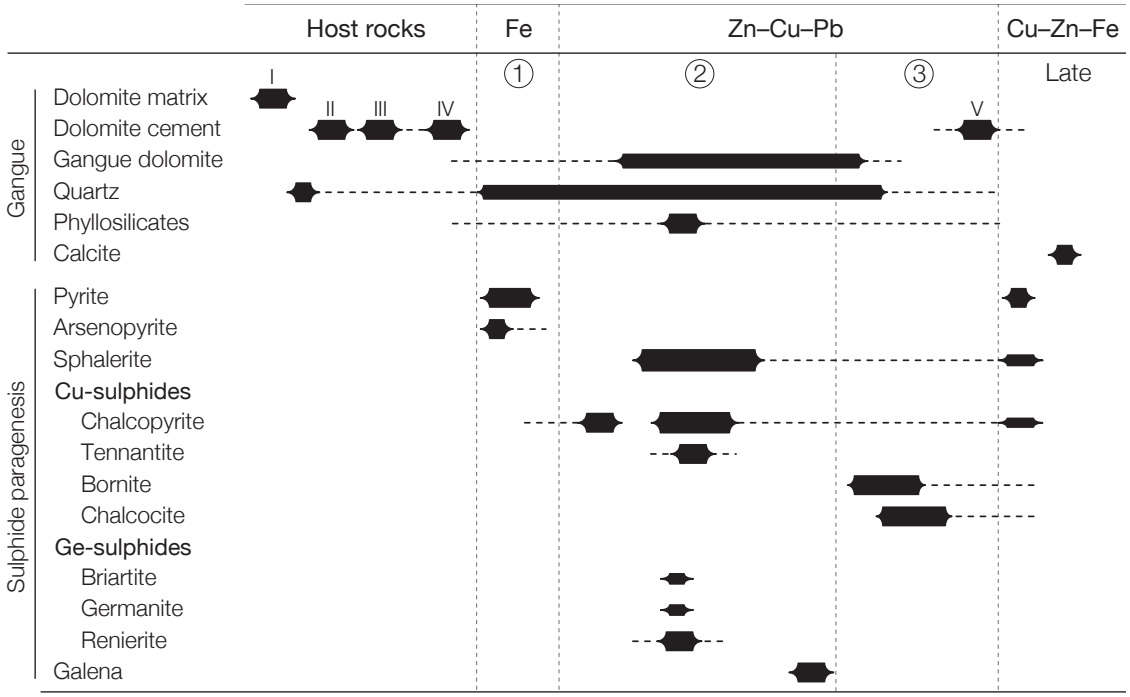

Fig. 4.12 – Paragenetic sequence of the host rock dolomite and sulphide mineralisation at Kipushi (modified from Heijlen et al., 2008; Van Wilderode et al., 2013).

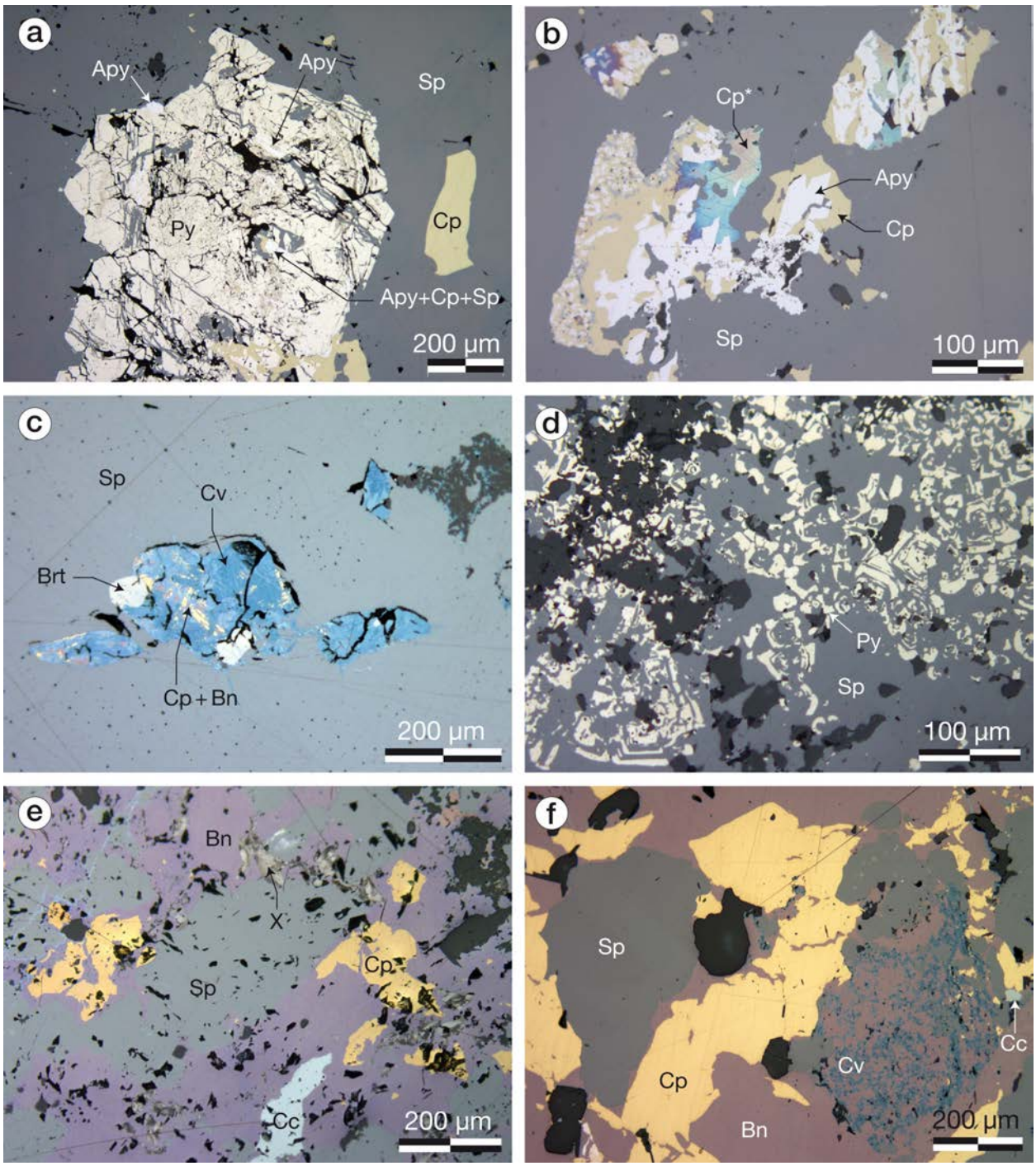

Fig. 4.13 – Ore textures in the Zn dominated ore at Kipushi. **a**. Pyrite grain (Py) replaced in places by chalcopyrite (Cp), later filled in micro-cracks with minor arsenopyrite (Apy) and sphalerite (Sp). **b**. Advanced replacement of pyrite by chalcopyrite, itself replaced by arsenopyrite (subhedral in places), then replaced by massive sphalerite deposition. Cp* is superficially oxidised. **c**. Covellite (Cv) and briartite (Brt) included in sphalerite. Covellite likely replaced former chalcopyrite as evidenced by relics of chalcopyrite and bornite (Bn). **d**. Skeletal pyrite (Py) that was replaced by sphalerite. **e** and **f**. Chalcopyrite replaced by bornite (corroded margins) and chalcocite (Cc), included in massive sphalerite.

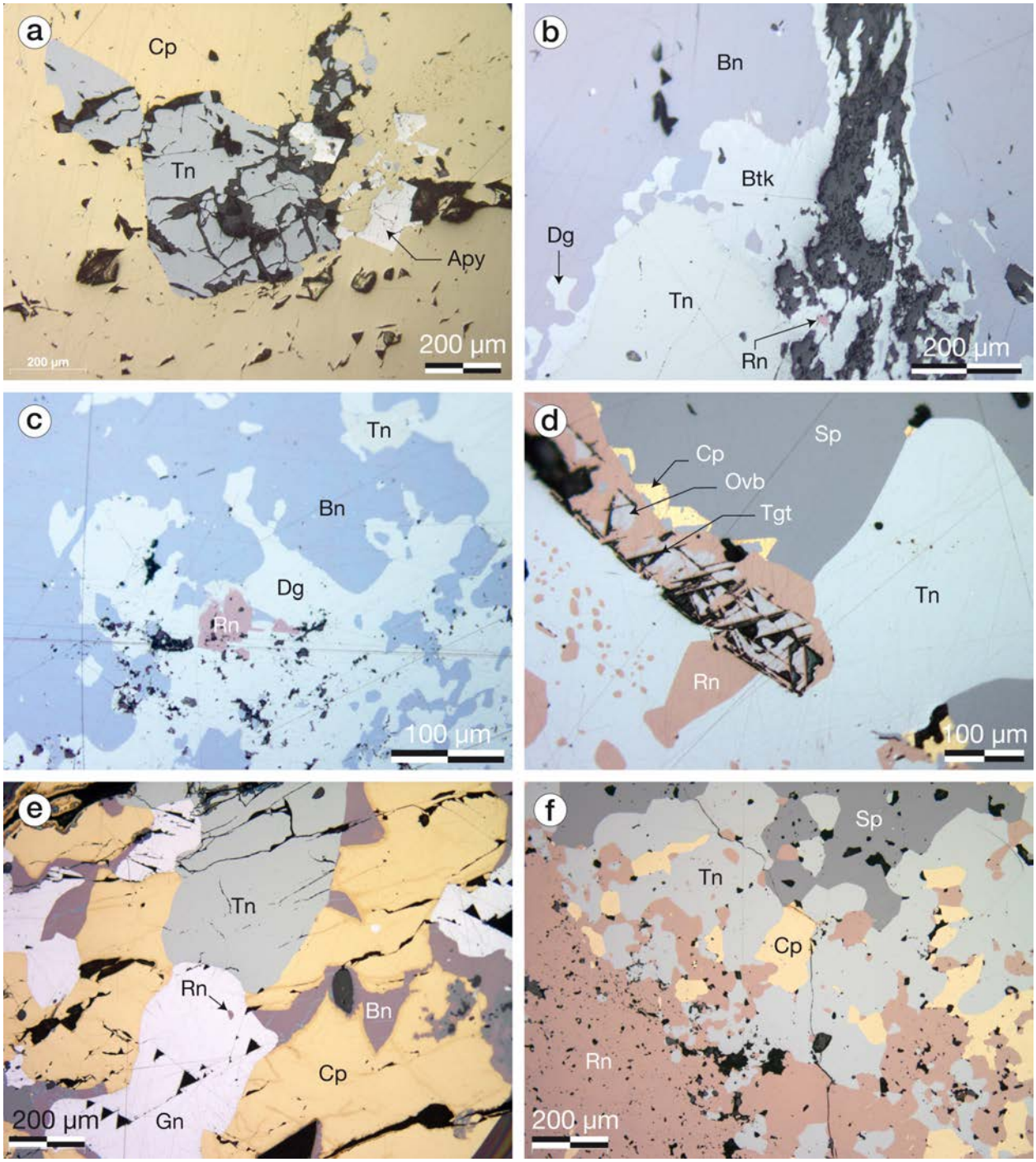

Fig. 4.14 – Ore textures in the Cu ore at Kipushi. **a**. Massive chalcopyrite (Cp) replacing fractured tennantite (Tn), that replaced arsenopyrite (Apy, refractory). **b**. Tennantite inclusion in massive bornite (Bn), replaced by betekhtinite (Btk) along a gangue-filled fracture. Digenite (Dg) inclusions in bornite along the tennanite boundary may be inherited from former chalcopyrite. Renierite (Rn) relic in digenite. **c**. Massive bornite replacing digenite (likely former chalcopyrite), renierite and tennantite. **d**. Ovamboite (Ovb) and tungstenite (Tgt) lamellae in renierite. Small chalcopyrite grains are replaced by sphalerite. Renierite, tennantite and sphalerite are mostly cogenetic. **e**. Tennantite–chalcopyrite–galena (Gn) assemblage. Chalcopyrite is replaced by bornite and little sphalerite in places. Renierite inclusion are visible in galena. **f**. Cogenetic renierite, chalcopyrite, tennantite and sphalerite.

Chapter 5

Minor and trace elements in Ge-bearing sulphides

5.1 Overview

This chapter is devoted to the study of Ge and related minor/trace elements in the studied ore deposits. The approach developed here is multi-scale. Firstly, at the scale of the deposit, we are to identify Ge hosts, outlining whether it occurs as Ge-sulphides or as minor/trace amounts in solid solutions, then, to study Ge distribution, associations, and its position within the paragenetic sequence. Secondly, at the scale of the mineral, if Ge occurs in trace/minor amounts, we are to determine whether Ge is distributed homogeneously or occurs in zoning patterns, for which it is crucial to determine whether it occurs in nano/micro-inclusions or in solid solutions. In the latter case, the nature of the substitution mechanism (direct or coupled) is to be understood, which require the identification of substituted sites, element correlations and possible crystal chemical constraints.

5.2 LA-ICP-MS analyses of minor and trace elements and bulk Ge isotopes in zoned Ge-rich sphalerites from the Noailhac – Saint-Salvy deposit (France)

This section is dedicated to the paper of Belissont R., Boiron M.-C., Luais B. and Cathelineau M. (2014) LA-ICP-MS analyses of minor and trace elements and bulk Ge isotopes in zoned Ge-rich sphalerites from the Noailhac – Saint-Salvy deposit (France): Insights into incorporation mechanisms and ore deposition processes. *Geochimica et Cosmochimica Acta* **126**, 518–540 (published on January 2014).

Available online at www.sciencedirect.com

ScienceDirect

Geochimica et Cosmochimica Acta 126 (2014) 518–540

Geochimica et Cosmochimica Acta

www.elsevier.com/locate/gca

LA-ICP-MS analyses of minor and trace elements and bulk Ge isotopes in zoned Ge-rich sphalerites from the Noailhac – Saint-Salvy deposit (France): Insights into incorporation mechanisms and ore deposition processes

Rémi Belissont [a,b,*], Marie-Christine Boiron [a], Béatrice Luais [b], Michel Cathelineau [a]

[a] GeoRessources, Université de Lorraine, CNRS, UMR 7359, Boulevard des Aiguillettes, B.P. 70239, F-54506 Vandoeuvre-lès-Nancy, France
[b] Centre de Recherches Pétrographiques et Géochimiques (CRPG), Université de Lorraine, CNRS, UMR 7358, 15 Rue Notre Dame des Pauvres, B.P. 20, F-54501 Vandoeuvre-lès-Nancy Cedex, France

Received 18 June 2013; accepted in revised form 30 October 2013; Available online 17 November 2013

Abstract

The increasing worldwide demand in germanium (Ge) is driving renewed research for understanding its geological cycle and the factors controlling its concentration in minerals. The advent of accurate, high-resolution trace element analysis by LA-ICP-MS, as well as the advances in MC-ICP-MS technique for Ge isotopes in sulphides, has enhanced studies in this field. Ge isobaric interferences, standard calibration and data interpretation remain outstanding issues needing to be addressed for more precise and comprehensive LA-ICP-MS analyses.

An integrated mineralogical and geochemical study was carried out on typical sphalerite (ZnS) samples from the main Ge deposit in western Europe: the vein-type Zn–Ge–Ag–(Pb–Cd) deposit of Noailhac – Saint-Salvy (Tarn, France). *In situ* coupled measurements of trace elements and S isotopes were performed using LA-ICP-MS and SIMS, respectively, together with bulk Ge isotopes by MC-ICP-MS. Principal component analyses revealed element clusters antithetically distributed within distinct zoning types in sphalerite: sector zonings are enriched in Cu, Ge, Ga, Sb and As, whereas rhythmic bandings (dark brown bands primarily) are enriched in Fe, Cd, In and Sn. This typical distribution points to crystallographic controls on trace element uptake during sphalerite growth, occurring with concomitant microscale variations in fluid compositions at the fluid–crystal interface. Regardless of the zoning type, in all spots, Cu contents approach the sum of tri- and tetravalent cations (Ge, Ga, In, etc.) so that Cu could provide charge-balance for the entire set of coupled substitution mechanisms responsible for the incorporation of the whole range of trace elements in this sphalerite. Strong binary correlations suggest direct substitutions as $Zn^{2+} \leftrightarrow (Fe^{2+}, Cd^{2+})$ and coupled substitutions as $2Zn^{2+} \leftrightarrow Cu^{+} + Sb^{3+}$, $3Zn^{2+} \leftrightarrow Ge^{4+} + 2Ag^{+}$, and $3Zn^{2+} \leftrightarrow In^{3+} + Sn^{3+} + \square$ (vacancy) despite no clear evidence for the presence of Sn^{4+}.

$\delta^{74}Ge_{NIST3120a}$ in bulk sphalerite varies from $-2.07 \pm 0.37‰$ to $+0.91 \pm 0.16‰$ (2σ SD) and positively correlates with bulk Ge content. This indicates considerable Ge isotopic fractionation within sphalerite during low-T hydrothermal deposition and zoning processes, associated with possible microscale open system fluid mixing. The trace element features in sphalerite from Saint-Salvy compared with those of other deposits confirm their use as discriminators among genetic types of ores (e.g., high In contents for magmatic-related deposits, and Ge for low-temperature deposits).

* Corresponding author at: GeoRessources, Université de Lorraine, CNRS, UMR 7359, Boulevard des Aiguillettes, B.P. 70239, F-54506 Vandoeuvre-lès-Nancy, France. Tel.: +33 3 83 68 47 14; fax: +33 3 83 68 47 01.
E-mail address: remi.belissont@univ-lorraine.fr (R. Belissont).

0016-7037/$ - see front matter © 2013 Elsevier Ltd. All rights reserved.
http://dx.doi.org/10.1016/j.gca.2013.10.052

INTRODUCTION

The increasing worldwide demand for germanium (Ge) for the high-tech industry (e.g., semi-conductors, infrared and fibre optics) has renewed research in the understanding of its geological cycle and the factors controlling its concentration in minerals. Ge is a semi-conductor metalloid that belongs to group IV of the periodic table, along with Si with which it shares chemical properties. Noticeably, Ge exhibits siderophile, lithophile, chalcophile and organophile behaviours and occurs in a wide variety of geologic environments (Bernstein, 1985; Höll et al., 2007). As such, it has important implications and applications in the fields of cosmochemistry and mantle geochemistry as a geological tracer (Luais, 2007, 2012 and references therein). Ge occurs as Ge^{2+} and Ge^{4+} oxidation states although the latter is the dominant form occurring in the environment and in natural compounds (Rosenberg, 2009). Even in the Ge-mineral of spinel-type structure, brunogeierite, Ge is now understood to occur as Ge^{4+} (Cempirek and Groat, 2013). Ge is not a particularly rare element in the oceanic and continental crusts, averaging 1.5 and 1.6 ppm, respectively (Taylor and McLennan, 1985). However, Ge is largely diluted in silicate minerals because of isomorphous substitutions Ge^{4+}(0.53 Å) ↔ Si^{4+}(0.40 Å) in tetrahedral sites (Bernstein, 1985). In the same way, Ge can also be incorporated in sulphide minerals, particularly sphalerite, which can contain up to 3000 ppm Ge (Bernstein, 1985).

The geochemical features of sphalerite were first investigated by Oftedahl (1940), who questioned the link between trace element content in sphalerite and its genetic type. Notably, several studies showed a temperature control on Ge and Ga contents in sphalerite (Möller and Dulski, 1993, 1996). A wide range of minor/trace elements can easily substitute for Zn within its tetrahedral sites in sphalerite, offering valuable by-products in sphalerite processing (e.g., Ge, In, Ga; Höll et al., 2007). The presence of some elements (e.g., Ag, Cu) is thought to enhance minor/trace element incorporation (Moh and Jäger, 1978). Several studies have pointed out that direct substitution of Zn^{2+} by bivalent cations accounts for the presence of common minor elements in sphalerite, i.e., Fe^{2+}, Mn^{2+}, Cd^{2+}, Co^{2+} or Ni^{2+} (e.g., Cook et al., 2009). Johan (1988) proposed a theoretical general coupled substitution mechanism, extended to tri- and tetravalent elements. This mechanism implies that incorporation of these cations in sphalerite is related to the formation of donor–acceptor pairs with monovalent ions. Compositional zoning and patterning (e.g., oscillatory zoning, rhythmic banding) implying variations in minor element contents in sphalerite have been extensively studied in the literature (e.g., Oen et al., 1980; Pattrick et al., 1993; Fowler and L'Heureux, 1996; Beaudoin, 2000; Di Benedetto et al., 2005a and references therein). However, the involvement of trace elements (notably, Ge) and related incorporation mechanisms in compositional zoning remain poorly documented (e.g., Johan, 1988) and understood. For Ge, this is at least partially due to analytical limitations with respect to the deposits, which have generally low and heterogeneous Ge concentrations. This gap in the current knowledge can be addressed using LA-ICP-MS technique.

Recent studies in sphalerite by LA-ICP-MS by Cook et al. (2009) and Ye et al. (2011) demonstrated that high-Ge contents occur in low-temperature hydrothermal deposits (e.g., carbonate-replacement MVT deposits) whereas low-Ge contents occur in high-temperature magmatic-related deposits (skarns, epithermal and massive sulphide deposits). These studies (in line with Danyushevsky et al., 2011) pointed out analytical issues in the quantification of low Ge contents using LA-ICP-MS related to external standard calibration and to isobaric interferences. These issues have to be overcome by testing isobaric interferences on Ge isotopes in well characterized matrix-matched materials and using proper external standard to better limit any matrix effects during laser ablation.

There are five naturally occurring stable Ge isotopes, ^{70}Ge (relative isotopic abundance of 20.8%), ^{72}Ge (27.5%), ^{73}Ge (7.73%), ^{74}Ge (36.28%) and ^{76}Ge (7.61%), whereas at least 27 synthetic radioisotopes have been artificially produced from ^{58}Ge to ^{89}Ge with half-lives from 110 ηs to 270.95 d (Audi et al., 2003). Ge isotope systems can provide useful information regarding processes triggering variable Ge contents in terrestrial reservoirs. To date, few Ge isotope data are available for meteorites and terrestrial rocks and fluids (Hirata, 1997; Xue et al., 1997; Luais et al., 2000; Luais, 2003, 2007, 2012; Rouxel et al., 2006; Siebert et al., 2006, 2011; Escoube et al., 2012). Recent advances in the development of multi-collector inductively coupled mass spectrometry (MC-ICP-MS) has improved the precision and reproducibility of heavy stable isotope measurements, reducing uncertainties to about 0.05‰ (depending on the element), allowing small isotopic anomalies to be detected (Luais, 2012). In the field of ore deposit research, stable isotopes (e.g., Zn, Fe, Cu, S) are typically used for tracing deposition temperatures, the origin, nature, and evolution of ore-forming fluids, as well as the sources of the ore components (e.g., metals) and depositional mechanisms (e.g., Wilkinson et al., 2005; Asael et al., 2012; Gagnevin et al., 2012).

This work presents an integrated mineralogical and geochemical study on typical sphalerite samples from the main Ge deposit in western Europe: the vein-type Zn–Ge–Ag–(Pb–Cd) deposit of Noailhac – Saint-Salvy (Tarn, France). Because this sphalerite exhibits high Ge contents (up to 2600 ppm; Halfon and Rosique, 1973) and very significant zoning patterns, it constitutes a key target for investigations of Ge and related minor/trace element enrichments in sphalerite. In addition, we describe new analytical approach for Ge quantification using LA-ICP-MS. *In situ* coupled measurements of trace elements and S isotopes were performed using LA-ICP-MS and SIMS, respectively, together with bulk Ge isotopes by MC-ICP-MS. Further, Ge isobaric interferences, as well as standard calibration and data treatment using multivariate statistics were carried out with particular care for LA-ICP-MS analyses. This study aims at providing new insights on where and how Ge and related minor/trace elements can reach several thousands of ppm in some sphalerite-bearing ores. It also intends to provide useful additions to address the gap in the current knowledge in Ge measurement, and to improve data interpreta-

tion and comparison with future or existing LA-ICP-MS datasets and Ge isotopes in sulphide minerals.

THE NOAILHAC – SAINT-SALVY DEPOSIT

Between 1975 and 1990, the Noailhac – Saint-Salvy Zn–Ge–Ag–(Pb–Cd) deposit (Tarn, France; also known as the Saint-Salvy deposit) produced 2 793 370 t of crude ore at 11.7% Zn and 547 300 t of sphalerite concentrate at about 55% Zn, 750 ppm Ge, 350 ppm Ag, 0.6% Pb and 0.3% Cd (Cassard et al., 1994). According to these data, this mine has produced about 300 000 t Zn, 400 t Ge and 200 t Ag.

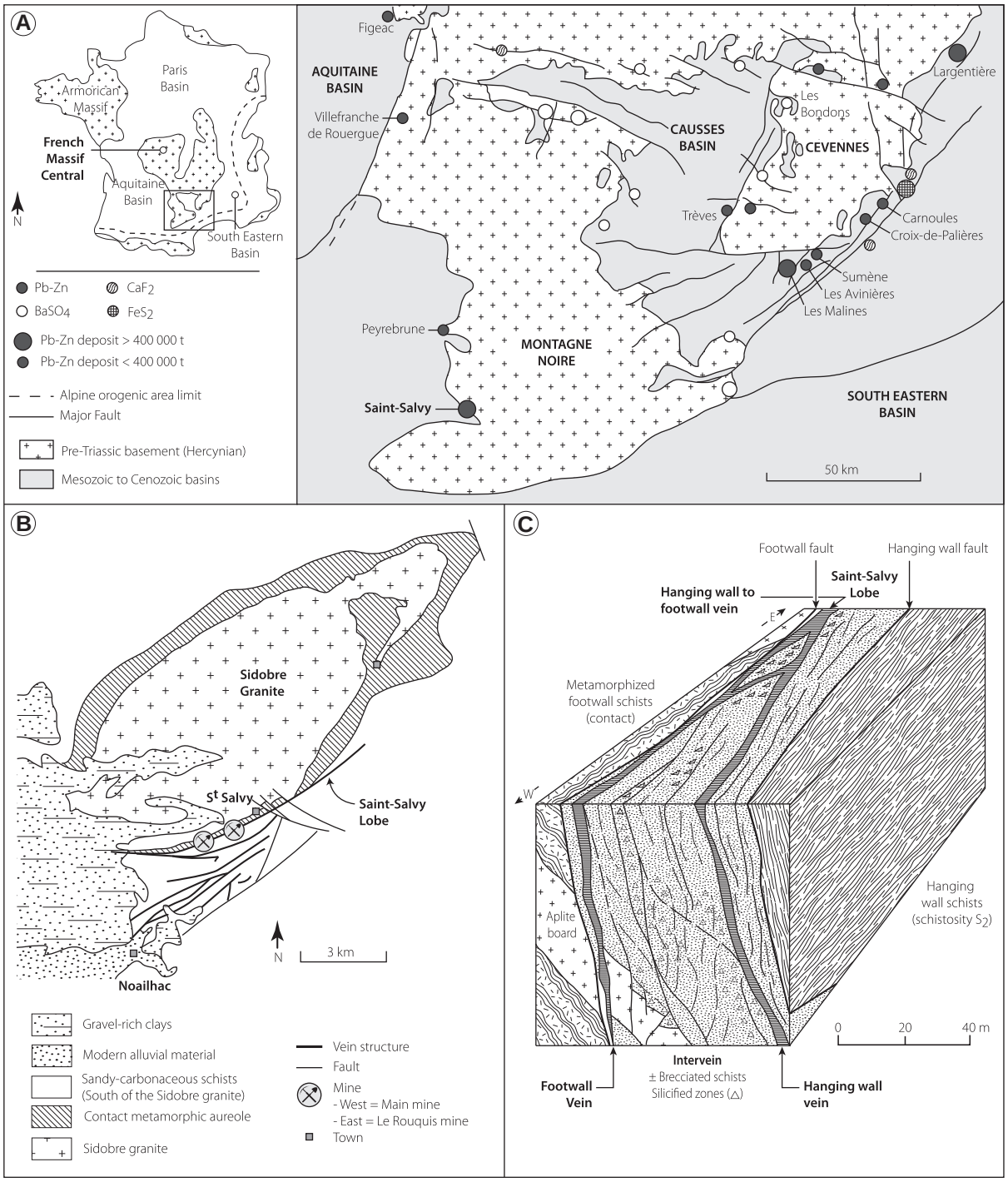

Fig. 1. (A) Location of the Saint-Salvy deposit in the French Massif Central and other major deposits (modified from Leach et al., 2006). (B) Location of the Saint-Salvy lobe south of the Sidobre granite, including the contact-metamorphism aureole (Cassard et al., 1994). (C) Main features of the East–West block diagram of the Saint-Salvy vein structure (Cassard et al., 1994).

Geological setting

The Saint-Salvy vein-type deposit is located on the southern border of the Sidobre granite massif, on the southwestern edge of the French Massif Central (Fig. 1a). The vein system is hosted by the western part of the Cambrian–Silurian unit between the Albigeois to the North and the Montagne Noire axial zone to the south. The deposit lies in a ENE–WSW strike slip fault partly mineralized over its 9 km length (Cassard et al., 1994 and references therein). The orebody extends along a 3 km section of the fault, striking N65 to N85, with an average dip of 80S, ~150 m from the granite, at the edge of the contact metamorphic aureole (Fig. 1b). Here, the vein system is 15–50 m wide and the mineralization is concentrated in two lenticular veins several meters wide, known as the hanging wall vein and the foot wall vein (Fig. 1c). The early movement of the fault started at the end of the syn-kinematic emplacement of the Sidobre granite, although mineralization events occurred significantly later. The mineralization occurs as anastomosed veinlets of siderite and/or sphalerite, as 0.6–1.0 m thick massive sphalerite veins, and as sphalerite-cemented breccias of silicified schist fragments covered with siderite and/or quartz.

The host-rocks, the Cambrian black schists series, bear primary uneconomic mineralization, which consists of stratiform and folded layers of disseminated syngenetic pyrite and sphalerite. The latter displays low Fe content (2–3 wt.%) and relatively high Ge content, up to 500 ppm (Halfon and Rosique, 1973). Stratiform skarns, outcropping at the southern edge of the Sidobre batholith, contain garnet, pyroxene, quartz and sulphides composed of pyrite, pyrrhotite and Fe-rich sphalerite (around 14 wt.%), and are thought to have formed along with the Cambrian syngenetic stratiform sphalerite (Barbanson, 1979).

The Saint-Salvy deposition model has been extensively reviewed in Cassard et al. (1994) and additional fluid inclusion and stable isotope studies were carried out by Munoz et al. (1994). Accordingly, the first stages of mineralization correspond (1) to development of a skarn by contact metamorphism and metasomatism and (2) to a massive quartz-stockwork formation inside the host schists and/or aplite dykes under strike-slip dynamics. Only a few sulphides formed during these stages (Cassard et al., 1994). These stages are related to a single hydrothermal event characterized by low-salinity H_2O–CO_2–(NaCl) fluids (⩽6 wt.% NaCl eq.) of 300–580 °C (Munoz et al., 1994). Later mineralization stages correspond to (3) a massive development of chalcedony and/or quartz-cemented breccias and veins, and (4) the formation of decametric veins of massive sphalerite and metric lenses of implosion-collapse breccias filled with siderite, quartz, and sphalerite, the whole forming the orebody (Cassard et al., 1994). These stages took place under an extensional strike-slip regime corresponding to high salinity H_2O–NaCl–$CaCl_2$ fluids (23–25 wt.% NaCl eq.) at a lower temperature (80–140 °C) (Munoz et al., 1994).

Samples studied

Ore samples were collected from the deep mine faces of the main mine, which is about 600 m deep and 1450 m long: 62E, 62W, 64W (64W-02 and 64W-08) and the deepest one,

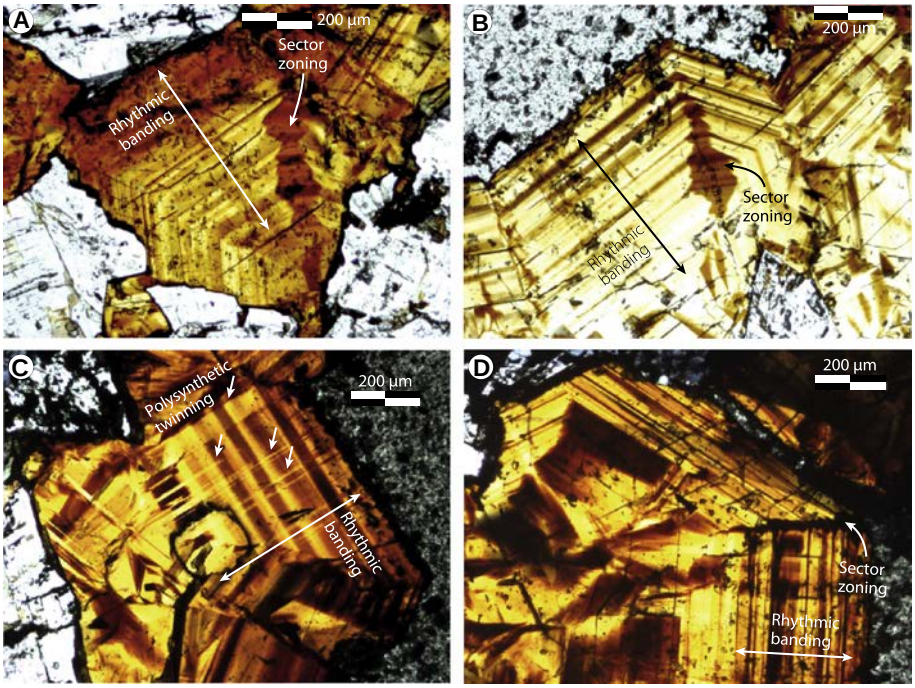

Fig. 2. Transmitted light microphotographs of zoned sphalerite from the Saint-Salvy deposit showing the main zoning patterns. (A) Sample SAL-UN. Banded sphalerite with well-defined dark-brown sector, in continuity with adjacent rhythmic bandings, getting darker towards the rim. (B) Sample 64W-02. Alternate light and dark-brown rhythmic bands, and sector zoning. (C) Sample 64W-08. Banded sphalerite with perpendicular polysynthetic twinning. (D) Sample 64W-08. Banded sphalerite with complex twinning, rhythmic banding and sector zoning at the core, and thin rhythmic bands with polysynthetic twinning at the rim.

74W (the first number indicates the mine level (depth) whereas the second indicates longitudes, see Cassard et al., 1994). Two additional samples representative of the mined ore were added to our study, K and SAL-UN. The samples were taken from economic veins so that only sphalerite from the economic mineralization stage (stage 4) was investigated. This sphalerite was sampled because it has the highest concentrations of minor and trace elements (Halfon and Rosique, 1973; Barbanson and Geldron, 1983; Cassard et al., 1994 and reference therein) and is there most relevant for study.

The ore samples consist of implosion-collapse breccias containing angular to rounded schist clasts coated with, in chronological order, palissadic layers of siderite and/or quartz, and Ge-bearing sphalerite, and terminal quartz filling. This paragenesis forms the typical "cockade" breccia texture (e.g., Cassard et al., 1994). Accessory sulphides, e.g., pyrite, pyrrhotite or galena (Cassard et al., 1994), have not been observed in our samples. The host-rock schist clasts are composed of quartz, siderite and phyllosilicates of hydrothermal alteration (e.g., illite, phengite). In addition, refractory minerals (e.g., zircons, titanium oxides) can also be observed, as well as sulphide minerals (e.g., pyrite, arsenopyrite, chalcopyrite) as described in Filia (2010).

Optical microscope observations of the Ge-bearing sphalerite on 150 μm-thick polished sections reveal well-developed supra-millimetric crystals heterogeneously coloured from light brown to dark reddish-brown without any micro-inclusions of other sulphide species (e.g., chalcopyrite). Two main typical optical compositional zoning patterns can be identified within sphalerite crystals, (i) rhythmic banding that occurs as alternating parallel dark brown and light brown growth bands, from the core to the rim (Fig. 2a–d), which is frequently associated with adjacent (ii) sector zoning occurring as crosscutting dark brown zones, consisting of a series of small and parallel truncation planes highly variable in size, and accounts for their highly indented boundaries (Fig. 2a, b and d). This sphalerite also shows dark brown geometric patterns such as triangles or multiple quadrangles (Fig. 2c) highlighting complex twinning (e.g., polysynthetic twins). These patterns can form complex areas over several dozens of μm^2 in some crystals.

ANALYTICAL TECHNIQUES AND METHODS

Preliminary SEM and EMPA analyses

Preliminary analyses were carried out using a scanning electron microscope (SEM) and an electron microprobe analyser (EMPA) at the Service Commun de Microscopie Electronique et Microanalyses X (SCMEM, GeoRessources laboratory, Vandoeuvre-lès-Nancy, France) in order to study major and minor element distribution within sphalerite zoning patterns. Back-scattered electron images and X-ray maps were created using a Jeol J7600F with both an energy dispersive spectrometer (EDS, SSD type) for major elements and a wavelength dispersive spectrometer (WDS, Oxford Wave) to detect minor/trace elements. The beam current was of 100 nA with an accelerating voltage of 25 kV to enhance chemical contrasts.

Major and minor element analyses were performed using a Cameca SX100 electron microprobe analyser (EMPA) with five wavelength dispersive spectrometers. Peak calibration on each element was carried out using reference materials. More specifically, sphalerite and metal Ge were used to calibrate Zn and Ge, respectively, and to compare their X-ray emission spectra to optimize the measurements. The beam current was of 100 nA with an accelerating voltage of 25 kV. The following 13 elements, standards, analytical lines, and monochromators were used for measurements: S (ZnS, Kα, PET), Fe (FeS_2, Kα, LIF), Zn (ZnS, Kα, LIF), Mn (Mn, Kα, LIF), Co (Co, Kα, LIF), Cu (Cu, Kα, LIF), Ga (AsGa, Lα, LIF/TAP), Ge (Ge, Lα, LIF/TAP), Ag (Ag, Lα, LPET), Cd (Cd, Lα, PET), In (InP, Lα, LPET), Sn (Sn/SnO_2, Kα, PET) and Pb (PbS, Mα, LPET). Peak counting times were scaled from 10 to 60 s, which were reduced by a half for background counting, depending on the element. Internal Cameca procedures were used for data reduction (i.e., quantification of element contents, uncertainties and limits of detection). Measurements were collected on 32 spot analyses in both 64W-02 and 64W-08 samples. Among the 13 elements monitored, Mn, Co and Ga were not detected. Further, Ge was only detected in two spots at 1100 and 1200 ppm, respectively, although the Ge detection limit was 470 ppm.

Recent developments by the SCMEM on the EMPA indicate that measuring Ge (Ge, Kα, LLIF) using a counting time of 60 s lowers the limit of detection to about 170 ppm. Nonetheless, trace element analyses using EMPA is limited due to the compromise between the counting time, the number of measured elements, and the required limits of detection.

Laser ablation inductively coupled plasma mass spectrometry (LA-ICP-MS)

The LA-ICP-MS technique was used to circumvent the EMPA limitations to analyse a wide range of trace elements (especially, Ge, Ga, In and Sn for our study). Trace element analyses in sphalerite were carried out using a LA-ICP-MS at the GeoRessources laboratory (Vandoeuvre-lès-Nancy, France) composed of a 193 nm MicroLas Pro ArF Excimer coupled with the Agilent 7500c quadrupole ICP-MS.

Analytical settings for laser ablation are detailed in Leisen et al. (2012) and Lach et al. (2013). Laser ablations were performed with a constant 5 Hz pulse rate at 90 mJ laser energy. The number of pulses depended on the section thickness, which allowed 100–200 pulses, sufficient to form a long and stable signal for integration. The ablated material is transported using a constant He flow and mixed with Ar in a cyclone coaxial mixer prior to entering the ICP torch and being ionized. The ions are then sampled, accelerated and focussed before being separated and analysed in the quadrupole mass spectrometer. Data were collected during a 30 ms dwell time per channel to enhance the number of counts for trace elements. Specific areas of the sample plates were ablated with 32, 44 or 60 μm spot diameters. The following isotopes were monitored: ^{57}Fe, ^{63}Cu, ^{66}Zn, ^{71}Ga, ^{74}Ge, ^{75}As, ^{107}Ag, ^{111}Cd, ^{115}In, ^{118}Sn, and ^{121}Sb. The choice of ^{74}Ge over ^{72}Ge is discussed in the next paragraph. The

total acquisition time was limited to 170 s, allowing a maximum of 2–3 spots per acquisition, generally in the same crystal.

Data reduction was carried out using in-house software (Leisen, 2011), following the standard methods of Longerich et al. (1996), and using Zn content – known from prior EMPA analyses – as an internal standard. No correction factors are introduced in the calculation. External standard calibration was performed with the synthetic polymetallic sulphide material MASS-1 (Wilson et al., 2002) using the certified Ge concentration of 57.8 ± 2.6 ppm (Dr. Stephen Wilson, personal communication). Limit of detection (LOD) and uncertainty depends on the ablation spot diameter and the analysed element. For each analysis, LOD was calculated using the 3σ criterion detailed in Longerich et al. (1996), uncertainty was calculated as in Lach et al. (2013), including the uncertainties on the net transient signal (σ) and on the internal standard concentration. Minimum LOD were usually lower than 1 ppm for the trace elements analysed at ablation spot diameters from 32 to 60 µm.

Isobaric interferences on Ge in the mass spectrometer prevent low-Ge concentrations to be measured with confidence as stated by Cook et al. (2009). The main interferences on Ge isotopes are the following: ^{70}Ge with ^{70}Zn and ^{36}Ar^{34}S; ^{72}Ge with ^{40}Ar^{32}S and ^{56}Fe^{16}O; ^{73}Ge with ^{40}Ar^{33}S, ^{57}Fe^{16}O, and ^{56}Fe^{16}O^{1}H; and ^{74}Ge with ^{40}Ar^{34}S and ^{58}Ni^{16}O. To address this interference issue, we used two homogeneous sphalerites whose bulk elemental concentrations have previously been analysed by the Service d'Analyses des Roches et des Minéraux (SARM) in the Centre de Recherches Pétrographiques et Géochimiques (CRPG-Nancy, France) following Carignan et al.'s (2001) routine procedure of liquid chromatography ICP-MS (Table 1). The two samples consist of a Ge-poor sphalerite (S1) from the epithermal ore deposit of Cavnic, Romanian Carpathians Mountains, and a Ge-rich sphalerite (S2) from the Zn-F vein-type deposit of Peyrebrune, S.W. Massif Central, France. Bulk Ge contents of these sphalerites are 0.4 ± 0.1 and 1360 ± 95 ppm Ge, respectively. LA-ICP-MS analyses were performed using the experimental setup detailed above except that the masses monitored were limited to ^{66}Zn, ^{70}Ge, ^{72}Ge, ^{73}Ge, and ^{74}Ge. The Ge-poor sphalerite S1 was used to test which Ge isotope is least affected by interferences in a sphalerite matrix. The Ge-rich sphalerite S2 was used to test the precision of the calculations using the different Ge isotopes, and so to track interferences in the external standard.

The resulting LA-ICP-MS ablation signal in S1 (Fig. 3a) shows major interferences on ^{70}Ge and ^{72}Ge leading to biased concentrations of 130 and 9 ppm respectively (true value of ~0.4 ppm). However, very limited interferences are seen on ^{73}Ge and ^{74}Ge, leading to concentrations of 1.1 and 0.1 ppm, respectively, which falls, within error, rather close to the bulk ICP-MS value. Calculations on S2 (Fig. 3b) showed that the best accuracy was obtained for ^{74}Ge and ^{73}Ge with concentrations of 1300 and 1280 ppm, respectively (true value of ~1360 ppm). However, Ge content using ^{70}Ge is only of 175 ppm. This large underestimation is due to significant interference by ^{70}Zn that is a major component in sphalerite. Ge content using ^{72}Ge is of 1000 ppm. Remarkably, this underestimation is due to the presence of oxygen in the MASS-1 external standard (~12.9 wt.%), allowing the

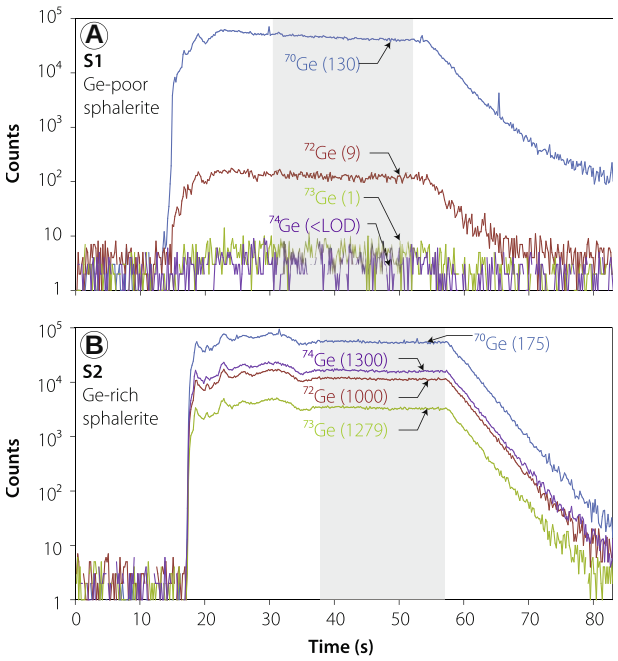

Fig. 3. Determination of the most effective isotope for accurate Ge analysis in sphalerite using LA-ICP-MS. Signals of ^{70}Ge, ^{72}Ge, ^{73}Ge and ^{74}Ge intensity in (A) Ge-poor sphalerite (S1, 0.4 ppm Ge) in order to quantify isobaric interferences, and (B) in Ge-rich sphalerite (S2, 1360 ppm Ge) to verify the precision of the measurement. Calculated contents are indicated for each signal (in ppm). In Ge-poor sphalerite, interferences on ^{70}Ge, ^{72}Ge, ^{73}Ge have been detected. No detectable interferences on ^{74}Ge make it the most relevant mass for accurate Ge content measurement using LA-ICP-MS (see text for details).

Table 1
Elemental compositions (in ppm) of S1 and S2 sphalerites analysed at the SARM (Nancy, France) using quadrupole ICP-MS.

		Mn	Fe	Co	Cu	Zn	Ga	As	Ge	Cd	In	Sb	Sn	Pb
S1	Content (ppm)	3330	117294	4.8	52	547400	4.3	<LOD	0.4	2030	0.3	46	17.6	11212
	Error (1σ SE, ppm)	238	5972	0.8	6	27870	0.4	–	0.1	103	0.1	2	2.0	571
S2	Content (ppm)	<LOD	26228	17.4	2296	661200	129	9.5	1363	1704	19.5	413	53.2	310
	Error (1σ SE, ppm)	–	1435	2.0	164	33664	9	1.1	97	87	1.4	21	3.8	16

LOD: limit of detection.
* Dissolution according to Luais (2007, 2012), trace element measurements at the SARM.

formation of $^{56}Fe^{16}O$ that interferes on ^{72}Ge and introduce a bias in the calculation. Therefore, the isotopes least affected by isobaric interferences are ^{73}Ge and ^{74}Ge, and, considering their relative isotopic abundance (7.73% and 36.28%, respectively; Audi et al., 2003), ^{74}Ge appears to be most suitable for LA-ICP-MS analysis in sphalerite (relative to the MASS-1 external standard). Interferences on this isotope being negligible, there is no need for further corrections.

Ge isotope determination by multi-collector inductively coupled plasma mass spectrometry (MC-ICP-MS)

The advent of high-precision and reproducible (i.e., less than 0.05‰/amu) MC-ICP-MS methods for measuring stable isotopes, have provided opportunities to measure and detect small variations of Ge isotopes in meteorites and terrestrial rocks (Hirata, 1997; Xue et al., 1997; Luais et al., 2000; Luais, 2003, 2007, 2012; Rouxel et al., 2006; Escoube et al., 2012). Bulk Ge isotopic measurements were carried out using an GV Instruments MC-ICP-MS Isoprobe at the CRPG–Nancy (France). The chemical procedures used to isolate Ge from the samples follow the analytical methods for iron meteorites and Ge-bearing ores (sphalerite ores included) developed by Luais (2007). Full descriptions of chemical procedures and Ge isotopic measurements have been detailed in Luais (2007, 2012).

Macroscopic sphalerites were separated and purified by handpicking under a stereomicroscope, avoiding grains with visible inclusions. About 10–30 mg were picked for each sample, which would represent 2.5–35 μg Ge (considering bulk sphalerite contents of 200–1200 ppm Ge) to ensure representative sampling. Note that 1 μg Ge is sufficient for replicate analyses using the MC-ICP-MS. Pure sphalerite samples were cleaned from any surface impurities by a weak and diluted acid leaching with 0.2 M HNO_3 during 5 min in an ultrasonic bath, then rinsed in ultra-pure water (18.2 MΩ cm), dried, weighed, and finally digested in screw-top Teflon vials using concentrated HNO_3 (~15 M). Chemical compositions of these solutions were analysed by quadrupole ICP-MS at the SARM (CRPG–Nancy, France) on an aliquot of the sample solution. For isotopic measurements, Ge was purified from dilute HNO_3 solution (0.5 M) using an AG 50 W-X8 cation-exchange resin (hydrogen form, 200–400 mesh, 2 ml). In parallel, a total chemistry blank, and the JMC and Aldrich Ge standards were submitted to the same procedure for control samples.

Germanium isotopes were measured using a GV Instrument *Isoprobe* MC-ICP-MS. The analytical settings have been described in Luais (2000). The external mass fractionation correction of Ge isotopic ratios relative to the international Ga isotopic standard SRM 994 ($^{69}Ga/^{71}Ga = 1.50676$, Machlan et al., 1986) is calculated using an exponential law. The multi-collection system simultaneously measures ^{70}Ge, ^{72}Ge, ^{73}Ge and ^{74}Ge for isotopic ratio calculations, ^{68}Zn for interference corrections on ^{70}Ge, and ^{69}Ga and ^{71}Ga for external mass bias corrections. Ge isotopic analyses were carried out on 200 ppb diluted Ge standards and samples in 0.01 N HNO_3 medium. Total procedural blanks, including total chemistry and MC-ICP-MS measurements, are better than 30 ρg for Ge, and 4 ηg for Zn.

Ge isotopic ratios are measured and expressed in δ units with respect to the JMC Ge standard using the sample-standard bracketing method as:

$$‰\delta^{x}Ge_{std}(sam) = \left[\left({}^{x}Ge/{}^{70}Ge\right)_{sam}/\left({}^{x}Ge/{}^{70}Ge\right)_{std} - 1\right] \times 1000$$

where x stands for the masses 72, 73 and 74 of Ge, for both sphalerite samples and the Aldrich Ge secondary standards. Re-calculations relative to the NIST SRM 3120a Ge standard (Escoube et al., 2012) were performed for normalization purpose using the formula:

$$‰\delta^{x}Ge_{NIST}(sam) = [(\delta^{x}Ge_{JMC}(sam) + 1000)/(\delta^{x}Ge_{JMC}(NIST) + 1000)] \times 1000$$

using the measured $\delta^{72}Ge$, $\delta^{73}Ge$ and $\delta^{74}Ge_{JMC}$ of the NIST SRM3120a standard of $+0.197 \pm 0.051‰$, $+0.261 \pm 0.109‰$ and $+0.366 \pm 0.131‰$ (2σ SD external reproducibility), respectively (Luais, 2012). During the course of sample measurements, the Aldrich Ge secondary standard gives average re-calculated $\delta^{72}Ge$, $\delta^{73}Ge$ and $\delta^{74}Ge_{NIST3120a}$ values of $-1.06 \pm 0.19‰$, $-1.67 \pm 0.32‰$ and $-1.93 \pm 0.37‰$, respectively, in agreement with long-term reproducibility values of $-1.05 \pm 0.14‰$, $-1.58 \pm 0.28‰$, and $-2.04 \pm 0.23‰$, respectively (Luais, 2012). Chemistry-processed JMC and Aldrich Ge standards give delta values similar to the unprocessed standards, indicating no analytical isotopic fractionation occurs during chemistry processing (Table 4).

Sulphur isotope measurements by secondary ion mass spectrometry (SIMS)

Sulphur isotopes can provide information on S sources and S reduction pathways from sulphate in hydrothermal systems (e.g., thermochemical or bacteriogenic, Pfaff et al., 2011 and references therein), and related conditions. *In situ* sulphur isotope analyses were performed using the Cameca IMS 1270 secondary ion mass spectrometer at the CRPG–Nancy (France). Analytical settings are detailed in Rollion-Bard et al. (2007) and Thomassot et al. (2009). Samples were sputtered with a primary mass-filtered Cs^+ beam with an impact energy of 10 kV and an intensity of ~7 nA. The aperture-delimited primary ion beam resulted in flat-bottomed 15 × 25 μm ellipsoid spots.

Sulphur isotopes were counted simultaneously in multi-collection mode by two off-axis Faraday cups (L'2 and H1) to yield ($^{34}S/^{32}S$) ratios. A presputtering of 5 min was necessary before the analyses. The typical acquisition time was of 90 s, comprising 30 cycles of 3 s analysis per cycle. Both Faraday cups were inter-calibrated at the beginning of each analytical session. Before each analysis, an automated procedure of peak centering was performed. Values are reported in ‰ relative to the Vienna–Cañon Diablo troilite (V-CDT, Ding et al., 2001) as:

$$\delta^{34}S_{V\text{-}CDT}(sam) = \left[\left(^{32}S/^{34}S\right)_{sam}/\left(^{32}S/^{34}S\right)_{V\text{-}CDT} - 1\right] \times 1000.$$

The instrumental mass fractionation (IMF) due to the analytical setting and matrix effect (e.g., Rollion-Bard and Marin-Carbonne, 2011) were corrected using the NBS-123 sphalerite standard of homogeneous isotopic composition (+17.44‰ V–CDT, Zhang and Ding, 1989). This instrumental fractionation, defined as the difference between the measured and the true isotopic values of the standard ($‰\Delta_{inst} = \delta^{34}S_{meas} - \delta^{34}S_{true}$), was measured at the beginning of each daily session and applied to correct each sample measurement ($‰\delta^{34}S_{corr} = \delta^{34}S_{meas} - \Delta_{inst}$). On the overall data acquisition, the IMF averaged −2.5‰. The precision, including errors from counting statistics and reproducibility based on repeated measurements of the standard, were of ±0.13‰ to ±0.29‰ (1σ SD) depending on the analytical session. The average overall precision was of ±0.25‰ (1σ SD).

In order to study sulphur isotopes with respect to compositional zoning in sphalerite, care was taken to couple spot analyses of $\delta^{34}S$ with those of LA-ICP-MS. The challenge was to aim the ion beam onto the different zoning patterns (only visible using transmitted light microscopy) with the camera on CAMECA IMS 1270. Transmitted light microphotographs of the samples were used to help us aiming the ion beam more accurately. Another issue rose from the analytical spot size that was bigger than some banding patterns. Considering the ion beam leaves slightly ovoid crater marks on the gold-coated sample surface after each spot analysis, their precise locations were verified after the measurements under transmitted light microscope.

Principal component analysis of *in situ* datasets

Multivariate statistical analyses provide unique tools to bring out concise description of high-dimensional data and highlight relationships among variables. Principal component analysis, one type of such multivariate statistical analysis, is a powerful variable-reduction technique designed to project data in two-dimensions with minimal data loss. Principal components are defined as orthogonal linear combinations of the initial variables, producing maximum variance and minimising data loss. They are directly computed as the eigenvectors of the correlation matrix and ordered by decreasing eigenvalues. For instance, the two first principal components carry the highest explained variance, corresponding to the most significant relationships between the variables. More detailed descriptions of the PCA method can be found in multivariate statistics textbooks (e.g., Koch, 2012), or in Le Maitre (1982) and Albarède (1995) as geochemistry-oriented textbooks.

Principal component analysis is widely used in the field of geochemical exploration on large-scale datasets (e.g., Samama et al., 1989) as it helps to better understand underlying ore mineralization and its organisation. Consequently, PCA is implemented in many geomodelling softwares (e.g., Lafferière et al., 2000). PCA has also found applications in isotope geochemistry (e.g., Cadoux et al., 2007; Iwamori et al., 2010) and sulphide geochemistry (e.g., Winderbaum et al., 2012) though it is still rarely used to treat large LA-ICP-MS datasets. Therefore, we emphasize the use of multivariate statistics to better interpret *in situ* minor/trace element data in mineral geochemistry, and understand their relationship. Consequently, PCA will be applied to the *in situ* LA-ICP-MS and SIMS datasets in our study.

RESULTS

Minor element distribution

Detailed observations of the zoning patterns in sphalerite using transmitted light microscopy (Fig. 4a) highlight complex relations between rhythmic bands and sector zonings (Fig. 4b). As shown in section 'Studied samples', rhythmic bandings and sector zoning occur in distinct crystallographic planes. By comparison with Johan (1988), the sectors correspond to [1 1 1] planes whereas alternating dark- and light-brown rhythmic bands correspond to [1 1 0] planes. However, within the sectors, dark inner bands are noticeable in the extension of adjacent rhythmic bands, suggesting an overlapping of these zoning patterns. Slight changes of colour within dark rhythmic bands are also visible (Fig. 4b, bands 2 and 3).

Element mapping using the SEM broadly show that Fe (EDS mapping, Fig. 4c) and Cd (WDS mapping, Fig. 4e) are mainly concentrated in rhythmic bands, especially the dark brown bands for Cd (Fig. 4e), and seem to be depleted in the sector. We also note that colour variations in dark rhythmic bands are due to variations in Cd (bands 2 and 3 on Fig. 4b). Antithetic with respect to Fe and Cd, Cu (WDS mapping, Fig. 4d) and Ge (WDS mapping, Fig. 4f) are enriched within the sector zoning part of the crystal. Cu is also enriched in dark brown bands.

However, within the sector, the dark inner bands are enriched in Fe, Cd, and Cu, in the extension of the adjacent the Fe–Cd–Cu-rich rhythmic bands. By contrast, in the sector, Ge seems to be slightly depleted in these dark inner bands, and is instead enriched in the lighter ones (Fig. 4a and b). Thus, this typical patterning in sectors is related to variations in the minor/trace element content and appears to overlap the rhythmic bandings in sector zonings.

Minor/trace element contents

Electron microprobe analyses for minor and some trace elements are listed in Table 2. The Saint-Salvy sphalerites are composed of 63.3 ± 0.6 wt.% Zn and 33.0 ± 0.2 wt.% S. Fe, Cd and Pb were consistently detected with mean concentrations of 2.1 ± 0.5, 0.22 ± 0.9 and 0.9 ± 0.2 wt.%, respectively. Moreover, Cu was detected in 28 spots, with contents up to about 1.0 wt.%. Sn is present in 11 spots with contents up to 4600 ppm, and Ag in 17 with contents up to 1000 ppm. In has been detected in only 4 spots, ranging from 200 to 1700 ppm, and finally, Ge has been detected in only 2 spots with concentrations of 1100 and 1200 ppm.

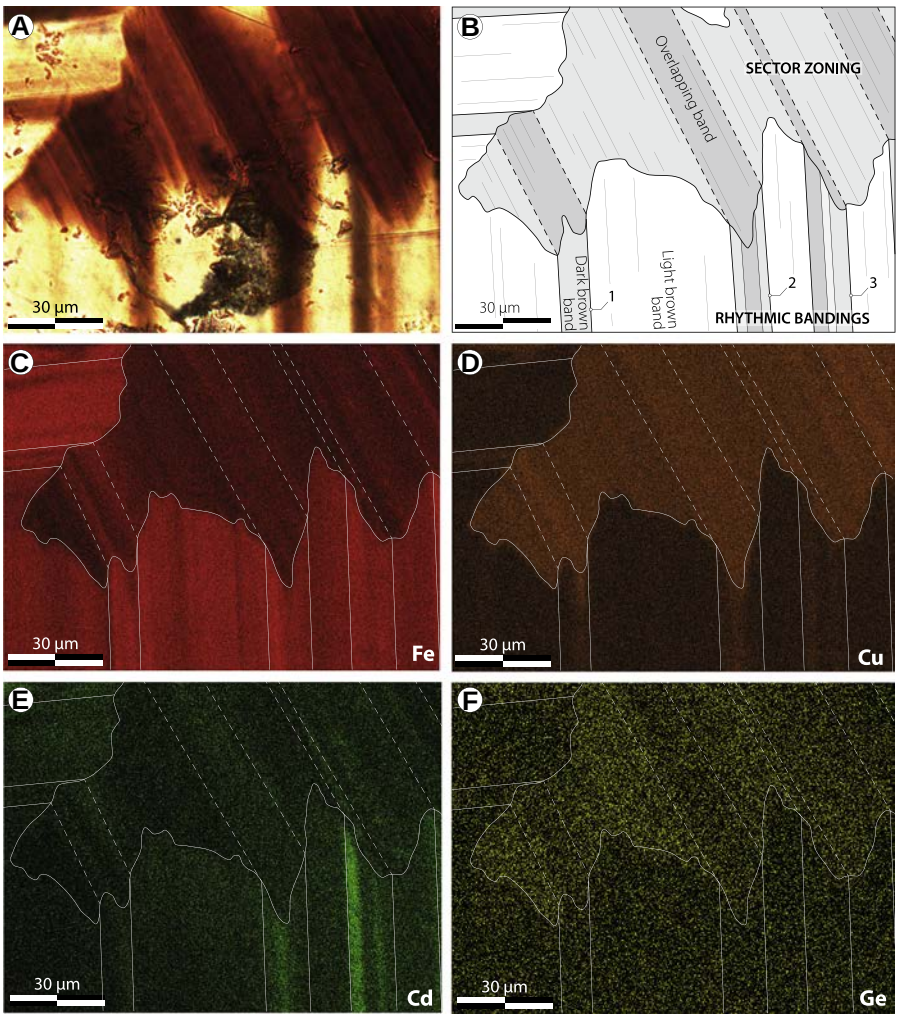

Fig. 4. Antithetic distribution of (Fe, Cd) and (Cu, Ge) within zoning patterns in sphalerite from the Saint-Salvy deposit (sample 64W-02). (A) Colour zoning patterns under transmitted light microscopy, i.e. rhythmic banding and sector zoning. (B) Interpretative scheme. Dark rhythmic bands are referred to as 1, 2 and 3 (see text for explanations). (C) EDS mapping of Fe, which is enriched in rhythmic banding patterns (slightly more in dark-brown rhythmic bands) and significantly depleted in sector zoning. (D) EDS mapping of Cu, which is enriched in sector zoning, and to a lesser extent in dark-brown rhythmic growth bands. (E) WDS mapping of Cd, which similarly to Fe is enriched in dark-brown rhythmic growth bands. (F) WDS mapping of Ge, which similarly to Cu is enriched in sector zoning. (For interpretation of the references to colour in this figure legend, the reader is referred to the web version of this article.)

Table 2
EMPA main results. Minimum, maximum, mean, corresponding standard deviation (1σ SD), and limit of detection (LOD) are presented.

	S (wt.%)	Fe (wt.%)	Zn (wt.%)	Cu (ppm)	Ge (ppm)	Ag (ppm)	Cd (ppm)	In (ppm)	Sn (ppm)	Pb (ppm)
n	32	32	32	28	2	17	32	4	11	32
Min.	32.48	1.41	62.42	300	1100	400	900	200	400	400
Max.	33.45	3.01	65.02	9900	1200	1000	4300	1700	4600	1400
Mean	32.9	2.11	63.3	5600	1150	600	2200	800	2100	900
1σ SD	0.24	0.48	0.63	3200	71	200	900	700	1400	200
LOD	0.07	0.09	0.18	231	471	235	351	155	290	314

n: number of measurements with higher contents than the limit of detection.

Table 3
LA-ICP-MS analyses results (in ppm) in the three compositional zoning patterns: sector zoning, dark brown bands and light brown zones (including light brown bands).

		Fe	Cu	Ga	Ge	As	Ag	Cd	In	Sn	Sb
Sector zonings ($n = 71$)	Min.	11696	664	33	59	<LOD	24	1071	<LOD	<LOD	122
	Max.	42021	7443	1054	2576	79	1091	4263	762	3028	5973
	Mean	19169	4003	359	1102	26	354	2048	44	351	1972
	1σ SD	5362	1713	264	716	21	230	644	128	630	1662
Dark brown bands ($n = 23$)	Min.	18410	789	137	46	1	27	1944	2	82	161
	Max.	30440	4074	919	340	32	581	5053	870	1751	3652
	Mean	25620	2447	332	142	8	142	3535	234	876	955
	1σ SD	2819	1014	201	96	7	119	815	238	534	766
Light brown zones (bands included, $n = 41$)	Min.	12875	3	<LOD	<LOD	<LOD	1	1058	<LOD	<LOD	<LOD
	Max.	32198	2496	425	1801	10	1654	8047	122	304	837
	Mean	21788	545	95	273	1	96	2938	7	37	128
	1σ SD	4834	568	109	461	2	272	1395	20	59	161

1σ SD: standard deviation.
LOD: limit of detection.

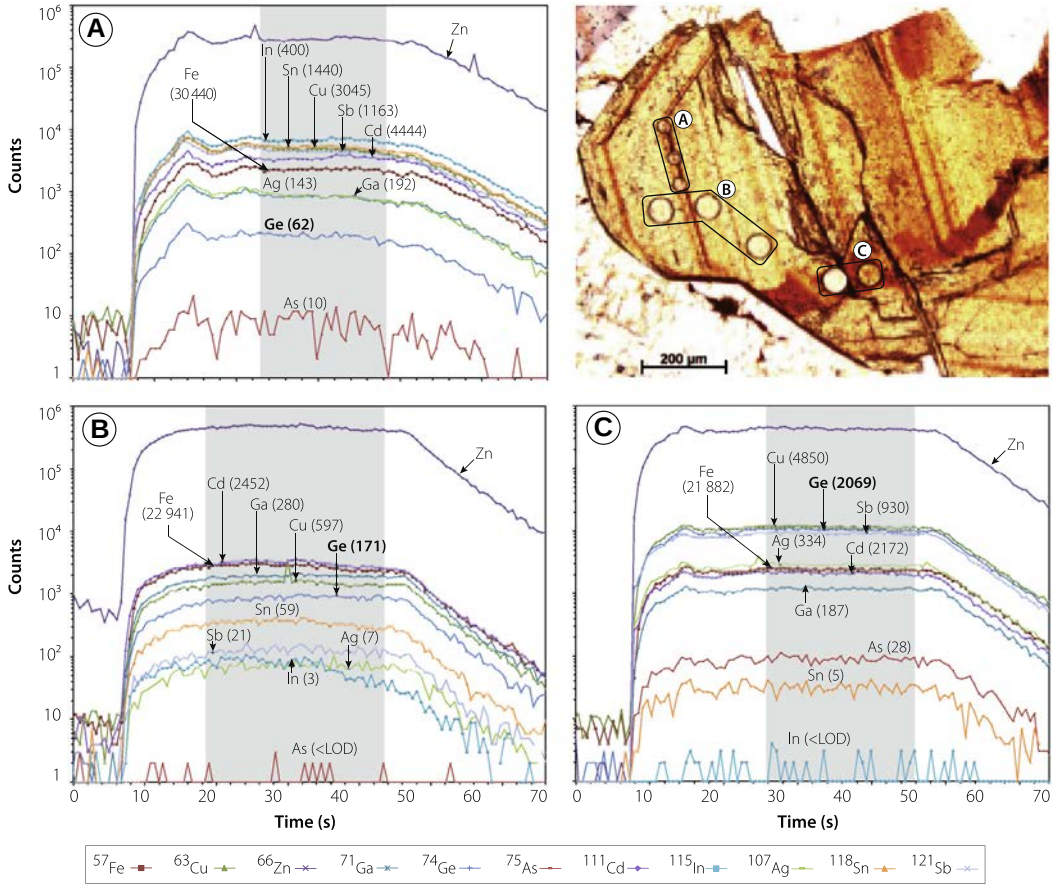

Fig. 5. Typical signals of intensity obtained by LA-ICP-MS and calculated element contents within the three studied zoning types, illustrated on a sphalerite crystal analysed with spot diameters of 32 and 60 µm (sample 64W-08). (A) Dark-brown bands. (B) Light-brown areas (rhythmic bands included). (C) Sector zoning.

Minor and trace element analysis by LA-ICP-MS are summarized in Table 3 for the three identified zones. The dataset consists of 71 spot analyses in sectors, 25 spot analyses in dark brown bands, and 52 spot analyses in light brown areas, including light brown bands, for a total of 135 spot analyses, performed on the 150 µm-thick polished sections. Ablation profiles were generally smooth, suggesting a homogeneous distribution of the elements in the spots

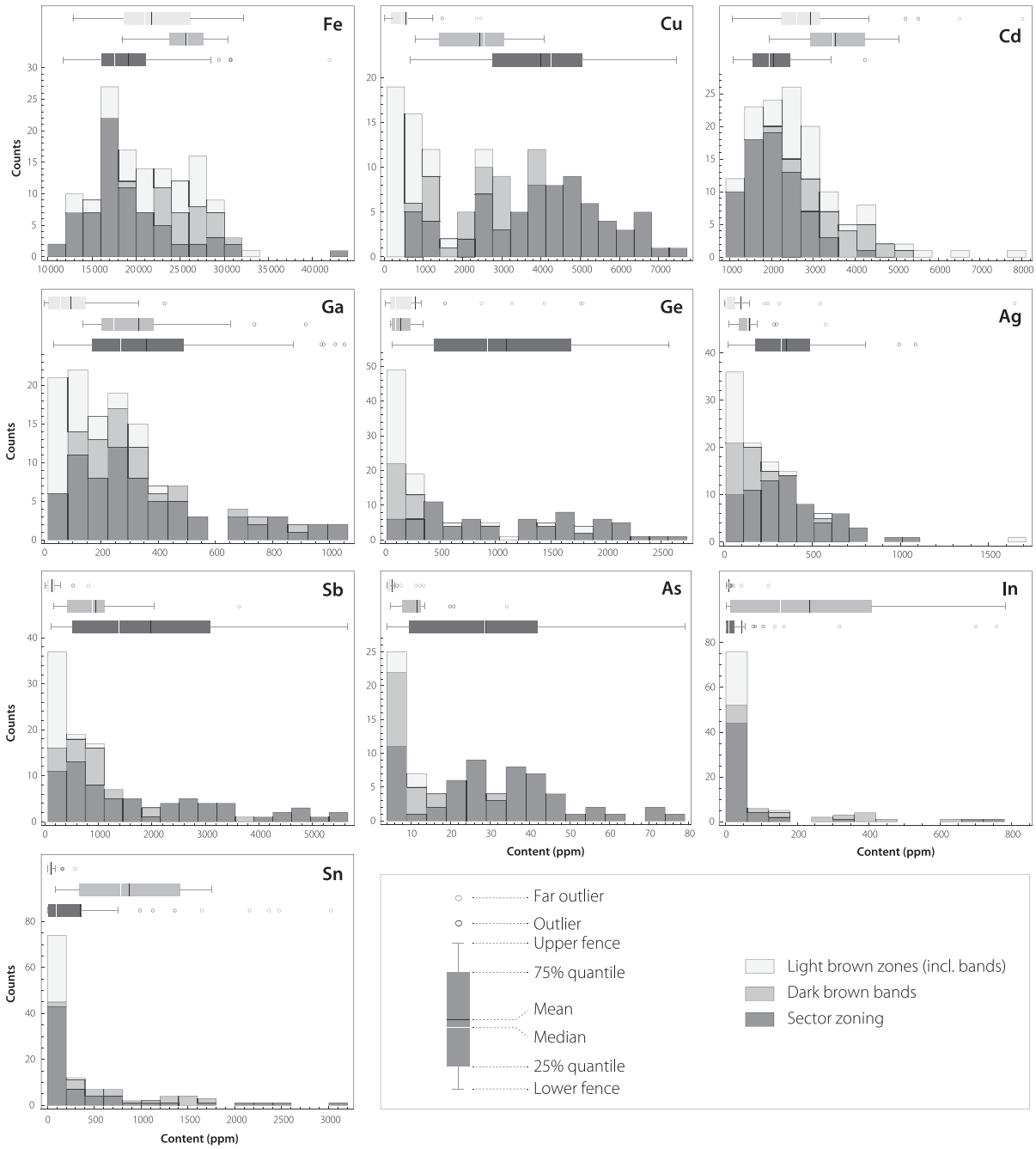

Fig. 6. Histograms of element contents in relation to the studied zoning types within sphalerite (LA-ICP-MS dataset) and corresponding box plots. Element contents vary over several orders of magnitude and complete basic statistics are presented in Table 3. The highest concentrations of Fe, Cd, In and Sn generally occur in rhythmic bandings whereas those of Cu, Ga, Ge, Ag, Sb and As occur in sector zonings. Noticeably, apart from sectors where concentrations of more than 2500 ppm are possible, Ge does not exceed 350 ppm in dark brown bands whereas it can locally reach ~1800 ppm in light brown zones.

analysed (Fig. 5). Histograms of element contents with respect to zoning patterns are shown in Fig. 6.

Sphalerite displays significant Fe and Cd contents (1.2–4.2 wt.% and 967–8047 ppm, respectively), which are enriched in the banded zone, especially in dark brown growth bands, with means of 2.56 wt.% Fe and 3535 ppm Cd. On the other hand, Cu varies over two orders of magnitude (50–7443 ppm) and is largely concentrated in sectors, averaging 4003 ppm.

Considering trace elements, Sb exhibits a wide range of concentrations (60–5973 ppm) and is enriched within sectors, averaging 1972 ppm. In addition, Ge, Sn and In

display approximately the same range of concentration, with highly variable contents. Ge displays concentrations from 14 to 2576 ppm whereas Sn and In contents extend from the limit of detection (~1 ppm) to 3028 and 870 ppm, respectively. Ge is mostly concentrated in sectors, averaging 1102 ppm, whereas Sn and In are enriched in dark brown bands with average contents of 876 and 234 ppm, respectively. Both Ga and Ag reveal quite similar distributions (4–1054 ppm and 11–1654 ppm, respectively) and are more concentrated in sectors with average contents of 359 and 354 ppm, respectively. Further, among the elements analysed in this study, As is the least abundant (1–79 ppm) although it was present in consistently higher concentrations in sectors, averaging 26 ppm.

Germanium isotopes

Ge isotopic compositions of the Saint-Salvy sphalerites are listed in Table 4, including the preliminary data of Filia (2010). The $\delta^{72}Ge_{JMC}$ vs. $\delta^{74}Ge_{JMC}$ diagram (Fig. 7) shows that Ge isotopic compositions of all sphalerite samples fall within error of the equilibrium and kinetic theoretical mass fractionation lines, as for both Aldrich and JMC Ge standards, indicating that isobaric interferences have been efficiently removed by the hexapole collision cell (argide interferences) and by the isobaric interference correction (e.g., Zn interferences) during measurements (Luais, 2012). Throughout the remainder of the manuscript, Ge isotopes will be discussed using the re-calculated $\delta^{74}Ge$ notation relative to the NIST SRM 3120a standard ($\delta^{74}Ge_{NIST3120a}$). The sphalerite of Saint-Salvy displays a wide range of $\delta^{74}Ge_{NIST3120a}$ values, from $-2.07 \pm 0.37‰$ to $+0.91 \pm 0.16‰$ (2σ SD external reproducibility). The samples that belong to the same level within the mine, 64W-02 and 64W-08, yield similar $\delta^{74}Ge_{NIST3120a}$ of $-2.06 \pm 0.37‰$ and $-2.03 \pm 0.39‰$ (2σ SD) despite different bulk Ge contents of 699 ± 35 and 270 ± 13 (1σ SD) ppm.

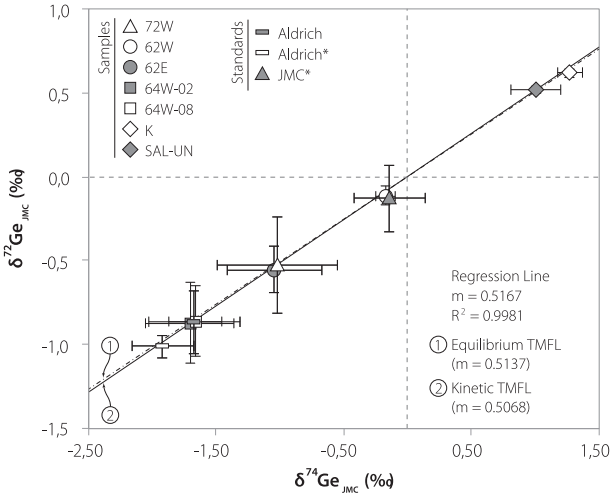

Fig. 7. $\delta^{72}Ge_{JMC}$ vs. $\delta^{74}Ge_{JMC}$ diagram for the sphalerite from Saint-Salvy (before re-calculation relative to the NIST SRM 3120a standard, see text for details), chemistry-processed JMC Ge standard and Aldrich secondary Ge standard (*) and an unprocessed Aldrich Ge standard. Error bars are 2σ (SD) external reproducibility, based on replicate samples. All samples fall on the equilibrium and kinetic theoretical mass fractionation lines (TMFL), for which the equations are $\delta^{72}Ge = (1/m_{72} - 1/m_{70})/(1/m_{74} - 1/m_{70}) \times \delta^{74}Ge \sim 0.5137 \times \delta^{74}Ge$ and $\delta^{72}Ge = \ln(m_{72} - m_{70})/\ln(m_{74} - m_{70}) \times \delta^{74}Ge \sim 0.5068 \times \delta^{74}Ge$, respectively, where m_x refers to the molar mass of the considered isotope (according to Young et al., 2002).

Sulphur isotopes

The *in situ* $\delta^{34}S_{V\text{-}CDT}$ values for the five analysed samples are shown as histograms in Fig. 8. The $\delta^{34}S_{V\text{-}CDT}$ values of both samples of the 64W (64W-08 and 64W-02) mine face are close in proximity and average $+6.09 \pm 0.55‰$ and $+6.00 \pm 0.91‰$, respectively. However the latter shows a wider range of $\delta^{34}S_{V\text{-}CDT}$. The 62W-02 sample shows $\delta^{34}S_{V\text{-}CDT}$ values matching those of the 64W samples,

Table 4
Germanium isotopic composition (‰) by MC-ICP-MS of the Aldrich Ge standard, the chemistry-processed Aldrich and JMC Ge standards (*), and the sphalerite samples of Saint-Salvy ore deposit (normalised to the NIST 3120a Ge standard). Ge contents (ppm) by solution MC-ICP-MS (measured on the solution used for isotopic measurements after column processing) and ICP-MS data (measured on an aliquot of the solution after total dissolution) for cross-checking. *n*: number of replicates. Errors as 1 or 2σ standard deviation.

		$\delta^{72}Ge_{NIST3120a}$		$\delta^{73}Ge_{NIST3120a}$		$\delta^{74}Ge_{NIST3120a}$		Ge (ppm) MC-ICP-MS		Ge (ppm) ICP-MS	
	n	Mean	2σ	Mean	2σ	Mean	2σ	Content	σ	Content	σ
Aldrich Ge	39	−1.06	0.19	−1.56	0.31	−2.04	0.38	–	–	–	–
Aldrich Ge*	2	−1.21	0.09	−1.69	0.27	−2.28	0.28	–	–	–	–
JMC Ge*	2	−0.33	0.2	−0.35	0.21	−0.51	0.31	–	–	–	–
62E	3	−0.75	0.15	−1.17	0.2	−1.41	0.39	813	34	909	45
62W	3	−0.31	0.08	−0.59	0.17	−0.54	0.15	908	69	861	43
64W-02	3	−1.07	0.24	−1.63	0.28	−2.07	0.37	699	49	699	35
64W-08	3	−1.06	0.21	−1.63	0.34	−2.03	0.39	240	13	270	13
72W	4	−0.73	0.29	−1.18	0.47	−1.39	0.49	470	19	557	28
SAL-UN	3	0.32	0.06	0.4	0.21	0.64	0.23	925	50	1000	50
K	2	0.42	0.06	0.51	0.25	0.91	0.16	1020	90	1125	56

* Chemistry-processed standards.

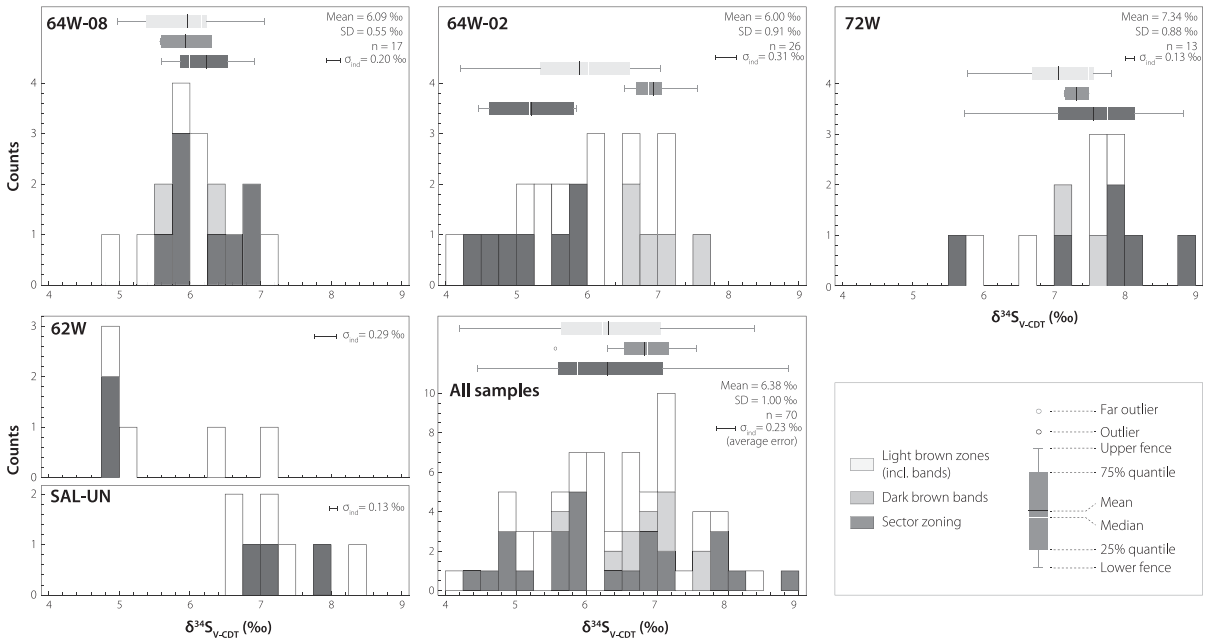

Fig. 8. Histogram of $\delta^{34}S_{V\text{-}CDT}$ relative to the three types of zoning patterns for each sample. Box plots, means and standard deviations (SD) are shown for samples with bell-shaped distribution. For those that are not bell-shaped, we choose not to indicate any mean and SD as they would not be representative due to an insufficient number of measurements. Average analytical errors of individual measurements are represented as σ_{ind}.

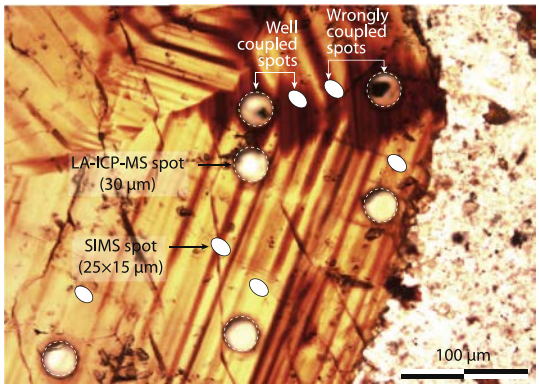

Fig. 9. Coupling of LA-ICP-MS and SIMS spot analysis. In some cases SIMS spot sizes were too large for precise measurements of the dark-brown band compositions, or were too far from the required location so that these were rejected and not spatially coupled with LA-ICP-MS spots.

ranging between $+4.84 \pm 0.29‰$ and $+7.13 \pm 0.29‰$. The deepest sample, 72W, shows a slightly higher range of $\delta^{34}S_{V\text{-}CDT}$ values, averaging $+7.34 \pm 0.88‰$, which are compatible with those of the SAL-UN sample, averaging $+7.26 \pm 0.62‰$. Overall sulphur isotope values range from $+4.21 \pm 0.29‰$ to $+8.85 \pm 0.13‰$ and average $+6.38 \pm 1.00‰$.

As regards the ability to couple $\delta^{34}S_{V\text{-}CDT}$ spot analyses to those by LA-ICP-MS, out of the 70 spot analyses, only 48 were correctly coupled with prior LA-ICP-MS spot analyses (see section 'Sulphur isotope measurements by secondary ion mass spectrometry (SIMS)'). Some spots were revealed to be out of the expected zone and could not be used for a proper comparison with adjacent LA-ICP-MS spots (Fig. 9). With the exception of sample 64W-02 which clearly shows high $\delta^{34}S$ in dark rhythmic bands and low $\delta^{34}S$ in sectors, all other samples and the overall data shows overlapping $\delta^{34}S$ irrespective of the zoning type, suggesting they are uncorrelated (see PCA results in the next section).

Principal component analysis of minor/trace elements and sulphur isotope data

The results of the PCA applied to the LA-ICP-MS dataset are shown in Fig. 10a where elements and spot analyses are projected on the PC1 *vs.* PC2 plane, accounting for 71.2% of element content variability. Element distributions (Fig. 10a, right frame) highlight two main groups, or element correlation clusters. One group is composed of Cu and trace elements Sb, Ag, Ge, Ga and As (loading PC1), whereas an other group is composed of Fe, Cd, In and Sn (loading PC2). This second group is divided into (Fe, Cd) and (In, Sn) sub-groups. The latter occupies an intermediate position between the (Fe, Cd) group and the Cu plus trace elements group along PC1. Spots representation in the PC1 vs. PC2 plane (Fig. 10a, left frame) refers to the zoning patterns described in section 'Samples studied'. PC1 (loaded by Cu and trace elements) is correlated with the spots in sector zonings, whereas PC2 (loaded by Fe,

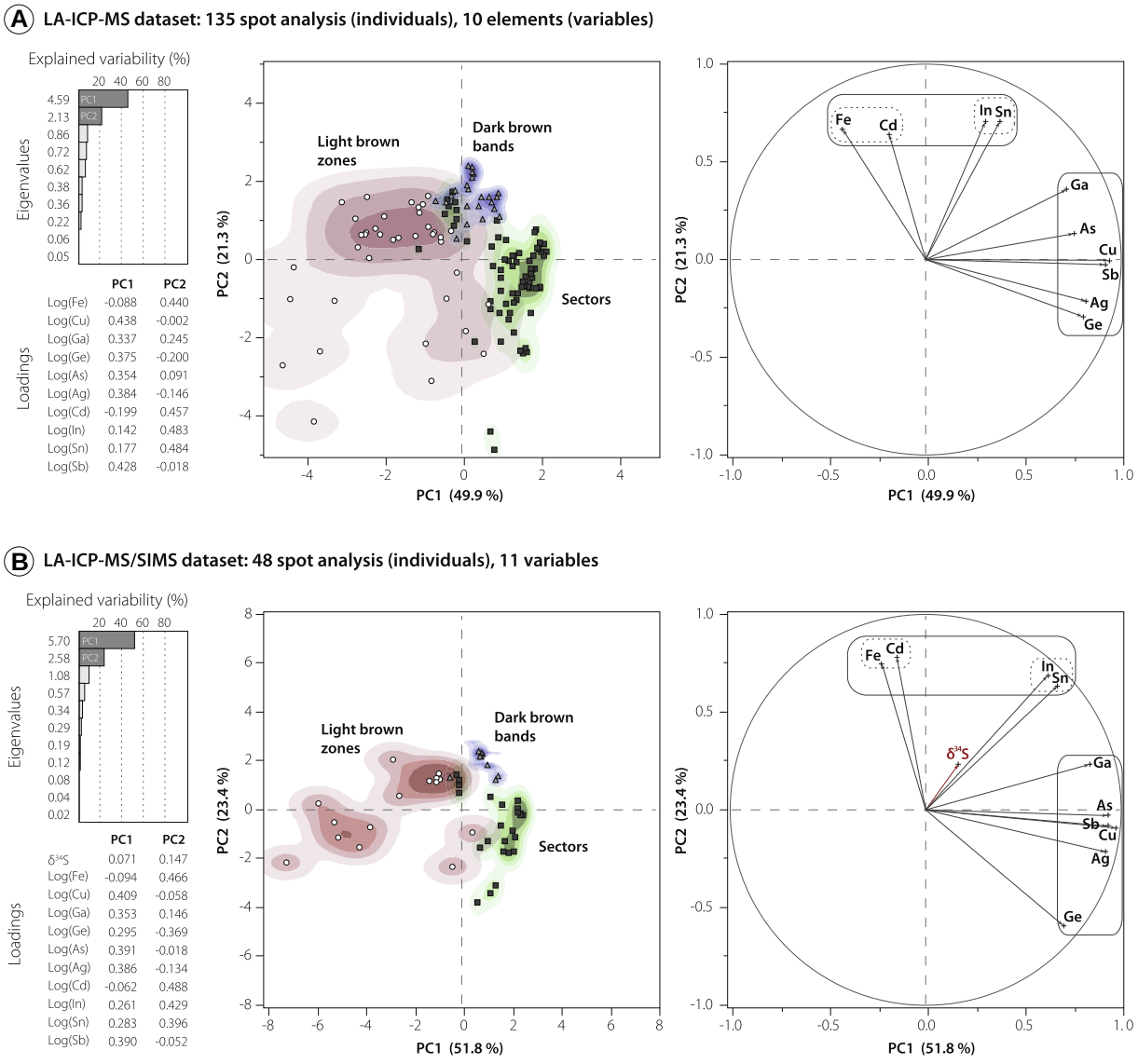

Fig. 10. (A) Principal component analysis of the LA-ICP-MS log-transformed dataset of trace element contents in sphalerite from Saint-Salvy. On the left hand side edge: eigenvalues (i.e., variance explanation) and loadings (i.e., eigenvector coefficients) of the principal components. Middle frame: spot analyses (i.e., individuals) plotted on the PC1 vs. PC2 plane (explaining 71.2% of element content variability). Right frame: elements (i.e., variables) plotted in the same plane. This PCA underlines two main, opposed clusters of elements distributed within the zoning patterns: (Fe, Cd) and (In, Sn) are enriched and correlated in rhythmic bandings whereas Cu, Ga, Ge, Ag, Sb and As are enriched and correlate in sector zoning. (B) PCA of the coupled LA-ICP-MS/SIMS of trace elements contents (log-transformed) and $\delta^{34}S_{V\text{-}CDT}$. On the left: eigenvalues and loadings. Middle frame: spot analyses plotted on the PC1 vs. PC2 plane (explaining 75.2% of total variability). Right frame: elements/$\delta^{34}S_{V\text{-}CDT}$ (variables) plotted in the same plane. This PCA suggests that there is no correlation between $\delta^{34}S_{V\text{-}CDT}$ and trace element content in sphalerite. To a lesser extent, the comments on (A) are applicable to this PCA regarding trace correlations and zoning patterns.

Cd, In and Sn) is correlated with dark brown bands, although these partly overlap. Spots analyses in the light brown growth areas exhibit a slight correlation with PC2 and a relatively well-marked anti-correlation with PC1. Indeed, as most spot analyses are performed in light brown rhythmic bands, it demonstrates that the element clustering that occurs in dark brown rhythmic bands also occur in light brown ones, though this element cluster is lower in concentration.

Principal component analysis was applied to the coupled SIMS/LA-ICP-MS spot analyses (48 spots) to investigate if any correlations exist between $\delta^{34}S$ and trace elements and whether or not they are also correlated with the different compositional zoning types. The results (Fig. 10b) show that $\delta^{34}S$ does not correlate with minor/trace element contents and zoning patterns. However, even using this limited dataset, element correlation clusters appear in agreement with those inferred from the whole dataset (Fig. 10a).

DISCUSSION

Element clustering in zoning patterns

The appearance of multi-element correlation groups specific to zoning patterns using PCA (Fig. 10), i.e., Cu and trace elements (Ge, Ga, Sb, Ag, As) in sectors, and (Fe, Cd) and (In, Sn) in rhythmic bands, may be reasonably linked to different processes of incorporation during sphalerite growth. The large angle between Ge and Cd in the PCA confirms the approximate anti-correlation previously reported in Cassard et al. (1994) and Halfon and Rosique (1973). Element mapping (Fig. 4) and PCA of minor/trace element data suggest a preferential enrichment of element clusters in zoning patterns in sphalerite, resulting in their antithetic distribution in sectors and rhythmic bands. This typical element distribution highlights crystallographic controls on the minor/trace element incorporation between sector zonings and rhythmic bandings. Similar antithetic distribution of element groups has been observed by Johan (1988) in sphalerite from the Saint-Martin-la-Sauveté district (Loire, France) where Fe and Cd are concentrated in (1 1 0) growth bands, whereas Cu and In are concentrated in (1 1 1) truncation faces (i.e. sectors) and complex twinning patterns, suggesting the coupled substitution mechanism $2Zn^{2+} \leftrightarrow Cu^{+} + In^{3+}$.

Compositional zoning has been documented by Vesselinov and Kerestedjian (1995) and Agrosì et al. (2002) for arsenopyrite and andradite crystals, respectively, and more recently in Di Benedetto et al. (2005a) for sphalerite crystals. A model for sector zoning has been proposed in Watson and Liang (1995) for slow grown crystals. Zoning patterns are generally considered to be related to self-organized non-equilibrium processes occurring during crystal growth under specific conditions (Di Benedetto et al., 2005a and references therein). Typically, large-scale variations of the mineralizing fluid composition in open systems and microscale variations of the fluid composition in closed systems are involved in the formation of banding patterns, and are seen as external and internal processes, respectively (Holten et al., 1997). At the micrometre-scale, the Saint-Salvy sphalerite does not show any systematic increase/decrease in element content from the core to the rim of the crystals, which suggests that only microscale (internal) processes at or near the growing crystal edges account for the observed types of zoning. Indeed, sector zoning and rhythmic banding occurred concomitantly during sphalerite growth. We can assume to some extent that preferential incorporation of Cu, Ge, Sb, Ag and Ga occured in sectors during sphalerite growth, implying that Fe, Cd, In and Sn were concentrated at the crystal-fluid interface and were therefore incorporated in more favourable crystal faces once they had reached a given threshold. This results in a feedback-driven reaction pathway forming the observed dark brown bands. According to Di Benedetto et al. (2005a), sector zoning is thought to be driven by out-of-equilibrium kinetically controlled factors such as surface atomic arrangement of the growing faces (Vesselinov and Kerestedjian, 1995; Agrosì et al., 2002), or by equilibrium crystal growth under given boundary constraints (Watson et al., 1995).

The lack of correlation between sulphur isotopes and minor/trace element contents (and zoning patterns) is consistent with $\delta^{34}S$ histograms (Fig. 8). It seems that the processes triggering cation enrichment and compositional zoning during sphalerite deposition (i.e., crystallographic controls, fluid evolution at the crystal interface) do not affect the sulphur isotopic system, which is thus rather a signature of the processes occurring in fluids before deposition of sphalerite (e.g., reduction mechanisms, sulphur sources; see section 'Source reservoirs of elements and the origin of mineralizing fluids').

Minor and trace element substitution mechanisms

The strong correlation between Fe and Cd in our data support specific studies on minor element incorporation in sphalerite (e.g., Di Benedetto et al., 2005b; Wright and Gale, 2010), which suggest direct substitutions of divalent cations as $Zn^{2+} \leftrightarrow (Fe^{2+}, Cd^{2+})$. For elements generally occurring in odd valences such as Cu, Sn, In, and other trace compounds (e.g., Sb, Ag, Ge, Ga, As), multiple coupled substitutions with Zn are thought to be involved to explain their enrichment in sphalerite (Bernstein, 1986; Johan, 1988; Cook et al., 2012).

To focus on trace element incorporation in sphalerite, binary plots (Fig. 11) have been constructed using the strongest element correlations (Fig. 10a) in order to observe potential coupled substitution schemes. The strong correlation between Sb and Cu with a trend sub-parallel to the molar ratio $(Sb/Cu)_{mol} = 1$ (Fig. 11a), suggests the coupled substitution $2Zn^{2+} \leftrightarrow Cu^{+} + Sb^{3+}$. These results are supported by previous suggestions of a Cu^{+} oxidation state in sphalerite and its coupled incorporation with In^{3+}, in agreement with Johan (1988) for the case of Saint-Salvy, and with Pattrick et al. (1998), Cook et al. (2012) and Murakami and Ishihara (2013) in sphalerite of various deposits.

The correlation between In and Sn with a trend sub-parallel to the $(In/Sn)_{mol} = 1$ line (Fig. 11b), suggests a potential coupled substitution $3Zn^{2+} \leftrightarrow In^{3+} + Sn^{3+} + \square$ ($\square$ denote a vacancy). If In^{3+} is generally assumed to be present in most materials (Epple et al., 2000), Sn^{3+} constitutes the best solution to match this 1:1 correlation although its main oxidation states are Sn^{+2} and Sn^{+4}. We would expect those valences to produce correlations with monovalent cations for charge compensation (as in Murakami and Ishihara, 2013), which would involve the following mechanisms: $3Zn^{2+} \leftrightarrow In^{3+} + Sn^{2+} + (Cu, Ag)^{+}$ or $4Zn^{2+} \leftrightarrow In^{3+} + Sn^{4+} + (Cu, Ag)^{+} + \square$. However, the involvement of monovalent cations is difficult to verify because Cu is more concentrated than In and Sn in most spot analyses and is likely involved in many coupled substitutions mechanisms that are impossible to distinguish in simple scatter plots. The oxidation state of Sn and of other elements (e.g., Ge, Ga) is problematic and requires further work using appropriate methods (e.g., X-ray absorption, μ-XANES/EXAFS) as in Pattrick et al. (1998), Goh et al. (2006) and more recently in Cook et al. (2012), concerning the oxidation state of Cu in In-Cu-rich sphalerite (μ-XANES).

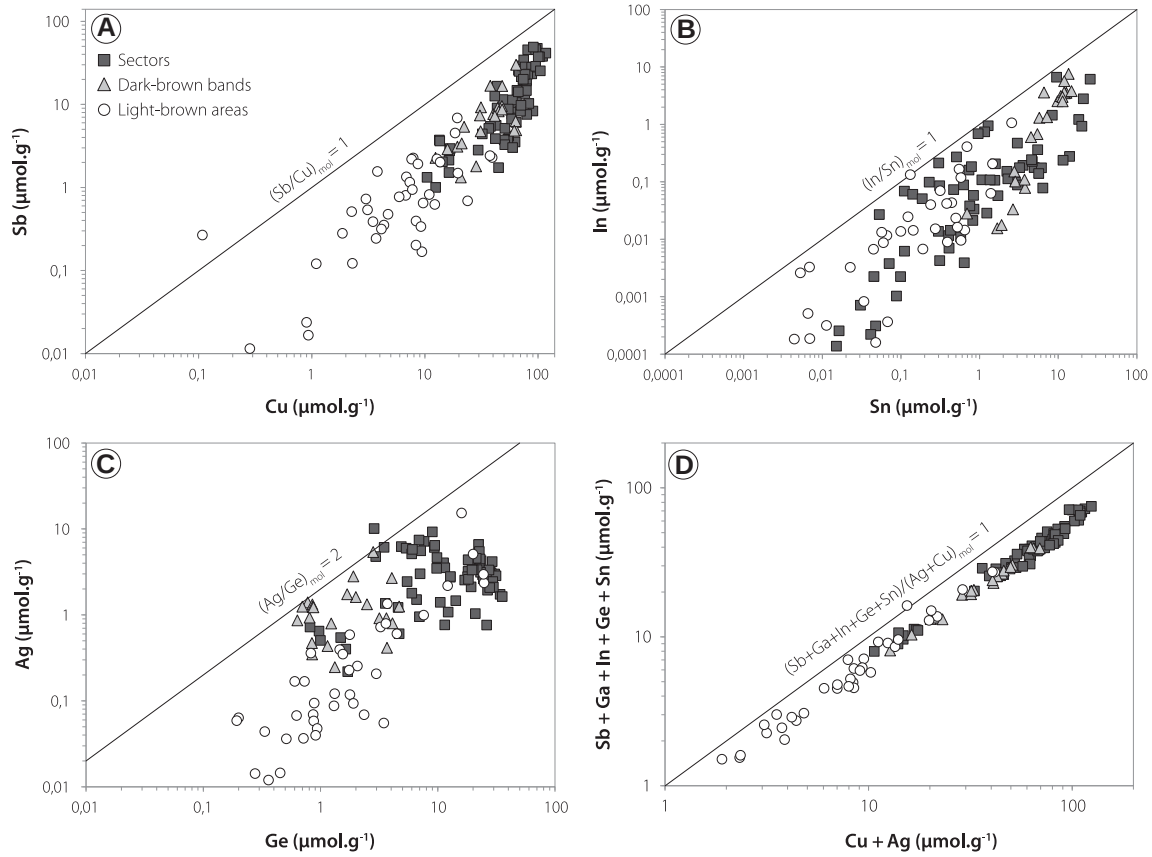

Fig. 11. Binary correlation plots, trend lines, and suggested coupled substitution mechanisms. (A) The correlation between Sb and Cu, with a trend sub-parallel to $(Sb/Cu)_{mol} = 1$, suggests the coupled substitution $2Zn^{2+} \leftrightarrow Cu^{+} + Sb^{3+}$. (B) In correlates with Sn along the $(In/Sn)_{mol} = 1$ line, suggesting the substitution $3Zn^{2+} \leftrightarrow In^{3+} + Sn^{3+} + \square$ ($\square$ = vacancy). (C) Ag correlates with Ge with a trend sub-parallel to the $(Ag/Ge)_{mol} = 2$ line, indicating the substitution $3Zn^{2+} \leftrightarrow Ge^{4+} + 2Ag^{+}$. (D) The strong correlation between Cu + Ag (monovalent cations) and Sb + Ga + Ge + In + Sn (tri- and tetravalent cations) along the 1/1 M ratio highlights a general coupled substitution mechanism for Cu (minor element) and trace elements in sphalerite, substituting for Zn.

The correlation between Ge and Ag, displaying a trend sub-parallel to the $(Ag/Ge)_{mol} = 2$ line (Fig. 11d), suggests the coupled substitution $3Zn^{2+} \leftrightarrow Ge^{4+} + 2Ag^{+}$. In dark brown sectors, Ge contents are considerably higher than those of Ag, i.e. around 1100 ppm against 360 ppm, respectively. Assuming that such a mechanism can account for the entire Ag incorporation in sphalerite, Ge has likely been involved in many other substitution mechanisms in order to reach these concentrations, primarily Cu, Ga and Sb (Fig. 10a). However, Johan (1988), and more recently Cook et al. (2009) and Ye et al. (2011) could not exclude a possible involvement of Ge^{2+} in direct substitution with Zn^{2+} or in a general substitution mechanism with minor/trace elements.

Cook et al. (2009) remarked that a general coupled substitution mechanism would result in monovalent cation enrichment (i.e. Ag^{+} and Cu^{+}) with respective tri- and tetravalent cation enrichments (e.g., Sb^{3+}, Ga^{3+}, In^{3+}, As^{3+}, Ge^{4+} and Sn^{4+}). The strong correlation between those elements has already been highlighted in sector zonings by PCA (Fig. 10a). Fig. 11d visualizes this observation in terms of contents. Taking into account its concentration, Cu is the predominant monovalent cation. Remarkably, within every spot, all zoning types considered, Cu (and Ag to a lesser extent) content approaches the sum of all available cations assumed to be tri- or tetravalent (Fig. 11d). Strikingly, Cu could provide charge-balance in the entire broad set of coupled substitution mechanisms, and could be responsible for incorporation of a large range of trace elements, especially Ge, Ga and Sb, regardless of the zoning type. It is impossible to separate the amounts of Fe and Cd involved in direct $Zn^{2+} \leftrightarrow (Fe^{2+}, Cd^{2+})$ substitutions from those involved in coupled substitutions (as Cd^{2+}, Fe^{2+} and/or Fe^{3+}) with monovalent cations (e.g., Cu, Ag), with which they should be correlated. For this reason Fe and Cd are not integrated in this plot, which can explain why the data are slightly scattered below the 1/1 M line, especially at high concentrations.

Implications for sphalerite deposition processes from germanium isotopes

The Ge isotopic variations in high-T mantle/crust and core planetary reservoirs display a restricted range of variations. Escoube et al. (2012) and Luais (2012) evaluated a mean δ^{74}Ge around $+0.59 \pm 0.18‰$ and $+0.53 \pm 0.16‰$ (2σ SD) for upper mantle/crust, respectively, based on Ge isotope measurements in various igneous rocks such as

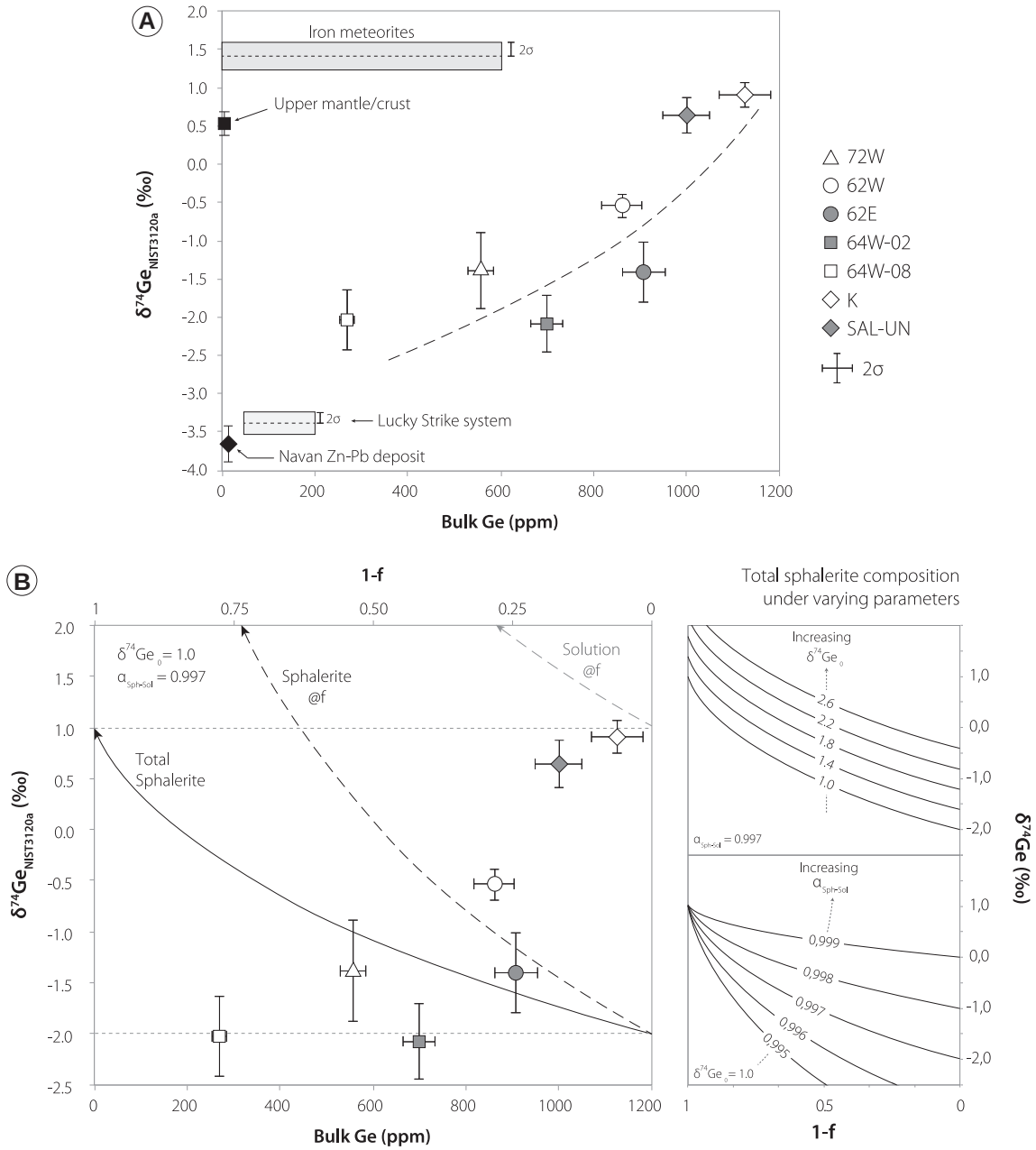

Fig. 12. (A) $\delta^{74}Ge_{NIST3120a}$ ‰ *vs.* bulk Ge content (ppm) diagram for the sphalerite of Saint-Salvy compared to the ranges of iron meteorites (representative of the Earth core composition; Luais, 2007), rocks representative of the igneous upper mantle/crust reservoirs (~1–2 ppm Ge; Luais, 2012; Escoube et al., 2012), sphalerite of the Navan Zn–Pb Irish-type deposit, Ireland (4–28 ppm Ge; Escoube et al., 2012), and sphalerite of the Lucky Strike modern seafloor hydrothermal system (40–200 ppm Ge; Escoube et al., 2012). See text for further explanation. (B) Rayleigh distillation model matching the observed $\delta^{74}Ge$ range. Equations are given in Johnson et al. (2004). The fractionation factor $\alpha_{sph-sol} = 0.997$ is in agreement with Li et al. (2009) calculations. The initial fluid composition $\delta^{74}Ge_0$ is assumed to be the $\delta^{74}Ge$ of the richest sphalerite, sample K. *f* indicates the fraction of residual Ge in solution ($1 - f$ the fraction of Ge incorporated in sphalerite) The observed $\delta^{74}Ge$ trend is not compatible with a Rayleigh-type fractionation process (main diagram), irrespective of the given fractionation factor ($\alpha_{sph-sol}$) and the initial fluid composition ($\delta^{74}Ge_0$) inputs (inserts on the right hand side).

peridotites, mantle-derived mid-ocean ridge and volcanic island basalts, and continental granites. Luais (2007, 2012) showed the mean $\delta^{74}Ge$ in magmatic iron meteorites is around $+1.41 \pm 0.22$‰ (2σ), representative of the core composition of planetesimals. By contrast, the Saint-Salvy sphalerite displays a broad range of $\delta^{74}Ge$ values (-2.07‰ to $+0.91$‰, Table 4), heavier than $\delta^{74}Ge$ values in sphalerite from the Navan Pb–Zn Irish-type deposits, Ireland (-4.28‰ to -2.82‰, Escoube et al., 2012), and $\delta^{74}Ge$ values in sphalerite from the Lucky Strike modern seafloor hydrothermal system (-4.00‰ to -2.98‰, Escoube et al., 2012). Ge isotopic data of Pb–Zn sulphides are displaced toward lower $\delta^{74}Ge$ values compared to mantle/crust samples, indicating a large Ge fractionation during

low-temperature (80–140 °C) and low-pressure crustal processes (i.e. leaching, transport and deposition).

There is a positive correlation between bulk Ge content and δ^{74}Ge in the Saint-Salvy data (Fig. 12a). Remarkably, the data of the Navan deposit and the Lucky Strike hydrothermal system are consistent with this trend. In a finite fluid reservoir from which sphalerite precipitated (Rayleigh fractionation), if decreasing Ge content in sphalerite is related to decreasing Ge content in solution during fluid evolution, this trend would suggest a progressive enrichment of light isotope in the fluid during sphalerite precipitation and an isotopic fractionation factor $\alpha_{sph-sol}$ higher than 1. However, theoretical *ab inito* prediction of Ge fractionation by Li et al. (2009) suggests the opposite, i.e., the lighter isotopes should be incorporated in the precipitating Ge-bearing sulphide phases. This would result in fluids becoming progressively enriched in heavy isotopes during cooling, and therefore the isotopic fractionation factor $\alpha_{sph-sol}$ would be lower than 1. These predictions are supported in Siebert et al. (2006, 2011) by measurements of heavy Ge isotope compositions of several continental high-T hydrothermal fluids. At present, the parameters of the law giving the equilibrium isotopic fractionation factor between aqueous Ge species and Ge-bearing precipitating sulphides as a function of fluid temperature remains unknown ($10^3 \ln\alpha_{sph-sol} = A\times10^6/T^2 + B\times10^3/T + C$ where A, B and C are the unknown parameters).

Accordingly, the predicted Rayleigh fractionation, implying that the precipitated sphalerite is isolated from isotopic exchange in a non-renewed but evolving hydrothermal fluid system, yields a trend opposite to that of the data (Fig. 12b). Thus, the conditions of Rayleigh distillation (finite reservoir) being incompatible with the data, sphalerite deposition has most likely occurred in open system. Nonetheless, assuming our samples represent cumulated deposited sphalerite, the observed range of Ge isotopic compositions in sphalerite can be matched by $\alpha_{sph-sol} = 0.997$, in good agreement with Li et al. (2009), and $\delta^{74}Ge_0 = 1.0‰$, chosen to correspond the isotopic composition of the first precipitated sphalerite, i.e., the sample richest in Ge, sample K (Ge = 1125 ppm, δ^{74}Ge = 0.91‰; Fig. 12b). The trend of the Rayleigh fractionation is irrespective of the given $\alpha_{sph-sol}$ and $\delta^{74}Ge_0$ (Fig. 12b inserts).

As shown in section 'Element clustering in zoning patterns', sector zoning and compositional banding imply crystallographic controls on Ge and minor/trace element incorporation, with rhythmic microscale compositional variations of the precipitating fluid at the crystal–fluid interface. We can speculate on how these processes affect Ge isotopic fractionation in each zoning type and how these contribute to the measured bulk Ge isotopes (e.g., kinetic effects), with respect to the proportion of Ge in the sampled sphalerite (even if special care has been taken to ensure that representative material has been sampled). If a Rayleigh fractionation process did occur close to the fluid–crystal interface during sphalerite precipitation, then mixing of these fluids with pulses of renewed fluids (responsible for rhythmic bandings) may have largely obscured its signature. Thus, in an open hydrothermal system, the Ge isotopic compositions of sphalerite might reflect isotopic variations in the upstream fluids, e.g., during metal leaching and transport.

Source reservoirs of elements and the origin of mineralizing fluids

The source reservoirs of metals and sulphur of the economic mineralization stage of the Saint-Salvy deposit has been widely discussed in the literature and its elemental and isotopic geochemical signatures have been the subject of major debate (Halfon and Rosique, 1973; Barbanson and Geldron, 1983; Cassard et al., 1994; Munoz et al., 1994).

The *in situ* δ^{34}S range of +4.21‰ to +8.85‰ is typical of hydrothermal systems (Ohmoto and Rye, 1979), and is similar to that of sphalerite containing thermochemically reduced S from the Navan Pb–Zn Irish-type deposit, Ireland (Blakeman et al., 2002; Gagnevin et al., 2012). These data are consistent with previous bulk sulphur isotope data on the Saint-Salvy sphalerite, displaying a $\delta^{34}S_{CDT}$ range of +6.2‰ to +8.8‰ (Munoz et al., 1994) and +5.7‰ to +7.5‰ (Cassard et al., 1994). According to Munoz et al. (1994), considering that there is no indication of the presence of sulphate or oxide in this paragenetic stage, and given temperatures ranging from 80 to 140 °C from fluid inclusion measurements, the dominant sulphur species in the fluids was most probably H_2S. Also, based on the abundance of carbonates in this stage, the pH of the fluids were therefore likely to be close to neutral (Moisy, 1993). Under these conditions, according to the compilation in Ohmoto and Rye (1979), equilibrium isotopic fractionation of sulphur in sphalerite is very small and δ^{34}S values in sphalerite are close to those of dissolved sulphur (H_2S) of the fluids. For instance, the calculated δ^{34}S values of H_2S in the fluids equilibrated with the deposited sphalerite, taking an average temperature of 110 °C, display a range of +3.53‰ to +8.16‰. Further, δ^{34}S values of the local Cambrian syngenetic sulphides (+4.7‰ to +9.4‰; Munoz et al., 1994 and references therein) are compatible with those of Saint-Salvy (+4.21‰ to +8.85‰), indicating a possible source of sulphur in the Cambrian black schists series. However, whether or not this signature is the result of contamination by the mineralizing fluids remains debatable (Cassard et al., 1994).

The comparison of the averaged δ^{34}S and bulk δ^{74}Ge in Saint-Salvy sphalerite did not reveal any clear trend between these two isotopic systems, although it appears that samples having high δ^{74}Ge also have high δ^{34}S (e.g., SAL-UN, $\delta^{74}Ge_{NIST3120a} = +0.64‰$, $\delta^{34}S_{V\text{-}CDT} = +7.3‰$) and vice-versa (e.g., 64W-08, $\delta^{74}Ge_{NIST3120a} = -2.03‰$, $\delta^{34}S_{V\text{-}CDT} = +6.1‰$). On the basis of our δ^{34}S measurements for some samples, it would be reasonable to conclude that similar thermochemical fractionation processes affected both S and Ge isotopic systems during deposition (e.g., reduction). Further δ^{34}S analyses should help us to evaluate this possibility.

There is an undisputable link between trace element contents of the ore sphalerite (our study) and those of the Cambrian black schists that contain about 550 ppm Ge,

300 ppm Ag and 2200 ppm Cd after Barbanson and Geldron (1983). Their study suggests that Ge and Ag may have been associated with organic matter in the fluorine-rich phosphate pellets of the Cambrian black schists, and were mobilized by hydrothermal solutions. Several types of ligands may facilitate Ge mobilization and transport could occur via complexation with fluorides, hydroxifluorides and/or aqueous organic compounds at the low temperatures involved during deposition (in agreement with Pokrovski and Schott, 1998; Wood and Samson, 2006). Furthermore, there would be sufficient Zn, Ge and Ag in the Cambrian black schists to account for the fluid concentrations from which the ore deposit formed. This idea is consistent with the "organic" character of these fluids as indicated by very low δD in fluid inclusions (Munoz et al., 1994).

Significance of trace element trends in sphalerite-bearing ore deposit types

Several authors suggest that the bulk trace element composition of sphalerite is intimately related to the type of ore

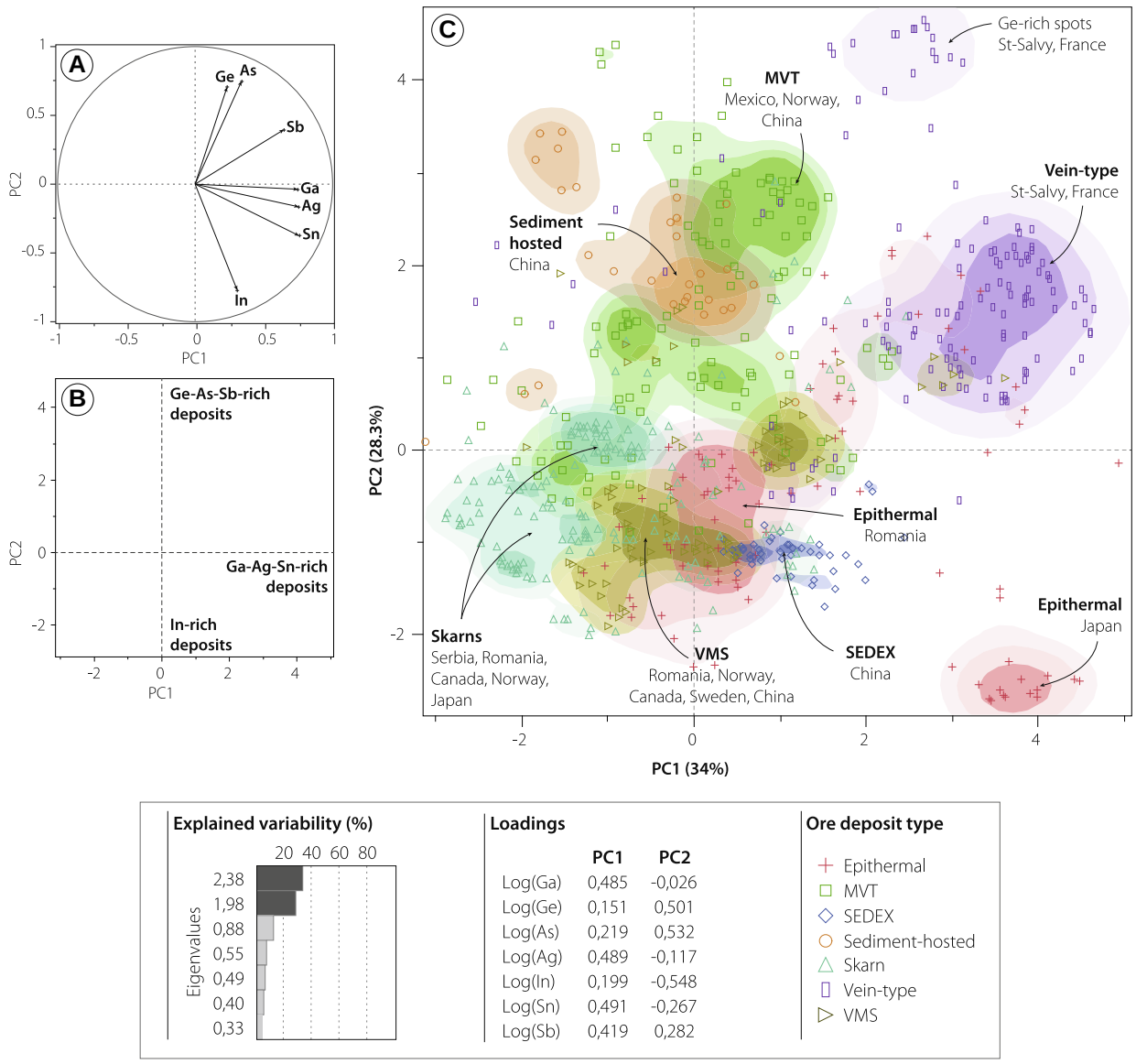

Fig. 13. PCA of Cook et al. (2009) and Ye et al. (2011) LA-ICP-MS dataset of sphalerite of different types of ore deposits worldwide. The Saint-Salvy dataset has been plotted after PCA in order to avoid introducing element variability due to crystallographic heterogeneities of any kind into the principal component calculation. This will allow us to focus on element variability at the scale of the ore deposit. Eigenvalues and loadings of the PCA are indicated. (A) Plot of the elements (variables), (B) interpretative scheme in terms of element enrichment for spot analysis (individuals), and (C) the scatterplot of the log-transformed spot analysis datasets (individuals) of the above publications including the Saint-Salvy dataset, plotted in the PC1 vs. PC2 plane. This PCA of the trace element contents in sphalerite from various deposits confirm their geochemical significance in discriminating between genetic ores types (e.g., high In contents for magmatic-related deposits, and Ge for low-temperature deposits). In the bottom insert, eigenvalues, eigenvector loadings and scores legend (i.e., ore deposit types) are shown.

deposit (e.g., in the pioneering work of Oftedahl, 1940; or more recently in Cook et al., 2009). The source of the ore components, the fluid history and evolution (lithologies, composition, temperature), sites and mechanisms of deposition, as well as the relative volumes of sphalerite within the orebody, will all influence elemental fractionation and the overall concentrations in sphalerite (Bethke and Borton, 1971). These parameters can be studied, combining our LA-ICP-MS minor/trace element dataset to those of recent studies (i.e., Cook et al., 2009; Ye et al., 2011), and treating them by multivariate statistics.

Reliable LA-ICP-MS minor/trace element datasets of sphalerite from different types of deposits and provinces worldwide are provided in Cook et al. (2009) and Ye et al. (2011). We compiled these data, log-transformed, and processed them using PCA only on trace element contents (Ga, Ge, As, Ag, In, Sn and Sb). This analysis aims to test if trace elements features (analysed in localised spots) in sphalerite may efficiently discriminate between ore genetic types using large datasets (Fig. 13). The Saint-Salvy dataset, which reflects strong microscale compositional variations, has been plotted in the PCA after the principal components calculation to focus the calculation on variations of trace element in sphalerite at the scale of the ore deposit (i.e., the scale of Cook et al. (2009) and Ye et al. (2011) studies).

The resulting PCA shows that the first factor of discrimination (PC1) is mainly loaded with Ga, Ag, Sn, Sb whereas the second order of discrimination (PC2) is primarily loaded with Ge, As, and In (Fig. 13a). Two element clusters are shown in Fig. 13a, (Ge, As) and (Ga, Ag, Sn); Sb occupies an intermediate position between these clusters, and In is anti-correlated with (Ge, As). On the one hand, high In contents in solid solution may typify magmatically-driven hydrothermal systems (i.e. skarn, epithermal and VMS deposits, and some SEDEX deposits, Fig. 13b and c). They are chiefly found in the bottom-left section of the graph. On the other hand, Ge, Ga and As tend to be enriched in low-T deposits unrelated to a magmatic source (i.e. the sediment-hosted deposit of Jinding, China, and MVT deposits, Fig. 13b and c) according to Cook et al.'s (2009) petrogenetic classification, although unusual signatures may reflect the local geological setting. These are located in the top-right section of the plot. Thus, this framework is likely to illustrate a positive temperature gradient and differences in metal sources from the top-right to the bottom-left corner.

As suggested by Cook et al. (2009) and Ye et al. (2011), specific trace element signatures may belong to a given deposit (e.g., Tres Marias, Mexico; Toyoha, Japan) or even an ore province (e.g., skarns of the Banatitic Magmatic and Metallogenic Belt (BMMB), Southeastern Europe). The Saint-Salvy sphalerite occupies the top-right corner of this structure, consistent with its low-T deposition and the non-magmatic nature of the depositional fluids. Some Ge-rich (In-poor) spot analysis within sectors form a very distinct subgroup, highlighting the huge microscale variability of the trace element content within the Saint-Salvy sphalerite. Finally, even if large variations in the trace element contents occur in the sphalerite of a given deposit, trace element trends show petrogenetic significance and may provide tools for discriminating between genetic types of ore deposits.

CONCLUSIONS

This integrated study coupling mineralogical observations, *in situ* LA-ICP-MS analyses of minor/trace elements and bulk Ge isotopes in zoned Ge-rich sphalerite from the Saint-Salvy deposit has allowed an investigation of their distribution and substitution mechanisms, an examination of the wide range of Ge isotopic fractionations in low-T processes, and provides implications for geochemical signatures of sphalerite ore deposits. The main results of this study are:

(1) The LA-ICP-MS technique is revealed to be a powerful tool to measure *in situ* trace and minor elements occurring as solid solutions in sphalerite. The ^{74}Ge isotope is most relevant for Ge analysis using the LA-ICP-MS, as this isotope shows the lowest isobaric interferences. Principal component analysis (PCA) of LA-ICP-MS dataset revealed an antithetic distribution of element clusters in sphalerite: Cu and trace elements Ge, Sb, Ag, and As are enriched and positively correlated in sector zoning whereas Fe, Cd, In and Sn are enriched in dark brown rhythmic bands. This distribution implies crystallographic controls on the incorporation of trace elements.

(2) Regardless of the zoning type, all spots considered, notable coupled substitutions have been suggested from binary scatter plots: $2Zn^{2+} \leftrightarrow Cu^{+} + Sb^{3+}$ and $3Zn^{2+} \leftrightarrow Ge^{4+} + 2Ag^{+}$. Also, the data suggest the substitution $3Zn^{2+} \leftrightarrow In^{3+} + Sn^{3+} + \square$ although Sn oxidation state needs verification using appropriate methods (e.g., XAS, μ-XANES/EXAFS). Fe and Cd are mainly involved in direct $Zn^{2+} \leftrightarrow (Fe^{2+}, Cd^{2+})$ substitutions. Noticeably, in all spots, Cu content approaches the sum of all available tri- and tetravalent cations. In this way, Cu (occurring as Cu^{+}) could provide charge-balance for the entire broad set of coupled substitution mechanisms responsible for incorporation of the whole range of trace elements in Saint-Salvy sphalerite, especially Ge, Ga and Sb.

(3) Germanium isotopes yield a broad range of $\delta^{74}Ge_{NIST3120a}$ values, from -2.07 ± 0.37 to $+0.91 \pm 0.16‰$ (2σ SD) that highlights large isotopic fractionation during sphalerite deposition in low-T hydrothermal systems. The positive correlation between bulk δ^{74}Ge and bulk Ge content in sphalerite suggests mixing processes between evolving microscale fluid layers at the fluid–crystal interface during sphalerite precipitation (Rayleigh fractionation) and pulsed renewed fluids in open hydrothermal system. We do not dismiss possible upstream variations of isotopic composition, e.g., during metal leaching and transport.

(4) *In situ* SIMS δ^{34}S values spread from $+4.21 \pm 0.29‰$ to $+8.85 \pm 0.13‰$ (1σ SD), averaging $+6.38 \pm 1.00‰$, and are compatible with those of

the enclosing Cambrian series sulphides. Yet, spot $\delta^{34}S$ values do not correlate with minor/trace element contents in zoning patterns, nor with bulk $\delta^{74}Ge$. The processes responsible for isotopic fractionation of sulphur appear to be decoupled from those triggering variations in minor/trace element contents in sphalerite.

(5) Multivariate statistics (PCA) applied on trace element features in sphalerite of Saint-Salvy and other types of sphalerite ores allow the establishment of a comprehensive framework to discriminate among ore genetic types as suggested by previous studies (e.g., In for magmatic-related hydrothermal systems, and Ge for amagmatic and low-*T* deposits).

Finally, the results point out the exceptional features of the Saint-Salvy deposit (France) considering the outstanding compositional zonings of sphalerite crystals, their very high Ge contents compared to other Ge-bearing sphalerite ores, as well as the broad range of Ge isotopic compositions.

ACKNOWLEDGMENTS

The authors thank the Bureau de Recherches Géologiques et Minières (BRGM), especially D. Cassard et C. Lerouge, for supplying of the Saint-Salvy sample material. P. Lach and C. Peiffert are thanked for their precious help on LA-ICP-MS measurements. A. Filia is thanked for his preliminary work on Saint-Salvy. J. Dubessy and J. Mercadier are kindly acknowledged for their insightful discussions and comments. Many thanks to S. Mathieu and O. Rouer (SCMEM) for their involvement in SEM and EMPA analyses, respectively. We are grateful to C. Rollion-Bard, A. Gurenko and E. Thomassot for their help with SIMS measurements. P. Burnard is warmly thanked for his careful English editing of the manuscript. The authors thank N.J. Cook, M.M. Osterloo and L.V. Danyushevsky for their detailed and insightful review of the manuscript, as well as M. Norman and E. Ripley, executive and associate editors, respectively. This work has been supported by the French National Research Agency through the national program "Investissements d'avenir" with the reference ANR-10-LABX-21–LABEX RESSOURCES21, the Observatoire Terre Environnement Lorraine (OTELo) program, and the INSU-CESSUR (CNRS) project. The LA-ICP-MS acquisition has been possible thanks to CNRS-INSU, ICEEL-CARNOT Institute, and the Region Lorraine through the CPER program. This is a CRPG contribution n° 2278.

REFERENCES

Agrosì G., Schingaro E., Pedrazzi G., Scandale E. and Scordari F. (2002) A crystal chemical insight into sector zoning of a titanian andradite ('melanite') crystal. *Eur. J. Mineral.* **14**, 785–794.

Albarède F. (1995) *Introduction to Geochemical Modeling*. Cambridge Univ. Press, New York.

Asael D., Matthews A., Bar-Matthews M., Harlavan Y. and Segal I. (2012) Tracking redox controls and sources of sedimentary mineralization using copper and lead isotopes. *Chem. Geol.* **310–311**, 23–25.

Audi G., Bersillon O., Blachot J. and Wapstra A. H. (2003) The NUBASE evaluation of nuclear and decay properties. *Nucl. Phys. A* **729**, 3–128.

Barbanson L. (1979) Etude des minéralisations du district zincifère de Saint-Salvy. Unpubl. Ph. D. thesis, Université de Toulouse, France, 184 p.

Barbanson L. and Geldron A. (1983) Distribution du germanium, de l'argent et du cadmium entre les schistes et les minéralisations stratiformes et filoniennes à blende-sidérite de la region de Saint-Salvy (Tarn). *Chron. Rech. Min.* **470**, 33–42.

Beaudoin G. (2000) Acicular sphalerite enriched in Ag, Sb, and Cu embedded within colour banded sphalerite from the Kokanee Range, BC. *Can. Mineral.* **38**, 1387–1398.

Bernstein L. R. (1985) Germanium geochemistry and mineralogy. *Geochim. Cosmochim. Acta* **49**, 2409–2422.

Bernstein L. R. (1986) Geology and mineralogy of the APEX germanium–gallium mine, Washington County, Utah. *USGS Bull.* **1577**, 1–9.

Bethke P. M. and Borton, Jr., P. B. (1971) Distribution of some minor elements between coexisting sulphide minerals. *Econ. Geol.* **66**, 140–163.

Blakeman R. J., Ashton J. H., Boyce A. J., Fallick A. E. and Russell M. J. (2002) Timing of interplay between hydrothermal and surface fluids in the Navan Zn+Pb orebody, Ireland: Evidence from metals distribution trends, mineral textures and $\delta^{34}S$ analyses. *Econ. Geol.* **97**, 73–91.

Cadoux A., Blichert-Toft J., Pinti D. L. and Albarède F. (2007) A unique lower mantle source for Southern Italy volcanics. *Earth Planet. Sci. Lett.* **259**, 227–238.

Carignan J., Hild P., Mevelle G., Morel J. and Yeghicheyan D. (2001) Routine analyses of trace elements in geological samples using flow injection and low pressure on-line liquid chromatography coupled to ICP-MS: A study of geochemical reference materials BR, DR-N, UB-N, AN-G and GH. *Geostand. Newlett.* **25**, 187–198.

Cassard D., Chabod J. C., Marcoux E., Bourgine B., Castaing C., Gros Y., Kosakevitch A., Moisy M. and Viallefon L. (1994) Mise en place et origine des minéralisations du gisement filonien à Zn, Ge, Ag, (Pb, Cd) de Noailhac – Saint-Salvy (Tarn, France). *Chron. Rech. Min.* **514**, 3–37.

Cempirek J. and Groat L. A. (2013) Note on the formula of brunogeierite and the first bond-valence parameters for Ge^{2+}. *J. Geosci.* **58**, 71–74.

Cook N. J., Ciobanu C. L., Pring A., Skinner W., Shimizu M., Danyushevsky L., Saini-Eidukat B. and Melcher F. (2009) Trace and minor elements in sphalerite: A LA-ICPMS study. *Geochim. Cosmochim. Acta* **73**, 4761–4791.

Cook N. J., Ciobanu C. L., Brugger J., Etschmann B., Howard D. L., De Jonge M. D., Ryan C. and Paterson D. (2012) Determination of the oxidation state of Cu in substituted Cu-In-Fe-bearing sphalerite via μ-XANES spectroscopy. *Am. Mineral.* **97**, 476–479.

Danyushevsky L. V., Robinson P., Gilbert S., Norman M., Large R., McGoldrick P. and Shelley J. M. G. (2011) Routine quantitative multi-element analysis of sulphide minerals by laser ablation ICP-MS: Standard development and consideration of matrix effects. *Geochem. Explor. Environ. Anal.* **11**, 51–60.

Di Benedetto F., Bernardini G. P., Costagliola P., Plant D. and Vaughan D. J. (2005a) Compositional zoning in sphalerite crystals. *Am. Mineral.* **90**, 1384–1392.

Di Benedetto F., Andreozzi G. B., Bernadini G. P., Borgheresi M., Caneschi A., Cipciani C., Gatteschi D. and Romanelli M. (2005b) Short range order of Fe^{2+} impurities, isolated and in pairs, in ZnS and CdS studies by the Mossbauer effect. *Phys. Chem. Miner.* **32**, 339–348.

Ding T., Valkiers S., Kipphardt H., De Bievre P., Taylor P. D. P., Gonfiantini R. and Krouse R. (2001) Calibrated sulfur isotope abundance ratios of three IAEA sulfur isotope reference

materials and V-CDT with a reassessment of the atomic weight of sulfur. *Geochim. Cosmochim. Acta* **65**, 2433–2437.

Epple M., Panthöfer M., Walther R. and Deiseroth H.-J. (2000) Crystal-chemical characterization of mixed valence indium chalcogenides by X-ray absorption spectroscopy (EXAFS). *Z. Kristallogr.* **215**, 445–453.

Escoube R., Rouxel O., Luais B., Ponzevera E. and Donard O. F. X. (2012) Intercomparison study of germanium isotope composition of geological and reference materials. *Geostand. Geoanal. Res.* **36**, 149–159.

Filia A. (2010) Le fractionnement isotopique du germanium comme traceur des conditions physicochimiques de formation des minéralisations de ZnS. Unpubl. M. Sc. thesis, Université Henri Poincaré, Nancy, France, 38 p.

Fowler A. D. and L'Heureux I. (1996) Self-organized banded sphalerite and branching galena in the Pine Point ore deposit, Northwest Territories. *Can. Mineral.* **34**, 1211–1222.

Gagnevin D., Boyce A. J., Barrie C. D., Menuge J. F. and Blakeman R. J. (2012) Zn, Fe and S isotope fractionation in a large hydrothermal system. *Geochim. Cosmochim. Acta* **88**, 183–198.

Goh S. W., Buckley A. N. and Lamb R. N. (2006) Copper (II) sulphide? *Miner. Eng.* **19**, 204–208.

Halfon J. and Rosique A. (1973) Comparaison des elements "en traces" dans les blendes du filon et les blendes du stratiforme de Saint-Salvy (81). *Bull. BRGM* **5**, 403–432 (2), sect. II.

Hirata T. (1997) Isotopic variations of germanium in iron and stony meteorites. *Geochim. Cosmochim. Acta* **61**, 4439–4448.

Höll R., Kling M. and Schroll E. (2007) Metallogenesis of germanium – a review. *Ore Geol. Rev.* **30**, 145–180.

Holten T., Jamtveit B., Meakin P., Cortini M., Blundy J. and Austrheim H. (1997) Statistical characteristics and origin of oscillatory zoning in crystals. *Am. Mineral.* **82**, 596–606.

Iwamori H., Albaréde F. and Nakamura H. (2010) Global structure of mantle isotopic heterogeneity and its implications for mantle differentiation and convection. *Earth Planet. Sci. Lett.* **299**, 339–351.

Johan Z. (1988) Indium and germanium in the structure of sphalerite: an example of coupled substitution with copper. *Mineral. Petrol.* **39**, 211–229.

Johnson C. M., Beard B. L. and Albarède F. (2004) Geochemistry of non-traditional stable isotopes: overview and general concepts. *Rev. Mineral. Geochem.* **55**, 1–24.

Koch I. (2012) *Analysis of multivariate and high-dimensional data theory and practice*. Cambridge University Press, Cambridge.

Lach P., Mercadier J., Dubessy J., Boiron M.-C. and Cuney M. (2013) *In situ* quantitative measurement of rare earth elements in uranium oxides by laser ablation-inductively coupled plasma-mass spectrometry. *Geostand. Geoanal. Res.* **2013**, 1–20.

Lafferière F., Royer J. J. and Mallet J. L. (2000) Multivariate Tools in gOcad. 20th Gocad Meeting, 1–14.

Leach D., Macquar J.-C., Lagneau V., Leventhal J., Emsbo P. and Premo W. (2006) Precipitation of lead-zinc ores in the Mississippi Valley-type deposit at Trèves, Cévennes region of Southern, France. *Geofluids* **6**, 24–44.

Le Maitre R. W. (1982) *Numerical Petrology: Statistical Interpretation of Geochemical Data*. Elsevier, Amsterdam.

Leisen M. (2011) Analyse chimique des inclusions fluides par ablation-laser couplée à l'ICP-MS et applications géochimiques. Unpubl. Ph. D. thesis, Nancy Université, 308 p.

Leisen M., Dubessy J., Boiron M.-C. and Lach P. (2012) Improvement of the determination of element concentrations in quartz-hosted fluid inclusions by LA-ICP-MS and Pitzer thermodynamic modeling of ice melting temperature. *Geochim. Cosmochim. Acta* **90**, 110–125.

Li X. F., Zhao H., Tang M. and Liu Y. (2009) Theoretical prediction for several important equilibrium Ge isotope fractionation factors and geological implications. *Earth Planet. Sci. Lett.* **287**, 1–11.

Longerich H. P., Jackson S. E. and Gunther D. (1996) Laser ablation inductively coupled plasma mass spectrometric transient signal data acquisition and analyte concentration calculation. *J. Anal. Atom. Spectrom.* **11**, 899–904.

Luais B., Framboisier X., Carignan J. and Ludden J. N. (2000) Analytical development of Ge isotopic analyses using multi-collection plasma source mass spectrometry: isoprobe MC-Hex-ICP-MS (Micromass). *Geoanalysis* **2000**, 45–46.

Luais B. (2003) Germanium isotopic systematics in meteorites. *Meteorit. Planet. Sci.* **38**, A31.

Luais B. (2007) Isotopic fractionation of germanium in iron meteorites: significance for nebular condensation, core formation and impact processes. *Earth Planet. Sci. Lett.* **262**, 21–36, Erratum: Earth Planet. Sci. Lett. 273, 400 (2008).

Luais B. (2012) Germanium chemistry and MC-ICPMS isotopic measurements of Fe-Ni, Zn alloys and silicate matrices: insights into deep Earth processes. *Chem. Geol.* **334**, 295–311.

Machlan L. A., Gramlich J. W., Powell L. J. and Lambert G. M. (1986) Absolute isotope abundance ratio and atomic weight of a reference sample of Gallium. *J. Res. Natl. Bur. Stand.* **91**, 323–331.

Moh G. H. and Jäger A. (1978) Phasengleichgewichte des systems Ge–Pb–Zn–S in relation zu germanium-gehalten alpiner Pb–Zn-Lagerstätten. *Verh. Geol. Bunde. Wien* **1978**, 437–440.

Moisy M. (1993) Évolution de la perméabilité et de la circulation des fluides hydrothermaux dans un zone de cisaillement fragile. *Doc. BRGM* **225**, 214.

Möller P. and Dulski P. (1993). Germanium and gallium distribution in sphalerite. In *Formation of Hydrothermal Vein Deposits – Case Study of the Pb-Zn, Barite and Fluorite Deposits of the Harz Mountains* (eds. P. Möller and V. Lüders). Monograph Series on Mineral Deposits, 30, Bornträger, Berlin-Stuttgart. pp. 189–196.

Möller P. and Dulski P. (1996) Germanium and gallium distribution in sphalerite: a key to the genesis of sediment-hosted sulphide mineralizations. *Z. Geol. Wiss.* **24**(3/4), 527–538.

Munoz M., Boyce A. J., Courjault-Rade P., Fallick A. E. and Tollon F. (1994) Multi-fluid incursion in the Paleozoic basement-hosted Saint-Salvy ore deposit (NW Montagne Noire, southern France). *Appl. Geochem.* **9**, 609–626.

Murakami H. and Ishihara S. (2013) Trace elements of Indium-bearing sphalerite from tin-polymetallic deposits in Bolivia, China and Japan: a femto-second LA-ICPMS study. *Ore Geol. Rev.* **53**, 223–243.

Oen I. S., Kager P. and Kieft C. (1980) Oscillatory zoning of a discontinuous solid–solution series: sphalerite–stannite. *Am. Mineral.* **65**, 1220–1232.

Ohmoto H. and Rye R. O. (1979) Isotopes of sulfur and carbon. In *Geochemistry of Hydrothermal Ore Deposits* (ed. H. L. Barnes), 2nd ed. Wiley, New York, pp. 509–567.

Oftedahl I. (1940) Untersuchungen über die Nebenbestandteile von Erzmineralien norwegischer zinkblendführender Vorkommen. *Skrift. Norsk Vidensk. Akad. Oslo, Math. Naturv. Kl.* **8**, 1–103.

Pattrick R. A. D., Dorling M. and Polya D. A. (1993) TEM study of indium- and copper-bearing growth-banded sphalerite. *Can. Mineral.* **31**, 105–117.

Pattrick R. A. D., Mosselmans F. W. and Charnock J. M. (1998) An X-ray absorption study of doped sphalerites. *Eur. J. Miner.* **10**, 239–249.

Pokrovski G. S. and Schott J. (1998) Thermodynamic properties of aqueous Ge(IV) hydroxide complexes from 25 to 350 °C: implications for the behaviour of germanium and the Ge/Si

ratio in hydrothermal fluids. *Geochim. Cosmochim. Acta* **62**, 1631–1642.

Pfaff K., Koenig A., Ridley I., Wenzel T., Adams D., Hildebrandt L. H., Leach D. L. and Markl G. (2011) Trace and minor element variations and sulfur isotopes in crystalline and colloform ZnS: incorporation mechanisms and implications for their genesis. *Chem. Geol.* **286**, 118–134.

Rollion-Bard C. and Marin-Carbonne J. (2011) Determination of SIMS matrix effects on oxygen isotopic compositions in carbonates. *J. Anal. Atom. Spectrom.* **26**, 1285–1289.

Rosenberg E. (2009) Germanium: occurrence, importance and speciation. *Rev. Environ. Sci. Biotechnol.* **8**, 29–57.

Rouxel O., Galy A. and Elderfield H. (2006) Germanium isotopic variations in igneous rocks and marine sediments. *Geochim. Cosmochim. Acta* **70**, 3387–3400.

Samama J. C., Royer J. J. and N'Ganzi C. (1989) Prise en compte de la surface spécifique des prélèvements en prospection géochimique: exemple de l'uranium dans les sediments de ruisseau. *J. Geochem. Explor.* **32**, 453–466.

Siebert C., Ross A. and McManus J. (2006) Germanium isotope measurements of high-temperature geothermal fluids using double-spike hydride generation MC-ICP-MS. *Geochim. Cosmochim. Acta* **70**, 3986–3995, Erratum: Geochim. Cosmochim. Acta 75, 6267–6269 (2011)..

Siebert C., Ross A. and McManus J. (2011) Erratum to "Germanium isotope measurements of high-temperature geothermal fluids using double-spike hydride generation MC-ICP-MS. Geochim. Cosmochim. Acta 70, 3986–3995". *Geochim. Cosmochim. Acta* **75**, 6267–6269.

Taylor S. R. and McLennan S. M. (1985) *The Continental Crust: Its Composition and Evolution*. Blackwell, Oxford, 312.

Thomassot E., Cartigny P., Harris J. W., Lorand J. P., Rollion-Bard C. and Chaussidon M. (2009) Metasomatic diamond growth: a multi-isotope study (^{13}C, ^{15}N, ^{33}S, ^{34}S) of sulphide inclusions and their host diamonds from Jwaneng (Botswana). *Earth Planet. Sci. Lett.* **282**(1–4), 79–90.

Vesselinov I. and Kerestedjian T. (1995) Kinetic aspects of sector zoning in arsenopyrite – a case study. *Miner. Petrol.* **52**, 85–106.

Watson E. B. and Liang Y. (1995) A simple model for sector zoning in slowly grown crystals implications for growth rate and lattice diffusion, with emphasis on accessory minerals in crustal rocks. *Am. Mineral.* **80**, 1179–1187.

Wilkinson J., Weiss D., Mason T. and Coles B. (2005) Zinc isotope variation in hydrothermal systems: preliminary evidence from the Irish Midlands ore field. *Econ. Geol.* **100**, 583–590.

Wilson S. A., Ridley W. I. and Koenig A. E. (2002) Development of sulfide calibration standards for the laser ablation inductively-coupled plasma mass spectrometry technique. *J. Anal. Atom. Spectrom.* **17**, 406–409.

Winderbaum L., Ciobanu C. L., Cook N. J., Paul M., Metcalfe A. and Gilbert S. (2012) Multivariate analysis of an LA-ICP-MS trace element dataset for pyrite. *Math. Geosci.* **44**(7), 823–842.

Wood S. A. and Samson I. M. (2006) The aqueous geochemistry of gallium, germanium, indium and scandium. *Ore Geol. Rev.* **28**, 57–102.

Wright K. V. and Gale J. D. (2010) A first principles study of the distribution of iron in sphalerite. *Geochim. Cosmochim. Acta* **74**, 3514–3520.

Xue S., Yang Y., Hall G. and Herzog G. (1997) Germanium isotopic compositions in Canyon Diablo spheroids. *Geochim. Cosmochim. Acta* **61**, 651–655.

Ye L., Cook N. J., Ciobanu C. L., Liu Y. P., Zhang Q., Liu T. G., Gao W., Yang Y. L. and Danyushevskiy L. (2011) Trace and minor elements in sphalerite from base metal deposits in South China: a LA-ICPMS study. *Ore Geol. Rev.* **39**, 188–217.

Young E. D., Galy A. and Nagahara H. (2002) Kinetic and equilibrium mass-dependent isotope fractionation laws in nature and their geochemical and cosmochemical significance. *Geochim. Cosmochim. Acta* **66**, 1095–1104.

Zhang Q. L., (Chang T. L.) and Ding T. (1989) Analysis of the reference material NBS-123 and the atomic weight of sulphur. *Chin. Sci. Bull.* **34**, 1086–1089.

Associate editor: Edward M. Ripley

5.3 Trace elements in copper-sulphides from Barrigão and Kipushi

The Cu-rich ores of Kipushi and Barrigão show distinct ore assemblages: Kipushi mostly is composed of a Cu-rich paragenesis (chalcopyrite, bornite), associated with a Zn–(Cu)–Ge-rich paragenesis (sphalerite, renierite), whereas the Barrigão ore is chiefly composed of chalcopyrite and the tennantite–tetrahedrite series, with minor sphalerite and pyrite. Gangue minerals consist of quartz and/or carbonates. These very contrasted ore paragenesis should carry valuable information on the Ge distribution and partitioning in Cu-rich ores with distinct formation conditions.

5.3.1 Chalcopyrite and tennantite–tetrahedrite series from Barrigão

Trace element distribution

In chalcopyrite, backscattered electron observations and element maps using SEM indicate the presence of Ge–Sn-rich zoning patterns associated with notable Fe depletion and Cu enrichment, which is illustrated in Fig. 5.1. Inside the Ge–Sn-rich zoning pattern there is marked 'core', richer in Sn, Cu, and depleted in Fe, whereas Ge content seems unchanged, suggesting that Sn and Ge likely behave independently. The regular boundaries of this enrichment zone evoke twinning patterns and possible crystal controls on element uptake. Given the relatively high atomic number of Sn, only the Sn-rich 'core' is visible in backscattered electron mode and not the wider, Ge-rich part of the zoning pattern.

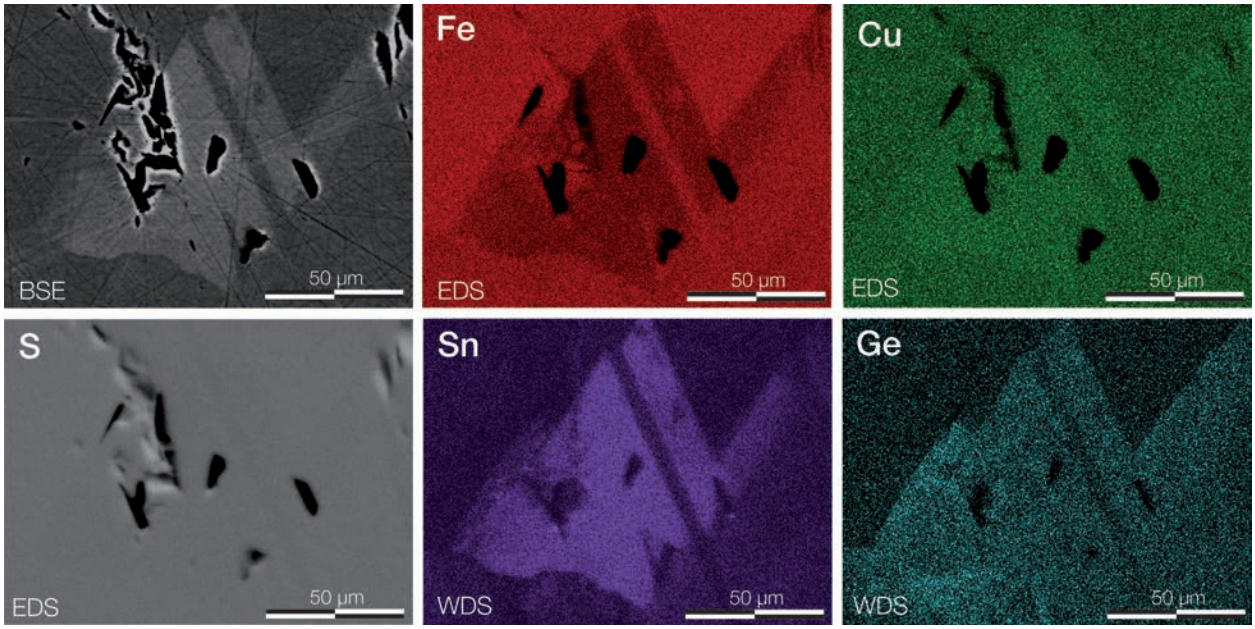

Fig. 5.1 – Secondary electron microscope observation (BSE mode) of a zoned-chalcopyrite in sample 2BARR5. Maps of Ge and Sn in wavelength dispersive X-ray spectroscopy (WDS), and maps of Fe and Cu in energy-dispersive X-ray spectroscopy (EDS).

Large scale element maps using EPMA (Fig. 5.2) outline the same element distribution as in SEM and bring out two layers of informations: (i) wide-scale Ge–Sn-rich zoning occurs in chalcopyrite, associated with marked Fe depletion (and Cu enrichment with minor respects), suggesting they substitute for Fe, and (ii) within Ge–Sn-rich zones, Sn and Ge are somewhat antithetically distributed, which suggests they could be in competition relatively to the Fe sute. Variations in Cu are semi-quantitatively minor relatively to Fe in the Ge–Sn enrichment patterns.

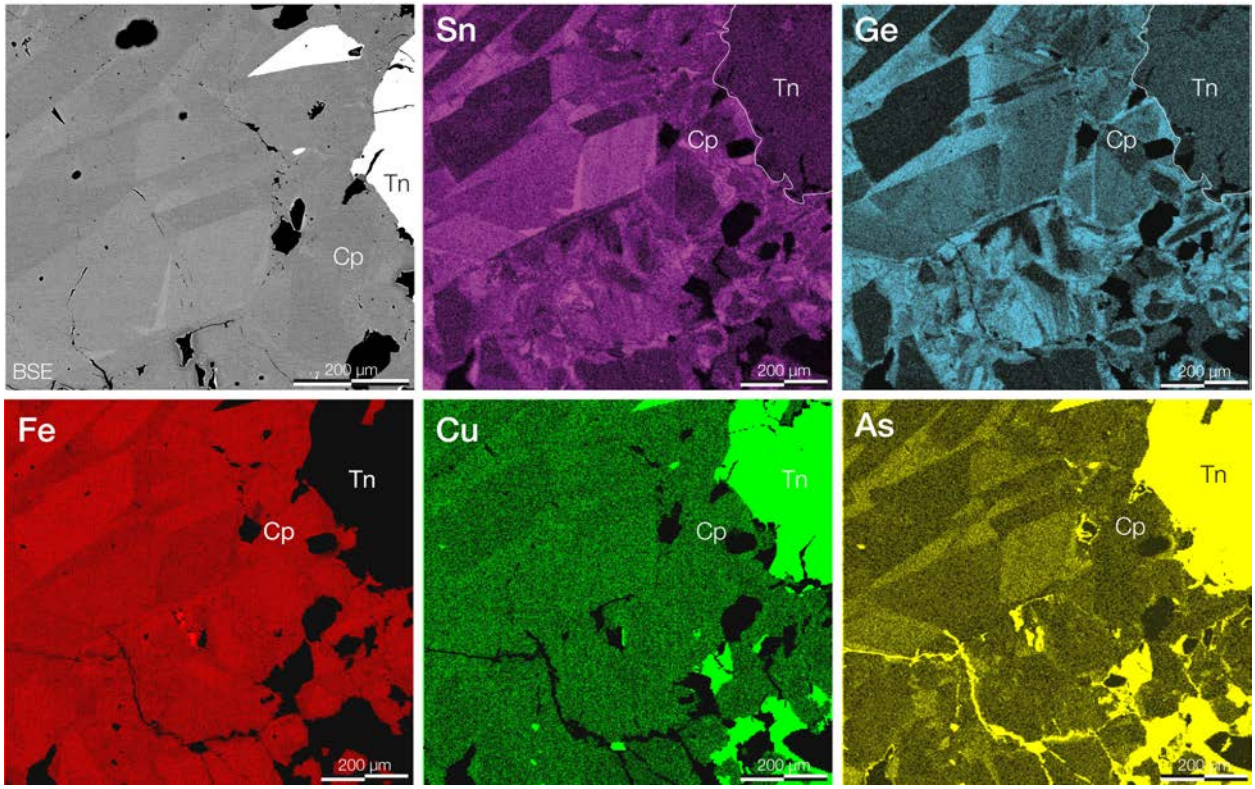

Fig. 5.2 – Secondary electron microscope observation (BSE mode) of a zoned-chalcopyrite in sample BARR8 (top-left corner) and electron-probe microanalyser maps of Sn, Ge, Fe, Cu and As.

In contrast, in fahlore (tennantite–tetrahedrite series), the observed large scale compositional zonings are primarily related to relative variations of As and Sb, i.e., displacement along the tennantite–tetrahedrite joint ($Cu_6[Cu_4(Fe,Zn)_2]As_4S_{13} \leftrightarrow Cu_6[Cu_4(Fe,Zn)_2]Sb_4S_{13}$). They generally occur as band- or twin-like patterns of up to hundreds μm^2 as outlined in Fig. 5.3.

Ge and related minor/trace element contents

Major and minor element analysis using EPMA are presented in Table 5.1. Ge and Sn reach minor concentrations in chalcopyrite, averaging 0.25 and 0.24 wt.%, respectively. In fahlore however, Ge and Sn rather occur as trace compounds, with only 0.09 wt.% and 0.03 wt.% mean contents, respectively. Copper being more homogeneous than Fe in chalcopyrite, with 34.6 ± 0.3 wt.% and 28.9 ± 0.6 wt.% (1σ SD), make it a better internal standard for calibrating in LA-ICP-MS analysis in chalcopyrite. Copper and Fe are both less homogeneous

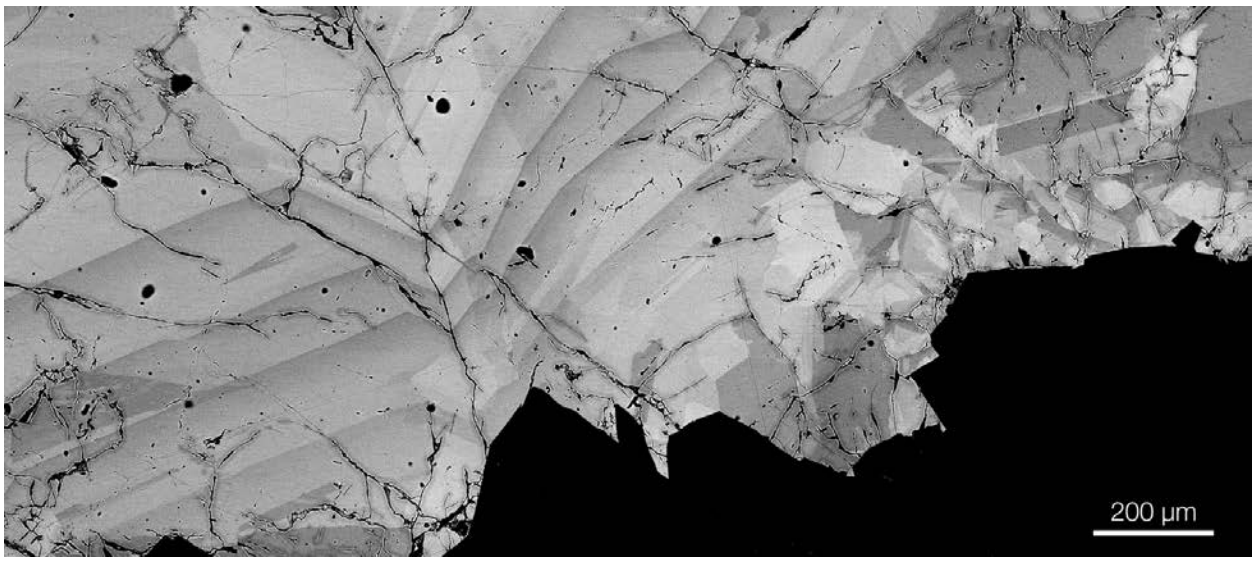

Fig. 5.3 – Secondary electron microscopic observation of compositional zoning in the tennantite–tetrahedrite series (grey scale) in equilibrium with chalcopyrite (black).

in tennantite, with 42.6±0.9 and 6.6±0.8 wt.%, respectively. Despite Cu have slightly higher standard deviation, Cu has been chosen as internal standard for calibrating LA-ICP-MS analyses in tennantite in order to better compare with chalcopyrite.

Table 5.1 – Results of EPMA analysis of the Barrigão ore assemblage (in wt.%).

	S	Fe	Cu	As	Sb	Co	Ge	Ag	In	Sn	Hg	Pb
Chalcopyrite (n=53)												
Min	33.95	26.99	33.87	<LOD	<LOD	<LOD	0.12	<LOD	<LOD	0.00	<LOD	0.03
Max	35.48	29.83	35.37	0.69	0.13	0.02	0.71	0.05	<LOD	1.72	0.04	0.15
Mean	34.90	28.90	34.55	0.19	0.02	0.01	0.25	0.01	–	0.24	–	0.09
SD	0.35	0.59	0.32	0.19	0.03	0.01	0.15	0.01	–	0.33	–	0.03
Tennantite–tetrahedrite (n=55)												
Min	26.19	3.57	39.47	3.86	0.90	<LOD	0.02	0.00	<LOD	0.00	<LOD	<LOD
Max	29.22	7.61	44.61	20.15	25.10	0.01	0.13	0.12	<LOD	0.14	<LOD	0.10
Mean	27.98	6.58	42.55	15.29	7.63	–	0.09	0.03	–	0.03	–	0.05
SD	0.69	0.80	0.93	3.44	5.08	–	0.02	0.03	–	0.03	–	0.03

Minor and trace element analysis by LA-ICP-MS are summarized in Table 5.2 for chalcopyrite and fahlore. The dataset consists of 60 spot analyses in chalcopyrite and 19 spot analyses in fahlore, all performed on 150 μm-thick polished sections. Ablation profiles were generally smooth, suggesting a homogeneous distribution of the elements in solid solution. Histograms of the element contents in each mineral are shown in Fig. 5.4. Minor/trace elements generally vary over several orders of magnitude. Remarkable concentrations of Ge and Sn occur in chalcopyrite, ranging 2–5750 and 1–6720 ppm, and averaging 1040 and 1760 ppm, respectively. Ag is by far the richest trace compound in fahlore, ranging 150–1875 ppm and averaging 750 ppm. Ge, however, is always present but markedly depleted compared to chalcopyrite, spanning from 1.1 to 91 ppm, for a mean of 22 ppm.

Table 5.2 – Results of LA-ICP-MS analysis of the Barrigão ore assemblage (in ppm).

	Mn	Fe	Co	Zn	Ga	Ge	As	Se	Ag	Cd	In	Sn	Sb	Pb
Chalcopyrite (n=58)														
Min	< LOD	55240	< LOD	0.3	0.1	1.7	43	< LOD	0.3	< LOD	1.0	1.1	5.0	< LOD
Max	6.0	308800	6.9	60	115	5750	10860	192	48	0.7	30	6720	439	79
Mean	0.7	297438	0.4	13	28	1079	1234	19	6	0.2	5.2	1761	119	9.3
SD	1.2	5326	1.3	13	27	1527	1887	41	7.1	0.2	5.3	1416	104	17
LOD*	0.08	11.34	0.03	0.25	0.04	0.04	0.46	1.63	0.04	0.45	0.01	0.07	0.08	0.12
Tennantite–tetrahedrite (n=19)														
Min	0.1	60210	16.8	228	2.6	1.1	265700	< LOD	151	2.9	2.0	0.3	52690	0.2
Max	8.3	73600	52	22020	115	91	416900	5.7	1875	195	19	30	245300	238
Mean	1.7	69757	32	3967	22	15	339789	1.3	753	68	5.1	5.2	156935	29
SD	2.1	3091	10	5528	28	22	54660	1.4	497	60	3.9	7.9	59158	59
LOD*	0.08	8.78	0.02	0.22	0.04	0.04	0.36	1.46	0.03	0.39	0.01	0.07	0.08	0.11

* Mean limit of detection (LOD)

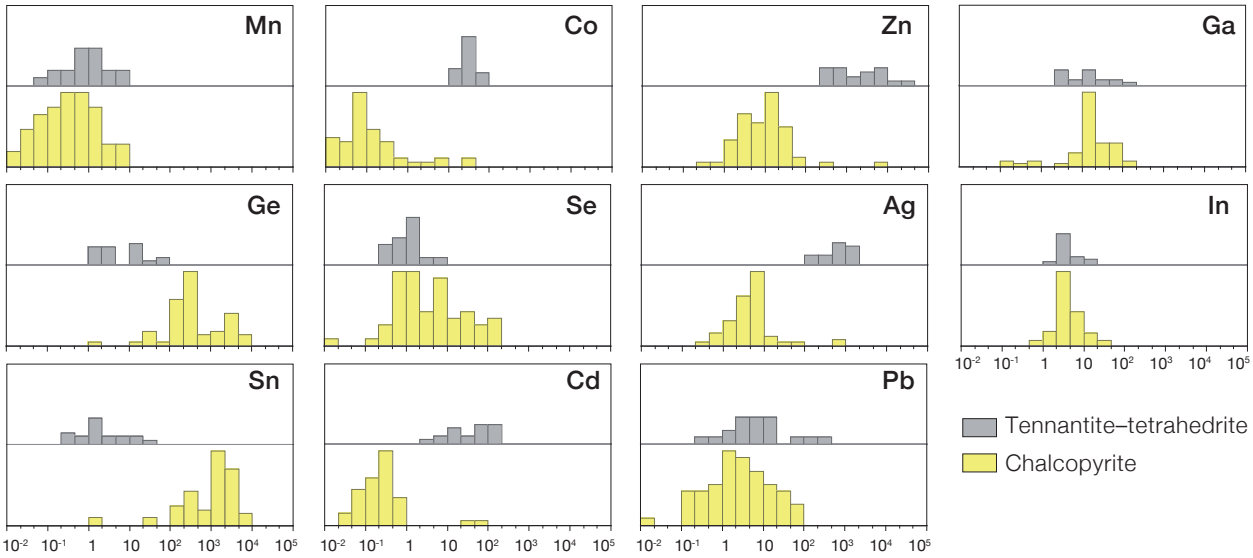

Fig. 5.4 – Histograms of trace element content in the Barrigão deposit (in ppm)

Element correlation and incorporation mechanisms

Chalcopyrite

Principal component analysis LA-ICP-MS data in chalcopyrite (n=58 spot analyses) is shown in Fig. 5.6a. Elements and spot analysis are plotted in the PC1 vs. PC2 plane, accounting for 63% of element content variability. Along the first component, which explains almost half of the total content variability (46%), a distinct anti-correlation is shown between Fe and the cluster composed of Sn, Ge and cations rarely exceeding 100 ppm (Fig. 5.4) such as Ga, As, Ag and Sb, underlying the substitution in the site of Fe by this cluster of elements. PC1 best explains the observation (i) on elements maps (section 5.3.1). Remarkably, In is uncorrelated to Fe and the main impurities Sn and Ge. The second component (17% of explained variability) basically split the cluster into a range from Sb down to Ge–Ga. Notably, Sn and Ge are separated by PC2, this component well explains the observation (ii) on element maps (section 5.3.1) of slight 'antithetic' distribution of Sn and Ge in zoning patterns. These results are qualitatively in agreement with binary correlations presented in Reiser et al. (2011).

The anticorrelation between Fe and Sn, Ge, and related trace elements as shown using binary plot (Fig. 5.5) and in PCA (Fig. 5.6a), which suggest they substitute in Fe sites (Fig. 5.5). Iron occurs as high-spin tetrahedral Fe^{3+} in chalcopyrite (e.g., Goh et al., 2006; Petiau et al., 1988). Direct substitutions $Fe^{3+} \leftrightarrow M^{3+}$ occur for elements usually trivalent such as Ga, As, In and Sb. Sn and Ge have chemical similarities and both can occur in divalent or tetravalent state. In sulphide minerals, Sn and Ge usually occur in tetravalent state in tetrahedral coordination with S, such as in stannite Cu_2FeSnS_4 and briartite $Cu_2(Fe,Zn)GeS_4$ that have chalcopyrite-like structures (Bernstein, 1985). Coupled substitution such as $3Fe^{3+} \leftrightarrow 2(Sn,Ge)^{4+}+Cu^{+}$ can reasonably account for Fe-depletion and slight Cu enrichment observed in Sn–Ge zones in Fig. 5.1 and Fig. 5.2, and the correlation of Ag with Sn and, to a lesser extent, Ge in the PCA (Fig. 5.6). Coupled mechanisms such as $2Fe^{3+} \leftrightarrow (Sn, Ge)^{4+} + (Pb, Zn)^{2+}$ may explain the observed microscale 'antithetic' distribution of Sn and Ge, and competition between these elements within Sn–Ge-rich patterns. In

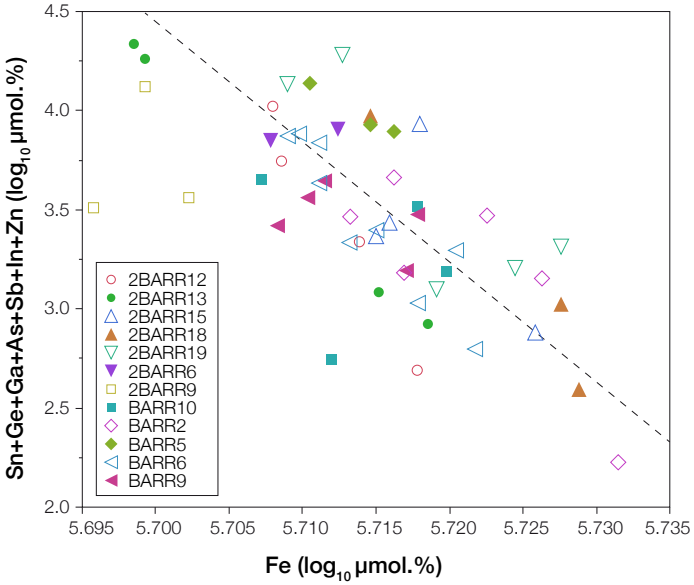

Fig. 5.5 – Fe *vs* Sn+Ge+Ga+As+Ag+Sb+In+Sn (log-transformed LA-ICP-MS data in μmol.%) in chalcopyrite from Barrigão. There is a clear anti-correlation between Fe and the total amount of incorporated cations, indicating substitutions in the Fe site.

the same way, coupled substitutions may also involve the creation of vacancies (□) through substitutions like $4Fe^{3+} \leftrightarrow 3(Sn, Ge)^{4+} + \square$.

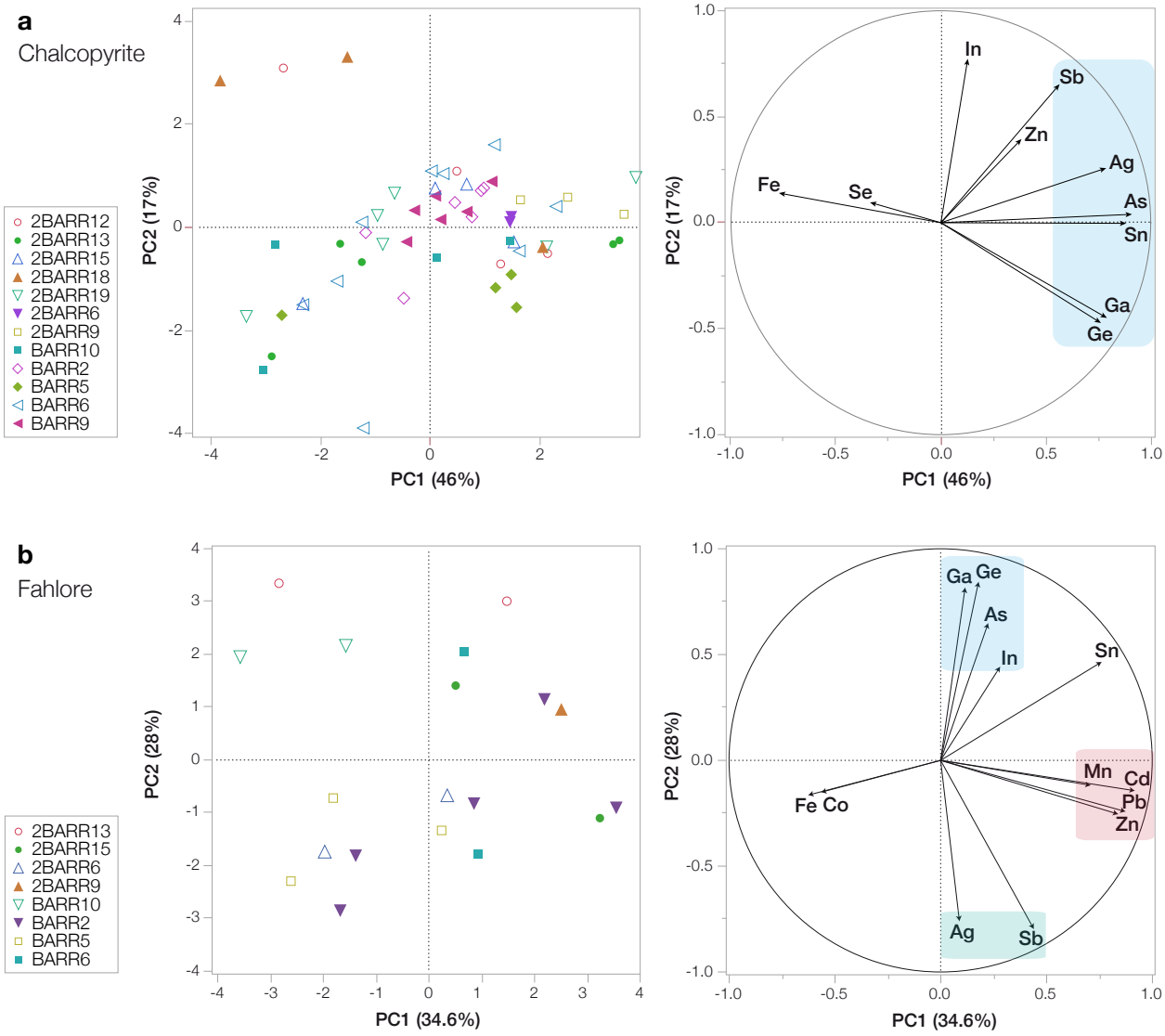

Fig. 5.6 – Principal component analysis of log-transformed LA-ICP-MS data in chalcopyrite (**a**) and fahlore (**b**) from Barrigão, Portugal. Spot analysis (i.e., individuals, left hand frame) and elements (i.e., variables) are plotted on the PC1 vs. PC2 plane (the most meaningful, explaining 63% and 62.6% of the total content variability, respectively). **a**. The blue box mark the correlation cluster (Ge, Ga, Sn, As, Ag, Sb), which is strongly anticorrelated with Fe along PC1, which carries most of the information (46%). PC2 is less significant (17%) but divides the blue large cluster into three clusters, (Ge, Ga), (Ag, As, Sn) and (Sb, Zn). **b**. The element cluster (As, Ge, Ga, In; blue box) is anticorrelated with elements (Sb, Ag; green box) along PC2. The cluster of divalent elements (Mn, Cd, Pb, Zn; red box) is anticorrelated with Fe and Co along PC1. See text for explanations.

Tennantite–tetrahedrite series

Principal component analysis of LA-ICP-MS data for the tennantite–tetrahedrite series (n=19 spot analyses) is shown in Fig. 5.6b. Elements and spot analysis are plotted in the PC1 vs. PC2 plane, accounting for 62.6% of element content variability. PC1 and PC2 almost equally explain the total content variability (34.6 and 28%, respectively). The first component (PC1) is loaded by Fe and Co, which are anti-correlated to Cd, Pb, Zn and Mn, all usually divalent, suggesting direct substitution of tetrahedrally coordinated Fe^{2+} (Charnock et al., 1989). The position of Co can reflect a competition with Cd, Pb, Zn and Mn in its incorporation in the Fe site. The second component (PC2) show that As, clustered with Ge, Ga, In (and Sn), is anticorrelated to Sb and Ag. Thus, Ge, Ga, In (and Sn) are most likely enriched towards the tennantite end-member, whereas Ag is most likely enriched towards the tetrahedrite end-member. In addition, Ge and Fe form an angle of 90° in PC1 *vs* PC2, indicating their content variations are independent, so, in contrast with chalcopyrite, Ge may substitute in the As site rather than in the Fe site. The size of Ge in tetrahedral coordination (1.20 Å in covalent bond) is closer to that of As (1.19 Å) than that of Sb (139 Å), which may explain the preferential Ge enrichment towards the tennantite end-member (covalent bond lengths from Cordero et al., 2008).

5.3.2 Sphalerite and copper-sulphides from Kipushi

Elements content and distribution

Electron-probe microanalyses of major and minor elements in the Kipushi ore minerals are presented in Table 5.3, including the compositions of the main sulphide paragenesis, bornite, chalcopyrite, galena, pyrite, sphalerite and tennantite, the Ge-sulphides, briartite, renierite (dominant species) and germanite, and accessory or rare sulphides, argentotennantite, arsenopyrite, barytine, betekhtinite, carrolite, chalcocite, covellite, digenite, ovamboite, tetrahedrite and tungstenite. The means and standard deviations of Cu was used for internal calibration in LA-ICP-MS analyses of bornite, chalcopyrite and tennantite, those of Fe was utilised for pyrite, and those of Zn was used for sphalerite.

Minor and trace element LA-ICP-MS analyses of sphalerite and Cu-sulphides from Kipushi are summarized in Table 5.4. The dataset includes 22 analyses in bornite, 53 in chalcopyrite, 21 in pyrite, 186 in sphalerite and 6 in tennantite. The frequency distribution of element contents for each mineral are shown in Fig. 5.7. As shown in the latter, all trace elements show a log-normal distribution, except for Cd (and Fe – not presented) in sphalerite and As in tennantite that show a normal distribution, because they are minor and major components, respectively.

Pyrite, which of the studied sulphides is the first to have precipitated (see Fig. 4.12 in Sec. 4.3.2 for the paragenetic sequence), shows the highest Co contents with up to 1220 ppm and an average of 134 ppm. Pyrite is also rather rich in Cu and Pb, for which the concentrations reach up to 3480 ppm and 17200 ppm, and average 720 and 841 ppm, respectively. Pyrite also host significant As concentrations, having up to 3.3 wt.% and a mean concentration of 6090 ppm. A notable Ge content of 148 ppm was measured, otherwise, its concentration barely reaches the ppm level.

Table 5.3 – Results of EPMA analysis of the Kipushi ore assemblage (concentrations in wt.%).

	S	V	Fe	Co	Ni	Cu	Zn	Ga	Ge	As	Se	Ag	Cd	Sn	Sb	W	Pb
Argento-tennantite (n=1)																	
Mean	14.37	–	0.29	–	–	43.53	–	–	0.17	–	–	48.71	0.44	–	–	–	–
SD	–	–	–	–	–	–	–	–	–	–	–	–	–	–	–	–	–
Min	14.37	–	0.29	–	–	43.53	–	–	0.17	–	–	48.71	0.44	–	–	–	–
Max	14.37	–	0.29	–	–	43.53	–	–	0.17	–	–	48.71	0.44	–	–	–	–
Arsenopyrite (n=2)																	
Mean	21.33	–	35.29	–	–	–	0.13	–	0.16	42.78	–	–	–	–	–	–	–
SD	0.19	–	0.47	–	–	–	0.18	–	0.01	1.26	–	–	–	–	–	–	–
Min	21.19	–	34.95	–	–	–	–	–	0.15	41.89	–	–	–	–	–	–	–
Max	21.46	–	35.62	–	–	–	0.25	–	0.17	43.67	–	–	–	–	–	–	–
Betekhtinite (n=7)																	
Mean	20.84	–	3.03	–	–	57.64	–	–	0.02	–	–	0.96	–	–	–	–	20.16
SD	0.27	–	1.81	–	–	7.86	–	–	0.06	–	–	0.21	–	–	–	–	7.90
Min	20.49	–	2.26	–	–	39.82	–	–	–	–	–	0.66	–	–	–	–	16.74
Max	21.31	–	7.13	–	–	60.90	–	–	0.17	–	–	1.32	–	–	–	–	38.06
Bornite (n=30)																	
Mean	26.02	–	10.80	–	–	62.22	0.06	–	0.03	0.05	–	1.11	–	–	–	–	–
SD	0.42	–	0.25	–	–	2.19	0.19	–	0.05	0.25	–	0.85	–	–	–	–	–
Min	25.30	–	10.01	–	–	57.37	–	–	–	–	–	–	–	–	–	–	–
Max	26.83	–	11.27	–	–	66.59	0.97	–	0.18	1.25	–	3.68	–	–	–	–	–
Briartite (n=1)																	
Mean	36.10	0.06	10.82	–	–	33.96	3.33	–	16.63	–	–	–	0.59	0.43	–	–	–
SD	–	–	–	–	–	–	–	–	–	–	–	–	–	–	–	–	–
Min	36.10	0.06	10.82	–	–	33.96	3.33	–	16.63	–	–	–	0.59	0.43	–	–	–
Max	36.10	0.06	10.82	–	–	33.96	3.33	–	16.63	–	–	–	0.59	0.43	–	–	–
Carrollite (n=2)																	
Mean	41.52	–	0.29	38.16	1.28	19.41	–	–	–	–	–	–	–	0.04	–	–	–
SD	0.01	–	0.25	0.38	0.25	0.13	–	–	–	–	–	–	–	0.06	–	–	–
Min	41.51	–	0.11	37.89	1.10	19.31	–	–	–	–	–	–	–	–	–	–	–
Max	41.53	–	0.47	38.43	1.45	19.50	–	–	–	–	–	–	–	0.08	–	–	–
Chalcopyrite (n=15)																	
Mean	34.65	–	29.38	–	–	34.56	0.15	–	0.03	–	–	–	–	0.01	–	–	0.04
SD	0.70	–	0.31	–	–	0.45	0.23	–	0.07	–	–	–	–	0.02	–	–	0.07
Min	32.69	–	28.51	–	–	33.53	–	–	–	–	–	–	–	–	–	–	–
Max	35.42	–	29.72	–	–	35.34	0.64	–	0.17	–	–	–	–	0.08	–	–	0.17
Chalcocite (n=2)																	
Mean	20.64	–	–	–	–	78.94	–	–	–	–	–	–	–	–	–	–	–
SD	0.53	–	–	–	–	1.59	–	–	–	–	–	–	–	–	–	–	–
Min	20.26	–	–	–	–	77.81	–	–	–	–	–	–	–	–	–	–	–
Max	21.01	–	–	–	–	80.06	–	–	–	–	–	–	–	–	–	–	–
Chalcopyrite (n=29)																	
Mean	34.82	–	28.07	1.24	0.09	33.99	0.25	0.15	0.03	0.16	–	0.36	–	0.01	–	–	0.02
SD	1.37	–	5.14	6.55	0.50	2.81	0.36	0.57	0.06	0.82	–	1.22	–	0.02	–	–	0.06
Min	31.72	–	1.78	0.00	0.00	20.03	0.00	0.00	0.00	0.00	–	0.00	–	0.00	–	–	0.00
Max	40.60	–	29.95	34.68	2.64	36.22	1.37	2.59	0.17	4.36	–	5.05	–	0.08	–	–	0.17
Covellite (n=4)																	
Mean	28.37	–	3.36	–	–	67.33	0.20	–	0.15	–	–	–	–	–	–	–	0.04
SD	0.71	–	5.51	–	–	9.09	0.24	–	0.18	–	–	–	–	–	–	–	0.08
Min	27.47	–	0.32	–	–	53.72	–	–	–	–	–	–	–	–	–	–	–
Max	29.05	–	11.60	–	–	72.46	0.48	–	0.35	–	–	–	–	–	–	–	0.16

Table 5.3 – *Continued*

	S	V	Fe	Co	Ni	Cu	Zn	Ga	Ge	As	Se	Ag	Cd	Sn	Sb	W	Pb
Digenite (n=6)																	
Mean	21.07	–	0.34	–	–	78.26	0.07	–	0.03	–	–	1.46	–	–	–	–	–
SD	0.68	–	0.49	–	–	0.89	0.17	–	0.07	–	–	0.92	–	–	–	–	–
Min	20.44	–	–	–	–	77.03	–	–	–	–	–	0.63	–	–	–	–	–
Max	22.32	–	1.31	–	–	79.54	0.41	–	0.16	–	–	2.64	–	–	–	–	–
Galena (n=20)																	
Mean	13.82	–	0.09	0.01	–	0.71	0.25	–	0.26	0.09	–	–	–	–	–	–	85.42
SD	0.26	–	0.26	0.04	–	1.28	0.91	–	0.04	0.40	–	–	–	–	–	–	1.17
Min	13.49	–	–	–	–	–	–	–	0.18	–	–	–	–	–	–	–	81.21
Max	14.58	–	1.11	0.17	–	4.36	4.09	–	0.32	1.80	–	–	–	–	–	–	86.49
Germanite (n=3)																	
Mean	32.11	3.53	0.32	–	–	49.00	3.08	–	7.80	5.58	–	0.10	–	0.03	–	–	–
SD	0.26	0.02	0.21	–	–	2.60	2.28	–	2.48	2.78	–	0.18	–	0.05	–	–	–
Min	31.81	3.51	0.11	–	–	47.42	0.44	–	4.93	3.82	–	–	–	–	–	–	–
Max	32.29	3.55	0.52	–	–	52.00	4.40	–	9.23	8.78	–	0.31	–	0.08	–	–	–
Ovamboite (n=2)																	
Mean	30.43	0.04	2.88	–	–	45.02	2.99	–	7.70	0.53	0.18	–	–	–	–	7.26	–
SD	0.23	0.01	0.56	–	–	0.01	0.07	–	0.20	0.09	0.03	–	–	–	–	0.62	–
Min	30.27	0.03	2.48	–	–	45.01	2.94	–	7.56	0.46	0.16	–	–	–	–	6.82	–
Max	30.59	0.04	3.27	–	–	45.02	3.04	–	7.84	0.59	0.20	–	–	–	–	7.69	–
Pyrite (n=62)																	
Mean	52.75	–	46.24	–	–	0.10	0.06	–	0.03	1.03	–	0.00	–	–	–	–	0.06
SD	0.55	–	0.41	–	–	0.50	0.24	–	0.06	0.71	–	0.03	–	–	–	–	0.10
Min	51.58	–	44.68	–	–	–	–	–	–	–	–	–	–	–	–	–	–
Max	54.14	–	47.10	–	–	3.69	1.34	–	0.17	1.99	–	0.21	–	–	–	–	0.40
Renierite (n=15)																	
Mean	32.62	0.25	12.61	0.01	–	42.59	2.51	0.13	7.72	1.75	–	0.06	–	0.02	–	–	–
SD	0.55	0.92	3.47	0.02	–	2.64	0.89	0.23	1.27	2.01	–	0.13	–	0.05	–	–	–
Min	31.03	–	0.11	–	–	40.82	0.49	–	5.03	0.47	–	–	–	–	–	–	–
Max	33.32	3.56	13.83	0.09	–	51.45	3.59	0.63	9.05	8.23	–	0.39	–	0.14	–	–	–
Sphalerite (n=88)																	
Mean	33.48	–	1.45	0.05	–	0.38	65.05	0.11	0.01	–	–	0.02	0.49	–	–	–	0.05
SD	0.58	–	1.20	0.29	–	1.21	1.97	0.74	0.05	–	–	0.11	0.54	–	–	–	0.25
Min	31.78	–	–	–	–	–	57.09	–	–	–	–	–	–	–	–	–	–
Max	34.50	–	3.98	1.88	–	8.12	68.56	5.09	0.29	–	–	0.68	4.50	–	–	–	2.14
Tennantite (n=18)																	
Mean	28.52	–	0.38	–	–	43.57	8.27	–	0.01	18.74	–	0.12	0.02	–	0.46	–	–
SD	0.30	–	0.50	–	–	0.73	0.30	–	0.04	1.07	–	0.17	0.07	–	0.32	–	–
Min	27.84	–	–	–	–	41.19	7.75	–	–	16.22	–	–	–	–	–	–	–
Max	29.20	–	1.73	–	–	44.48	8.75	–	0.16	19.98	–	0.39	0.31	–	0.98	–	–
Tetrahedrite (n=1)																	
Mean	23.74	–	5.02	–	–	27.28	3.73	–	0.23	2.37	–	17.75	0.31	–	22.57	–	–
SD	–	–	–	–	–	–	–	–	–	–	–	–	–	–	–	–	–
Min	23.74	–	5.02	–	–	27.28	3.73	–	0.23	2.37	–	17.75	0.31	–	22.57	–	–
Max	23.74	–	5.02	–	–	27.28	3.73	–	0.23	2.37	–	17.75	0.31	–	22.57	–	–
Tungstenite (n=4)																	
Mean	26.01	–	0.73	–	–	4.21	0.16	–	–	–	1.69	–	–	–	–	68.59	0.65
SD	2.06	–	0.27	–	–	2.55	0.32	–	–	–	0.23	–	–	–	–	4.83	0.87
Min	23.05	–	0.32	–	–	2.30	–	–	–	–	1.42	–	–	–	–	61.64	–
Max	27.75	–	0.92	–	–	7.87	0.64	–	–	–	1.96	–	–	–	–	72.26	1.93

In sphalerite, deposited after pyrite in the paragenetic sequence, Fe and Cd can reach concentrations of up to 7.3 and 1.4 wt.%, with averages of 1.47 and 0.48 wt.%, respectively. Sphalerite is often referred to as 'Fe-poor' for such concentrations. Otherwise, of all the analysed sulphides, sphalerite hosts the most important number of elements that can be present in significant amounts (up to hundreds ppm, Table 5.4) and vary over several orders of magnitude (Fig. 5.7), including Mn, Cu, Co, Ga, Ge, As, Cd, Sn, Sb and Tl. Of particular interest, Ge concentrations spread from the limit of detection (∼0.2 ppm) to 5930 ppm (sample P712). Its frequency distribution show a main mode around 0.3 ppm with a long tail at higher concentrations having a slight mode around 250 ppm. Moreover, a huge Cu–Ga enrichment occur in P712, which contains up to 2.93 wt.% Cu and 5.20 wt.% Ga. This sample aside, Cu and Ga respectively show maximum concentrations of only 4049 and 283 ppm, and average grades of 263 and 35 ppm.

Chalcopyrite, which is generally coeval with sphalerite, shows the most significant Ga and Ge enrichments, with concentrations spanning from about 1 to 1340 ppm (mean 176 ppm) and 13 to 686 ppm (216 ppm), respectively. Quite significant Sn concentration, of up to 533 ppm (sample B40), also occur in chalcopyrite, with an average grade of 99 ppm. The few LA-ICP-MS analyses in tennantite (sample P712), also coeval with sphalerite and chalcopyrite, show remarkable trace concentrations in Ga, ranging 560–630 ppm with a mean of 600 ppm, Ag, ranging 185–205 ppm with a mean of 193 ppm, and Cd, ranging 2480–2730, averaging 2600 ppm. Ge generally shows concentrations below the ppm level, except in one spot, where it reaches 182 ppm.

Finally, bornite, which deposited later in the paragenetic sequence, shows the highest Ag concentrations, grading 410–2260 ppm for an average of 1205 ppm. Ge only reaches a maximum of 14 ppm (sample A114). Therefore, through the whole paragenetic sequence, the average Ge content decreases in the following order, chalcopyrite > sphalerite > tennantite > pyrite > bornite, and its most significant contents occur in the sulphides that were deposited coevally with Ge-sulphides (mostly renierite), i.e., sphalerite and chalcopyrite, and with minor respects, tennantite. In addition, regarding sphalerite, the Ge distribution mode around 0.3 ppm likely corresponds to sphalerite precipated before and/or after the deposition of Ge-sulphides and Ge-bearing sphalerite, chalcopyrite and tennantite, and the latter may correspond the a Ge peak in the timing of ore mineralisation.

Table 5.4 – Results of LA-ICP-MS analysis of the Kipushi ore assemblage (concentrations in ppm).

	Mn	Fe	Co	Zn	Cu	Ga	Ge	As	Se	Ag	Cd	In	Sn	Sb	Te	Hg	Tl	Pb
Bornite (n=22)																		
Min	–	101400	–	–	*i.s.*	0.2	2.2	4.7	–	406	–	–	0.4	–	–	–	–	0.8
Max	16	113600	0.08	22	*i.s.*	53	14	118	13	2260	1.4	0.08	5.0	0.4	0.9	4.4	0.14	53
Mean	1.4	107355	0.01	1.5	*i.s.*	11	6.0	31	4.6	1205	0.4	0.03	1.4	0.1	0.1	1.1	0.02	8.4
LOD*	0.40	18.24	0.09	0.73	*i.s.*	0.11	0.12	0.78	4.02	0.11	1.38	0.04	0.18	0.18	1.71	3.46	0.14	0.47
Chalcopyrite (n=53)																		
Min	–	282000	–	0.4	*i.s.*	0.9	13.2	4.3	–	0.3	–	–	0.4	–	–	–	–	–
Max	21	312000	22	15600	*i.s.*	1338	686	124	25	42	117	37	533	5	3.9	7	0.47	66
Mean	1.0	298326	1.86	380	*i.s.*	179	218	31	10	7.4	4	7.8	99	0.4	0.6	1.7	0.03	7.8
LOD*	0.56	21.73	0.10	1.16	*i.s.*	0.13	0.14	0.98	4.89	0.12	1.60	0.04	0.20	0.19	2.01	4.33	0.14	0.50
Pyrite (n=21)																		
Min	–	*i.s.*	0.1	–	–	–	–	23	–	–	–	–	–	–	–	–	–	–
Max	13	*i.s.*	1220	431	3160	32	148	33160	46	78	7.7	1.6	87	18	2.9	2.0	1.35	17200
Mean	3.1	*i.s.*	151	31	392	2.1	8.3	6090	15	4.9	0.8	0.1	4.6	4.6	0.6	0.1	0.16	873
LOD*	0.45		0.13	0.76	1.13	0.11	0.13	0.86	4.17	0.11	1.38	0.04	0.16	0.15	1.64	3.40	0.11	0.39
Sphalerite (n=186)																		
Min	13	–	–	*i.s.*	1.56	0.1	–	–	–	0.5	2343	–	0.2	–	–	–	–	–
Max	252	73000	368	*i.s.*	29300	52000	5930	920	27	29	14240	48	924	202	–	–	238	70
Mean	79	14656	36	*i.s.*	1350	2105	128	25	3.3	2.1	4894	4.7	21	2.1	–	–	36	4.8
LOD*	1.00	43.59	0.19	*i.s.*	1.88	0.12	0.17	0.75	3.59	0.11	2.12	0.02	0.14	0.08	0.93	1.69	0.08	1.02
Tennantite (n=6)																		
Min	78	1831	78	101000	*i.s.*	562	1.0	530000	33	185	2476	1.2	0.3	1288	4.1	112	–	16
Max	173	2217	83	108000	*i.s.*	630	182	584000	41	205	2726	1.6	0.4	3362	5.0	145	0.07	25
Mean	104	2014	81	104000	*i.s.*	601	32	562667	37	193	2599	1.4	0.3	2455	4.5	124	0.03	18
LOD*	0.33	12.21	0.06	6.24	*i.s.*	0.36	0.07	0.57	2.50	0.06	0.85	0.02	0.09	0.08	1.03	2.32	0.06	0.18

i.s. LA-ICP-MS internal standard
– Not detected or below the limit of detection (LOD)
* Mean LOD calculated with the 3σ criterion – depend on the element and its concentration

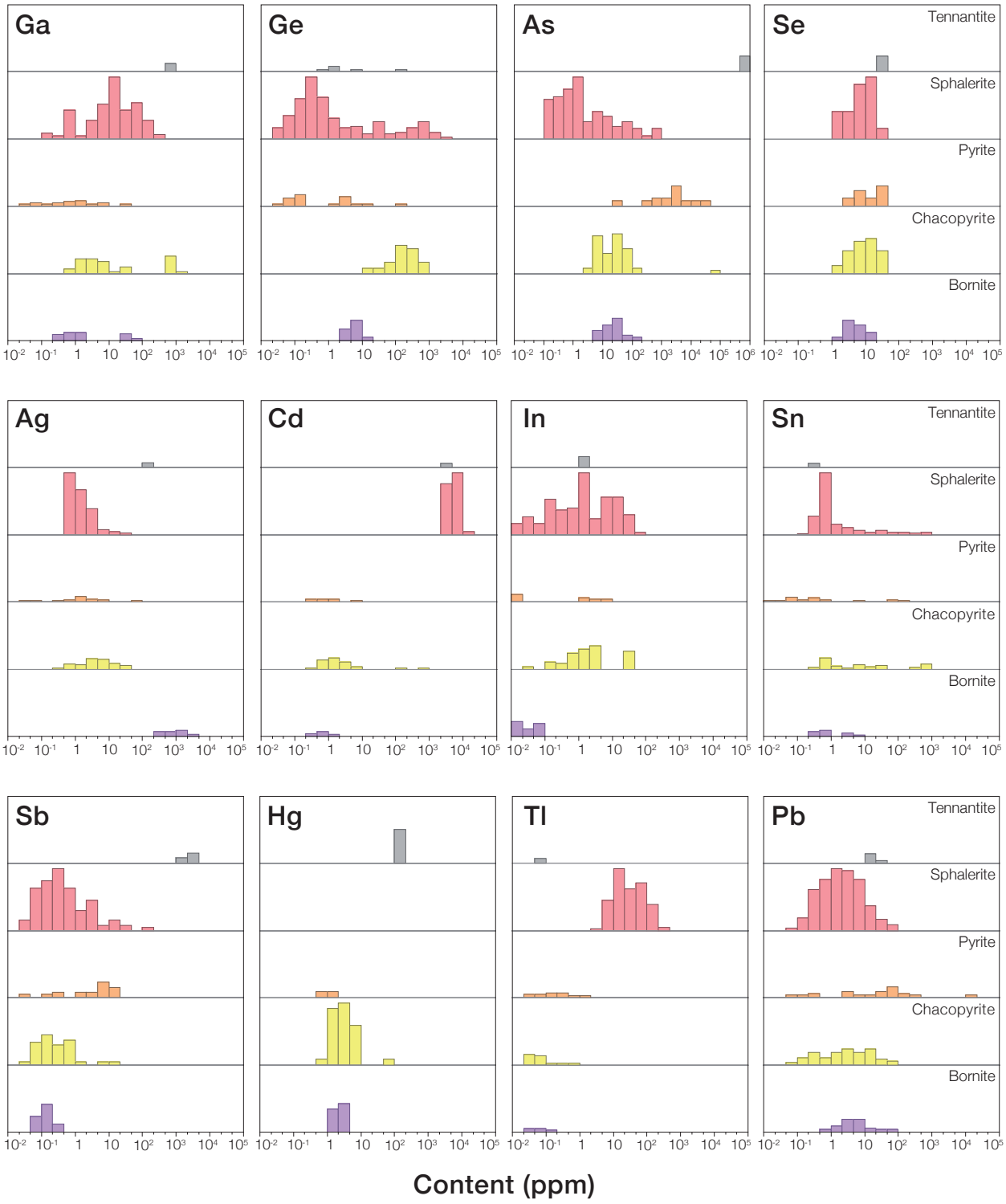

Fig. 5.7 – Histograms of the trace element contents in the Kipushi deposit (in ppm).

Correlation trends and incorporation mechanisms

Principal component analysis (PCA) has been applied on the log-transformed LA-ICP-MS dataset for each type of sulphide (see Sec. 3.4), in order to bring out a comprehensive overview of the underlying correlation trends, as well as discerning the most significant element associations. The results of the PCA are shown in Fig. 5.8 and Fig. 5.10. Elements and spot analyses are projected on the PC1 *vs* PC2 plane, which carry the highest explained variance.

For pyrite (Fig. 5.8a), PC1 *vs* PC2 yield 55.5% of explained variance and PC1 carries most of the information (41.1%). PC1 is mainly loaded by Ge, Ga, Sb, Pb, Mn, Cu and Ag, with almost equal weights, along which two populations can be distinguished, the pyrites rich in the trace elements previously enumerated, and the pyrites poor in those elements. These trace element obviously substitute for Fe in the pyrite lattice, hence, if present in the PCA (internal LA-ICP-MS standard), it would likely be anticorrelated to trace elements along PC1. In geological and temporal context, the trace-rich pyrite population, especially samples A51, A87, U37 and A78, likely relates to the arrival of Zn–Cu rich fluids.

For sphalerite (Fig. 5.8b), although the explained variance by PC1 *vs* PC2 is rather low (40.7%), three marked element clusters can be identified and they are correlated one another (the smaller the angle, the stronger the correlation). These three clusters are composed of heterovalent cations, Sn–Sb–Tl, Ge–As and Ga–Cu. In addition, two anticorrelated element clusters are observed for divalent cations, Fe(–Cd) and Co–Mn. The clear segregation between divalent and heterovalent elements may originate from independent incorporation mechanisms. Divalent cations can readily enter the sphalerite lattice through direct substitutions such as $Zn^{2+} \leftrightarrow (Fe, Cd, Co, Mn)^{2+}$, whereas heterovalent cations require some form of charge compensation to enter the sphalerite lattice, via coupled substitutions, e.g., $5Zn^{2+} \leftrightarrow (Ge, Sn)^{4+} + (Ga, As)^{3+} + 3(Cu, Ag, Tl)^{+}$, or through the creation of vacancies. In Fig. 5.9, the strong correlation between the sum of tri- and tetravalent elements (Ga, Ge, As, In, Sn and Sb) with monovalent elements (Cu, Ag, Tl) along the 1/1 molar ratio well illustrates the charge compensation effect by coupled substitutions for heterovalent cations.

Moreover, in the individuals plot (Fig. 5.8), two spot populations are present, one with a marked trend correlating with the Sn–Ge cluster, and one that relates to enrichment in Co–Mn and Ga–Cu, which can be interpreted in a the folowing temporal context: (1) since pyrite was enriched in Co and was deposited before sphalerite, the Co-rich sphalerite individuals (e.g., U22, A108, U48) may represent the first precipitated sphalerite. (2) The Ga–Cu- and Sn–Ge-rich individuals (e.g., P712, D32, A51) would mark the fluid peak in Ge and other related metals (Ga, Sb, Sb). Then, (3) the displacement of individuals down the Sn–Ge trend would indicate the end of progressive depletion in Ge and related metals in the fluid past the ‘Ge peak’.

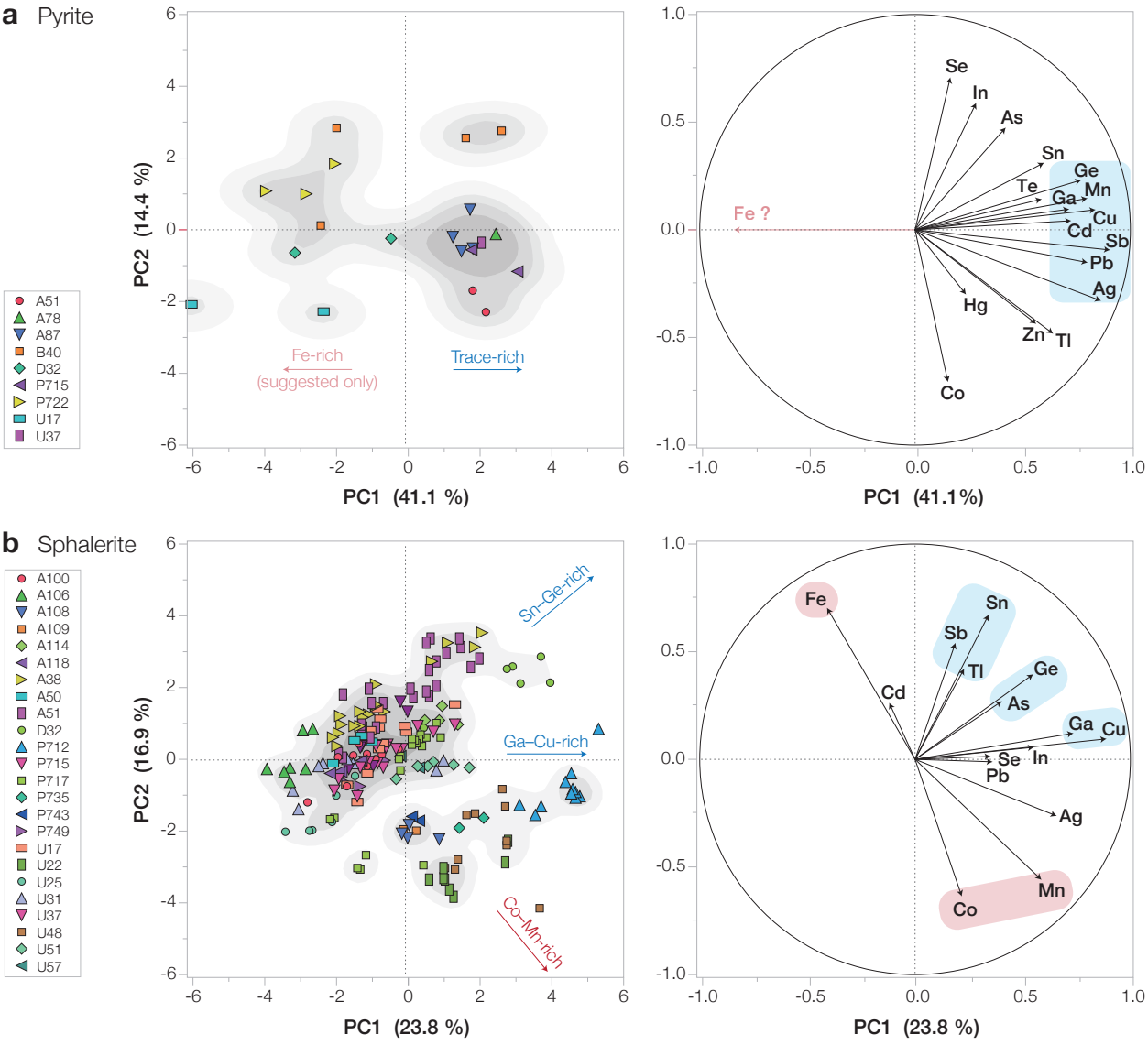

Fig. 5.8 – Principal component analysis of log-transformed, μmol%-converted LA-ICP-MS data in pyrite (**a**) and sphalerite (**b**) from Kipushi (D.R. Congo). Spot analysis (i.e., individuals, left hand frame) and elements (i.e., variables) are plotted on the PC1 *vs* PC2 plane. See text for detailed explanations.

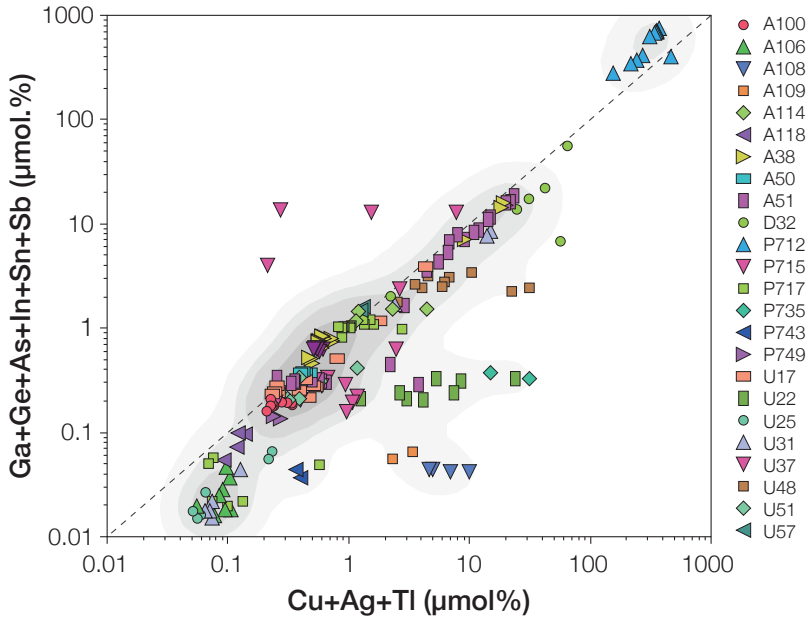

Fig. 5.9 – Sum of Ge plus related tri- and tetravalent (Ga, As, In, Sn, Sb) elements *vs* monovalent elements (Cu, Ag, Tl) in sphalerite. Most of the spot analyses align along the 1/1 ratio line, suggesting the existence of coupled substitutions.

For chalcopyrite (Fig. 5.10a), PC1 and PC2 explain, with almost similar weight, only 38.2% of the total variance. The element plot is clearly different to that observed in chalcopyrite from Barrigão (Fig. 5.6 in Sec. 5.3.1). The individuals for each sample are well grouped in distinct positions in PC1 *vs* PC2, indicating that the samples have markedly different trace element compositions, therefore, the correlations observed here appear to reflect mostly gross elemental enrichments rather than incorporation mechanisms. Given the trace element concentrations in Table 5.4, the individuals are mostly distinguished through two trends; along PC1, Sn–Ga(–In)-rich chalcopyrite and Sn–Ga(–In)-depleted chalcopyrite (with slight Pb enrichment) and; along PC2, Zn–Ge-rich chalcopyrites and Zn–Ge-poor chalcopyrite (with slight Ag–Co–Hg enrichment). Due to the relatively low information carried by PC1 *vs* PC2, it is difficult to go any further with the interpretation.

For tennantite (Fig. 5.10b), the few LA-ICP-MS have been collected in the same sample, hence, the element correlations are only representative of the incorporation mechanisms. Understandably, the PC1 *vs* PC2 plane explains almost 3/4 of the total variance (70.8%). Two main, anticorrelated clusters (having a major compound) can be distinguished, Zn–Ga–Co, and Fe–Ge–Mn. The former may suggest the direct substitution, $Fe^{3+} \leftrightarrow (Ga, Co)^{3+}$, while the latter may indicate direct substitutions for divalent cations, $Zn^{2+} \leftrightarrow (Mn, Cd, Pb)^{2+}$, and more complex substitutions for Ge, e.g., involving vacancy creation, $2Zn^{2+} \leftrightarrow Ge^{4+} + \square$, or a coupled substitution with Cu (not presented since it is the internal LA-ICP-MS standard), $3Zn^{2+} \leftrightarrow Ge^{4+} + 2Cu^{+}$, as shown in sphalerite (Sec. 6.2).

Finally, for bornite (Fig. 5.10c), PC1 *vs* PC2 yields a total explained variance of 53.6%. The most significant element clusters are Ga–Sn along PC1 and Ag–Ge along PC2. Individuals can therefore be mainly distinguished relatively to their Ga–Sn content, and with minor respect, their Ag(–Ge) content. The correlation of Ge with Ag suggests the coupled substitution, $3Fe^{3+} \leftrightarrow 2Ge^{4+} + Ag^{+}$. Ge in unlikely to substitute in the Cu site because it would require an important creation of lattice vacancies to maintain the charge balance. However, the marked Ag enrichment can be explained by the direct substitution, $Cu^{+} \leftrightarrow Ag^{+}$.

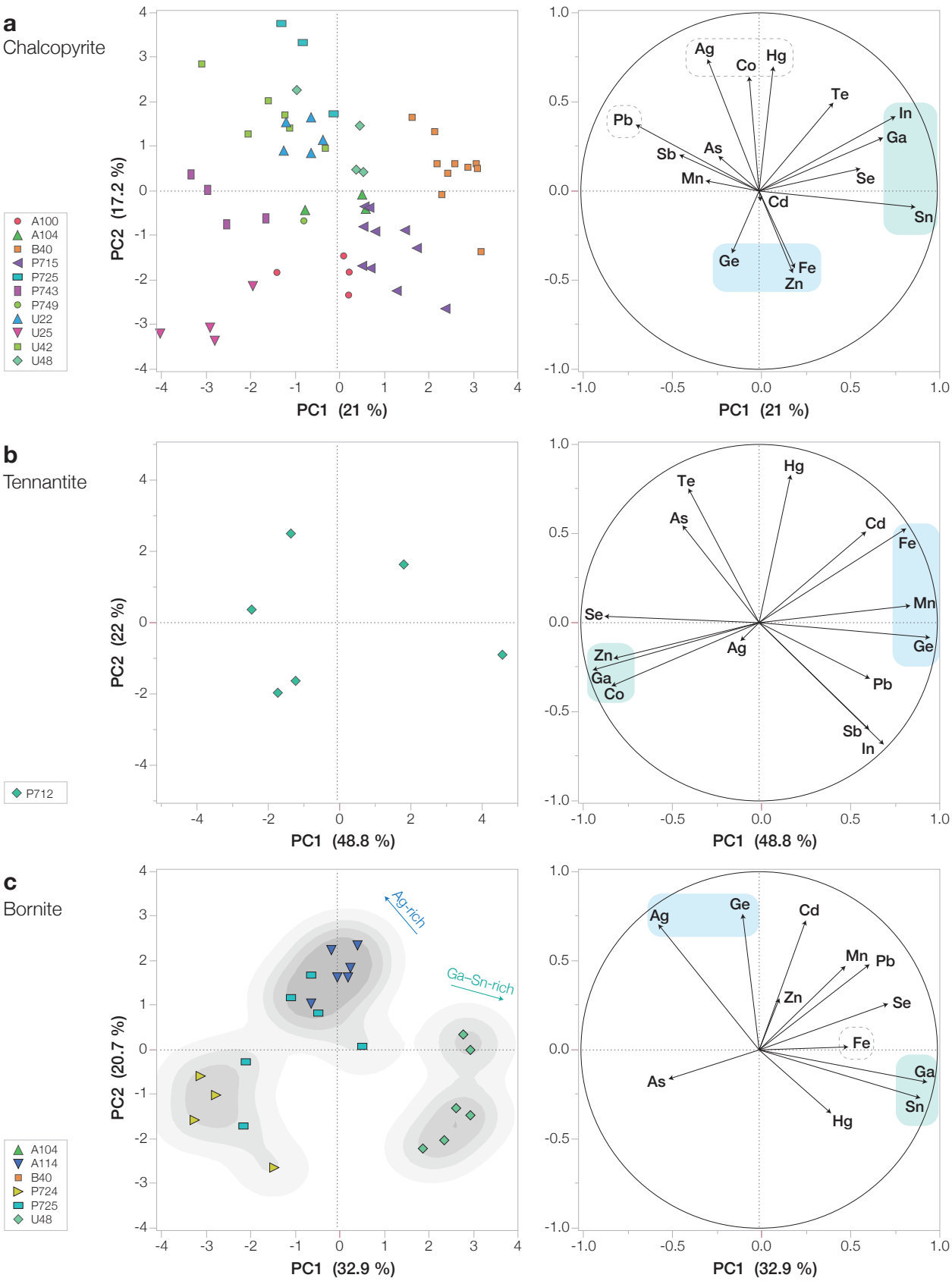

Fig. 5.10 – Principal component analysis of log-transformed, μmol%-converted LA-ICP-MS data in chalcopyrite (**a**), tennantite (**b**), and bornite (**c**) from Kipushi (D.R. Congo). Spot analysis (i.e., individuals, left hand frame) and elements (i.e., variables) are plotted on the PC1 *vs* PC2 plane.

Signification of trace element contents in sphalerite

Finally, the averaged, log-transformed trace element signatures of the sphalerite samples have been compared to their position within the mine using PCA with 'NE' and 'Up' as illustrative variables (i.e., not taken into account in the calculation of principal components). Results are shown in Fig. 5.11. The PCA roughly outline similar element clusters as the PCA showed Fig. 5.8b. Most remarkably, this PCA indicates that Ge, Ga, In and As, but also Cu and Sn decrease towards the North-East. With minor respects, Cu contents decreases with depth while that of Cd and Fe tend to increase. Intiomale (1982) and Intiomale and Oosterbosch (1974) noted that below the 1350 m level, the concentration of Zn in the Zn–Cu ores decreases while the amount of Fe progressively increases. The trend observed here is consistent with the later, hence, the Cu and Fe trace contents in sphalerite from levels between 290 and 850 m could be related to variations in ore mineralogy with depth.

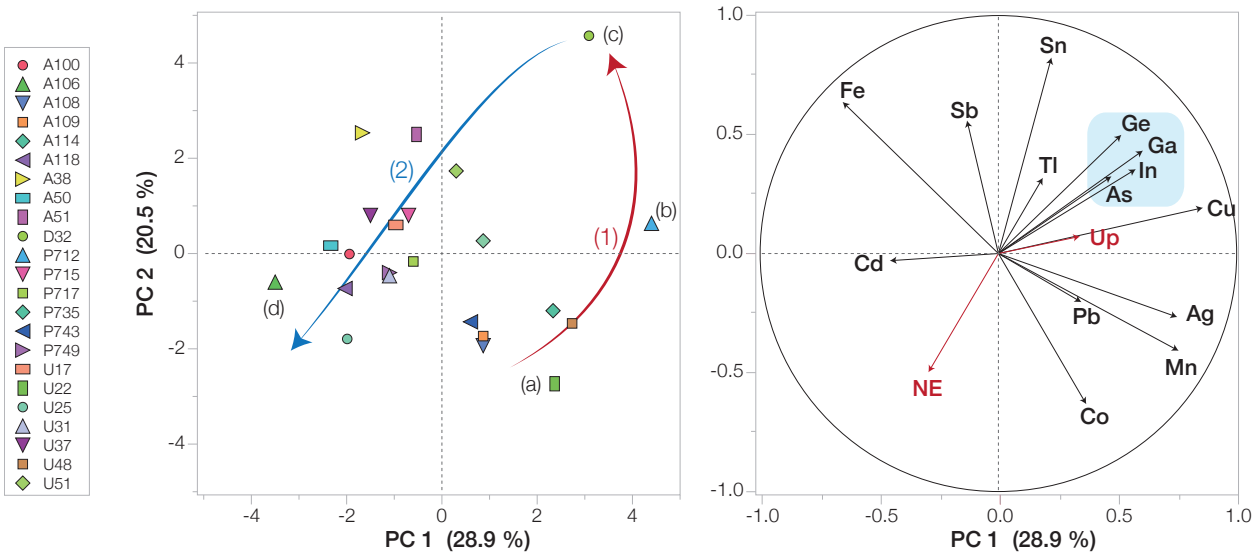

Fig. 5.11 – Principal component analysis of log-transformed, average sphalerite trace element signatures. 'NE' (North-East) and 'Up' are illustrative variables. (1) Upward fluid branch associated to the deposition of (a) early Co-rich sphalerite, (b) Ga–Cu-rich sphalerite and (c) Ge–Sn-rich sphalerite ('Ge peak'), after which a (2) north-eastward/downward branch corresponds to progressive fluid depletion in Ge.

From observations of Fig. 5.8b and Fig. 5.11, the trace element contents in sphalerite may relate to the fluid evolution through time and space. This model (Fig. 5.11) involves two fluid circulation branches, an upward fluid branch associated to the deposition of early Co-rich sphalerite before precipitation of Ga–Cu-rich sphalerite (coeval with gallite), and Ge–Sn-rich sphalerite (coeval with renierite), which indicate the 'Ge peak', either through fluid cooling or through the injection of a Ga- and Ge-rich fluids in the system. Then, past the 'Ge peak', a north-eastward/downward branch would correspond to the progressive depletion in Ge and related metals in the fluid trough circulation within the Kipushi fault.

5.4 Conclusions

Germanium concentrations vary over several orders of magnitude in sulphides from the studied deposits (Fig. 5.12). The most remarkable trace concentrations of Ge occur in sphalerite from Saint-Salvy and chalcopyrite from Barrigão, averaging 780 and 1100 ppm, respectively. However, fahlore from Barrigão, which is fairly in equilibrium with chalcopyrite, contains only ∼15 ppm. Chalcopyrite is therefore enriched in Ge by almost one hundred-fold. In the Kipushi deposit, Ge averages only 220 ppm in chalcopyrite and 6 ppm in bornite. Ge content histogram for sphalerite exhibits an intense mode under 1 ppm, with a long tail stretching up to 5900 ppm. The trace element contents in sphalerite from Kipushi may be a good proxy of the fluid evolution through time and space.

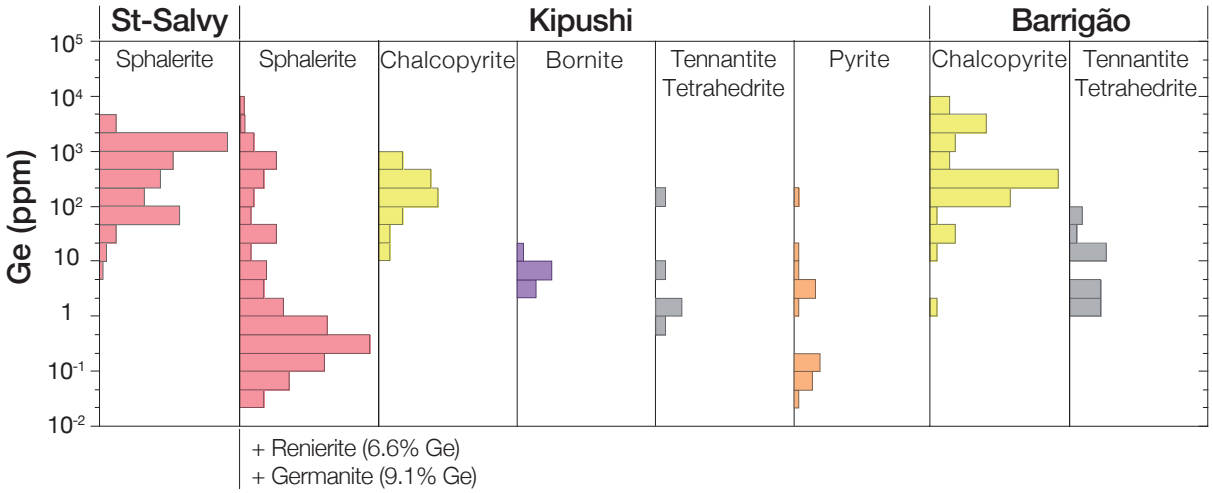

Fig. 5.12 – Histograms comparing Ge concentration in Ge–bearing minerals at Saint-Salvy, Kipushi (except for Ge-sulphides) and Barrigão.

Several substitution mechanisms have been inferred from element correlations in Ge-bearing sulphides, all of which involving coupled substitutions or the creation of vacancies to accommodate Ge entry within the sulphide lattice. In the above sections, Ge is thought to occur as Ge^{4+} rather than as Ge^{2+} because it is the dominant state in known natural compounds (Bernstein, 1985), yet, the oxidation state of Ge needs verification if we are to refine its incorporation mechanisms in sulphide minerals.

Chapter 6

Ge crystal chemistry in sulphide minerals

6.1 Overview

As shown above (Chap. 5) and in a number of studies, incorporation of minor and trace elements into sulphide minerals is often, in the first place, addressed trough the prism of element correlations from which substitution mechanisms are inferred. The limits of this approach lie in the uncertainties about the oxidation state for some substituting elements. Elements occurring in minor amounts are generally strongly anticorrelated to one of the essential component in the site of which they substitute, and, since there are usually little doubts concerning their oxidation state, isovalent direct substitution is the most straightforward and privileged interpretation. Taking sphalerite for instance, the substitutions $Zn^{2+} \leftrightarrow (Fe, Mn, Cd)^{2+}$ is known for long to be responsible for the presence of these elements in minor amounts (up to tens wt.%; e.g., Bernardini et al., 2004; Di Benedetto et al., 2005a; Wright, 2009; Wright and Gale, 2010).

Elements in trace amounts are often heterovalent, so, given that the substituted site is known from a broad anticorrelation of trace elements with one of the essential component, coupled substitutions or the creation of lattice vacancies are required to maintain charge balance. In sphalerite from Saint-Salvy for example, for substituting divalent Zn, a large coupled substitution mechanism was inferred from the correlation of monovalent elements with tri- and tetravalent elements, basically such as $(2x + 3y)Zn^{2+} \leftrightarrow (x + 2y)(Cu, Ag)^{+} + x(Ga, In, Sb)^{3+} + y(Ge, Sn)^{4+}$ (Sec.5.2). To do so, the oxidation state of the elements are assumed *a priori* and the possible creation of vacancies ignored, which show the limit of this method.

In particular, the oxidation state of Ge and other substituting elements with which it correlates remain poorly constrained and their questioning is still open to debate. Despite Ge^{4+} is the most encountered form in the mineral world, some authors argued in favour of the presence of Ge^{2+}. In sphalerite, Cook et al. (2009) proposed the isovalent substitution $Zn^{2+} \leftrightarrow Ge^{2+}$ where Ge is not associated with monovalent elements (Très Marias deposit, Mexico; Sec.2.3.4), and Bonnet (2014), after a synchrotron XAFS experiment, suggested the

presence of Ge^{2+} in sphalerite from MVT deposits in Tennessee (USA).

Other unresolved questions include the influence of the oxidation state of substituting elements on crystallography-controlled zoning in sphalerite and whether or not variations exist between different types of zoning. In addition, as shown in Sec. 2.4.1, the oxidation state, together with ligands and coordination numbers, is one of the key parameters involved in inducing large isotopic equilibrium fractionation, especially at low temperatures. In an attempt to answer these questions, synchrotron X-ray absorption spectroscopy is the most powerful, element-specific, technique for obtaining information about the oxidation state of Ge and its coordination symmetry in the sulphide minerals studied here. The study is centred on two case studies, (1) μ-XANES in Ge-bearing sphalerite and (2) μ-XANES/EXAFS in Ge-bearing copper sulphides (chalcopyrite, tennantite, bornite, covellite).

6.2 Distribution and oxidation state of Ge, Cu and Fe in sphalerite by μ-XRF and *K*-edge μ-XANES

This section is devoted to the paper of Belissont R. *et al.*, "Distribution and oxidation state of Ge, Cu and Fe in sphalerite by μ-XRF and K-edge μ-XANES: insights into Ge incorporation, partitioning and isotopic fractionation.", accepted on January, 3rd, 2016 in *Geochimica et Cosmochimica Acta* (edited version in Appendix).

Abstract

Synchrotron-based microscale X-ray absorption near edge structure spectroscopy (μ-XANES) has been combined with X-ray fluorescence (μ-XRF) mapping to investigate Ge, Cu and Fe oxidation states in compositionally zoned Ge-rich sphalerite from the Saint-Salvy deposit (France). The present study aims at improving our understanding of substitution mechanisms and trace element uptake relative to Ge isotope fractionation in sphalerite. K-edge XANES records of various Ge-, Cu- and Fe-bearing sulphides are presented for comparison with sphalerite, and *ab initio* calculations at the Ge K-edge complete our experimental data. The Ge K-edge spectra of the Ge-bearing sphalerite are identical to those of germanite, renierite and briartite, indicating the presence of tetrahedrally-coordinated Ge^{4+}. In addition, Cu and Fe K-edge spectra suggest the presence of Cu^{+} and Fe^{2+}, respectively, in the tetrahedral site. No significant differences in the oxidation states of Ge, Cu and Fe were observed within or between the zoning types or between the samples. The intake of Ge^{4+} in sphalerite may therefore occur in the tetrahedral divalent metal site via coupled substitutions charge-balanced by monovalent elements such as $3Zn^{2+} \leftrightarrow Ge^{4+} + 2Cu^{+}$, resulting in a strong Ge–Cu elemental correlation, or, when Ge does not correlate with monovalent elements, through the creation of lattice vacancies such as $2Zn^{2+} \leftrightarrow Ge^{4+} + \square$ (vacancy). The tetravalent state of Ge is compatible with temperature-related Ge isotopic fractionation and can explain the large range of δ^{74}Ge measured in the Saint-Salvy sphalerite. Moreover, the exceptional enrichment in Ge and the large variations in the 'bulk' Ge contents in these sphalerites do not appear to be related to charge effects but would instead result from the effect of temperature-related partitioning.

6.2.1 Introduction

Germanium (Ge) is increasingly in demand for use in a variety of high-tech devices. Its strategic importance as well as its scarcity in most geological environments necessitates a refinement of our understanding of its geological cycle. The concentration of Ge in the Earth's crust averages 1.3 ppm (updated in Hu and Gao, 2008), mostly incorporated into silicate minerals through $Ge^{4+} \leftrightarrow Si^{4+}$ isovalent substitutions in tetrahedral sites. However, enrichment of Ge relative to this average can occur in iron meteorites, iron oxides/hydroxides, Cu-, Ag-, As-rich sulphides and Zn sulphides, and coal. Thus, depending on the geological setting, Ge can be distinctly lithophile, siderophile, chalcophile or organophile, making it a useful geochemical tracer in the fields of cosmochemistry, planetary differentiation, hydrothermal and tectonic activity and fluid sources, as well as continental weathering (e.g., Dickinson et al., 1989; Luais, 2007, 2012; Rouxel et al., 2006; Escoube et al., 2015; Kurtz et al., 2002). Germanium can occur as Ge^{2+} and Ge^{4+} although the latter is thought to be the dominant form found in aqueous fluids (Wood and Samson, 2006) and natural compounds such as sulphide minerals (e.g., renierite, germanite, briartite), oxides (e.g., argutite) and hydroxides (e.g., stottite; Höll et al., 2007). Even in the spinel-type oxide, brunogeierite, Ge is now understood to occur as Ge^{4+} (Cempirek and Groat, 2013).

Sphalerite (ZnS) and coal are the main primary sources of Ge and concentrations in sphalerite can reach around 3000 ppm, mostly in low-temperature hydrothermal systems (e.g., Mississippi valley type deposits, MVT; Bernstein, 1985; Höll et al., 2007; Frenzel et al., 2014). Since the study of Stoiber (1940) was published over seventy years ago, the wide range of minor/trace elements entering the sphalerite diamond-type lattice has been the subject of numerous studies. Microscale compositional zoning often occurs in sphalerite (Pattrick et al., 1993a; Beaudoin, 2000; Di Benedetto, 2005), and, in particular, antithetical partitioning of minor/trace elements between different types of compositional zoning has been reported, indicating the involvement of crystallographic controls in the incorporation process (Johan, 1988; Belissont et al., 2014). Accordingly, huge Ge enrichments, correlated with minor Cu plus tri- and tetravalent element enrichments, have been reported in sector zoning patterns, whereas Ge is depleted in rhythmic bands. Despite these findings, the parameters that influence these crystal structure controls remain poorly constrained.

The incorporation of divalent elements (e.g., Fe^{2+}, Mn^{2+}, Cd^{2+}) via direct substitution of Zn^{2+} has been widely demonstrated (e.g., Bernardini et al., 2004; Di Benedetto et al., 2005a; Wright, 2009; Wright and Gale, 2010). Tri- and tetravalent elements (e.g., Ga^{3+}, Ge^{4+}) are thought to enter sphalerite via either coupled substitutions with monovalent elements (e.g., Cu^{+}, Ag^{+}) for charge compensation or through the creation of vacancies (e.g., Johan, 1988; Bernstein, 1985). However, the oxidation states of incorporated elements, including Ge, remain poorly constrained and are still open to debate. For instance, Cook et al. (2009) proposed the isovalent substitution $Ge^{2+} \leftrightarrow Zn^{2+}$ in sphalerite where Ge is not associated with monovalent elements. Other unresolved questions include the influence of the oxidation state of substituting elements on crystallography-controlled zoning in sphalerite and whether or not variations exist between different types of zoning.

The oxidation state, together with ligands and coordination numbers, is one of the key parameters involved in inducing large isotopic equilibrium fractionation at low temperatures (e.g., Schauble, 2004). Thus, heavy isotopic compositions typically correlate with high ox-

idation states, as seen for example in Fe isotope systematics, where $^{56}Fe/^{54}Fe$ ratios are usually higher in Fe^{3+}-bearing compounds than in Fe^{2+}-bearing compounds (e.g., Polyakov and Mineev, 2000). The oxidation states of incorporated elements (and the substitution mechanisms) also affect their partition coefficients, which drive elemental enrichment from the ore-forming fluids into the growing solid phase. Advanced study of the oxidation state of Ge and related elements is thus highly important if we are to improve our understanding of substitution mechanisms, impurity uptake, and Ge isotope fractionation in sphalerite.

Synchrotron X-ray absorption near edge structure (XANES) spectroscopy is a powerful element-specific technique for obtaining information on the oxidation state of the absorbing atom and its coordination symmetry. Advances in XANES spectroscopy have meant that high-resolution *in situ* analysis is now possible and elements can be probed in minor or trace amounts in various types of material (e.g., Muñoz et al., 2006). Germanium K-edge data from natural Ge-bearing specimens are scarce in the literature. The few studies of note include that of Bernstein and Waychunas (1987), who studied the Ge-bearing iron oxides, hematite, goethite and stottite. More recently, Cook et al. (2015) focused on the oxidation state of Ge in sphalerite from the Très Marias Zn deposit (Mexico), which was thought to carry Ge^{2+} (Cook et al., 2009). Many studies have investigated the (bulk) oxidation state of Fe in sphalerite using Mössbauer spectroscopy, and these have shown that the uptake of Fe by sphalerite depends on temperature and sulphur fugacity, with high sulphur fugacity being related to increased Fe^{3+} in order to compensate for the charge deficiency induced by Zn^{2+} vacancies (e.g., Manning, 1967; Gerard et al., 1971; Di Benedetto et al., 2005a; Lepetit et al., 2003). Finally, Cook et al. (2012) investigated the copper oxidation state in In-rich sphalerite by Cu K-edge μ-XANES and suggested that incorporation of indium occurs via the coupled substitution, $2Zn^{2+} \leftrightarrow Cu^{+} + In^{3+}$.

The present study aims at probing the oxidation state of Ge at the microscale using K-edge μ-XANES in zoned Ge-rich sphalerite in order to gain further insights into Ge enrichment processes related to direct and coupled substitution mechanisms, crystallography-controlled zoning and Ge isotopic fractionation. The sphalerite studied here comes from the very typical Noailhac – Saint-Salvy deposit in France. Ge-bearing sphalerite from the Kipushi deposit (D.R. Congo) is used for comparison. The sphalerite from Saint-Salvy contains Cu and Fe in minor amounts that are, respectively, positively and negatively correlated with Ge, both spatially and in terms of concentration (Belissont et al., 2014). Cu and Fe K-edge μ-XANES spectra were therefore determined in addition to the Ge K-edge spectra. Synchrotron-based μ-XRF mapping was used to determine element distributions and beam positioning for subsequent μ-XANES records. *Ab initio* Ge K-edge calculations complement our experimental XANES data and improve our interpretation.

6.2.2 Experimental methods

Sample description

Three Ge-rich compositionally zoned sphalerites representative of the Saint-Salvy vein-type Zn–Ge–Ag deposit (France) were selected. The three samples exhibit increasing bulk Ge contents and isotopic compositions (δ^{74}Ge relative to the NIST 3120a Ge standard) as shown in the study of Belissont et al. (2014): 64W (∼500 ppm, -2.05‰), 62E (∼900 ppm, -1.41‰)

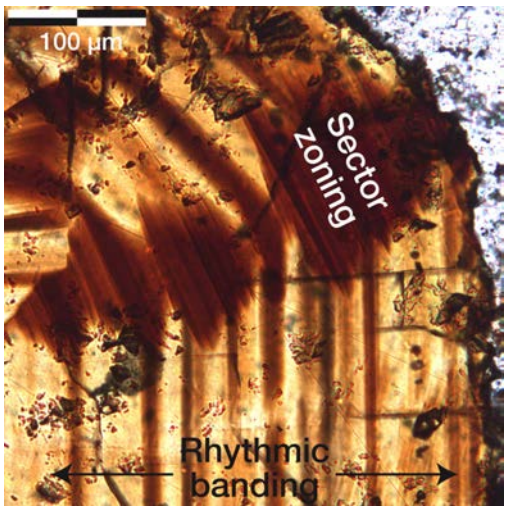

Fig. 6.1 – Microphotograph of the typical zoning types observed in sphalerite from Saint-Salvy (France): rhythmic bands and overlapping cross-cutting-like sector zones, corresponding to the (110) and (111) planes, respectively (planes are referenced according to the study of Johan, 1988).

and SALUN (∼1000 ppm, +0.64‰). The sphalerites were collected from different locations in the mine (Cassard et al., 1994). The specimens, prepared as 150 μm-thick polished sections, occur as supra-millimetric zoned crystals, light brown to dark reddish-brown in colour. Trace element spot analyses were performed using LA-ICP-MS and bulk Ge isotopic compositions were measured by MC-ICP-MS (Belissont et al., 2014). Exsolutions of other minerals (e.g., chalcopyrite) were not detected by optical and electron microscopy, and were not observed in LA-ICP-MS down-hole profiles. Furthermore, the amount of Fe in this sphalerite (3–4 mol.%) is below the critical content required to initiate diffusion-induced segregation (DIS) processes (>5 mol.%; Bente and Doering, 1995).

Minor and trace elements are antithetically distributed among two types of compositional zoning that can be distinguished optically (Fig. 6.1). (i) Rhythmic banding, along (110) planes, occurs as alternating parallel dark brown and light brown growth-bands from the core to the rim. The dark brown bands are enriched in Fe (2.6 wt.%), Cd (3500 ppm), Sn (880 ppm) and In (230 ppm). Ge and Cu average 140 and 2450 ppm, respectively. The light bands are relatively depleted in all elements, including Cu (550 ppm) and Fe (2.2 wt.%), except Ge, which averages 270 ppm. (ii) The sector zoning, along (111) planes, forms cross-cutting-like dark brown zones that overlap rhythmic bands and which consist of a series of small and parallel truncation planes of variable size. The sector zones are enriched in Cu (4000 ppm), Sb (1970 ppm), Ge (1100 ppm), Ga (370 ppm) and Ag (360 ppm). Fe (1.9 wt.%) is depleted relative to the rhythmic bands. This antithetic zoning in element concentration suggests a crystallographic control on the incorporation of trace elements (Belissont et al., 2014).

One of the sphalerite samples, sample A38, originates from the Kipushi vein-type Cu–Zn–(Ge–Pb) ore deposit (D.R. Congo) and consists of supra-millimetric orange crystals in a gangue of dolomite and quartz. A few optically dark zones, up to 1 μm^2 in size, can be observed, though these are distinct from those observed in the Saint-Salvy sphalerite. Sample A38 is relatively enriched in Ge (∼170 ppm) compared to other sphalerites within the deposit, and concentrations of up to 950 ppm have been measured in the optically dark zones.

Three Ge-bearing sulphides were analysed for calibration: renierite, germanite, and briartite as the major Ge carrier. Synthetic GeS (Sigma Aldrich, 99.99%) was used as a divalent Ge reference. Chalcopyrite and covellite specimens contained trace to minor amounts of

Ge. Stannite, pyrite and arsenopyrite were used specifically for the collection of Fe *K*-edge XANES spectra. The known crystal chemistries of the sphalerite and calibration compounds are listed in Table 6.1. The compositions of the minerals analysed in this study are given in Table 6.2. Major and minor elements were analysed by EPMA and trace quantities of Ge were analysed by LA-ICP-MS (GeoRessources, Vandoeuvre-lès-Nancy, France).

Table 6.1 – Known crystal chemistry of analysed compounds.

Mineral	Formula	CN	Ge	Fe	Cu	Technique	Reference
Sphalerite	ZnS	4	?	$Fe^{2+/3+}$ (*h*)	Cu^{+}	Mössbauer (^{57}Fe) μ-XANES (Cu *K*-edge)	Lepetit et al. (2003) Cook et al. (2012)
Germanite	$Cu_{13}Fe_2Ge_2S_{16}$	4	Ge^{4+}	Fe^{3+} (*h*)	Cu^{+}	Mössbauer (^{57}Fe)	Vaughan and Craig (1978)
Renierite	$Cu_{10}ZnGe_2Fe_4S_{16}$	4	Ge^{4+}	Fe^{3+} (*h*)	Cu^{+}	Mössbauer (^{57}Fe)	Bernstein (1986b)
Briartite	$Cu_2(Zn,Fe)GeS_4$	4	Ge^{4+}	Fe^{2+} (*h*)	Cu^{+}	Mössbauer (^{57}Fe)	Imbert et al. (1973)
GeS	GeS	4	Ge^{2+}	–	–	XRD	Wiedemeier and Schnering (1978)
Chalcopyrite	$CuFeS_2$	4	?	Fe^{3+} (*h*)	Cu^{+}	XANES (Fe, Cu L-edges)	Goh et al. (2006)
Covellite	CuS	4	?	–	Cu^{+}	XANES (Cu L-edge)	Goh et al. (2006)
Stannite	Cu_2FeSnS_4	4	–	Fe^{2+} (*h*)	Cu^{+}	Mössbauer (^{57}Fe, ^{119}Sn)	Di Benedetto et al. (2005b)
Pyrite	FeS_2	6	–	Fe^{2+} (*l*)	–	Mössbauer (^{57}Fe)	Vaughan and Craig (1978)
Arsenopyrite	FeAsS	6	–	Fe^{2+} (*l*)	–	Mössbauer (^{57}Fe)	Vaughan and Craig (1978)

CN coordination number
? unknown oxidation state
h high spin Fe
l low spin Fe

Table 6.2 – Origins and compositions of analysed samples. Concentrations were determined by EPMA (wt.%) and LA-ICP-MS (ppm). Experimental methods are detailed in Belissont et al. (2014).

Mineral	Sample	Ge	Cu	Fe	Origin
Sphalerite	64W, 62E, SAL-UN	15–2580 ppm	41–8170 ppm	1.2–3.1 wt.%	Saint-Salvy, France
	A38	*bdl*–950 ppm	20–1280 ppm	1.4–1.8 wt.%	Kipushi, D.R. Congo
Germanite	TSU1	6.0–11.1 wt.%	41.2–45.0 wt.%	3.7–14.0 wt.%	Tsumeb, Namibia
	U48	9.2 wt.%	47.5 wt.%	0.2–0.5 wt.%	Kipushi, D.R. Congo
Renierite	K2208, U48	7.8–9.0 wt.%	40.8–42.8 wt.%	13.2–13.5 wt.%	Kipushi, D.R. Congo
Briartite	P717	16.6 wt.%	34.0 wt.%	10.8 wt.%	Kipushi, D.R. Congo
GeS	GeS	69.4 wt.%	–	–	Synthetic
Chalcopyrite	2BARR5	160–4660 ppm	34.6 wt.%	29.1 wt.%	Barrigão, Portugal
Covellite	P717	0.3 wt.%	71.6 wt.%	0.3 wt.%	Kipushi, D.R. Congo
Stannite	Oruro	*nm*	29.6 wt.%	13.0 wt.%	Oruro, Bolivia
Pyrite	2BARR5	*nm*	0.12–0.29 wt.%	46.5 wt.%	Barrigão, Portugal
Arsenopyrite	LAU20	*nm*	*nm*	34.3 wt.%	Lauriéras, France

nm not measured
bdl below detection limit (~1 ppm with LA-ICP-MS)

μ-XRF and μ-XANES data collection

μ-XRF and μ-XANES measurements were performed on the BM23 beamline at the European Synchrotron Radiation Facility (ESRF, Grenoble, France). The storage ring was operated at 6 GeV in multibunch mode with a ~200 mA current. X-rays were generated using a bending magnet (BM) and monochromatised with a fixed-exit double-crystal Si(111) monochromator. Micro-focusing of X-rays into an incident beam of ~3×3 μm^2 was achieved using two mirrors

in Kirkpatrick-Baez (KB) geometry. For the sphalerite samples and reference compounds, XRF and XANES (fluorescence mode) data were collected with a Vortex silicon-drift energy-dispersive detector located 90° from the incident beam. μ-XRF maps were collected at 11.3 keV in order to measure Ge, Cu and Fe Kα-lines. Selected regions in sphalerite samples were mapped with a typical step-size of 10 μm depending on the area mapped. Dwell-time was adjusted to 0.5 s. Using the μ-XRF maps, several spots of interest were selected in sector zones and dark and light brown bands in order to measure μ-XANES spectra. The XRF spectra (one spectrum per pixel) were converted into element-specific XRF-intensity maps using batch curve fitting of Ge-Kα (convolved with the Zn-Kβ line), Cu-Kα, and Fe-Kα lines, using the PyMCA software (Solé et al., 2007).

XANES spectra were collected at room temperature by scanning the monochromator over the energy ranges of 10970–11500 eV for Ge, 8870–9220 eV for Cu, and 7025–7305 eV for Fe. Constant energy increments of 0.5 eV for Ge and Cu and 0.2 eV for Fe were used around the absorption edges. Above this region, the energy increment was progressively increased, to about 2 eV at the upper end of the scan. The spectrum of a Fe foil, collected in transmission mode, was used to calibrate the energy (edge inflexion at 7112.0 eV). The drift of the incident X-ray beam was less than 3 μm between 7 and 11 keV. Complementary XANES spectra were collected on the ID26 beamline (ESRF, Grenoble, France). X-rays were generated using an insertion device (ID), monochromatised using a cryogenically-cooled fixed-exit double-crystal Si(111) monochromator, and focused into an incident beam of $\sim$1$\times$2 mm^2 with a high X-ray photon flux. Five analyser crystals were used to resolve the Zn-Kβ interference with Ge-Kα, allowing absorption studies to be conducted on very dilute samples. Thorough examination of incident beam (I_0) glitches showed the occurrence of long-term instrumental drift of up to 0.67, 2.10 and 1.18 eV for Ge, Cu and Fe, respectively. The data were therefore corrected using the glitches of I_0 for 'internal calibration'. For cubic lattices, electronic dipole transitions (e.g., $1s \rightarrow 4p$) are isotropic whereas electronic quadrupole transitions (e.g., $1s \rightarrow 3d$) are anisotropic (e.g., Juhin et al., 2008; Muñoz et al., 2013). Orientation effects are therefore unlikely to be significant in the XANES spectra of single cubic crystals (e.g., sphalerite, germanite and pyrite), with the exception of the Fe-K pre-edge feature, which is primarily related to $1s \rightarrow 3d$ transitions.

XANES data reduction was carried out using the Athena package based on the IFEFFIT program (Newville, 2001), including data merging and normalisation. Edge centroid positions were determined using the main peak centroid on the first derivative spectra, from which the centroid of the main positive peak was calculated. This method is particularly useful for comparing highly structured edges such as Cu or Fe K-edges. For the sphalerite samples, the uncertainty in the pre-edge position chiefly originates from the merging procedure; the uncertainty was less than 0.20 eV at the Ge K-edge (due to relatively noisy spectra) and less than 0.05 eV at the Cu and Fe K-edges. Fits of Fe-K pre-edge features were performed in batch processing mode using the XasMap package, initially designed for dispersive μ-XANES mapping applications (Muñoz et al., 2006, 2008). Pre-edge background modelling was based on the adjustment of the tail of a Gaussian function, while peaks were fitted using two or three pseudo-Voigt functions. Errors in the centroid energy position are estimated to be $\pm$0.05 eV.

Ab initio calculations

The energy and intensity of the electronic transitions that give rise to the absorption K-edge spectrum depend upon the oxidation state of the excited atom, the coordination symmetry, and the ligand type. Like many elements, Ge, Cu and Fe show significant edge-feature shifts toward higher energies with increasing oxidation state, as well as variations in intensity and shape with changes in coordination and differences in both edge feature position and shape with changes in ligand type (Pugsley et al., 2011; Kau et al., 1987; Waychunas et al., 1983, respectively).

Because the availability of Ge K-edge XANES data is rather limited in the literature, *ab initio* XANES calculations were used to better understand the variations observed in our experimental data in terms of oxidation state, coordination and ligand type, and to improve the calibration with model compounds. Computations were performed using the FEFF8.2 software (Ankudinov et al., 1998; Rehr et al., 1992) for selected compounds at the Ge K-edge. A self-consistent field (SCF card) multiple-scattering procedure was used to model charge transfer between atoms during the photo-electronic process, up to 3.3 Å. Full multiple scattering (FMS card) calculations were performed for the first eight shells of atoms.

The crystal structures of the Ge-bearing sulphides used in the calculations were those of GeS_2 (Zachariasen, 1936), renierite (Bernstein et al., 1989), germanite (Tettenhorst and Corbato, 1984) and argyrodite (Eulenberger, 1977). The crystal structure of GeS was approximated by the substitution of Sn by Ge in the natural compound herzenbergite (SnS) available in Schnering and Wiedemeier (1981). Calculations for GeO_2 were performed on the crystal structures of rutile-like polymorphs (argutite) with octahedral Ge^{4+} (Haines et al., 2000; Shiraki et al., 2003).

6.2.3 Results

Element distribution

X-ray fluorescence maps of Ge, Cu and Fe in sphalerite from Saint-Salvy are shown in Fig. 6.2. In sample 64W (Fig. 6.2a), Cu is enriched in the sector zoning and to a lesser extent in the adjacent optically-dark rhythmic bands. Germanium is enriched in the sector zoning and depleted in the dark rhythmic bands. Conversely, Fe is enriched in the rhythmic bands (especially in the optically-dark bands) and depleted in the sector zoning. This typical antithetic distribution of Cu, Ge and Fe is also observed in samples 62E (Fig. 6.2b) and SAL-UN (Fig. 6.2c-d), and is consistent with the observations of Belissont et al. (2014) from secondary electron microscope (SEM) and multivariate statistical analysis of LA-ICP-MS data.

The Ge-rich sphalerite sample from Kipushi (Fig. 6.3) displays sector-like zoning that is enriched in Ge (Fig. 6.3a). In contrast with the sphalerite from Saint-Salvy, neither Cu nor Fe show any distinguishable variations. SEM mapping performed in energy dispersive mode (EDS, Fig. 6.3b) shows that the Ge instead occurs in Ge–Cu-rich micro- or nano-clusters, substituting for Zn.

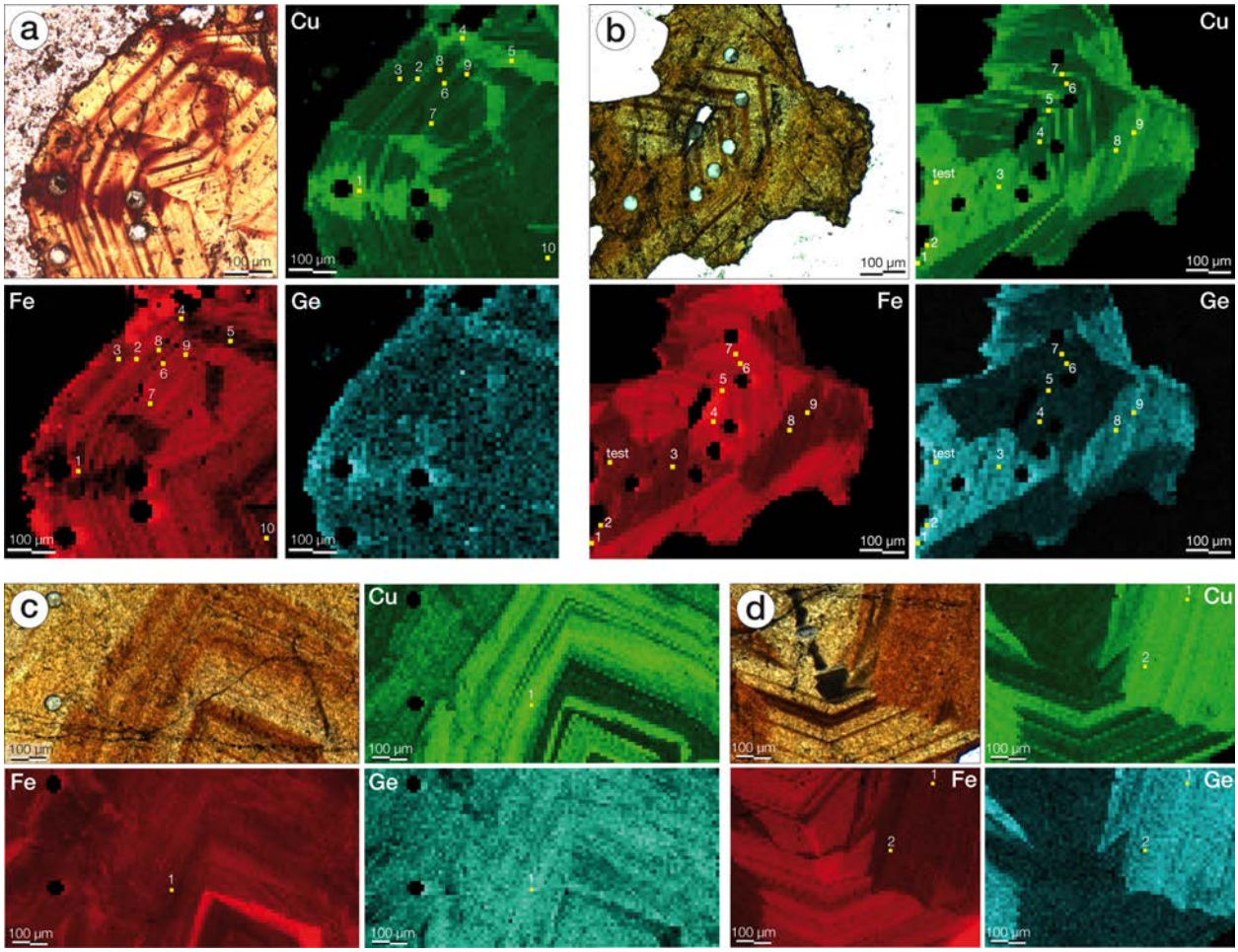

Fig. 6.2 – Microphotograph of the region of interest in transmitted light (top left) and XRF maps of Cu (green), Fe (red) and Ge (blue) in Saint-Salvy sphalerite samples. Holes of 44 μm diameter are LA-ICP-MS craters (see Belissont et al., 2014). Numbered spots correspond to μ-XANES acquisitions. **a**. Sample 64W. **b**. Sample 62E. **c**. Sample SAL-UN (rhythmic bands) **d**. Sample SAL-UN (rhythmic bands between two overlapping sector zones).

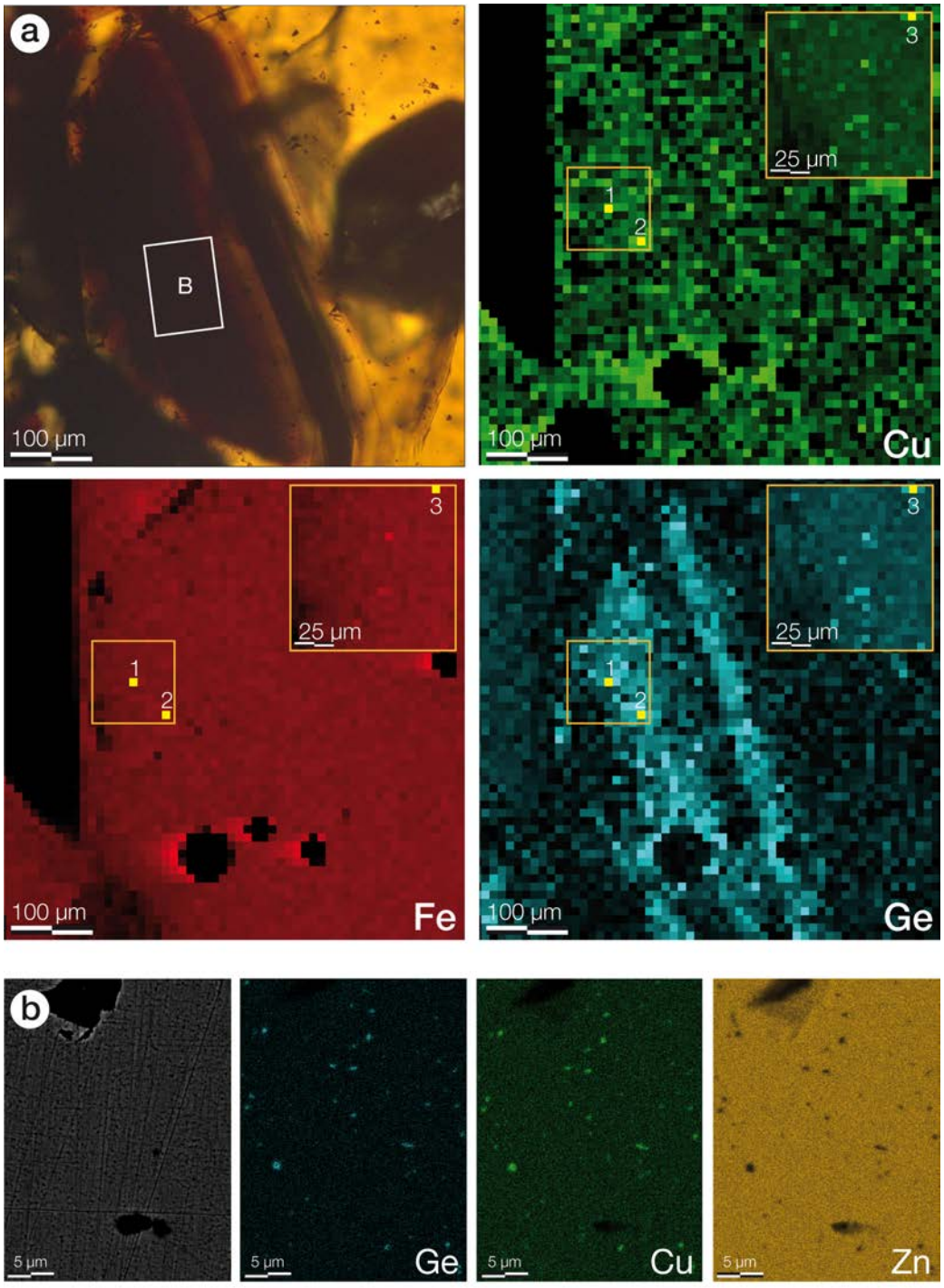

Fig. 6.3 – **a**. Microphotograph of the region of interest in transmitted light (top left) and XRF maps of Cu (green), Fe (red)and Ge (blue) in the Kipushi Ge-rich sphalerite sample (A38). Holes of 60 and 32 μm diameter are LA-ICP-MS craters. Numbered spots indicate μ-XANES acquisitions. **b**. SEM maps in energy dispersive mode (EDS) of Ge, Cu and Zn showing Ge-Cu nano- or micro-inclusions. Map locations are indicated on the top-left microphotograph shown in (a).

Germanium *K*-edge

Model compounds

Germanium K-edge XANES spectra for Ge-bearing model compounds are shown in Fig. 6.4a and their known crystal chemistries are presented in Table 6.1. With the exception of GeS, the model compounds all show steep white lines of similar height originating from $1s \rightarrow 4p$ transitions, as well as similar post-edge features corresponding to transitions towards p–like partially filled states and multiple scattering resonances. GeS, however, exhibits less-intense post-edge features together with an absorption edge shifted towards lower energies. The edge positions are located at 11108.9 ± 0.2 eV in the Ge^{4+}-bearing model compounds (renierite, germanite, and briartite) and at 11107.2 eV in Ge^{2+}-bearing GeS (Table 6.3), indicating a shift of 1.7 eV between Ge^{2+} and Ge^{4+} in sulphide compounds. Accordingly, Ge-bearing chalcopyrite and covellite show edge positions at 11109.1 and 11108.9 eV, respectively, suggesting a formal Ge^{4+} oxidation state in these minerals.

In Fig. 6.5, *ab initio* XANES calculations performed at the Ge K-edge for GeS and Ge^{4+}-bearing sulphides perfectly support the edge-shift of about 1.7 eV observed in the experimental data. The edge positions of renierite, germanite and argyrodite are similar to that of GeS_2, indicating that the formal oxidation state Ge^{4+} in these compounds is unequivocal. Rutile-like GeO_2 (r-GeO_2, octahedral Ge) spectra are in good agreement with experimental spectra reported in the literature (Andrault et al., 1995; Bertini et al., 2003; Vaccari et al., 2009; Baldini et al., 2010). The edge shift of 5.1 eV between r-GeO_2 and GeS is similar to the experimental shift of 5.8 eV reported in Pugsley et al. (2011). For Ge^{4+} compounds, the edge shift of 3.6 eV between r-GeO_2 and Ge-bearing sulphides highlights the strong differences in Ge K-edge positions in the case of Ge–S and Ge–O bonds, indicating that the use of GeO_2 as a standard for the estimation of Ge oxidation state in sulphides would result in a severe underestimation.

The differences in the bond nature and length between oxide/silicate and sulphide compounds are indeed significant. Although Ge favours covalent bonding with many ligands, Ge–O bonds have about 31% ionic character and are shorter (about 1.75 Å) and stronger than Ge–S bonds, which have only 7% ionic character and are about 2.27 Å long (Bernstein, 1985; Li et al., 2009). This shifts the core electron binding energy in oxides/silicates, and thus likewise the onset of the absorption edge, to higher values compared to sulphides. In addition, in experimental spectra, the edge of q-GeO_2, the quartz-like GeO_2 polymorph with tetrahedral Ge, is reported as being about 0.8–1.0 eV below the edge of r-GeO_2 (Vaccari et al., 2009; Baldini et al., 2010; Pugsley et al., 2011). This indicates that changes in coordination also affect Ge K-edge features. According to our calculations and the literature data, only sulphide standards are therefore suitable for calibrating sphalerite if we are to avoid any misinterpretation.

Sphalerite samples

Germanium K-edge XANES spectra in sphalerite are shown in Fig. 6.6a. Due to interferences between the Ge K-α and Zn K-β lines, the spectra were recorded only in spots with Ge contents higher than about 700 ppm, thus enabling the signal-to-noise ratio to be significantly reduced. In the sphalerite from Saint-Salvy, such concentrations mostly occur in the

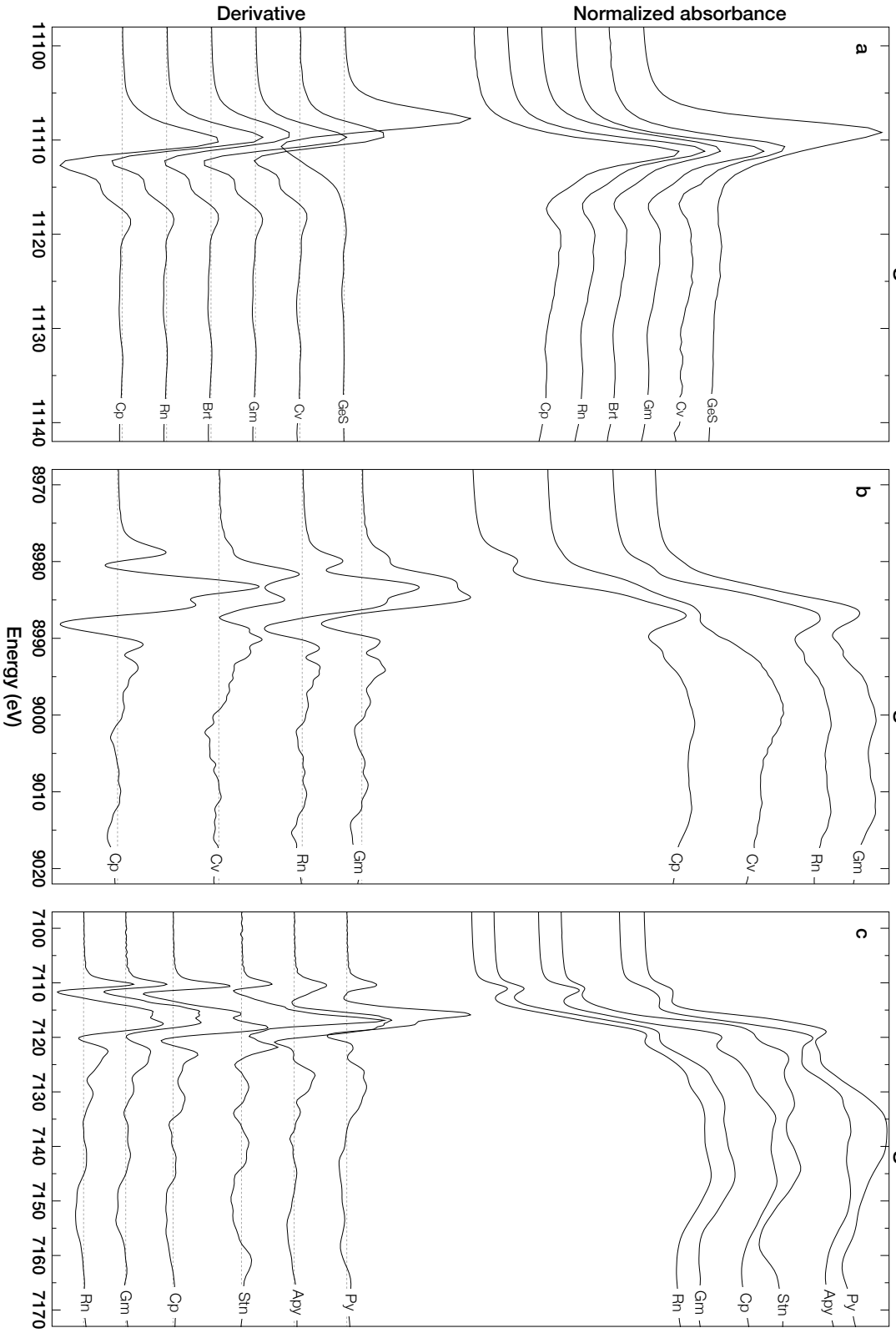

Fig. 6.4 – Normalised XANES spectra and corresponding derivatives at the Ge (**a**), Cu (**b**) and Fe (**c**) *K*-edges for renierite (Rn), germanite (Gm), briartite (Brt), chalcopyrite (Cp), covellite (Cv), stannite (Stn), pyrite (Py) and arsenopyrite (Apy).

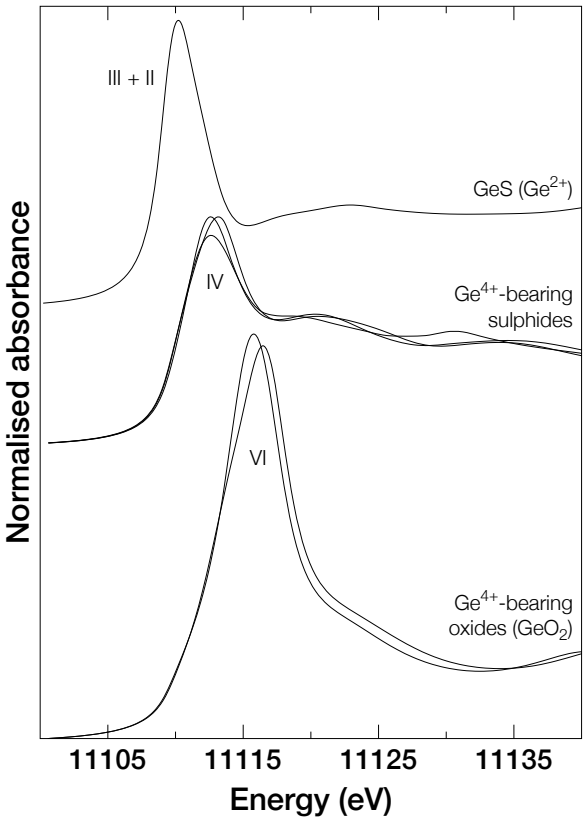

Fig. 6.5 – Ab initio calculations at the Ge *K*-edge of Ge^{2+}- and Ge^{4+}-bearing compounds, with sulphur and oxygen ligands. Ge^{4+}-bearing sulphides include GeS_2, renierite, and argyrodite, all of which have tetragonal Ge. GeO_2 have rutile-like structures with octahedral Ge. Roman numerals refer to coordination number.

sector zoning and Ge contents rarely exceed 500 ppm in the rhythmic bands. Consequently, Ge *K*-edge XANES were recorded in both types of zoning in sample SAL-UN (the richest in Ge), but only in the sector zoning in sample 62E. None of the XANES records for sample 64W were considered acceptable due to the presence of significant noise. To overcome this issue, additional 'bulk' XANES spectra were recorded in samples 64W and SAL-UN on the ID26 beamline. SAL-UN was then used to match energy calibration between the BM23 and ID26 spectra.

The average Ge *K*-edge position of sphalerite from both Saint-Salvy and Kipushi (A38) is 11109.0 ± 0.2 eV. This is close to the average position of Ge^{4+}-bearing model compounds (11108.9 ± 0.2 eV, Table 6.3), which suggests a dominantly Ge^{4+} oxidation state for the sphalerites from the two localities. In the Ge-rich zoned sphalerite from the Saint-Salvy deposit, the edge positions obtained for different spots within the same type of zoning varied by a maximum of 0.2 eV in any given crystal. These spectra were therefore merged into a 'bulk' spectrum in order to improve the counting statistics (as presented in Table 6.4). The shift in edge position between the sector zoning and the dark rhythmic bands is only 0.03 eV in sample SAL-UN (Table 6.4). The maximum edge shift between the edge positions of samples 64W and 62E is 0.2 eV. Assuming that the edge energy increases linearly with increasing valence from +2 to +4 by a shift of 1.7 eV (Table 6.3), the above variations in edge position within and between zoning types (0.2 and 0.03 eV, respectively), and between samples (0.2 eV) can therefore be considered negligible and can be neglected. There is therefore no evidence for significant redox variation, suggesting a formal Ge^{4+} oxidation state for the sphalerite from Saint-Salvy.

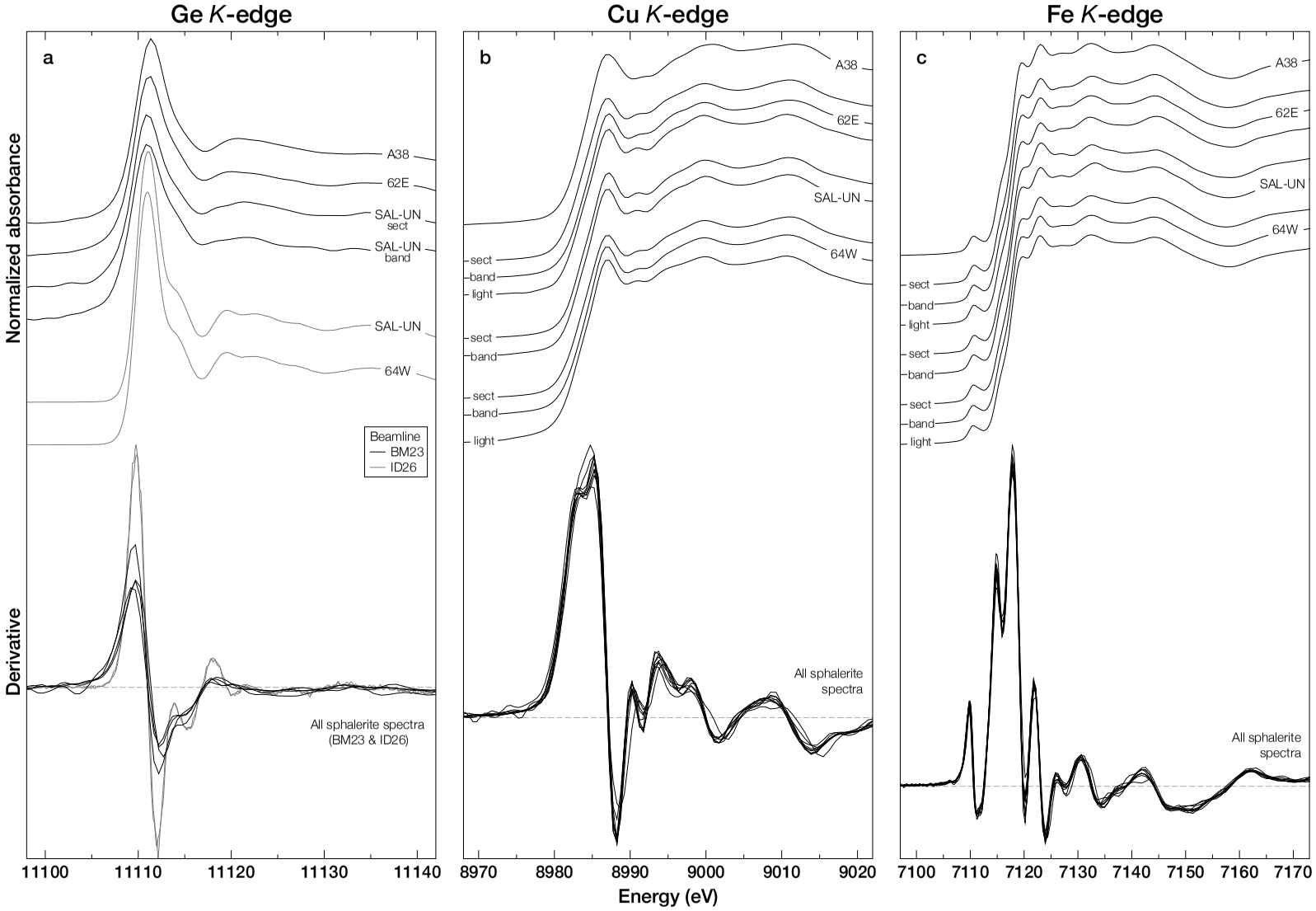

Fig. 6.6 – Normalised and derivative XANES spectra at the Ge (**a**), Cu (**b**) and Fe (**c**) *K*-edges for the studied sphalerite samples and zoning types. Samples 64W, 62E and SAL-UN are from Saint-Salvy (France) and A38 is from Kipushi (D.R. Congo).

Copper *K*-edge

Model compounds

Copper *K*-edge XANES spectra in Cu-bearing model compounds are shown in Fig. 6.4b and their known crystal chemistries are presented in Table 6.1. Cu-bearing model compounds show an absorption edge at about 8983.1 ± 0.6 eV, as is typical for Cu^{+} (Kau et al., 1986). The edge is structured with two shoulders from about 8980 to 8989 eV as highlighted on the first derivative spectra. The edge positions of renierite and germanite are at 8983.0 and 8982.9 eV, respectively, similar to the edge position of chalcopyrite (8983.9 eV; Table 6.3). All compounds show a distinct pre-edge feature below 8980 eV, which decreases in intensity from chalcopyrite, to renierite, germanite and covellite, where it forms only a tiny shoulder below the edge threshold.

The presence of a pre-edge feature below 8980 eV usually corresponds to transitions towards the $3d$ empty state due to the d^9 configuration of Cu^{2+} in the ground state (Kau et al., 1987; Petiau et al., 1988). However, Cu $2p$ XPS and Cu *L*-edge XANES have shown that copper in chalcopyrite and covellite is formally Cu^{+}, with the ground state being a mixture of Cu $3d^{10}4s^{0}$, Cu $3d^{10}4s^{1}\underline{S}$ ($\underline{S}$ = hole in a sulphide ligand) and Cu $3d^{9}4s^{1}$ configurations (Pearce et al., 2006; Goh et al., 2006, and references therein). Therefore, the d-like unfilled states allow $1s \rightarrow 3d$ electronic quadrupole transitions to occur, resulting in the observed pre-edge. Because of the greater availability of d-like empty states in the nominally d^9 system, the pre-edge feature should be more intense in Cu^{2+} compounds than in Cu^{+}-bearing compounds. Chalcopyrite, renierite and germanite all share sphalerite-type structures with Cu in a tetrahedral site. The very similar XANES features observed in these compounds therefore strongly suggest the presence of Cu^{+} in renierite and germanite.

The choice of relevant compounds is difficult for Cu^{2+} because no evidence has yet been found for the presence of Cu^{2+} in any sulphide minerals (Goh et al., 2006) and also because, if present, its site would be distorted (Petiau et al., 1988). Kau et al. (1987) presented XANES spectra for complexes with Cu^{+} and Cu^{2+} surrounded by four S ligands in tetrahedral geometry, showing an edge energy difference of 1.6 eV. This edge shift should be a good analogue for what we might expect to find between tetrahedral Cu^{+} and Cu^{2+} (if present) in a sulphide lattice. Of note, the presence of a pre-edge feature for the Cu^{+} complex, similar to that which we observe for chalcopyrite, has been attributed to the highly covalent nature of the S_4 ligand field (Kau et al., 1987).

Sphalerite samples

Copper *K*-edge XANES spectra for sphalerites from Saint-Salvy and Kipushi are shown in Fig. 6.6b. The XANES features for sphalerite are similar in shape and position (edge energy of 8983.5 ± 0.2) to those for chalcopyrite, renierite and germanite (edge energy of 8984.9 ± 0.1 eV), albeit that no pre-edge feature is observed in the sphalerite. For the Saint-Salvy samples, the variability in the Cu *K*-edge position is less than 0.3 eV within and between the different types of zoning (Table 6.4). In sample 62E, the maximum variability in the edge position between sector zones and light rhythmic bands is about 0.27 eV. Again, between samples 64W and SAL-UN, a maximum shift of 0.39 eV is observed. Compared to the energy shift of 1.6 eV in going from Cu^{+} to Cu^{2+} tetrahedrally-complexed with S, the

edge variations measured in sphalerite from Saint-Salvy (i.e., a maximum of 0.39 eV) are thus negligible and can be neglected. Thus, no significant variation in the Cu oxidation state is observed in sphalerite from Saint-Salvy, suggesting that the copper is monovalent.

Iron *K*-edge

Model compounds

Iron *K*-edge XANES spectra of model sulphides are shown in Fig. 6.4c and their known crystal chemistries are given in Table 6.1. The spectra show a main absorption edge located at about 7117.0 ± 0.2 eV. All spectra show a distinct pre-edge peak at 7111–7112 eV due to $1s \rightarrow 3d$ electronic quadrupole transitions (Waychunas et al., 1983). Fe^{3+} compounds (i.e., renierite, germanite, chalcopyrite) show an edge structure characterised by two features (or shoulders) between 7112 and 7119 eV for all compounds, highlighted by a doublet on the first derivative spectra. Renierite and germanite have similar edge positions (∼7116.6 eV) and shapes, as well as similar post-edge features. The edge for chalcopyrite, however, is located 0.7 eV higher (7117.3 eV), and slight differences are observed in the doublet relative intensity and post-edge features. The edge for Fe^{2+} compounds (i.e., stannite, pyrite, arsenopyrite) rises monotonically, showing a single peak on the first derivative spectra. The edge positions of pyrite and arsenopyrite (∼7117.2 eV, octahedral low-spin Fe) are located 0.8 eV above that of stannite (7116.4 eV, high-spin Fe), probably due to their different coordination and spin-state configurations. In addition, these two compounds have very distinct post-edge features. In particular, there is an edge shift of only 0.2 eV (stannite → renierite/germanite) or 0.9 eV (stannite → chalcopyrite) from Fe^{2+} and Fe^{3+} in high-spin tetrahedral configuration. However, the pre-edge features vary in the most clearly systematic manner with site geometry, metal-ligand bond type and oxidation state (e.g., Waychunas et al., 1983).

Fe-*K* pre-edge characteristics (centroid position and integrated intensity) have been extensively used to quantify the redox state of Fe in a number of earth materials, mostly oxide and silicate minerals and glasses (e.g., Waychunas et al., 1983; Galoisy et al., 2001; Wilke et al., 2001; Prietzel et al., 2007; Wilke et al., 2009; Muñoz et al., 2013). The pre-edge region is primarily related to quadrupolar $1s \rightarrow 3d$ electronic transitions. Non-centrosymmetric sites (e.g., tetrahedral sites) have more intense pre-edge features than centrosymmetric sites (e.g., octahedral sites) due to the addition of dipolar allowed $1s \rightarrow 4p$ electronic transitions, attributed to mixing of Fe $4p$ into the $3d$ orbital (e.g., Dräger et al., 1988; Westre et al., 1997). Normalized pre-edge peaks reveal three different shapes depending on the spin state and the coordination of iron (Fig. 6.7a). Peak fitting allows integrated intensity and centroid energy values to be derived, as shown in Fig. 6.7c).

The pre-edge centroids for pyrite and arsenopyrite (octahedral Fe^{2+}) are located at high energy (at 7111.7 eV and 7111.9 eV, respectively) due to the low-spin configuration of iron (e_g-like first empty states). The pre-edge shapes of pyrite and arsenopyrite can be modelled reasonably well using two peaks of similar intensity (i.e., at ∼7111.2 eV and ∼7112.7 eV). Pyrite and arsenopyrite have a distorted iron octahedron site (point group S_6), therefore, only electronic quadrupole transitions are permitted. The strong hybridisation of the Fe $3d$ e_g-like states with Fe $4p$ and S $3p\sigma^*$ states (covalent bonds) can explain their relatively

Sample	Edge position (eV)			
	Ge	Cu	Fe	pre-edge
Germanite	11108.97	8982.88	7116.47	7111.08
Renierite	11109.05	8983.04	7116.73	7111.09
Briartite	11108.72	–	–	–
GeS	11107.20	–	–	–
Chalcopyrite	11109.09	8983.91	7117.30	7111.40
Covellite	11108.87	8982.45	–	–
Stannite	–	–	7116.38	7110.80
Pyrite	–	–	7117.06	7111.70
Arsenopyrite	–	–	7117.28	7111.87

Table 6.3 – Ge, Cu and Fe edge positions and measured concentrations for the zoning types in each sphalerite sample.

intense pre-edge features for an octahedral arrangement (e.g., Petiau et al., 1988; Mosselmans et al., 1995) as well as the appearance of a doublet rather than a singlet as is observed in low-spin ferrous complexes (Westre et al., 1997).

The pre-edge peak for stannite (high-spin tetrahedral Fe^{2+}) is less intense, located at a lower energy, around 7110.8 eV, and is primarily defined by two contributions (~7110.6 and ~7112.0 eV). The pre-edge peaks for germanite and renierite are positioned at higher energy, around 7111.1 eV, and the pre-edge peak for chalcopyrite is located at around 7111.4 eV. All three have high-spin tetrahedral Fe^{3+} and show a more intense pre-edge, largely defined by a single peak. The $1s \rightarrow 3d$ features for tetrahedral Fe^{2+}- and Fe^{3+}-bearing sulphides are similar to those observed for iron complexes, oxides, and silicates (Westre et al., 1997; Wilke et al., 2001; Berry et al., 2010; Muñoz et al., 2013). For both high-spin Fe^{2+} and Fe^{3+} in tetrahedral coordination, the pre-edge feature gains intensity through allowed quadrupole and dipole electronic transitions to mixed $3d$-$4p$ orbitals in a non-centrosymmetric environment. The pre-edge centroid energy varies by ~0.6 eV between the divalent and trivalent states. The ~0.3 eV variation in the centroid position between germanite/renierite and chalcopyrite can be attributed to crystal orientation effects on the quadrupole transition.

Sphalerite samples

Iron K-edge XANES spectra for sphalerite samples are presented in Fig. 6.6c. The average K-edge position is 7116.7 ± 0.05 eV, close to that of renierite and germanite (7116.60 ± 0.19 eV). The sphalerite from Saint-Salvy does not exhibit any significant variation in the Fe K-edge position, neither within or between the two zoning types nor between samples. A maximum edge variation of 0.13 eV occurs between sector zones and dark bands in sample SAL-UN (Table 6.4). Moreover, the sphalerite spectra are all very similar throughout the XANES region, which may suggest a unique Fe oxidation state and speciation in this mineral.

Pre-edge centroid positions and integrated intensity are plotted in Fig. 6.7c. The points corresponding to the Saint-Salvy sphalerite samples are grouped around 7110.8 eV in an area of 0.2 eV in energy (Fig. 6.7b-c), and there is no direct correlation with the type of zoning. The pre-edge peaks of sphalerite are composed of a single intense peak at around 7110.6 eV and a shoulder at 7111.7 eV, with a total intensity (0.26) that is about half that of

Table 6.4 – Ge, Cu and Fe edge positions for the zoning types in each sphalerite sample and their respective contents

		Edge position (eV)				Content⋆ (ppm)		
Sample	**Zoning**	**Ge**	**Cu**	**Fe**	**pre-edge**	**Ge**	**Cu**	**Fe**
Saint-Salvy, France								
64W	Sector	–	8983.21	7116.63	7110.81	726	4887	19601
	Dark band	11108.84†	8983.34	7116.62	7110.75	98	2328	26552
	Light area	–	8983.19	7116.62	7110.75	95	336	22753
62E	Sector	11109.06	8983.47	7116.68	7110.88	2203	4306	16308
	Dark band	–	8983.68	7116.69	7110.88	249	2858	25302
	Light area	–	8983.74	7116.68	7110.86	242	555	26465
SAL-UN	Sector	11108.93	8983.61	7116.77	7110.92	1544	3647	17649
	Dark band	11108.90	8983.67	7116.63	7110.85	360	1799	19882
Kipushi, D.R. Congo								
A38	Sector	11109.33	8983.51	7116.66	7110.78	883	1270	17360

– when not determined

⋆ LA-ICP-MS data from Belissont et al. (2014)

† bulk measurement on ID26 beamline (ESRF)

chalcopyrite (0.45), consistent with the previous observations of Petiau et al. (1988). The pre-edge positions and structures for sphalerite are similar to those obtained for stannite (though slightly more intense), suggesting that high-spin Fe^{2+} occur in tetrahedral coordination. The 0.2 eV variation in the pre-edge centroid positions and the higher intensities can be attributed to crystal orientation effects and/or rare occurrences of Fe^{3+} in the tetrahedral site.

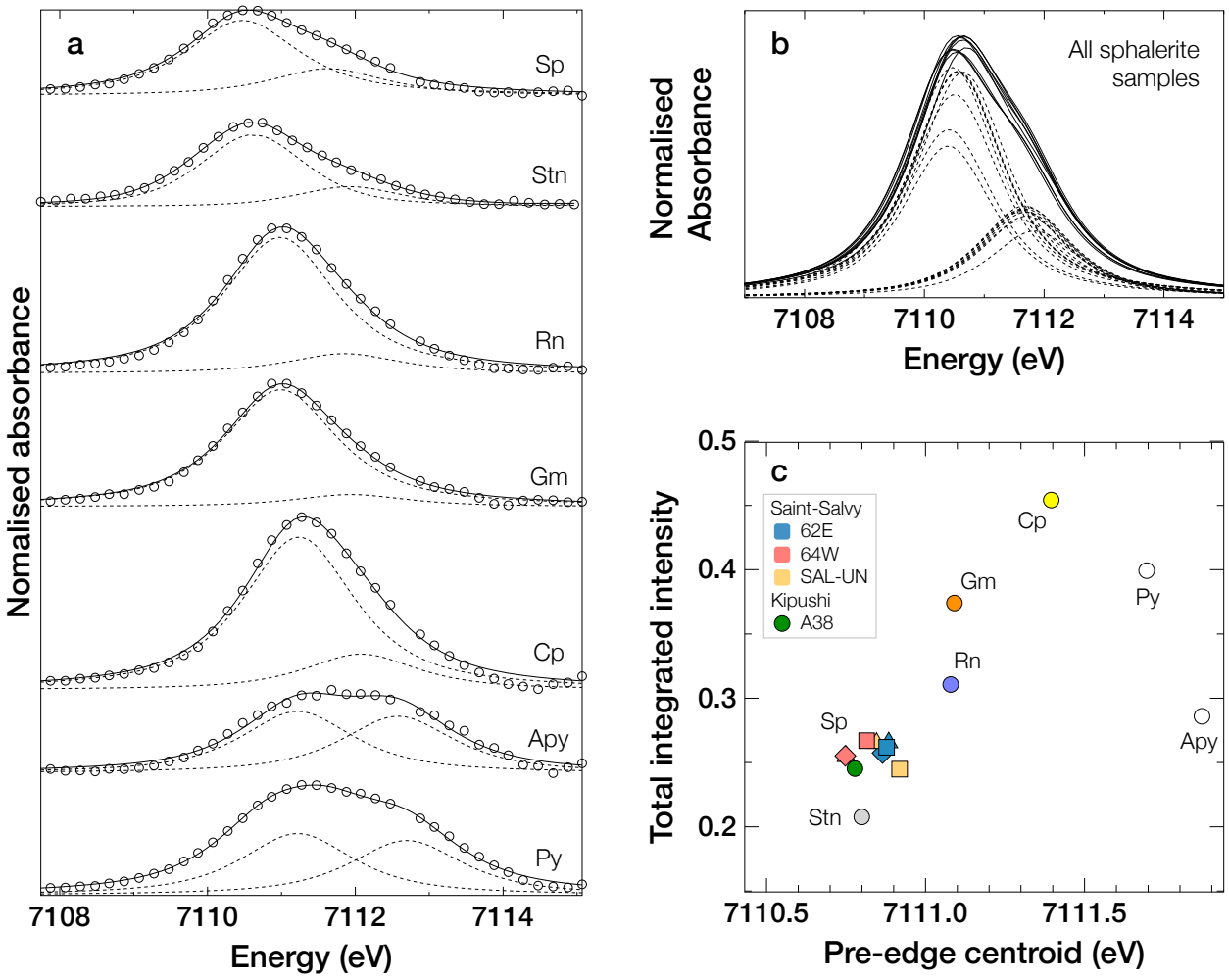

Fig. 6.7 – a. Normalised Fe-*K* pre-edge spectra and model fits (XasMap) for a sphalerite sample (A38) and for the model sulphide compounds. Open circles represent experimental data, the dotted lines show the contributions of each transition to the model, and solid lines show the resulting fit. **b**. Normalised Fe-*K* pre-edge fitted curves for all sphalerite samples (solid lines) and the two transition contributions to the model (dotted lines). The curves are all near-identical in shape. **c**. Fe-*K* pre-edge information (total integrated intesity vs. centroid position) for the model compounds and sphalerite samples. Renierite (Rn), germanite (Gm) and chalcopyrite (Cp) have high-spin $^{IV}Fe^{3+}$. Stannite (Stn) has high-spin $^{IV}Fe^{2+}$. Pyrite (Py) and arsenopyrite (Apy) have low-spin $^{VI}Fe^{2+}$. In sphalerite from Saint-Salvy, □ refers to sector zoning, △ is for dark rhythmic bands, and ◇ is for light rhythmic bands.

6.2.4 Discussion

Formal oxidation states of Ge, Cu and Fe

Our data support the presence of tetrahedral Ge^{4+} in sphalerite, whatever the zoning type and sample, as well as in chalcopyrite and covellite where Ge is present as a trace component. We find no evidence for the presence of Ge^{2+} which would be compatible with a direct substitution $Zn^{2+} \leftrightarrow Ge^{2+}$ in sphalerite. The presence of Ge^{2+} in the Ge-rich sphalerite from Tres Marias (Mexico) was previously inferred due to the lack of correlation between Ge and monovalent ions for charge compensation (Cook et al., 2009), however, a recent XANES study has provided formal evidence for tetrahedral Ge^{4+} (Cook et al., 2015). Indeed, in a covalently bonded crystal, Ge^{2+} is unlikely to occupy tetrahedral sites but instead occurs in trigonal-pyramidal coordination. The latter is similar to tetrahedral coordination, though one of the apices is composed of a lone pair of electrons (Bernstein, 1985). For instance, GeS (orthorhombic) is composed of a double layer structure in which Ge^{2+} occurs in a 3-fold coordination (ionic bonds of ∼3.494 Å) and also shares two covalent bonds (∼2.443 Å) inside one of the layers, resulting in a (3+2) coordination (Wiedemeier and Schnering, 1978). The presence of Ge^{2+} in sulfosalts with trigonal-pyramidal Sn^{2+} has previously been suggested for $PbSnS_2$ containing ∼700 ppm Ge (Moh, 1976) without discarding coupled substitution of Sn^{2+} by Ge^{4+} with some form of charge compensation, and also for morozeviczite $Pb_3Ge_{1-x}S_4$ (Harańczyk, 1975). Even in the germanate spinel brunogeierite Fe_2GeO_4 (Johan et al., 1983; Welch et al., 2001), Ge is now understood to occur in the tetravalent state (Cempirek and Groat, 2013).

The oxidation state of copper in sulphide minerals has for many years been quite controversial. It is now generally accepted that the Cu in sulphide minerals is nominally Cu^+, though a d^9 character can be observed in chalcopyrite, triggering the presence a Cu-K pre-edge that is usually diagnostic of the Cu^{2+} state (Kau et al., 1987; Folmer and Jellinek, 1980; Goh et al., 2006; Buckley et al., 2007). The only exception may be in the tetrahedrite group, where small amounts of Cu^{2+} may occur in divalent metal sites (Pattrick et al., 1993b), even though tetrahedral coordination for Cu^{2+} is somewhat unlikely (Pattrick et al., 1997). Cu^+ has been reported in Cu-bearing sphalerite (Cook et al., 2012) at the *K*-edge and no evidence for the presence of Cu^{2+} in the sphalerite lattice has been found at the *L*-edge (Buckley et al., 2007). Our results, in line with these observations, support the presence of tetrahedral Cu^+ in sphalerite, whatever the type of zoning or sample considered.

Fe-*K* pre-edge features suggest a formal Fe^{2+} oxidation state in sphalerite in agreement with the findings of previous Mössbauer spectroscopic studies (e.g., Gerard et al., 1971; Lepetit et al., 2003; Di Benedetto et al., 2005a). Gerard et al. (1971) detected the presence of 'very small amounts' of Fe^{3+} in Fe-rich sphalerite (> 6 mol.% Fe). Lepetit et al. (2003) showed that temperature and sulphur fugacity control the Fe^{3+}/Fe^{2+} ratio in sphalerite containing more than 7 mol.% Fe. In turn, the Fe^{3+}/Fe^{2+} ratio, with the oxidation of Fe^{3+} to Fe^{2+}, plays on the lattice parameters in summarising the effects of local shrinkage by the creation of vacancies and the effects of dilatations by incoming elements (e.g., Cu). The Fe content in sphalerite from Saint-Salvy and Kipushi (3-4 mol.%) is well below this critical Fe content (around 7 mol.%).

Incorporation of trace elements into sphalerite

In sphalerite from Saint-Salvy, spot concentrations for Ge and Cu range from the ppm level to 2580 and 4080 ppm, respectively, and there is a well-defined Cu–Ge correlation. Iron contents range from 1.2 to 4.2 wt.% (and correlate with isovalent Cd; Belissont et al., 2014). The incorporation of Fe via the isovalent substitution $Zn^{2+} \leftrightarrow Fe^{2+}$ has already been discussed extensively in a number of studies (e.g., Wright, 2009; Di Benedetto et al., 2005a; Wright and Gale, 2010). For the remainder of the discussion, we therefore focus on the incorporation of the heterovalent elements, Ge and Cu.

The incorporation of trace elements into sphalerite is governed by crystal–fluid partition coefficients ($K_{\mathrm{d}}^{i} = [i]_{\mathrm{crystal}}/[i]_{\mathrm{fluid}}$) and their bulk concentrations in the ore-forming fluids. Lattice-strain theory predicts that apart from the ionic radius, the partition coefficient of an element may vary by several orders of magnitude, depending primarily on the pressure, temperature, charge, and phase composition (e.g., McIntire, 1963; Bruce et al., 1998; Blundy and Wood, 1994, 2003). Speciation in the aqueous fluid also exerts a strong influence on the partition coefficient in hydrothermal systems (van Hinsberg et al., 2010). Crystal-scale crystallographic controls on Ge and minor/trace element partitioning associated with rhythmic microscale compositional variations in fluid at the crystal–fluid interface are responsible for the contrast in compositional zoning (Belissont et al., 2014). However, the large difference in bulk sphalerite composition must result either from other parameters that act on the partition coefficients or from large variations in the ore-forming fluid composition.

Metal speciation in aqueous solutions depends on several parameters, including salinity, pH, and the fluid redox condition, which involves f_{O_2} and f_{S_2}. Ge^{4+} and Cu^{+} are the most stable oxidation states in environmental fluids. Being a relatively hard acid in the sense of Pearson (1963), germanium forms the strongest complexes with hard ligands such as hydroxide or fluoride (Wood and Samson, 2006). In contrast, copper, being a transition metal and softer material, predominantly forms complexes with chloride. Pokrovski and Schott (1998b) showed that $Ge(OH)^{\circ}_{4(\mathrm{aq})}$ is the dominant Ge-bearing species in hydrothermal solutions, at concentrations of up to at least 0.05 M over a wide range of pH (0–8) and temperatures (20–350°C). Brugger et al. (2007) found that linear $CuCl_x^{1-x}$ (x=1,2) complexes are stable up to supercritical conditions (P=600 bar, T=25-400°C, salinities up to 17.2 M Cl). The Saint-Salvy ore-forming fluids fall within this range of compositions, with close to neutral pH, high salinity fluids (3.9-4.3 M Cl) and temperatures ranging from 80 to 140°C (Moisy, 1993; Munoz et al., 1994). Therefore, it seems unlikely that modifications of the metal speciation have occurred during ZnS deposition at Saint-Salvy.

Next we consider the charge effect. For elements of similar ionic radius, Wood and Blundy (2001) showed that charge effects yield $K_{\mathrm{d}}^{i^{2+}} > K_{\mathrm{d}}^{j^{3+}} \simeq K_{\mathrm{d}}^{k^{+}} > K_{\mathrm{d}}^{l^{4+}}$, and a strong correlation was found between the partition coefficients of highly charged ions and the bulk composition of the crystal. Large variations in $K_{\mathrm{d}}^{\mathrm{Ge}}$ would therefore be expected if either Ge^{2+} and/or Ge^{4+} can enter the ZnS lattice. However, our μ-XANES data clearly indicate that only Ge^{4+} occurs in the sphalerite from Saint-Salvy, regardless of the zoning type (or Ge content). Likewise, only Cu^{+} and Fe^{2+} are present in the sphalerite from Saint-Salvy, as well as in that from Kipushi.

Thermodynamically, partition coefficients are expected to rely on the entropy of the doped crystal, which for heterovalent elements (e.g., Ge^{4+}, Cu^{+}) depends upon the charge-balancing substitution mechanism (McIntire, 1963; Blundy and Wood, 1994). Our data strongly support a coupled substitution mechanism such as $3Zn^{2+} \leftrightarrow 2Cu^{+} + Ge^{4+}$ (crystal radii of 0.74, 0.53 and 0.74 Å, respectively). *In situ* LA-ICP-MS data from the Saint-Salvy sphalerite (Belissont et al., 2014) show that the Cu content in any part of the crystal is nearly equal to that of the tri- and tetravalent elements (Ge, Ga, In, Sn, Sb). Increased Cu fluid activity should therefore 'enhance' the incorporation of Ge and related trace elements in precipitating sphalerite. However, in sphalerite from Très Marias (Mexico), a high Ge content (∼1081 ppm in Fe-rich zones) unrelated to monovalent element concentrations has been reported (Cook et al., 2009), even though there is no doubt that the Ge occurs as Ge^{4+} (Cook et al., 2015). This suggests that Ge can also enter the sphalerite lattice through the creation of vacancies such as $2Zn^{2+} \leftrightarrow Ge^{4+} + \square$ (vacancy).

No evidence has been found for the presence of divalent Ge and Cu. Hence, the direct substitution $Zn^{2+} \leftrightarrow (Ge^{2+},Cu^{2+})$ seems highly unlikely in sphalerite from Saint-Salvy and Kipushi. Indeed, even though divalent copper may form stable chloro-aqua complexes in the highly saline low-T (20–90°C) hydrothermal fluids and brines generally found in oxidizing near-surface environments (Brugger et al., 2001), the redox potentials of hydrothermal fluids and near-surface environments are generally too high to induce significant formation of divalent Ge species such as Ge^{2+}, $GeOH^{+}$ or $Ge(OH)_2^{\circ}$ (Arnórsson, 1984; Pokrovski and Schott, 1998b) and incorporate them into sphalerite.

Finally, pressure-related effects should be insignificant since deposition of the Saint-Salvy deposit occurred in a small upper-crustal region where the pressure remained constant during the time of deposition (Cassard et al., 1994; Munoz et al., 1994). The sphalerite appears to have been unaffected by any variations in pressure, speciation, or charge effects. Therefore, bulk compositional differences due to the variation in $K_{\mathrm{d}}^{\mathrm{Ge}}$ may be more significantly affected by temperature. For Ge, this is discussed further in the next section, using Ge isotopes as well as variations in concentration in the ore-forming fluid.

Implications for Ge isotopic fractionation

Temperature is a key parameter in controlling both crystal–fluid element partitioning and isotopic fractionation. Belissont et al. (2014) showed a positive correlation between Ge content and the Ge isotopic composition, δ^{74}Ge, in the Saint-Salvy sphalerite, which was interpreted as resulting from kinetic isotope fractionation in an open fault-related depositional system. Theoretical *ab initio* predictions by Li et al. (2009) simulated Ge^{2+} and Ge^{4+} in a sphalerite-like structure, resulting in $[GeS_4]$ tetrahedrons with Ge–S bond lengths of ∼2.262 and 2.275 Å, respectively. Our data indicate only the presence of Ge^{4+}, and variations in δ^{74}Ge cannot therefore be related to mixed oxidation states. For Ge^{4+}, the theoretical predictions yield $\Delta_{\mathrm{sp-fluid}}$ of −11.4‰ at 25°C, implying that sphalerite should be preferentially enriched in the lighter isotopes during precipitation. These results entail an isotopic fractionation factor, $\alpha_{\mathrm{sp-fluid}}$ of 0.9887, and a temperature parameter, A of −1.0134 (as in many instances, B is approximated to zero), as given by the following relation:

$$\Delta_{\mathrm{sp-fluid}} = \delta^{74}\mathrm{Ge}_{\mathrm{sp}} - \delta^{74}\mathrm{Ge}_{\mathrm{fluid}} \simeq 10^3 \ln \alpha_{\mathrm{sp-fluid}} = A\,\frac{10^6}{T^2} + B$$

If parameter A is known, backward calculations can allow us to estimate $\Delta_{\text{sp-fluid}}$ for different temperatures. Given our current understanding of the Saint-Salvy deposition model, the enclosing Cambrian black schist is the most plausible source of metals (Munoz et al., 1994; Barbanson and Geldron, 1983), including Ge, which were mobilised by fluid circulation and leaching on a regional scale. The metal-rich fluids were channelled into the Noailhac–Saint-Salvy vein network that developed against the Sidobre granite intrusion and the sphalerite deposition then occurred in an open-system (Belissont et al., 2014). The fluid inclusions in this sphalerite are too scarce and too small for analysis, Munoz et al. (1994) therefore used quartz-hosted fluids inclusions of the same paragenesis to constrain the range of temperature for this mineralisation stage (i.e., massive sphalerite, quartz, and/or siderite). These fluid inclusions, trapped under low-P conditions, indicate homogenisation temperatures of 80–140°C (mean of 110°C from 30 measurements). These temperatures should be similar to the trapping temperatures since pressure corrections are negligible (minimum pressure <100 bars).

Similar surface-derived brines have been described for most of the Pb–Zn–(F–Ba) deposits of the southern Massif Central margins, for example Peyrebrune (Munoz et al., 1997), Les Malines (Charef and Sheppard, 1988) and Trèves (Leach et al., 2006), which belong to a widespread early Jurassic hydrothermal event in western Europe that formed a number of large F-Ba-Pb-Zn mineralisations (e.g., Bruce et al., 1998; Muchez et al., 2005; Boiron et al., 2010; Cathelineau et al., 2012; Munoz et al., 2015). Accordingly, the composition of the fluid (i.e., the $\delta^{74}\text{Ge}_{\text{fluid}}$ and the Ge content) most likely remained constant over the period of sphalerite deposition. Thus, $\Delta^{140^\circ\text{C}}_{\text{sp-fluid}} - \Delta^{80^\circ\text{C}}_{\text{sp-fluid}}$ gives $\delta^{74}\text{Ge}^{140^\circ\text{C}}_{\text{sp}} - \delta^{74}\text{Ge}^{80^\circ\text{C}}_{\text{sp}}$, the isotopic fractionation range for sphalerite precipitated between 80 and 140°C, which yields a value of 2.19‰. In comparison with the value of 2.98‰ previously measured for these sphalerites (Belissont et al., 2014), a temperature-related isotopic fractionation could partly explain variations in δ^{74}Ge at Saint-Salvy. Alternatively, a 2.98‰ variation in δ^{74}Ge can be obtained for a slightly extended range of temperature, e.g., 70–150°C

Furthermore, because δ^{74}Ge correlates with Ge content, variations in the latter might suggest temperature-related changes in the Ge partition coefficient. The logarithm of the partition coefficient varies linearly with temperature in the form of $\ln K_{\text{d}} = \ln K^0_{\text{d}} - \Delta G/RT$ (Brice, 1975), where K^0_{d} denotes the strain-free partition coefficient, ΔG is the free enthalpy for inserting a cation into the crystal lattice, R is the gas constant and T is the temperature in K. Thus, the positive correlation between δ^{74}Ge and Ge content could imply that the partition coefficient D_{Ge} increases with temperature (i.e., $\Delta G < 0$, exothermic reaction). In comparison, Wright and Gale (2010) showed that the reaction energies for incorporating Fe are exothermic when sphalerite is Zn deficient, which involves high sulphur fugacity.

6.2.5 Conclusions

Experimental Ge, Cu and Fe K-edge μ-XANES combined with μ-XRF element maps in zoned Ge-rich sphalerite from the remarkable Saint-Salvy (France) and Kipushi ore deposits (R.D. Congo) indicate the occurrence of Ge^{4+}, Cu^{+}, and Fe^{2+} in tetrahedral sites, with no significant differences in intra- and inter-zoning type for the Saint-Salvy sphalerite. Theoretical *ab initio* calculations show that the nature of the Ge K-edge features strongly depend on the Ge oxidation state, the coordination symmetry, and the ligand type. The marked

differences between Ge–S and Ge–O bonds imply that only sulphide standards should be used for comparing sphalerite Ge K-edge XANES data. Our results strongly suggest that incorporation of Ge in sphalerite occurs via the $3Zn^{2+} \leftrightarrow 2Cu^{+} + Ge^{4+}$ coupled substitution, consistent with Ge–Cu correlations observed in previous studies. There is no evidence to support the presence of divalent Ge. It is now clear that the Ge enrichment in sphalerite and its partitioning among distinct zoning type do not result from variations in Ge oxidation state. Likewise, the large isotopic fractionation measured in sphalerite from Saint-Salvy is rather a result of variations in the temperature of the mineralising fluid than redox modifications. Precise quantification of the Fe^{3+}/Fe_{tot} ratio in sulphide minerals is beyond the scope of this study and could not be achieved here due to the lack of model compounds. However, the collection of XANES data for a range of Fe-bearing minerals in different oxidation states, coordination and spin-states would be of considerable use for performing a solid empirical calibration for the quantification of Fe redox states in sulphide minerals.

Acknowledgments The authors thank D. Cassard and C. Lerouge (BRGM) for supplying the Saint-Salvy sample material. We are grateful to P. Muchez (KU Leuven, Belgium) and D. Oliveira (LNEG, Lisbon, Portugal) for the Kipushi and Barrigão samples, M. Cathelineau (GeoRessources, Nancy) for the germanite sample, and P. Marion (ENSG, Nancy) for the stannite. This work has been possible thanks to the ESRF facilities (Project ES64, BM23 beamline, October 2013). P. Glatzel and K. Kvashnina are kindly acknowledged for allowing complementary XANES records to be performed on the ID26 beamline. Two anonymous reviewers and the Associate Editor, E. Ripley, are thanked for their detailed and insightful comments which significantly improved this manuscript. A. Williams is warmly thanked for her careful English editing of the manuscript. This work was supported by the French National Research Agency through the 'Investissements d'avenir' national research program (ANR-10-LABX-21–LABEX RESSOURCES21), the Observatoire Terre Environnement Lorraine (OTELo) program, and the INSU-CESSUR (CNRS) project.

6.3 Distribution and crystal chemistry of Ge in chalcopyrite by μ-XRF and μ-XANES

Along with the Zn-sulphide sphalerite, Cu-sulphides in Cu ores can show significant Ge enrichments, up to thousands ppm, such as the chalcopyrite from Barrigão (Reiser et al., 2011), and in Cu–Zn ores, can be associated with accessory Ge-sulphides, grading 6–18 wt.% Ge (e.g., renierite and briartite at Kipushi; Heijlen et al., 2008). Moreover, like sphalerite, chalcopyrite can exhibit compositional zoning in trace elements, including Ge, but their study is relatively complex utilising classic characterisation techniques primarily due to the opaque character of chalcopyrite. Incorporation mechanisms of minor/trace metals remain poorly studied and, like sphalerite in above section (Sec.6.2), Ge-bearing chalcopyrite deserve a fine examination of the oxidation state and coordination of Ge at the microscale and *in situ*. Germanium crystal chemistry were therefore addressed by μ-XRF combined with μ-XANES, in order to confront the substitution mechanisms suggested by trace element data (Sec. 5.3 above) as well as gaining insights into Ge elemental partitioning and isotopic fractionation (presented below in Sec. 7.3).

6.3.1 Samples, data acquisition and treatment

Several samples from Barrigão were selected for μ-XRF mapping, Barr1, Barr3, and Barr8, among which only chalcopyrite of Barr8 was used for collecting Ge K-edge μ-XAFS spectra. In samples from Kipushi, μ-XRF mapping and subsequent μ-XAFS data were collected in covellite from sample P717 and chalcopyrite from both samples U25 and U48. Tennantite, either from Barrigão or Kipushi, have very low concentrations and could not be studied due to a severe As K-α interference on Ge K-α, which result in a significantly increased statistic noise. Bornite from Kipushi could not be measured as well because of its low Ge contents (2–14 ppm Ge, see Table 5.4). The edge position of Ge^{4+} was calibrated using renierite from sample K2221, briartite from P717, and a germanite sample from Tsumeb (Namibia) used both in the form of pellet of pressed powder and polished section. Other reference compounds include synthetic GeS for Ge^{2+}, and GeO_2 for Ge^{4+} with O ligands.

The experimental set-up is similar to that for the preceding experiment on sphalerite (Sec. 6.2). Data were collected on the BM23 beamline at the European Synchrotron Radiation Facility (ESRF, Grenoble, France). The storage ring was operated at 6 GeV in 16 bunch mode with a current from 90 to 75 mA between each refill. X-rays were generated using a bending magnet (BM) and monochromatised with a fixed-exit double-crystal Si(111) monochromator. Micro-focusing of X-rays into an incident beam of $\sim$5$\times$5 μm^2 was achieved using two mirrors in Kirkpatrick-Baez (KB) geometry. The spectrum of a Ge foil, collected in transmission mode, was used to calibrate the energy (edge inflexion at 11103.0 eV). Data collection in samples and reference compounds were performed in fluorescence mode using a Vortex silicon-drift energy-dispersive detector, located 90° from the incident beam.

XRF maps were collected at 12 keV, yielding X-ray emission lines up to As-Kβ (11726.2 eV). Selected regions in the samples were mapped with step-sizes of 10 μm to 3 μm depending on the level of detail required. Dwell-time was adjusted to 0.5 s. XRF spectra (one spectrum per pixel) were converted into element XRF-intensity maps using the PyMca software (ESRF

Software Group; Solé et al., 2007), either with region of interest imaging or with batch curve fitting of the emission lines. Resulting μ-XRF maps were used for selecting the spots to be analysed in μ-XAFS.

Germanium K-edge XANES spectra were collected at room temperature by scanning the monochromator over the energy range of 11000–11600 eV with the smallest energy increments around the absorption edge (11070–11110 eV), above which the energy increment was progressively increased, to about 2.5 eV at the upper end of the scan (11600 eV). XANES spectra were cut at 11600 eV because in samples having low Ge contents, the L_3-edge absorption of Pt (at 11564 eV) that constitutes the KB mirrors was visible. The drift in the incident X-ray beam positioning is generally lower than 3 μm. For optimal fluorescence counting, deadtime was adjusted to 10%. Except germanite, the crystal system of the samples studied in polished section is not cubic, therefore, orientation effects may likely affect the XANES region (about 11080–11200 eV). Data reduction was carried out using *Athena* (Demeter suite), which is based on the *Ifeffit* program (Ravel and Newville, 2005), including data merging and normalisation. Absorption edge position is referred to as the inflexion point of the edge, which was determined visually as the root of the second derivative spectra.

6.3.2 Element distribution

X-ray fluorescence maps in sulphide minerals from Kipushi showed homogeneous Ge distributions (e.g., see Fig. 6.8), so, XRF maps were used only for beam positioning. Unlike samples from Kipushi, chalcopyrite showed significant variations in Ge contents. XRF maps in samples Barr1, Barr3 and Barr8 from Barrigão are presented in Fig. 6.9, Fig. 6.10 and Fig. 6.11, respectively. Fig. 6.9 shows a fracture through a large chalcopyrite grain rather devoid of Ge, containing tennantite at the center, surrounded by Ge-rich chalcopyrite grains of various size. Ge enrichments occur mostly in grain borders (insert 2), which clearly underline the micro-fracture network seen on the secondary electron microphotograph (insert 1). Remarkably, in Fig. 6.10, Ge is correlated to As in chalcopyrite and Ge-rich zones mostly surround tennantite inclusions. The core of the chalcopyrite grain is, however, depleted in Ge. Finally, Fig. 6.11 shows vein-like, Ge(–As)-rich zones in chalcopyrite. Enriched zones occur primarily on the grain border, others appear to extend radially from the hole/inclusion at the centre of the grain. These XRF-intensity maps suggest that Ge-rich zones, either coating grain borders or in vein-like networks, are superimposed to a primary, Ge-poor chalcopyrite, complementing the petrological observations Sec. 4.3.2. In addition, the broad correlation of Ge with As and the proximity of Ge-rich zones with tennantite grains appear to involve a late-stage hydrothermal overprint that deposited both Ge-rich chalcopyrite and, maybe afterwards, tennantite.

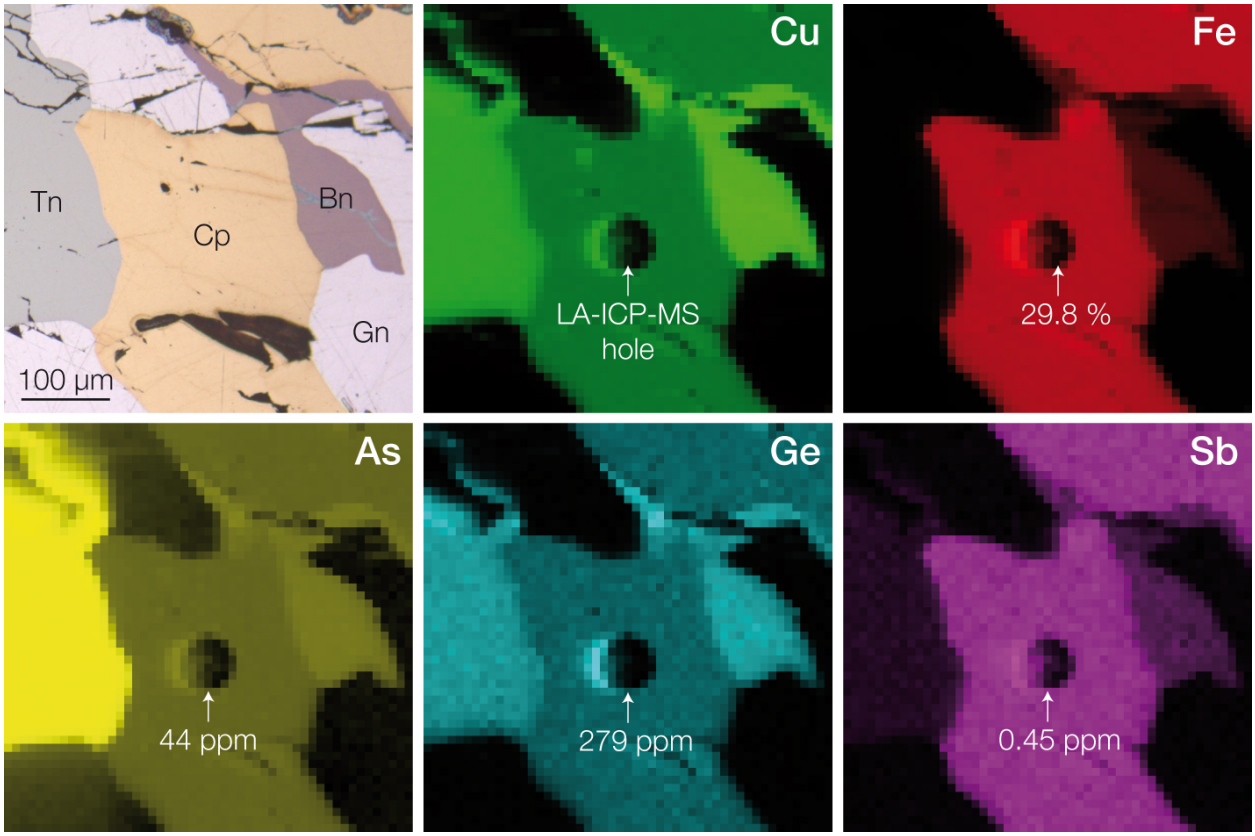

Fig. 6.8 – XRF-intensity maps of Cu, Fe, As (log-scaled), Ge, and Sb in sample U48 from Kipushi, consisting of tennantite (Tn), chalcopyrite (Cp), bornite (Bn) and galena (Gn). 500×500 μm^2, step size 10 μm.

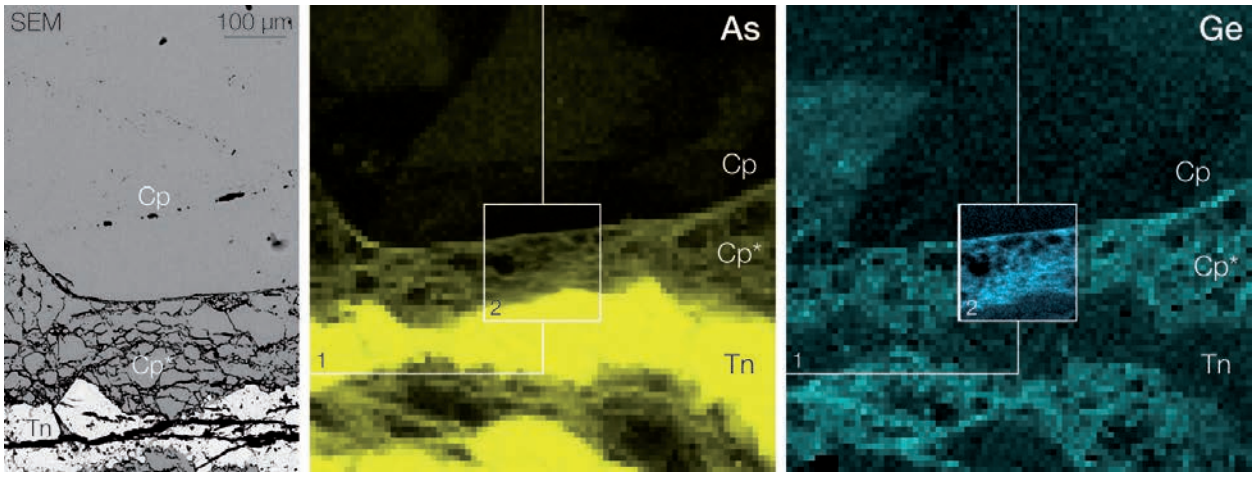

Fig. 6.9 – XRF-intensity maps of As (log-scaled) and Ge in sample Barr1 (800×800 μm^2, step size 10 μm) showing a fracture through a large chalcopyrite (Cp) grain, containing tennantite (Tn) at the center, surrounded by Ge-rich chalcopyrite grains (Cp*). Insert 1 represent the secondary electron microphotograph on the left hand side. Is sumperimposed in insert 2 a detailed map of the fractured zone (200×200 μm^2, step size 2.5 μm).

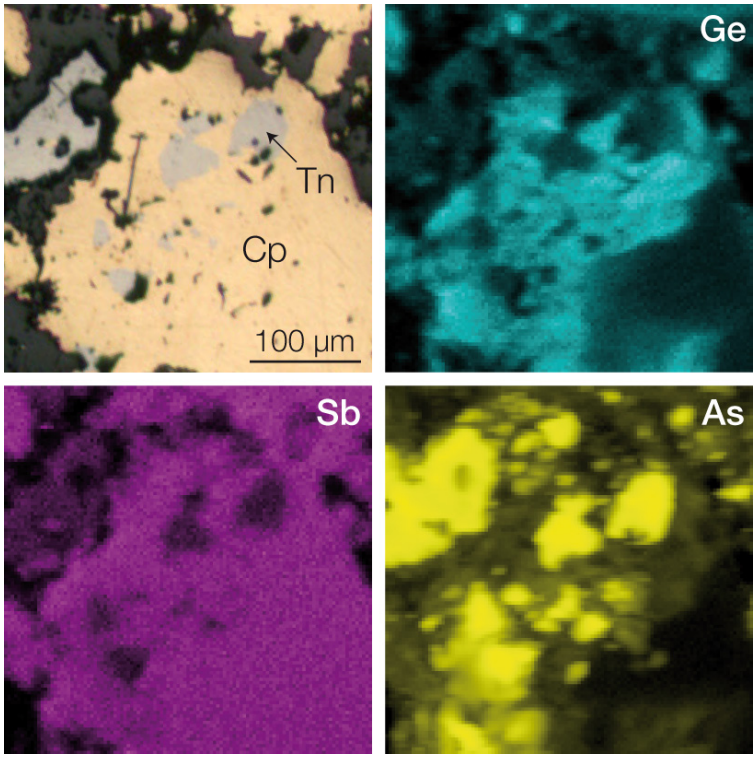

Fig. 6.10 – XRF-intensity maps of As (log-scaled), Ge and Sb in sample Barr3 (330×330 μm^2, step size 3 μm). Ge is correlated to As in chalcopyrite and Ge-rich zones surround tennantite inclusions.

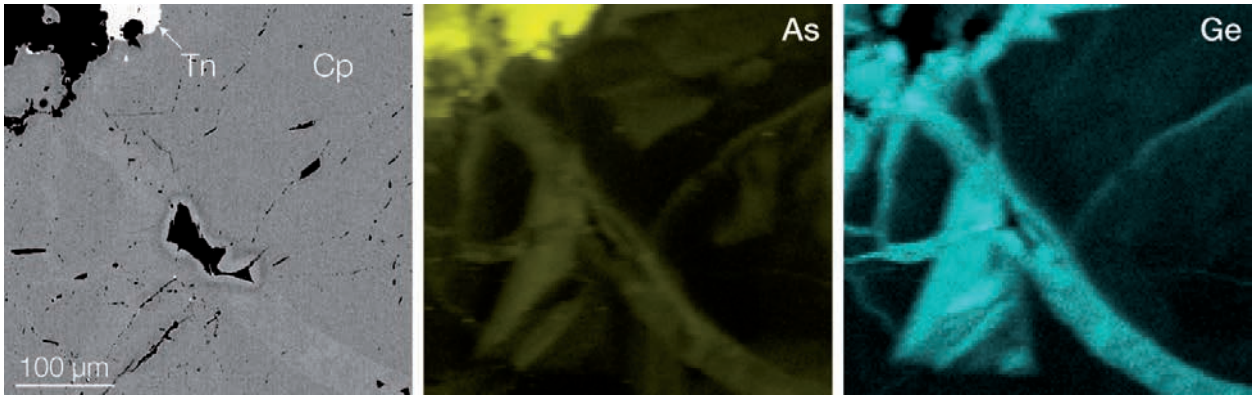

Fig. 6.11 – XRF-intensity maps of As (log-scaled) and Ge in sample Barr8 (400 × 400 μm^2, step size 3 μm) showing vein-like Ge-rich zones in chalcopyrite (Cp). Tn stands for tennantite.

6.3.3 Germanium *K*-edge XANES

Germanium K-edge XANES spectra for Ge-bearing model compounds are shown in Fig. 6.12. Ge^{4+}-bearing sulphide model compounds (renierite, briartite and germanite) all have similar XANES spectra, with an average edge position of 11105.1±0.1 eV, a steep white line ($1s \rightarrow 4p$ transitions) of similar height (at 11106.4 eV), and similar post-edge features, which represent transitions towards p–like partially filled states and multiple scattering resonances. GeS, the Ge^{2+}-bearing standard, however, exhibits less-intense post-edge features, together with an absorption edge shifted 2.2 eV below (11102.8). Remarkably, the Ge^{4+}-bearing oxide K-edge (11107.1 eV), GeO_2, is located 2.1 eV above Ge^{4+}-bearing sulphides, which is fairly consistent with the shift of 3.6 eV calculated *ab initio* in the previous section (Sec. 6.2). This edge shift towards higher energy primarily originates from the strong difference in the bond nature and length between Ge–S and Ge–O, as well as from the difference in coordination symmetry. The shorter/stronger Ge–O bond increases the core electron binding energy, and likewise, the onset of the absorption edge.

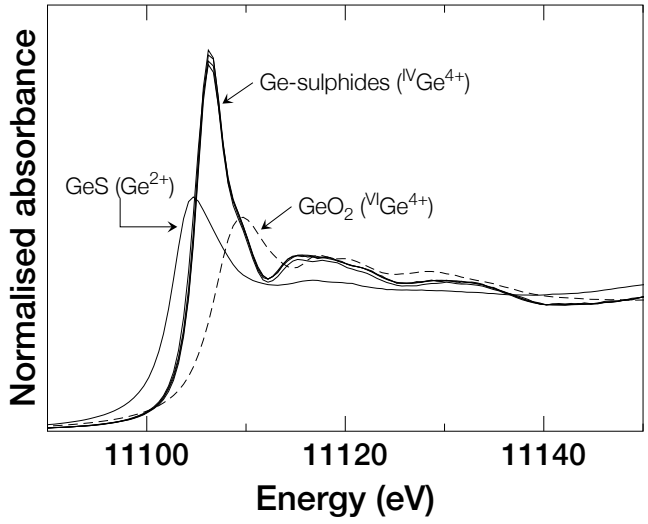

Fig. 6.12 – Detail of the XANES region for reference compounds. The reader can report to Sec. 6.2 to compare with *ab initio* FEFF8 calculations.

Germanium K-edge XANES spectra for Ge-bearing chalcopyrite and covellite are shown in Fig. 6.13. Chalcopyrite spectra show highly similar spectra, with an average edge position of 11105.0±0.1 eV, which is nearly identical to that for Ge^{4+}-bearing sulphides (11105.1±0.1 eV). This suggests that only tetravalent Ge is present in chalcopyrite regardless of the sample or the Ge content (e.g., Ge-rich *vs* Ge-poor zones). Post-edge features for chalcopyrite and Ge^{4+} are also identical in all respects up to at least 150 eV above the edge, which outlines very similar coordination environments, i.e., tetrahedral coordination. This is consistent with the first Ge K-edge XANES results for chalcopyrite (sample 2Barr5, Barrigão) that is presented above in Sec. 6.2. Finally, covellite show an edge position of 11104.6 eV, which is about 0.5 eV below Ge^{4+}-bearing sulphides though with similar post-edge features. This edge difference was not observed in the previous experiment (Sec. 6.2) so it appears that this difference would be related to a slight drift in the monochromator calibration, rather than the presence of Ge^{2+}. The occurrence of tetrahedral Ge^{4+} is therefore most likely.

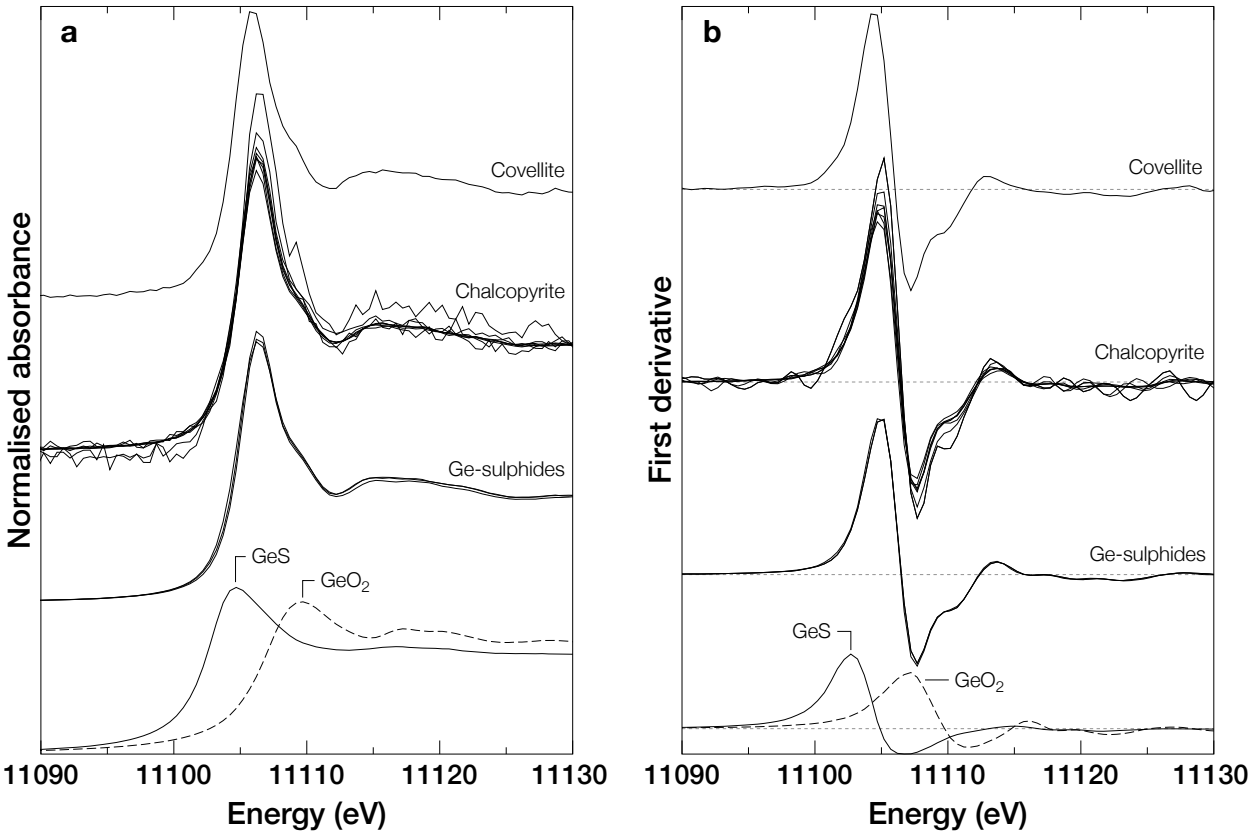

Fig. 6.13 – Germanium *K*-edge XANES normalised spectra (**a**) and first derivatives (**b**). Model compounds include GeS (Ge^{2+}), GeO_2 (Ge^{4+} bonded to O), and Ge^{4+}-bearing sulphides, i.e., renierite and briartite from Kipushi, and germanite from Tsumeb. Studied samples include chalcopyrite from Barrigão and Kipushi, and covellite from Kipushi.

6.4 Concluding remarks

Germanium crystal chemical studies in sphalerite by XANES spectroscopy formally indicated the presence of Ge^{4+}, Cu^{+}, and Fe^{2+} in tetrahedral sites, with no significant differences neither within nor between zoning type. Likewise, tetrahedral Ge^{4+} was identified in all of the studied Ge-bearing sulphide minerals, either in those where Ge is an essential component, i.e., renierite, briarite and germanite, or in sulphide having Ge in trace amounts, in solid solution, i.e., sphalerite, chalcopyrite, covellite, or in micro/nano-inclusion of Ge-sulphides, which is rare but was observed in one sphalerite from Kipushi (A38). The knowledge of the oxidation state of Ge allowed to refine the incorporation mechanisms of Ge and help for interpreting Ge isotope data in next chapter.

Chapter 7

Ge isotope fractionation in sulphide minerals

7.1 Overview

This chapter is devoted to the study of stable isotope signatures of the Ge-bearing sulphide minerals. Ge isotopes are important for understanding Ge enrichment processes in ore sulphides and deposits as well as related ore-forming conditions. Ge isotopes can be combined with other isotope systematics in order to gain perspective on the metallogenesis of hydrothermal systems, because ore components may be affected either by similar (e.g., fluid mixing, kinetic fractionation) or distinct processes (biologic activity, redox process). Significant Fe isotope fractionation can occur through redox processes, yielding δ^{56}Fe ranges as high as 5‰ (Beard and Johnson, 2004). Germanium isotopes, however, appear to be insensitive to redox processes since only Ge^{4+} is found. Atomistic calculations by Wright and Gale (2010) showed that reaction energies for incorporating Fe^{2+} and Fe^{3+} in sphalerite are different. In turn, S isotopes can provide information on S sources or sulphate reduction pathways in hydrothermal systems (Seal, 2006, e.g., thermochemical or bacteriogenic;).

Our approach consists in the multi-isotopic characterisation of Ge-bearing sulphides, using the Ge isotope systematic, together with those of Fe and S, in order to gain insights into the thermodynamic conditions and processes triggering sulphide deposition for the three studied deposits. In this sense, our approach can be compared to that of Gagnevin et al. (2012), who examined the Zn, Fe and S isotope systematics in the Navan Zn Irish-type deposit, and demonstrated the combined effects of kinetic Zn and Fe isotope fractionation during sphalerite precipitation, associated to S isotope variation through mixing of hot, metal-rich hydrothermal fluids with cool, bacteriogenic S-bearing brines.

7.2 Stable isotope studies in sphalerite from Saint-Salvy

This section presents the studies of Ge, S and Fe isotope systematics in sphalerite from Saint-Salvy, compared to sphalerite from various deposits. The data are presented in Table 7.1, including the original Ge isotope study presented in Belissont et al. (2014) (Sec. 5.2), that is also discussed in Sec. 6.2. Bulk S isotopes (δ^{34}S) were analysed by EA-IRMS and complementary Fe isotope measurements were performed on the Neptune *Plus* MC-ICP-MS at the CRPG-Nancy following the chemistry procedure and analytical setting presented in Marin-Carbonne et al. (2011) and Liu et al. (2014). New samples concerns sphalerite samples from the collection of Prof. Christian Marignac, including three samples from Saint-Salvy (SALMAR 1 to 3), two samples from other deposits in the French Massif Central, Peyrebrune (PEY) and Saint-Laurent-le-Minier (ST LAU), two samples from low-T MVT deposits, Elmwood-Gordonsville, Tennessee, USA (ELM) and Weardale, North Pennine district, England (WEAR). These samples from MVT deposits were compared to Saint-Salvy because the latter is associated to a widespread late Triassic–early Jurassic hydrothermal event (∼180 Ma) that formed a number of Zn–Pb MVT deposits in the French Massif Central (e.g., Muchez et al., 2005; Boiron et al., 2010). Data for both Fe and Ge isotopes fall on the theoretical mass fractionation lines (Fig. 7.1a,b), indicating that all interferences were efficiently removed.

Table 7.1 – Stable isotopes (Ge, S, Fe) in sphalerite from Saint-Salvy and other sphalerites for comparison. Ge isotopes data include those presented in Sec.5.2 (Belissont et al., 2014). Errors in 2σ SD.

	Ge isotopes (*vs* NIST 3120a)						S isotopes (*vs* VCDT)		Fe isotopes (*vs* IRMM)			
	δ^{72}Ge	2σ	δ^{73}Ge	2σ	δ^{74}Ge	2σ	δ^{34}S	2σ	δ^{56}Fe	2σ	δ^{57}Fe	2σ
Saint-Salvy												
K	0.42	0.06	0.51	0.25	0.91	0.16	9.09	0.01	-0.60	0.04	-0.92	0.10
62W	-0.31	0.08	-0.59	0.17	-0.54	0.15	8.59	0.43	-0.67	0.06	-0.97	0.09
72W	-0.73	0.29	-1.18	0.47	-1.39	0.49	7.80	0.17	-0.71	0.15	-1.01	0.15
64W-02	-1.07	0.24	-1.63	0.28	-2.07	0.37	7.84	0.43	-0.76	0.06	-1.05	0.15
62E	-0.75	0.15	-1.17	0.2	-1.41	0.39	6.45	0.36	-0.67	0.06	-0.97	0.20
SAL-UN	0.32	0.06	0.4	0.21	0.64	0.23	8.73	0.08	-0.70	0.09	-1.11	0.14
64W-08	-1.06	0.21	-1.63	0.34	-2.03	0.39	7.15	0.03	-0.67	0.13	-0.96	0.12
SALMAR 1	-0.58	0.24	-1.44	0.11	-1.73	0.08	8.34	0.06	-0.68	0.04	-1.02	0.10
SALMAR 2	-0.71	0.64	-3.8	0.19	-5.06	0.26	6.46	0.17	-0.64	0.05	-0.99	0.11
SALMAR 3	0.06	0.11	-0.81	0.1	-1.07	0.04	9.06	0.12	-0.61	0.12	-0.91	0.08
Various												
PEY	-0.82	0.15	-2.37	0.13	-3.01	0.13	8.15	0.19	–	–	–	–
ELM	2.81	0.35	-0.39	0.4	-0.62	0.16	-2.58	0.18	–	–	–	–
ST LAU	0.07	0.25	-1.63	0.19	-2.17	0.11	5.65	0.25	–	–	–	–
WEAR	-0.89	0.14	-3.55	0.35	-4.79	0.25	7.02	0.25	–	–	–	–

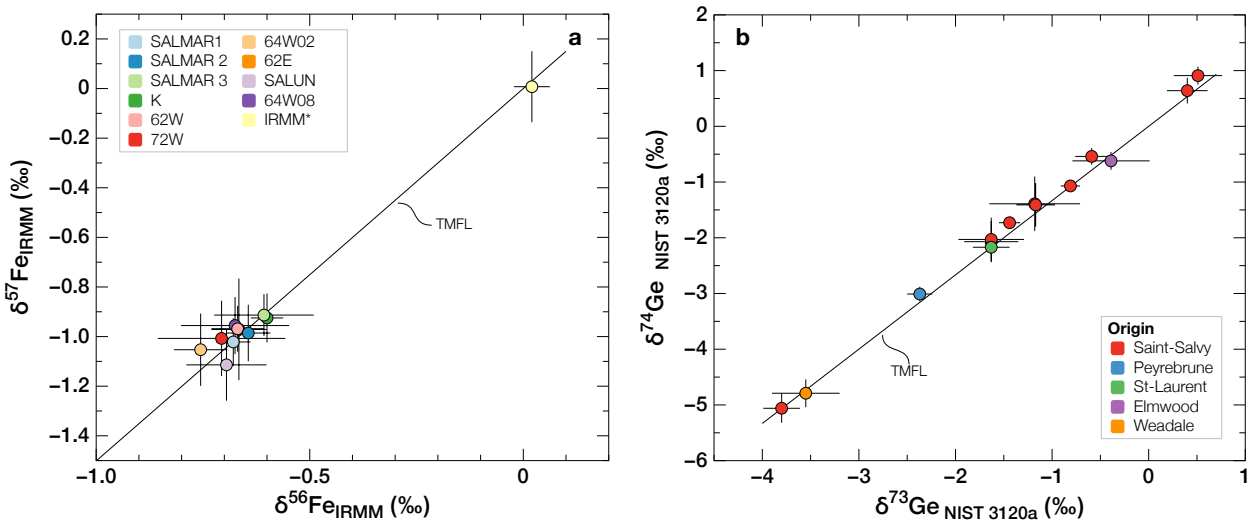

Fig. 7.1 – **a**. δ^{57}Fe *vs* δ^{56}Fe diagram for the Saint-Salvy samples and chemistry-processed IRMM standard (*). All the data fall on the theoretical mass fractionation line within error, expressed as $\delta^{74}\text{Ge} = \ln(m_{74} - m_{70})/\ln(m_{73} - m_{70})\,\delta^{73}\text{Ge}$ (Young et al., 2002). **b**. δ^{74}Ge *vs* δ^{73}Ge diagram for the samples from Saint-Salvy and other locations. All samples fall on the TMFL within error. Errors in 2σ SD.

7.2.1 Ge isotopes

The original Ge isotope study in sphalerite from Saint-Salvy concerns samples K, 62W, 72W, 64W-02, 62E, 64W-08 and SAL-UN, which were performed using the Isoprobe MC-ICP-MS. They yield a broad range of $\delta^{74}\text{Ge}_{\text{NIST3120a}}$ values, from -2.07 ± 0.37‰ to $+0.91 \pm 0.16$‰ (2σ SD), highlighting a significant isotopic fractionation during sphalerite deposition in low-T hydrothermal systems. Given the tetravalent state of Ge, the *ab initio* predictions for Ge isotope fractionation by Li et al. (2009) and the deposition temperatures (80–140°C) measured by Munoz et al. (1994) from fluid inclusions, the large range of δ^{74}Ge values of 2.98‰ can be readily explained by temperature variations, e.g., between 70°C and 150°C. The positive correlation between bulk δ^{74}Ge and bulk Ge content in sphalerite cannot be explained by a closed-system Rayleigh fractionation, which instead suggests that precipitation likely occurred in open-system (Sec. 5.2). In addition, this correlation may imply that the partition coefficient of Ge between sphalerite and fluid, K_{d}^{Ge}, increases with temperature, suggesting that the reaction of Ge incorporation in sphalerite is exothermic ($\Delta G < 0$, Sec. 6.2.4). In comparison, Wright and Gale (2010) showed that exothermic reactions occur for incorporating Fe when sphalerite is Zn deficient, which involves high sulphur fugacity.

Germanium isotope analyses in other samples from Saint-Salvy, SALMAR 1, 2 and 3, were performed on the Neptune *Plus* MC-ICP-MS. Remarkably, sample SALMAR 3 yields a δ^{74}Ge value of –5.06‰, which could indicate deposition temperatures as low as ~50°C using *ab initio* fractionation factors of Li et al. (2009) (see Sec. 6.2.4), without dismiss possible kinetic effects. Samples from Peyrebrune and Saint-Laurent-le-Minier show negative δ^{74}Ge values of −3.01‰ and −2.17‰, falling in the δ^{74}Ge range measured for Saint-Salvy. Indeed, these similar δ^{74}Ge values are consistent with the fact that most of the Pb–Zn–(F–Ba) deposits of the southern Massif Central margins are related to a widespread, early Jurassic hydrothermal event in western Europe (e.g., Bruce et al., 1998; Muchez et al., 2005; Boiron

et al., 2010; Cathelineau et al., 2012; Munoz et al., 2015).

Sphalerite from Elmwood and Weardale show distinct δ^{74}Ge compositions, yielding –0.62‰ and –4.79‰, respectively. Sphalerite from the Elmwood-Gordonsville district were precipitated from moderately hot (97–133°C) and highly saline Na–Ca–Mg–Cl fluids (21–23 wt.% NaCl eq.; Gratz and Misra, 1987). The relatively low fractionation of the Elmwood sample (–0.62‰) could be either an expression of the higher end of the fluid temperature range (e.g., $T \simeq 150$°C). The other possibility involve fluids of heavy δ^{74}Ge that can be either attained in a Rayleigh fractionation process during sulphide precipitation, or inherited from the Ge source, which can be Ge-bearing silicate igneous/sedimentary rocks having generally high δ^{74}Ge (see Sec. 2.4.2). The few data regarding Weardale report fluid inclusion studies in fluorite and quartz from the North Pennine district that indicate hydrothermal fluid temperatures between 100 and 200°C of high salinity (20 wt.% NaCl eq.; Sawkins, 1966). Low-temperature equilibrium or kinetic Ge isotope fractionation could therefore readily explain the light δ^{74}Ge value of the Weardale sphalerite (–4.79‰).

7.2.2 Sulphur isotopes

In situ SIMS δ^{34}S values spread from +4.21‰ to +8.85‰ and do not correlate with minor/trace element contents in zoning patterns, nor with bulk δ^{74}Ge. However, it appeared that there were notable variations in the average δ^{34}S between the sample. Bulk S isotopes were therefore measured to verify this observation. Sulphur isotopes in sphalerite from Saint-Salvy show $\delta^{34}S_{VCDT}$ values spanning from 6.45‰ to 9.09‰ (Table 7.1), which is typical of hydrothermal systems (Ohmoto and Rye, 1979) and thermochemically reduced sulphur. These data are consistent with previous bulk sulphur isotope data which displayed $\delta^{34}S_{CDT}$ ranges of 6.2–8.8‰ (Munoz et al., 1994) and 5.7–7.5‰ (Cassard et al., 1994). Sulphur isotope data for sphalerite from Mississippi Valley-type deposits of the French Massif Central (Peyrebrune, Saint-Laurent-le-Minier) and the North Pennin district (Weardale) have similar compositions (5.65–8.15‰), while that from the Elmwood–Gordonsville displays a lighter S composition (-2.58 ± 0.18‰). These compositions are consistent with those reported for Mississippi Valley-type deposits, which involve two major sulphide reservoirs, one centred between –5 to 15‰ and one greater than 20‰ (Seal, 2006).

7.2.3 Iron isotopes

Sphalerite from Saint-Salvy all exhibit very close $\delta^{56}Fe_{IRMM}$ values, between –0.76‰ and –0.60‰ (range of 0.16‰, Table 7.1). These values fall in the range of δ^{56}Fe data reported in sphalerite from the Irish-type Zn–Pb deposit of Navan, Ireland (Gagnevin et al., 2012), spreading from -2.11‰ to –0.14‰ for a greater range of Fe isotopic fractionation (2‰), for which kinetic processes are invoked. The small variations in $\delta^{56}Fe_{IRMM}$ in sphalerite is consistent with the fact that no redox variations occurs in sphalerite, as indicated by XANES spectroscopy (only Fe^{2+} was observed; Sec. 6.2).

Although Fe isotopes have received the most attention of the transition elements due to its high abundance and its prominent role in a number of high and low temperature processes, there remain few data from low to moderate temperature ore systems to compare

our δ^{56}Fe data with, especially for economic sulphides in large deposits such as those of the Mississippi Valley type.

7.2.4 Multi-isotopic comparison

The comparison of the averaged *in situ* δ^{34}S (by SIMS) and bulk δ^{74}Ge in the Saint-Salvy sphalerite did not reveal any clear trend between these two isotopic systems (Sec. 5.2). There is, however, a correlation trend between bulk δ^{34}S (by EA-IRMS) and δ^{74}Ge (Fig. 7.2a). Sample 62E and sphalerite from Saint-Laurent-le-Minier are however shifted above this trend, while the Peyrebrune sphalerite align with it. Several processes may be considered to account for the correlation between δ^{34}S and δ^{74}Ge, including fluid mixing, kinetic fractionation, temperature variation during sphalerite precipitation, or a combination of the three. The correlation along a straight line in Fig. 7.2a indicate that if a mixing process occurred, both of the end-members had the same Ge/S ratio. Kinetic fractionation would account for the isotopically light δ^{34}S and δ^{74}Ge due to sphalerite that precipitated rapidly from solution by addition of sulphide.

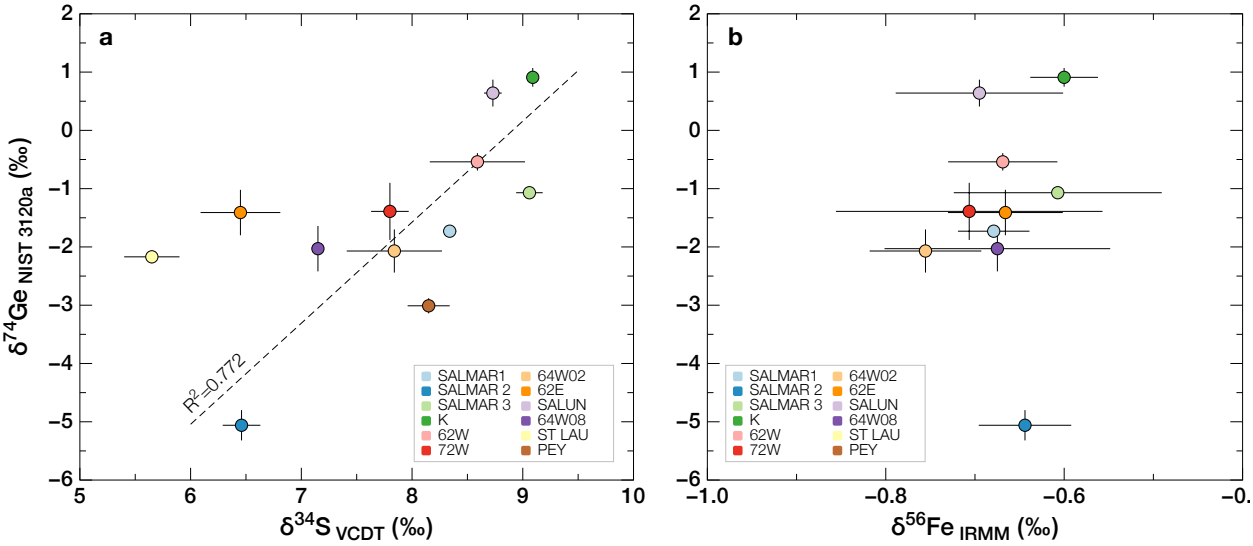

Fig. 7.2 – a. δ^{74}Ge *vs* δ^{34}S plot for sphalerite from Saint-Salvy and two other Zn MVT deposits in the French Massif Central (Saint-Laurent-le-Minier, Peyrebrune) showing a correlation trend. **b**. δ^{57}Fe *vs* δ^{74}Ge plot. There is no clear correlation between these two isotopic systems.

However, the non-correlation between δ^{74}Ge and δ^{56}Fe observed in Fig. 7.2b is a good indication that kinetic fractionation is unsignificant, otherwise we would expect these two isotopic systems to be correlated. For instance, Gagnevin et al. (2012) demonstrate that kinetic effects yield light and correlated δ^{66}Zn and δ^{56}Fe in sphalerite from Navan Zn–Pb deposit (Ireland) as the result of rapid precipitation. Considering the ore textures at Saint-Salvy, rapid precipitation is unlikely for the Saint-Salvy sphalerite because it exhibits supra-millimetric, euhedral crystals in comb structures, evidencing a slow growth in open space. Moreover, Li et al. (2009) demonstrated that the weak, highly covalent Ge–S bond can yield extremely low ^{74}Ge/^{70}Ge in equilibrium fractionation, and, as shown above, the observed δ^{74}Ge range can be readily explained by temperature changes ($T < 150$°C). Temperature variations of a single fluid is compatible with the straight line δ^{74}Ge–δ^{34}S which requires that

the Ge/S ratio to remain constant. A mixing process is therefore rather unlikely since a single fluid with evolving temperature (i.e., cooling) is the simplest explanation for the correlation between δ^{34}S and δ^{74}Ge observed in Fig. 7.2a for the given textural and low-temperature characteristics of the Saint-Salvy sphalerite.

7.3 Germanium isotopes in Ge-rich sulphides from MVT-related and VMS-remobilised ore deposits

7.3.1 Ge isotopes in chalcopyrite and tennantite–tetrahedrite from Barrigão

Germanium isotopic compositions of chalcopyrite and fahlore (tennantite–tetrahedrite) from the Barrigão deposit are presented in Table 7.2. The δ^{74}Ge *vs* δ^{73}Ge diagram (Fig. 7.3) shows that Ge isotopic compositions of both the Aldrich and JMC Ge standards are perfectly aligned along the theoretical mass fractionation line (TMFL) within error. Some of the samples, however, fall slightly away from the TMFL, especially fahlore. Deviations from the TMFL may originate either from isobaric interferences or matrix effects. A mass scan in the chemistry-processed solution of fahlore from sample Barr6 (under a dilution of 10) showed that all impurities were efficiently removed from the sample during chemistry except sulphur. ^{72}Ge is strongly affected by ^{40}Ar^{32}S interferences, which causes δ^{72}Ge values to be shifted out of the TMFL (Table 7.2). ^{73}Ge and ^{74}Ge are affected to a lesser extent by ^{40}Ar^{33}S and (Fig. 7.3), respectively, because they involve the S isotopes of lower abundance (0.76% and 4.29%, respectively).

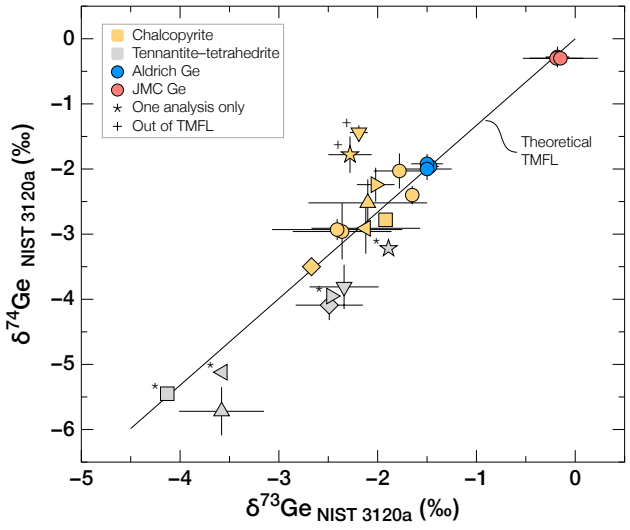

Fig. 7.3 – δ^{74}Ge *vs* δ^{73}Ge diagram for chalcopyrite and fahlore (tennantite–tetrahedrite) from Barrigão. Slight isobaric interference occur on ^{73}Ge, which slightly push the data away from the theoretical mass fractionation line (TMFL). Chalcopyrite and fahlore originating from the same sample are paired with the same marker.

Chalcopyrite and fahlore have negative δ^{74}Ge compositions but fahlore is distinctly lighter and have lower Ge contents (Table 7.2). δ^{74}Ge values in chalcopyrite range from –3.50‰ to –1.44‰, with a mean of -2.50 ± 0.60‰, and δ^{74}Ge values in fahlore span from –5.72‰ to –3.22‰, with a mean of -4.48 ± 0.95‰. Remarkably, high δ^{74}Ge values are associated

Table 7.2 – Ge bulk isotope compositions with respect to the SRM NIST 3120a reference for chalcopyrite and the tennantite–tetrahedrite series in Barrigão (Portugal). Data for δ^{72}Ge (in grey) in the samples are presented for informational purpose only as major S interferences occured on ^{72}Ge (especially in the tennantite–tetrahedrite series). Errors in 2σ SD.

	n	δ^{72}Ge (‰)	2σ (‰)	δ^{73}Ge (‰)	2σ (‰)	δ^{74}Ge (‰)	2σ (‰)	Ge (ppm)	2σ (ppm)
Chalcopyrite									
Barr1	5	-1.01	0.60	-2.36	0.50	-2.96	0.43	100.6	8.0
Barr2	5	-0.61	1.83	-2.41	0.66	-2.93	0.16	88.5	7.1
Barr3	3	-0.38	0.10	-1.92	0.06	-2.78	0.06	133.7	10.7
Barr4	4	-0.93	0.07	-2.67	0.07	-3.50	0.11	198.8	15.9
Barr5	5	-0.89	0.59	-2.10	0.60	-2.52	0.36	119.8	9.6
Barr6 *	4	-0.52	0.09	-2.19	0.09	-1.44	0.11	180.1	14.4
Barr8	3	-0.37	0.06	-1.78	0.26	-2.03	0.27	201.3	16.1
2Barr5	3	-0.67	0.02	-1.65	0.02	-2.40	0.14	302.2	24.2
2Barr8	5	-0.10	2.10	-2.12	0.55	-2.91	0.39	350.2	28.0
2Barr12	4	-0.70	0.10	-2.02	0.19	-2.24	0.26	243.6	19.5
2Barr13	0	–	–	–	–	–	–	224.4	17.9
2Barr19 *	4	-0.01	0.19	-2.28	0.22	-1.78	0.28	125.0	10.0
Tennantite–tetrahedrite									
Barr1	0	–	–	–	–	–	–	17.3	1.4
Barr2	0	–	–	–	–	–	–	14.0	1.1
Barr3	1	7.69	–	-4.13	–	-5.45	–	19.0	1.5
Barr4	6	12.99	4.08	-2.49	0.34	-4.09	0.23	36.2	2.9
Barr5	2	19.03	0.95	-3.58	0.43	-5.72	0.37	22.3	1.8
Barr6	2	10.61	1.83	-2.34	0.35	-3.81	0.34	27.5	2.2
Barr8	0	–	–	–	–	–	–	17.8	1.4
2Barr5	0	–	–	–	–	–	–	10.3	0.8
2Barr8	0	–	–	–	–	–	–	18.2	1.5
2Barr12	1	8.69	–	-3.57	–	-5.12	–	51.6	4.1
2Barr13	1	13.45	–	-2.47	–	-3.95	–	39.6	3.2
2Barr19	1	10.42	–	-1.89	–	-3.22	–	52.1	4.2
Standards									
Aldrich July	11	-1.00	0.07	-1.47	0.09	-1.96	0.11	–	–
Aldrich Aug.	13	-0.99	0.10	-1.50	0.16	-1.92	0.15	–	–
Aldrich Sept.	15	-1.02	0.11	-1.50	0.25	-2.00	0.17	–	–
JMC July	8	-0.13	0.10	-0.18	0.12	-0.28	0.16	–	–
JMC Aug.	10	-0.13	0.09	-0.19	0.27	-0.30	0.11	–	–
JMC Sept.	15	-0.13	0.10	-0.15	0.38	-0.30	0.10	–	–

n Number of replicates

σ Standard deviation

– Not measured

* Data out of the TMFL due to S interferences ^{73}Ge

with high Ge contents (Fig.7.4a). In samples for which Ge isotopes have been measured in both chalcopyrite and fahlore, the isotope fractionation between these species, calculated as $\Delta^{74}Ge_{cp-fhl} = \delta^{74}Ge_{cp} - \delta^{74}Ge_{fhl}$, yields values between 0.60‰ to 3.20‰. In the same manner, the Ge partition coefficient, expressed as $D^{Ge}_{cp-fhl} = [Ge]_{cp}/[Ge]_{fhl}$, gives values between 6.6 and 21.1.

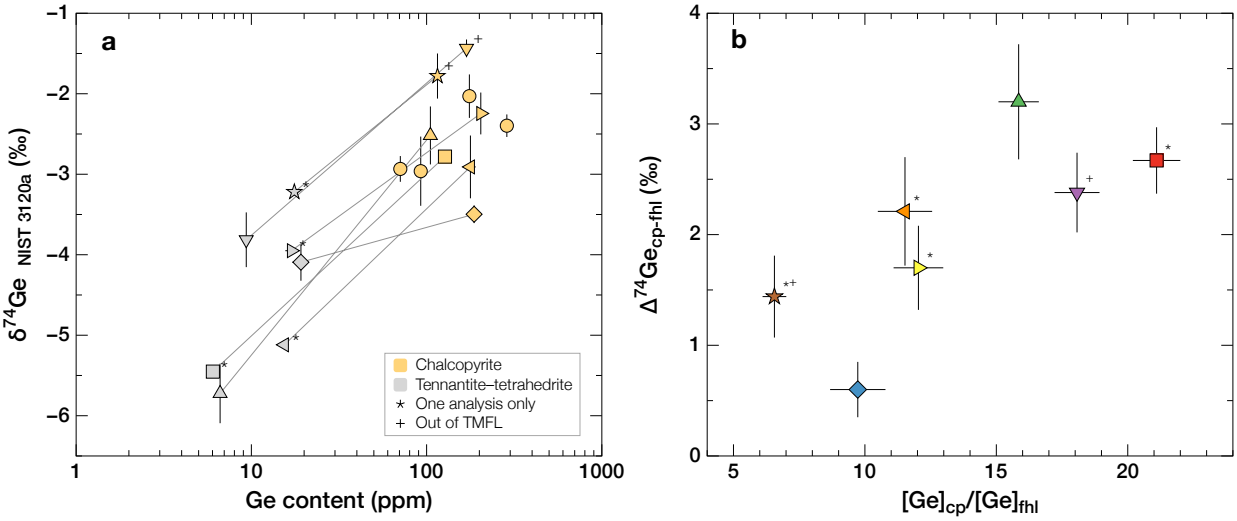

Fig. 7.4 – a. δ^{74}Ge *vs* Ge content. Chalcopyrite and fahlore (tennantite–tetrahedrite) originating from the same sample are paired with the same marker. **b**. Isotope fractionation between chalcopyrite and fahlore ($\Delta^{74}Ge_{cp-fhl} = \delta^{74}Ge_{cp} - \delta^{74}Ge_{fhl}$) *vs* Ge partitioning between chalcopyrite and fahlore ($[Ge]_{cp}/[Ge]_{fhl}$).

In Fig.7.4b, there is a marked correlated between the Ge chalcopyrite–fahlore isotopic fractionation ($\Delta^{74}Ge_{cp-fhl}$) and partitioning (D^{Ge}_{cp-fhl}), which likely indicates that both these sulphides are in equilibrium, and that they may be affected by variations in the same underlying parameter; temperature for instance. Indeed, we can expect that decreasing temperature may enhance the differences in crystal–fluid fractionation ($\Delta^{74}Ge_{cp-fluid}$ and $\Delta^{74}Ge_{fhl-fluid}$) and partitioning ($D^{Ge}_{cp-fluid}$ and $D^{Ge}_{fhl-fluid}$) coefficients between chalcopyrite and fahlore, which results in positively correlated $\Delta^{74}Ge_{cp-fhl}$ and D^{Ge}_{cp-fhl}.

Table 7.3 – Isotope fractionation between chalcopyrite and fahlore ($\Delta^{74}Ge_{cp-fhl} = \delta^{74}Ge_{cp} - \delta^{74}Ge_{fhl}$) and associated Ge partitioning ($[Ge]_{cp}/[Ge]_{fhl}$). Errors propagated in 2σ SD.

	$\Delta^{74}Ge_{cp-fhl}$ (‰)	2σ (‰)	$[Ge]_{cp}/[Ge]_{fhl}$	2σ
Barr3 *	2.67	0.06	21.1	0.9
Barr4	0.60	0.25	9.7	1.1
Barr5	3.20	0.52	15.8	0.8
Barr6 *	1.69	0.36	18.1	0.9
2Barr12 *	2.21	0.39	11.5	1.0
2Barr13 *	1.70	0.26	12.0	0.9
2Barr19 *	1.44	0.28	6.6	0.5

* The error is that of chalcopyrite, fahlore has been analysed once

7.3.2 Ge isotopes in sulphide minerals from Kipushi

Germanium isotopic compositions of the ore sulphides from the Kipushi deposit are presented in Table 7.4. Renierite and germanite from Tsumeb (Namibia) are presented for comparison. The δ^{74}Ge *vs* δ^{73}Ge plot (Fig. 7.3a) shows that Ge isotopic compositions of both the Aldrich and JMC Ge standards are perfectly aligned along the theoretical mass fractionation line (TMFL) within error. Only one sample, A114, is slightly shifted out of the TMFL due to the interferences discussed in the previous section (7.3.1). The δ^{74}Ge *vs* δ^{72}Ge plot (Fig. 7.3b) shows a perfect alignment of the standards and most of the samples on the TMFL, except samples A51, A114, A109, P724, and U29, which are strongly affected by ^{40}Ar^{32}S interferences (isotopes of major abundances) on ^{72}Ge.

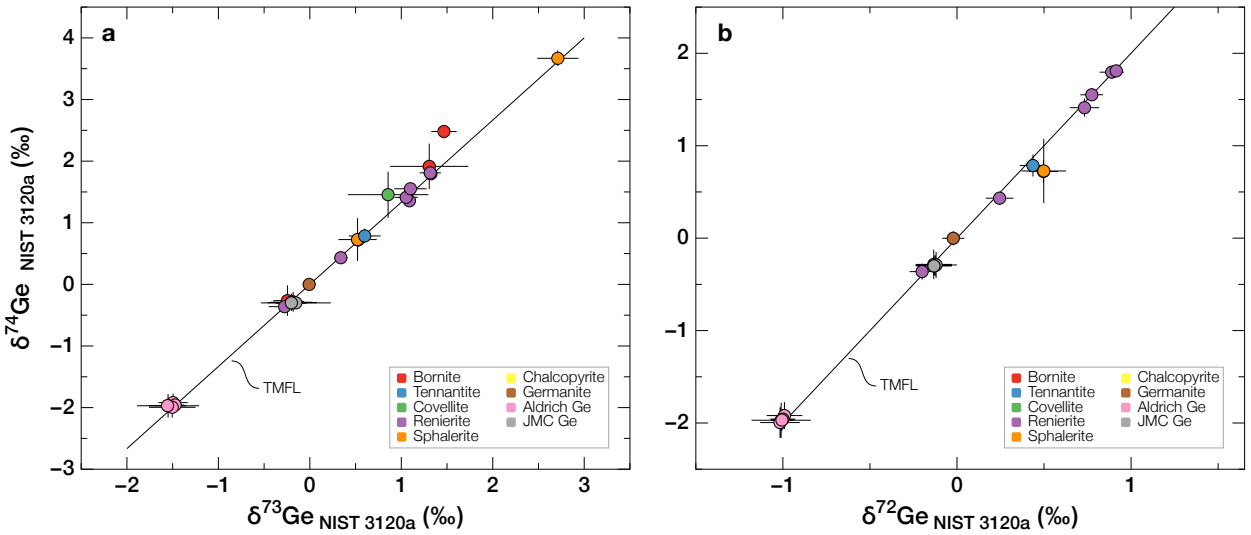

Fig. 7.5 – a. δ^{74}Ge *vs* δ^{73}Ge diagram for ore sulphides from Kipushi (D.R. Congo) and theoretical mass fractionation line. All samples fall on the TMFL within error, except bornite A114. **b**. δ^{74}Ge *vs* δ^{72}Ge diagram. Most of the samples fall on the TMFL within error, except A51, A114, A109, P724, and U29. See text for details.

Renierite and the Ge-bearing sulphides, bornite, chalcopyrite, covellite, sphalerite and tennantite have δ^{74}Ge values ranging from –0.26‰ to +3.67‰ (Fig.7.6), but there are no systematic variations in δ^{74}Ge between the sulphide species. There is a 0.56‰ difference between microsampled and bulk bornite A114 that indicates that the Ge isotope composition can be slightly heterogeneous within a given sample. The Ge-sulphides from Tsumeb (Namibia), renerite and germanite, have close compositions (0.00‰ and –0.28‰, respectively) but are isotopically lighter than renierite from Kipushi.

Table 7.4 – Ge bulk isotope compositions with respect to the SRM NIST 3120a reference for ore sulphides from Kipushi (D.R. Congo). δ^{72}Ge data in grey are presented for informational purpose only as major S interferences occured on ^{72}Ge. Likewise for Ge content data in grey. Of note, there may be a contamination of Ge-sulphides in chalcopyrite, sphalerite and tennantite in sample P712. Gm, germanite; Rn, renierite. Errors in 2σ SD.

	n	δ^{72}Ge ‰	2σ ‰	δ^{73}Ge ‰	2σ ‰	δ^{74}Ge ‰	2σ ‰	Ge ppm	2σ ppm	X m	Y m	Z m	'Up' coord.	'NE' coord.
Bornite														
A114 μ	5	6.29	3.69	1.31	0.43	1.92	0.37	140	8.6	-252	-220	-850	-1.69	1.04
P724	4	6.38	0.26	-0.24	0.16	-0.26	0.25	53	1.4	-27	-50	-417	1.79	0.70
A114	3	9.38	0.62	1.47	0.14	2.48	0.11	13	0.2	-252	-220	-850	-1.69	1.04
Chalcopyrite														
P712	6	0.50	0.08	0.53	0.07	0.72	0.12	3128	221.1	-218	125	-290	2.09	-1.76
Covellite														
A109	2	22.12	0.30	0.86	0.44	1.46	0.37	15	0.7	-251	-200	-850	-1.60	0.88
Renierite														
U29 μ *	1	5.64	–	1.09	–	1.36	–	119		-24.5	-75.5	-500	1.37	0.94
K1703	4	0.73	0.08	1.05	0.13	1.41	0.10	58667	14079	–	–	-290	–	–
U4	4	0.77	0.07	1.10	0.18	1.55	0.06	61473	4374	–	–	–	–	–
P712	8	0.24	0.08	0.34	0.07	0.43	0.07	21500	3493	-218	125	-290	2.09	-1.76
K2201	3	0.89	0.07	1.32	0.05	1.80	0.03	54957	1375	–	–	–	–	–
K2208	3	0.91	0.04	1.32	0.12	1.81	0.04	71371	2978	–	–	–	–	–
Sphalerite														
P712	8	0.50	0.13	0.52	0.21	0.73	0.35	3280	157.7	-218	125	-290	2.09	-1.76
A51	3	6.64	0.32	2.71	0.23	3.67	0.13	99	0.9	-350	-89	-850	-1.63	-0.54
Tennantite														
P712	6	0.44	0.08	0.60	0.17	0.79	0.12	22395	2109	-218	125	-290	2.09	-1.76
Sulphides from Tsumeb (Namibia)														
Tsu1 Gm	4	-0.02	0.06	-0.01	0.07	0.00	0.08	65643	3510	–	–	–	–	–
Tsu2 Rn	4	-0.20	0.07	-0.28	0.17	-0.36	0.09	51830	3883	–	–	–	–	–
Standards														
Aldrich Aug.	13	-0.99	0.10	-1.50	0.16	-1.92	0.15	–	–	–	–	–	–	–
JMC Aug.	10	-0.13	0.09	-0.19	0.27	-0.30	0.11	–	–	–	–	–	–	–
Aldrich July	11	-1.00	0.07	-1.47	0.09	-1.96	0.11	–	–	–	–	–	–	–
JMC July	8	-0.13	0.10	-0.18	0.12	-0.28	0.16	–	–	–	–	–	–	–
Aldrich Oct.	13	-1.01	0.17	-1.55	0.34	-1.97	0.19	–	–	–	–	–	–	–
JMC Oct.	12	-0.12	0.12	-0.20	0.23	-0.29	0.14	–	–	–	–	–	–	–
Aldrich Sep.	15	-1.02	0.11	-1.50	0.25	-2.00	0.17	–	–	–	–	–	–	–
JMC Sep.	15	-0.13	0.10	-0.15	0.38	-0.30	0.10	–	–	–	–	–	–	–
Aldrich Nov.	8	-1.01	0.06	-1.56	0.20	-1.97	0.11	–	–	–	–	–	–	–
JMC Nov.	8	-0.13	0.04	-0.20	0.17	-0.30	0.03	–	–	–	–	–	–	–

– Not measured

* Measured once – no error estimation

μ sampled by micro-milling

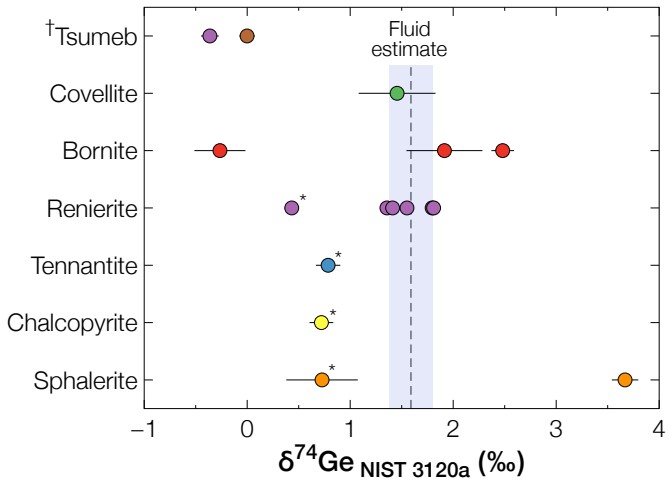

Fig. 7.6 – δ^{74}Ge of Kipushi (D.R. Congo) ore sulphides compared to those of the Tsumeb deposit (Namibia), †renierite (purple) and germanite (brown). *Minerals in equilibrium texture in P712.

It was shown in Sec. 5.3.2 that the deposition of Ge-sulphides at Kipushi (i.e., mostly renierite) is confined to a limited period in the paragenetic sequence, which happens to coincide with the few occurrences of Ge-rich sphalerite, and was referred to as a 'Ge peak'. Considering mass balance effects, the precipitation of Ge-sulphides, as they absorb the greater part of the Ge stock from the fluid, likely represent the initial isotopic composition of the fluid. In renierite δ^{74}Ge ranges from 1.36‰ to 1.81‰ and averages 1.59±0.21‰ (sample P712 appart; 0.43‰), which can be an estimation of the initial fluid isotopic composition. This value fall in the range of hydrothermal fluid compositions reported in the literature (1.15–1.64‰ in various contexts; Siebert et al., 2006; Escoube et al., 2015).

Given that sulphide minerals are expected to be enriched in the lighter isotopes while they precipitate (Li et al., 2009), hence, during Ge-bearing sulphide deposition, and especially after that of Ge-sulphides, Ge remaining in the fluid likely reached a very heavy isotopic composition through a Rayleigh fractionation process (see Fig. 2.15). As a good evidence of such a process, sphalerite A51, which shows the very high δ^{74}Ge of 3.67‰ (Table 7.4), precipitated from a fluid of very heavy isotopic composition and therefore was likely deposited after the deposition of Ge-sulphides. Bornite A114 (2.48‰) is heavier than the initial fluid δ^{74}Ge estimate, so, its deposition probably occured after Ge-sulphides. In turn, the samples that have lighter δ^{74}Ge than the initial fluid estimate (1.59‰), were likely deposited before the Ge peak, e.g., sulphides from sample P712. Hence, δ^{74}Ge appears to be a good proxy of the fluid evolution.

Germanium isotope compositions roughly increases downwards in the orebody (Fig. 7.7a), however, there is no clear trend with the North-eastward coordinate (Fig. 7.7a). In the current understanding of the deposition model, the mineralisation is though to result from ascending metal-bearing brines. However, increased δ^{74}Ge values in sulphides downwards suggest that the fluid attained heavier isotopic compositions through a Rayleigh fractionation process in a downward flow. The model of fluid circulation in the hydrothermal system would therefore imply convective movements implying a hot upward branch were little amounts of Ge are incorporated in precipitating sulphides, while the downward branch may be associated to Ge incorporation in sulphides (and fractionation), perhaps due to fluid cooling or change in composition, e.g., an increase in the Ge/(Zn+Cu) ratio. This observation is fairly consistent with what was outlined from the trace element signatures of sphalerite shown in Sec. 5.3.2.

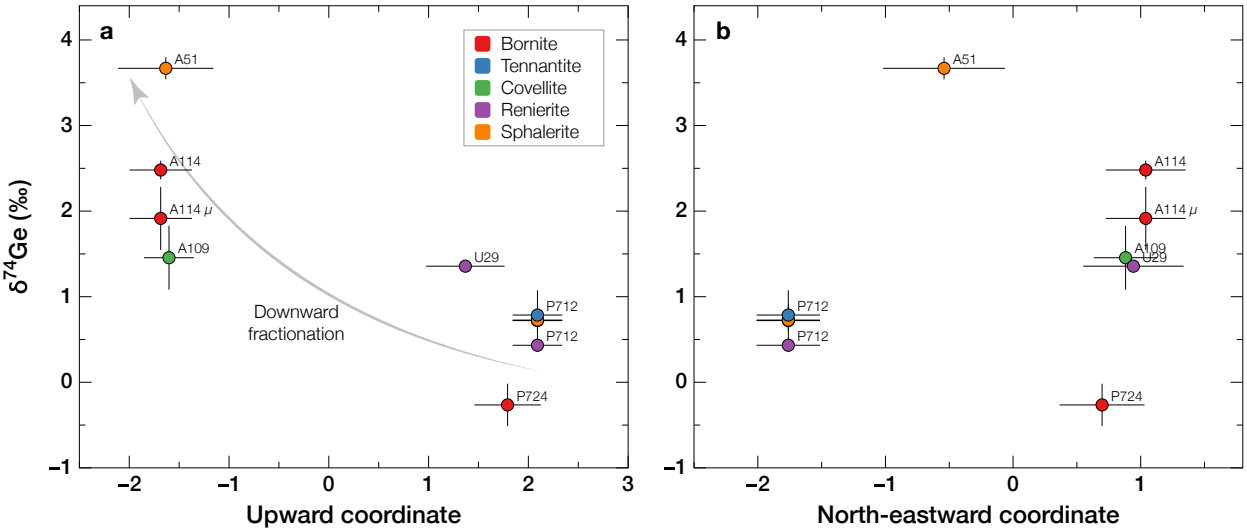

Fig. 7.7 – δ^{74}Ge of Kipushi (D.R. Congo) ore sulphides *vs* their position within the orebody (when known), i.e., (a) upward (b) North-eastward coordinates.

7.3.3 Discussion and conclusions

Germanium isotopes in sulphide minerals yield a large range of δ^{74}Ge values, from –5.72‰ to +3.67‰ compared to Earth core and silicate reservoirs (Fig. 7.8). The total isotopic fractionation is of 5.97‰ in sphalerite from Saint-Salvy, 1.52‰ and 2.5‰ in chalcopyrite and fahlore from Barrigão, respectively, and 3.41‰ in the ore assemblage from Kipushi. The isotopically light compositions of Saint-Salvy and Barrigão vein-type ores appear to relate to variations in the fluid temperature, while for the Kipushi ore sulphides, given the hot fluid temperatures (290–380°C) and the lack of systematic difference in δ^{74}Ge between the mineral species, the clear trend observed towards heavier isotopic composition suggests that temperature variations did not likely play a key role in Ge isotope fractionation, but rather a Rayleigh fractionation effect.

At Saint-Salvy and Barrigão, since Ge is a trace component in ore sulphides, mass balance effects due to the incorporation of Ge during sulphide depositions were likely insignificant, so the isotopic composition may have remained fairly constant during ore formation. Chalcopyrite and fahlore from Barrigão are shifted towards light values compared to sphalerite from Saint-Salvy (Fig. 7.8). Ore deposition at Barrigão was suggested to occur in the temperature range of ∼260–300°C (post deformation peak; prehnite-pumpellyite facies, ∼250–350°C, 2–6 kbar), while ore formation at Saint-Salvy occured at lower temperatures (80–140°C; Munoz et al., 1994). If the fluid δ^{74}Ge composition was similar for these deposits, we would expect Barrigão to be heavier than Saint-Salvy.

One explanation for the significantly lighter δ^{74}Ge composition of Barrigão could be that the fluid–Cu-sulphide fractionation factor (α) was significantly greater than the fluid–sphalerite one, which we assume unlikely since Ge in sphalerite and chalcopyrite occur in similar states (see Chap. 6) and given the temperature difference evoked above. A second explanation would be that the late Ge overprint at Barrigão is associated to a low temperature event, but evidences are however lacking at present for supporting this idea such as the presence of a sphalerite–galena assemblage which characterises a late low-T event in other

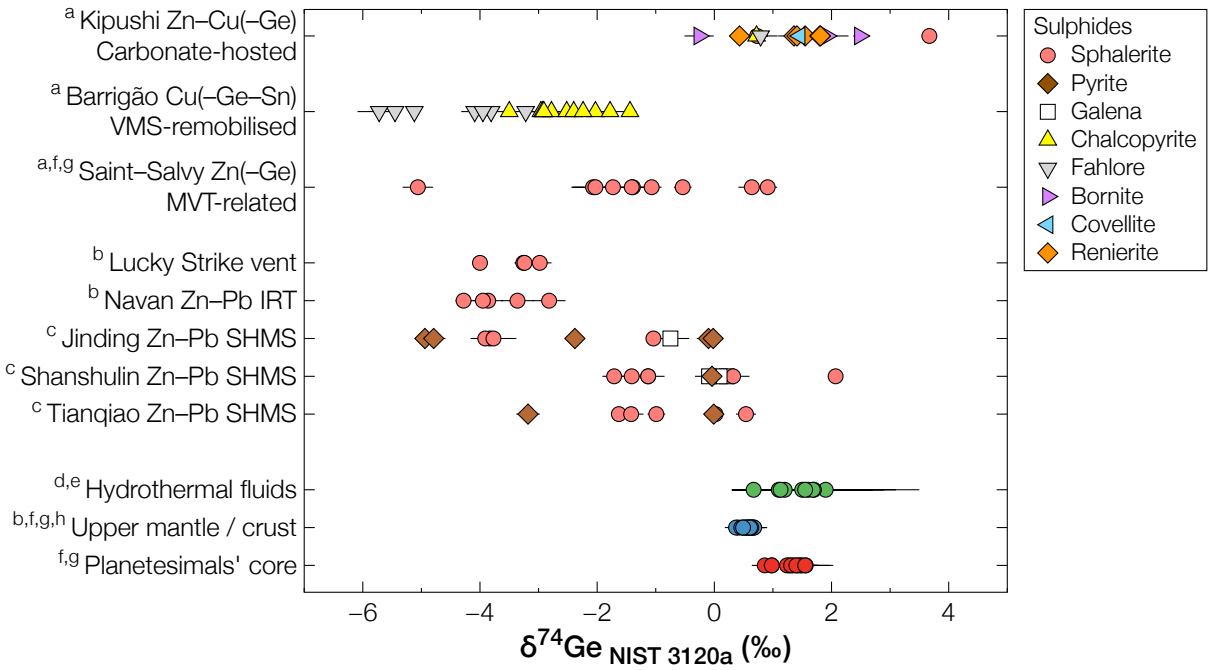

Fig. 7.8 – δ^{74}Ge compositions of planetesimals' core (Fe meteorites), Bulk Silicate Earth (upper mantle/crust rocks), hydrothermal fluids and sulphide minerals from various ore deposits. Data from [a]this study, [b]Escoube et al. (2012), [c]Meng et al. (2015), [d]Escoube et al. (2015), [e]Siebert et al. (2006, 2011), [f]Luais (2007), [g]Luais (2012), [h]Rouxel et al. (2006). Errors bars are 2σ SD.

Cu deposits of the region (Mateus et al., 2003), or fluid inclusion data. Another explanation would be a source effect on the fluid δ^{74}Ge composition. Indeed, the remobilisation of Ge from pre-enriched sulphides (having light δ^{74}Ge), e.g., from large VMS deposits such as Neves Corvo as suggest in Reiser et al. (2011), would result in Ge-bearing fluids of light δ^{74}Ge, and therefore, in sulphides with even lighter δ^{74}Ge at Barrigão.

The trend towards heavy isotopic compositions at Kipushi suggest that ore-forming fluids have significantly evolved trough ore deposition, as in 'closed system', while those involved for Saint–Salvy sphalerite deposition and the Ge overprint at Barrigão were either unaffected by Ge incorporation in sulphides or regularly renewed in 'open system'. Ge deposition at Kipushi occurred downwards, perhaps through fluid cooling and/or smooth variations in the fluid composition during precipitation (e.g., Ge/(Zn+Cu) ratio). Indeed, a dramatic change in the way metal source operates that would result in significant, time-limited input of Ge in the ore-forming system is hardly conceivable. The convective fluid circulation proposed in the previous section for Kipushi would explain the massive precipitation of Ge-sulphides during a limited period in the paragenetic sequence; Ge would be relatively enriched in the fluid during early sulphides precipitation (pyrite, arsenopyrite, massive sphalerite and chalcopyrite), then, both Ge deposition and isotopic fractionation would be triggered past a given threshold in composition and/or temperature (e.g., cooling). Enhanced understanding of the Ge sulphide–fluid partitioning and fractionation would require experimental studies to constrain the parameters acting on Ge behaviour in hydrothermal systems. Such an attempt is presented in the next chapter for sphalerite.

Chapter 8

Experimental study of Ge partitioning and isotope fractionation in sphalerite

8.1 Overview

The study of critical metals and their *non-traditional* stable isotopes, including the recent renaissance of Ge geochemistry, not only is economically motivated, but is largely driven by the development and improvement of new analytical techniques, especially laser ablation and multi-collector inductively coupled plasma mass spectrometers (LA-ICP-MS and MC-ICP-MS, respectively). This scientific field is rich with opportunities and challenges but the studies of natural objects are somewhat outpacing the experimental and theoretical basis required for fully interpret empirical observations (e.g., Shanks, 2014). Regarding Ge geochemistry, very little is known about elemental partitioning and isotopic fractionation of Ge between coexisting phases in controlled environments and most of the existing work is still confined in field and analytical studies. In order to address the gap in our current understanding of the broad variability of Ge concentration and isotopic compositions in sphalerite, this experimental study is the first attempt to decipher Ge partitioning and fractionation in a fluid where sphalerite precipitates, as a function of temperature.

8.2 Materials and methods

8.2.1 Hydrothermal synthesis of Ge-doped sphalerite

Ge-doped sphalerite have been precipitated experimentally in order to study the elemental partitioning and isotopic fractionation of Ge between sphalerite and an hydrothermal solution for different temperatures. The experiments have been performed at GeoRessources in collaboration with Laurent Truche. Four experiments have been conducted at temperature of 25 °C, 90 °C, 150 °C and 200 °C in a 400 mL Parr Ti autoclave, using the same initial reactants and procedure. A summary of the experimental conditions is shown in Table 8.1. The autoclave is loaded with 380 ml NaOH 0.026 M, closed, stirring is activated and the autoclave

is flushed with Ar. $H_2S_{(g)}$ is injected until total replacement of NaOH by NaHS as indicated by the formation of Ag_2S in the AgCl trap on the exit. The autoclave is closed and heated up to the desired temperature using a oven mounted around the autoclave tank. About 18 ml of the a Zn–Ge stock solution (0.4 M Zn, 150 ppm Ge) is injected using a piston presser, which brings the solution to 400 ml of 0.025 M NaHS (plus dissolved H_2S in excess), 0.02 M Zn, and about 7 ppm Ge. We expect the reaction, $H_2S + Zn(OH)^+ \leftrightarrow ZnS + H_3O^+$, to form about 65 mg ZnS which can host up to 4150 ppm Ge if the latter is totally incorporated in ZnS.

Table 8.1 – Experimental starting conditions and reactants volumes/concentrations before and after metal stock injection in the autoclave.

	Starting conditions				Pre-injection					Post-injection			
	T (°C)	P (bar)	pH	H_2S (M)	V_{NaHS} (ml)	C_{H2S} (M)	V_{Zn-Ge} (ml)	C_{Zn} (M)	C_{Ge} (ppm)	V_{tot} (ml)	C_{H2S} (M)	C_{Zn} (M)	C_{Ge} (ppm)
ZnSGe 2	25	7	5.50	0.070	369.8	0.070	18	0.370	151	387.8	0.067	0.017	7.0
ZnSGe 3	90	6	6.00	0.050	379.6	0.050	18	0.370	151	397.6	0.048	0.017	6.8
ZnSGe 4	150	6	5.90	0.110	379.4	0.110	18	0.370	151	397.4	0.105	0.017	6.8
ZnSGe 5	200	6	6.00	0.088	349.9	0.088	18	0.370	151	367.9	0.084	0.018	7.4

During the course of each experiment, six samplings of about 13 ml are performed; 1 ml of purge, about 2 ml for pH measurements and H_2S titration, and 10 ml are filtered (0.2 μm) and saved for ICP-MS elemental analyses. The first sampling, P_0, is performed just after Zn–Ge injection, at $\sim T_0 + 5$ min. P_1 is sampled at T_0+30 min, P_2 at T_0+1h, P_3 at T_0+2h min, P_4 is performed overnight, at $\sim T_0$+17h min. After cooling down to ambient temperature, the autoclave is opened the solution is filtered using a Büchner funnel equipped with 0.2 μm membrane filter. The recovered solid product is then rinsed with ultra-pure water and ethanol to ensure rapid drying (in heating chamber at 90 °C) and prevent oxidation. The filtered solutions (referred to as P_{End}) are saved in PET bottles for Ge isotope measurements.

8.2.2 Analytical methods

Observations of the powders have been performed using SEM (Jeol J7600F, GeoRessources), and their phase composition have been characterised using XRD (Bruker D2, GeoRessources, and Bruker D8, Laboratoire environnement et minéralurgie, LEM, Nancy). The germanium content (and other possible trace elements) have been analysed by LA-ICP-MS on pressed pellets of the powder (see section 3.3). Trace elements in the solutions sampled during each experimental run have been analysed using ICP-MS (SARM, CRPG-Nancy) and both the final solid products and final solutions have been processed for Ge isotope measurements using MC-ICP-MS (see section 3.6).

8.3 Reaction kinetic and fluid composition evolution

Results of the fluid sample analysis are shown in Table 8.2. The kinetics of precipitation can be observed in Fig. 8.1, using the concentration evolution of Zn content. According to the latter, the precipitation occur immediately after the metal injection with a very fast kinetic. Indeed, the reaction is complete after 15 min (most likely less), Zn concentration

remains fairly stable afterwards, below the ppm level in fluid samples P_1 to P_{End} (remaining Zn fraction <0.1%). The erratic Zn content evolution in experiment ZnSGe5 (200°C), most notably for P_3, likely results from a sampling issue such as contamination or a bad filtration of the fluid sample. Similarly, Ge concentration is not measurable in almost every fluid samples, from P_1 to P_{End}, and the possible sampling issue is also observed on the Ge content in P_3 of ZnSGe5 (200°C). Most of ZnS precipitation therefore occured within the first minutes of the experiments for which only P_0 is the witness.

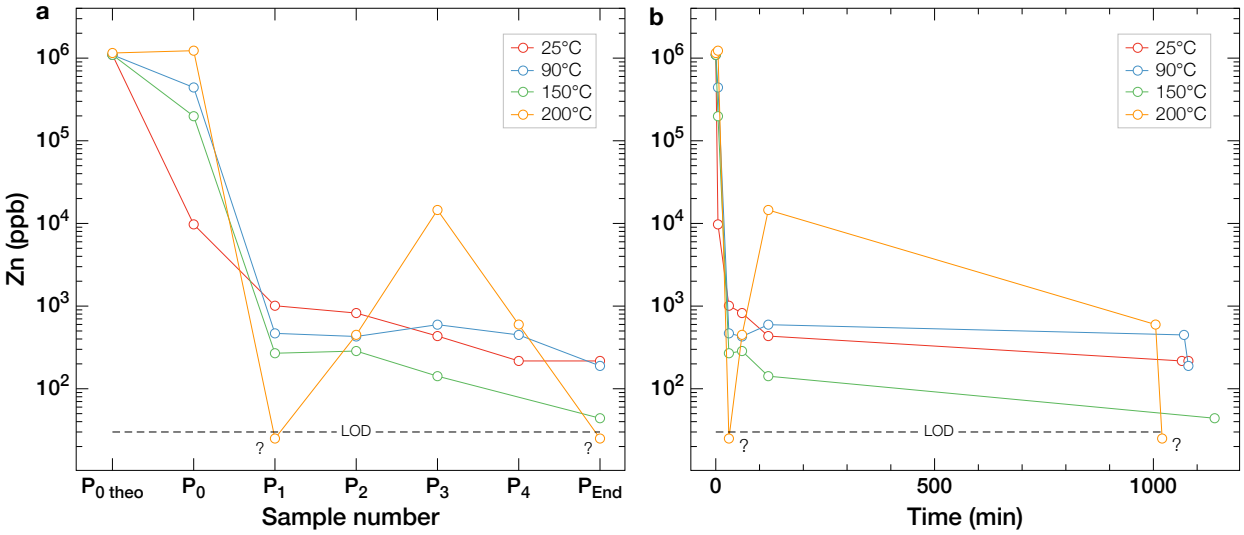

Fig. 8.1 – Evolution of Zn concentration through the experiments, *vs* the sample number (**a**) and, *vs* time (**b**). $P_{i\ theo}$ represents the theoretical concentration of Zn at the injection of the stock Zn–Ge solution in the autoclave. P_{End} is sample when autoclave has cooled down. It can be inferred that the precipitation of sphalerite was completed at P_1. The points marked with '?' have concentrations below the limit of detection for which virtual concentrations are used for representation only.

Given the very fast kinetic of the reaction and since it was impossible to perform a sampling on time to the second, there are obviously time discrepancies when comparing the first sampling (P_0) for each experimental run. However, as shown in Fig. 8.2, Ge and Zn concentrations in solution (P_0) markedly correlates with the experiment temperature, suggesting that the reaction kinetic would decrease with increasing temperature.

Table 8.2 – Fluid compositions in Ge and Zn trough each experiments. Element contents were determined using ICP-MS at the SARM (CRPG-Nancy) trough the 'Trace element' process.

	Time	pH	H_2S (M)	Ge (ppb)	1σ	Zn (ppb)	1σ	$Ge_{cons.}$ (%)	$Zn_{cons.}$ (%)
Stock solution									
		–	–	150772	12062	24219062	2421906	–	–
ZnSGe2 – 25°C									
$P_{0\ theo}$	Injection	5.50	0.070	6999	560	1124260	112426	0	0
P_0	5'	1.30	0.071	0.37	0.03	9740	974	99.99	99.13
P_1	30'	2.07	–	0.07	0.01	1010	101	100.00	99.91
P_2	1 h	2.15	–	0.07	0.01	824	82	100.00	99.93
P_3	2 h	2.15	0.057	–	–	434	43	100.00	99.96
P_4	17 h 45'	2.13	0.055	–	–	217	22	100.00	99.98
P_{End}	18 h	–	–	–	–	217	22	100.00	99.98
ZnSGe3 – 90°C									
$P_{0\ theo}$	Injection	6.00	0.050	6826	546	1096547	109655	0	0
P_0	5'	2.15	0.039	17.7	1	441569	44156.9	99.75	60.72
P_1	30'	2.09	–	–	–	468	46.80	100.00	99.96
P_2	1 h	2.09	–	–	–	429	42.90	100.00	99.96
P_3	2 h	2.15	0.035	–	–	596	59.60	100.00	99.95
P_4	17 h 50'	2.20	0.024	0.07	0.01	448	44.80	100.00	99.96
P_{End}	18 h	–	–	–	–	189	18.90	100.00	99.98
ZnSGe4 – 150°C									
$P_{0\ theo}$	Injection	5.90	0.110	6829	546	1096961	109696	0	0
P_0	5'	2.73	0.085	56.90	4.55	198203	19820	99.19	82.37
P_1	30'	2.15	–	–	–	269	26.90	100.00	99.98
P_2	1 h	2.25	–	–	–	286	28.60	100.00	99.97
P_3	2 h	2.25	0.039	–	–	142	14.20	100.00	99.99
P_{End}	19 h	–	–	–	–	44	4.40	100.00	100.00
ZnSGe5 – 200°C									
$P_{0\ theo}$	Injection	6.00	0.088	7376	590	1184918	118492	0	0
P_0	5'	2.20	0.037	1006	80	1230156	123016	86.36	0.00
P_1	30'	–	–	–	–	–	–		
P_2	1 h	1.70	–	0.11	0.01	449	45	100.00	99.96
P_3	2 h	1.75	0.032	126	10.08	14542	1454	98.29	98.77
P_4	16 h 45'	3.10	0.010	1661	132.88	598	60	77.48	99.95
P_{End}	17 h	–	–	1179	94	–	–	84.02	100.00

– Not detected

Data in grey are suggested

P_{End} corresponds to cooled down autoclave

P = 6 bar for all experiments

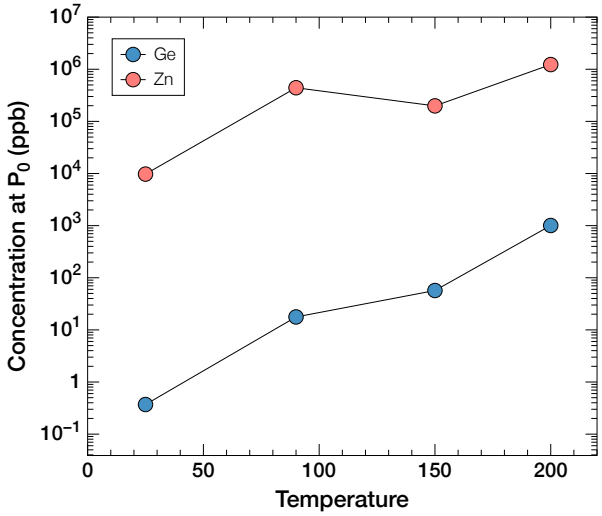

Fig. 8.2 – Concentrations of Ge and Zn in solution at P_0 in function of the experiment temperature. Ge concentrations, and to a lesser extent, Zn concentration, increases with increasing temperature, suggesting that ZnS precipitates faster towards low temperatures and that Ge incoporation is controlled by the ZnS precipitation kinetic.

8.4 Solid product characterisation

Secondary electron microscope observations highlight that the powders are composed of highly agglomerated fine particles (Fig. 8.3a). Even dispersed, the particles size is hardly measurable (Fig. 8.3b, few ηm only) although particles of larger size are present (roughly about 40–80 ηm). Energy dispersive analysis display a ZnS chemical composition for all the powders.

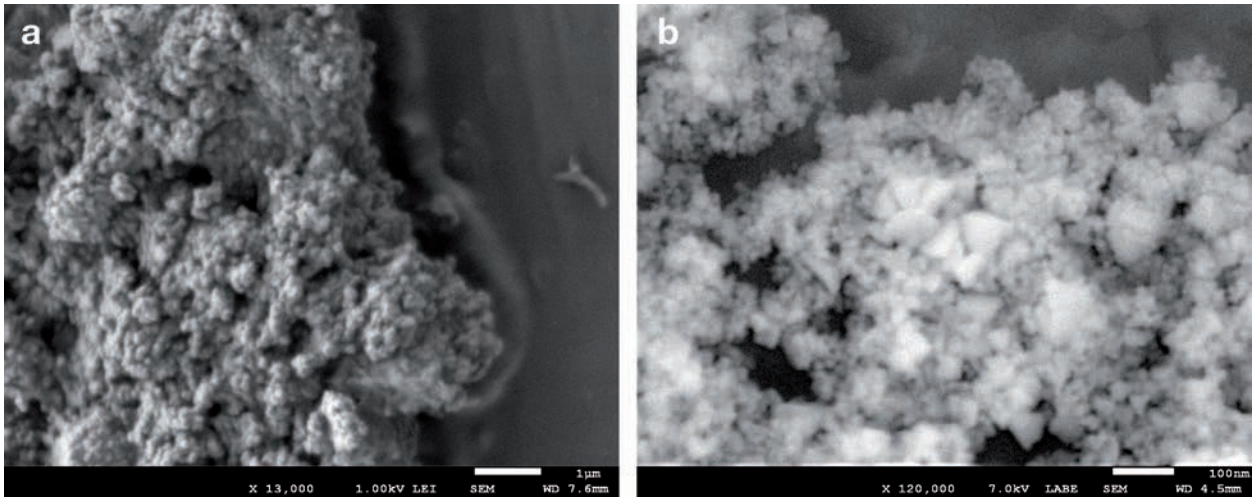

Fig. 8.3 – Secondary electron microphotograhs of the synthetic powder ZnSGe3 (90°C). **a** Powder as it stands, composed of highly agglomerated fine particles. **b** Dispersed particles. A small amount of powder is dispersed in ethanol using ultrasonic bath. A drop of it then drown on the sample holder. The smallness of the particles can be appreciated (few ηm) though they are still agglomerated. Particles of larger size are however present (about 40–80 ηm).

X-ray diffraction were performed in collaboration with Renaud Gley and Isabelle Bihannic (LIEC, Nancy) in order to better characterise the powders, especially to verify the crystal structure of ZnS (sphalerite or wurtzite) and the crystallinity of the powders. XRD spectra were acquired on a Brüker D8 at the LIEC, Nancy; they are presented in Fig. 8.4. All show diffraction peaks characteristic of sphalerite ($F\bar{4}3m$ space group). Moreover, in ZnSGe5

(200°C), the characteristic peaks of native sulphur (α form) are observed. In addition, the peaks width vary between the samples, the broader being those of ZnSGe2 (25°C), the narrower being those of ZnSGe4 (150°C).

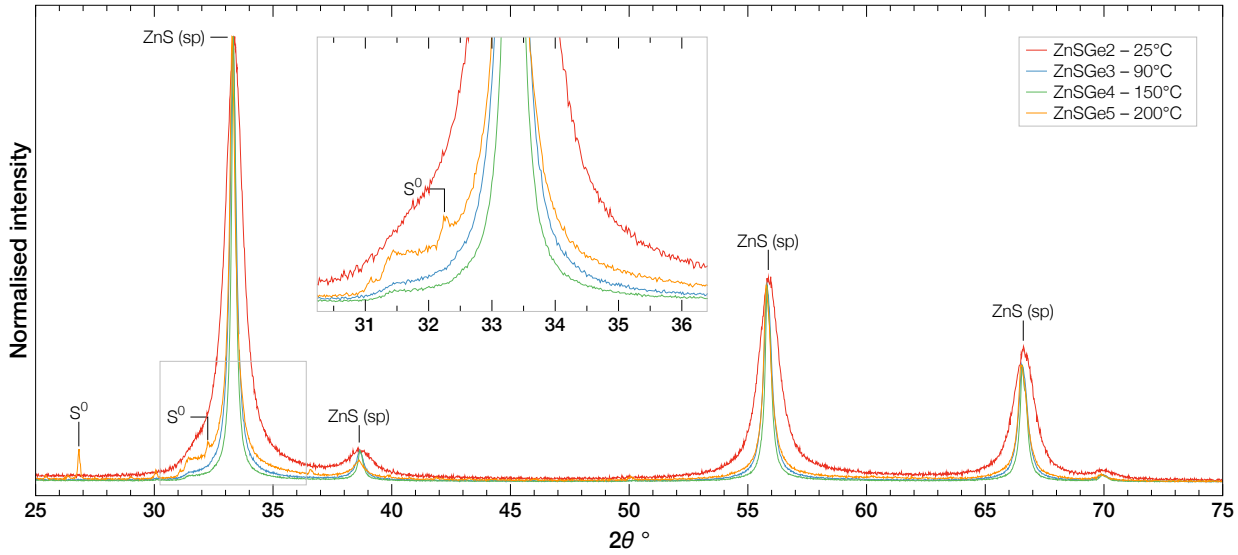

Fig. 8.4 – X-ray diffraction patterns of the four experiment solid products performed at the LIEC (Nancy) using a Brüker D8.

The powder characterisation was refined by the Rietveld method with X-ray diffraction data using the TOPAS software (Brüker-AXS). The fitted parameters were (i) the cubic unit cell parameter, a, (ii) the crystallite size using a Lorentz distribution and (iii) the Ge/Zn substitution rate. Strain broadening coefficients were not applied since they did not improved the fits. Particularly, the results (Table 8.3) show that the crystallinity increases with temperature from 25°C to 150°C (in line with the peak narrowing), but decreases in the experiment performed at 200°C, along with the appearance of sulphur α (5.75%). The crystal growth rate would therefore increase with temperature and decrease at higher sulphur activity. In addition, the Ge/Zn ratio of the site occupancy is fairly similar for temperatures of 25°C to 150°C, but is found to be higher at 200°C. This higher substitution rate would either be related to higher Ge content in the solution of this experiment (see P_{0theo} in Table 8.2), or associated with higher sulphur activity as suggests the presence of native sulphur.

Germanium concentrations were measured by LA-ICP-MS on pellets of the sphalerite powder. Ge concentration in sphalerite is similar between 25°C and 90°C (Fig. 8.5), grading 2641±144 and 2655±120 ppm Ge, respectively, but increases significantly at 150°C, attaining 3202 ± 212 ppm Ge. However, at 200°C, the Ge concentration falls down to 2014 ± 91 ppm.

Table 8.3 – Key results of the Rietveld method applied on X-ray diffraction patterns of the experimental sphalerite powders.

	ZnSGe2 25°C	ZnSGe3 90°C	ZnSGe4 150°C	ZnSGe5 200°C
R-values				
R_{wp}	7.41	8.45	10.44	16.11
R_{exp}	3.11	3.00	3.11	3.02
GOF	2.39	2.82	3.36	5.34
Structure parameters				
R-Bragg	3.121	2.888	2.447	6.180
Scale ($\times 10^3$)	9.434	9.566	8.744	8.865
Cell mass (g)	372.6	376.1	374.5	363.5
Cell volume (nm^3)	157.7	158.1	158.0	158.3
Crystallite size (nm)	11.7	30.2	43.4	23.2
Absorption coeff. (cm^{-1})	463.7	465.3	464.6	454.9
Crystal density ($g.cm^{-3}$)	3.922	3.949	3.937	3.813
Cubic cell lenght (nm)	5.403	5.408	5.406	5.409
Atom occupancy				
Zn^{2+}	0.852	0.882	0.869	0.774
Ge^{4+}	0.074	0.059	0.066	0.113
S^{2-}	1	1	1	1

R_{wp} Weighted profile R-factor
R_{exp} Expected R factor ("best possible R_{wp}")
GOF Goodness-of-fit

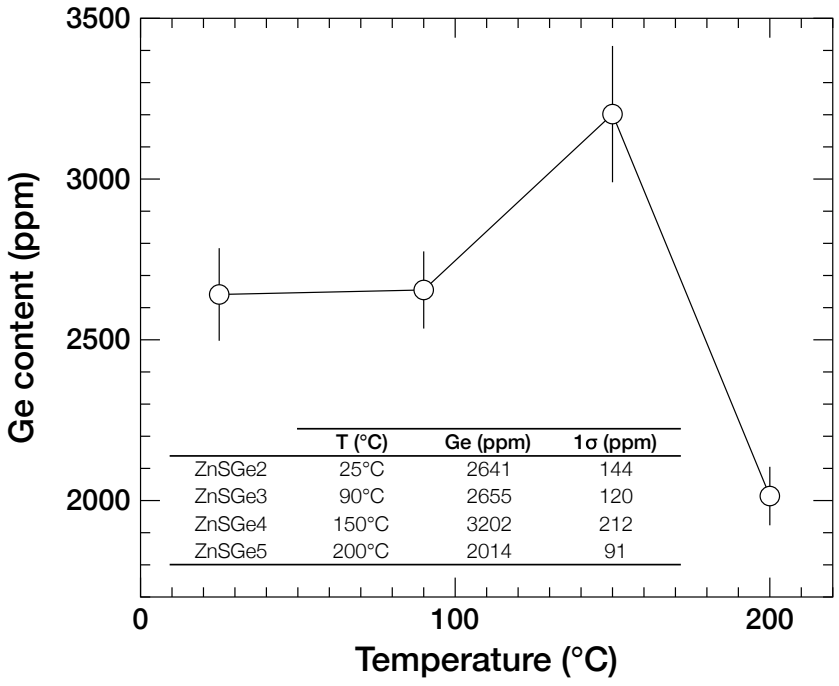

Fig. 8.5 – Ge concentrations in experimental sphalerites by LA-ICP-MS.

8.5 Ge isotope compositions

Given the high Ge content of the synthesised sphalerites, only a small amount was necessary to perform MC-ICP-MS analyses of several replicates. The Ge isotopic composition of the fluid before precipitation were determined in analysing synthetic GeO_2 that was used for preparing the Zn–Ge stock solution, both before and after dissolution. Unfortunately, despite our efforts to recover all of the remaining Ge in the final experimental solutions though an entire fluid evaporation followed by two-step column processing, only the ZnSGe5 solution was finally found to contain enough Ge to measure its isotopic composition. In addition, two external Ge standards were analysed during each analytical session for controlling the accuracy and reproducibility of the measurements. The results are presented in Table 8.4. δ^{72}Ge, δ^{73}Ge and δ^{74}Ge are plotted against one another in Fig. 8.6a–b, their alignment on the theoretical mass fractionation line attests to the reliability of the data.

Table 8.4 – Ge bulk isotope compositions with respect to the SRM NIST 3120a reference for experimental sphalerite and solutions. Errors in 2σ SD.

	T (°C)	n	δ^{72}Ge (‰)	2σ (‰)	δ^{73}Ge (‰)	2σ (‰)	δ^{74}Ge (‰)	2σ (‰)	Ge (ppm)*	1σ (ppm)
Sphalerite										
ZnSGe2	25°C	6	0.01	0.09	-0.03	0.20	-0.03	0.09	2641	144
ZnSGe3	90°C	6	-0.01	0.06	-0.02	0.08	-0.04	0.11	2655	120
ZnSGe4	150°C	8	0.05	0.06	-0.05	0.11	-0.06	0.20	3202	212
ZnSGe5	200°C	6	-0.19	0.06	-0.56	0.17	-0.69	0.12	2014	91
Solution										
GeO_2	–	9	-0.15	0.06	-0.25	0.28	-0.27	0.10	–	–
ZnSGe5	200°C	3	3.00	0.26	2.93	0.15	3.91	0.18	1179	94.32
Standards										
Aldrich Sep.	–	15	-1.02	0.11	-1.50	0.25	-2.00	0.17	–	–
JMC Sep.	–	15	-0.13	0.10	-0.15	0.38	-0.30	0.10	–	–
Aldrich Nov.	–	8	-1.01	0.06	-1.56	0.20	-1.97	0.11	–	–
JMC Nov.	–	8	-0.13	0.04	-0.20	0.17	-0.30	0.03	–	–

* Measured by LA-ICP-MS for sphalerite powders (as pellets), by ICP-MS for solutions.

Sphalerites produced at 25°C, 90°C and 150°C (ZnSGe2, 3 and 4, respectively) display very similar δ^{74}Ge compositions (Fig. 8.7), around -0.04 ± 0.25‰ (including SD of the mean and 2σ SD errors), which is also similar (within error), though slightly heavier, that the initial fluid composition, which is represented by GeO_2 at -0.27 ± 0.1‰ (2σ SD). Since almost all Ge has been integrated into sphalerite, their composition tend to that of the initial fluid δ^{74}Ge value. Sphalerites being isotopically heavier than the initial fluid is somewhat unexpected because all naturalistic observations of crystal–fluid fractionation (e.g., Siebert et al., 2006; Escoube et al., 2015) and theoretical predictions (Li et al., 2009) show that light δ^{74}Ge compositions always occur in sulphide minerals relatively to hydrothermal fluids. Unfortunately, it is difficult to address properly this matter without knowing the respective final-state fluid composition.

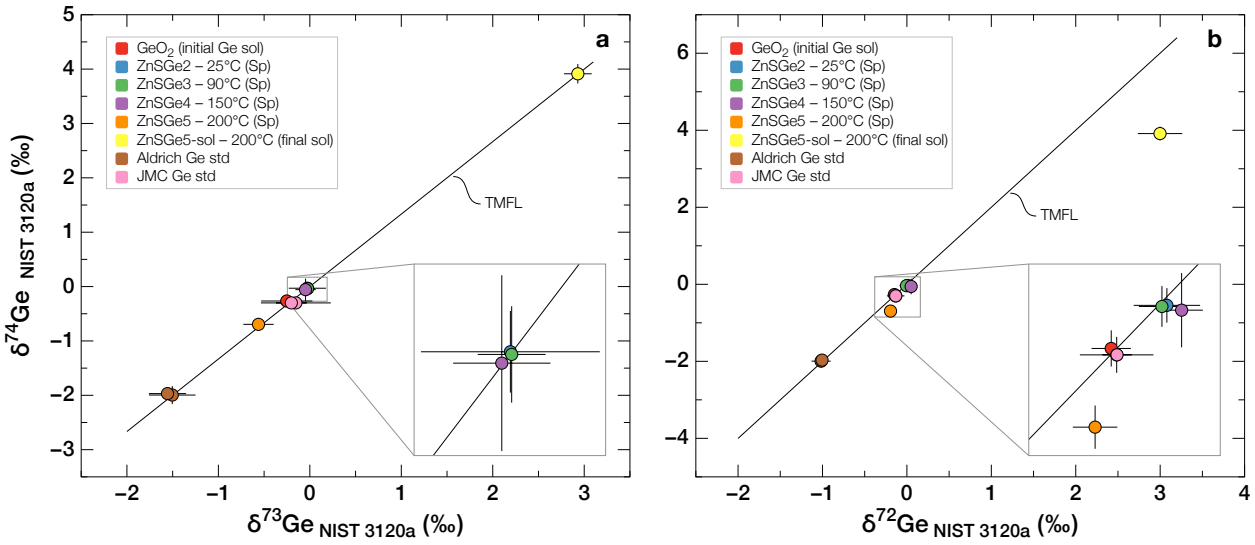

Fig. 8.6 – **a**. δ^{74}Ge *vs* δ^{73}Ge plot of the four experimental sphalerite products and fluid compositions. All the data fall on the theoretical mass fractionation line within error. **b**. δ^{74}Ge *vs* δ^{72}Ge plot. Only the final solution of experiment ZnSGe5 is out of the TMFL due to S interferences on ^{72}Ge.

The experiment performed at 200°C (ZnSGe5), however, exhibits a δ^{74}Ge of -0.69 ± 0.12‰ (Fig. 8.7), which is therefore about 0.42‰ lighter than the initial fluid composition, thus in line with the empirical and theoretical background. This composition is obviously close to that of the initial fluid since 83‰ of the Ge stock has been integrated in the precipitated sphalerite. Inverserly, in the fluid, the remaining 17% of the intial Ge stock shows a δ^{74}Ge composition of $+3.91 \pm 0.18$‰ significantly heavier than sphalerite. The mass balance calculation yields +0.09‰, making a difference of only 0.36‰ compared to the expected value of the intial fluid composition, i.e., -0.27‰. This small difference most likely originates from the uncertainties associated with either fluid samples dilutions and their analysis by ICP-MS (about 8% on Ge, 10% on Zn).

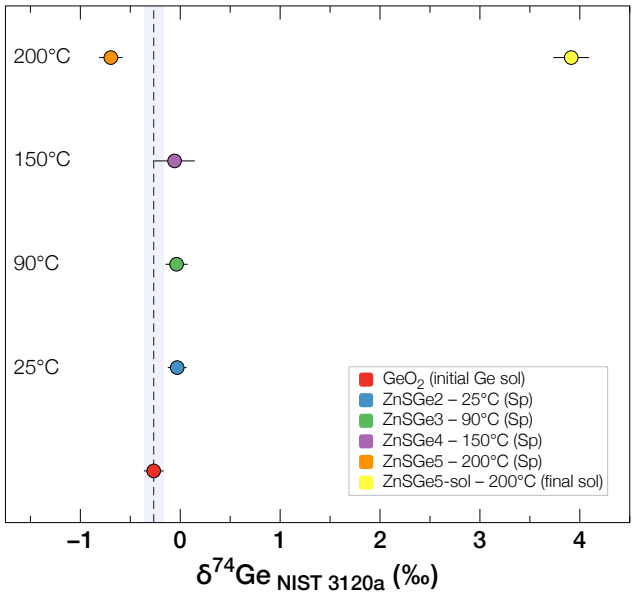

Fig. 8.7 – δ^{74}Ge compositions experimental sphalerites (ZnSGe2 to ZnSGe5), the initial fluid composition (GeO_2), and the final fluid composition (only experiment ZnSGe5 was found to have enough Ge for isotopic analysis).

8.6 Discussion

For sphalerite precipitated at 25°C, 90°C and 150°C, the entire Ge stock in solution was pumped into sphalerite, so we cannot calculate the sphalerite–fluid partition coefficient, $K_{\mathrm{d}}^{\mathrm{Ge}} = [\mathrm{Ge}]_{\mathrm{sp}}/[\mathrm{Ge}]_{\mathrm{fluid}}$. At 200°C, we can however estimate a $K_{\mathrm{d}}^{\mathrm{Ge}}$ of 1708 ± 157 (propagated 1σ SD). Remarkably, up to 150°C, Ge concentration in sphalerite smoothly increases with temperature, from 2641 to 3202 ppm, which is consistent with the idea suggested in Sec. 6.2.4, i.e., at high S activity (Zn deficient sphalerite), Ge concentration in sphalerite may increase with temperature due to an exothermic reaction of incorporation. However, the Ge content falls down to 2014 ppm Ge at 200°C, which suggests an inversion in the evolution partition coefficient in function of temperature somewhere between 150°C and 200°C.

As a shown in section 2.4.1, the equation associated with the Ge isotopic fractionation for sphalerite precipitating in a hydrothermal fluid can be cast as

$$\Delta^{74}\mathrm{Ge}_{\mathrm{sp-fluid}} = \delta^{74}\mathrm{Ge}_{\mathrm{sp}} - \delta^{74}\mathrm{Ge}_{\mathrm{fluid}} \simeq 1000 \ln \alpha_{\mathrm{sp-fluid}} = \frac{A}{T^2} + B$$

where T is the temperature in Kelvin and A and B two constant parameters. The ZnSGe5 experiment is associated with an isotopic fractionation, $\Delta^{74}\mathrm{Ge}_{\mathrm{sp-fluid}}$, of –4.58‰, which makes a $\alpha_{\mathrm{sp-fluid}}$ of about 0.9954 at 200°C. Using first-principles density functional theory, Li et al. (2009) predicted that $\Delta^{74}\mathrm{Ge}_{\mathrm{sp-fluid}} = -11.4‰$ at 25°C, yielding a temperature parameter, A, of -1.0134×10^6 (as in many instances, B is approximated to zero). Using the latter parameter, at 200°C, we can calculate that $\Delta_{\mathrm{sp-fluid}} = -4.53‰$, which is in good agreement with our measured value of –4.58‰. In the same manner, using our experimental value, $\Delta_{\mathrm{sp-fluid}} = -4.58‰$, we can calculate a temperature parameter A, of -1.0253×10^6, yielding the following first-assumption relation:

$$\Delta^{74}\mathrm{Ge}_{\mathrm{sp-fluid}} = \frac{-1.0253 \times 10^6}{T^2}$$

Finally, the above equation would be significantly refined if the fluid composition of the experiments at 25°C, 90°C and 150°C were measurable, such as parameter A and B would be obtained using a data regression. In this state, we could expect the isotopic compositions of the fluid ($\delta^{74}\mathrm{Ge}_{\mathrm{fluid}}$) at 25°C, 90°C and 150°C, to be as high as +11.50‰, 7.74‰, and 5.56‰, respectively. The sphalerite–fluid isotopic fractionation measured at 200°C, $\Delta^{74}\mathrm{Ge}_{\mathrm{sp-fluid}}$, of –4.58‰ is consistent with that measured by Escoube et al. (2015) between Fe–Zn sulphides (sphalerite ± pyrite) and fluids, of about $-5.6 \pm 0.6‰$ at the East Pacific Rise (Bio9 vent) for sphalerite precipitation temperatures below 250°C along the chimney wall.

Chapter 9

Summary and conclusions

Germanium-bearing sulphide minerals were studied in a series of contrasted types of ore deposits, combining mineralogical observations associated with both *in situ* and bulk analyses of trace elements and stable isotopes, and XAFS spectroscopy. A detailed multi-scale investigation of Ge geochemistry, spanning from the scale of the sulphide mineral lattice, up to that of minerals and ore deposits was carried out thanks to the study of Ge distribution, substitution mechanisms, and deposition or enrichment processes. The main features of Ge behaviour in the most important minerals of this study, i.e., sphalerite, chalcopyrite and renierite, are summarised in Table 9.1, and a comparison of the main characteristics of the Saint-Salvy, Barrigão, and Kipushi deposit is presented in Table 9.2.

9.1 Ge crystal chemistry and incorporation mechanisms

Germanium crystal chemical studies in sphalerite by XAFS spectroscopy formally indicated the occurrence of Ge^{4+}, Cu^{+}, and Fe^{2+} in tetrahedral sites, with no significant differences neither within nor between zoning type. Likewise, tetrahedral Ge^{4+} was formally identified in all of the studied Ge-bearing sulphide minerals, either in those where Ge is an essential component, i.e., renierite, briarite and germanite, or in sulphide having Ge in trace amounts, in solid solution, i.e., sphalerite, chalcopyrite, covellite, or in micro/nano-inclusion of Ge-sulphides, which is rare but was observed in one sphalerite from Kipushi (A38).

Germanium analysis by LA-ICP-MS has been refined in order to provide reliable data for Ge and related trace elements in a number of sulphide minerals in the studied deposits. Multivariate statistics, especially principal component analysis, was applied to the LA-ICP-MS dataset in order to gain statistical power in the identification of element correlation and their interpretation. Sphalerite consistently shows a strong correlation of tri- and tetravalent elements (Ge, Ga, Sb, In, Sn) with monovalent elements (Cu, Ag), outlining the occurrence of coupled substitution mechanisms for heterovalent elements, cast as $(2x + 3y)Zn^{2+} \leftrightarrow (x+2y)(Cu, Ag)^{+} + x(Ga, In, Sb)^{3+} + y(Ge, Sn)^{4+}$. In contrast with previous studies, notably that of Johan (1988), divalent elements are not included in this mechanism given the broad lack of correlation with heterovalent elements. Instead, divalent elements can readily enter the sphalerite structure trough direct substitutions, such as $Zn^{2+} \leftrightarrow (Fe,Cd,Mn)^{2+}$.

Table 9.1 – Main Ge geochemical features in the most important Ge-bearing sulphides of this study.

	Sphalerite **ZnS**	**Chalcopyrite** **$CuFeS_2$**	**Renierite** **$(Cu,Zn)_{11}(Ge,As)_2Fe_4S_{16}$**
Deposit	Saint-Salvy Kipushi	Barrigão Kipushi	Kipushi
Ore texture	**Saint-Salvy** – Cockade breccia, slow growth rate, open-space filling **Kipushi** – Locally massive or in equilibrium in mixed Pb–Zn and Zn–Cu ores. Chalcopyrite DIS in places	**Barrigão** – Subhedral grains interlocked with fahlore, replacement textures in places. **Kipushi** – Mostly in equilibrium in Zn–Cu or locally massive in Cu ores	Locally massive or in equilibrium with various sulphides in Zn–Cu ores.
Ge crystal chemistry	Tetrahedral Ge^{4+}	Tetrahedral Ge^{4+}	Tetrahedral Ge^{4+}
Observed Ge contents	up to 2576 ppm (S) up to 5930 ppm (K)	2 – 5750 ppm (B) 13 – 686 ppm (K)	5.03 – 16.63 wt.%
Substitution mechanism	$3Zn^{2+} \leftrightarrow Ge^{4+} + (Ag,Cu)^{+}$ $2Zn^{2+} \leftrightarrow Ge^{4+} + \square$	$3Fe^{3+} \leftrightarrow 2(Ge,Sn)^{4+} + Cu^{+}$ $2Fe^{3+} \leftrightarrow Ge^{4+} + (Pb,Zn)^{+}$	Ge is a major element
Crystal-scale distribution	**Saint-Salvy** – Sector zoning in slow-grown, euhedral grains due to crystal controls. **Kipushi** – Rather homogeneous or as micro/nano-inclusions of Ge-sulphide.	**Barrigão** – Patchy zoning around chalcopyrite grain relics, coating grain borders in fractured zones, or vein-like. **Kipushi** – Homogeneous	Homogeneous
Ge uptake timing	**Saint-Salvy** – Synchronous, associated with both crystal-structural controls (sector zoning) and micro-scale rhythmic variation of fluid composition (banding) **Kipushi** – Likely related to a fluid 'Ge peak' event, probably contemporary or close to the precipitation of Ge-sulphides	**Barrigão** – Late hydrothermal overprint **Kipushi** – Likely related to a fluid 'Ge peak' event, probably contemporary or close to the precipitation of Ge-sulphides	Characteristic of a Zn–Cu–Ge-rich fluid event, probably at high S activity, as attest the presence of sulfosalts

More specifically, Ge was found to be incorporated as $3Zn^{2+} \leftrightarrow Ge^{4+} + 2(Cu,Ag)^{+}$, but our experimental study indicate that large amounts of Ge can be readily incorporated in sphalerite, most likely trough the creation of vacancies, as $2Zn^{2+} \leftrightarrow Ge^{4+} + \square$, probably at high S activity, in which condition sphalerite is Zn deficient. Consequently, the positive $\delta^{74}\mathrm{Ge} - \mathrm{Ge}$ content correlation observed in sphalerite from Saint-Salvy indicate that Ge partition coefficient, $K_{\mathrm{d}}^{\mathrm{Ge}} = [\mathrm{Ge}]_{\mathrm{ZnS}}/[\mathrm{Ge}]_{\mathrm{sol}}$, may increase with temperature, in which case the reaction of Ge incorporation would be exothermic (i.e., $\Delta G < 0$) and thermodynamically spontaneous.

Chalcopyrite showed a marked anticorrelation of Ge and the related, Ga, Sn, Sb and Ag, with Fe, indicating that these elements substitute in the Fe site through coupled substitutions. Particularly, Ge incorporation can occur via the following coupled substitutions, $3Fe^{3+} \leftrightarrow 2Ge^{4+} + Cu^{+}$ and $2Fe^{3+} \leftrightarrow (Sn, Ge)^{4+} + (Pb, Zn)^{2+}$. In the tennantite–tetrahedrite series, Ge is found to be towards the tennantite end-member. One explanation for this is that Ge substitutes in the As site rather than in the Fe site. Ge anticorrelates with Zn in tennantite from Kipushi, which suggest it may also substitutes in the site of Zn through the mechanisms identified for sphalerite. In bornite, Ge correlates with Ag, suggesting a coupled substitution mechanism such as $3Fe^{3+} \leftrightarrow 2Ge^{4+} + Ag^{+}$ though the anticorrelation expected with Fe is unclear. In pyrite, Ge correlates with Cu, which brings to mind the coupled substitution observed in sphalerite.

Table 9.2 – Comparison of the main features of the deposits of Saint-Salvy, Barrigão, and Kipushi.

	Saint-Salvy French Massif Central	**Barrigão** Iberian pyrite belt	**Kipushi** Central-african copperbelt
Deposit type	Sediment-hosted Zn vein-type Fluid characteristics of MVT	Sediment-hosted Cu vein-type Re-mobilised VMS	Carbonate-hosted Cu–Zn Kipushi-type
Age	Late triassic–early Jurassic (~180 Ma) Late Variscan, extensional regime	Late Variscan, possible Eo-Alpine overprint	Late ordovician (~451 Ma) Post Lufilian (peak 530 Ma)
Ore type	Cockade breccia	Breccia	Massive sulphides
Ore paragenesis	Sp	Cp, Tn–Tht and minor Py	Sp, Cp, Bn, Cc, Py, Apy, Tn, Gn and accessory Rn, Shg
Elements	Zn ± Ge, Ag, Cd, Pb	Cu ± Ge, Sn	Zn, Cu ± Pb, Ge, Ga, Mo, W, V
Fluid nature	H_2O–NaCl–$CaCl_2$	Not presumed *	NaCl–KCl–$CaCl_2$
Salinity	23–25 wt.% NaCl eq.	2–25 wt.% NaCl eq.*	~30–43 eq.wt.% NaCl eq.
Temperature	80–140°C	260–300°C * perhaps lower during Ge overprint	~290–380°C
Source of metals	Cambrian black schists ± Sidobre granite ?	VMS remobilisation and/or metasediments	Felsic basement leaching
δ^{74}Ge (‰)	–5.06‰ to +0.91‰ (5.97‰ ampl.)	–3.50‰ to –1.44‰ in Cp (1.52‰ ampl.) –5.72‰ to –3.22‰ in Tn–Tht (2.50‰ ampl.)	–0.36‰ to (3.41‰ ampl.)
Inferred process	Temperature effect, fluid cooling	Temperature effect	Rayleigh fractionation process

* Theoretical considerations of Mateus et al. (2003)
Abbreviations: Sp, sphalerite; Cp, chalcopyrite: Tn, tennantite; Tht, tetrahedrite; Bn, bornite; Cc, chalcocite; Py, pyrite; Gn, galena; Rn, renierite, Shg, shungite

9.2 Ge distribution and trends: from the crystal-scale to ore deposits and beyond

Germanium concentrations of up to ∼5900 ppm was measured in sphalerite (at Kipushi). In sphalerite from Saint-Salvy (max. 2580 ppm Ge), principal component analysis of trace element data outlined the antithetic clustering of Ge, Ga, Sb, Ag and Cu in sector zoning, while Fe, Cd, In and Sn are clustered in dark brown rhythmic bands. This contrasted element distribution point to crystal-structural controls on the incorporation of trace elements. Sphalerite from Kipushi show local Ge enrichments, whether Ge occurs in solid solution or in micro/inclusion is still unclear, but in contrast to sphalerite from Saint-Salvy, the average Ge concentration is relatively low (128 ppm). At Saint-Salvy, to best of our knowledge, the Ge-rich sphalerite is associated to a single hydrothermal event of low–T (80–140°C) and there is no clear relationship with the location within the orebody.

Chalcopyrite can also show strong enrichments in Ge, and concentrations of up to ∼5800 ppm have been measured in this study. With the exception of covellite (up to 0.35 wt.% Ge by EPMA), Ge concentrations were fairly low in the Cu-sulphides, bornite (max. 14 ppm) and tennantite (max. 182 ppm), as well as in pyrite (max. 182 ppm). In contrast to sphalerite from Saint-Salvy, chalcopyrite from Barrigão displays Ge enrichments coating grain borders in micro-fissures, as patchy zoning highlighting the relics of former chalcopyrite grains, or as vein-like zones through coarser grain, indicating that chalcopyrite incorporated

Ge during a late hydrothermal overprint. Mateus et al. (2003) theoretically estimated that the Cu veins though the Ossa Morena Zone were deposited in temperatures of ∼260–300°C under $10^{-33} < fO_2 < 10^{-28}$. The chalcopyrite deposition mechanism is however unclear and many processes are envisaged, such as local T decrease, H_2S increase, salinity depletion, reduction, or pH rise. Nevertheless, one would wonder whether there is a temperature difference associated with the late hydrothermal Ge overprint observed in chalcopyrite from Barrigão.

The link between trace element signature in sphalerite and its genetic type was already questioned since the pioneering studies of the 1940s (Stoiber, 1940; Oftedal, 1940; Evrard, 1945), but it was not until the 1980s that the first attempts to discriminate among sphalerite from various Zn–Pb deposit types on the basis of their trace element content and their relation with temperature were published (Qian, 1987; Möller et al., 1983). This topic was further fuelled in recent LA-ICP-MS studies (Cook et al., 2009; Ye et al., 2011; Murakami and Ishihara, 2013), in which was noted that metal source and ore-forming conditions appear to systematically influence the trace element signature in sphalerite. In an attempt to bring together these observations and ours in a single, statistically powerful perspective, these data were treated using principal component analysis. The results clearly indicated a first order relation with temperature: Ge, along with Ga and Sb, are correlated to low-T, sediment- and carbonate-hosted deposits, while In is markedly correlated to high-T, magmatic-related deposits (Belissont et al., 2014). This approach was put forward very recently, in the meta-analysis by Frenzel et al. (2016) on a large minor/trace element dataset compiled from the literature, who concluded that fluid temperature exerts a strong influence of the Ge and Ga contents in sphalerite while there appears that the In content is strongly controlled by Cu activity, and that metamorphic overprinting at T below $\sim 310 \pm 50$°C may lead to a relative loss of Ge and Ga by re-equilibration of sphalerite in high-T environments.

9.3 Germanium isotope implications into ore-forming processes

Germanium isotopes in sulphide minerals yield a range of δ^{74}Ge values, from –5.72‰ to +3.67‰ (Table 9.2). An isotopic fractionation amplitude as high as 5.97‰ was observed in sphalerite from Saint-Salvy, 1.52‰ and 2.5‰ in chalcopyrite and fahlore from Barrigão, respectively, and 3.41‰ in the ore assemblage from Kipushi.

The isotopically light compositions of Saint-Salvy and Barrigão vein-type ores appear to relate to variations in the low to moderate fluid temperature. In contrast, given the hot fluid temperatures (290–380°C) and the lack of systematic difference in δ^{74}Ge for the Kipushi ore minerals, the clear trend observed towards heavier isotopic composition suggests that temperature variations did not likely play a key role in the Ge isotope fractionation, but rather a Rayleigh fractionation effect. The ore-forming fluid at Kipushi may have therefore significantly evolved through ore deposition, as in 'closed system', while those involved for the Saint–Salvy sphalerite deposition and the Ge overprint at Barrigão were likely renewed and precipitation occurred in open system.

9.4 Outstanding issues

9.4.1 Parameters influencing Ge uptake in ore deposits

This study has provided new insights into Ge geochemistry in sulphide-bearing ore deposits and brings new facts for understanding the Ge geological cycle. Ultime Ge enrichements primarily occur in unmetamorphosed, sulphide-bearing ore deposits of two types: (1) those where Ge concentrations can reach up to few thousands ppm — low-grade high-tonnage deposits — such as ∼3000 ppm in sphalerite or ∼6000 ppm in chalcopyrite; and (2) those, scarcer, where Ge forms thiogermanates — high grade low tonnage — such as renierite or germanite. Of the parameters that favour Ge enrichements in hydrothermal ore systems, low-T deposition process is the requirement that comes up from every naturalistic-oriented studies (this study and those of Bernstein, 1985; Cook et al., 2009; Frenzel et al., 2014, 2016) and our experimental study — Ge incorporation may severely decrease between 150°C and 200°C.

High monovalent element activity may enhance Ge incorporation due to the formation of donor–acceptor pairs which may result in the formation of clusters. Of prime importance in our opinion, the sulphur activity play a important role in the Ge crystal–fluid partitioning. High S activity in Zn–Cu-rich fluids is essential for the formation of thiogermanates, but also in sulphide minerals where Ge occur in trace/minor amounts. For instance, we noted that Ge uptake in sphalerite appears to increase with temperature — most likely at $T < 200$°C as suggested by our experiments — which implies a thermodynamically favourable, exothermic reaction. Such as process was predicted to be possible for incorporating Fe^{3+} in sphalerite from atomistic calculations by Wright (2009) because high S activity, sphalerite can readily accommodate the entrance of heterovalent elements through the creation of vacancies.

Therefore, an extension of our experimental study, using the same protocol, would be the testing of Ge solubility in sphalerite with increased Ge activity in order to find $K_{\mathrm{d}}^{\mathrm{Ge}}$. Once the Ge solubility reached, study the $K_{\mathrm{d}}^{\mathrm{Ge}}$ and $\Delta^{74}\mathrm{Ge}_{\mathrm{sp-fluid}}$ evolutions with temperatures up to 450°C, or study the effect of S activity — and/or possibly that of Cu — on $K_{\mathrm{d}}^{\mathrm{Ge}}$ would be of prime importance. In addition, the understanding of the Ge uptake in chalcopyrite from Barrigão would greater benefit from fluid inclusion studies to decipher whether significantly distinct fluid events occurred by tracing fluid nature, salinity and temperature.

9.4.2 Ge sources and extraction

However, one largely unresolved, non-addressed issue remains the Ge source of these ore deposits, which is, in most cases, a crucial point for the metallogenesis of Ge-bearing deposits and for future exploration targeting. Potential Ge sources or pre-enrichment processes are poorly understood because, as for many metallogenic studies, they are physically inaccessible and/or depleted in metals partly due to hydrothermal alteration, which is not always readily identifiable. We emphasise that such study would require enhanced data regarding the two major sources from which Ge in hydrothermal fluids can be derived: (1) hydrothermal alteration of late igneous differentiates where Ge may be concentrated through fractional crystallisation, and (2) fluids migration in sedimentary basin sequences, particularly those

rich in organic matter. Specifically, the study of Ge sources would benefit from enhanced Ge budget calculations, which requires further analyses of Ge contents and stable isotopes, possibly combined with stable isotope systematics (e.g., Zn, Fe, S, Pb).

Of particular importance, the involvement of organic matter as a Ge pre-enriched source or in the Ge transport in low-T environments with aqueous organic species (Pokrovski and Schott, 1998a, e.g.,) should be a prime scientific target since most of the largest Ge-bearing deposits are related in some way to organic matter. At Saint-Salvy, Ge (and possibly Ag) were associated with organic matter in fluorine-rich phosphate pellets of the enclosing, Cambrian black schists (Barbanson and Geldron, 1983), that could have both acted as a Ge source and facilitated its mobilisation by hydrothermal solutions. At Kipushi, the occurence of shungite (amorphous organic matter) is widely recognised in the sulphide paragenesis as well as both close to and well away from the orebody in the black carbonaceous dolomite of the Kipushi, the Kakontwe Moyen and the Kakontwe Supérieur formation. Shungite may evidence the migration of bitumen/oil (now pyrobitumen; Melezhik et al., 1999) in which Ge may had been transported as relatively stable organo-germanium complexes (Höll et al., 2007).

The aqueous chemistry of Ge is well constrained (Wood and Samson, 2006) and was particularly refined by the study of Pokrovski and Schott (1998a) and Pokrovski et al. (2005). However, the Ge uptake in hydrothermal fluids requires further thermodynamic and kinetic data as well as experimental phase equilibria studies that are lacking to understand the functioning of Ge source. Likewise, the understanding of ultimate Ge crystal–fluid partitioning and isotopic fractionation in sulphide-bearing ore deposits requires enhanced experimental studies of sulphide precipitation in controlled, hydrothermal environment. For instance, an extension of our preceding experimental work on sphalerite would require to study the P_0 fluid and sphalerite samples that may both carry enough Ge for measuring the sphalerite–fluid partitioning, $K_{\mathrm{d}}^{\mathrm{Ge}}$, and isotopic fractionation, $\Delta^{74}\mathrm{Ge}_{\mathrm{sp-fluid}}$.

9.4.3 Ore beneficiation

Large efforts are ongoing for co-operating major and their minor/trace elements through implementation of trace element concentrations, mineral-processing and metallurgical and/or hydrometallurgical yields into the estimation of ore/metal reserves in 3D geosystems modelling. This encourages systematic detections of critical trace elements in major ore components, e.g., Ge, Ga and In in sphalerite. Geometallurgy will have to take better into consideration the future feasibility of co-processing, as most deposits will be probably operated for low grade ores, and treated using hydrometallugy.

Bibliography

Albarède, F. (2004). The stable isotope geochemistry of copper and zinc. *Reviews in Mineralogy and Geochemistry*, 55:409–427.

Andrault, D., Peryronneau, J., Farges, F., and Itié, J. P. (1995). High pressure and high temperature XAFS study of germanate: Fourfold versus sixfold coordination changes. *Physica B: Condensed Matter*, 208:327–329.

Ankudinov, A. L., Ravel, B., Rehr, J. J., and Conradson, S. D. (1998). Real-space multiple-scattering calculation and interpretation of x-ray-absorption near-edge structure. *Phys. Rev. B*, 58:7565–7576.

Arnórsson, S. (1984). Germanium in Icelandic geothermal systems. *Geochimica et Cosmochimica Acta*, 48(12):2489–2502.

Asael, D., Matthews, A., Bar-Matthews, M., Harlavan, Y., and Segal, I. (2012). Tracking redox controls and sources of sedimentary mineralization using copper and lead isotopes. *Chemical Geology*, 310-311:23–35.

Audi, G., Bersillon, O., Blachot, J., and Wapstra, A. H. (2003). The NUBASE evaluation of nuclear and decay properties. *Nuclear Physics A*, pages 3–128.

Avdonin, V. V. and Sergeeva, N. E. (1999). Rare metals in the evolutionary sequences of base-metal massive-sulfide deposits. *Moscow University Geology Bulletin*, 54(4):43–53.

Baldini, M., Aquilanti, G., Mao, H.-k., Yang, W., Shen, G., Pascarelli, S., and Mao, W. L. (2010). High-pressure EXAFS study of vitreous GeO2 up to 44 GPa. *Physical Review B*, 81(2):024201–024201.

Barbanson, L. and Geldron, A. (1983). Distribution du germanium, de l'argent et du cadmium entre les schistes et les minéralisations stratiformes et filoniennes a blende-sidérite de la region de Saint-Salvy (Tarn). *Chronique de la recherche minière*, 470:33–42.

Beard, B. L. and Johnson, C. M. (2004). Fe isotope variations in the modern and ancient earth and other planetary bodies. *Reviews in Mineralogy and Geochemistry*, 55:319–357.

Beaudoin, G. (2000). Acicular sphalerite enriched in Ag, Sb, and Cu embedded within color-banded sphalerite from the Kokanee Range, British Columbia, Canada. *The Canadian Mineralogist*, 38(6):1387–1398.

Belissont, R., Boiron, M.-C., Luais, B., and Cathelineau, M. (2014). LA-ICP-MS analyses of minor and trace elements and bulk Ge isotopes in zoned Ge-rich sphalerites from the

Noailhac – Saint-Salvy deposit (France): Insights into incorporation mechanisms and ore deposition processes. *Geochimica et Cosmochimica Acta*, 126:518–540.

Bente, K. and Doering, T. (1995). Experimental studies on the solid state diffusion of Cu + In in ZnS and on "Disease", DIS (Diffusion Induced Segregations), in sphalerite and their geological applications. *Mineralogy and Petrology*, 53(4):285–305.

Bernardini, G. P., Borgheresi, M., Cipriani, C., Di Benedetto, F., and Romanelli, M. (2004). Mn distribution in sphalerite: an EPR study. *Physics and Chemistry of Minerals*, 31(2):80–84.

Bernstein, L. R. (1985). Germanium geochemistry and mineralogy. *Geochimica et Cosmochimica Acta*, 49(11):2409–2422.

Bernstein, L. R. (1986a). Geology and mineralogy of the Apex germanium-gallium mine, Washington County, Utah. *United States Geological Survey Bulletin*, 1577:1–9.

Bernstein, L. R. (1986b). Renierite, $Cu_{10}ZnGe_2Fe_4S_{16}$-$Cu_{11}GeAsFe_4S_{16}$: a coupled solid solution series. *American Mineralogist*, 71:210–221.

Bernstein, L. R., Reichel, D. G., and Merlino, S. (1989). Renierite crystal structure refined from Rietveld analysis of powder neutron-diffraction data. *American Mineralogist*, 74:1177–1181.

Bernstein, L. R. and Waychunas, G. A. (1987). Germanium crystal chemistry in hematite and goethite from the Apex Mine, Utah, and some new data on germanium in aqueous solution and in stottite. *Geochimica et Cosmochimica Acta*, 51(3):623–630.

Berry, A. J., Yaxley, G. M., Woodland, A. B., and Foran, G. J. (2010). A XANES calibration for determining the oxidation state of iron in mantle garnet. *Chemical Geology*, 278(1-2):31–37.

Bertini, L., Ghigna, P., Scavini, M., and Cargnoni, F. (2003). Germanium K edge in GeO2 polymorphs. Correlation between local coordination and electronic structure of germanium. *Physical Chemistry Chemical Physics*, 5(7):1451–1456.

Blundy, J. and Wood, B. (1994). Prediction of crystal melt partition coefficients from elastic moduli.

Blundy, J. and Wood, B. (2003). Partitioning of trace elements between crystals and melts. *Earth and Planetary Science Letters*, 210(3-4):383–397.

Boiron, M. C., Cathelineau, M., and Richard, A. (2010). Fluid flows and metal deposition near basement/cover unconformity: lessons and analogies from Pb-Zn-F-Ba systems for the understanding of Proterozoic U deposits. *Geofluids*, 10:270–292.

Bonev, I. K., Kerestedjian, T., Atanassova, R., and Andrew, C. J. (2002). Morphogenesis and composition of native gold in the Chelopech volcanic-hosted Au–Cu epithermal deposit, Srednogorie zone, Bulgaria. *Mineralium Deposita*, 37(6-7):614–629.

Boni, M., Balassone, G., and Iannace, A. (1996). Base metal ores in the lower Paleozoic of southwestern Sardinia. *Economic Geology*, 75th Anniversary Volume:18–28.

Bonnet, J. (2014). *Distribution et contrôle cristallographique des éléments Ge, Ga et Cd dans les sphalérites des gisements de type Mississippi Valley dans les districts de Central et East Tennessee, USA*. PhD thesis.

Bradley, D. C. and Leach, D. L. (2003). Tectonic controls of Mississippi Valley-type lead–zinc mineralization in orogenic forelands. *Mineralium Deposita*, 38(6):652–667.

Brice, J. C. (1975). Some thermodynamic aspects of the growth of strained crystals. *Journal of crystal growth*, 28:249–253.

Bruce, S., Banks, D., Munoz, M., Courjault-Rade, P., Tollon, F., Boyce, A., and Fallick, A. (1998). The genesis of mineralising brines in the South West Massif Central, France. *Mineralogical Magazine*, 62A:238–239.

Brugger, J., Etschmann, B., Liu, W., Testemale, D., Hazemann, J. L., Emerich, H., van Beek, W., and Proux, O. (2007). An XAS study of the structure and thermodynamics of Cu(I) chloride complexes in brines up to high temperature (400 °C, 600bar). *Geochimica et Cosmochimica Acta*, 71(20):4920–4941.

Brugger, J., McPhail, D. C., Black, J., and Spiccia, L. (2001). Complexation of metal ions in brines: application of electronic spectroscopy in the study of the Cu(II)-LiCl-H_2O system between 25 and 90°C. *Geochimica et Cosmochimica Acta*, 65(16):2691–2708.

Brugger, J., Pring, A., Reith, F., Ryan, C., Etschmann, B., Liu, W., O'Neill, B., and Ngothai, Y. (2010). Probing ore deposits formation: New insights and challenges from synchrotron and neutron studies. *Radiation Physics and Chemistry*, 79(2):151–161.

Buckley, A. N., Skinner, W. M., Harmer, S. L., Pring, A., Lamb, R. N., Fan, L.-J., and Yang, Y.-w. (2007). Examination of the proposition that Cu (II) can be required for charge neutrality in a sulfide lattice-Cu in tetrahedrites and sphalerite. *Canadian Journal of Chemistry*, 85(10):767–781.

Butterman, W. C. and Jorgenson, J. D. (2005). Germanium. U.S. Geological Survey Mineral Commodity Profiles.

Cadoux, A., Blichert-Toft, J., Pinti, D. L., and Albaréde, F. (2007). A unique lower mantle source for Southern Italy volcanics. *Earth and Planetary Science Letters*, 259:227–238.

Cassard, D., Chabod, J.-C., Marcoux, E., Bourgine, B., Castaing, C., Gros, Y., Kosakevitch, A., Moisy, M., and Viallefond, L. (1994). Mise en place et origine des minéralisations du gisement filonien à Zn, Ge, Ag, (Pb, Cd) de Noailhac – Saint-Salvy (Tarn, France). *Chronique de la recherche minière*, 514:3–37.

Cathelineau, M., Boiron, M.-C., Fourcade, S., Ruffet, G., Clauer, N., Belcourt, O., Coulibaly, Y., Banks, D. a., and Guillocheau, F. (2012). A major Late Jurassic fluid event at the basin/basement unconformity in western France: 40Ar/39Ar and K–Ar dating, fluid chemistry, and related geodynamic context. *Chemical Geology*, 322-323:99–120.

Cempirek, J. and Groat, L. A. (2013). Note on the formula of brunogeierite and the first bond-valence parameters for Ge^{2+}. *Journal of Geosciences*, 58:71–74.

Charef, A. and Sheppard, S. (1988). The Malines Cambrian carbonate-shale-hosted Pb-Zn deposit, France: thermometric and isotopic (H, O) evidence for pulsating hydrothermal mineralization. *Mineralium Deposita*, 23:86–95.

Charnock, J. M., Garner, C. D., Pattrick, R., and Vaughan, D. J. (1989). EXAFS and Mossbauer spectroscopic study of Fe-bearing tetrahedrites. *Mineral Mag*, 53:193–199.

Ciobanu, C. L., Cook, N. J., and Stein, H. (2002). Regional setting and geochronology of the Late Cretaceous Banatitic Magmatic and Metallogenetic Belt. *Mineralium Deposita*, 37(6-7):541–567.

Cook, N., Etschmann, B., Ciobanu, C., Geraki, K., Howard, D., Williams, T., Rae, N., Pring, A., Chen, G., Johannessen, B., and Brugger, J. (2015). Distribution and Substitution Mechanism of Ge in a Ge-(Fe)-Bearing Sphalerite. *Minerals*, 5(2):117–132.

Cook, N. J., Ciobanu, C. L., and Bogdanov, K. (2002). Trace mineralogy of the Upper Cretaceous banatitic Magmatic and metallogenetic Belt, SE Europe. In *11th Quadrennial IAGOD Symposium and Geocongress*, Windhoek, Namibia.

Cook, N. J., Ciobanu, C. L., Brugger, J., Etschmann, B., Howard, D. L., de Jonge, M. D., Ryan, C., and Paterson, D. (2012). Determination of the oxidation state of Cu in substituted Cu-In-Fe-bearing sphalerite via μ-XANES spectroscopy. *American Mineralogist*, 97(2-3):476–479.

Cook, N. J., Ciobanu, C. L., Danyushevsky, L. V., and Gilbert, S. (2011). Minor and trace elements in bornite and associated Cu–(Fe)-sulfides: A LA-ICP-MS study. *Geochimica et Cosmochimica Acta*, 75(21):6473–6496.

Cook, N. J., Ciobanu, C. L., Pring, A., Skinner, W., Shimizu, M., Danyushevsky, L., Saini-Eidukat, B., and Melcher, F. (2009). Trace and minor elements in sphalerite: A LA-ICPMS study. *Geochimica et Cosmochimica Acta*, 73(16):4761–4791.

Cordero, B., Gomez, V., Platero-Prats, A. E., Reves, M., Echeverria, J., Cremades, E., Barragan, F., and Alvarez, S. (2008). Covalent radii revisited. *Dalton Trans.*, 21:2832–2838.

Danyushevsky, L., Robinson, P., Gilbert, S., Norman, M., Large, R., McGoldrick, P., and Shelley, M. (2011). Routine quantitative multi-element analysis of sulphide minerals by laser ablation ICP-MS: Standard development and consideration of matrix effects. *Geochemistry: Exploration, Environment, Analysis*, 11(1):51–60.

Dasch, E. J., editor (1996). *Encyclopedia of Earth Sciences*. Macmillan Reference USA, New York.

De Vos, W., Viaene, W., Moreau, J., and Wautier, J. (1974). Minéralogie du gisement de Kipushi, Shaba, Zaïre. *Annales de la Société géologique de Belgique*, Publication spéciale, Gisements stratiformes et provinces cuprifères - Centenaire de la Société Géologique de Belgique:165–183.

Di Benedetto, F. (2005). Compositional zoning in sphalerite crystals. *American Mineralogist*, 90(8-9):1384–1392.

Di Benedetto, F., Andreozzi, G. B., Bernardini, G. P., Borgheresi, M., Caneschi, A., Cipriani, C., Gatteschi, D., and Romanelli, M. (2005a). Short-range order of Fe2+ in sphalerite by 57Fe Mössbauer spectroscopy and magnetic susceptibility. *Physics and Chemistry of Minerals*, 32(5-6):339–348.

Di Benedetto, F., Bernardini, G. P., Borrini, D., Lottermoser, W., Tippelt, G., and Amthauer, G. (2005b). ^{57}Fe– and ^{119}Sn– Mössbauer study on stannite (Cu_2FeSnS_4)-kesterite (Cu_2ZnSnS_4) solid solution. *Physics and Chemistry of Minerals*, 31(10):683–690.

Dickinson, T., Taylor, G. J., and Keil, K. (1989). Germanium abundances in lunar basalts-Evidence of mantle metasomatism? *Lunar and Planetary Science ....*

Dimanche, F. (1974). Paragenèse des sulfures de cuivre dans les gisements du Shaba (Zaïre) : I. Kipushi ; II. Kamoto. *Annales de la Société géologique de Belgique*, Publication spéciale, Gisements stratiformes et provinces cuprifères - Centenaire de la Société Géologique de Belgique:185–201.

Ding, T., Valkiers, H., Kipphardt, H., De Bièvre, P., Taylor, P. D. P., Gonfiantini, R., and Krouse, R. (2001). Calibrated sulfur isotope abundance ratios of three IAEA sulfur isotope reference materials and V-CDT with a reassessment of the atomic weight of sulfur. *Geochimica et Cosmochimica Acta*, 65(15):2433–2437.

Dräger, G., Frahm, R., Materlik, G., and Brümmer, O. (1988). On the Multipole Character of the X-Ray Transitions in the Pre-Edge Structure of Fe K Absorption Spectra. An Experimental Study. *physica status solidi (b)*, 146:287–294.

El Korh, A., Luais, B., Boiron, M.-C., Deloule, E., and Cividini, D. Tracing fluid-related HP metamorphism in subduction zones using Ge and Ga trace elements and Ge isotopes: implications for the fore-arc mantle wedge composition (*in revision*). *Geochimica et Cosmochimica Acta*, pages 1–39.

Escoube, R., Rouxel, O. J., Edwards, K., Glazer, B., and Donard, O. F. X. (2015). Coupled Ge/Si and Ge isotope ratios as geochemical tracers of seafloor hydrothermal systems: Case studies at LoihiSeamount and East Pacific Rise 9 °50. *Geochimica et Cosmochimica Acta*, 167(C):93–112.

Escoube, R., Rouxel, O. J., Luais, B., Ponzevera, E., and Donard, O. F. X. (2012). An Intercomparison Study of the Germanium Isotope Composition of Geological Reference Materials. *Geostandards and Geoanalytical Research*, 36(2):149–159.

Eulenberger, G. (1977). Die Kristallstruktur der Tieftemperaturmodifikation von Ag_8GeS_6. *Monatshefte für Chemie/Chemical Monthly*, 108(4):901–913.

European Commission, X. (2010). Critical raw materials for the EU. Report of the Ad hoc Working Group on defining critical raw materials. Technical report, Brussels, Belgium.

European Commission, X. (2014). Critical raw materials for the EU. Report of the Ad hoc Working Group on defining critical raw materials. Technical report, Brussels, Belgium.

Evrard, P. (1945). Minor elements in sphalerites from Belgium. *Economic Geology*, 40(8):568–574.

Farquhar, J., Bao, H., and Thiemens, M. (2000). Atmospheric influence of Earth's earliest sulfur cycle. *Science*, 289:756–758.

Foglierini, F., Beziat, D., Tollon, F., and Chabod, J.-C. (1980). Le gisement filonien de Noailhac – Saint-Salvy (Tarn). In *26th International Geology Congress – Gisements français*, pages 1–43, Paris, France.

Folmer, J. and Jellinek, F. (1980). The valence of copper in sulphides and selenides: an x-ray photoelectron spectroscopy study. *Journal of the Less Common Metals*, 76(1):153–162.

Franklin, J. M., Lydon, J. W., and Sangster, D. F. (1981). Volcanic-associated massive sulphide minerals. *Economic Geology*, 75th Anniversary Volume:485–627.

Frenzel, M., Hirsch, T., and Gutzmer, J. (2016). Gallium, germanium, indium, and other trace and minor elements in sphalerite as a function of deposit type — A meta-analysis. *Ore Geology Reviews*, in press.

Frenzel, M., Ketris, M. P., and Gutzmer, J. (2014). On the geological availability of germanium. *Mineralium Deposita*, 49(4):471–486.

Frenzel, M. and Woodcock, N. H. (2014). Cockade breccia: Product of mineralisation along dilational faults. *Journal of Structural Geology*, 68(PA):194–206.

Froelich, P. N., Hambrick, G. A., and Andreae, M. O. (1985). The geochemistry of inorganic germanium in natural waters. *Journal of Geophysical Research*, 90(C1):1133–1141.

Gagnevin, D., Boyce, A. J., Barrie, C. D., Menuge, J. F., and Blakeman, R. J. (2012). Zn, Fe and S isotope fractionation in a large hydrothermal system. *Geochimica et Cosmochimica Acta*, 88:183–198.

Galoisy, L., Calas, G., and Arrio, M. A. (2001). High-resolution XANES spectra of iron in minerals and glasses: structural information from the pre-edge region. *Chemical Geology*, 174(1):307–319.

Gerard, A., Imbert, P., Prange, H., Varret, F., and Wintenberger, M. (1971). Fe^{2+} impurities, isolated and in pairs, in ZnS and CdS studied by the Mössbauer effect. *Journal of Physics and Chemistry of Solids*, 32:2091–2100.

Goh, S. W., Buckley, A. N., Lamb, R. N., Rosenberg, R. A., and Moran, D. (2006). The oxidation states of copper and iron in mineral sulfides, and the oxides formed on initial exposure of chalcopyrite and bornite to air. *Geochimica et Cosmochimica Acta*, 70(9):2210–2228.

Goodfellow, W. D., Lydon, J. W., and RJW, T. (1993). Geology and genesis of stratiform sediment-hosted (SEDEX) zinc–lead–silver sulphide deposits. In Kirkham, R. V., Sinclair, W. D., and Thorpe, R. I., editors, *Mineral Deposit Modelling*, pages 201–251. Geological Association of Canada Special Paper.

Grassineau, N. V. (2006). High-precision EA-IRMS analysis of S and C isotopes in geological materials. *Applied Geochemistry*, 21(5):756–765.

Gratz, J. C. and Misra, K. C. (1987). Fluid inclusion study of the Gordonsville zinc deposit, central Tennessee. *Economic Geology*, 82(7):1790–1804.

Guberman, D. E. (2013). Germanium. U.S. Geological Survey 2012 Minerals Yearbook.

Guberman, D. E. (2016). Germanium. U.S. Geological Survey, Mineral Commodity Summaries.

Haines, J., Leger, J. M., Chateau, C., and Pereira, A. S. (2000). Structural evolution of rutile-type and CaCl2-type germanium dioxide at high pressure. *Physics and Chemistry of Minerals*, 27(8):575–582.

Halfon, J. and Rosique, A. (1973). Comparaison des elements "en traces" dans les blendes du filon et les blendes du stratiforme de Saint-Salvy (81). *Bulletin du BRGM*, 5(2):403–432.

Haller, E. E. (2006). Germanium: From its discovery to SiGe devices. *Materials Science in Semiconductor Processing*, 9(4-5):408–422.

Hannington, M. D., Bleeker, W., and Kjaesgaard, I. (1999). Sulphide mineralogy, geochemistry, and ore genesis of the Kidd Creek deposit. Part I: north, central, and south orebodies. *Economic Geology Monographs*, 10:163–224.

Harańczyk, C. (1975). Morozewiczite and polkowicite – typo-chemical minerals of mesozoic mineralization in copper deposits of the fore-Sudetic monocline. *Rudy i Metale*, 20:288–293.

Heijlen, W., Banks, D. A., Muchez, P., Stensgard, B. M., and Yardley, B. (2008). The nature of mineralizing fluids of the Kipushi Zn-Cu deposit, Katanga, Democratic Repubic of Congo: quantitative fluid inclusion analysis using laser ablation ICP-. *Economic Geology*, 103:1459–1482.

Hilton, Sr, A. R. (1993). Chalcogenide glasses for passive FLIR systems. 2018:46–57.

Hirata, T. (1997). Isotopic variations of germanium in iron and stony iron meteorites. *Geochimica et Cosmochimica Acta*, 61(20):4439–4448.

Hoefs, J. (2009). Stable isotope geochemistry.

Höll, R., Kling, M., and Schroll, E. (2007). Metallogenesis of germanium—A review. *Ore Geology Reviews*, 30(3-4):145–180.

Hu, Z. and Gao, S. (2008). Upper crustal abundances of trace elements: A revision and update. *Chemical Geology*, 253(3-4):205–221.

Imbert, P., Varret, F., and Wintenberger, M. (1973). Etude par effet Mössbauer de la briartite (Cu_2FeGeS_4). *Journal of Physics and Chemistry of Solids*, 34(10):1675–1682.

Intiomale, M. M. (1982). *Le gisement Zn–Pb–Cu de Kipushi (Shaba–Zaire). Étude géologique et métallogénique*. PhD thesis, Université Catholique de Louvain, Louvain-la-Neuve.

Intiomale, M. M. and Oosterbosch, R. (1974). Géologie et géochimie du gisement de Kipushi, Zaïre. *Annales de la Société géologique de Belgique*, Publication spéciale, Gisements stratiformes et provinces cuprifères - Centenaire de la Société Géologique de Belgique:123–164.

Iwamori, H., Albaréde, F., and Nakamura, H. (2010). Global structure of mantle isotopic heterogeneity and its implications for mantle differentiation and convection. *Earth and Planetary Science Letters*, 299:339–351.

Johan, Z. (1988). Indium and Germanium in the Structure of Sphalerite : an Example of Coupled Substitution with Copper. *Mineralogy and Petrology*, 39:211–229.

Johan, Z., Oudin, E., and Picot, P. (1983). Analogues germanifères et gallifères des silicates et oxydes dans les gisements de zinc des Pyrénées centrales, France; argutite et carboirite, deux nouvelles espèces minérales. *Tschermaks Mineralogische und Petrographische Mitteilungen*, 31:97–119.

Johnson, C. A., Kelley, K. D., and Leach, D. L. (2004a). Sulfur and oxygen isotopes in barite deposits of the western Brooks Range, Alaska, and implications for the origin of the Red Dog massive sulfide deposits. *Economic Geology*, 99:1435–1448.

Johnson, C. M., Beard, B. L., and Albaréde, F. (2004b). Geochemistry of Non-Traditional Stable Isotopes: Overview and General Concepts. *Reviews in Mineralogy and Geochemistry*, 55:1–24.

Juhin, A., Brouder, C., Arrio, M.-A., Cabaret, D., Sainctavit, P., Balan, E., Bordage, A., Calas, G., Eeckhout, S. G., and Glatzel, P. (2008). X-ray Linear Dichroism in cubic compounds: the case of Cr3+ in MgAl2O4. *Physical Review B*, 78(195103):1–18.

Kampunzu, A. B., Cailteux, J. L. H., Kamona, A. F., Intiomale, M. M., and Melcher, F. (2009). Sediment-hosted Zn–Pb–Cu deposits in the Central African Copperbelt. *Ore Geology Reviews*, 35(3-4):263–297.

Kau, L.-S., Penner-Hahn, J. E., Solomon, E. I., and Hodgson, K. O. (1986). Quantitative Cu X-ray absorption edge studies: oxidation state and site structure determination. *Le Journal de Physique Colloques*, 47(C8):C8–1177–C8–1180.

Kau, L.-S., Spira-Solomon, D. J., Penner-Hahn, J. E., Hodgson, K. O., and Solomon, E. I. (1987). X-ray absorption edge determination of the oxidation state and coordination number of copper. Application to the type 3 site in Rhus vernicifera laccase and its reaction with oxygen. *Journal of the American Chemical Society*, 109(21):6433–6442.

Kelley, K. D., Leach, D. L., Johnson, C. A., Clark, J. L., Fayek, M., Slack, J. F., Anderson, V. M., Ayuso, R. A., and Ridley, W. I. (2004). Textural, Compositional, and Sulfur Isotope Variations of Sulfide Minerals in the Red Dog Zn-Pb-Ag Deposits, Brooks Range, Alaska: Implications for Ore Formation. *Economic Geology*, 99:1509–1532.

Kelley, K. D., Wilkinson, J. J., Chapman, J. B., Crowther, H. L., and Weiss, D. J. (2009). Zinc isotopes in sphalerite from base metal deposits in the Red Dog district, northern Alaska. *Economic Geology*, 104:767–773.

Kuhlemann, J., Vennemann, T., Herlec, U., Zeeh, S., and Bechstadt, T. (2001). Variations of sulfur isotopes, trace element compositions, and cathodoluminescence of Mississippi Valley-type Pb-Zn ores from the Drau Range, eastern Alps (Slovenia-Austria):. *Economic Geology*, 96:1931–1941.

Kurtz, A. C., Derry, L. A., and Chadwick, O. A. (2002). Germanium–silicon fractionation in the weathering environment. *Geochimica et Cosmochimica Acta*, 66(9):1525–1537.

Lach, P., Mercadier, J., Dubessy, J., Boiron, M.-C., and Cuney, M. (2013). In Situ Quantitative Measurement of Rare Earth Elements in Uranium Oxides by Laser Ablation-Inductively Coupled Plasma-Mass Spectrometry. *Geostandards and Geoanalytical Research*, (1):1–20.

Lafferière, F., Royer, J.-J., and Mallet, J. L. (2000). Multivariate Tools in gOcad. *20th Gocad meeting*, pages 1–14.

Large, R. R., McPhie, J., and Gemmell, J. B. (2001). The Spectrum of Ore Deposit Types, Volcanic Environments, Alteration Halos, and Related Exploration Vectors in Submarine Volcanic Successions: Some Examples from Australia. *Economic Geology*, 96:913–938.

Leach, D., Bradley, D., Lewchuk, M., Symons, D., de Marsily, G., and Brannon, J. (2001). Mississippi Valley-type lead-zinc deposits through geological time: implications from recent age-dating research. *Mineralium Deposita*, 36(8):711–740.

Leach, D., Macquar, J. C., Lagneau, V., Leventhal, J., Emsbo, P., and Premo, W. (2006). Precipitation of lead–zinc ores in the Mississippi Valley-type deposit at Trèves , Cévennes region of southern France. *Geofluids*, 6:24–44.

Leach, D. L., Marsh, E., Emsbo, P., Rombach, C. S., Kelley, K. D., and Anthony, M. (2004). Nature of hydrothermal fluids at the shale-hosted Red Dog Zn–Pb–Ag deposits, Brooks Range, Alaska. *Economic Geology*, 99:1449–1480.

Lecoy, P. (2013). *Fiber-Optic Communications*. John Wiley & Sons.

Leisen, M. (2011). *Analyse chimique des inclusions fluides par ablation-laser couplée à l'ICP-MS et applications géochimiques*. PhD thesis.

Leisen, M., Dubessy, J., Boiron, M.-C., and Lach, P. (2012). Improvement of the determination of element concentrations in quartz-hosted fluid inclusions by LA-ICP-MS and Pitzer thermodynamic modeling of ice melting temperature. *Geochimica et Cosmochimica Acta*, 90:110–125.

Lepetit, P., Bente, K., Doering, T., and Luckhaus, S. (2003). Crystal chemistry of Fe-containing sphalerites. *Physics and Chemistry of Minerals*, 30(4):185–191.

Li, X., Zhao, H., Tang, M., and Liu, Y. (2009). Theoretical prediction for several important equilibrium Ge isotope fractionation factors and geological implications. *Earth and Planetary Science Letters*, 287(1-2):1–11.

Liu, P. P., Zhou, M. F., Luais, B., Cividini, D., and Rollion-Bard, C. (2014). Disequilibrium Fe isotope fractionation during the high-temperature magmatic differentiation of the Baima Fe-Ti oxide-bearing mafic intrusion, SW China. *Earth and Planetary Science Letters*, 339:21–29.

Longerich, H. P., Jackson, S. E., and Günther, D. (1996). Inter-laboratory note. Laser ablation inductively coupled plasma mass spectrometric transient signal data acquisition and analyte concentration calculation. *Journal of Analytical Atomic Spectrometry*, 11(September):899–904.

Luais, B. (2003). Germanium isotope systematics in meteorites. *Meteoritics and Planetary Science Supplement*, 38:5048.

Luais, B. (2007). Isotopic fractionation of germanium in iron meteorites: Significance for nebular condensation, core formation and impact processes. *Earth and Planetary Science Letters*, 262(1-2):21–36.

Luais, B. (2012). Germanium chemistry and MC-ICPMS isotopic measurements of Fe–Ni, Zn alloys and silicate matrices: Insights into deep Earth processes. *Chemical Geology*, 334:295–311.

Luais, B. (2015). *Du noyau à la croûte : apport de la géochimie isotopique du germanium.* HDR thesis. Centre de Recherches Pétrographiques et Géochimiques, Nancy.

Luais, B., Framboisier, X., Carignan, J., and Ludden, J. N. (2000). Analytical development of Ge isotopic analyses using multi-collection plasma source mass spectrometry: Isoprobe MC-Hex-ICP-MS (Micromass). *Geoanalysis 2000*, pages 45–46.

Luais, B., Telouk, P., and Albaréde, F. (1997). Precise and accurate neodymium isotopic measurements by plasma-source mass spectrometry. . *Geochimica et Cosmochimica Acta*, 61:4847–4854.

Machlan, L. A., Gramlich, J. W., Powell, L. J., and Lambert, G. M. (1986). Absolute isotope abundance ratio and atomic weight of a reference sample of gallium. *Journal of Research of the National Bureau of Standards*, 91:323–331.

Magnée, I. and Francois, A. (1988). The Origin of the Kipushi (Cu, Zn, Pb) Deposit in Direct Relation with a Proterozoic Salt Diapir. Copperbelt of Central Africa, Shaba, Republic of Zaire. pages 74–93. Springer Berlin Heidelberg, Berlin, Heidelberg.

Manning, P. G. (1967). Absorption spectra of Fe(III) in octahedral sites in sphalerite. *The Canadian Mineralogist*, 9:57–64.

Marignac, C. and Cuney, M. (1999). Ore deposits of the French Massif Central: insight into the metallogenesis of the Variscan collision belt. *Mineralium Deposita*, 34(5-6):472–504.

Marin-Carbonne, J., Rollion-Bard, C., and Luais, B. (2011). In-situ measurements of iron isotopes by SIMS: MC-ICP-MS intercalibration and application to a magnetite crystal from the Gunflint chert. *Chemical Geology*, 285:50–61.

Mateus, A., Matos, J. X., Rosa, C., and Oliveira, V. (2003). Cu-ores in quartz-carbonate veins at Estremoz-Alandroal and Barrancos-Sto Aleixo regions (Ossa Morena Zone): A result of Late-Variscan hydrothermal activity ? *Ciências da Terra (UNL), Lisboa*, pages F90–F93.

May, T. W. and Wiedmeyer, R. H. (1998). A table of polyatomic interferences in ICP-MS. *Atomic Spectroscopy*, 19(5):150–155.

McDonough, W. F. (2003). Compositional model for the Earth's core. *Treatise on geochemistry*, 2:547–568.

McDonough, W. F. and Sun, S.-S. (1995). The composition of the Earth. *Chemical Geology*, 120(3):223–253.

McIntire, W. L. (1963). Trace element partition coefficients—a review of theory and applications to geology. *Geochimica et Cosmochimica Acta*, 27:1209–1264.

Melcher, F. (2003). The Otavi Mountain Land in Namibia: Tsumeb, Germanium and Snowball Earth. pages 1–23.

Melcher, F. and Buchholz, P. (2013). Germanium. In Gunn, G., editor, *Critical Metal Handbook*, pages 177–203. Wiley Online Library.

Melezhik, V. A., Fallick, A. E., Filippov, M. M., and Larsen, O. (1999). Karelian shungite—an indication of 2.0-Ga-old metamorphosed oil-shale and generation of petroleum: geology, lithology and geochemistry. *Earth-Science Reviews*, 47(1–2):1–40.

Meng, Y.-M., Qi, H.-W., and Hu, R.-Z. (2015). Ore Geology Reviews. *Ore Geology Reviews*, 65(P4):1095–1109.

Misra, K. C., Gratz, J. C., and Lu, C. (1996). Carbonate-hosted Mississippi Valley-type mineralizations in the Elmwood-Gordonsville deposits, Central Tennessee zinc district, a synthesis. In Sangster, D. F., editor, *Carbonate-Hosted Lead–Zinc Deposits*, pages 58–73. Society of Economic Geologists Special Publication.

Moh, G. H. (1976). Experimental and descriptive ore mineralogy. *Neues Jahrbuch für Mineralogie Abhandlungen*, 128:115–188.

Moisy, M. (1993). *Evolution de la perméabilité et de la circulation des fluides hydrothermaux dans une zone de cisaillement fragile.* PhD thesis, Université Joseph-Fourier-Grenoble I.

Möller, P. and Dulski, P. (1993). *Germanium and gallium distribution in sphalerite.* Formation of Hydrothermal Vein Deposits: A Case Study of the Pb-Zn, Barite and Fluorite Deposits of the Harz Mountains (No. 30). Gebrüder Borntraeger.

Möller, P. and Dulski, P. (1996). Germanium and gallium distribution in sphalerite: a key to the genesis of sediment-hosted sulphide mineralizations. *Zeitschrift Für Geologische Wissenschaften*, 24:527–538.

Möller, P., Dulski, P., and Schneider, H.-J. (1983). Interpretation of Ga and Ge content in sphalerite from the Triassic Pb-Zn deposits of the Alps. pages 213–222.

Mosselmans, J., Pattrick, R., Van Der Laan, G., Charnock, J. M., Vaughan, D. J., Henderson, C., and Garner, C. D. (1995). X-ray absorption near-edge spectra of transition metal disulfides FeS2 (pyrite and marcasite), CoS2, NiS2 and CuS2, and their isomorphs FeAsS and CoAsS. *Physics and Chemistry of Minerals*, 22(5):311–317.

Muchez, P., Heijlen, W., Banks, D., Blundell, D., Boni, M., and Grandia, F. (2005). Extensional tectonics and the timing and formation of basin-hosted deposits in Europe. *Ore Geology Reviews*, 27(1-4):241–267.

Müller, D., Kaminski, K., Uhlig, S., Graupner, T., Herzig, P. M., and Hunt, S. (2002). The transition from porphyry- to epithermal-style gold mineralization at Ladolam, Lihir Island, Papua New Guinea: a reconnaissance study. *Mineralium Deposita*, 37(1):61–74.

Munoz, M., Baron, S., Boucher, A., Béziat, D., and Salvi, S. (2015). Mesozoic vein-type Pb–Zn mineralization in the Pyrenees: Lead isotopic and fluid inclusion evidence from the Les Argentières and Lacore deposits. *Comptes Rendus Geoscience (in-press)*, pages 1–11.

Munoz, M., Boyce, A., Courjault-Rade, P., Fallick, A., and Tollon, F. (1997). Le filon (Zn, F) de Peyrebrune (SW Massif central, France): caractérisation géochimique des fluides au cours du Mésozoïque à la bordure orientale du bassin d'Aquitaine. *Comptes Rendus de l'Académie des Sciences de Paris*, 324(II a):899–906.

Munoz, M., Boyce, A. J., Courjault-Rade, P., Fallick, A. E., and Tollon, F. (1994). Multi-stage fluid incursion in the Palaeozoic basement-hosted Saint-Salvy ore deposit (NW Montagne Noire, southern F. *Applied Geochemistry*, 9:609–626.

Muñoz, M., De Andrade, V., Vidal, O., Lewin, E., Pascarelli, S., and Susini, J. (2006). Redox and speciation micromapping using dispersive X-ray absorption spectroscopy: Application to iron in chlorite mineral of a metamorphic rock thin section. *Geochemistry, Geophysics, Geosystems*, 7(11):1–10.

Muñoz, M., Pascarelli, S., Aquilanti, G., Narygina, O., Kurnosov, A., and Dubrovinsky, L. (2008). Hyperspectral μ-XANES mapping in the diamond-anvil cell: analytical procedure applied to the decomposition of (Mg,Fe)-ringwoodite at the upper/lower mantle boundary. *High Pressure Research*, 28(4):665–673.

Muñoz, M., Vidal, O., Marcaillou, C., Pascarelli, S., Mathon, O., and Farges, F. (2013). Iron oxidation state in phyllosilicate single crystals using Fe-K pre-edge and XANES spectroscopy: Effects of the linear polarization of the synchrotron X-ray beam. *American Mineralogist*, 98(7):1187–1197.

Murakami, H. and Ishihara, S. (2013). Trace elements of Indium-bearing sphalerite from tin-polymetallic deposits in Bolivia, China and Japan: A femto-second LA-ICPMS study. *Ore Geology Reviews*, 1.

Murnane, R. J. and Stallard, R. F. (1990). Germanium and silicon in rivers of the Orinoco drainage basin. *Nature*, 344:749–752.

Newville, M. (2001). IFEFFIT: interactive XAFS analysis and FEFF fitting. *Journal of synchrotron radiation*, 8(2):322–324.

Newville, M. (2014). Fundamentals of XAFS. *Reviews in Mineralogy and Geochemistry*, 78(1):33–74.

Oftedal, I. W. (1940). Untersuchungen über die Nebenbestandteile von Ermineralien norwegischer zinkblendeführender Vorkommen. Skrifter utgit av Det Norske Videnskaps-Akademi i Oslo, I. Mat. *Naturv. Klasse*, 8:103.

Ohmoto, H. and Rye, R. O. (1979). Isotopes of sulfur and carbon. In Barnes, H. L., editor, *Geochemistry of Hydrothermal Ore Deposits*, pages 509–567. John Wiley & Sons.

Oliveira, J. T. s., Pacheco, N., and Carvalho, P. (1997). The Neves–Corvo mine and the Paleozoic geology of Southwest Portugal. In Barriga, F. J. and Carvalho, P., editors, *Geology and VMS Deposits of the Iberian Pyrite Belt*. Society of Economic Geologists Neves–Corvo Field Conference 1997. SEG Guidebook Series.

Omotowa, B. (2010). Processes for producing halocarbon compounds using inorganic fluoride. US Patent Office.

Paar, W. H. and Putz, H. (2005). Germanium associated with epithermal mineralization: examples from Bolivia and Argentina. In Zhao, C. S. and Guo, B. J., editors, *Mineral Deposit Research: Meeting the Global Challenge*, pages 48–51. China Land Publishing House, Beijing.

Paar, W. H., Roberts, A. C., Berlepsch, P., Armbruster, T., Topa, D., and Zagler, G. (2004). Putzite, $(Cu_{4.7}Ag_{3.3})_8GeS_6$, a new mineral species from Capillitas, Catamarca, Argentina: description and mineral structure. *The Canadian Mineralogist*, 42:1757–1769.

Pascua, M. I., Murciego, A., Pellitero, E., Babkine, J., and Dusausoy, Y. (1997). Sn–Ge–Cd–Cu–Fe-bearing sulfides and sulfosalts from the Barquilla Deposit, Salamanca, Spain. *The Canadian Mineralogist*, 35:39–52.

Paton, C., Hellstrom, J., Paul, B., Woodhead, J., and Hergt, J. (2011). Iolite: Freeware for the visualisation and processing of mass spectrometric data. *Journal of Analytical Atomic Spectrometry*, 26(12):2508.

Pattrick, R. A. D., Dorling, M., and Polya, D. A. (1993a). TEM study of indium-and copper-bearing growth-banded sphalerite. *The Canadian Mineralogist*, 31:105–117.

Pattrick, R. A. D., Mosselmans, J., Charnock, J. M., England, K., Helz, G. R., Garner, C. D., and Vaughan, D. J. (1997). The structure of amorphous copper sulfide precipitates: An X-ray absorption study. *Geochimica et Cosmochimica Acta*, 61(10):2023–2036.

Pattrick, R. A. D., Van Der Laan, G., Vaughan, D. J., and Henderson, C. (1993b). Oxidation state and electronic configuration determination of copper in tetrahedrite group minerals by L-edge X-ray absorption spectroscopy. *Physics and Chemistry of Minerals*, 20(6):395–401.

Pearce, C. I., Pattrick, R. A. D., Vaughan, D. J., Henderson, C., and Van Der Laan, G. (2006). Copper oxidation state in chalcopyrite: Mixed Cu d^9 and d^{10} characteristics. *Geochimica et Cosmochimica Acta*, 70(18):4635–4642.

Pearson, R. G. (1963). Hard and soft acids and bases. *Journal of the American Chemical Society*, 85(22):3533–3539.

Petiau, J., Sainctavit, P., and Calas, G. (1988). K X-ray absorption spectra and electronic structure of chalcopyrite $CuFeS_2$. *Materials Science and Engineering: B*, 1(3):237–249.

Pfaff, K., Koenig, A., Wenzel, T., Ridley, I., Hildebrandt, L. H., Leach, D. L., and Markl, G. (2011). Trace and minor element variations and sulfur isotopes in crystalline and colloform ZnS: Incorporation mechanisms and implications for their genesis. *Chemical Geology*, 286(3-4):118–134.

Pokrovski, G. S., Roux, J., Hazemann, J.-L., and Testemale, D. (2005). An X-ray absorption spectroscopy study of argutite solubility and aqueous Ge(IV) speciation in hydrothermal fluids to 500 °C and 400 bar. *Chemical Geology*, 217(1-2):127–145.

Pokrovski, G. S. and Schott, J. (1998a). Experimental study of the complexation of silicon and germanium with aqueous organic species: implications for germanium and silicon transport and Ge/Si ratio in natural waters. *Geochimica et Cosmochimica Acta*, 62(21-22):3413–3428.

Pokrovski, G. S. and Schott, J. (1998b). Thermodynamic properties of aqueous Ge(IV) hydroxide complexes from 25 to 350 °C: implications for the behavior of germanium and the Ge/Si ratio in hydrothermal fluids. *Geochimica et Cosmochimica Acta*, 62(9):1631–1642.

Polyakov, V. B. and Mineev, S. D. (2000). The use of Mössbauer spectroscopy in stable isotope geochemistry. *Geochimica et Cosmochimica Acta*, 64(5):849–865.

Prietzel, J., Thieme, J., Eusterhues, K., and Eichert, D. (2007). Iron speciation in soils and soil aggregates by synchrotron-based X-ray microspectroscopy (XANES, μ-XANES). *European Journal of Soil Science*, 58(5):1027–1041.

Pugsley, A. J., Bull, C. L., Sella, A., Sankar, G., and McMillan, P. F. (2011). XAS/EXAFS studies of Ge nanoparticles produced by reaction between Mg2Ge and GeCl4. *Journal of Solid State Chemistry*, 184(9):2345–2352.

Qi, H.-W., Rouxel, O., Hu, R.-Z., Bi, X.-W., and Wen, H.-J. (2011). Germanium isotopic systematics in Ge-rich coal from the Lincang Ge deposit, Yunnan, Southwestern China. *Chemical Geology*, 286(3-4):252–265.

Qian, Z. (1987). Trace elements in galena and sphalerite and their geochemical significance in distinguishing the genetic types of Pb-Zn ore deposits. *Chinese Journal of Geochemistry*, 6(2):177–190.

Ravel, B. and Newville, M. (2005). *ATHENA*, *ARTEMIS*, *HEPHAESTUS*: data analysis for X-ray absorption spectroscopy using *IFEFFIT*. *Journal of synchrotron radiation*, 12(4):537–541.

Rehr, J. J., Albers, R. C., and Zabinsky, S. I. (1992). High-order multiple-scattering calculations of x-ray-absorption fine structure. *Phys. Rev. Lett.*, 69:3397–3400.

Reiser, F. K. M., Rosa, D. R. N., Pinto, Á. M. M., Carvalho, J. R. S., Matos, J. X., Guimarães, F. M. G., Alves, L. C., and de Oliveira, D. P. S. (2011). Mineralogy and geochemistry of tin- and germanium-bearing copper ore, Barrigão re-mobilized vein deposit, Iberian Pyrite Belt, Portugal. *International Geology Review*, 53(10):1212–1238.

Richter, F. M., Davis, A. M., DePaolo, D. J., and Watson, E. B. (2003). Isotope fractionation by chemical diffusion between molten basalt and rhyolite. *Geochimica et Cosmochimica Acta*, 67(20):3905–3923.

Richter, F. M., Liang, Y., and Davis, A. M. (1999). Isotope fractionation by diffusion in molten oxides. *Geochimica et Cosmochimica Acta*, 63(18):2853–2861.

Righter, K., King, C., Danielson, L., Pando, K., and Lee, C. T. (2011). Experimental determination of the metal/silicate partition coefficient of Germanium: Implications for core and mantle differentiation. *Earth and Planetary Science Letters*, 304(3):379–388.

Rollion-Bard, C., Mangin, D., and Champenois, M. (2007). Development and Application of Oxygen and Carbon Isotopic Measurements of Biogenic Carbonates by Ion Microprobe. *Geostandards and Geoanalytical Research*, 31(1):39–50.

Rollion-Bard, C. and Marin-Carbonne, J. (2011). Determination of SIMS matrix effects on oxygen isotopic compositions in carbonates. *Journal of Analytical Atomic Spectrometry*, 26(6):1285–1289.

Rosenberg, E. (2008). Germanium: environmental occurrence, importance and speciation. *Reviews in Environmental Science and Bio/Technology*, 8(1):29–57.

Rouxel, O., Galy, A., and Elderfield, H. (2006). Germanium isotopic variations in igneous rocks and marine sediments. *Geochimica et Cosmochimica Acta*, 70(13):3387–3400.

Samama, J. C., Royer, J. J., and N'Ganzi, C. (1989). Prise en compte de la surface spécifique des prélèvements en prospection géochimique: exemple de l'uranium dans les sédiments de ruisseau. *Journal of Geochemical Exploration*, 32(1):453–466.

Sangster, D. F. (1990). Mississippi Valley-type and sedex lead–zinc deposits: a comparative examination. *Transactions, Institution of Mining and Metallurgy. Section B, Applied Earth Science*, 99:21–42.

Sangster, D. F. (2001). The role of dense brines in the formation of vent-distal sedimentary-exhalative (SEDEX) lead–zinc deposits: field and laboratory evidence. *Mineralium Deposita*, 37(2):149–157.

Sawkins, F. J. (1966). Ore genesis in the North Pennine orefield, in the light of fluid inclusion studies. *Economic Geology*, 61:385–401.

Schauble, E. A. (2004). Applying stable isotope fractionation theory to new systems. *Reviews in Mineralogy and Geochemistry*, 55(1):65–111.

Schneider, J., Melcher, F., and Brauns, M. (2007). Concordant ages for the giant Kipushi base metal deposit (DR Congo) from direct Rb–Sr and Re–Os dating of sulfides. *Mineralium Deposita*, 42(7):791–797.

Schnering, H. G. v. and Wiedemeier, H. (1981). The high temperature structure of β-SnS and β-SnSe and the B16-to-B33 type λ-transition path. *Zeitschrift fur Kristallographie*, 156:143–150.

Schroll, E. (2005). Alpine-type Pb–Zn deposits (APT) hosted by Triassic carbonates. In JW, M. and Bierlein, F. P., editors, *Mineral Deposit Research: Meeting the Global Challenge*, pages 175–178. Springer, Berlin.

Seal, R. R. (2006). Sulfur Isotope Geochemistry of Sulfide Minerals. *Reviews in Mineralogy and Geochemistry*, 61(1):633–677.

Shanks, W. C. P. (2014). Stable Isotope Geochemistry of Mineral Deposits. In *Treatise on Geochemistry*, pages 59–85. Elsevier Ltd.

Shikazono, N. (2003). *Geochemical and tectonic evolution of arc–backarc hydrothermal systems: implication for the origin of Kuroko and epithermal vein-type mineralizations and the global geochemical cycle.*, volume 8. Developments in Geochemistry, Elsevier, Amsterdam.

Shiraki, K., Tsuchiya, T., and Ono, S. (2003). Structural refinements of high-pressure phases in germanium dioxide. *Acta Crystallographica Section B*, 59(6):701–708.

Siebert, C., Hammond, D. E., Ross, A., and McManus, J. (2011). Erratum to C. Siebert, A. Ross and J. McManus (2006) "Germanium isotope measurements of high-temperature geothermal fluids using double-spike hydride generation MC-ICP-MS", Geochimica et Cosmochimica Acta 70, 3986–3995. *Geochimica et Cosmochimica Acta*, 75(20):6267–6269.

Siebert, C., Ross, A., and McManus, J. (2006). Germanium isotope measurements of high-temperature geothermal fluids using double-spike hydride generation MC-ICP-MS. *Geochimica et Cosmochimica Acta*, 70(15):3986–3995.

Skarpelis, N. (1995). Minor elements in the base metal part of an epithermal system: the Kirki (St. Phillippe) Mine, Thrace, Northern Greece. In *Terra—Proceedings of the 8th EUG Meeting*, page 293, Strasbourg.

Slack, J. F., Dumoulin, J. A., Schmidt, J. M., Young, L. E., and Rombach, C. S. (2004). Paleozoic sedimentary rocks in the Red Dog Zn– Pb–Ag district and vicinity, Western Brooks Range, Alaska: provenance, deposition, and metallogenic significance. *Economic Geology*, 99:1385–1414.

Solé, V. A., Papillon, E., Cotte, M., Walter, P., and Susini, J. (2007). A multiplatform code for the analysis of energy-dispersive X-ray fluorescence spectra. *Spectrochimica Acta Part B: Atomic Spectroscopy*, 62(1):63–68.

Soler, P. (1987). Variations des teneurs en éléments mineurs (Cd, In, Ge, Ga, Ag, Bi, Se, Hg, Sn) des minerais de Pb-Zn de la province polymétallique des Andes du Pérou central. *Mineralium Deposita*, 22:135–143.

Stoiber, R. E. (1940). Minor elements in sphalerite. *Economic Geology*, 35:501–519.

Taylor, S. R. and McLennan, S. M. (1995). The geochemical evolution of the continental crust. *Reviews of Geophysics*, 33:241–265.

Tettenhorst, R. T. and Corbato, C. E. (1984). Crystal structure of germanite, $Cu_{26}Ge_4Fe_4S_{32}$ determined by powder X-ray diffraction. *American Mineralogist*, 69(9-10):943–947.

Thiele, U. K. (2001). The Current Status of Catalysis and Catalyst Development for the Industrial Process of Poly(ethylene terephthalate) Polycondensation. *International Journal of Polymeric Materials*, 50(3-4):387–394.

Thomas, D. W., Mahmood, T., and Lindhal, C. B. (2000). Germanium and Germanium Compounds. In *Kirk-Othmer Encyclopedia of Chemical Technology*. John Wiley & Sons, Inc.

Thomassot, E., Cartigny, P., Harris, J. W., Lorand, J. P., Rollion-Bard, C., and Chaussidon, M. (2009). Metasomatic diamond growth: A multi-isotope study (^{13}C, ^{15}N, ^{33}S, ^{34}S) of sulphide inclusions and their host diamonds from Jwaneng (Botswana). *Earth and Planetary Science Letters*, 282(1-4):79–90.

Tourigny, G., Doucet, D., and Bourget, A. (1993). Geology of the Bousquet 2 Mine: an example of a deformed, gold-bearing, polymetallic sulfide deposit. *Economic Geology*, 88(6):1578–1597.

Tsirambides, A. and Filippidis, A. (2012). Metallic Mineral Resources of Greece. *Central European Journal of Geosciences*, 4(4):641–650.

Vaccari, M., Aquilanti, G., Pascarelli, S., and Mathon, O. (2009). A new EXAFS investigation of local structural changes in amorphous and crystalline GeO(2) at high pressure. *Journal of Physics: Condensed Matter*, 21(14):145403–145403.

van Hinsberg, V. J., Migdisov, A. A., and Williams-Jones, A. E. (2010). Reading the mineral record of fluid composition from element partitioning. *Geology*, 38(9):847–850.

Van Wilderode, J., Heijlen, W., De Muynck, D., Schneider, J., Vanhaecke, F., and Muchez, P. (2013). The Kipushi Cu–Zn deposit (DR Congo) and its host rocks: A petrographical, stable isotope (O, C) and radiogenic isotope (Sr, Nd) study. *Journal of African Earth Sciences*, 79:143–156.

Vaughan, D. J. and Craig, J. R. (1978). *Mineral Chemistry of Metal Sulfides*. Cambridge Earth Science Series. Cambridge, cambridge university press edition.

Viets, J. G., Hopkins, R. T., and Miller, B. M. (1992). Variations in minor and trace metals in sphalerite from Mississipi Valley-type deposits of the Ozark Region: Genetic implications. *Economic Geology*, 87:1897–1905.

Wasson, J. T. (1966). Butler, Missouri: An Iron Meteorite with Extremely High Germanium Content. *Science*, 153(3739):976–978.

Waychunas, G. A., Apted, M. J., and Brown, Jr, G. E. (1983). X-ray K-edge absorption spectra of Fe minerals and model compounds: near-edge structure. *Physics and Chemistry of Minerals*, 10(1):1–9.

Welch, M. D., Cooper, M. A., and Hawthorne, F. C. (2001). The crystal structure of brunogeierite, Fe2GeO4 spinel. *Mineralogical Magazine*, 65(3):441–444.

Westre, T. E., Kennepohl, P., and DeWitt, J. G. (1997). A multiplet analysis of Fe K-edge $1s \rightarrow 3d$ pre-edge features of iron complexes. *Journal of the American Chemical Society*, 119:6297–6314.

Wiedemeier, H. and Schnering, H. G. (1978). Refinement of the structures of GeS, GeSe, SnS and SnSe. *Z. Kristallogr*, 148:295–303.

Wiederhold, J. G. (2015). Metal Stable Isotope Signatures as Tracers in Environmental Geochemistry. *Environmental Science and Technology*, 49:2606–2624.

Wilke, M., Farges, F., Petit, P. E., Brown, G. E. J., and Martin, F. (2001). Oxidation state and coordination of Fe in minerals: An Fe K-XANES spectroscopic study. *American Mineralogist*, 86(1998):714–730.

Wilke, M., Hahn, O., Woodland, A. B., and Rickers, K. (2009). The oxidation state of iron determined by Fe K-edge XANES—application to iron gall ink in historical manuscripts. *Journal of Analytical Atomic Spectrometry*, 24(10):1364–1372.

Wilkinson, J. J. (2014). Sediment-Hosted Zinc–Lead Mineralization: Processes and Perspectives. In *Treatise on Geochemistry*, volume 13: Geochemistry of Mineral Deposits, chapter 9, pages 219–249. Elsevier Ltd.

Wilkinson, J. J., Eyre, S. L., and Boyce, A. J. (2005a). Ore-Forming Processes in Irish-Type Carbonate-hosted Zn-Pb Deposits : Evidence from Mineralogy , Chemistry , and Isotopic Composition of Sulfides at the Lisheen Mine. *Economic Geology*, 100:63–86.

Wilkinson, J. J., Weiss, D. J., Mason, T., and Coles, B. J. (2005b). Zinc isotope variation in hydrothermal systems: Preliminary evidence from the Irish Midlands ore field. *Economic Geology*, 100:583–590.

Wilson, S. a., Ridley, W. I., and Koenig, a. E. (2002). Development of sulfide calibration standards for the laser ablation inductively-coupled plasma mass spectrometry technique. *Journal of Analytical Atomic Spectrometry*, 17(4):406–409.

Winderbaum, L., Ciobanu, C. L., Cook, N. J., Paul, M., Metcalfe, A., and Gilbert, S. (2012). Multivariate Analysis of an LA-ICP-MS Trace Element Dataset for Pyrite. *Mathematical Geosciences*, 44(7):823–842.

Wood, B. J. and Blundy, J. D. (2001). The effect of cation charge on crystal–melt partitioning of trace elements. *Earth and Planetary Science Letters*, 188(1):59–71.

Wood, S. a. and Samson, I. M. (2006). The aqueous geochemistry of gallium, germanium, indium and scandium. *Ore Geology Reviews*, 28(1):57–102.

Wright, K. (2009). The Incorporation of Cadmium, Manganese and Ferrous Iron in Sphalerite: Insights From Computer Simulations. *The Canadian Mineralogist*, 47(3):615–623.

Wright, K. and Gale, J. D. (2010). A first principles study of the distribution of iron in sphalerite. *Geochimica et Cosmochimica Acta*, 74(12):3514–3520.

Xue, S., Yang, Y.-L., Hall, G. S., and Herzog, G. F. (1997). Germanium isotopic compositions in Canyon Diablo spheroids. *Geochimica et Cosmochimica Acta*, 61(3):651–655.

Ye, L., Cook, N. J., Ciobanu, C. L., Yuping, L., Qian, Z., Tiegeng, L., Wei, G., Yulong, Y., and Danyushevskiy, L. (2011). Trace and minor elements in sphalerite from base metal deposits in South China: A LA-ICPMS study. *Ore Geology Reviews*, 39(4):188–217.

Young, E., Stansberry, J., and Gordon, K. (2003). Properties of germanium photoconductor detectors. *The Calibration Legacy of the ISO Mission*, 481:231–235.

Young, E. D., Galy, A., and Nagahara, H. (2002). Kinetic and equilibrium mass-dependent isotope fractionation laws in nature and their geochemical and cosmochemical significance. *Geochimica et Cosmochimica Acta*, 66(6):1095–1104.

Zachariasen, W. H. (1936). The Crystal Structure of Germanium Disulphide. *The Journal of Chemical Physics*, 4(9):618.

Zhang, Q. L. and Ding, T. P. (1989). Analysis of the reference material NBS-123 and the atomic weight of sulfur. *Chinese Science Bulletin*, 34(13):1086–1089.

Appendix

Available online at www.sciencedirect.com

ScienceDirect

Geochimica et Cosmochimica Acta 177 (2016) 298–314

Geochimica et Cosmochimica Acta

www.elsevier.com/locate/gca

Distribution and oxidation state of Ge, Cu and Fe in sphalerite by μ-XRF and *K*-edge μ-XANES: insights into Ge incorporation, partitioning and isotopic fractionation

Rémi Belissont [a,b,*], Manuel Muñoz [c], Marie-Christine Boiron [a], Béatrice Luais [b], Olivier Mathon [d]

[a] *GeoRessources, Université de Lorraine, CNRS, UMR 7359, Boulevard des Aiguillettes, BP 70239, F-54506 Vandoeuvre-lès-Nancy, France*
[b] *Centre de Recherches Pétrographiques et Géochimiques (CRPG), Université de Lorraine, CNRS, UMR 7358, 15 Rue Notre Dame des Pauvres, BP 20, F-54501 Vandoeuvre-lès-Nancy Cedex, France*
[c] *Institut des Sciences de la Terre (ISTerre), Université Joseph Fourier, 1381 Rue de la Piscine – BP 53, F-38041 Grenoble cedex 9, France*
[d] *European Synchrotron Radiation Facility, BP 220, F-38043 Grenoble, France*

Received 18 August 2015; accepted in revised form 3 January 2016; Available online 11 January 2016

Abstract

Synchrotron-based microscale X-ray absorption near edge structure spectroscopy (μ-XANES) has been combined with X-ray fluorescence (μ-XRF) mapping to investigate Ge, Cu and Fe oxidation states in compositionally zoned Ge-rich sphalerite from the Saint-Salvy deposit (France). The present study aims at improving our understanding of substitution mechanisms and trace element uptake relative to Ge isotope fractionation in sphalerite. *K*-Edge XANES records of various Ge-, Cu- and Fe-bearing sulphides are presented for comparison with sphalerite, and *ab initio* calculations at the Ge *K*-edge complete our experimental data. The Ge *K*-edge spectra of the Ge-bearing sphalerite are identical to those of germanite, renierite and briartite, indicating the presence of tetrahedrally-coordinated Ge^{4+}. In addition, Cu and Fe *K*-edge spectra suggest the presence of Cu^{+} and Fe^{2+}, respectively, in the tetrahedral site. No significant differences in the oxidation states of Ge, Cu and Fe were observed within or between the zoning types or between the samples. The intake of Ge^{4+} in sphalerite may therefore occur in the tetrahedral divalent metal site via coupled substitutions charge-balanced by monovalent elements such as $3Zn^{2+} \leftrightarrow Ge^{4+} + 2Cu^{+}$, resulting in a strong Ge–Cu elemental correlation, or, when Ge does not correlate with monovalent elements, through the creation of lattice vacancies such as $2Zn^{2+} \leftrightarrow Ge^{4+} + \square$ (vacancy). The tetravalent state of Ge is compatible with temperature-related Ge isotopic fractionation and can explain the large range of δ^{74}Ge measured in the Saint-Salvy sphalerite. Moreover, the exceptional enrichment in Ge and the large variations in the 'bulk' Ge contents in these sphalerites do not appear to be related to charge effects but would instead result from the effect of temperature-related partitioning.

1. INTRODUCTION

Germanium (Ge) is increasingly in demand for use in a variety of high-tech devices. Its strategic importance as well as its scarcity in most geological environments necessitates a refinement of our understanding of its geological cycle. The concentration of Ge in the Earth's crust averages

* Corresponding author at: GeoRessources, Université de Lorraine, CNRS, UMR 7359, Boulevard des Aiguillettes, BP 70239, F-54506 Vandoeuvre-lès-Nancy, France.
E-mail address: remi.belissont@univ-lorraine.fr (R. Belissont).

http://dx.doi.org/10.1016/j.gca.2016.01.001
0016-7037/

1.3 ppm (updated in Hu and Gao, 2008), mostly incorporated into silicate minerals through $Ge^{4+} \leftrightarrow Si^{4+}$ isovalent substitutions in tetrahedral sites. However, enrichment of Ge relative to this average can occur in iron meteorites, iron oxides/hydroxides, Cu-, Ag-, As-rich sulphides and Zn sulphides, and coal. Thus, depending on the geological setting, Ge can be distinctly lithophile, siderophile, chalcophile or organophile, making it a useful geochemical tracer in the fields of cosmochemistry, planetary differentiation, hydrothermal and tectonic activity and fluid sources, as well as continental weathering (e.g., Dickinson et al., 1989; Kurtz et al., 2002; Rouxel et al., 2006; Luais, 2007, 2012; Escoube et al., 2015). Germanium can occur as Ge^{2+} and Ge^{4+} although the latter is thought to be the dominant form found in aqueous fluids (Wood and Samson, 2006) and natural compounds such as sulphide minerals (e.g., renierite, germanite, briartite), oxides (e.g., argutite) and hydroxides (e.g., stottite; Höll et al., 2007). Even in the spinel-type oxide, brunogeierite, Ge is now understood to occur as Ge^{4+} (Cempirek and Groat, 2013).

Sphalerite (ZnS) and coal are the main primary sources of Ge and concentrations in sphalerite can reach around 3000 ppm, mostly in low-temperature hydrothermal systems (e.g., Mississippi valley type deposits, MVT; Bernstein, 1985; Höll et al., 2007; Frenzel et al., 2014). Since the study of Stoiber (1940) was published over 70 years ago, the wide range of minor/trace elements entering the sphalerite diamond-type lattice has been the subject of numerous studies. For instance, the recent meta-analysis by Frenzel et al. (2016) showed that the Ge, Ga, In, Fe and Mn contents in sphalerite best discriminate among different type of deposits; concentrations of Ge and Ge increase, while those of In, Fe, Mn decrease with increasing formation temperature. Microscale compositional zoning often occurs in sphalerite (Pattrick et al., 1993; Beaudoin, 2000; Di Benedetto, 2005), and, in particular, antithetical partitioning of minor/trace elements between different types of compositional zoning has been reported, indicating the involvement of crystallographic controls in the incorporation process (Johan, 1988; Belissont et al., 2014). Accordingly, large Ge enrichments, correlated with minor Cu plus tri- and tetravalent element enrichments, have been reported in sector zoning patterns, whereas Ge is depleted in rhythmic bands. Despite these findings, the parameters that influence these crystal structure controls remain poorly constrained.

The incorporation of divalent elements (e.g., Fe^{2+}, Mn^{2+}, Cd^{2+}) via direct substitution of Zn^{2+} has been widely demonstrated (e.g., Bernardini et al., 2004; Di Benedetto et al., 2005a; Wright, 2009 Wright and Gale, 2010). Tri- and tetravalent elements (e.g., Ga^{3+}, Ge^{4+}) are thought to enter sphalerite via either coupled substitutions with monovalent elements (e.g., Cu^{+}, Ag^{+}) for charge compensation or through the creation of vacancies (e.g., Bernstein, 1985; Johan, 1988). However, the oxidation states of incorporated elements, including Ge, remain poorly constrained and are still open to debate. For instance, Cook et al. (2009) proposed the isovalent substitution $Ge^{2+} \leftrightarrow Zn^{2+}$ in sphalerite where Ge is not associated with monovalent elements. Other unresolved questions include the influence of the oxidation state of substituting elements on crystallography-controlled zoning in sphalerite and whether or not variations exist between different types of zoning.

The oxidation state, together with ligands and coordination numbers, is one of the key parameters involved in inducing large isotopic equilibrium fractionation at low temperatures (e.g., Schauble, 2004). Thus, heavy isotopic compositions typically correlate with high oxidation states, as seen for example in Fe isotope systematics, where $^{56}Fe/^{54}Fe$ ratios are usually higher in Fe^{3+}-bearing compounds than in Fe^{2+}-bearing compounds (e.g., Polyakov and Mineev, 2000). The oxidation states of incorporated elements (and the substitution mechanisms) also affect their partition coefficients, which drive elemental enrichment from the ore-forming fluids into the growing solid phase. Advanced study of the oxidation state of Ge and related elements is thus highly important if we are to improve our understanding of substitution mechanisms, impurity uptake, and Ge isotope fractionation in sphalerite.

Synchrotron X-ray absorption near edge structure (XANES) spectroscopy is a powerful element-specific technique for obtaining information on the oxidation state of the absorbing atom and its coordination symmetry. Advances in XANES spectroscopy have meant that high-resolution *in situ* analysis is now possible and elements can be probed in minor or trace amounts in various types of material (e.g., Muñoz et al., 2006). Germanium *K*-edge data from natural Ge-bearing specimens are scarce in the literature. The few studies of note include that of Bernstein and Waychunas (1987), who studied the Ge-bearing iron oxides, hematite, goethite and stottite. More recently, Cook et al. (2015) focused on the oxidation state of Ge in sphalerite from the Tres Marias Zn deposit (Mexico), which was thought to carry Ge^{2+} (Cook et al., 2009). Many studies have investigated the (bulk) oxidation state of Fe in sphalerite using Mössbauer spectroscopy, and these have shown that the uptake of Fe by sphalerite depends on temperature and sulphur fugacity, with high sulphur fugacity being related to increased Fe^{3+} in order to compensate for the charge deficiency induced by Zn^{2+} vacancies (e.g., Manning, 1967; Gerard et al., 1971; Di Benedetto et al., 2005a; Lepetit et al., 2003). Finally, Cook et al. (2012) investigated the copper oxidation state in In-rich sphalerite by Cu *K*-edge μ-XANES and suggested that incorporation of indium occurs via the coupled substitution, $2Zn^{2+} \leftrightarrow Cu^{+} + In^{3+}$.

The present study aims at probing the oxidation state of Ge at the microscale using *K*-edge μ-XANES in zoned Ge-rich sphalerite in order to gain further insights into Ge enrichment processes related to direct and coupled substitution mechanisms, crystallography-controlled zoning and Ge isotopic fractionation. The sphalerite studied here comes from the very typical Noailhac – Saint-Salvy deposit in France. Ge-bearing sphalerite from the Kipushi deposit (D.R. Congo) is used for comparison. The sphalerite from Saint-Salvy contains Cu and Fe in minor amounts that are, respectively, positively and negatively correlated with Ge, both spatially and in terms of concentration (Belissont et al., 2014). Cu and Fe *K*-edge μ-XANES spectra were

therefore determined in addition to the Ge *K*-edge spectra. Synchrotron-based μ-XRF mapping was used to determine element distributions and beam positioning for subsequent μ-XANES records. *Ab initio* Ge *K*-edge calculations complement our experimental XANES data and improve our interpretation.

2. EXPERIMENTAL METHODS

2.1. Sample description

Three Ge-rich compositionally zoned sphalerites representative of the Saint-Salvy vein-type Zn–Ge–Ag deposit (France) were selected. The three samples exhibit increasing bulk Ge contents and isotopic compositions (δ^{74}Ge relative to the NIST 3120a Ge standard) as shown in the study of Belissont et al. (2014): 64W (~500 ppm, −2.05‰), 62E (~900 ppm, −1.41‰) and SAL-UN (~1000 ppm, +0.64‰). The sphalerites were collected from different locations in the mine (Cassard et al., 1994). The specimens, prepared as 150 µm-thick polished sections, occur as supra-millimetric zoned crystals, light brown to dark reddish-brown in colour. Trace element spot analyses were performed using LA-ICP-MS and bulk Ge isotopic compositions were measured by MC-ICP-MS (Belissont et al., 2014). Exsolutions of other minerals (e.g., chalcopyrite) were not detected by optical and electron microscopy, and were not observed in LA-ICP-MS down-hole profiles. Furthermore, the amount of Fe in this sphalerite (3–4 mol.%) is below the critical content required to initiate diffusion-induced segregation (DIS) processes (>5 mol.%; Bente and Doering, 1995).

Minor and trace elements are antithetically distributed among two types of compositional zoning that can be distinguished optically (Fig. 1). (i) Rhythmic banding, along (110) planes, occurs as alternating parallel dark brown and light brown growth-bands from the core to the rim. The dark brown bands are enriched in Fe (2.6 wt.%), Cd (3500 ppm), Sn (880 ppm) and In (230 ppm). Ge and Cu average 140 and 2450 ppm, respectively. The light bands are relatively depleted in all elements, including Cu (550 ppm) and Fe (2.2 wt.%), except Ge, which averages 270 ppm. (ii) The sector zoning, along (111) planes, forms cross-cutting-like dark brown zones that overlap rhythmic bands and which consist of a series of small and parallel truncation planes of variable size. The sector zones are enriched in Cu (4000 ppm), Sb (1970 ppm), Ge (1100 ppm), Ga (370 ppm) and Ag (360 ppm). Fe (1.9 wt.%) is depleted relative to the rhythmic bands. This antithetic zoning in element concentration suggests a crystallographic control on the incorporation of trace elements (Belissont et al., 2014).

One of the sphalerite samples, sample A38, originates from the Kipushi carbonate-hosted Cu–Zn–(Ge–Pb) ore deposit (D.R. Congo) and consists of supra-millimetric orange crystals in a gangue of dolomite and quartz. A few optically dark zones, up to 1 µm^2 in size, can be observed, though these are different from those observed in the Saint-Salvy sphalerite. Sample A38 is relatively enriched in Ge (~170 ppm) compared to other sphalerites within the deposit, and concentrations of up to 950 ppm have been measured in the optically dark zones.

Three Ge-sulphides were analysed for calibration: renierite, germanite, and briartite. Synthetic GeS (Sigma Aldrich, 99.99%) was used as a divalent Ge reference. Chalcopyrite and covellite specimens contained trace to minor amounts of Ge. Stannite, pyrite and arsenopyrite were used specifically for the collection of Fe *K*-edge XANES spectra. The known crystal chemistries of the sphalerite and calibration compounds are listed in Table 1. The compositions of the minerals analysed in this study are given in Table 2. Major and minor elements were analysed by EPMA and trace quantities of Ge were analysed by LA-ICP-MS (GeoRessources, Vandoeuvre-lès-Nancy, France).

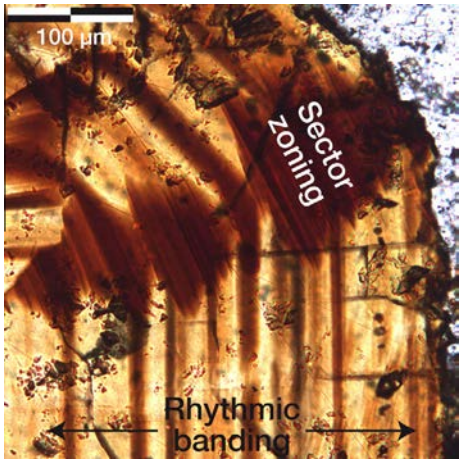

Fig. 1. Microphotograph of the typical zoning types observed in sphalerite from Saint-Salvy (France): rhythmic bands and overlapping cross-cutting-like sector zones, corresponding to the (110) and (111) planes, respectively (planes are referenced according to the study of Johan, 1988).

2.2. μ-XRF and μ-XANES data collection

μ-XRF and μ-XANES measurements were performed on the BM23 beamline at the European Synchrotron Radiation Facility (ESRF, Grenoble, France). The storage ring was operated at 6 GeV in multibunch mode with a ~200 mA current. X-rays were generated using a bending magnet (BM) and monochromatised with a fixed-exit double-crystal Si(111) monochromator. Micro-focusing of X-rays into an incident beam of ~3×3 µm^2 was achieved using two mirrors in Kirkpatrick–Baez (KB) geometry. For the sphalerite samples and reference compounds, XRF and XANES (fluorescence mode) data were collected with a Vortex silicon-drift energy-dispersive detector located 90° from the incident beam. μ-XRF maps were collected at 11.3 keV in order to measure Ge, Cu and Fe Kα-lines. Selected regions in sphalerite samples were mapped with a typical step-size of 10 µm depending on the area mapped. Dwell-time was adjusted to 0.5 s. Using the μ-XRF maps, several spots of interest were selected in sector zones and dark and light brown bands in order to measure μ-XANES spectra. The XRF spectra (one

Table 1
Known crystal chemistry of analysed compounds.

Mineral	Formula	CN	Ge	Fe	Cu	Technique	Reference
Sphalerite	ZnS	4	?	$Fe^{2+/3+}$ (*h*)	Cu^{+}	Mössbauer (^{57}Fe)	Lepetit et al. (2003)
						μ-XANES (Cu *K*-edge)	Cook et al. (2012)
Germanite	$Cu_{13}Fe_2Ge_2S_{16}$	4	Ge^{4+}	Fe^{3+} (*h*)	Cu^{+}	Mössbauer (^{57}Fe)	Vaughan and Craig (1978)
Renierite	$(Cu,Zn)_{11}(Ge,As)_2Fe_4S_{16}$	4	Ge^{4+}	Fe^{3+} (*h*)	Cu^{+}	Mössbauer (^{57}Fe)	Bernstein (1986)
Briartite	$Cu_2(Zn,Fe)GeS_4$	4	Ge^{4+}	Fe^{2+} (*h*)	Cu^{+}	Mössbauer (^{57}Fe)	Imbert et al. (1973)
GeS	GeS	4	Ge^{2+}	–	–	XRD	Wiedemeier and Schnering (1978)
Chalcopyrite	$CuFeS_2$	4	?	Fe^{3+} (*h*)	Cu^{+}	XANES (Fe, Cu L-edges)	Goh et al. (2006)
Covellite	CuS	4	?	–	Cu^{+}	XANES (Cu L-edge)	Goh et al. (2006)
Stannite	Cu_2FeSnS_4	4	–	Fe^{2+} (*h*)	Cu^{+}	Mössbauer (^{57}Fe, ^{119}Sn)	Di Benedetto et al. (2005b)
Pyrite	FeS_2	6	–	Fe^{2+} (*l*)	–	Mössbauer (^{57}Fe)	Vaughan and Craig (1978)
Arsenopyrite	FeAsS	6	–	Fe^{2+} (*l*)	–	Mössbauer (^{57}Fe)	Vaughan and Craig (1978)

CN, coordination number.
?, unknown oxidation state.
h, high spin Fe.
l, low spin Fe.

Table 2
Origins and compositions of analysed samples. Concentrations were determined by EPMA (wt.%) and LA-ICP-MS (ppm). Experimental methods are detailed in Belissont et al. (2014).

Mineral	Sample	Ge	Cu	Fe	Origin
Sphalerite	64W, 62E, SAL-UN, A38	15–2580 ppm	41–8170 ppm	1.2–3.1 wt.%	Saint-Salvy, France
		bdl–950 ppm	20–1280 ppm	1.4–1.8 wt.%	Kipushi, D.R. Congo
Germanite	TSU1, U48	6.0–11.1 wt.%	41.2–45.0 wt.%	3.7–14.0 wt.%	Tsumeb, Namibia
		9.2 wt.%	47.5 wt.%	0.2–0.5 wt.%	Kipushi, D.R. Congo
Renierite	K2208, U48	7.8–9.0 wt.%	40.8–42.8 wt.%	13.2–13.5 wt.%	Kipushi, D.R. Congo
Briartite	P717	16.6 wt.%	34.0 wt.%	10.8 wt.%	Kipushi, D.R. Congo
GeS	GeS	69.4 wt.%	–	–	Synthetic
Chalcopyrite	2BARR5	160–4660 ppm	34.6 wt.%	29.1 wt.%	Barrigão, Portugal
Covellite	P717	0.3 wt.%	71.6 wt.%	0.3 wt.%	Kipushi, D.R. Congo
Stannite	Oruro	*nm*	29.6 wt.%	13.0 wt.%	Oruro, Bolivia
Pyrite	2BARR5	*nm*	0.12–0.29 wt.%	46.5 wt.%	Barrigão, Portugal
Arsenopyrite	LAU20	*nm*	*nm*	34.3 wt.%	Lauriéras, France

nm, not measured.
bdl, below detection limit (~1 ppm with LA-ICP-MS).

spectrum per pixel) were converted into element-specific XRF-intensity maps using batch curve fitting of Ge–Kα (convolved with the Zn–Kβ line), Cu–Kα, and Fe–Kα lines, using the PyMCA software (Solé et al., 2007).

XANES spectra were collected at room temperature by scanning the monochromator over the energy ranges of 10970–11500 eV for Ge, 8870–9220 eV for Cu, and 7025–7305 eV for Fe. Constant energy increments of 0.5 eV for Ge and Cu and 0.2 eV for Fe were used around the absorption edges. Above this region, the energy increment was progressively increased, to about 2 eV at the upper end of the scan. The spectrum of an Fe foil, collected in transmission mode, was used to calibrate the energy (edge inflexion at 7112.0 eV). The drift of the incident X-ray beam was less than 3 μm between 7 and 11 keV. Complementary XANES spectra were collected on the ID26 beamline (ESRF, Grenoble, France). X-rays were generated using an insertion device (ID), monochromatised using a cryogenically-cooled fixed-exit double-crystal Si(111) monochromator, and focused into an incident beam of ~1×2 mm^2 with a high X-ray photon flux. Five analyser crystals were used to resolve the Zn–Kβ interference with Ge–Kα, allowing absorption studies to be conducted on very dilute samples. Thorough examination of incident beam (I_0) glitches showed the occurrence of long-term instrumental drift of up to 0.67, 2.10 and 1.18 eV for Ge, Cu and Fe, respectively. The data were therefore corrected using the glitches of I_0 for 'internal calibration'. For cubic lattices, electronic dipole transitions (e.g., $1s \rightarrow 4p$) are isotropic whereas electronic quadrupole transitions (e.g., $1s \rightarrow 3d$) are anisotropic (e.g., Juhin et al., 2008; Muñoz et al., 2013). Orientation effects are therefore unlikely to be significant in the XANES spectra of single cubic crystals (e.g., sphalerite, germanite and pyrite), with the exception of the Fe-*K* pre-edge feature, which is primarily related to $1s \rightarrow 3d$ transitions.

XANES data reduction was carried out using the Athena package based on the IFEFFIT program (Newville, 2001), including data merging and normalisation. Edge centroid positions were determined using the main peak centroid on the first derivative spectra, from which the centroid of the main positive peak was

calculated. This method is particularly useful for comparing highly structured edges such as Cu or Fe *K*-edges. For the sphalerite samples, the uncertainty in the pre-edge position chiefly originates from the merging procedure; the uncertainty was less than 0.20 eV at the Ge *K*-edge (due to relatively noisy spectra) and less than 0.05 eV at the Cu and Fe *K*-edges. Fits of Fe-*K* pre-edge features were performed in batch processing mode using the XasMap package, initially designed for dispersive μ-XANES mapping applications (Muñoz et al., 2006, 2008). Pre-edge background modelling was based on the adjustment of the tail of a Gaussian function, while peaks were fitted using two or three pseudo-Voigt functions. Errors in the centroid energy position are estimated to be $\pm$0.05 eV.

2.3. *Ab initio* calculations

The energy and intensity of the electronic transitions that give rise to the absorption *K*-edge spectrum depend upon the oxidation state of the excited atom, the coordination symmetry, and the ligand type. Like many elements, Ge, Cu and Fe show significant edge-feature shifts toward higher energies with increasing oxidation state, as well as variations in intensity and shape with changes in coordination and differences in both edge feature position and shape with changes in ligand type (Waychunas et al., 1983; Kau et al., 1987; Pugsley et al., 2011, respectively).

Because the availability of Ge *K*-edge XANES data is rather limited in the literature, *ab initio* XANES calculations were used to better understand the variations observed in our experimental data in terms of oxidation state, coordination and ligand type, and to improve the calibration with model compounds. Computations were performed using the FEFF8.2 software (Rehr et al., 1992; Ankudinov et al., 1998) for selected compounds at the Ge *K*-edge. A self-consistent field (SCF card) multiple-scattering procedure was used to model charge transfer between atoms during the photo-electronic process, up to 3.3 Å. Full multiple scattering (FMS card) calculations were performed for the first eight shells of atoms.

The crystal structures of the Ge-bearing sulphides used in the calculations were those of GeS_2 (Zachariasen,

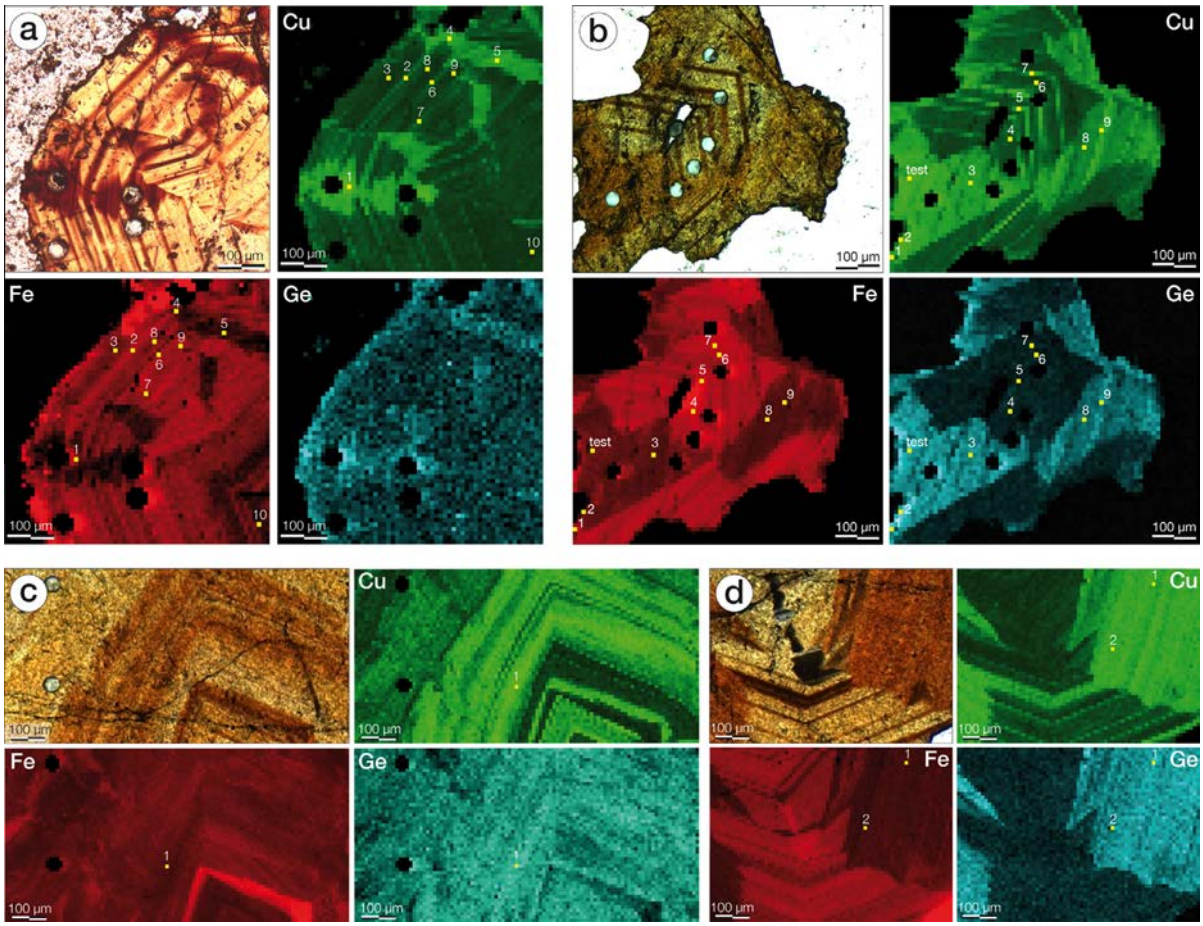

Fig. 2. Microphotograph of the region of interest in transmitted light (top left) and XRF maps of Cu (green), Fe (red) and Ge (blue) in Saint-Salvy sphalerite samples. Holes of 44 µm diameter are LA-ICP-MS craters (see Belissont et al., 2014). Numbered spots correspond to μ-XANES acquisitions. (a) Sample 64W. (b) Sample 62E. (c) Sample SAL-UN (rhythmic bands). (d) Sample SAL-UN (rhythmic bands between two overlapping sector zones). (For interpretation of the references to colour in this figure legend, the reader is referred to the web version of this article.)

1936), renierite (Bernstein et al., 1989), germanite (Tettenhorst and Corbato, 1984) and argyrodite (Eulenberger, 1977). The crystal structure of GeS was approximated by the substitution of Sn by Ge in the natural compound herzenbergite (SnS) available in Schnering and Wiedemeier (1981). Calculations for GeO_2 were performed on the crystal structures of rutile-like polymorphs (argutite) with octahedral Ge^{4+} (Haines et al., 2000; Shiraki et al., 2003).

3. RESULTS

3.1. Element distribution

X-ray fluorescence maps of Ge, Cu and Fe in sphalerite from Saint-Salvy are shown in Fig. 2. In sample 64W (Fig. 2a), Cu is enriched in the sector zoning and to a lesser extent in the adjacent optically-dark rhythmic bands. Germanium is enriched in the sector zoning and depleted in the dark rhythmic bands. Conversely, Fe is enriched in the rhythmic bands (especially in the optically-dark bands) and depleted in the sector zoning. This typical antithetic distribution of Cu, Ge and Fe is also observed in samples 62E (Fig. 2b) and SAL-UN (Fig. 2c and d), and is consistent with the observations of Belissont et al. (2014) from secondary electron microscope (SEM) and multivariate statistical analysis of LA-ICP-MS data.

The Ge-rich sphalerite sample from Kipushi (Fig. 3) displays sector-like zoning that is enriched in Ge (Fig. 3a). In contrast with the sphalerite from Saint-Salvy, neither Cu nor Fe show any distinguishable variations. SEM mapping performed in energy dispersive mode (EDS, Fig. 3b) shows that the Ge instead occurs in Ge–Cu-rich micro- or nanoclusters, substituting for Zn.

3.2. Germanium *K*-edge

3.2.1. Model compounds

Germanium *K*-edge XANES spectra for Ge-bearing model compounds are shown in Fig. 4a and their known crystal chemistries are presented in Table 1. With the exception of GeS, the model compounds all show steep white lines of similar height originating from $1s \rightarrow 4p$ transitions, as well as similar post-edge features corresponding to transitions towards *p*-like partially filled states and multiple scattering resonances. GeS, however, exhibits less-intense post-edge features together with an absorption edge shifted towards lower energies. The edge positions are located at 11108.9 ± 0.2 eV in the Ge^{4+}-bearing model compounds (renierite, germanite, and briartite) and at 11107.2 eV in Ge^{2+}-bearing GeS (Table 3), indicating a shift of 1.7 eV between Ge^{2+} and Ge^{4+} in sulphide compounds. Accordingly, Ge-bearing chalcopyrite and covellite show edge positions at 11109.1 and 11108.9 eV, respectively, suggesting a formal Ge^{4+} oxidation state in these minerals.

In Fig. 5, *ab initio* XANES calculations performed at the Ge *K*-edge for GeS and Ge^{4+}-bearing sulphides perfectly support the edge-shift of about 1.7 eV observed in the experimental data. The edge positions of renierite, germanite and argyrodite are similar to that of GeS_2, indicating that the formal oxidation state Ge^{4+} in these compounds is unequivocal. Rutile-like GeO_2 (*r*-GeO_2, octahedral Ge) spectra are in good agreement with experimental spectra reported in the literature (Andrault et al., 1995; Bertini et al., 2003; Vaccari et al., 2009; Baldini et al., 2010). The edge shift of 5.1 eV between *r*-GeO_2 and GeS is similar to the experimental shift of 5.8 eV reported in Pugsley et al. (2011). For Ge^{4+} compounds, the edge shift of 3.6 eV between *r*-GeO_2 and Ge-bearing sulphides highlights the strong differences in Ge *K*-edge positions in the case of Ge–S and Ge–O bonds, indicating that the use of GeO_2 as a standard for the estimation of Ge oxidation state in sulphides would result in a severe underestimation.

The differences in the bond nature and length between oxide/silicate and sulphide compounds are indeed significant. Although Ge favours covalent bonding with many ligands, Ge–O bonds have about 31% ionic character and are shorter (about 1.75 Å) and stronger than Ge–S bonds, which have only 7% ionic character and are about 2.27 Å long (Bernstein, 1985; Li et al., 2009). This shifts the core electron binding energy in oxides/silicates, and thus likewise the onset of the absorption edge, to higher values compared to sulphides. In addition, in experimental spectra, the edge of *q*-GeO_2, the quartz-like GeO_2 polymorph with tetrahedral Ge, is reported as being about 0.8–1.0 eV below the edge of *r*-GeO_2 (Vaccari et al., 2009; Baldini et al., 2010; Pugsley et al., 2011). This indicates that changes in coordination also affect Ge *K*-edge features. According to our calculations and the literature data, only sulphide standards are therefore suitable for calibrating sphalerite if we are to avoid any misinterpretation.

3.2.2. Sphalerite samples

Germanium *K*-edge XANES spectra in sphalerite are shown in Fig. 6a. Due to interferences between the Ge *K*-α and Zn *K*-β lines, the spectra were recorded only in spots with Ge contents higher than about 700 ppm, thus enabling the signal-to-noise ratio to be significantly reduced. In the sphalerite from Saint-Salvy, such concentrations mostly occur in the sector zoning and Ge contents rarely exceed 500 ppm in the rhythmic bands. Consequently, Ge *K*-edge XANES were recorded in both types of zoning in sample SAL-UN (the richest in Ge), but only in the sector zoning in sample 62E. None of the XANES records for sample 64W were considered acceptable due to the presence of significant noise. To overcome this issue, additional 'bulk' XANES spectra were recorded in samples 64W and SAL-UN on the ID26 beamline. SAL-UN was then used to match energy calibration between the BM23 and ID26 spectra.

The average Ge *K*-edge position of sphalerite from both Saint-Salvy and Kipushi (A38) is 11109.0 ± 0.2 eV. This is close to the average position of Ge^{4+}-bearing model compounds (11108.9 ± 0.2 eV, Table 3), which suggests a dominantly Ge^{4+} oxidation state for the sphalerites from the two localities. In the Ge-rich zoned sphalerite from the Saint-Salvy deposit, the edge positions obtained for different spots within the same type of zoning varied by a maximum of 0.2 eV in any given crystal. These spectra were therefore merged into a 'bulk' spectrum in order to improve

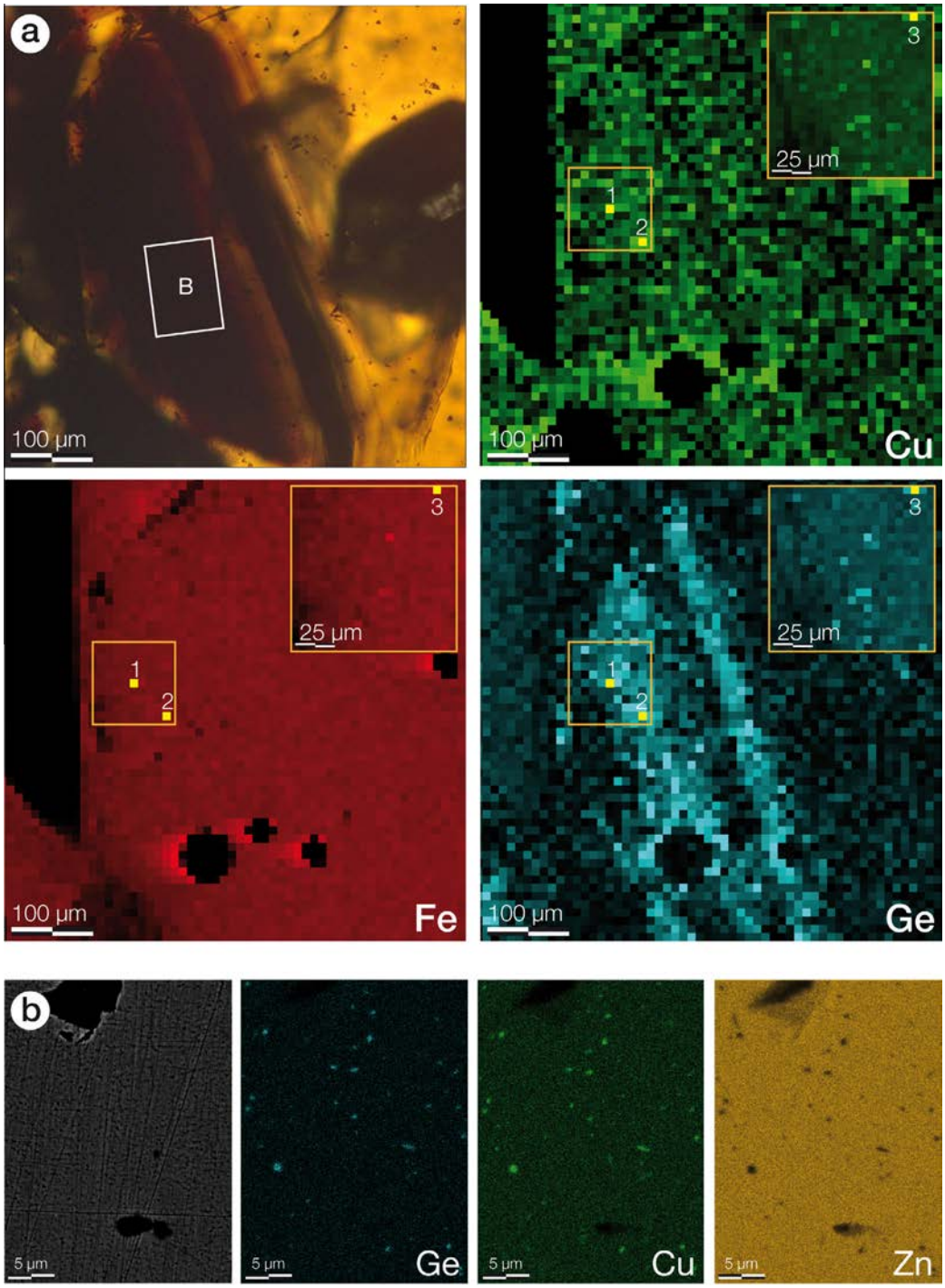

Fig. 3. (a) Microphotograph of the region of interest in transmitted light (top left) and XRF maps of Cu (green), Fe (red)and Ge (blue) in the Kipushi Ge-rich sphalerite sample (A38). Holes of 60 and 32 µm diameter are LA-ICP-MS craters. Numbered spots indicate μ-XANES acquisitions. (b) SEM maps in energy dispersive mode (EDS) of Ge, Cu and Zn showing Ge–Cu nano- or micro-inclusions. Map locations are indicated on the top-left microphotograph shown in (a). (For interpretation of the references to colour in this figure legend, the reader is referred to the web version of this article.)

the counting statistics (as presented in Table 4). The shift in edge position between the sector zoning and the dark rhythmic bands is only 0.03 eV in sample SAL-UN (Table 4). The maximum edge shift between the edge positions of samples 64W and 62E is 0.2 eV. Assuming that the edge energy increases linearly with increasing valence from +2 to +4 by a shift of 1.7 eV (Table 3), the above variations in edge position within and between zoning types (0.2 and

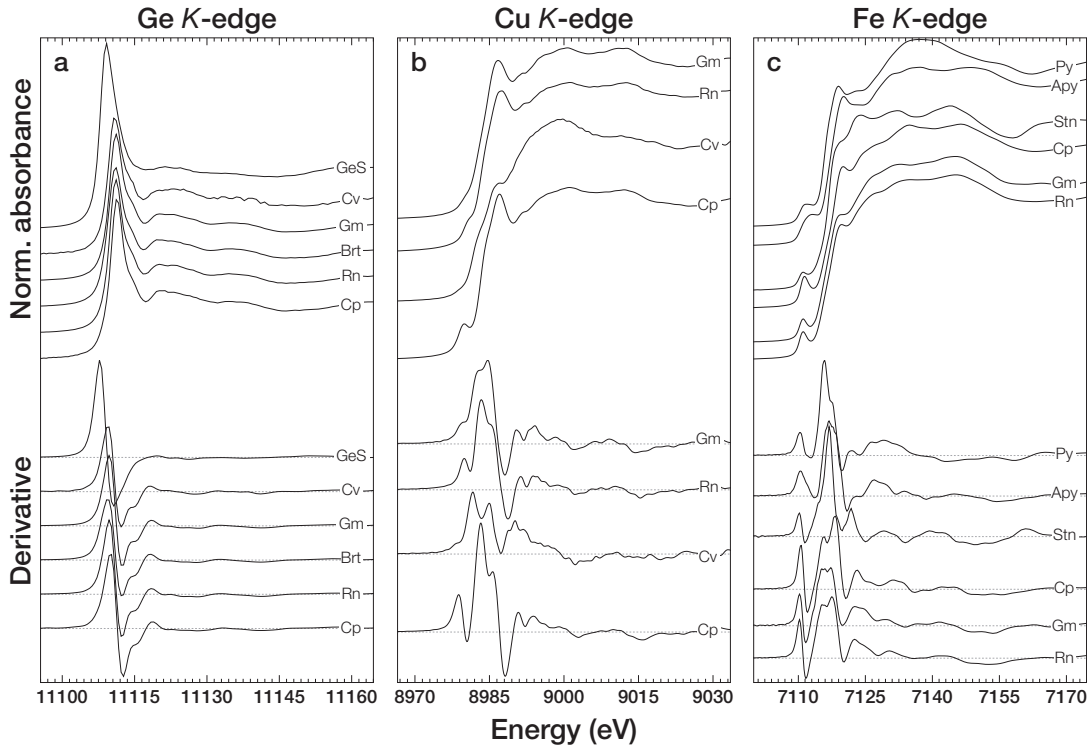

Fig. 4. Normalised XANES spectra and corresponding derivatives at the Ge (a), Cu (b) and Fe (c) *K*-edges for renierite (Rn), germanite (Gm), briartite (Brt), chalcopyrite (Cp), covellite (Cv), stannite (Stn), pyrite (Py) and arsenopyrite (Apy).

Table 3
Ge, Cu and Fe *K*-edge positions (peak centroid of the first derivative) in model compounds.

Sample	Edge position (eV)			
	Ge	Cu	Fe	Pre-edge
Germanite	11108.97	8982.88	7116.47	7111.08
Renierite	11109.05	8983.04	7116.73	7111.09
Briartite	11108.72	–	–	–
GeS	11107.20	–	–	–
Chalcopyrite	11109.09	8983.91	7117.30	7111.40
Covellite	11108.87	8982.45	–	–
Stannite	–	–	7116.38	7110.80
Pyrite	–	–	7117.06	7111.70
Arsenopyrite	–	–	7117.28	7111.87

0.03 eV, respectively), and between samples (0.2 eV) can therefore be considered negligible. There is therefore no evidence for significant redox variation, suggesting a formal Ge^{4+} oxidation state for the sphalerite from Saint-Salvy.

3.3. Copper *K*-edge

3.3.1. Model compounds

Copper *K*-edge XANES spectra in Cu-bearing model compounds are shown in Fig. 4b and their known crystal chemistries are presented in Table 1. Cu-bearing model compounds show an absorption edge at about 8983.1 ± 0.6 eV, as is typical for Cu^{+} (Kau et al., 1986). The edge is structured with two shoulders from about 8980–8989 eV as highlighted on the first derivative spectra. The edge positions of renierite and germanite are at 8983.0 and 8982.9 eV, respectively, similar to the edge position of chalcopyrite (8983.9 eV; Table 3). All compounds show a distinct pre-edge feature below 8980 eV, which decreases in intensity from chalcopyrite, to renierite, germanite and covellite, where it forms only a tiny shoulder below the edge threshold.

The presence of a pre-edge feature below 8980 eV usually corresponds to transitions towards the 3*d* empty state due to the d^9 configuration of Cu^{2+} in the ground state (Kau et al., 1987; Petiau et al., 1988). However, Cu 2*p* XPS and Cu *L*-edge XANES have shown that copper in chalcopyrite and covellite is formally Cu^{+}, with the ground state being a mixture of Cu $3d^{10}4s^{0}$, Cu $3d^{10}4s^{1}\underline{S}$ ($\underline{S}$ = hole in a sulphide ligand) and Cu $3d^{9}4s^{1}$ configurations (Goh et al., 2006, Pearce et al., 2006, and references therein). Therefore, the *d*-like unfilled states allow $1s \rightarrow 3d$ electronic quadrupole transitions to occur, resulting in the observed pre-edge. Because of the greater availability of *d*-like empty states in the nominally d^9 system, the pre-edge feature should be more intense in Cu^{2+} compounds than in Cu^{+}-bearing compounds. Chalcopyrite, renierite and germanite all share sphalerite-type structures with Cu in a tetrahedral site. The very similar XANES features observed in these compounds therefore strongly suggest the presence of Cu^{+} in renierite and germanite.

The choice of relevant compounds is difficult for Cu^{2+} because no evidence has yet been found for the presence of Cu^{2+} in any sulphide minerals (Goh et al., 2006) and also

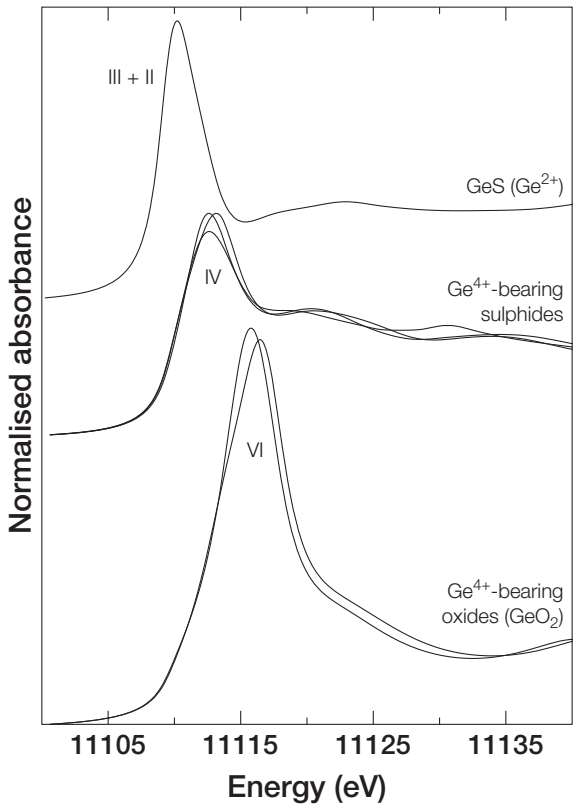

Fig. 5. Ab initio calculations at the Ge *K*-edge of Ge^{2+}- and Ge^{4+}-bearing compounds, with sulphur and oxygen ligands. Ge^{4+}-bearing sulphides include GeS_2, renierite, and argyrodite, all of which have tetragonal Ge. GeO_2 have rutile-like structures with octahedral Ge. Roman numerals refer to coordination number.

because, if present, its site would be distorted (Petiau et al., 1988). Kau et al. (1987) presented XANES spectra for complexes with Cu^+ and Cu^{2+} surrounded by four S ligands in tetrahedral geometry, showing an edge energy difference of 1.6 eV. This edge shift should be a good analogue for what we might expect to find between tetrahedral Cu^+ and Cu^{2+} (if present) in a sulphide lattice. Of note, the presence of a pre-edge feature for the Cu^+ complex, similar to that which we observe for chalcopyrite, has been attributed to the highly covalent nature of the S_4 ligand field (Kau et al., 1987).

3.3.2. Sphalerite samples

Copper *K*-edge XANES spectra for sphalerites from Saint-Salvy and Kipushi are shown in Fig. 6b. The XANES features for sphalerite are similar in shape and position (edge energy of 8983.5 ± 0.2 eV) to those for chalcopyrite, renierite and germanite (edge energy of 8984.9 ± 0.1 eV), albeit that no pre-edge feature is observed in the sphalerite. For the Saint-Salvy samples, the variability in the Cu *K*-edge position is less than 0.3 eV within and between the different types of zoning (Table 4). In sample 62E, the maximum variability in the edge position between sector zones and light rhythmic bands is about 0.27 eV. Again, between samples 64W and SAL-UN, a maximum shift of 0.39 eV is observed. Compared to the energy shift of 1.6 eV from Cu^+ to Cu^{2+} tetrahedrally-complexed with S, the edge variations measured in sphalerite from Saint-Salvy (i.e., a maximum of 0.39 eV) can be neglected. Thus, no significant variation in the Cu oxidation state is observed in sphalerite from Saint-Salvy, suggesting that the copper is monovalent.

3.4. Iron *K*-edge

3.4.1. Model compounds

Iron *K*-edge XANES spectra of model sulphides are shown in Fig. 4c and their known crystal chemistries are given in Table 1. The spectra show a main absorption edge located at about 7117.0 ± 0.2 eV. All spectra show a distinct pre-edge peak at 7111–7112 eV due to $1s \rightarrow 3d$ electronic quadrupole transitions (Waychunas et al., 1983). Fe^{3+} compounds (i.e., renierite, germanite, chalcopyrite) show an edge structure characterised by two features (or shoulders) between 7112 and 7119 eV for all compounds, highlighted by a doublet on the first derivative spectra. Renierite and germanite have similar edge positions (~7116.6 eV) and shapes, as well as similar post-edge features. The edge for chalcopyrite, however, is located 0.7 eV higher (7117.3 eV), and slight differences are observed in the doublet relative intensity and post-edge features. The edge for Fe^{2+} compounds (i.e., stannite, pyrite, arsenopyrite) rises monotonically, showing a single peak on the first derivative spectra. The edge positions of pyrite and arsenopyrite (~7117.2 eV, octahedral low-spin Fe) are located 0.8 eV above that of stannite (7116.4 eV, high-spin Fe), probably due to their different coordination and spin-state configurations. In addition, these two compounds have very distinct post-edge features. In particular, there is an edge shift of only 0.2 eV (stannite → renierite/germanite) or 0.9 eV (stannite → chalcopyrite) from Fe^{2+} and Fe^{3+} in high-spin tetrahedral configuration. However, the pre-edge features vary in the most clearly systematic manner with site geometry, metal-ligand bond type and oxidation state (e.g., Waychunas et al., 1983).

Fe-*K* pre-edge characteristics (centroid position and integrated intensity) have been extensively used to quantify the redox state of Fe in a number of earth materials, mostly oxide and silicate minerals and glasses (e.g., Waychunas et al., 1983; Galoisy et al., 2001; Wilke et al., 2001, 2009; Prietzel et al., 2007; Muñoz et al., 2013). The pre-edge region is primarily related to quadrupolar $1s \rightarrow 3d$ electronic transitions. Non-centrosymmetric sites (e.g., tetrahedral sites) have more intense pre-edge features than centrosymmetric sites (e.g., octahedral sites) due to the addition of dipolar allowed $1s \rightarrow 4p$ electronic transitions, attributed to mixing of Fe $4p$ into the $3d$ orbital (e.g., Dräger et al., 1988; Westre et al., 1997). Normalized pre-edge peaks reveal three different shapes depending on the spin state and the coordination of iron (Fig. 7a). Peak fitting allows integrated intensity and centroid energy values to be derived, as shown in Fig. 7c).

The pre-edge centroids for pyrite and arsenopyrite (octahedral Fe^{2+}) are located at high energy (at 7111.7 eV and 7111.9 eV, respectively) due to the low-spin configuration of iron (e_g-like first empty states). The pre-edge shapes of pyrite and arsenopyrite can be modelled reasonably well

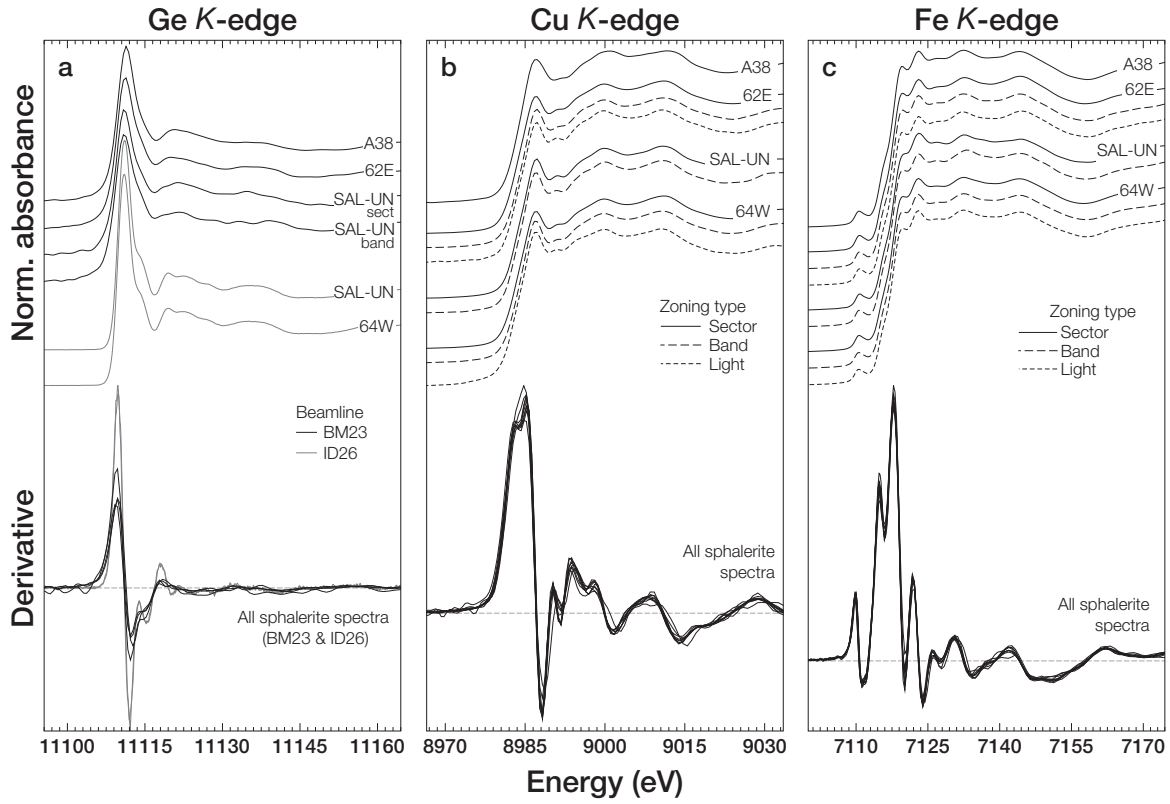

Fig. 6. Normalised and derivative XANES spectra at the Ge (a), Cu (b) and Fe (c) *K*-edges for the studied sphalerite samples and zoning types. Samples 64W, 62E and SAL-UN are from Saint-Salvy (France) and A38 is from Kipushi (D.R. Congo).

Table 4
Ge, Cu and Fe edge positions for the zoning types in each sphalerite sample and their respective contents.

Sample	Zoning	Edge position (eV)				Content★ (ppm)		
		Ge	Cu	Fe	Pre-edge	Ge	Cu	Fe
Saint-Salvy, France								
64W	Sector	–	8983.21	7116.63	7110.81	726	4887	19601
	Dark band	11108.84	8983.34	7116.62	7110.75	98	2328	26552
	Light area	–	8983.19	7116.62	7110.75	95	336	22753
62E	Sector	11109.06	8983.47	7116.68	7110.88	2203	4306	16308
	Dark band	–	8983.68	7116.69	7110.88	249	2858	25302
	Light area	–	8983.74	7116.68	7110.86	242	555	26465
SAL-UN	Sector	11108.93	8983.61	7116.77	7110.92	1544	3647	17649
	Dark band	11108.90	8983.67	7116.63	7110.85	360	1799	19882
Kipushi, D.R. Congo								
A38	Sector	11109.33	8983.51	7116.66	7110.78	883	1270	17360

–, when not determined.
★, LA-ICP-MS data from Belissont et al. (2014).
†, bulk measurement on ID26 beamline (ESRF).

using two peaks of similar intensity (i.e., at ~7111.2 eV and ~7112.7 eV). Pyrite and arsenopyrite have a distorted iron octahedron site (point group S_6), therefore, only electronic quadrupole transitions are permitted. The strong hybridisation of the Fe 3*d* e_g-like states with Fe 4*p* and S 3*pσ** states (covalent bonds) can explain their relatively intense pre-edge features for an octahedral arrangement (e.g., Petiau et al., 1988; Mosselmans et al., 1995) as well as the appearance of a doublet rather than a singlet as is observed in low-spin ferrous complexes (Westre et al., 1997).

The pre-edge peak for stannite (high-spin tetrahedral Fe^{2+}) is less intense, located at a lower energy, around 7110.8 eV, and is primarily defined by two contributions (~7110.6 and ~7112.0 eV). The pre-edge peaks for

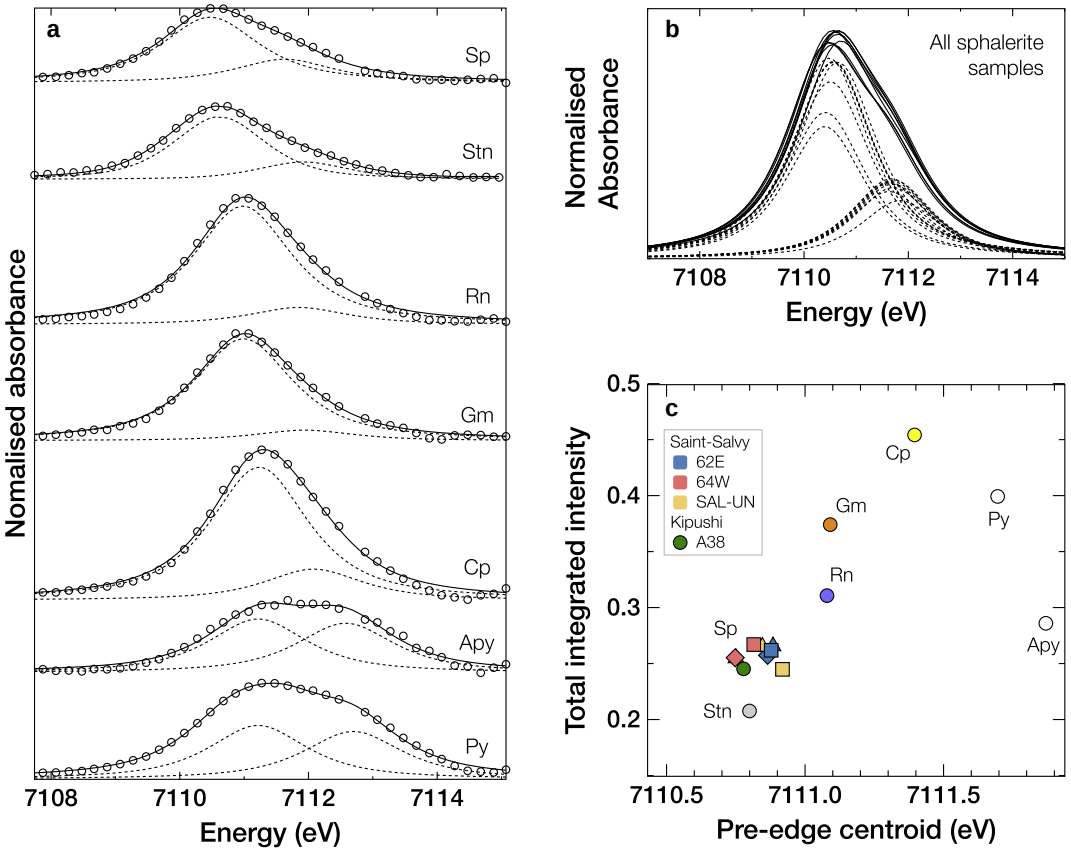

Fig. 7. (a) Normalised Fe-*K* pre-edge spectra and model fits (XasMap) for a sphalerite sample (A38) and for the model sulphide compounds. Open circles represent experimental data, the dotted lines show the contributions of each transition to the model, and solid lines show the resulting fit. (b) Normalised Fe-*K* pre-edge fitted curves for all sphalerite samples (solid lines) and the two transition contributions to the model (dotted lines). The curves are all near-identical in shape. (c) Fe-*K* pre-edge information (total integrated intesity vs. centroid position) for the model compounds and sphalerite samples. Renierite (Rn), germanite (Gm) and chalcopyrite (Cp) have high-spin $^{IV}Fe^{3+}$. Stannite (Stn) has high-spin $^{IV}Fe^{2+}$. Pyrite (Py) and arsenopyrite (Apy) have low-spin $^{VI}Fe^{2+}$. In sphalerite from Saint-Salvy, □ refers to sector zoning, △ is for dark rhythmic bands, and ◇ is for light rhythmic bands.

germanite and renierite are positioned at higher energy, around 7111.1 eV, and the pre-edge peak for chalcopyrite is located at around 7111.4 eV. All three have high-spin tetrahedral Fe^{3+} and show a more intense pre-edge, largely defined by a single peak. The $1s \rightarrow 3d$ features for tetrahedral Fe^{2+}- and Fe^{3+}-bearing sulphides are similar to those observed for iron complexes, oxides, and silicates (Westre et al., 1997; Wilke et al., 2001; Berry et al., 2010; Muñoz et al., 2013). For both high-spin Fe^{2+} and Fe^{3+} in tetrahedral coordination, the pre-edge feature gains intensity through allowed quadrupole and dipole electronic transitions to mixed 3*d*–4*p* orbitals in a non-centrosymmetric environment. The pre-edge centroid energy varies by ~0.6 eV between the divalent and trivalent states. The ~0.3 eV variation in the centroid position between germanite/renierite and chalcopyrite can be attributed to crystal orientation effects on the quadrupole transition.

3.4.2. Sphalerite samples

Iron *K*-edge XANES spectra for sphalerite samples are presented in Fig. 6c. The average *K*-edge position is 7116.7 ± 0.05 eV, close to that of renierite and germanite (7116.60 ± 0.19 eV). The sphalerite from Saint-Salvy does not exhibit any significant variation in the Fe *K*-edge position, neither within or between the two zoning types, nor between samples. A maximum edge variation of 0.13 eV occurs between sector zones and dark bands in sample SAL-UN (Table 4). Moreover, the sphalerite spectra are all very similar throughout the XANES region, which may suggest a unique Fe oxidation state and speciation in this mineral.

Pre-edge centroid positions and integrated intensity are plotted in Fig. 7c. The points corresponding to the Saint-Salvy sphalerite samples are grouped around 7110.8 eV in an area of 0.2 eV in energy (Fig. 7b and c), and there is no direct correlation with the type of zoning. The pre-edge peaks of sphalerite are composed of a single intense peak at around 7110.6 eV and a shoulder at 7111.7 eV, with a total intensity (0.26) that is about half that of chalcopyrite (0.45), consistent with the previous observations of Petiau et al. (1988). The pre-edge positions and structures for sphalerite are similar to those obtained for stannite (though slightly more intense), suggesting that high-spin Fe^{2+} occur in tetrahedral coordination. The 0.2 eV variation in the

pre-edge centroid positions and the higher intensities can be attributed to crystal orientation effects and/or rare occurrences of Fe^{3+} in the tetrahedral site.

4. DISCUSSION

4.1. Formal oxidation states of Ge, Cu and Fe

Our data support the presence of tetrahedral Ge^{4+} in sphalerite, whatever the zoning type and sample, as well as in chalcopyrite and covellite where Ge is present as a trace component. We find no evidence for the presence of Ge^{2+} which would be compatible with a direct substitution $Zn^{2+} \leftrightarrow Ge^{2+}$ in sphalerite. The presence of Ge^{2+} in the Ge-rich sphalerite from Tres Marias (Mexico) was previously inferred due to the lack of correlation between Ge and monovalent ions for charge compensation (Cook et al., 2009), however, a recent XANES study has provided formal evidence for tetrahedral Ge^{4+} (Cook et al., 2015). Indeed, in a covalently bonded crystal, Ge^{2+} is unlikely to occupy tetrahedral sites but instead occurs in trigonal–pyramidal coordination. The latter is similar to tetrahedral coordination, though one of the apices is composed of a lone pair of electrons (Bernstein, 1985). For instance, GeS (orthorhombic) is composed of a double layer structure in which Ge^{2+} occurs in a threefold coordination (ionic bonds of ~3.494 Å) and also shares two covalent bonds (~2.443 Å) inside one of the layers, resulting in a (3+2) coordination (Wiedemeier and Schnering, 1978). The presence of Ge^{2+} in sulfosalts with trigonal–pyramidal Sn^{2+} has previously been suggested for $PbSnS_2$ containing ~700 ppm Ge (Moh, 1976) without discarding coupled substitution of Sn^{2+} by Ge^{4+} with some form of charge compensation, and also for morozeviczite $Pb_3Ge_{1-x}S_4$ (Harańczyk, 1975). Even in the germanate spinel brunogeierite Fe_2GeO_4 (Johan et al., 1983; Welch et al., 2001), Ge is now understood to occur in the tetravalent state (Cempirek and Groat, 2013).

The oxidation state of copper in sulphide minerals has for many years been quite controversial. It is now generally accepted that the Cu in sulphide minerals is nominally Cu^+, though a d^9 character can be observed in chalcopyrite, triggering the presence a Cu-*K* pre-edge that is usually diagnostic of the Cu^{2+} state (Folmer and Jellinek, 1980; Kau et al., 1987; Goh et al., 2006; Buckley et al., 2007). The only exception may be in the tetrahedrite group, where small amounts of Cu^{2+} may occur in divalent metal sites (Pattrick et al., 1993), even though tetrahedral coordination for Cu^{2+} is somewhat unlikely (Pattrick et al., 1997). Cu^+ has been reported in Cu-bearing sphalerite (Cook et al., 2012) at the *K*-edge and no evidence for the presence of Cu^{2+} in the sphalerite lattice has been found at the *L*-edge (Buckley et al., 2007). Our results, in line with these observations, support the presence of tetrahedral Cu^+ in sphalerite, whatever the type of zoning or sample considered.

Fe-*K* pre-edge features suggest a formal Fe^{2+} oxidation state in sphalerite in agreement with the findings of previous Mössbauer spectroscopic studies (e.g., Gerard et al., 1971; Lepetit et al., 2003; Di Benedetto et al., 2005a). Gerard et al. (1971) detected the presence of 'very small amounts' of Fe^{3+} in Fe-rich sphalerite (>6 mol.% Fe). Lepetit et al. (2003) showed that temperature and sulphur fugacity control the Fe^{3+}/Fe^{2+} ratio in sphalerite containing more than 7 mol.% Fe. In turn, the Fe^{3+}/Fe^{2+} ratio, with the oxidation of Fe^{3+} to Fe^{2+}, plays on the lattice parameters in summarising the effects of local shrinkage by the creation of vacancies and the effects of dilatations by incoming elements (e.g., Cu). The Fe content in sphalerite from Saint-Salvy and Kipushi (3–4 mol.%) is well below the critical Fe content (~7 mol.%).

4.2. Incorporation of trace elements into sphalerite

In sphalerite from Saint-Salvy, spot concentrations for Ge and Cu range from the ppm level to 2580 and 4080 ppm, respectively, and there is a well-defined Cu–Ge correlation. Iron contents range from 1.2 to 4.2 wt.% (and correlate with isovalent Cd; Belissont et al., 2014). The incorporation of Fe via the isovalent substitution $Zn^{2+} \leftrightarrow Fe^{2+}$ has already been discussed extensively in a number of studies (e.g., Di Benedetto et al., 2005a; Wright, 2009; Wright and Gale, 2010). The remainder of the discussion is therefore focused on the incorporation of the heterovalent elements, Ge and Cu.

The incorporation of trace elements into sphalerite is governed by crystal–fluid partition coefficients ($D_i = [i]_{crystal}/[i]_{fluid}$) and their bulk concentrations in the ore-forming fluids. Lattice-strain theory predicts that apart from the ionic radius, the partition coefficient of an element may vary by several orders of magnitude, depending primarily on the pressure, temperature, charge, and phase composition (e.g., McIntire, 1963; Bruce et al., 1998; Blundy and and Wood, 1994; Blundy and Wood, 2003). Speciation in the aqueous fluid also exerts a strong influence on the partition coefficient in hydrothermal systems (van Hinsberg et al., 2010). Crystal-scale crystallographic controls on Ge and minor/trace element partitioning associated with rhythmic microscale compositional variations in fluid at the crystal–fluid interface are responsible for the contrast in compositional zoning (Belissont et al., 2014). However, the large difference in bulk sphalerite composition must result either from other parameters that act on the partition coefficients or from large variations in the ore-forming fluid composition.

Metal speciation in aqueous solutions depends on several parameters, including salinity, pH, and the fluid redox condition, which involves fO_2 and fS_2. Ge^{4+} and Cu^+ are the most stable oxidation states in environmental fluids. Being a relatively hard acid in the sense of Pearson (1963), germanium forms the strongest complexes with hard ligands such as hydroxide or fluoride (Wood and Samson, 2006). In contrast, copper, being a transition metal and softer material, predominantly forms complexes with chloride. Pokrovski and Schott (1998) showed that $Ge(OH)^\circ_{4(aq)}$ is the dominant Ge-bearing species in hydrothermal solutions, at concentrations of up to at least 0.05 M over a wide range of pH (0–8) and temperatures (20–350 °C). Brugger et al. (2007) found that linear $CuCl_x^{1-x}$ ($x = 1, 2$) complexes are stable up to supercritical conditions ($P = 600$ bar, $T = 25$–400 °C, salinities up to

17.2 M Cl). The Saint-Salvy ore-forming fluids fall within this range of compositions, with close to neutral pH, high salinity fluids (3.9–4.3 M Cl) and temperatures ranging from 80 to 140 °C (Moisy, 1993; Munoz et al., 1994). Therefore, it seems unlikely that modifications of the metal speciation have occurred during ZnS deposition at Saint-Salvy.

Next we consider the charge effect. For elements of similar ionic radius, Wood and Blundy (2001) showed that charge effects yield $D_i^{2+} > D_j^{3+} \simeq D_k^{+} > D_l^{4+}$, and a strong correlation was found between the partition coefficients of highly charged ions and the bulk composition of the crystal. Large variations in D_{Ge} would therefore be expected if either Ge^{2+} and/or Ge^{4+} can enter the ZnS lattice. However, our μ-XANES data clearly indicate that only Ge^{4+} occurs in the sphalerite from Saint-Salvy, regardless of the zoning type (or Ge content). Likewise, only Cu^{+} and Fe^{2+} are present in the sphalerite from Saint-Salvy, as well as in that from Kipushi.

Thermodynamically, partition coefficients are expected to rely on the entropy of the doped crystal, which for heterovalent elements (e.g., Ge^{4+}, Cu^{+}) depends upon the charge-balancing substitution mechanism (McIntire, 1963; Blundy and and Wood, 1994). Our data strongly support a coupled substitution mechanism such as $3Zn^{2+} \leftrightarrow 2Cu^{+} + Ge^{4+}$ (crystal radii of 0.74, 0.53 and 0.74 Å, respectively). *In situ* LA-ICP-MS data from the Saint-Salvy sphalerite (Belissont et al., 2014) show that the Cu content in any part of the crystal is nearly equal to that of the tri- and tetravalent elements (Ge, Ga, In, Sn, Sb). Increased Cu fluid activity should therefore 'enhance' the incorporation of Ge and related trace elements in precipitating sphalerite. However, in sphalerite from Tres Marias (Mexico), a high Ge content (~1081 ppm in Fe-rich zones) unrelated to monovalent element concentrations has been reported (Cook et al., 2009), even though there is no doubt that the Ge occurs as Ge^{4+} (Cook et al., 2015). This suggests that Ge can also enter the sphalerite lattice through the creation of vacancies such as $2Zn^{2+} \leftrightarrow Ge^{4+} + \square$ (vacancy).

No evidence has been found for the presence of divalent Ge and Cu. Hence, the direct substitution $Zn^{2+} \leftrightarrow (Ge^{2+}, Cu^{2+})$ seems highly unlikely in sphalerite from Saint-Salvy and Kipushi. Indeed, even though divalent copper may form stable chloro-aqua complexes in the highly saline low-T (20–90 °C) hydrothermal fluids and brines generally found in oxidizing near-surface environments (Brugger et al., 2001), the redox potentials of hydrothermal fluids and near-surface environments are generally too high to induce significant formation of divalent Ge species such as Ge^{2+}, $GeOH^{+}$ or $Ge(OH)^{\circ}_2$ (Arnórsson, 1984; Pokrovski and Schott, 1998) and incorporate them into sphalerite.

Finally, pressure-related effects should be insignificant since deposition of the Saint-Salvy deposit occurred in a small upper-crustal region where the pressure remained constant during the time of deposition (Cassard et al., 1994; Munoz et al., 1994). The sphalerite appears to have been unaffected by any variations in pressure, speciation, or charge effects. Therefore, bulk compositional differences due to the variation in D_{Ge} may be more significantly affected by temperature. For Ge, this is discussed further in the next section, using Ge isotopes as well as variations in concentration in the ore-forming fluid.

4.3. Implications for Ge isotopic fractionation

Temperature is a key parameter in controlling both crystal–fluid element partitioning and isotopic fractionation. Belissont et al. (2014) showed a positive correlation between Ge content and the Ge isotopic composition, δ^{74}Ge, in the Saint-Salvy sphalerite, which was interpreted as resulting from kinetic isotope fractionation in an open fault-related depositional system. Theoretical *ab initio* predictions by Li et al. (2009) simulated Ge^{2+} and Ge^{4+} in a sphalerite-like structure, resulting in $[GeS_4]$ tetrahedrons with Ge–S bond lengths of ~2.262 and 2.275 Å, respectively. Our data indicate only the presence of Ge^{4+}, and variations in δ^{74}Ge cannot therefore be related to mixed oxidation states. For Ge^{4+}, the theoretical predictions yield $\Delta_{sp-fluid}$ of −11.4‰ at 25 °C, implying that sphalerite should be preferentially enriched in the lighter isotopes during precipitation. These results entail an isotopic fractionation factor, $\alpha_{sp-fluid}$ of 0.9887, and a temperature parameter, A of −1.0134 (as in many instances, B is approximated to zero), as given by the following relation:

$$\Delta_{sp-fluid} = \delta^{74}Ge_{sp} - \delta^{74}Ge_{fluid} \simeq 10^3 \ln \alpha_{sp-fluid} = A\frac{10^6}{T^2} + B$$

If parameter A is known, backward calculations can allow us to estimate $\Delta_{sp-fluid}$ for different temperatures. Given our current understanding of the Saint-Salvy deposition model, the enclosing Cambrian black schist is the most plausible source of metals (Barbanson and Geldron, 1983; Munoz et al., 1994), including Ge, which were mobilised by fluid circulation and leaching on a regional scale. The metal-rich fluids were channelled into the Noailhac–Saint-Salvy vein network that developed against the Sidobre granite intrusion and the sphalerite deposition then occurred in an open-system (Belissont et al., 2014). The fluid inclusions in this sphalerite are too scarce and too small for analysis, Munoz et al. (1994) therefore used quartz-hosted fluids inclusions of the same paragenesis to constrain the range of temperature for this mineralisation stage (i.e., massive sphalerite, quartz, and/or siderite). These fluid inclusions, trapped under low-P conditions, indicate homogenisation temperatures of 80–140 °C (mean of 110 °C from 30 measurements). These temperatures should be similar to the trapping temperatures since pressure corrections are negligible (minimum pressure <100 bars). Similar surface-derived brines have been described for most of the Pb–Zn–(F–Ba) deposits of the southern Massif Central margins, for example Peyrebrune (Munoz et al., 1997), Les Malines (Charef and Sheppard, 1988) and Trèves (Leach et al., 2006), which belong to a widespread early Jurassic hydrothermal event in western Europe that formed a number of large F–Ba–Pb–Zn mineralisations (e.g., Bruce et al., 1998; Muchez et al., 2005; Boiron et al., 2010; Cathelineau et al., 2012; Munoz et al., 2015). Accordingly, the composition of the fluid (i.e., the $\delta^{74}Ge_{fluid}$ and the Ge content) most likely remained

constant over the period of sphalerite deposition. Thus, $\Delta^{140°C}_{sp–fluid} - \Delta^{80°C}_{sp–fluid}$ gives $\delta^{74}Ge^{140°C}_{sp} - \delta^{74}Ge^{80°C}_{sp}$, the isotopic fractionation range for sphalerite precipitated between 80 and 140 °C, which yields a value of 2.19‰. In comparison with the value of 2.98‰ previously measured for these sphalerites (Belissont et al., 2014), a temperature-related isotopic fractionation could partly explain variations in δ^{74}Ge at Saint-Salvy. Alternatively, a 2.98‰ variation in δ^{74}Ge can be obtained for a slightly extended range of temperature, e.g., 70–150 °C.

Furthermore, because δ^{74}Ge correlates with Ge content, variations in the latter might suggest temperature-related changes in the Ge partition coefficient. The logarithm of the partition coefficient varies linearly with temperature in the form of $\ln D = \ln D_0 - \Delta G/RT$ (Brice, 1975), where D_0 denotes the strain-free partition coefficient, ΔG is the free enthalpy for inserting a cation into the crystal lattice, R is the gas constant and T is the temperature in K. Thus, the positive correlation between δ^{74}Ge and Ge content could imply that the partition coefficient D_{Ge} increases with temperature (i.e., $\Delta G < 0$, exothermic reaction). In comparison, Wright and Gale (2010) showed that the reaction energies for incorporating Fe are exothermic when sphalerite is Zn deficient, which involves high sulphur fugacity.

5. CONCLUSIONS

Experimental Ge, Cu and Fe *K*-edge μ-XANES combined with μ-XRF element maps in zoned Ge-rich sphalerite from the remarkable Saint-Salvy (France) and Kipushi ore deposits (R.D. Congo) indicate the occurrence of Ge^{4+}, Cu^{+}, and Fe^{2+} in tetrahedral sites, with no significant differences neither within or between the zoning types, nor between the Saint-Salvy sphalerite samples. Theoretical *ab initio* calculations show that the nature of the Ge *K*-edge features strongly depend on the Ge oxidation state, the coordination symmetry, and the ligand type. The marked differences between Ge–S and Ge–O bonds imply that only sulphide standards should be used for comparing sphalerite Ge *K*-edge XANES data. Our results strongly suggest that incorporation of Ge in sphalerite occurs via the $3Zn^{2+} \leftrightarrow 2Cu^{+} + Ge^{4+}$ coupled substitution, consistent with Ge–Cu correlations observed in previous studies. There is no evidence to support the presence of divalent Ge. It is now clear that the Ge enrichment in sphalerite and its partitioning among distinct zoning types do not result from variations in Ge oxidation state. Likewise, the large isotopic fractionation measured in sphalerite from Saint-Salvy is rather a result of variations in the temperature of the mineralising fluid than redox modifications. Precise quantification of the Fe^{3+}/Fe_{tot} ratio in sulphide minerals is beyond the scope of this study and could not be achieved here due to the lack of model compounds. However, the collection of XANES data for a range of Fe-bearing minerals in different oxidation states, coordination and spin-states would be of considerable use for performing a solid empirical calibration for the quantification of Fe redox states in sulphide minerals.

ACKNOWLEDGMENTS

The authors thank D. Cassard and C. Lerouge (BRGM) for supplying the Saint-Salvy sample material. We are grateful to P. Muchez (KU Leuven, Belgium) and D. Oliveira (LNEG, Lisbon, Portugal) for the Kipushi and Barrigão samples, respectively, M. Cathelineau (GeoRessources, Nancy) for germanite, and P. Marion (ENSG, Nancy) for stannite. This work has been possible thanks to the ESRF facilities (Project ES64, BM23 beamline, October 2013). P. Glatzel and K. Kvashnina are kindly acknowledged for allowing complementary XANES records to be performed on the ID26 beamline. Two anonymous reviewers and the Associate Editor, E. Ripley, are thanked for their detailed and insightful comments which significantly improved this manuscript. A. Williams is warmly thanked for her careful English editing of the manuscript. This work was supported by the French National Research Agency through the 'Investissements d'avenir' national research program (ANR-10-LABX-21-LABEX RESSOURCES21), the Observatoire Terre Environnement Lorraine (OTELo) program, and the INSU-CESSUR (CNRS) project. This is a CRPG contribution n°2425.

REFERENCES

Andrault D., Peryronneau J., Farges F. and Itié J. P. (1995) High pressure and high temperature XAFS study of germanate: fourfold versus sixfold coordination changes. *Phys. B Condens. Matter* **208**, 327–329.

Ankudinov A. L., Ravel B., Rehr J. J. and Conradson S. D. (1998) Real-space multiple-scattering calculation and interpretation of X-ray-absorption near-edge structure. *Phys. Rev. B* **58**, 7565–7576.

Arnórsson S. (1984) Germanium in Icelandic geothermal systems. *Geochim. Cosmochim. Acta* **48**(12), 2489–2502.

Baldini M., Aquilanti G., Mao H.-K., Yang W., Shen G., Pascarelli S. and Mao W. L. (2010) High-pressure EXAFS study of vitreous GeO2 up to 44 GPa. *Phys. Rev. B* **81**(2), 024201-024201.

Barbanson L. and Geldron A. (1983) Distribution du germanium, de l'argent et du cadmium entre les schistes et les minéralisations stratiformes et filoniennes a blende-sidérite de la region de Saint-Salvy (Tarn). *Chronique de la recherche minière* **470**, 33–42.

Beaudoin G. (2000) Acicular sphalerite enriched in Ag, Sb, and Cu embedded within color-banded sphalerite from the Kokanee Range, British Columbia, Canada. *Canad. Mineral.* **38**(6), 1387–1398.

Belissont R., Boiron M.-C., Luais B. and Cathelineau M. (2014) LA-ICP-MS analyses of minor and trace elements and bulk Ge isotopes in zoned Ge-rich sphalerites from the Noailhac – Saint-Salvy deposit (France): insights into incorporation mechanisms and ore deposition processes. *Geochim. Cosmochim. Acta* **126**, 518–540.

Bente K. and Doering T. (1995) Experimental studies on the solid state diffusion of Cu + In in ZnS and on Disease, DIS (Diffusion Induced Segregations), in sphalerite and their geological applications. *Mineral. Petrol.* **53**(4), 285–305.

Bernardini G. P., Borgheresi M., Cipriani C., Di Benedetto F. and Romanelli M. (2004) Mn distribution in sphalerite: an EPR study. *Phys. Chem. Min.* **31**(2), 80–84.

Bernstein L. R. (1985) Germanium geochemistry and mineralogy. *Geochim. Cosmochim. Acta* **49**(11), 2409–2422.

Bernstein L. R. (1986) Renierite, $Cu_{10}ZnGe_2Fe_4S_{16}$–$Cu_{11}GeAsFe_4S_{16}$: a coupled solid solution series. *Am. Mineral.* **71**, 210–221.

Bernstein L. R., Reichel D. G. and Merlino S. (1989) Renierite crystal structure refined from Rietveld analysis of powder neutron-diffraction data. *Am. Mineral.* **74**, 1177–1181.

Bernstein L. R. and Waychunas G. A. (1987) Germanium crystal chemistry in hematite and goethite from the Apex Mine, Utah, and some new data on germanium in aqueous solution and in stottite. *Geochim. Cosmochim. Acta* **51**(3), 623–630.

Berry A. J., Yaxley G. M., Woodland A. B. and Foran G. J. (2010) A XANES calibration for determining the oxidation state of iron in mantle garnet. *Chem. Geol.* **278**(1–2), 31–37.

Bertini L., Ghigna P., Scavini M. and Cargnoni F. (2003) Germanium K edge in GeO_2 polymorphs. Correlation between local coordination and electronic structure of germanium. *Phys. Chem. Chem. Phys.* **5**(7), 1451–1456.

Blundy J. and Wood B. (1994) Prediction of crystal melt partition coefficients from elastic moduli. *Nature* **372**, 452–454.

Blundy J. and Wood B. (2003) Partitioning of trace elements between crystals and melts. *Earth Planet. Sci. Lett.* **210**(3–4), 383–397.

Boiron M. C., Cathelineau M. and Richard A. (2010) Fluid flows and metal deposition near basement/cover unconformity: lessons and analogies from Pb–Zn–F–Ba systems for the understanding of Proterozoic U deposits. *Geofluids* **10**, 270–292.

Brice J. C. (1975) Some thermodynamic aspects of the growth of strained crystals. *J. Cryst. Growth* **28**, 249–253.

Bruce S., Banks D., Munoz M., Courjault-Rade P., Tollon F., Boyce A. and Fallick A. (1998) The genesis of mineralising brines in the South West Massif Central, France. *Mineral. Mag.* **62A**, 238–239.

Brugger J., Etschmann B., Liu W., Testemale D., Hazemann J. L., Emerich H., van Beek W. and Proux O. (2007) An XAS study of the structure and thermodynamics of Cu(I) chloride complexes in brines up to high temperature (400 °C, 600 bar). *Geochim. Cosmochim. Acta* **71**(20), 4920–4941.

Brugger J., McPhail D. C., Black J. and Spiccia L. (2001) Complexation of metal ions in brines: application of electronic spectroscopy in the study of the Cu(II)–LiCl–H_2O system between 25 and 90 °C. *Geochim. Cosmochim. Acta* **65**(16), 2691–2708.

Buckley A. N., Skinner W. M., Harmer S. L., Pring A., Lamb R. N., Fan L.-J. and Yang Y.-W. (2007) Examination of the proposition that Cu (II) can be required for charge neutrality in a sulfide lattice-Cu in tetrahedrites and sphalerite. *Canad. J. Chem.* **85**(10), 767–781.

Cassard D., Chabod J.-C., Marcoux E., Bourgine B., Castaing C., Gros Y., Kosakevitch A., Moisy M. and Viallefond L. (1994) Mise en place et origine des minéralisations du gisement filonien à Zn, Ge, Ag, (Pb, Cd) de Noailhac – Saint-Salvy (Tarn, France). *Chronique de la recherche minière* **514**, 3–37.

Cathelineau M., Boiron M.-C., Fourcade S., Ruffet G., Clauer N., Belcourt O., Coulibaly Y., Banks D. a. and Guillocheau F. (2012) A major Late Jurassic fluid event at the basin/basement unconformity in western France: 40Ar/39Ar and K-Ar dating, fluid chemistry, and related geodynamic context. *Chem. Geol.* **322–323**, 99–120.

Cempirek J. and Groat L. A. (2013) Note on the formula of brunogeierite and the first bond-valence parameters for Ge^{2+}. *J. Geosci.* **58**, 71–74.

Charef A. and Sheppard S. (1988) The Malines Cambrian carbonate-shale-hosted Pb–Zn deposit, France: thermometric and isotopic (H, O) evidence for pulsating hydrothermal mineralization. *Mineralium Deposita* **23**, 86–95.

Cook N., Etschmann B., Ciobanu C., Geraki K., Howard D., Williams T., Rae N., Pring A., Chen G., Johannessen B. and Brugger J. (2015) Distribution and substitution mechanism of Ge in a Ge-(Fe)-bearing sphalerite. *Minerals* **5**(2), 117–132.

Cook N. J., Ciobanu C. L., Brugger J., Etschmann B., Howard D. L., de Jonge M. D., Ryan C. and Paterson D. (2012) Determination of the oxidation state of Cu in substituted Cu-In-Fe-bearing sphalerite via μ-XANES spectroscopy. *Am. Mineral.* **97**(2–3), 476–479.

Cook N. J., Ciobanu C. L., Pring A., Skinner W., Shimizu M., Danyushevsky L., Saini-Eidukat B. and Melcher F. (2009) Trace and minor elements in sphalerite: A LA-ICPMS study. *Geochim. Cosmochim. Acta* **73**(16), 4761–4791.

Di Benedetto F. (2005) Compositional zoning in sphalerite crystals. *Am. Mineral.* **90**(8–9), 1384–1392.

Di Benedetto F., Andreozzi G. B., Bernardini G. P., Borgheresi M., Caneschi A., Cipriani C., Gatteschi D. and Romanelli M. (2005a) Short-range order of Fe^{2+} in sphalerite by 57Fe Mössbauer spectroscopy and magnetic susceptibility. *Phys. Chem. Min.* **32**(5–6), 339–348.

Di Benedetto F., Bernardini G. P., Borrini D., Lottermoser W., Tippelt G. and Amthauer G. (2005b) ^{57}Fe- and ^{119}Sn-Mössbauer study on stannite (Cu_2FeSnS_4)-kesterite (Cu_2ZnSnS_4) solid solution. *Phys. Chem. Min.* **31**(10), 683–690.

Dickinson T., Taylor G. J. and Keil K. (1989) Germanium abundances in lunar basalts-Evidence of mantle metasomatism? Proceedings of the 19th Lunar and Planetary Science Conference, pp. 189–198.

Dräger G., Frahm R., Materlik G. and Brümmer O. (1988) On the multipole character of the X-ray transitions in the pre-edge structure of Fe K absorption spectra. An experimental study. *Phys. Status Solidi (b)* **146**, 287–294.

Escoube R., Rouxel O. J., Edwards K., Glazer B. and Donard O. F. X. (2015) Coupled Ge/Si and Ge isotope ratios as geochemical tracers of seafloor hydrothermal systems: case studies at LoihiSeamount and East Pacific Rise 9°50N. *Geochim. Cosmochim. Acta* **167**(C), 93–112.

Eulenberger G. (1977) Die Kristallstruktur der Tieftemperatur-modifikation von Ag_8GeS_6. *Monatshefte für Chemie* **108**(4), 901–913.

Folmer J. and Jellinek F. (1980) The valence of copper in sulphides and selenides: an X-ray photoelectron spectroscopy study. *J. Less Common Met.* **76**(1), 153–162.

Frenzel M., Ketris M. P. and Gutzmer J. (2014) On the geological availability of germanium. *Miner. Deposita* **49**, 471–486.

Frenzel Max, Hirsch Tamino and Gutzmer Jens (2016) Gallium, germanium, indium, and other trace and minor elements in sphalerite as a function of deposit type — A meta-analysis. *Ore Geol. Rev.* http://dx.doi.org/10.1016/j.oregeorev.2015.12.017, in press.

Galoisy L., Calas G. and Arrio M. A. (2001) High-resolution XANES spectra of iron in minerals and glasses: structural information from the pre-edge region. *Chem. Geol.* **174**(1), 307–319.

Gerard A., Imbert P., Prange H., Varret F. and Wintenberger M. (1971) Fe^{2+} impurities, isolated and in pairs, in ZnS and CdS studied by the Mössbauer effect. *J. Phys. Chem. Solids* **32**, 2091–2100.

Goh S. W., Buckley A. N., Lamb R. N., Rosenberg R. A. and Moran D. (2006) The oxidation states of copper and iron in mineral sulfides, and the oxides formed on initial exposure of chalcopyrite and bornite to air. *Geochim. Cosmochim. Acta* **70**(9), 2210–2228.

Haines J., Leger J. M., Chateau C. and Pereira A. S. (2000) Structural evolution of rutile-type and $CaCl_2$-type germanium dioxide at high pressure. *Phys. Chem. Min.* **27**(8), 575–582.

Harańczyk C. (1975) Morozewiczite and polkowicite – typochemical minerals of mesozoic mineralization in copper deposits of the fore-Sudetic monocline. *Rudy i Metale* **20**, 288–293.

Höll R., Kling M. and Schroll E. (2007) Metallogenesis of germanium—a review. *Ore Geol. Rev.* **30**(3–4), 145–180.

Hu Z. and Gao S. (2008) Upper crustal abundances of trace elements: a revision and update. *Chem. Geol.* **253**(3–4), 205–221.

Imbert P., Varret F. and Wintenberger M. (1973) Etude par effet Mössbauer de la briartite (Cu_2FeGeS_4). *J. Phys. Chem. Solids* **34**(10), 1675–1682.

Johan Z. (1988) Indium and germanium in the structure of sphalerite : an example of coupled substitution with copper. *Mineral. Petrol.* **39**, 211–229.

Johan Z., Oudin E. and Picot P. (1983) Analogues germanifères et gallifères des silicates et oxydes dans les gisements de zinc des Pyrénées centrales, France; argutite et carboirite, deux nouvelles espèces minérales. *Tschermaks Mineralogische und Petrographische Mitteilungen* **31**, 97–119.

Juhin A., Brouder C., Arrio M.-A., Cabaret D., Sainctavit P., Balan E., Bordage A., Calas G., Eeckhout S. G. and Glatzel P. (2008) X-ray Linear Dichroism in cubic compounds: the case of Cr^{3+} in $MgAl_2O_4$. *Phys. Rev. B* **78**(195103), 1–18.

Kau L.-S., Penner-Hahn J. E., Solomon E. I. and Hodgson K. O. (1986) Quantitative Cu X-ray absorption edge studies: oxidation state and site structure determination. *J. Phys. Colloques* **47**(C8), pp. C8-1177–C8-1180.

Kau L.-S., Spira-Solomon D. J., Penner-Hahn J. E., Hodgson K. O. and Solomon E. I. (1987) X-ray absorption edge determination of the oxidation state and coordination number of copper. Application to the type 3 site in Rhus vernicifera laccase and its reaction with oxygen. *J. Am. Chem. Soc.* **109**(21), 6433–6442.

Kurtz A. C., Derry L. A. and Chadwick O. A. (2002) Germanium–silicon fractionation in the weathering environment. *Geochim. Cosmochim. Acta* **66**(9), 1525–1537.

Leach D., Macquar J. C., Lagneau V., Leventhal J., Emsbo P. and Premo W. (2006) Precipitation of lead–zinc ores in the Mississippi Valley-type deposit at Trèves, Cévennes region of southern France. *Geofluids* **6**, 24–44.

Lepetit P., Bente K., Doering T. and Luckhaus S. (2003) Crystal chemistry of Fe-containing sphalerites. *Phys. Chem. Min.* **30**(4), 185–191.

Li X., Zhao H., Tang M. and Liu Y. (2009) Theoretical prediction for several important equilibrium Ge isotope fractionation factors and geological implications. *Earth Planet. Sci. Lett.* **287** (1–2), 1–11.

Luais B. (2007) Isotopic fractionation of germanium in iron meteorites: significance for nebular condensation, core formation and impact processes. *Earth Planet. Sci. Lett.* **262**(1–2), 21–36.

Luais B. (2012) Germanium chemistry and MC-ICPMS isotopic measurements of Fe–Ni, Zn alloys and silicate matrices: insights into deep Earth processes. *Chem. Geol.* **334**, 295–311.

Manning P. G. (1967) Absorption spectra of Fe(III) in octahedral sites in sphalerite. *Canad. Mineral.* **9**, 57–64.

McIntire W. L. (1963) Trace element partition coefficients—a review of theory and applications to geology. *Geochim. Cosmochim. Acta* **27**, 1209–1264.

Moh G. H. (1976) Experimental and descriptive ore mineralogy. *Neues Jahrbuch für Mineralogie Abhandlungen* **128**, 115–188.

Moisy M. (1993) *Evolution de la perméabilité et de la circulation des fluides hydrothermaux dans une zone de cisaillement fragile.* PhD thesis. Université Joseph-Fourier-Grenoble I, 214 p.

Mosselmans J., Pattrick R., Van Der Laan G., Charnock J. M., Vaughan D. J., Henderson C. and Garner C. D. (1995) X-ray absorption near-edge spectra of transition metal disulfides FeS_2 (pyrite and marcasite), CoS_2, NiS_2 and CuS_2, and their isomorphs FeAsS and CoAsS. *Phys. Chem. Min.* **22**(5), 311–317.

Muchez P., Heijlen W., Banks D., Blundell D., Boni M. and Grandia F. (2005) Extensional tectonics and the timing and formation of basin-hosted deposits in Europe. *Ore Geol. Rev.* **27** (1–4), 241–267.

Munoz M., Baron S., Boucher A., Béziat D. and Salvi S. (2015) Mesozoic vein-type Pb–Zn mineralization in the Pyrenees: lead isotopic and fluid inclusion evidence from the Les Argentières and Lacore deposits. *Comptes Rendus Geosci.*, 1–11 (in press).

Munoz M., Boyce A., Courjault-Rade P., Fallick A. and Tollon F. (1997) Le filon (Zn, F) de Peyrebrune (SW Massif central, France): caractérisation géochimique des fluides au cours du Mésozoïque à la bordure orientale du bassin d'Aquitaine. *Comptes Rendus de l'Académie des Sciences de Paris* **324**(II a), 899–906.

Munoz M., Boyce A. J., Courjault-Rade P., Fallick A. E. and Tollon F. (1994) Multi-stage fluid incursion in the Palaeozoic basement-hosted Saint-Salvy ore deposit (NW Montagne Noire, southern F. *Appl. Geochem.* **9**, 609–626.

Muñoz M., De Andrade V., Vidal O., Lewin E., Pascarelli S. and Susini J. (2006) Redox and speciation micromapping using dispersive X-ray absorption spectroscopy: Application to iron in chlorite mineral of a metamorphic rock thin section. *Geochem. Geophys. Geosyst.* **7**(11), 1–10.

Muñoz M., Pascarelli S., Aquilanti G., Narygina O., Kurnosov A. and Dubrovinsky L. (2008) Hyperspectral μ-XANES mapping in the diamond-anvil cell: analytical procedure applied to the decomposition of (Mg, Fe)-ringwoodite at the upper/lower mantle boundary. *High Pressure Res.* **28**(4), 665–673.

Muñoz M., Vidal O., Marcaillou C., Pascarelli S., Mathon O. and Farges F. (2013) Iron oxidation state in phyllosilicate single crystals using Fe-K pre-edge and XANES spectroscopy: effects of the linear polarization of the synchrotron X-ray beam. *Am. Mineral.* **98**(7), 1187–1197.

Newville M. (2001) IFEFFIT: interactive XAFS analysis and FEFF fitting. *J. Synchrotron Radiat.* **8**(2), 322–324.

Pattrick R. A. D., Dorling M. and Polya D. A. (1993) TEM study of indium-and copper-bearing growth-banded sphalerite. *Canad. Mineral.* **31**, 105–117.

Pattrick R. A. D., Mosselmans J., Charnock J. M., England K., Helz G. R., Garner C. D. and Vaughan D. J. (1997) The structure of amorphous copper sulfide precipitates: an X-ray absorption study. *Geochim. Cosmochim. Acta* **61**(10), 2023–2036.

Pattrick R. A. D., Van Der Laan G., Vaughan D. J. and Henderson C. (1993) Oxidation state and electronic configuration determination of copper in tetrahedrite group minerals by L-edge X-ray absorption spectroscopy. *Phys. Chem. Min.* **20**(6), 395–401.

Pearce C. I., Pattrick R. A. D., Vaughan D. J., Henderson C. and Van Der Laan G. (2006) Copper oxidation state in chalcopyrite: mixed Cu d^9 and d^{10} characteristics. *Geochim. Cosmochim. Acta* **70**(18), 4635–4642.

Pearson R. G. (1963) Hard and soft acids and bases. *J. Am. Chem. Soc.* **85**(22), 3533–3539.

Petiau J., Sainctavit P. and Calas G. (1988) K X-ray absorption spectra and electronic structure of chalcopyrite $CuFeS_2$. *Mater. Sci. Eng. B* **1**(3), 237–249.

Pokrovski G. S. and Schott J. (1998) Thermodynamic properties of aqueous Ge(IV) hydroxide complexes from 25 to 350 °C: implications for the behavior of germanium and the Ge/Si ratio in hydrothermal fluids. *Geochim. Cosmochim. Acta* **62**(9), 1631–1642.

Polyakov V. B. and Mineev S. D. (2000) The use of Mössbauer spectroscopy in stable isotope geochemistry. *Geochim. Cosmochim. Acta* **64**(5), 849–865.

Prietzel J., Thieme J., Eusterhues K. and Eichert D. (2007) Iron speciation in soils and soil aggregates by synchrotron-based X-ray microspectroscopy (XANES, μ-XANES). *Eur. J. Soil Sci.* **58**(5), 1027–1041.

Pugsley A. J., Bull C. L., Sella A., Sankar G. and McMillan P. F. (2011) XAS/EXAFS studies of Ge nanoparticles produced by reaction between Mg_2Ge and $GeCl_4$. *J. Solid State Chem.* **184** (9), 2345–2352.

Rehr J. J., Albers R. C. and Zabinsky S. I. (1992) High-order multiple-scattering calculations of X-ray-absorption fine structure. *Phys. Rev. Lett.* **69**, 3397–3400.

Rouxel O., Galy A. and Elderfield H. (2006) Germanium isotopic variations in igneous rocks and marine sediments. *Geochim. Cosmochim. Acta* **70**(13), 3387–3400.

Schauble E. A. (2004) Applying stable isotope fractionation theory to new systems. *Rev. Mineral. Geochem.* **55**(1), 65–111.

Schnering H. G. v. and Wiedemeier H. (1981) The high temperature structure of β-SnS and β-SnSe and the B16-to-B33 type λ-transition path. *Zeitschr. Kristallogr.* **156**, 143–150.

Shiraki K., Tsuchiya T. and Ono S. (2003) Structural refinements of high-pressure phases in germanium dioxide. *Acta Crystallogr. Sect. B* **59**(6), 701–708.

Solé V. A., Papillon E., Cotte M., Walter P. and Susini J. (2007) A multiplatform code for the analysis of energy-dispersive X-ray fluorescence spectra. *Spectrochim. Acta B At. Spectrosc.* **62**(1), 63–68.

Stoiber R. E. (1940) Minor elements in sphalerite. *Econ. Geol.* **35**, 501–519.

Tettenhorst R. T. and Corbato C. E. (1984) Crystal structure of germanite, $Cu_{26}Ge_4Fe_4S_{32}$ determined by powder X-ray diffraction. *Am. Mineral.* **69**(9–10), 943–947.

Vaccari M., Aquilanti G., Pascarelli S. and Mathon O. (2009) A new EXAFS investigation of local structural changes in amorphous and crystalline GeO(2) at high pressure. *J. Phys. Condens. Matter* **21**(14), 145403.

van Hinsberg V. J., Migdisov A. A. and Williams-Jones A. E. (2010) Reading the mineral record of fluid composition from element partitioning. *Geology* **38**(9), 847–850.

Vaughan D. J. and Craig J. R. (1978) *Mineral Chemistry of Metal Sulfides. Cambridge Earth Science Series*. Cambridge University Press edition, Cambridge.

Waychunas G. A., Apted M. J. and Brown, Jr, G. E. (1983) X-ray K-edge absorption spectra of Fe minerals and model compounds: near-edge structure. *Phys. Chem. Min.* **10**(1), 1–9.

Welch M. D., Cooper M. A. and Hawthorne F. C. (2001) The crystal structure of brunogeierite, Fe_2GeO_4 spinel. *Mineral. Mag.* **65**(3), 441–444.

Westre T. E., Kennepohl P. and DeWitt J. G. (1997) A multiplet analysis of Fe K-edge $1s \rightarrow 3d$ pre-edge features of iron complexes. *J. Am. Chem. Soc.* **119**, 6297–6314.

Wiedemeier H. and Schnering H. G. (1978) Refinement of the structures of GeS, GeSe, SnS and SnSe. *Z. Kristallogr.* **148**, 295–303.

Wilke M., Farges F., Petit P. E., Brown G. E. J. and Martin F. (2001) Oxidation state and coordination of Fe in minerals: an Fe K-XANES spectroscopic study. *Am. Mineral.* **86**(1998), 714–730.

Wilke M., Hahn O., Woodland A. B. and Rickers K. (2009) The oxidation state of iron determined by Fe K-edge XANES—application to iron gall ink in historical manuscripts. *J. Anal. At. Spectrometry* **24**(10), 1364–1372.

Wood B. J. and Blundy J. D. (2001) The effect of cation charge on crystal–melt partitioning of trace elements. *Earth Planet. Sci. Lett.* **188**(1), 59–71.

Wood S. A. and Samson I. M. (2006) The aqueous geochemistry of gallium, germanium, indium and scandium. *Ore Geol. Rev.* **28** (1), 57–102.

Wright K. (2009) The incorporation of cadmium, manganese and ferrous iron in sphalerite: insights from computer simulations. *Canad. Mineral.* **47**(3), 615–623.

Wright K. and Gale J. D. (2010) A first principles study of the distribution of iron in sphalerite. *Geochim. Cosmochim. Acta* **74** (12), 3514–3520.

Zachariasen W. H. (1936) The crystal structure of germanium disulphide. *J. Chem. Phys.* **4**(9), 618.

Associate editor: Edward M. Ripley